Microporomechanical Modeling of Shale

by

J. Alberto Ortega

B.S., Texas A&M University (2002)
S.M., Massachusetts Institute of Technology (2006)

Submitted to the Department of Civil and Environmental Engineering
in partial fulfillment of the requirements for the degree of

Doctor of Philosophy

at the

MASSACHUSETTS INSTITUTE OF TECHNOLOGY

February 2010

Signature of Author .....
Department of Civil and Environmental Engineering
December 30, 2009

Certified by .....
Franz-Josef Ulm
Professor of Civil and Environmental Engineering
Thesis Supervisor

Accepted by .....
Daniele Veneziano
Chairman, Departmental Committee for Graduate Students

Microporomechanical Modeling of Shale

by

J. Alberto Ortega

Submitted to the Department of Civil and Environmental Engineering
on December 30, 2009, in partial fulfillment of the
requirements for the degree of
Doctor of Philosophy in the field of Structures and Materials

Abstract

Shale, a common type of sedimentary rock of significance to petroleum and reservoir engineering, has recently emerged as a crucial component in the design of sustainable carbon and nuclear waste storage solutions and as a prolific natural gas source. Despite its importance, the highly heterogeneous and anisotropic nature of shale has challenged the theoretical modeling and prediction of its mechanical properties. This thesis presents a comprehensive microporomechanics framework for developing predictive models for shale poroelasticity and strength. Modeling is accomplished through a multi-scale approach, in which the experimental evidence gathered from novel nanoindentation techniques and conventional macroscopic tests informs the development of a suit of micromechanics tools for linking composition and microstructure to material performance.

Based on a closed loop approach of calibration and validation of elastic and strength properties at different length scales, it was possible to deconstruct shale to the scale of an elementary material unit with mechanical behaviors governed by invariant properties, and to upscale these behaviors from the nanoscale to the macroscale of engineering applications. The elementary building block for elasticity is an anisotropic solid characterizing the in situ stiffness of highly consolidated clay. This intrinsic behavior represents the composite response of clay platelets, interlayer galleries, and interparticle contacts, yielding an invariant stiffness with respect to clay mineralogy. The anisotropic nanogranular nature of the porous clay in shale as inferred from nanoindentation is confirmed through micromechanics modeling. The intrinsic anisotropy of the clay fabric is suggested as the dominant factor driving the multi-scale anisotropic poroelasticity of unfractured shale compared to the contributions of geometrical sources related to shapes and orientations of particles. For strength properties, the micromechanics approach revealed that the frictional behavior of the elementary unit of compacted clay is scale independent, whereas a scale effect modifies its cohesive behavior.

Having established a fundamental material unit and the adequate micromechanics representation for the microstructure, the macroscopic diversity of shale predominantly depends on two volumetric properties derived from mineralogy and porosity: the clay packing density and the silt inclusion volume fraction. The proposed two-parameter microporoelastic and strength models represent appealing alternatives for use in geomechanics and geophysics applications.

Thesis Supervisor: Franz-Josef Ulm
Title: Professor of Civil and Environmental Engineering

Contents

List of Figures

Acknowledgments

My doctoral studies at MIT were possible thanks to the support of many people. First, I want to thank my research supervisor, Prof. Franz-Josef Ulm. I am sincerely grateful to him for his unconditional support, for challenging me everyday to advance the field of engineering mechanics, and for bringing the best of me as a researcher and as a person. I cherish every conversation of the past four years. It has been truly an honor working with you. My deepest gratitude also goes to Prof. Younane Abousleiman from the University of Oklahoma, who is the director of the GeoGenome Industry Consortium (G2IC) which provided the financial support for the work presented in this dissertation. My participation in the GeoGenome project has been a remarkable and enriching experience. Thank you for your trust and leadership.

I am thankful to Prof. Brian Evans and Prof. Ruben Juanes, who served in my thesis committee. I sincerely appreciate your support and encouragement. I highly regard your advice and suggestions, which constantly inspired me to improve my research efforts. I am grateful for the support of the G2IC. In particular, I want to thank Dr. Greg Perez from Halliburton, who has contributed with his industrial perspective and insightful comments to help me refine my modeling work.

During my years at MIT, I have been blessed to work and collaborate with the finest of researchers: Dr. Christopher Bobko, Dr. Matthieu Vandamme, Konrad Krakowiak, Sophie Cariou, Benjamin Gathier, and Romain Bard. I am grateful to all of you for contributing to my work, for developing together exciting research, and most importantly, for your friendship. I want to thank my officemates: James Vanzo, Zenzile Brooks, Rouzbeh Shah, and Oguz Gunes. Everyday at MIT was special thanks to you. I also want to thank the G2IC team at the University of Oklahoma: Minh Tran, Son Hoang, and Dr. Vinh Nguyen, for the fruitful

collaborations. It has been a pleasure working with you. Thanks to all the wonderful people at the Department of Civil and Environmental Engineering, for their support and kindness: Pat Dixon, Patty Glidden, Donna Hudson, Kris Kipp, Jeanette Marchocki, Cynthia Steward, Andre Dixon, Denise Brehm, Debbie Levey, Marygrace Aboudou, and Stephen Rudolph.

Finally, I would like to thank some people whom I love dearly. To Samar and Guadalupe, who always believed in me. To Dr. Adrian KC Lee and Dr. Eduardo Torres-Jara, for their invaluable friendship. To my family in Boston: Jon, Jeri and Nancy, for their encouragement and love. And to my family and my beloved Yvonne. You are the light of my life.

Part I

General Presentation

Chapter 1

Introduction

1.1 Industrial Context and Research Motivation

Shale, a sedimentary rock composed mainly of highly consolidated clay particles and some portion of silt-size minerals, constitutes one of the Earth's most common rock formations. In many hydrocarbon reservoirs, shale serves as a geological seal that prevents the migration of oil and gas from source rocks due to its low permeability characteristics (Figure 1-1). Besides working as sealing formation, some shale layers rich in organic content can be source rocks for hydrocarbon and natural gas.

The ubiquitous presence of shale in oil fields underscores its importance to many aspects of petroleum and reservoir engineering, ranging from seismic exploration to well drilling and production. An adequate understanding of shale's seismic and poroelastic behaviors are pivotal to seismic data interpretation, reservoir modeling, design of hydraulic fracturing schemes, and predictions of flow paths in oil recovery applications. The mechanical characterization of elastic and strength properties is also crucial for drill bit performance and the prediction of wellbore stability and failure. It is estimated that wellbore instability problems translate into significant economic losses of approximately US$ 8 billion per year worldwide [209]. In addition to petroleum engineering applications, the mechanics of shale may also be important for the development of sustainable nuclear waste storage solutions.

Despite the mentioned significance of shale to many geomechanics problems, a comprehensive knowledge of its poroelastic and strength behaviors is limited compared to the developments

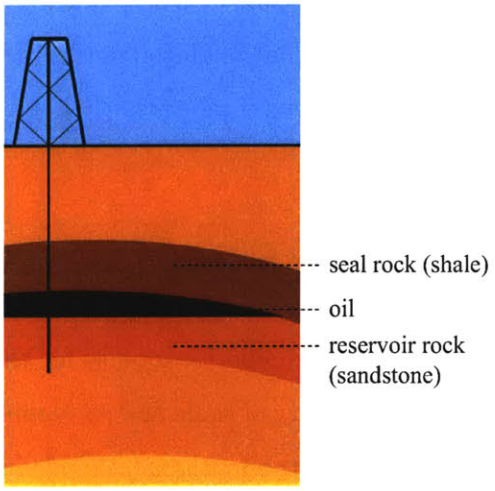

Figure 1-1: Schematic of shale as a geological seal for oil reservoirs.

for other reservoir rocks. The challenge of linking material composition and microstructure to mechanical performance has been accomplished with some success for sandstones and limestones through the implementation of classical approaches such as fitted empirical relations between velocity measurements and porosity, clay content, and other statistically significant parameters [88, 99, 112]. Some more refined methods have taken this approach a step further by linking porosity and clay content to seismic velocity through the application of effective medium theory [49, 221, 299]. However, modeling attempts have had a limited success when it comes to shale mainly due to the fact that shales - in contrast to sandstones, limestones, and synthetic clay-silt mixtures - are both highly heterogeneous and anisotropic from the micro- to the macroscale of engineering applications.

Important research efforts have been pursued in the past two decades to improve the understanding and modeling of shale in view of its growing importance to the petroleum industry for enhanced oil recovery applications and as major resource of natural gas [3]. Recently, the MIT-OU GeoGenome Industry Consortium (G2IC) has conducted a pioneering experimental and theoretical multi-scale investigation aiming at the development of the next generation of poroelastic and strength modeling of shale. The mechanical testing of shale using advanced instrumented indentation techniques, probing length scales never reached before in geomechanics investigations, and conventional macroscopic experiments form the foundation for the devel-

opment of robust predictive models for shale. The work presented in this thesis develops a multi-scale micromechanics framework that enables translating the learned mechanical behaviors at different length scales into effective predictive tools for the poromechanics description of shale.

1.2 Problem Statement and Approach

This thesis aims at the development of predictive models for the poroelasticity and strength of shale materials. The macroscopic diversity of shale and its complex composition and microstructure call for a reductionist approach to the mechanical modeling task. Hence, the challenge to be addressed in this thesis is:

Is it possible to deconstruct the diverse macroscopic behavior of shale rocks to a scale where the mechanical behaviors are governed by material invariant properties, and to successfully upscale those behaviors from microscopic scales to the macroscopic scales of engineering applications?

Such endeavor is accomplished through a multi-scale modeling approach, in which the experimental evidence at the various length scales informs the development of a suit of micro-poromechanics theoretical tools as means to fulfill the material science paradigm for shale; that is, to link of material composition and microstructure to material performance. Using independent and comprehensive data sets from shale materials of diverse origins and compositions, the micromechanics models are calibrated and validated as useful predictive tools of shale poromechanics.

1.3 Research Objectives

A comprehensive theoretical approach is presented to address the scientific challenge. Five primary research objectives guide the proposed approach:

- **Objective 1** *Establish a comprehensive database of mechanical properties of shale at different length scales of observation.* The proposed multi-scale modeling of shale requires a collection of experimental data aiming at the comprehensive characterization of mechanical and compositional properties of shale materials from diverse origins. In addition

to conventional testing approaches at macroscales, recently available data from direct mechanical testing of shale at nanometer length scales becomes a crucial element for new modeling approaches by elucidating the grain-scale mechanics of shale.

- **Objective 2** *Develop a multi-scale micromechanics framework for modeling shale poroelasticity.* The multi-scale behavior of shale poroelasticity is modeled through the implementation of microporomechanics theory. A comprehensive suit of homogenization techniques and tools is developed to model its poroelastic and anisotropic properties at different length scales.

- **Objective 3** *Conduct hypothesis testing of various micromechanics descriptions of shale's multi-scale anisotropic elasticity using independent experimental data sets.* The microporoelasticity modeling framework for shale is used for the implementation of several configurations of microstructural features and material properties. Through a series of calibration and validation exercises using independent sets of elasticity data, the different micromechanics descriptions of shale are tested against the multi-scale responses of shale measured by different experimental techniques. The aim of the hypothesis testing approach is to establish a set of material invariant properties and effective definitions for the microstructure of shale that collectively allow for the successful prediction of the macroscopic diversity of shale's anisotropic elasticity.

- **Objective 4** *Assess the features and predictive capabilities of the adopted microporoelastic model for shale.* Based on accomplishing our third objective, a thorough assessment of the modeling features and capabilities of the adopted micromechanics model for shale is necessary. The relevance of the concept of an elementary building block for shale associated with the proposed multi-scale approach is examined along with the micromechanics description of the clay fabric, which successfully captures the macroscopic diversity of shale. The assessment of model capabilities is also crucial for defining its domain of application for predictions of properties in laboratory and field conditions. The model predictions of poroelastic parameters, elastic anisotropy, and model extensions are investigated in detail for potential uses in field applications.

- **Objective 5** *Develop a multi-scale strength model for shale.* Using a similar multi-scale

approach, a strength homogenization framework for geomaterials is presented. Based on yield design and non-linear micromechanics, the multi-scale strength modeling approach is implemented for shale in an exploratory work.

1.4 Industrial and Scientific Benefits

Accomplishing the proposed research objectives would translate into various industrial and scientific benefits:

- Enhanced understanding of the multi-scale structure of shale, and the effects of grain-scale mechanics on the overall macroscopic response.
- Design of a baseline model for shale anisotropy that enables physics-based predictions at engineering scales based on sensible input parameters easily obtained from logging tools or standard laboratory measurements.
- Development of a suit of micromechanics tools for poroelasticity and strength upscaling of heterogeneous microstructures.

1.5 Outline of Thesis

This report is divided into four parts. Part I contains this introductory material and the presentation of the research topic.

Part II - Experimental Mechanics of Shale - is divided into two chapters that address the first research objective. Chapter 2 introduces relevant aspects of the nature and composition of shale rocks and delineates a multi-scale structure thought-model for shale that provides a framework for introducing experimental information and guiding the theoretical investigation. Chapter 3 reviews the experimental information gathered in this thesis for modeling shale. A comprehensive database of mechanical properties for numerous shale specimens investigated by the G2IC and others obtained from open literature sources is compiled in this chapter, including experimental data at fundamental scales of minerals, recently developed nanomechanics results from instrumented indentation techniques, and conventional macroscopic seismic and strength testing.

Part III - Microporoelasticity of Shale - is devoted to the development of a micromechanics model aiming at the prediction of shale's anisotropic, multi-scale poroelasticity. This part consists of three chapters. Chapter 4 fulfills the second research objective of establishing a general microporomechanics foundation for modeling heterogeneous, multi-scale materials. A particular focus of these micromechanics developments is the treatment of different sources of anisotropy related to shale, which include structural factors such as particle shapes and orientation distributions, as well as intrinsic anisotropic sources of material phases. Chapter 5 presents a series of calibration and validation exercises involving micromechanics modeling and the experimental data introduced in Chapter 3, hence implementing the third research objective. The evaluation of different model configurations of shale's microstructure and intrinsic properties at multiple scales using original developments of the micromechanics of granular anisotropic media developed in Chapter 4 leads to determining a baseline modeling approach for shale materials from different origins and compositions. Chapter 6 examines the predictive capabilities of the micromechanics model for shale adopted based on the findings of the previous chapters. This chapter satisfies the fourth research objective by establishing the physical bases of the developed multi-scale model that underlie its predictive capabilities. Chapter 7 presents a model extension to kerogen-rich shale and a first assessment of the micromechanics model as a predictive engineering tool for field applications.

Part IV contains two chapters dealing with the development of a strength upscaling model for shale, which accomplishes the fifth research objective. Chapter 8 develops the theoretical formulation of a two-scale strength model using yield design theory and non-linear homogenization approaches. The strength modeling framework is examined in detail, and extended for the application to dual-porosity geomaterials. Chapter 9 covers the first implementation of the multi-scale strength model for the prediction of strength properties of shale.

Finally, Part V of this thesis summarizes the findings of this study and its scientific and industrial contributions, and providing suggestions for future research directions.

Part II

Multi-Scale Mechanical Properties of Shale

Chapter 2

Multi-Scale Structure and Thought-Model of Shale

Shale is a complex porous material with heterogeneities (porosities and particulate phases) that manifest themselves at scales much below the macroscale of engineering applications. The adequate knowledge of composition, microstructure, and mechanical properties at different scales of observation is pivotal to any successful modeling endeavor.

The first part of this report is devoted to the compilation of experimental data for a diversity of shale materials that will assist our multi-scale modeling investigation. Chapter 2 offers a brief review of shale as a sedimentary rock, its compositional characteristics, and microstructural features. This information sets the stage for introducing a multi-scale structure thought-model for shale, which defines the material length scales of relevance to our mechanics modeling endeavor. The multi-scale structure model guides the theoretical investigation. Chapter 3 assists the objective of this part of the thesis by presenting a comprehensive database of material properties for various shale materials of diverse origins and compositions. The database offers the necessary experimental data for our multi-scale investigation of shale by including data at fundamental scales of minerals, recently developed nanomechanics results from instrumented indentation techniques, and conventional macroscopic seismic and strength testing.

2.1 Shale and Sedimentary Rocks

Sedimentary rocks constitute a large portion of the Earth's surface. In addition to their ubiquitous presence, their characteristics such as textures, compositions, structures, and organic content are of importance for the investigation and understanding of past Earth environments, landscapes, life forms, and their evolution with time. Sedimentary rocks may also contain minerals and fossil fuels, consolidating their importance with respect to economic reasons.

The origins of sedimentary rocks are related to the deposition of sediments by water, wind, and ice over extensive periods of time. Their formation is the product of a complex series of geological processes involving physical, chemical, and biological activities explained by the following:

- At first, physico/chemical processes disintegrate source rocks, leading to the concentration of resistant particulates (e.g. silicate minerals, rock fragments), in addition to the creation of secondary products (e.g. clay minerals, iron oxides) and the release of soluble elements (e.g. calcium, potassium, sodium).

- The resulting particulates and soluble constituents are removed from land by erosion, and subsequently transported by various agents (water, wind, ice) to depositional basins. The transported sediments eventually reach a basin and are deposited.

- At the depositional basin, sediments are buried by younger ones, and diagenesis[1] occurs at increasing temperatures and pressures. At this stage, dissolution of some constituents and the generation of new minerals occur. Finally, the consolidation and lithification of these products result in the creation of a sedimentary rock [29].

Depending on the particular sequence of sedimentary processes, three main types of constituents are generated: terrigenous siliciclastic particles, chemical/biological elements, and carbonaceous constituents. Their relative proportions determine the fundamental types of sedimentary rocks, as displayed in Table 2.1. Interestingly, from the many types of sedimentary

[1] Diagenesis corresponds to a series of physical, chemical, or biological processes affecting sediments after their deposition and before their final lithification. It encompases processes such as compaction, cementation, leaching, hydration, and recrystalization. Diagenesis occurs at relatively low pressures and temperatures. Porosity typically decreases during diagenesis [241].

rocks shown in Table 2.1 in terms of compositions and grain sizes (from a petrology perspective), three particular rock types constitute the dominant forms of sedimentary rocks encountered in the rock record from a volumetric perspective: shale, sandstone, and limestone. In what follows, the most salient aspects of shale petrology are presented.

2.2 Shale Petrology

Fine-grained siliciclastic rocks composed mainly by particles smaller than hundreds of micrometers are known by several names such as lutites, siltstones, mudrocks, mudstones, claystones, and shales. From a historical perspective, the term *shale* has been used for two particular cases: 1) as a restrictive definition of laminated clayey rocks, and 2) as a general group name for all fine-grained siliciclastic rocks [260]. Other geologists instead differentiate the mudrock and shale groups: the former encompasses fine-grained sedimentary rocks, while the latter is reserved for laminated or fissile fine-grained rock. Today, the terms shale, mudstone, and mudrock continue to be employed as group names for fine-grained siliciclastic rocks [29]. In this work, we investigate shale materials from a geomechanics perspective, in which shale materials are considered as a sedimentary rock that exhibits high amounts of clay content and whose small scale layering associated with the bedding direction and a slow sedimentation process dictates specific elasticity and strength behaviors.

While not an exhaustive description, the following presentations describe some of the most salient physical characteristics of shale materials including grain sizes, particle shapes and orientations, mineralogy, porosity, and permeability. These characteristics are critical to the understanding of the relations between material composition, microstructure and the rock's mechanical behaviors[2].

2.2.1 Grain Size

Shale is mainly composed of small-sized grains, which prevent the application of established methods to characterize the material. As expected, the grain size of sedimentary rocks is highly

[2]The presentation of the petrology of shale is organized according to Boggs Jr. [29].

Siliciclastic Rocks	
Composition	< 50% terrigenous siliciclastic grains < 15% carbonaceous residue
Particle size	(1) > 2 mm (2) 1/16 - 2 mm (3) < 1/16 mm
Principal constituents	(1) Rock fragments [Conglomerates, breccias] (2) Silicate minerals, rock fragments [Sandstones] (3) Silicate minerals [Shales, mudrocks]
Chemical-biochemical Rocks	
Composition	> 50% chemical-biochemical constituents, < 15% carbonaceous residues
Particle size	Variable
Principal constituents	Carbonate minerals, grains, skeletal fragments [Carbonate rocks (limestones, dolomites)] Evaporite minerals (sulfates, chlorides) [Evaporites (rock salt, gypsum, anhydrite)] Chalcedony, opal, siliceous skeletal remains [Siliceous rocks (cherts)] Ferruginous minerals [Ironstones, iron formations] Phosphate minerals [Phosphorites]
Carbonaceous Rocks	
Composition	> 15% carbonaceous residues
Particle size	Variable
Principal constituents	Siliciclastic/chemical-biochemical constituents: carbonaceous residues [Sapropelites (oil shales), impure coals] Carbonaceous residues [Humic coals, cannel coals, solid hydrocarbons (bitumens)]

Table 2.1: Classification of sedimentary rocks [29]. The main rock types for each category of sedimentary rock are presented in brackets.

variable. For some mudrocks and shales, an approximated average grain size distribution[3] consists of 45 percent silt, 40 percent clay, and 15 sand [212].

2.2.2 Particle Shape

Although sediments undergo long processes until becoming rock masses, the shape of fine silts and clay-size particles found in shale are only slightly modified by erosion and transport. In contrast to sand-size particles, clays and fine silts tend to keep the original shapes of the detrital[4] sources or those of the mineral sources generated during diagenesis. In general, their shapes are angular, especially for clay minerals. Scanning electron microscopy (SEM) studies reveal that most clay minerals exhibit flaky structures. Due to the high concentration of clay minerals in shale, these rocks may display microfabrics with preferred orientations and bedding planes.

2.2.3 Orientation of Clay Minerals and Shale Microfabric

The fabric or microstructure of shale is intimately related to the orientations of clay particles, which are the results of complex processes during rock formation. During stages of suspension settling, particles associate in different modes such as a flocculation and aggregation. Several factors control the dynamics of clay particle settling in suspensions such as pH levels, presence of electrolytes, mineralogy content, and particle size [272]. At the stages of fresh sedimentation, clays are not yet subjected to significant compaction, forming sub-microscopic regions in which particles are structured in parallel arrays or *domains* [12]. These groups of clay crystals are oriented randomly in the overall clay matrix, and reach up to 700 Å in length depending on the clay type.

Finally, in consolidated shales, clay domains are tightly packed due to compaction. Some clay sediments develop *fissility*, the ability of some rocks to split into thin slabs along narrowly spaced planes parallel to the directions of natural bedding. Important factors such as geochemistry are pivotal for the development of fissility in shale [189]. In this perspective, the presence of dispersing agents in water such as organic substances dictates whether clay precipitates as

[3] In sieve analysis, clay is considered finer than 4 μm, silt is between 4 and 63 μm, and sand is between 63 μm and 2 mm.

[4] Related to rock particles derived from the mechanical breakdown of pre-existing rocks by weathering and erosion.

dispersed particles or as flocculated structures. The major microstructural changes occurring during deposition and lithification of clay sediments are displayed in Figure 2-1.

2.2.4 Mineralogy Composition

A list of minerals typically found in shale materials is listed in Tables 2.2 and 2.3. Generally, shale is composed mostly of clay minerals, fine-grained mica, quartz and feldspars. The particular mineralogy composition of shale is dependent on various factors such as tectonic settings, depositional environments, formation age, and diagenetic processes. In particular, diagenesis provokes important changes in the mineralogy make-up of shale. Smectite is transformed into illite or chlorite at burial temperatures of approximately 70°C to 150°C. Kaolinite is transformed into illite at similar temperatures. Hence, quantities of illite and chlorite tend to increase with deeper burial depths and longer time periods [29].

Regarding the main group of minerals in shale, clays belong to the mineral family of *phyllosilicates*, whose unit cells ordinarily have a residual negative charge that is balanced by the absorption of cations from solution. Common layer silicates are composed by the combination of two basic structural units: the *silicon tetrahedron*, and the *aluminum* or *magnesium octahedron*. The stacking arrangement of sheets of these units and the way in which two successive layers are held together determine the different clay mineral groups [187]. The basic structures of clay mineral groups are shown schematically in Figure 2-2.

Three clay minerals are particularly common in shale: kaolinite, smectite and illite [187]. Kaolinite is a 1:1 clay mineral type as it is composed of alternating silica and octahedral sheets. The bonding between successive layers, dominated by van der Waals forces and hydrogen bonds, is relatively strong, inhibiting any interlayer swelling due to the presence of water. Kaolinite can occur as either well or poorly crystallized particles with lateral and thickness dimensions ranging between 0.1 - 4 μm and 0.05 - 2 μm, respectively, for well-crystallized kaolinite. Smectite is a 2:1 clay mineral type, consisting of an octahedral sheet situated between two silica sheets. The bonding between layers provided by van der Waals forces and cations balancing charge deficiencies are relatively weak, allowing layer separation by cleavage or water/liquid adsorption. In smectite-rich shale, for instance, a large proportion of water content is to some degree electrostatically bound to clay particle surfaces [246]. A common smectite-type mineral,

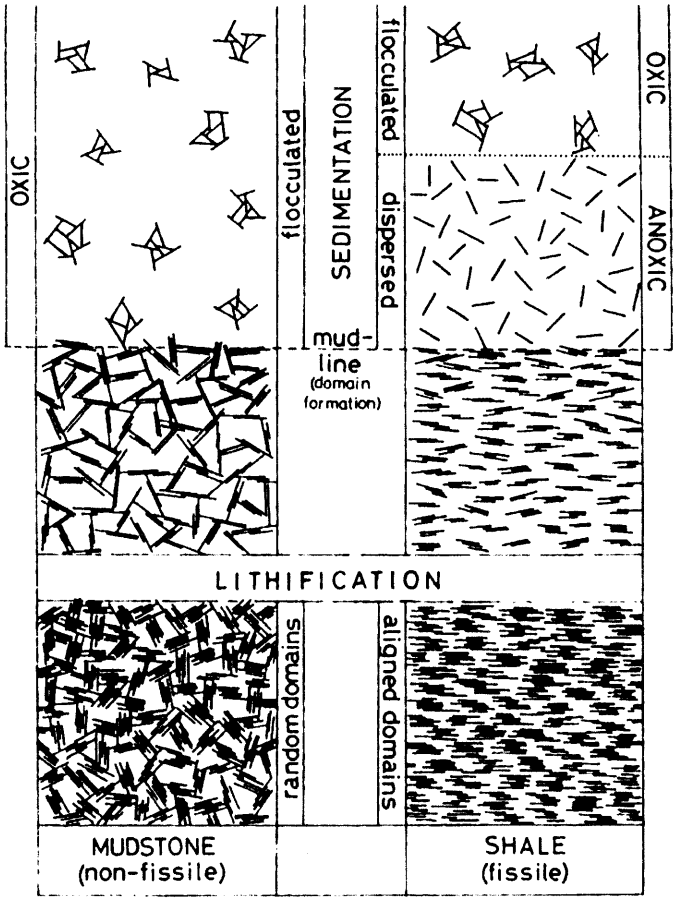

Figure 2-1: Schematic representation of the major microstructural changes in clay sediments during deposition and lithification. In anoxic environments, the abundant presence of organic substances prevents the formation or causes the dispersion of flocs. Domains formed in fresh deposits of sediments are randomly oriented in oxic sediments and highly aligned in anoxic sediments. During lithification, oxic sediments are further compacted, yet preserving the random orientation of clay domains. In contrast, lithification enhances the alignment of clay domains in anoxic sediments, leading to fissility. Adapted from [189], and reprinted by permission of Geological Society Publishing House, UK.

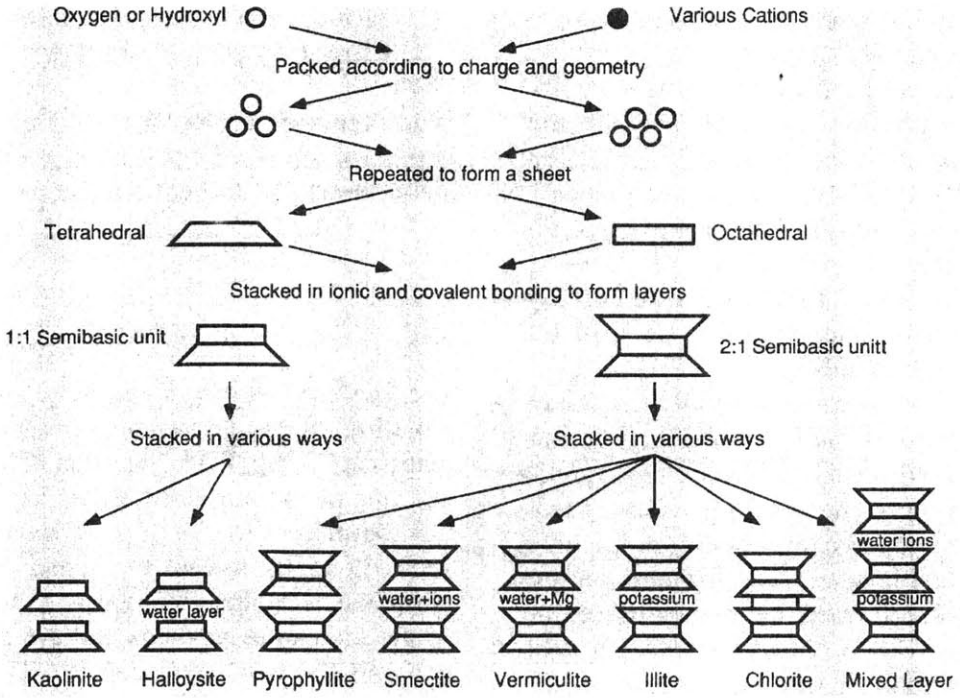

Figure 2-2: Synthesis pattern for clay minerals. Adapted from [187].

montmorillonite, occurs as film-like, equi-dimensional structures with particle thickness in the nanometer range, while the characteristic long dimension can reach 1 - 2 μm. Illite is another 2:1 mineral type, whose atomic structure is similar to that of muscovite mica. Muscovite follows the three-layer silica-gibbsite-silica unit structure, with the particularity that some silicon positions are filled by aluminium creating a charge deficiency that is balanced by potassium between layers. Illite differs from mica in a few important aspects such as containing lesser amounts of potassium, exhibiting some randomness in the stacking of layers, and its smaller particle size. Illite occurs as flaky particles, with characteristic long dimensions in the sub- and micrometer ranges, while the thickness is of nanometer dimensions [156, 187].

Among the non-clay minerals present in shale, quartz is the most abundant. Quartz in shale is typically of silt-grade although coarser grains do occur. Compared to the more rounded quartz in sand, quartz silt tends to be angular and derived from grain collisions in aqueous media and from glacial grinding. Only a small portion of quartz in shale is diagenetic rather than detrital [263].

2.2.5 Organic Matter

The most abundant organic matter in shale is sapropel, which consists of phytoplankton, zooplankton, pollen, and fragments of higher plants. During burial and diagenesis, chemical/biological processes lead to the dissolution of some part of the organic matter and to the transformation of the rest into an insoluble substance called kerogen. Kerogen is the solid, high-molecular weight component of sedimentary organic matter, which is typically identified by optical or chemical methods. In petroleum chemistry, different types of kerogen (I through IV) are defined depending on the composition of the organic matter, most of which generate oil and gas upon burial and diagenesis [184].

2.2.6 Porosity

In general, porosity describes the part of the material that is not occupied by mineral grains. Porosity is defined as the ratio of the volume of pore space in the sedimentary rock over the total volume, and it is typically measured by fluid intrusion and density difference methods. In contrast to this total or physical porosity, petroleum scientists and hydrologists are concerned

Framework Silicates	
Quartz	Constitutes 20-30% of an average shale, and is most likely of detrital origin. Other varieties of silica include opal CT, chalcedony, and amorphous silica.
Feldspar	Commonly less abundant than quartz. Plagioclase is more abundant than alkali feldspars.
Zeolites	Commonly present as alterations of volcanic glass. Clinoptilolite and phillipsite are common zeolites in modern marine sediments.
Clay Minerals	
Kaolinite (7 Å)	Forms in soils developed under abundant rainfall, adequate drainage, and acid waters. Typically concentrated near shore in marine basins.
Smectite-Illite-Muscovite (10 Å and greater)	Members of this structurally complex group form in different ways. Smectite, a hydrated expandable clay, forms from volcanic glass (bentonites); it transforms to illite during burial. Illite, the most abundant clay mineral, derives from pre-existing shales, and it converts to muscovite during diagenesis. Muscovite also occurs as detrital particles in unaltered shale. A iron-rich variety of illite-smectite is glauconite.
Chlorite, Corrensite, and Vermiculite	Chlorite forms by burial diagenesis, especially in Mg-rich pore waters. It is commonly the second most abundant clay in Paleozoic and older shales. Vermeculite may convert to corrensite and finally to chlorite during diagenesis.
Sepiolite and Attapulgite	Magnesium-rich clays that form under special conditions, such as saline lakes.

Table 2.2: Principal constituents of shale and mudstones [219].

Oxides / Hydroxides	
Iron oxides and hydroxides	Present in shale mostly as coatings on clay minerals. In reducing environments, they convert into pyrite and siderite. Hematite is another common iron oxide in shales.
Gibbsite	It represents the product of acid leaching. May be associated with kaolinite in marine shale.
Carbonates	
Calcite	More common in marine than non-marine shales. As with quartz and feldspar, little is known about its distribution and form in shale.
Dolomite	Common in shale as a cementing agent.
Siderite and Ankerite	Occurs in shales commonly as concretions.
Sulfur Minerals	
Sulfates	Gypsum, anhydrite, and barite occur in shale as concretions and may indicate hypersalinity during or after deposition.
Sulfides	Shale typically exhibits iron sulfides such as pyrite and marcasite.
Other Constituents	
Apatite	A phosphatic mineral that forms nodules in slowly deposited marine muds.
Glass	Found in modern muds associated with volcanism. It converts into zeolites and smectites during burial.
Organic Materials	
Organic particles	Mostly either palynomorphs or small coaly fragments.
Kerogen	Amorphous organic material of complex chemical characterization that is present in almost all shales except red ones. It informs about gas and oil potential of a basin and its thermal history.

Table 2.3: Principal constituents of shale and mudstones [219] (*continued*).

in the movement and transport of fluids. Hence, an effective or transport porosity is of interest:

$$\text{effective porosity:} \quad \phi_{eff} = \frac{V_{ip}}{V} \tag{2.1}$$

where V_{ip} is the volume of interconnected pore space, and V the total volume of rock. The effective porosity is commonly less than the total porosity, although their differences may be relatively small for coarse-grained rocks.

From a length scale perspective, the occurrence of porosity in shale at particularly small length scales sets the mechanical and transport behaviors of this sedimentary rock apart from those observed in rocks such as sandstones. The sequence of burial and diagenetic processes cause the formation of the majority of pore space at nanometer scales. The so-called inter-domain porosity present between groupings or conglomerates of clays is known to be very low, with maximum radii at 4.2 nm [228]. From a combination of techniques such as mercury intrusion porosimetry and small angle neutron scattering, the characteristic pore size in shale is of some nanometers (e.g. 25 nm [77], 8 nm [111], 20 nm [130]). By way of illustration, Figure 2-3 shows the measured pore size distributions of two shale materials in comparison with a sandstone specimen. The pore space in shale has a much smaller characteristic length scale, in contrast to the pore distribution for a common sandstone, which may exhibit a wide range of pore sizes from the nanometer to the micrometer scales.

The nano-sized pores in shale cause some amount of water or other pore fluids to be ordered or structured by their association with mineral surfaces. The potential transport or chemical reactions between solutes and water may be inhibited through some particularly small pore throats, creating osmotic membrane properties in some shales [207].

2.2.7 Permeability

In sedimentary rocks, permeability, or the ability of the medium to transmit a fluid, is a complex function of particle size, shape, orientation, and sorting. Shale permeability vary up to ten orders of magnitude and by three orders of magnitude at a single porosity, which can be explained by differences in grain sizes. Silt-rich mudstones are more permeable than finer mudstones, as illustrated by studies of pore size distributions. In addition, the losses of porosity and permeability with increasing effective stress are related mainly to the collapse of larger pore

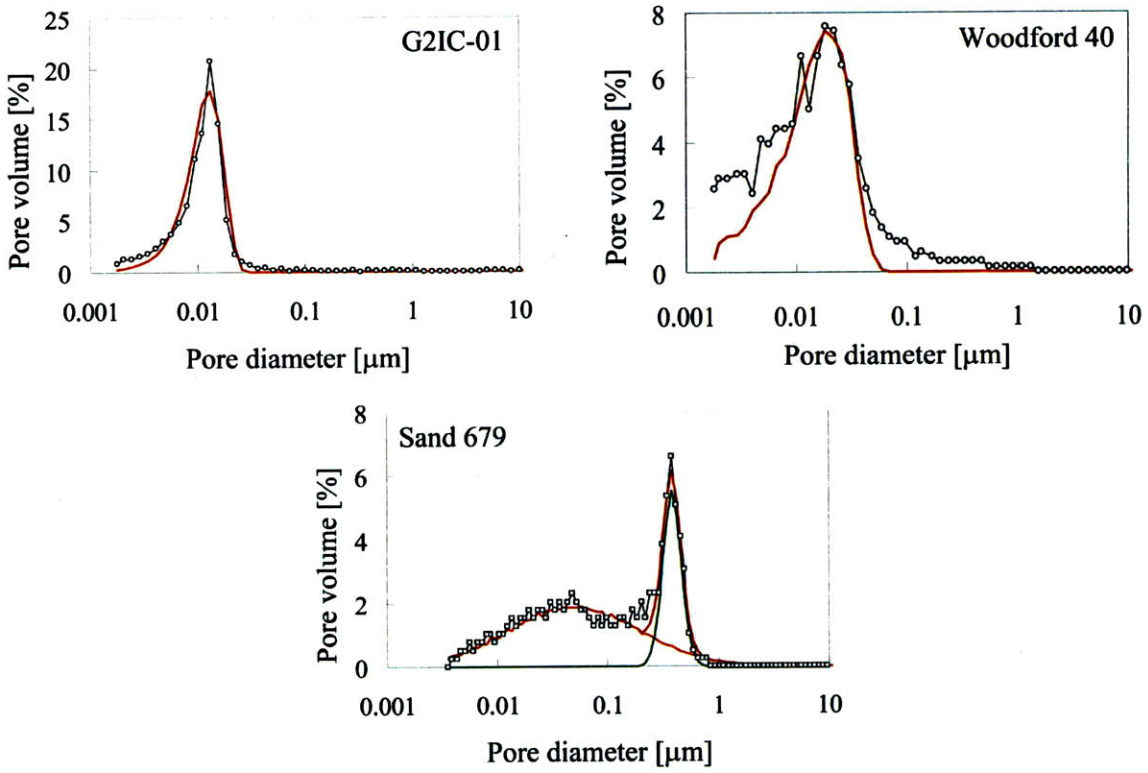

Figure 2-3: Pore size distributions for two shale specimens (G2IC-01 and Woodford 40, [30]) and a sandstone specimen (Sand 679, [31]).

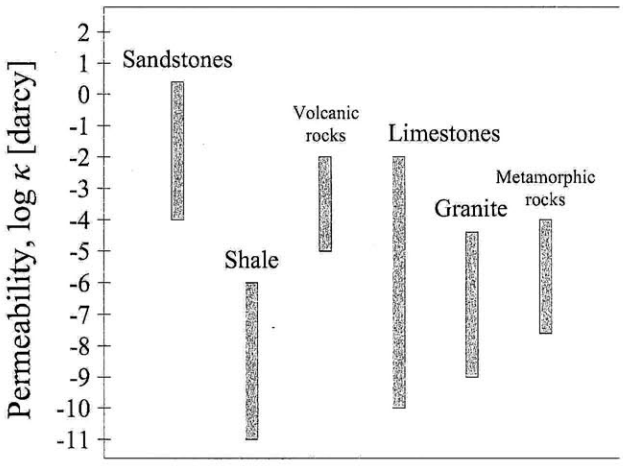

Figure 2-4: Compilation of laboratory-measured permeabilities for various rock types. The vertical bars display the range of measured values. 1 darcy $= 0.97 \times 10^{-12}$ m^2. The hydrostatic pressure during testing was less than 10 MPa and the temperature of about 25° C. Adapted from [41].

spaces [78]. Permeability in shale can be as low as 1 nD (10^{-21} m^2) [149]. Figure 2-4 displays a comparison of the permeability for different rock types as measured in laboratory experiments. The figure clearly illustrates the known nature of shale as a geological seal due to its extremely low permeability.

2.2.8 Clay Terminology

The thriving field of grain-scale mechanics of rocks is bringing together research contributions from a variety of experimental and theoretical disciplines. As this micromechanics investigation will add to the discourse of nanomechanics of shale, it is important to clearly define certain terms and concepts in order to minimize any errors in the dissemination of results [303]. Given the importance of clay mechanics to the present study, definitions of certain terminologies are provided hereafter [108]:

- *Mineral.* "A mineral is an element or chemical compound that is normally crystalline and that has been formed as a result of geological processes."
- *Crystalline.* "It is considered to be a material with sufficient atomic ordering such that

a (X-ray, electron, neutron, etc.) diffraction pattern containing well-defined maxima can be indexed using Miller indices."

- *On planes, sheets, and layers.* "The terms 'plane', 'sheet', and 'layer' cannot be used interchangeably and they refer to specific parts of the structure, with atomic arrangements that increase with thickness."

- *Plane.* "A 'plane' of one or more types of atoms (e.g. a plane of Si (silicon) and Al (aluminium) atoms, a plane of basal oxygen atoms) can occur."

- *Sheet.* "A 'tetrahedral sheet' or 'octahedral sheet' is composed of continuous two-dimensional corner-sharing tetrahedra involving three corners and the fourth corner pointing in any direction or edge-sharing octahedra, respectively."

- *Layer.* "A layer contains one or more tetrahedral and an octahedral sheet. There are two types of layers, depending on the ratios of the component sheets: a 1:1 layer has one tetrahedral sheet and one octahedral sheet, whereas a 2:1 layer has an octahedral sheet between two opposing tetrahedral sheets."

- *Interlayer material.* "Interlayer material separates the layers and generally may consist of cations, hydrated cations, organic material, hydroxide octahedra, and/or hydroxide octahedral sheets."

- *Unit structure.* "A 'unit structure' is the total assembly and includes the layer and interlayer material."

- *Clay mineral.* "The term 'clay mineral' refers to phyllosilicate minerals and to minerals which impart plasticity to clay and which harden upon drying or firing". "Clay minerals are not defined a priori as fine-grained because clays are fine-grained, but rather they may be of any crystallite size so that the term 'clay mineral' is consistent with the definition of 'mineral', which is unrelated to crystallite size."

These definitions are most relevant to our modeling of shale rocks, in which the mechanical behaviors of the clay-particle scale dominate the macroscopic response. Precision in handling these terms will enrich the modeling descriptions of the clay fabric in shale.

2.3 Multi-Scale Structure Thought-Model for Shale

Shale is complex, highly heterogeneous geological material, with heterogeneities that manifest themselves at different length scales. The presence of fine-grained clay minerals, nanometric porosities, and silt-size detrital grains imply a broad range of heterogeneities at multiple length scales of observation. In this geomechanics investigation of shale, we establish the macroscopic length scale to be that of an intact rock specimen at the centimeter length scale and higher. These length scales correspond to those of laboratory specimens used in standard mechanical characterization experiments such as acoustic measurements for elasticity and triaxial testing for strength properties. The intact rock sample should not exhibit macroscopic types of discontinuities such as joints, sheared zones [9].

This micromechanics investigation begins by defining a multi-scale structure thought-model for shale, which provides a consistent framework for separating the length scales that are most relevant to the micromechanics of shale. Originally proposed by Ulm et al. [268], the adopted multi-scale model establishes three characteristic length scales of observation, as displayed in Figure 2-5. The thought-model spans roughly seven orders of magnitude, from the scale of elementary clay particles (level 0), to the scale of a macroscopic clay-silt composite (level II). The rationale for each of the model levels is discussed in the following sections.

2.3.1 Level 0: Elementary Clay Particles

Level 0 is the scale of the elementary clay particles, which constitute the solid clay phase in shale. This scale has classically been designated as the fundamental scale of clay mineralogy. While the atomic structures of the clay minerals are well-known, their mechanical properties are rarely documented in handbooks [175]. The small nature of clay particles in pure solid form becomes the main obstacle for performing direct measurements of clay mineral stiffness or strength. For instance, several attempts to assess the elasticity of various clays have been reported [150, 171, 220, 273, 287]. However, the large range of estimated solid clay stiffness values emphasize the difficulty to assess the intrinsic properties of single clay crystals.

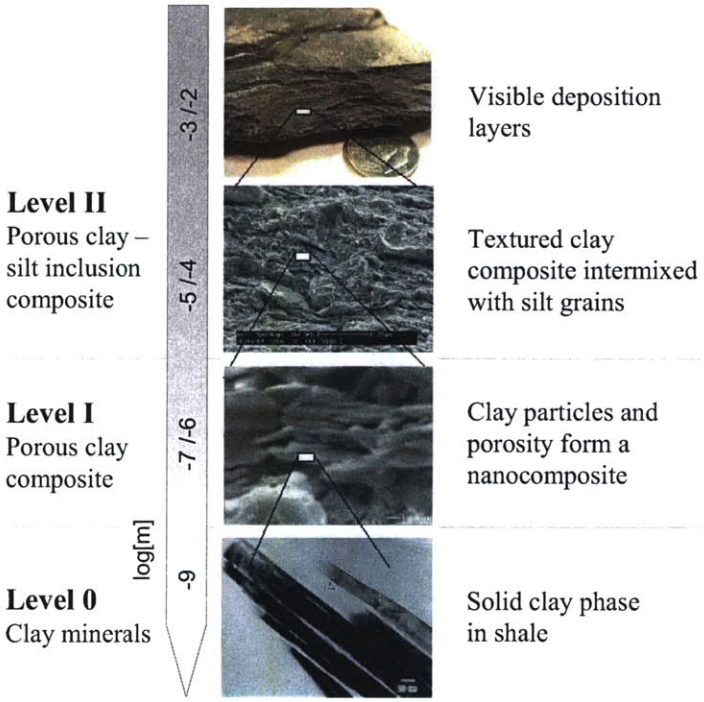

Figure 2-5: Multi-scale structure thought-model of shale. The level II and level I images come from scanning electron microscopy (SEM) imaging. The level 0 image comes from transmission electron microscopy (TEM) imaging [161], reprinted with the kind permission of Springer Science and Business Media. Adapted from [202, 265, 267, 268].

2.3.2 Level I: Porous Clay Composite

Level I is the scale of the porous clay composite, which manifests itself at the sub-micrometer scale (10^{-7} to 10^{-6} m). This scale is classically that of advanced observational methods, which aim at linking the morphology of the clay fabric to physico-chemical, electro-chemical, bio-organic, and burial diagenesis processes (see e.g. [18]). In particular, it has been long understood that the microstructure of the clay phase plays an important role in the macroscopic behavior of shale and other clay-bearing geomaterials [128, 145, 166, 228]. In particular, three methods of observing this clay microstructure in shale have provided important contributions to the topic. The most commonly employed visual observation technique is scanning electron microscopy (SEM) in secondary electron mode [146, 267]. These images give a visual understanding of the surface topography of a sample. Figure 2-6a displays a typical SEM image of a shale surface, which exposes the bedding planes associated with the depositional history of the material. The SEM image shows a typically observed flaky structure, with characteristic dimensions of clay platelets of about $500-1000$ nm and $20-50$ nm thickness. The shape of clay particles typically has been characterized by approximate thickness-to-diameter aspect ratios of $1/25-1/20$ [267]. A related technique is transmission electron microscopy (TEM), which gives high resolution information about the relative atomic density of a very thin section of material. Figures 2-6b and 2-6c display typical TEM images from Bryant et al. [44], who produced a series of images of consolidated marine clay[5]. Darker regions in TEM images correspond to higher atomic densities. Hence, the TEM images in Figures 2-6 may suggest a granular microstructure with equi-dimensional, submicron-sized groupings of aligned clay minerals. Finally, atomic force microscopy (AFM) has also been used to probe the surface topography of a shale sample. In AFM imaging, a sharp tip is rastered across the sample surface, and the heights at which the tip makes contact with the surface are recorded. Figures 2-6d and 2-6e show typical AFM images of a polished shale surface [32]. These images also may suggest a granular microstructure consisting of equi-dimensional, submicron-sized structures.

Regarding the porosity in shale, porosimetry testing (Section 2.2.6) has determined that the space in between clay mineral units accounts for almost the totality of the pore space in shale,

[5] TEM images of clay in shale are not found in the open literature due to difficulties with TEM sample preparation.

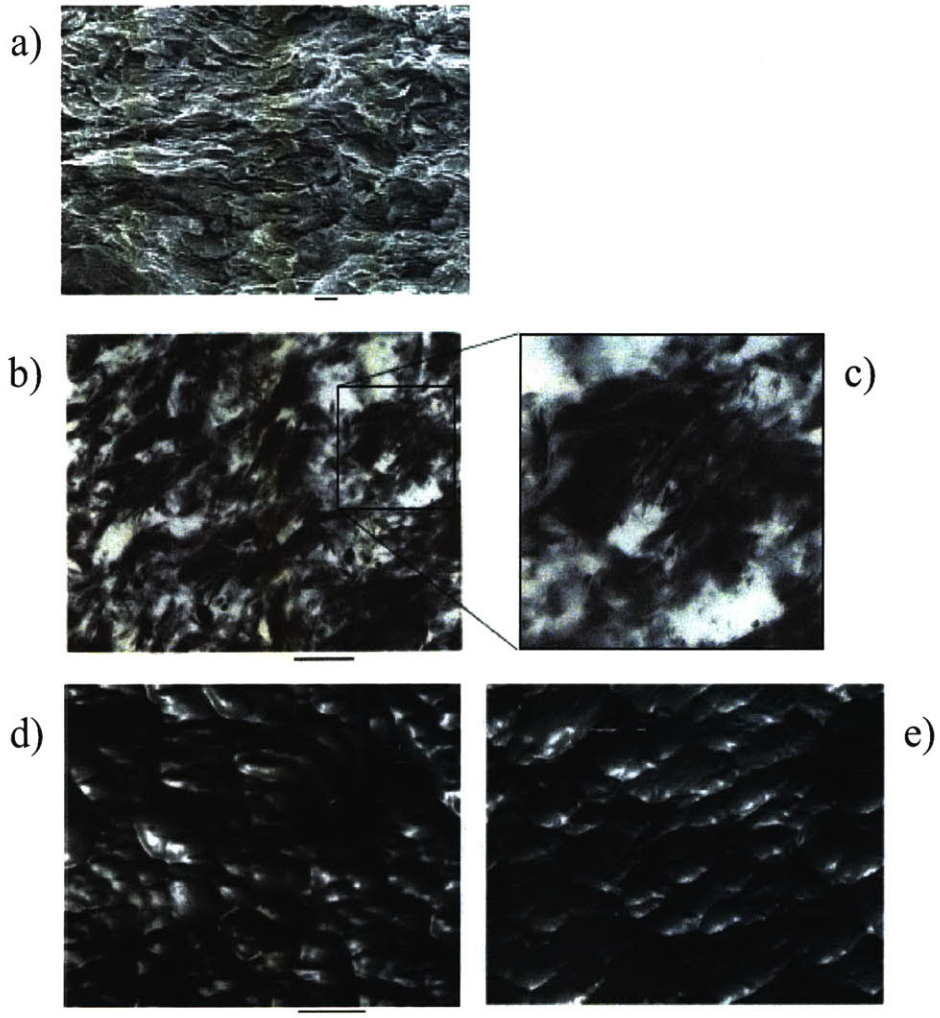

Figure 2-6: Visual observations of the microstructure of the porous clay in shale. The scale bar for each image is 1 μm. a) SEM image of shale G2IC-03 adapted from Ulm et al. [267], showing well-aligned flaky structures. b) TEM image of consolidated clay from Bryant et al. [44], showing an equi-dimensional, submicron-sized granular structure consisting of c) aligned clay minerals. d-e) AFM images of shale G2IC-03 in the normal-to-bedding and in-bedding planes from Bobko and Ulm [32], showing an equi-dimensional submicron-sized granular structure. Adapted from [31].

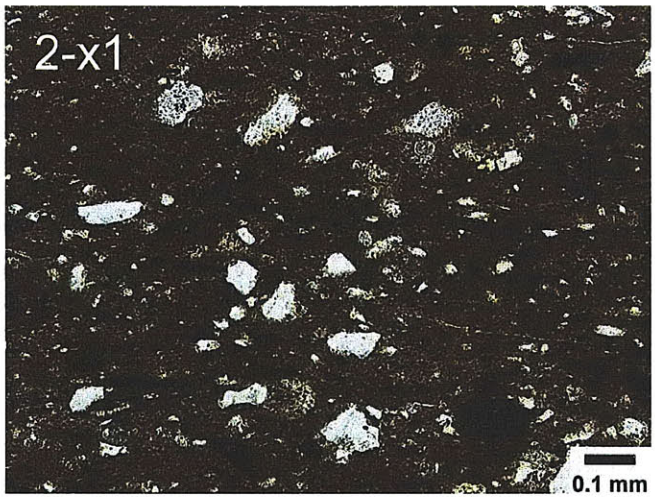

Figure 2-7: Plane polarized light thin-section photomicrographs at 25X magnification for shale G2IC-02. Courtesy of Chevron. Adapted from [267].

with characteristic pore access radii of some nanometers. Consequently, the porosity in shale is assigned to length scales of level I.

2.3.3 Level II: Composite of Porous Clay and Silt Inclusions

Level II is deemed as the macroscopic scale of characteristic size in the sub-millimeter and millimeter range (10^{-5} to 10^{-4} m). At this scale, the material is composed of the porous clay fabric intermixed with an abundant population of poorly sorted detrital grains (mainly quartz and feldspar inclusions), which are either concentrated into laminations or homogeneously distributed throughout, as observed in Figure 2-7.

This scale is the designated scale for exploration geophysics and experimental geomechanics. The material characterization at level II is based on the application of various methodologies, e.g. acoustic testing (ultrasonic pulse velocity measurements), conventional triaxial testing, tensile split testing, and inclined direct shear testing [2], in order to determine deformation and strength behaviors and properties. Laboratory measurements using this different experimental techniques involve the characterization of intact rock specimens with no macroscopic discontinuities.

2.4 Chapter Summary

This chapter has briefly introduced some of the most relevant aspects of composition and microstructure of shale. Properties and microstructural features such as the clay mineralogy, particle shapes and orientations, permeability, and nanoporosity have direct effects on the macroscopic mechanical response of this type of sedimentary rocks. The discussions in Chapter 3 regarding the mechanical properties of shale materials will quickly reveal the links between material performance to each of these compositional and microstructural aspects. In particular, the porous clay phase in shale shall be found to dominate the elastic and strength responses of shale as assessed through different experimental means.

The complex, heterogeneous nature of shale has been structured through a hierarchical, multi-scale thought-model, which allows separating the different length scales of relevance to this micromechanics investigation. This multi-scale structure thought model for shale will provide the framework for introducing a comprehensive experimental database in Chapter 3 used for model development. It will also guide the theoretical modeling efforts presented in subsequent parts of this thesis.

Chapter 3

Shale Materials and Multi-Scale Properties

Despite their ubiquitous presence as sealing formation in hydrocarbon reservoirs or as host rocks, the knowledge of the poroelastic and strength behaviors of shale is limited compared to the developments for other reservoir rocks. Well-preserved shale specimens are difficult to retrieve from the field for adequate mechanical characterization. Laboratory experimental programs tend to be time-consuming because of the experimental constraints imposed by low permeability of shale. In addition, one of shale's prominent properties, its anisotropic mechanical behavior, requires special suits of theoretical and experimental techniques for valid assessment. However, in the past two decades, significant research progress has been made in the characterization of mechanical properties of shale, in particular at the macroscopic scale of engineering testing. More recently, advances in experimental techniques have also contributed to the direct assessment of the elasticity and strength at the scale of the clay fabric, the binding phase in shale.

The aim of this chapter is to establish a comprehensive database of mechanical properties for shale measured at different length scales of observation. The chapter begins with the description of the different shale samples that will be considered throughout this investigation and the corresponding information regarding material composition (mineralogy, porosity, bulk density). This information is vital to our modeling efforts. The chapter then introduces experimental

data on clay mineral properties, recently developed nanomechanics results from instrumented indentation, and conventional macroscopic seismic and strength testing. In an original development, the indentation data gathered by the G2IC Industry Consortium is reanalyzed using a robust statistical approach, which ensures the accuracy and reliability of the inferred information about the nanomechanical response of shale. The database established in this chapter becomes the experimental foundation for our micromechanics modeling investigation of shale.

3.1 Materials

A set of 47 shale specimens will be used in this investigation to develop the microporomechanics models for elasticity and strength[1]. This compilation of shale material information serves as a comprehensive database which brings together specimens from diverse geological origins, burial depths, and compositional characteristics. The database is composed of experimental data developed internally by the members of the GeoGenome Industry Consortium[2] and data obtained from the open literature on shale. The motivation for developing such comprehensive database of material behaviors is to advance the multi-scale mechanics understanding and modeling of shale.

GeoGenome Shales

A total of twelve shale samples were characterized by the G2IC for this study. Their compositional and mechanical properties cover a broad spectrum of shale formation properties. The shale samples were provided by Chevron, Norsk Hydro (now StatoilHydro), and the University of Oklahoma. Although detailed experimental information was disclosed for all samples, information regarding their geological origins was not generally provided. Only two shale samples are known to belong to a Pierre formation and a North Sea formation. The remaining samples are identified by a reference number (G2IC-0X) or by their physical appearance ("light" and "dark" shales).

[1] A total of 28 specimens will be consider for developing the microporoelastic model, whereas 19 specimens will be considered for the strength homogenization model.

[2] The dataset of shale materials developed by the G2IC was first presented in Bobko and Ulm [32], although some experimental information (especially regarding macroscopic measurements) does not appear in that report.

Woodford Shales

The Woodford shale samples were cored from a well in the Woodford formation located at the Northern flank of the Arbuckle uplift in Pontatoc County, Oklahoma. The Woodford shale formation, deposited during the lower Mississippian and upper Devonian periods under anaerobic marine environments, is one of the major source rocks along the US Midwest region. The five samples of Woodford shale belong to the same single core, and were retrieved from a total distance of approximately 20 m. Compared to the composition of the GeoGenome shales, which did not display significant amounts of organic compounds, the Woodford shale specimens will be used in the investigation of the effects of kerogen (a precursor of hydrocarbon) on the overall mechanical properties of shale. The Woodford specimens are denoted by their depth of burial in meters (i.e. Woodford 40, 47, 51, 53, 56 m).

Highly Consolidated Boston Blue Clay

The highly consolidated Boston Blue Clay is a synthetic sedimentary material which can be seen as an analogue of shale. The raw material is resedimented Boston Blue Clay (RBBC), which has been well-studied and characterized at MIT for more than four decades [101]. Among the many advantages of such a material is that samples are derived from a natural material, so while the behavior of RBBC is similar to what is expected for materials encountered in nature, inherent variations between samples are largely eliminated. To synthesizing rock-like samples from RBBC, the samples of RBBC considered here experienced consolidation pressures of up to 10 MPa [1]. All samples were unloaded to an over-consolidation ratio[3] (OCR) of 4. The Boston Blue Clay samples are identified by their final consolidation pressure (i.e. 2, 4, 6, 8, 10 MPa).

Shales from the Literature

The last component of the database of shale materials is compiled from a literature review of shale mechanics. Although several research projects have been conducted on shale materi-

[3] Overconsolidation ratio (OCR) is a soil mechanics term, referring to ratio of maximum compressive effective stress to the current compressive effective stress a certain soil deposit has experienced. In the case of OCR = 4, the soil is unloaded in the oedometer to a compressive stress 1/4 of the maximum consolidation stress.

Source	Specimen	Location	Depth, [m]
G2IC	G2IC-01, -02, -03, -04, -05, -06, -07, -08, Dark, Light, Pierre, North Sea	Not disclosed Pierre / North Sea	Not disclosed
Woodford	40, 47, 51, 53, 56	Woodford formation, Oklahoma	40–56
[146]	CRE	Cretaceous shale, Williston basin, North Dakota	1,524
[129]	KIM	Kimmeridge clay formation, North Sea	3,750
	JUR	Jurassic age shale, from reference outcrop	-
[138]	3492, 3506, 3525, 3536, 3564	Brage field, North Sea basin	3,492–3,564
[81]	108/111	North Sea basin	3,000–4,000
[77]	MUD	Muderong shale, from Carnarvon basin, Australia	1,120
[226]	CO	Jurassic-age, Callovo-Oxfordian shale, France	613
[142]	9898, 10151, 6275, 7053, 6853, 8675	Travis Peak Formation, East Texas	1,800–3,000
[130]	B, D, E, H, J, K	North Sea	1,570-4,870
[195]	TOU	Toarcian massive shale, Tournemire site, France	-
[68]	SH1	Jurassic age, English coast	-
[1]	RBBC-2,-4,-6,-8,-10	-	-

Table 3.1: List of shale samples considered in this study, their geological origins, and corresponding burial depths.

als, especially at the macroscopic scales of engineering testing, only a few references provide complete descriptions of the material composition and mechanical properties of interest to this study. The selected references from the open literature on shale are: Jones and Wang [146], Hornby [129], Jakobsen and Johansen [138], Domnesteanu et al. [81], Dewhurst and Siggins [77], Sarout and Gueguen [226], Jizba [142], Horsrud et al. [130], Niandou et al. [195], and Cook et al. [68].

Table 3.1 provides a list of all shale specimens considered in this investigation, their geological origin and location, and their burial depth. In the following sections, the mineralogy, porosity, and density information are detailed for these shale samples, as those properties are critical inputs to the multi-scale modeling efforts.

Sample	Inclusions	Total clay	Kaolinite	Illite/Smectite	Other clay	Amorphous
G2IC-01	22	76	36	38	2	-
G2IC-02	28	72	21	42	9	-
G2IC-03	30	70	9	54	7	-
G2IC-04	40	57	7	44	6	-
G2IC-05	36	60	8	40	12	-
G2IC-06	17	82	42	37	3	-
G2IC-07	31	67	37	21	9	-
G2IC-08[a]	56	15	N.A.	N.A.	N.A.	-
Dark	66	35	20	10	6	-
Pierre	64	36	0	25	11	-
Light	71	30	N.A.	N.A.	N.A.	-
40	53	30	1	26	3	17
47	55	28	0	25	3	17
51	51	31	0	27	4	18
53	52	36	0	31	5	12
56	49	36	3	29	4	15
North Sea	45	55	19	11	25	-

Table 3.2: Mineralogy composition for shale specimens gathered in collaboration with the G2IC, in mass percents. The mineralogy data was obtained by X-ray diffraction. N.A. (*non available*) refers to information not disclosed. *Inclusions* refers to components mainly of the sand and carbonate mineral groups such as quartz, feldspar, plagioclase, calcite, ankerite, as well as other silt minerals such as pyrite, halite, and anhydrite. *Other clays* refers to minerals such as chlorite, glauconite, biotite, serpentine, berthierine, and montmorillonite. *Amorphous* refers mainly to kerogen content.
(a) Mineralogy in volume percent.

3.2 Mineralogy Data

The characterization of the relative amounts of solid constituents in a composite becomes a critical input for material modeling. For shale modeling, the assessment of mineralogy composition is crucial for quantifying the volumetric contributions of clay and non-clay minerals to the overall mechanical response. The quantitative analysis of the mineralogy composition of shale specimens is typically obtained through X-ray diffraction measurements (XRD analysis), although other methodologies are also used, such as infrared spectroscopy and energy dispersive spectroscopy. Tables 3.2, 3.3, and 3.4 summarize the mineralogy compositions of all considered shale specimens. Evidently, a wide range of mineralogy make-ups for the different samples testifies to the diversity of materials included in this investigation.

Sample	Inclusions	Total clay	Kaolinite	Illite/Smectite	Other clay
CRE	73	27	5	19	4
KIM	41	59	22	35	2
JUR	42	58	0	58	0
3492[(a)]	69	17	4	9	4
3506	35	53	14	17	22
3525	35	55	23	8	24
3536	31	59	14	10	35
3564	52	38	6	15	17
108/111	59	41	25	16	0
MUD	33	65	15	45	5
CO	52	47	3	31	14
9898[(b)]	55	42	-	-	-
9763	75	20	-	-	-
10151	43	52	-	-	-
6275	32	63	-	-	-
7053	57	38	-	-	-
6853	64	31	-	-	-
8675	38	56	-	-	-

Table 3.3: Mineralogy composition for shale data gathered from the literature sources, in mass percents. *Inclusions* refers to components mainly of the sand and carbonate mineral groups such quartz, feldspar, plagioclase, calcite, ankerite, as well as other silt minerals such as pyrite, halite, and anhydrite. *Other clays* refers to minerals such as chlorite, glauconite, biotite, serpentine, berthierine, and montmorillonite. The mineralogy data was obtained by X-ray diffraction, except for the specimens KIM (infrared spectrometry), 3492-3564 (energy dispersive spectroscopy), and 9898-8675 (clay content determined by thin-section point count).

(a) Mineralogies for specimens 3492 to 3564 are in volume percents. 10-14 percent of solid volume was specified as *Other clay* without distinction between clay or non-clay mineral.

(b) Mineralogies for specimens 9898 to 8675 are in volume percents.

Sample	Inclusions	Total clay	Kaolinite	Illite/Smectite	Other clay
RBBC-2[(a)]	11	45	-	-	-
RBBC-4	12	48	-	-	-
RBBC-6	12	49	-	-	-
RBBC-8	12	50	-	-	-
RBBC-10	13	51	-	-	-
B	18	82	-	-	-
D	44	56	-	-	-
E	48	52	-	-	-
H	42	58	-	-	-
I	53	47	-	-	-
J	35	65	-	-	-
K	51	49	-	-	-
TOU	45	55	28	25	2
SH1	51	49	22	18	9

Table 3.4: Mineralogy composition of shale data gathered from the literature sources, in mass percents. *Inclusions* refers to components mainly of the sand and carbonate mineral groups such quartz, feldspar, plagioclase, calcite, ankerite, as well as other silt minerals such as pyrite, halite, and anhydrite. *Other clays* refers to minerals such as chlorite, glauconite, biotite, serpentine, berthierine, and montmorillonite.
(a) Mineralogies for RBBC specimens are in volume percents.

3.3 Porosity and Bulk Density

There are different ways to determine the porosity in rocks. One method consists in the combination of experimental bulk density measurements and mineralogy data (solid constituents):

$$\overline{\rho}^{sat} = \frac{1-\phi_0}{\sum_{i=1}^{N} m_i/\rho_i} + \phi_0 \rho^{fl} \Rightarrow \phi_{0,\rho} = \frac{\overline{\rho}^{sat} - \left[\sum_{i=1}^{N} (m_i/\rho_i)\right]^{-1}}{\left[\sum_{i=1}^{N} (m_i/\rho_i)\right]^{-1} - \rho^{fl}} \tag{3.1}$$

where $\overline{\rho}^{sat}$ is the saturated bulk density and ρ^{fl} the density of the fluid phase saturating the pore space[4]. Another convenient way of determining the porosity is from weighing a saturated and a dried sample:

$$\phi_{0,d} = \frac{\overline{\rho}^{sat} - \overline{\rho}^{dry}}{\rho^{fl}} \tag{3.2}$$

[4]For most shale specimens, specific information regarding the composition of the pore fluids was not provided. For shales G2IC-01 through G2IC-05, the saturating fluid was a brine solution (14.2% NaCl), whose corresponding bulk density is similar to that of water. In most cases, the assumption of compressibility properties of water assigned to the pore fluid is adequate for our micromechanics modeling efforts.

Sample	MIP porosity [%]	Drying porosity [%]	Bulk density [g/cm^3]
G2IC-01	26	26	2.20
G2IC-02	13	17	2.43
G2IC-03	7	13	2.55
G2IC-04	20	21	2.33
G2IC-05	26	29	2.19
G2IC-06	12	16	2.41
G2IC-07	7	11.5	2.51
G2IC-08	29	-	N.A.
Dark	4	-	2.57
Pierre(*)	N.A.	-	2.25-2.40
Light	8	-	2.48
40	13	-	2.21
47	12	-	2.18
51	16	-	2.18
53	19	-	2.26
56	14	-	2.11
North Sea	13-16	-	N.A.

Table 3.5: Porosity and bulk density data for shale specimens gathered in collaboration with the G2IC. N.A. (*non available*) refers to information not disclosed. MIP stands for mercury intrusion porosimetry.
(a) Data from [231].

where $\overline{\rho}^{sat} = M^{sat}/V_0$ and $\overline{\rho}^{dry} = M^{dry}/V_0$ are the mass densities of the fully saturated and the oven-dried sample, respectively (M^{sat} and M^{dry} are the masses of the fully saturated and oven-dried samples, respectively). Provided an initially saturated state and adequate drying of the shale sample, the drying method yields estimates of the total porosity that generally coincide well with estimate (3.1) based on bulk density measurements. Finally, independent measurements of the porosity are provided by fluid intrusion or gas expansion techniques, among which mercury intrusion porosimetry (MIP) is the most prominent test. MIP consists of forcing mercury (a non-wetting liquid for most porous earth materials at atmospheric conditions) into a porous solid by means of increasing pressure on the mercury. With increasing pressure, the fluid is forced into smaller pores, and the mercury intrusion volume is translated into a pore volume. It is well documented that mercury intrusion porosimetry underestimates the actual porosity [79], while estimation of porosity by using the bulk density and mineralogy information provides a higher value of porosity.

Sample	Porosity [%]	Density [g/cm^3]	Remarks (porosity / density)
CRE	11	2.42	Estimated from weight loss experiments / Measured by immersion in water (after waterproofing samples)
KIM	2	-	JUR: weight loss experiments, KIM: Helium expansion test /
JUR	10	-	Matrix density was estimated for both shales from mineral composition and standard set of mineral densities
3492	10	2.43	Standard helium expansion technique /
3506	16	2.44	Measurements of volume and weight of cylindrical specimens
3525	8	2.38	
3536	14	2.44	
3564	7	2.41	
108/111	15	2.38	Helium porosimetry test / Experimental method not specified
MUD	21	2.20	Mercury intrusion capillary pressure / Experimental method not specified
CO	10	2.45	Mercury intrusion porosimetry (200 MPa mercury pressure)
9898[(a)]	3.3	2.69	Helium porosimetry at 15-28 MPa confining pressure /
9763	4.8	2.69	Experimental method not specified
10151	4.9	2.68	
6275	5.0	2.72	
7053	5.2	2.71	
6853	5.4	2.62	
8675	5.8	2.72	

Table 3.6: Porosity and bulk density data for shale specimen data obtained from literature sources.
(a) Density data for specimens 9898-8675 correspond to grain density values.

Sample	Porosity [%]	Density [g/cm^3]	Remarks (porosity / density)
RBBC-2	44	-	Porosity estimated from consolidation data.
RBBC-4	40	-	
RBBC-6	39	-	
RBBC-8	38	-	
RBBC-10	36	-	
B	41	-	Standard helium injection technique
D	34	-	
E	31	-	
H	10	-	
I	17	-	
J	15	-	
K	3	-	
TOU	13	2.72	Mercury intrusion porosimetry
SH1	8	-	Mercury intrusion porosimetry

Table 3.7: Porosity and bulk density data for shale specimen data obtained from literature sources.

3.4 Volume Fractions

In view of the forthcoming development of multi-scale micromechanics models for shale, the mineralogy and porosity information for all considered shale samples is transformed into appropriate volumetric parameters. The volumetric quantities become critical inputs for mechanics modeling as they weigh the contributions of the relevant phases to the mechanical response of the composite material at different length scales. Following the multi-scale structure thought-model for shale outlined in Section 2.3, we define two shale-specific volumetric parameters: the clay packing density η, and the inclusion volume fraction f^{inc}, which neatly summarize the porosity and mineralogy information of the material sample into two simply understood parameters.

At the macroscopic scale, or level II, shale is classically partitioned into three characteristic components; non-clay minerals, clay minerals, and porosity:

$$\text{Level II: } f^{inc} + f^{c} + \phi_0 = 1 \tag{3.3}$$

where f^{inc} is the volume fraction occupied by the non-clay mineral (NCM) phases (quartz,

feldspar, plagioclase, etc.) in the macroscopic sample volume, f^c is the volume fraction occupied by the clay mineral (CM) phases (kaolinite, illite, smectite, montmorillonite, etc.) in the macroscopic sample volume, and ϕ_0 is the porosity. The *inclusion volume fraction* and the *clay volume fraction* can be determined from mineralogy data:

$$f^{inc} = (1-\phi_0)\frac{\sum_{i=1}^{i=NCM}(m_i/\rho_i)}{\sum_{i=1}^{N}(m_i/\rho_i)} \tag{3.4a}$$

$$f^{c} = (1-\phi_0)\frac{\sum_{i=1}^{i=CM}(m_i/\rho_i)}{\sum_{i=1}^{N}(m_i/\rho_i)} \tag{3.4b}$$

where m_i are for the mass fractions of the $N = NCM + CM$ shale solid constituents provided by e.g. X-ray diffraction (XRD) measurements, and ρ_i the corresponding mineral densities (refer to Table 3.8). The *clay packing density* of the porous clay phase is obtained from:

$$\eta = \frac{f^c}{1-f^{inc}} = \frac{(1-\phi_0)\sum_{i=1}^{i=CM}(m_i/\rho_i)}{\sum_{i=1}^{i=CM}(m_i/\rho_i) + \phi_0\sum_{i=1}^{i=NCM}(m_i/\rho_i)} \tag{3.5}$$

In contrast to the macroscopic volume fractions in (3.3), the clay packing density is defined at level I of the clay fabric in shale, composed of the solid clay particles and *clay porosity*, $\varphi_0 = \phi_0/\left(1-f^{inc}\right)$, typically of nanometer size:

$$\text{Level I: } \eta + \varphi_0 = 1 \tag{3.6}$$

For kerogen-rich shale, such as the Woodford shale, the volumetric characterization of the kerogen phase is necessary for appropriate modeling. In our multi-scale modeling approach, kerogen is treated akin to a clay mineral phase, and thus the (relative) volume fraction of kerogen is calculated as:

$$f^k = \frac{V^k}{\sum_{i=1}^{i=CM} V_i} \tag{3.7}$$

where V^k is the volume of kerogen, and $\sum_{i=1}^{i=CM} V_i$ the total volume of clay mineral phases and kerogen. For the computation of the clay packing density for kerogen-rich shales is modified accordingly[5].

[5]The modeling of kerogen-rich shale (Woodford shale) will be undertaken as a extension of the modeling of kerogen-free shale (G2IC and shales from the literature), which represents the main target of our modeling

		Density, ρ_i [g/cm^3]
Inclusion	Quartz	2.65
	Kspar	2.57
	Plagioclase	2.68
	Calcite	2.71
	Dolomite	2.90
	Pyrite	5.00
	Siderite	3.74
	Ankerite	3.00
	Hematite	2.90
Clay minerals	Kaolinite	2.64
	Illite / Smectite	2.65
	Chlorite	2.95

Table 3.8: Density information of some minerals present in shale.

Beside mineralogy data, the determination of the clay packing density and the non-clay inclusion volume fraction requires as input the total porosity ϕ_0. There are different ways to determine the porosity of a rock sample depending on the combinations of experimental techniques. As explained in Section 3.3, traditional methods such as mercury intrusion porosimetry (MIP), drying experiments, and estimations from density and mineralogy data may yield different estimates for the total porosity. This may lead to some variability in the estimation of the clay packing density and the inclusion volume fraction.

The determination of the clay packing density and the non-clay inclusion volume fraction for the shale data considered in this investigation is accomplished through a combination of test results from mineralogy, porosity, and bulk density experiments. A first set of packing density and inclusion volume fraction estimates is derived from direct porosity and mineralogy tests. A second set of estimates is derived from experimental bulk density and mineralogy tests (using relation (3.1) for estimating the porosity). A third set is obtained from drying porosity and mineralogy tests. For some shale samples, only a limited set of properties was available.

The derived estimates of clay packing density and inclusion volume fraction for the G2IC and Woodford shale specimens and the shale data gathered from the literature are presented in Tables 3.9 and 3.10. By way of illustration, Figure 3-1 displays the comparisons of clay packing density and inclusion volume fraction estimates obtained by the three methodologies

efforts.

Sample	$\eta_{\max}$	$\eta_{\min}$	η_{dry}	$f^{inc}_{\max}$	$f^{inc}_{\min}$	f^{inc}_{dry}	f^k
G2IC-01	69	65	69	16	16	16	-
G2IC-02	83	78	78	24	23	23	-
G2IC-03	90	90	82	28	28	26	-
G2IC-04	71	68	69	33	32	33	-
G2IC-05	64	58	61	27	26	26	-
G2IC-06	86	80	82	14	13	13	-
G2IC-07	90	85	84	28	27	27	-
G2IC-08	34	-	-	56	-	-	-
Dark	90	79	-	62	59	-	-
Pierre[(a)]	65	52	-	52	47	-	-
Light	82	75	-	64	62	-	-
40	79	70	-	40	37	-	49
47	80	64	-	40	35	-	51
51	75	68	-	36	34	-	49
53	69	70	-	38	38	-	36
56	77	61	-	38	33	-	39
North Sea[(b)]	79	75	-	38	37	-	-

Table 3.9: Volume fractions for the data gathered by the G2IC, in terms of the clay packing density η, the inclusion volume fraction f^{inc}, and the relative volume fraction of kerogen f^k. Minimum volume fractions were calculated using mineralogy and bulk density information. Maximum volume fractions were calculated using mineralogy and MIP porosity information.
(a) The variability in volume fractions was calculated using the bulk density data.
(b) The variability in volume fractions was calculated using the range in porosity measured for this specimen.

previously discussed. The figures show a greater variability across estimates of clay packing density compared to inclusion volume fraction estimates. Furthermore, and as it was expected, estimates of clay packing density and inclusion volume fraction using porosity and mineralogy information are higher compared to those obtained from bulk density and mineralogy information, which recognizes that fluid/gas intrusion techniques underestimate the actual porosity, and hence overestimate clay packing density and inclusion volume fraction values.

3.5 Mechanical Properties of Clay Minerals - Level 0

The review of the mechanical properties of shale begins by first focusing at the scale of clay minerals. The clay phase in shale, which is its dominating material component (see mineralogy compositions in Section 3.2), dictates the overall rock deformation and strength behaviors. In clay-rich sedimentary rocks and soils, the extremely small particle sizes in the sub-micrometer

Sample	$\eta_{\max}$	$\eta_{\min}$	$f^{inc}_{\max}$	$f^{inc}_{\min}$
CRE	69	53	64	58
KIM	96	-	39	-
JUR	84	-	36	-
3492	64	38	72	61
3506	76	76	34	33
3525	88	71	36	31
3536	80	66	30	26
3564	86	67	54	48
108/111	71	65	50	48
MUD	72	62	26	23
CO	81	72	47	44
9898	93	-	55	-
9763	81	-	75	-
10151	91	-	43	-
6275	93	-	32	-
7053	88	-	57	-
6853	85	-	64	-
8675	91	-	38	-

Table 3.10: Volume fractions for the data obtained from the open literature, in terms of the clay packing density η, and the inclusion volume fraction f^{inc}. Minimum volume fractions were calculated using mineralogy and bulk density information, whenever available. Maximum volume fractions were calculated using mineralogy and MIP porosity information.

Sample	$\eta_{\max}$	$\eta_{\min}$	$f^{inc}_{\max}$	$f^{inc}_{\min}$
RBBC-2	51	-	11	-
RBBC-4	54	-	12	-
RBBC-6	56	-	12	-
RBBC-8	57	-	12	-
RBBC-10	59	-	13	-
B	54	-	11	-
D	52	-	29	-
E	54	-	33	-
H	84	-	38	-
I	70	-	44	-
J	79	-	30	-
K	94	-	49	-
TOU	92	86	40	38
SH1	41	-	79	-

Table 3.11: Volume fractions for the data obtained from the open literature, in terms of the clay packing density η, and the inclusion volume fraction f^{inc}. Minimum volume fractions were calculated using mineralogy and bulk density information, whenever available. Maximum volume fractions were calculated using mineralogy and MIP porosity information.

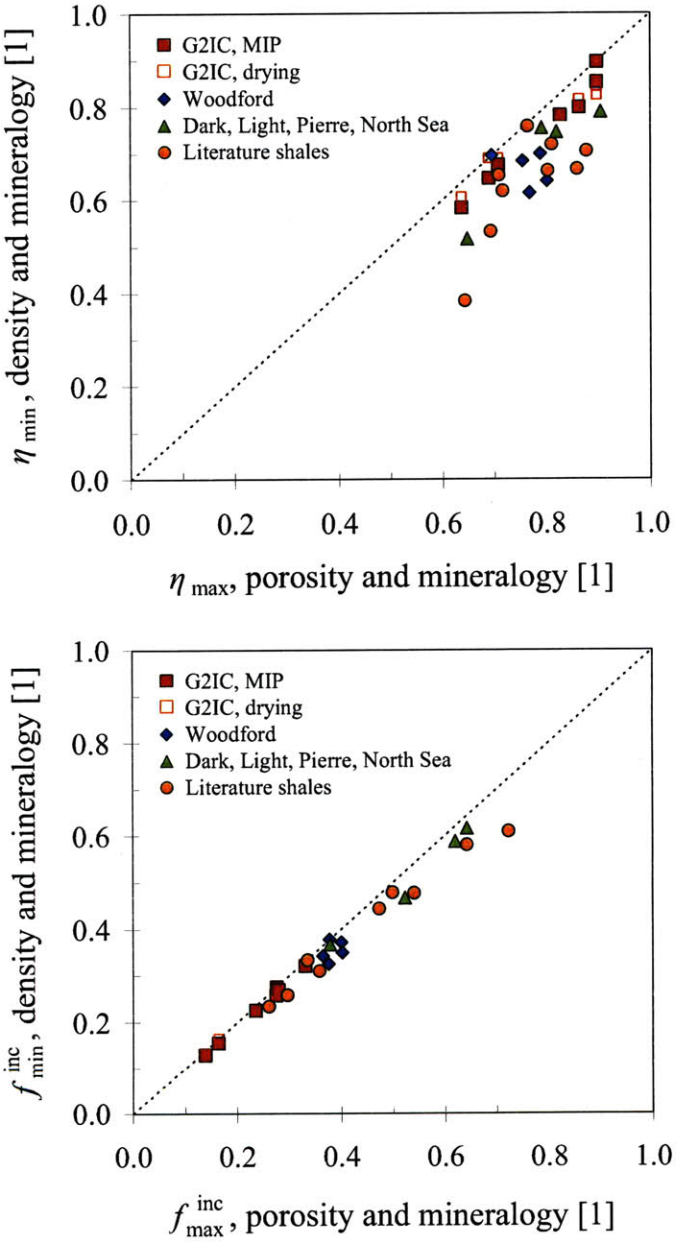

Figure 3-1: Comparisons of clay packing density (top) and inclusion volume fraction (bottom) estimates obtained from porosity and bulk density tests in addition to mineralogy information.

range, large specific surfaces (tens to hundreds of m^2/g), and unbalanced surface electrical forces associated with clay particles result in a colloidal behavior at fundamental length scales [187]. For such configuration, the behavior of the material system is governed by surface forces, which can act between solid and liquid bodies at distances larger than interatomic spacings in a crystal, as well as in the presence of a third interacting medium such as water [137]. These surface forces are related to different physical scenarios of repulsive and attractive interactions between bodies [105]:

- Electrical double-layer forces rise from the contributions of electrostatic interactions and an osmotic pressure derived from the confinement of a cationic layer in the interlayer gap between charged crystals. This type of repulsive force is dominant at large separation distances.

- Hydration forces at small separation distances occur due to the hydration of crystal surfaces and interlayer cations.

- Van der Waals attractive forces originate from dipolar interactions. Although relatively weak compared to hydration forces, they are non-directional and additive between atoms.

- Capillary attractive forces develop due to the surface tension at fluid/solid interfaces. The influence of this type of attractive force may be more significant in partially saturated media.

The combination of ionic and electrostatic forces defines the behavior of clay systems. In particular, material domains, or quasi-crystals (refer to Section 2.2.3), form from the grouping of several clay layers held together by short-range attractive forces, depending on the specific clay group[6]. These layered arrangements are the bases for the structures of clay particles, whose morphologies are strongly linked to the development of the signature microfabric in shale.

It is at the level of clay particles where physical chemistry meets the mechanics of clays in terms of deformation and strength behaviors. Unfortunately, most clay minerals do not exist as large crystal structures, which has become a recurrent challenge for experimental programs

[6]The stacking of clay layers depends on the particular clay group. Layers may be stacked closely together or water layers in the interlayer gap may occur.

aiming at their mechanical characterization. In what follows, the results of experimental tests on clay particles are presented. These experimental investigations are aimed particularly at the characterization of the elastic behavior of single crystals through the use of various methodologies. Numerical simulations of clay particles are also discussed, which address similar behaviors as those related to experiments on single clay minerals. In addition, a series of experimental values for *pure clay* in shale are discussed. These values have been reported based on extrapolations from results of macroscopic experiments on clay-mixtures and shale rocks, with the specific intent to define the in situ mechanical properties of the clay phase in shale. Indeed, the results for in situ clay behavior encompass mechanical behaviors such as particle contacts, crystal deformation, and grain boundaries, in addition to the complex intermolecular and surface behaviors attributed to clay systems. Finally, the discussions about clay mineral behavior focus on the elastic deformation which is a central aspect of this investigation.

3.5.1 Single Clay Mineral Elasticity

The challenge in the implementation of experimental testing techniques to assess the elasticity of clay minerals is intrinsically related to their small particle size. Nevertheless, successful experiments have been conducted on certain clay types such as muscovite or rectorite, which can manifest themselves as crystal structures of adequate size for direct measurements. One of the earliest direct tests on muscovite was conducted by Aleksandrov and Ryzhova [7] using ultrasonic techniques. However, experimental limitations resulted in an incomplete characterization of its elastic anisotropy, assuming henceforth hexagonal symmetry properties (5 independent elastic constants). Vaughan and Guggenheim [276] provided new measurements of muscovite using Brillouin scattering techniques. This type of light scattering technique that measures Brillouin spectra allows for the measurement of small samples such as a natural crystal of 1 mm characteristic size. The measured elasticity for the muscovite sample revealed a monoclinic elastic symmetry (13 independent elastic constants). A similar study and findings were also presented by McNeil and Grimsditch [183]. In turn, Katahara [148] proposed estimates of acoustic properties for illite minerals in shale based on muscovite data [7]. Katahara also provided estimates for chlorite and kaolinite based on acoustic velocity-density trends. A later review of Chen and Evans [57] confirmed the proposed scaling of elastic properties and density

for silicate materials. Table 3.12 summarizes the anisotropic elasticity values measured through the acoustic and optical methods here discussed. Isotropized values estimated through the Voigt-Reuss-Hill average are also listed in Table 3.12. The Voigt-Reuss-Hill (VRH) average is an empirical estimate based on the arithmetic mean of the Voigt and Reuss averages, both of which provide rigorous bounds for the elastic properties of an isotropic aggregate of crystals [123]. The VRH estimates of isotropic elastic properties of an aggregate of crystals can be calculated using the full elastic tensor of the single crystal and the arithmetic mean of the Voigt and Reuss averaging schemes. The Voigt and Reuss averages are based on the assumptions of uniform strain and stress fields, respectively. For transversely isotropic crystals, the VRH estimates yield (see e.g. [10]):

$$K_V = \frac{1}{9}(2C_{11} + C_{33}) + \frac{2}{9}(C_{12} + 2C_{13}) \tag{3.8a}$$

$$G_V = \frac{1}{15}(2C_{11} + C_{33}) - \frac{1}{15}(C_{12} + 2C_{13}) + \frac{1}{5}(2C_{44} + C_{66}) \tag{3.8b}$$

$$K_R = \frac{1}{A(C_{11} + C_{12} + 2C_{33} - 4C_{13})} \tag{3.9a}$$

$$G_R = \frac{15}{2A[2(C_{11} + C_{12}) + 4C_{13} + C_{33}] + 6(1/C_{44} + 1/C_{66})} \tag{3.9b}$$

$$K_{VRH} = \frac{1}{2}(K_V + K_R) \tag{3.10a}$$

$$G_{VRH} = \frac{1}{2}(G_V + G_R) \tag{3.10b}$$

where, K_J is the bulk modulus, G_J is the shear modulus, and $A = \left[C_{33}(C_{11} + C_{12}) - 2C_{13}^2\right]^{-1}$.

The experimental studies related to the mechanical characterization of clay minerals have been supplemented by computational modeling. Molecular dynamic (MD) simulations conducted by Seo et al. [237] yielded estimates of the anisotropic elastic properties of muscovite. The MD simulations using partial ionic two-body interatomic potentials were carried out under uniaxial and tensile stress conditions. The estimated monoclinic elasticity for muscovite is also presented in Table 3.12. High stiffness values of similar order of magnitude as those predicted

Clay mineral	Reference	Elastic constants [GPa] C_{11}	C_{12}	C_{13}	C_{33}	C_{44}	VRH averages [GPa] k^{VRH}	g^{VRH}
Acoustic and optical experiments								
Muscovite	[7]	178.0	42.4	14.5	54.9	12.2	52.2	31.6
Muscovite	[276]	184.3	48.3	23.8	59.1	16.0	59.1	34.4
Acoustic velocity - density scaling								
Kaolinite	[148]	171.5	38.9	26.9	52.6	14.8	55.4	31.8
Chlorite	[148]	181.8	56.8	90.1	96.8	11.4	99.7	24.4
Instrumented nanoindentation								
Muscovite	[302]						36.9	22.1
Rectorite	[302]						10.0	6.0
Molecular simulations								
Muscovite	[237]	250	60	35	80	35	80	49

Table 3.12: Reported anisotropic elasticity properties of single clay minerals estimated using ultrasonic, optical, and nanoindentation experiments, as well as calculated through molecular simulations. Most references report elastic properties corresponding to hexagonal (transverse isotropic) symmetry of the stiffness tensor, except for the data of Vaughan and Guggenheim [276] and Seo et al. [237]. The experiments of [276] and the molecular simulations of [237] characterized muscovite as a monoclinic elastic solid. For clarity, only a subset of elastic constants for those referenced results are presented. The Voigt-Reuss-Hill (VRH) averages for the bulk k^{VRH} and shear g^{VRH} moduli were calculated assuming a hexagonal symmetry for all the elastic estimates of clay minerals (the error of this assumption for the data of [237], [276] is less than two percent). The VRH values for Zhang et al. [302] correspond to isotropic elastic properties measured by nanoindentation.

for muscovite were also found in MD simulations of single lamella of montmorillonite conducted by Manevitch and Rutledge [169].

The collection of results presented in Table 3.12 attest to the highly anisotropic nature of clay minerals. The results of ultrasonic and optical experiments and molecular simulations also elucidate the links between particular clay atomic structures and the resulting elasticity attributes of clay crystals [169, 276]. The particularly stiff response of the minerals noted in Table 3.12 already hints towards a characteristic behavior of clay particles with well-crystallized structures. In contrast, the in situ behavior of clay particles in sedimentary rocks, which display different crystalline structures and interlayer galleries highly modified by aqueous solutions, may develop a different response. The effective in situ behavior of clay minerals in shale is presented hereafter.

3.5.2 Consolidated Clay

In contrast to direct measurements and atomistic simulations of clay minerals, the open literature on shale elasticity provides data on clay properties that correspond to extrapolated values at zero porosity for some clay samples. This type of clay properties is seen as representative of the in situ elastic behavior of the solid clay phase in clay-bearing rocks. Due to the different nature of this clay data compared to mechanical properties of single crystals, we refer to these effective properties of clay in rocks as *compacted* or *consolidated* clay. A summary of elastic properties for compacted clay reported in the open literature is presented in Table 3.13.

The clay properties reported by Hornby et al. [128] were obtained by extrapolating to zero porosity the results of core analysis by Marion et al. [171] for a saturated shale specimen with 25 percent porosity. The extrapolation procedure was based on the application of effective medium theory and an isotropic-elasticity version of the self-consistent scheme of micromechanics. Berge and Berryman [20] suggested their values to be representative properties of natural clays based on a compilation of laboratory measurements documented in Castagna et al. [52]. The values referred by Mavko et al. [175] correspond to clay acoustic properties interpreted by Castagna et al. [53] for mixed lithologies through extrapolating empirical relations to 100 percent clay content. The data used by Castagna et al. was gathered by Han et al. [112] and Blangy [28]. The values presented by Jorstad et al. [147], which are viewed as representative of pure

Reference	Bulk modulus k^s [GPa]	Shear modulus g^s [GPa]
Hornby et al. [128]	22.9	10.6
Berge and Berryman [20]	21.4	6.7
Mavko et al. [175]	25	9
Jorstad et al. [147]	26.6	7.5
Vanorio et al. [273]	12	6

Table 3.13: Reported elastic properties of compacted (consolidated) clay.

shale, were derived from an implementation of effective medium theory to the modeling of a shaley sand formation. Finally, the clay properties suggested by Vanorio et al. [273] were obtained from acoustic velocity measurements of kaolinite and Na-montmorillonite powders in dry, compacted form and in water suspension.

The comparison of Tables 3.12 and 3.13 suggests two different types of effective behavior of clay. The elasticity measured for single clay minerals clearly corresponds to the stiff nature of highly crystalline stacks of clay layers. This clay particle stiffness is of a different magnitude - two times larger or more - compared to the elasticity inferred for the solid clay phase in shale rocks. The extrapolated behaviors of clay in shale define an effective response of both clay particles and interlayer materials (water, brine solutions). Furthermore, the mechanics of interparticle contacts and grain boundaries may also contribute to the different behavior of in situ or compacted clay compared to that of stiff, single clay platelets. Further discussion of these noted elasticity behaviors will be pursued in Section 6.2, which will also include the results of the micromechanics model for shale.

3.6 Instrumented Indentation Analysis and Shale Nanomechanics - Level I

Access to the mechanical behavior of shale at nanometer length scales has become possible through the application of instrumented indentation. Indeed, it is of upmost interest to gain access to the properties of the porous clay fabric in shale (or level I of the multi-scale structure of shale) through direct measurements in order to fill in the gap in experimental understanding of these rocks. The recent application of nanoindentation to shale and other natural compos-

ites (see e.g. [66, 270, 275]) has required extending the experimental and analysis techniques for homogeneous materials to heterogeneous materials by developing experimental setups and statistical tools for identifying the properties of material constituents. In this section, brief introductions of the most salient aspects of instrumented indentation experiments and analyses are presented[7], followed by a summary of the experimental results for the mechanical properties of shale at nanoscales developed by Ulm and co-workers [2, 32]. In addition, a recent development in the statistical analysis of nanoindentation data is presented, which provides a more robust interpretation of indentation data for shale. Finally, the relevant experimental data of shale at nanoscales used for the development of shale micromechanics models are summarized.

3.6.1 Overview of the Indentation Experiment

Instrumented indentation is a surface test that provides access to the bulk properties of the investigated material using the tools of continuum mechanics for interpreting the measured mechanical responses. An indentation test consists in pressing an indenter tip of known geometric and mechanical properties orthogonally onto the surface of the material of interest. During such a test, the load P applied to the indenter and the depth h of the indenter with respect to the material surface are continuously recorded, as shown in Figure 3-2. The resulting load–displacement curve defines the characteristic mechanical response of the tested material system and could be used for extracting elastic, strength, and creep properties.

The apparent simplicity of this test belies its complexity when aiming at measuring mechanical responses at sub-micrometer length scales, for which advanced measuring devices based on electromechanical components have been developed. The development and use of instrumented nanoindentation has been the target of significant research over the past two decades (see e.g. [59, 200] for recent reviews). The current and most common applications of this technique are for homogeneous material samples and thin films. The reader is referred to the works of Ulm and co-workers [31, 64, 274] for comprehensive reviews of instrumented nanoindentation applications, details of the experimental procedures, testing equipment, specimen preparation, and other important aspects relevant to the implementation of the experimental technique. In what

[7] The presentation of the principles of instrumented indentation experiments and analysis is inspired from the works of G. Constantinides, C. Bobko, and M. Vandamme [31, 64, 274].

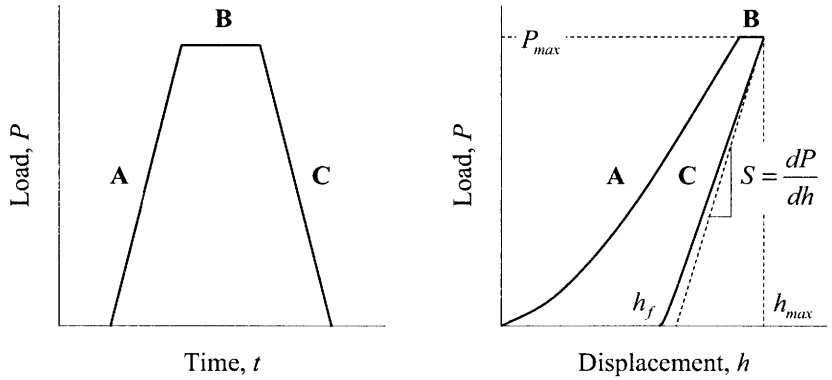

Figure 3-2: Schematic illustrations of the indentation loading function (left) and a typical load-displacement response (right), showing important measured parameters. The loading phases are: (A) loading, (B) holding, and (C) unloading. S corresponds to the slope of the unloading curve at the maximum indentation load $P_{\max}$, $h_{\max}$ is the maximum displacement or indentation depth, and h_f is the final depth, corresponding to the permanent depth of penetration after full unloading.

follows, this presentation focuses on the theoretical background necessary to assess the results from experimental nanoindentation. In particular, the discussions will lead to the presentation of an extension of instrumented nanoindentation for elasticity and strength characterization of heterogenous materials and the specific application to shale.

3.6.2 Self-Similarity of the Indentation Test

One important feature in the analysis of indentation experiments that allows linking measured parameters to material properties is the self-similarity of the indentation test. A time-developing phenomenon is noted as *self-similar* if the spatial distributions of its properties at different times can be obtained from one another by a similarity transformation [13]. As a result, the self-similarity property of a problem simplifies its investigation. In indentation testing, self-similarity implies that the displacement fields at any load P can be inferred from the displacement fields at a different load P_0. A set of three conditions determine the self-similarity character of an indentation problem [39, 40]. First, the shape of the indenter probe must be described by a homogeneous function with degree greater than or equal to unity. Second, the constitutive relations of the indented material must be homogeneous functions of stress and

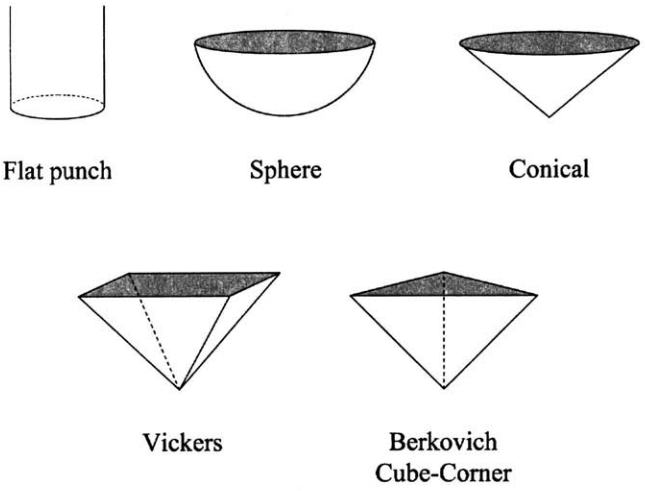

Figure 3-3: Indenter probes of different geometries.

strain. Finally, the loading at any point must be increasing during the contact process. These conditions related to the self-similarity of indentation tests are further detailed in this section[8].

Indenter Shapes and Geometric Similarity

A series of relevant indenter probes is schematically shown in Figure 3-3. Although rarely used in indentation testing, the flat punch indenter probe is important from a theoretical perspective. The related analysis of the indentation contact problem is greatly simplified by the constant contact surface between the probe and the indented surface during testing. The spherical indenter probe enables the testing of elastic properties at small load magnitudes, and it is mostly used for soft materials. In practice, the most used indenter shapes are pyramidal indenter probes such as the Berkovich, Vickers and Cube-Corner probes. Their sharp geometries allow for the testing of volumes of material smaller than what other geometries can probe. However, this same feature generates stress concentrations at the probe tip, which result in plastic deformation for the material being solicited even at low load magnitudes. The indentation testing of shale materials involved the extensive use of the Berkovich indenter [32].

[8]This section follows the presentation of M. Vandamme [274] of the subject.

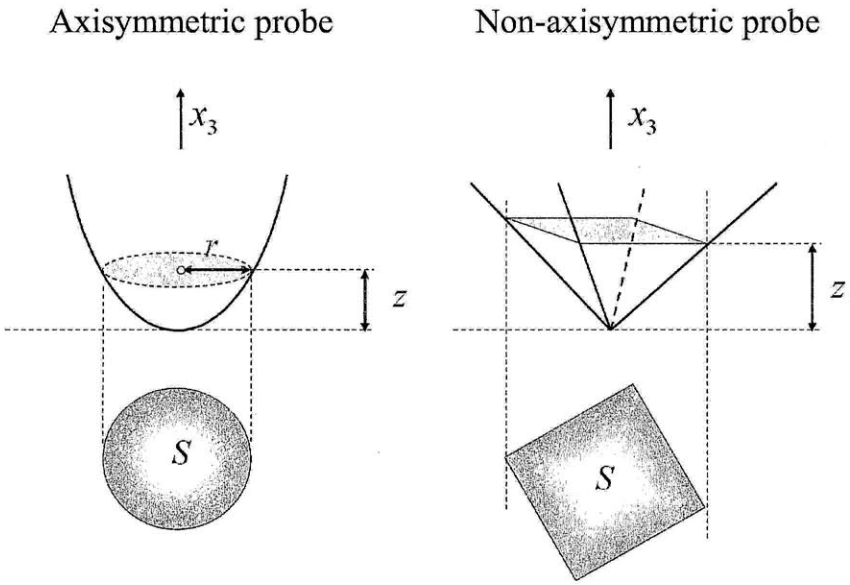

Figure 3-4: Parameters defining the geometry of an indenter probe. z is the indentation height, and S the cross-sectional area. For an axisymmetric probe, r is the radius. Adapted from [274].

For a given probe within a Cartesian coordinate system $O(x_1, x_2, x_3)$ where the probe tip is at the origin and the depth of the probe is in the direction x_3 (Figure 3-4), the height z of the surface of the probe verifies the following relation:

$$z(\lambda x_1, \lambda x_2) = \lambda^d z(x_1, x_2) \text{ with } \lambda > 0 \tag{3.11}$$

where d is the degree of the homogeneous function. For axisymmetric problems, (3.11) simplifies to:

$$z(r) = Br^d \tag{3.12}$$

where r is the radius of the probe at a given height z, and B a proportionality factor that represents the radius at $r = 1$, as shown in Figure 3-4. The degree d and the proportionality factor B for the probes presented in Figure 3-3 are provided in Table 3.14.

Two objects that can be transformed into each other by dilation or contraction are *geometrically similar.* Applied to the shapes in Figure 3-3, all flat punch probes are geometrically similar. Two spherical probes of different radii are also geometrically similar to each other. In contrast,

Probe type	d	B
Flat punch	$\to \infty$	$1/(a^n)$
Spherical	2	$1/(2R)$
Conical	1	$\cot(\theta)$
Pyramidal	1	$\cot(\theta^{eq})$

Table 3.14: Degree d of the homogeneous function and proportionality factor B for various indenter probes.

Probe type	Equivalent half-cone angle, θ_{eq}
Berkovich	70.32°
Vickers	70.32°
Cube Corner	42.28°

Table 3.15: Equivalent half-cone angle θ_{eq} for various pyramidal probes.

pyramidal indenter probes are invariant when contracted or dilated. That is, pyramidal and conical indenters are similar to themselves, and hence said to be *geometrically self-similar*. For the purpose of indentation analysis and making use of this geometric self-similarity, the non-axisymmetric pyramidal probes are approximated by axisymmetric cones of same degree $d = 1$. Such approximation greatly simplifies the analysis of the indentation experiment. The mentioned approximation is achieved by the implementation of an equivalent half-cone angle θ_{eq}, whose corresponding cone gives the same projected cross-section area S for a given height z as the original pyramidal indenter probe. The equivalent half-cone angles of common pyramidal probes are provided in Table 3.15.

Material Behavior

The self-similarity of an indentation experiment entails that the constitutive relations of the indented material must be homogeneous with respect to the resulting strains (or strain rates) or stresses. This condition expresses that the operator of constitutive relations F, and thus the stress tensor $\boldsymbol{\sigma}(\boldsymbol{\varepsilon})$, must scale as:

$$F(\lambda\boldsymbol{\varepsilon}) = \lambda^{\kappa} F(\boldsymbol{\varepsilon}) \tag{3.13}$$

where $\boldsymbol{\varepsilon}$ is the strain tensor, and κ the degree of the homogeneous constitutive function F. Linear and non-linear elasticity satisfy this requirement provided that [38]:

$$\boldsymbol{\sigma} = \mathbb{C}(\boldsymbol{\varepsilon}) : \boldsymbol{\varepsilon} \tag{3.14}$$

$$\mathbb{C}(\lambda\boldsymbol{\varepsilon}) = \lambda^{\kappa-1}\mathbb{C}(\boldsymbol{\varepsilon}) \tag{3.15}$$

where $\mathbb{C}(\boldsymbol{\varepsilon})$ is the secant stiffness tensor. $\kappa = 1$ corresponds to the case of linear elasticity. Condition (3.13) is also satisfied for the behavior at the rigid plastic limit, for which the stress derives from the dissipation (or support) function $\boldsymbol{\sigma} : \boldsymbol{\varepsilon} = \pi(\mathbf{d})$ [83]:

$$\boldsymbol{\sigma} = \frac{\partial \pi}{\partial \mathbf{d}}(\mathbf{d}) \tag{3.16}$$

where $\pi(\mathbf{d})$ is a homogeneous function of degree 1 with respect to the strain rate $\mathbf{d}$, such that:

$$\pi(\lambda\mathbf{d}) = \lambda\pi(\mathbf{d}) \tag{3.17}$$

Consequently for the rigid plastic limit, yield design solutions applied to indentation analysis satisfy the self-similarity condition (3.13) with $\kappa = 0$.

It is worth noting that not all materials satisfy condition (3.13). For instance, consider the case of linear-elastic, perfectly-plastic materials, for which $\kappa = 1$ within the elastic domain, and $\kappa = 0$ at the limit of the elastic domain, corresponding to the strength limit. In this case, there is no unique value of parameter κ for which condition (3.13) holds for all strain levels eventually present in the indentation test. Consequently, indentation testing performed on linear-elastic, perfectly-plastic materials are not self-similar. In general terms, whenever the material response of the indented half-space is not governed uniformly by the same class of material behavior characterized by the parameter κ, the non-homogeneous stress distribution within the indented half-space may imply the loss of self-similarity of the indentation test.

Self-Similar Scaling Relations

Provided that conditions (3.11) and (3.13) are satisfied, the loading phase of an indentation test possesses self-similarity (see Figure 3-2). Hence, given a known indentation response,

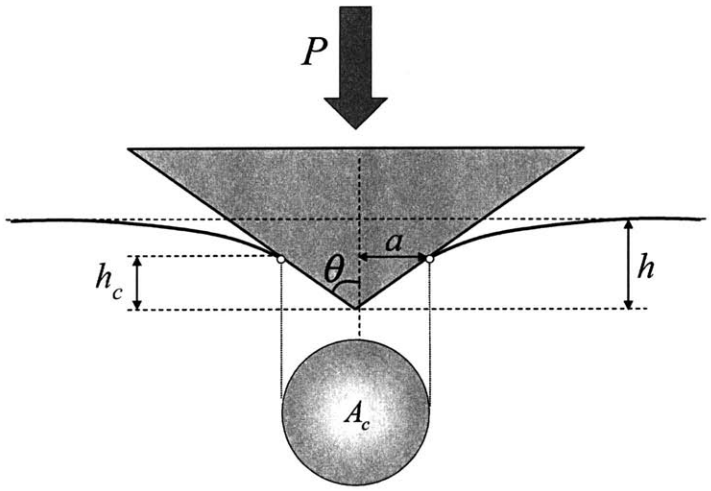

Figure 3-5: Geometric description of a conical indentation test. P is the indentation load, h the indentation depth, h_c the contact depth, A_c the projected area of contact, and a the contact radius [274].

represented by load P_0, indentation depth h_0, contact depth $(h_c)_0$, and projected area of contact $(A_c)_0$ (see Figure 3-5), the indentation response (P, h, h_c, A_c) is obtained from a similarity transformation [37]:

$$\frac{P}{P_0} = \left(\frac{h}{h_0}\right)^{\frac{2+\kappa(d-1)}{d}} \tag{3.18}$$

For the case of elastic behavior ($\kappa = 1$), $P \propto h$ for a flat punch, and $P \propto h^{3/2}$ for a spherical indenter. In contrast, for a conical or pyramidal indenter probe ($d = 1$), $P \propto h^2$ irrespective of the material behavior. This scaling relation provides a strong argument in favor of using the Berkovich indenter, as self-similarity will prevail irrespective of the constitutive relations.

Another relation obtained from the self-similarity of the indentation test is [37]:

$$\frac{h}{h_0} = \left(\frac{A_c}{(A_c)_0}\right)^{\frac{d}{2}} \tag{3.19}$$

A combination of the previous two scaling relations readily shows that the average pressure below the indenter – or indentation hardness $H = P/A_c$ – scales as:

$$\frac{H}{H_0} = \left(\frac{h}{h_0}\right)^{\frac{\kappa(d-1)}{d}} \tag{3.20}$$

Consequently, the hardness H is constant throughout the loading process and does not depend on the applied load for any rigid plastic behavior ($\kappa = 0$) or for any pyramidal or conical indenter shape ($d = 1$).

Finally, (3.19) can be rewritten as follows by noting that $A_c = \pi a^2$, where a is the contact radius:

$$\frac{a^d}{h} = cst. \tag{3.21}$$

For axisymmetric probes, in which the contact radius a and the contact depth h_c are linked by $h_c = Ba^d$, an equivalent expression is given by:

$$\frac{h_c}{h} = cst. \tag{3.22}$$

Expression (3.22) determines that the contact height-to-indentation depth ratio h_c/h does not depend on the load P, provided the self-similarity of the indentation test. This result is of critical importance for indentation analysis and forms much of the basis of indirect methods of determination of the projected area of contact A_c in the contact problem, which is a key quantity used for linking measured responses to material properties.

3.6.3 Indentation Analysis of Elastic and Strength Properties

The translation of the material response measured in an indentation test into mechanical quantities requires the solution of the contact problem between the indenter and the material surface using the tools of continuum mechanics modeling. For indentation testing, the measured response is condensed into two indentation properties: the indentation modulus M, and the indentation hardness H:

$$M \overset{def}{=} \frac{\sqrt{\pi}}{2}\frac{S}{\sqrt{A_c}} \tag{3.23}$$

$$H \overset{def}{=} \frac{P_{\max}}{A_c} \tag{3.24}$$

where P is the applied maximum indentation load, $S = dP/dh$ the measured initial slope of the unloading branch of the $P - h$ curve, and A_c the projected area of contact between the indenter tip and the indented material (see Figure 3-5). Although elastic indentation solutions

provide direct means to determine the contact area A_c from the contact depth-to-indentation depth relation h_c/h (the Galin-Sneddon solution [94, 244]), the projected contact area for other material behaviors (e.g. elasto-plasticity) is a priori an unknown of the contact problem[9]. Fortunately, indirect methods have been designed for determining the contact area in terms of the maximum depth measured in the indentation experiment, $h_{\max}$. One of the most prominent methods was proposed by Oliver and Pharr [199], which is based on the determination of the contact height h_c from the elastic contact solution involving measurable quantities:

$$h_c = h_{\max} - \epsilon \frac{P_{\max}}{S} \tag{3.25}$$

where the constant ϵ does not vary much for different indenter probes (0.72, 0.75, 1 for cone, sphere, and flat punch geometries, respectively). Once this estimate is available, the contact area can be calculated using the self-similar properties of the indentation test, which for the case of a Berkovich indenter yields:

$$A_c\left(h_c\right) = 24.56 h_c^2 \tag{3.26}$$

The next task of indentation analysis is to link the measured indentation parameters (the indentation modulus and hardness) to meaningful mechanical properties of the indented material.

Indentation Modulus

The definition of the indentation modulus M (3.23), introduced by Bulychev, Alekhin, and Shorshorov [48], derives from the consideration of the contact problem between an elastic half-space and a rigid axisymmetric indenter[10]. The indentation modulus linked to an isotropic

[9] It is important to note that definition (3.23) was developed in the framework of elastic media. However, extensive research has shown that such definition can be applied to the unloading branch for material systems exhibiting e.g. elasto-plastic behavior, to extract their elasticity content [35, 58, 211].

[10] The contact-mechanics problem related to the indentation setup finds its theoretical basis in the works of Hertz, Love, Galin, Sneddon, and Boussinesq, among others. The form of the BASh formula in (3.23) is the preferred presentation of the indentation problem in terms of measurable quantities.

medium corresponds to the plane-stress modulus [94, 244]:

$$M = \frac{E}{1-\nu^2} \tag{3.27}$$

where E is the Young's modulus, and ν the Poisson's ratio of the indented isotropic material. The solution for the case of anisotropic elasticity is more involved, as the indentation modulus depends on the direction of the indentation load with respect to the material elasticity symmetry. General solutions for anisotropic media have been proposed (e.g. [250, 279]); however, more compact expressions have been derived for specific material symmetries. Of particular importance to this investigation is the case of transversely isotropic elasticity, which is an attribute of shale materials (at least from a macroscopic scale perspective). For a transverse isotropic half-space with the material symmetry oriented in the x_3-direction, the indentation moduli $M_i = M(x_i)$ obtained from indentation directed in the principal material axis x_i are related to the five independent elastic constants by [72]:

$$M_1 = M(x_1) = M(x_2) \approx \sqrt{\sqrt{\frac{C_{11}}{C_{33}}}\frac{C_{11}^2 - C_{12}^2}{C_{11}} M_3} \tag{3.28a}$$

$$M_3 = M(x_3) = 2\sqrt{\frac{C_{11}C_{33} - C_{13}^2}{C_{11}}\left(\frac{1}{C_{44}} + \frac{2}{\sqrt{C_{11}C_{33}} + C_{13}}\right)^{-1}} \tag{3.28b}$$

where the Voigt notation was used to denote the elastic constants $C_{11} = C_{1111}$, $C_{12} = C_{1122}$, $C_{13} = C_{1133}$, $C_{33} = C_{3333}$, $C_{44} = C_{1313} = C_{2323}$.

Indentation Hardness

One of the primary intents of indentation testing, from its early applications, was the measurement of hardness as a parameter used for material characterization. Early experimental observations linked hardness measurements to the strength of metals [42]. Based on a slip-line field solution for the indentation problem involving a rigid, cohesive plastic solid and a frictionless rigid wedge, Tabor suggested a hardness-to-yield strength relation of the form $H/Y = 3$, which is a well-known rule of thumb for cohesive materials [251]. For frictional materials, a variability of the hardness-to-compressive strength on the order of $H/Y_C \simeq 20 - 30$ has been observed experimentally [63, 151, 136], which highlights the contribution of the internal fric-

tion to the measured hardness. Numerous studies on a several types of material behaviors (e.g. elastic-perfectly plastic, work-hardening plasticity) have suggested that hardness is not an intrinsic material properties, but rather a snapshot of mechanical properties of the indented material and the influence of the indenter geometry [59, 144].

Recently, the use of yield design approaches have advanced the application of indentation analysis for linking the hardness measured in indentation testing and strength properties of the cohesive-frictional materials, which are of relevance to our topic of investigation. Ganneau et al. [95] developed a dual indentation approach based on the upper bound theorem of yield design to access the cohesion and friction of a Mohr-Coulomb solid from the dependence of hardness and cohesion on the indenter cone angle. Cariou et al. [50] and Gathier and Ulm [98] extended the use of the yield design approach to treat the hardness response of porous solids with a Drucker-Prager solid phase. In particular, the approach of Gathier and Ulm [98] offers a robust means for establishing the relations between measured hardness H, porosity (expressed as one minus the packing density η), and the solid's cohesion and friction properties (c^s, α). The simulated scaling relations[11] follow the form [98]:

$$H = h^s\left(c^s, \alpha\right) \times \Pi_H\left(\alpha, \eta\right) \tag{3.29}$$

where $\Pi_H\left(\alpha, \eta\right)$ is a dimensionless function to be developed, and $h^s\left(c^s, \alpha\right) = \lim_{\eta \to 1} H$ is the asymptotic hardness of the cohesive-frictional solid phase that obeys the Drucker-Prager criterion[12]. This asymptotic value relates the solid's cohesion c^s, and friction coefficient α, by the function:

$$h^s = c^s \times a\left(1 + b\alpha + (c\alpha)^3 + (d\alpha)^{10}\right) \tag{3.30}$$

[11] The relations between the measured indentation hardness and the material's strength properties correspond to a simulated indentation experiment on a granular, isotropic porous solid with a conical indenter with equivalent cone angle to a Berkovich tip. This configuration of the simulated indentation experiment is relevant for applications to shale.

[12] The Drucker-Prager plasticity criterion is an isotropic shear-friction strength criterion, which will be used for the strength modeling of shale in Part IV of this thesis.

with fitted parameters:

$$\begin{cases} a = 4.7644 \\ b = 2.5934 \\ c = 2.1860 \\ d = 1.6777 \end{cases}$$

The dimensionless function $\Pi_H \in [0,1]$ depends on the packing density η and the friction coefficient α, and it given by a limit development around α:

$$\Pi_H(\alpha,\eta) = \Pi_1(\eta) + \alpha(1-\eta)\ \Pi_2(\alpha,\eta) \tag{3.31}$$

where the first part of the function is independent of the friction coefficient. The expressions for $\Pi_1(\eta)$ and $\Pi_2(\alpha,\eta)$ are given by:

$$\Pi_1(\eta) = \frac{\sqrt{2(2\eta-1)} - (2\eta-1)}{\sqrt{2}-1}\left(1 + g(1-\eta) + h(1-\eta)^2 + j(1-\eta)^3\right) \tag{3.32a}$$

$$\Pi_2(\alpha,\eta) = \frac{2\eta-1}{2}\left(k + m(1-\eta) + p(1-\eta)\alpha + q\alpha^3\right) \tag{3.32b}$$

with fitted parameters:

$$\begin{cases} g = -5.3678 & k = 6.7374 \\ h = 12.1933 & m = -39.5893 \\ j = -10.3071 & p = 34.3216 \\ & q = -21.2053 \end{cases}$$

These smooth, closed-form functional relations between packing density, cohesive-frictional strength parameters, and indentation hardness have been implemented for inferring the strength properties of the solid clay phase in shale from nanoindentation data [31].

3.6.4 Grid Indentation Technique for Heterogeneous Materials

The extensive use of indentation testing for material characterization has been related so far to applications for homogeneous materials and thin films. For heterogeneous materials, the direct application of the indentation technique is challenged by the occurrence of heterogeneities manifesting themselves at different length scales, such as in natural composites (e.g. concrete,

rocks, bone). In principle, one approach is the indentation on specific material phases previously identified through visual means. However, this method clearly becomes not practical for large scale testing programs. Ulm and co-workers [63, 65, 270] have proposed the so-called *grid indentation technique*, which is based on conducting a large grid of indentations over the surface of the heterogeneous medium of interest. Provided the adequate choices for the indentation depth and grid size, each indentation experiment could be regarded as statistically independent, which opens a way for the application of statistical techniques to interpret the indentation results in terms of mechanical properties of the material phases.

The grid indentation principle can be introduced by considering an indentation test on an infinite half-space composed of two different material phases with contrasting properties, as schematically shown in Figure 3-6. Performing an indentation on a random location in the specimen surface should provide access to the properties of either of the phases given that the indentation depth is much smaller than their characteristic sizes. In contrast, a much deeper indentation compared to the size of the phases should probe the composite mechanical response via mechanical homogenization [65]. Consequently, the adequate choice of an indentation depth for soliciting the mechanical properties of the material phases involves a more detailed analysis, because the new length scales added to the indentation problem must meet criteria for statistical sampling and scale separability conditions from continuum mechanics analysis.

To achieve statistical independence in the sampling process, the grid size L must be much larger than the imprint of the indentation test. Furthermore, a large number of tests N are necessary in order to avoid sampling effects, which entails the use of a sufficiently large testing surface compared to the individual material phases of size D. Keeping in mind the objective of retrieving properties of the individual phases, the indentation depth h (which is related to the size of the indentation imprint) should be much smaller than the length scale of the phases[13]. The previous conditions can be summarized as:

$$h \ll D \ll L\sqrt{N} \tag{3.33}$$

[13] Finite element simulations for indentation testing using a Berkovich probe have shown that the measured elastic response during testing corresponds to a material volume that is 3 to 5 times the depth of indentation [157].

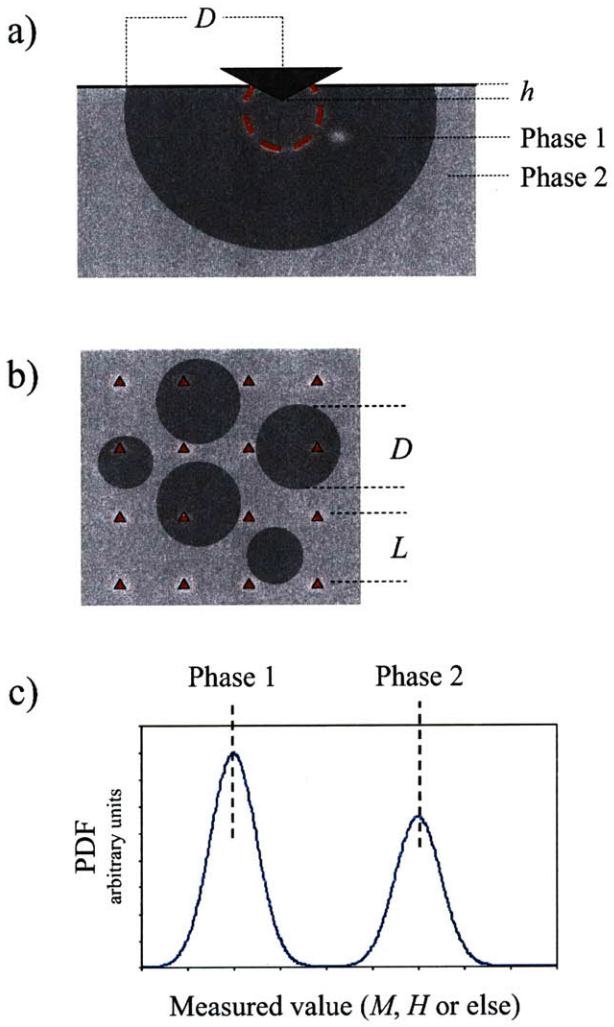

Figure 3-6: Schematic of the principle of grid indentation analysis performed on a two-phase, heterogeneous material. a) Characterization of intrinsic phase properties from shallow indentation depths. The dashed circle represents the volume of the material probed during testing. b) Indentation tests, represented as triangles, provide access to the mechanical properties of either of the two phases. Indentations are performed in a grid arrangement. c) Resulting probability density function (PDF) for each of the measured properties. Adapted from [274].

With regard to the interpretation of indentation results, the length scales involved in the indentation test must conform to the scale separability condition of continuum mechanics for the use of continuum scale modeling:

$$d \ll l \ll h \tag{3.34}$$

where l is the characteristic size of the representative elementary volume, which must be larger than the characteristic length scale of the largest heterogeneity d contained in the representative elementary volume (rev), and smaller than the scale of indentation defined by the indentation depth h. A more detailed discussion about the scale separability condition of continuum mechanics will be presented in Chapter 4.

The application of the grid indentation entails performing a large set of indentations as displayed in Figure 3-6b. Although a few indentations may probe the composite response of the two material phases (e.g. at phase boundaries or thin layers), enforcing the scale separability condition will result in a majority of the indentations capturing the intrinsic properties of the phases. As an illustration, the experimental results are displayed as probability density functions (Figure 3-6c) of the measured indentation properties: the indentation modulus M and the indentation hardness H. For the discussed two-phase material, two peaks are present, whose mean values represent the mean mechanical properties of the phases.

The next challenge for the grid indentation technique is very evident for the case of a real material specimen that diverges from the discussed two-phase composite. To illustrate this challenge, Figure 3-7 displays three different nanoindentation responses measured by Bobko and Ulm [32] for a shale sample. At the length scale of the experiment, the measured indentation curves characterize the responses of a typical quartz inclusion (curve a) and of the porous clay composite in different indentation directions (curves b,c). The measured load–depth curves testify to the contrast of mechanical properties between the stiffer quartz inclusions and the more compliant clay fabric. In addition, atomic force microscopy (AFM) photo images were performed on similar material locations, which provide a visual perspective of the indentation imprints on the material surfaces. Clearly in this case, we can characterize the response of these two material phases by combining the visual information and the measured mechanical response for each indentation event. However, for a large array of indentation tests such an approach is not feasible. Figure 3-8 displays the measured indentation modulus and hardness

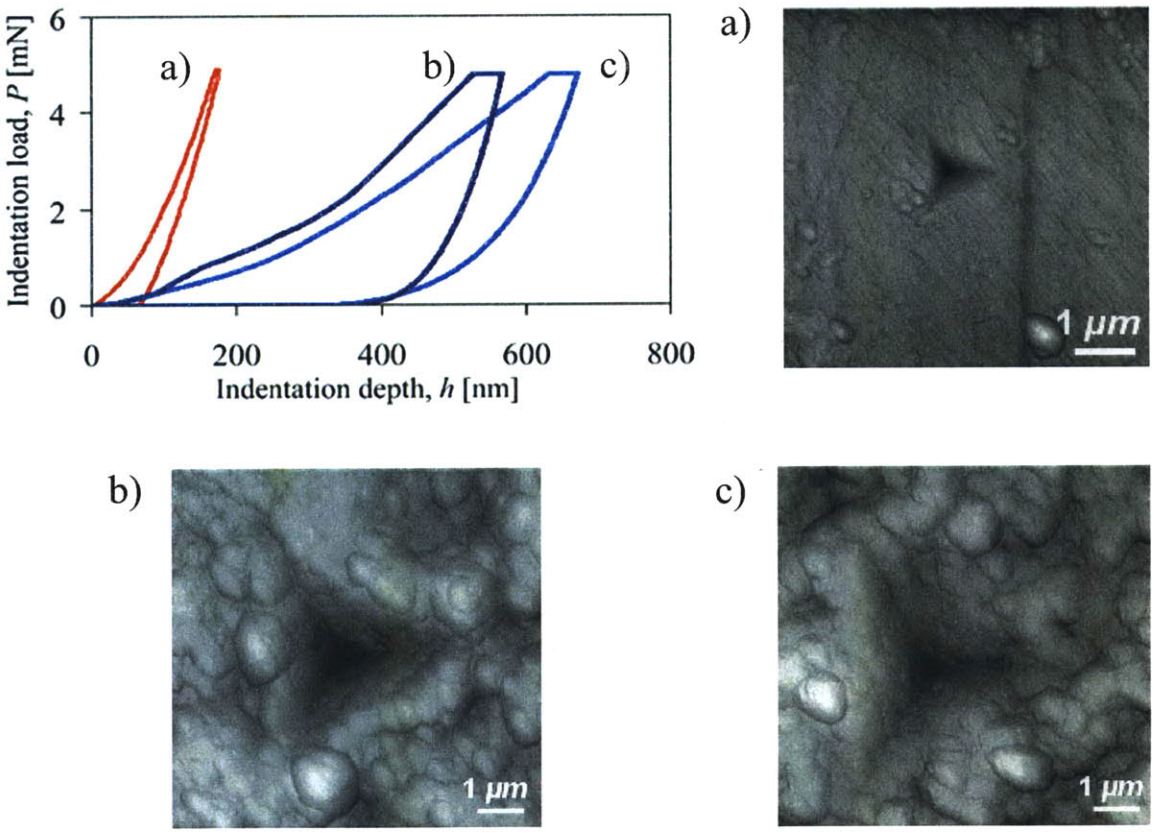

Figure 3-7: Indentation responses on shales indented to a maximum load of 4.8 mN. Curve (a) is typical of indentation on a quartz inclusion, whereas the curves (b) and (c) are typical of indentation on the porous clay composite. Curve (b) is from indentation in the x_1-direction and curve (c) is from indentation in the x_3-direction. The other three images are AFM photo simulations after a 4.8 mN indent on (a) a quartz inclusion in the x_3-direction, (b) the porous clay composite in shale G2IC-03 in the x_1-direction, and (c) the porous clay composite in G2IC-03 in the x_3-direction. Adapted from [32].

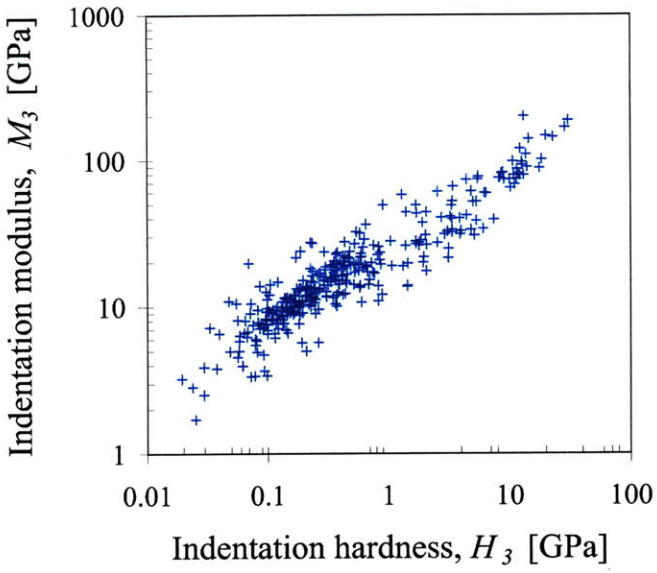

Figure 3-8: Indentation properties measured for the G-03 shale sample in the normal-to-bedding (x_3) direction. Each experimental point corresponds to a single indentation event.

for a shale specimen in terms of a scatter plot, in which each data point corresponds to a single indentation test. The standing challenge is to identify and characterize the active mechanical phases measured by instrumented indentation as in Figure 3-8. With the framework of the grid indentation testing in place, we turn to the application of statistical tools to extract mechanical information for each material phase present from the measured indentation properties.

3.6.5 Statistical Analysis of Indentation Data

The analysis of the experimental data collected through the grid indentation technique calls for the use of statistical methods for identifying the different phases present in the composite material. A first development addressing this need was proposed by Constantinides et al. [63]: the so-called deconvolution technique, which was further developed in subsequent works [65, 66]. In essence, the deconvolution technique seeks to fit a number of probability density functions to the experimental frequency plot of the measured indentation quantity (indentation modulus or hardness). Improved algorithms regarding the automatization of the deconvolution procedures using cumulative distributions functions have been later introduced [270]. More recently,

Krakowiak et al. [153] resorted to the use of multi-variate mixture modeling for addressing the statistical analysis of indentation data. Before the presentations of these methods, a common issue to both approaches is first discussed regarding the choice of the phase distribution functions characterizing the material phase data.

Choice of Phase Distribution Functions

The first task in the statistical modeling of the grid indentation data is specifying the form of the model distributions associated with the properties of each material phase. For simplicity, the display of the material properties in the forms of probability distribution functions (PDF) is adopted in this discussion, as shown in Figure 3-9.

A distribution function is uniquely defined by its moments (i.e. mean, variance, skewness, and higher-order moments). The first assumption in the statistical modeling is that each phase of the heterogeneous material has its own indentation property values, associated with the actual properties of the phase. These phase properties correspond to the mean of the model phase distribution. If the indentation measurements were perfect, the resulting data would be expected as sharp peaks (Figure 3-9a). However, some spread of the data is anticipated, related to noise in experimental measurements and the intrinsic variability of the phase properties in a natural material. The second assumption is that such variability is distributed evenly around the mean value (Figure 3-9b). Finally, the application of grid indentation on the heterogeneous surface of the material will invariably result in some measurements probing composite responses of two or more material phases at a particular grid indentation location. The analysis of such a composite response is clearly a challenge; although, it is expected that it will be bounded by the values of the individual phases (Figure 3-9c). The event of a mechanical composite response measured by grid indentation will result in asymmetries in the modeled peaks. In a first approach, a symmetric form of distribution (i.e. zero skewness) could be adopted to characterize all peaks. The previous set of observations and assumptions leads to adopting the normal, or Gaussian, distribution as a first approximation for modeling the experimental data of each material phase.

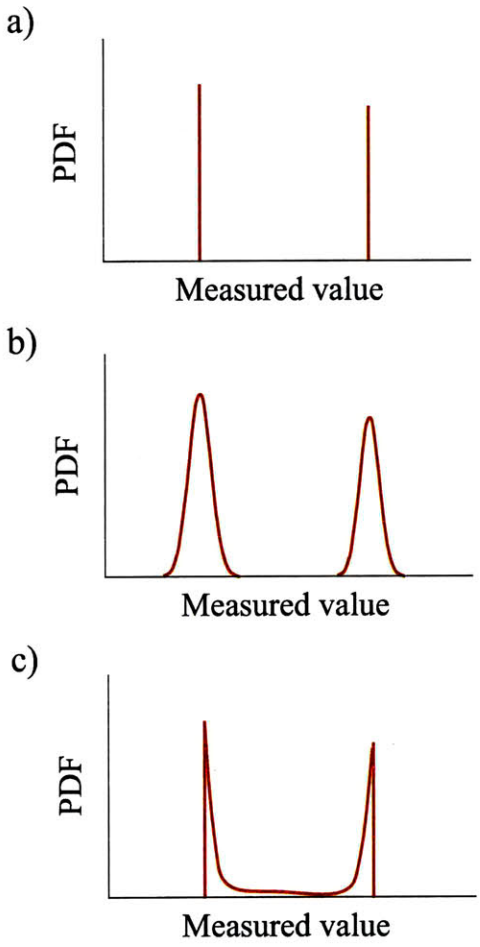

Figure 3-9: Probability density functions (PDF) for a two-phase material. a) Perfect measurements and materials. b) Imperfect measurements or materials. c) Perfect measurements and material with some composite responses. Adapted from [274].

Deconvolution Technique

The implementation of the deconvolution technique [31, 63, 274] for the analysis of indentation data begins with the generation of the experimental cumulative distribution function (CDF). Let n be the number of indentation tests performed on a specimen and $\{Y_j\}_{j=1..n}$ the sorted values of the measured property to be deconvoluted. The Y_j parameter can be the indentation modulus M or the indentation hardness H obtained from the indentation test. The points of the experimental CDF of Y, denoted by F^Y, are obtained from:

$$F^Y(Y_j) = \frac{j}{n} - \frac{1}{2n};\ \text{for } j \in [1, n] \tag{3.35}$$

Once the experimental CDFs are known, the form of the model CDFs are specified. For this, consider the heterogeneous material to be composed of g-material phases with sufficient contrast in mechanical phase properties. Each phase occupies a volume fraction π_i of the indented surface. In an a priori analysis, an adequate choice for the distribution of the mechanical properties of each phase is a Gaussian distribution, designated by its mean value μ_i^Y and its standard deviation σ_i^Y. The CDF of the i-th Gaussian distributed phase is given by:

$$F(Y_j; \mu_i^Y, \sigma_i^Y) = \frac{1}{\sigma_i^Y \sqrt{2\pi}} \int_{-\infty}^{Y_j} \exp\left(\frac{-(u-\mu_i^Y)^2}{2(\sigma_i^Y)^2}\right) du \tag{3.36}$$

The unknowns $\{\pi_i, \mu_i^Y, \sigma_i^Y\}$ for $j \in [1, n]$ are determined by minimizing the difference between the experimental CDFs and the weighted model CDFs:

$$\min \sum_{j=1}^{n} \sum_{Y} \left(\sum_{i=1}^{g} \pi_i F(Y_j; \mu_i^Y, \sigma_i^Y) - F^Y(Y_j) \right)^2$$

$$s.t. \tag{3.37}$$

$$\sum_{i=1}^{g} \pi_i = 1$$

where the constraint of the minimization problem requires that the volume fractions of the different phases sum to one. To ensure that phases have sufficient contrast in properties, and thus to avoid that two neighboring Gaussians completely overlap, the optimization problem is

additionally constrained by:

$$\mu_i^Y + \sigma_i^Y \leq \mu_{i+1}^Y + \sigma_{i+1}^Y \tag{3.38}$$

The deconvolution methodology can be automated and performed by a non-linear solver in MATLAB [31, 274].

The deconvolution technique has two important drawbacks. First, the construction of the probability or cumulative distribution functions from the indentation data relies on the sorting of measured values for the indentation modulus and hardness. Consequently, an underlying assumption to the method is that the measured properties follow a trend of increasing indentation modulus – increasing hardness, which may be only appropriate for heterogeneous composites in which the dominating heterogeneities affect the elasticity and hardness properties in similar manners. A clear example would be a weakening effect of porosity on the response of a solid matrix. A second limitation of the deconvolution technique is the a priori choice of the number of model phases used for the fitting of experimental data. In the next section, the implementation of a maximum likelihood mixture model is discussed for treating the multi-variate data of grid indentation.

Multi-Variate Mixture Modeling

An alterative statistical analysis to the deconvolution technique is the application of a mixture modeling technique for the interpretation of grid indentation data. The maximum likelihood mixture modeling approach to clustering analysis provides a robust means for identifying the mechanical active phases in shale and their corresponding elasticity and hardness properties. In addition to treating multi-variate data, the maximum likelihood mixture modeling approach identifies the optimal number of constitutive phases and the degree of accuracy for the clustering of data corresponding to each identified phase. The use of the mixture modeling to resolve the clustering problem of grid indentation was introduced by Krakowiak et al. [153], who presented applications of the technique to different data sets of composites (e.g. cement paste, masonry).

Finite mixture modeling is a well-established approach for the statistical characterization of data derived from multiple populations or components in varying proportions. Mixture models are also widely adopted in cluster analysis due to their usefulness in identifying groups (components) for which no prior information is provided regarding their structures or properties.

In particular, normal mixture models are increasingly used to model multi-variate data based on efficient iterative solutions by maximum likelihood (ML) via the expectation-maximization (EM) algorithm [73, 178, 180, 258]. This methodology is certainly well-suited for the analysis of grid indentation data.

The mixture modeling for grid indentation data begins by considering each indentation event $\mathbf{y}_j$ to be a realization of the random, two-dimensional vector $\mathbf{Y} = \left(\mathbf{Y}_1^T, ..., \mathbf{Y}_n^T\right)$, where n is the total number of grid indentations. The two dimensions correspond to the indentation modulus and hardness attributes, respectively, that were measured for each of the n tests. For the case of a mixture of normal components, the probability density function $f(\mathbf{y}_j)$ of the observed data $\mathbf{y}_j$ in $\mathbf{Y}_j$ with a g-component mixture is:

$$f(\mathbf{y}_j; \boldsymbol{\Psi}) = \sum_{i=1}^{g} \pi_i c(\mathbf{y}_j; \boldsymbol{\mu}_i, \boldsymbol{\Sigma}_i) \tag{3.39}$$

where π_i are the mix proportions with $0 \leq \pi_i \leq 1$ and $\sum_{i=1}^{g} \pi_i = 1$, $\boldsymbol{\Psi} = \left(\pi_1, ..., \pi_{g-1}, \boldsymbol{\xi}^T\right)^T$ with $\boldsymbol{\xi}$ containing the (unknown) elements of the group means $\boldsymbol{\mu}_i$ and variance-covariance matrices $\boldsymbol{\Sigma}_i$, and $c(\mathbf{y}_j; \boldsymbol{\mu}_i, \boldsymbol{\Sigma}_i)$ corresponds to the multi-variate normal density:

$$c(\mathbf{y}_j; \boldsymbol{\mu}_i, \boldsymbol{\Sigma}_i) = \frac{1}{\sqrt{2\pi}} (\boldsymbol{\Sigma}_i)^{-\frac{1}{2}} \exp\left[-\frac{1}{2} (\mathbf{y}_j - \boldsymbol{\mu}_i)^T (\boldsymbol{\Sigma}_i)^{-1} (\mathbf{y}_j - \boldsymbol{\mu}_i)\right] \tag{3.40}$$

Assuming that indentations $\mathbf{y}_1, ..., \mathbf{y}_n$ are independent and identically distributed realizations from the vector $\mathbf{Y}$, the log likelihood function for $\boldsymbol{\Psi}$ is [180]:

$$\log L(\boldsymbol{\Psi}) = \sum_{j=1}^{n} \log f(\mathbf{y}_j; \boldsymbol{\Psi}) \tag{3.41}$$

An estimate of the likelihood can be obtained from an appropriate root of the likelihood equation (3.41):

$$\frac{\partial \log L(\boldsymbol{\Psi})}{\partial \boldsymbol{\Psi}} = \mathbf{0} \tag{3.42}$$

Mixture models are usually faced with the problem of multiple roots. Fortunately, the EM algorithm of Dempster et al. [73] allows for a consistent and efficient solution of (3.41). Following the discussion of [181], the EM algorithm proceeds iteratively in two steps, expectation and

maximization (E and M, respectively), for the solution of the complete-data log likelihood of the form:

$$\log L_c(\mathbf{\Psi}) = \sum_{i=1}^{g}\sum_{j=1}^{n} z_{ij} \log\left[\pi_i c\left(\mathbf{y}_j; \boldsymbol{\mu}_i, \mathbf{\Sigma}_i\right)\right] \tag{3.43}$$

where z_{ij} $(i = 1, ..., g; j = 1, ..., n)$ are denoted as component-label variables, with values of $z_{ij} =$ 1 or 0 corresponding to if $\mathbf{y}_j$ arose or not from the ith component of the mixture model. The variables z_{ij} and the measured data are regarded together as a complete-data vector $\mathbf{x}_c$:

$$\mathbf{x}_c = \left(\mathbf{x}_1^T, ..., \mathbf{x}_n^T\right)^T \tag{3.44}$$

where $\mathbf{x}_j = \left(\mathbf{y}_j^T, \mathbf{z}_j^T\right)^T$.

In the E-step and $(k+1)$th iteration, the conditional expectation of (3.43) given the measured data $\mathbf{y}_{\text{exp}}$ and the current fit $\mathbf{\Psi}^{(k)}$ of $\mathbf{\Psi}$ is calculated:

$$Q\left(\mathbf{\Psi}; \mathbf{\Psi}^{(k)}\right) = E_{\mathbf{\Psi}^{(k)}}\left[\log L_c(\mathbf{\Psi}) \,|\mathbf{y}_{\text{exp}}\right] \tag{3.45}$$

Given the linearity of $\log L_c(\mathbf{\Psi})$ with respect to z_{ij}, the E-step is accomplished by replacing z_{ij} by its current conditional expectation on $\mathbf{y}_j$, namely $z_{ij}^{(k)}$:

$$E_{\mathbf{\Psi}^{(k)}}\left[Z_{ij}|\mathbf{y}_j\right] = \text{pr}_{\mathbf{\Psi}^{(k)}}\left[Z_{ij} = 1|\mathbf{y}_j\right] = z_{ij}^{(k)} \tag{3.46}$$

where by Bayes Theorem,

$$z_{ij}^{(k)} = \tau_i\left(\mathbf{y}_j; \mathbf{\Psi}^{(k)}\right) = \frac{\pi_i c\left(\mathbf{y}_j; \boldsymbol{\mu}_i, \mathbf{\Sigma}_i\right)}{\sum_{h=1}^{g} \pi_h c\left(\mathbf{y}_j; \boldsymbol{\mu}_h, \mathbf{\Sigma}_h\right)} \tag{3.47}$$

for $(i = 1, ..., g; j = 1, ..., n)$. Thus, $\tau_i\left(\mathbf{y}_j; \mathbf{\Psi}^{(k)}\right)$ is the current estimate of the posterior probability that $\mathbf{y}_j$ belongs to the ith g-component.

The M-step on the $(k+1)$th iteration aims at the global maximization of $Q\left(\mathbf{\Psi}; \mathbf{\Psi}^{(k)}\right)$ with respect to $\mathbf{\Psi}$ based on the updated estimate $\mathbf{\Psi}^{(k+1)}$. The current fitting for the mix proportions and the component means and variance-covariance matrices are calculated explicitly by:

$$\pi_i^{(k+1)} = \frac{\sum_{j=1}^{n} \tau_{ij}^{(k)}}{n} \tag{3.48}$$

$$\boldsymbol{\mu}_i^{(k+1)} = \frac{\sum_{j=1}^{n} \tau_{ij}^{(k)} \mathbf{y}_j}{n\pi_i^{(k+1)}} \tag{3.49}$$

$$\boldsymbol{\Sigma}_i^{(k+1)} = \frac{\sum_{j=1}^{n} \tau_{ij}^{(k)} \left(\mathbf{y}_j - \boldsymbol{\mu}_i^{(k+1)}\right)\left(\mathbf{y}_j - \boldsymbol{\mu}_i^{(k+1)}\right)^T}{n\pi_i^{(k+1)}} \tag{3.50}$$

for $(i = 1, ..., g)$, where $\tau_{ij}^{(k)} = \tau_i\left(\mathbf{y}_j; \boldsymbol{\Psi}^{(k)}\right)$. The E- and M-steps are alternated repeatedly until the difference in likelihoods $L\left(\boldsymbol{\Psi}^{(k+1)}\right) - L\left(\boldsymbol{\Psi}^{(k)}\right)$ changes by a small amount in the case of convergence. Dempster et al. [73] demonstrated the remarkable feature of the EM algorithm that the mixture likelihood is not decreased after an EM iteration:

$$L\left(\boldsymbol{\Psi}^{(k+1)}\right) \geq L\left(\boldsymbol{\Psi}^{(k)}\right) \tag{3.51}$$

and consequently convergence is attained with a sequence of likelihoods bounded above. The reader is referred to [179] for a detailed discussion of the EM algorithm. The mixture-likelihood approach allows for the formal assessment of the mixture order (number of components in the mixture) based on the application of a likelihood criteria such as penalized likelihood (Akaike's information criterion (AIC), Bayesian information criterion (BIC)) and likelihood ratios (based on hypothesis testing and confidence levels). Additionally, it can assess the effectiveness of the clustering for a particular number of components in the form of individual and overall allocation rates using the estimated posterior probabilities of component membership [178]. The application of the ML-EM methodology for the analysis of grid indentation data on shale was accomplished using the EMMIX algorithm developed by McLachlan et al. [181]. The EMMIX algorithm automatically fits a range of normal mixture distributions with unrestricted variance-covariance matrices. The optimal number of mixture components is determined using the BIC criterion.

3.6.6 Results of Grid Indentation of Shale Materials

Bobko and Ulm [32] conducted a comprehensive indentation campaign on shale materials to characterize the mechanical properties of their clay fabric at nanometer length scales. A total of fourteen shale samples from different origins and formations were tested at various loads, ranging between $P = 0.3$ mN and $P = 19.2$ mN. These materials belong to the data set

developed by the G2IC, and were introduced in Section 3.1. Given the transversely isotropic elastic nature of shale, specimens were tested in the direction of symmetry (normal-to-bedding or x_3-axis) and normal to the direction of symmetry (parallel-to-bedding or x_1-axis). These orientations were related to the macroscopically observed bedding planes for each specimen. The reader is referred to the works of Bobko and Ulm [31, 32] for detailed explanations of the experimental aspects of the indentation campaign on shale materials (e.g. surface preparation, instrument calibration, load and depth selections). In what follows, we recall only the relevant information from the nanoindentation campaign in the context of the application of the EM-ML modeling approach for the interpretation of the grid indentation data for shale specimens.

By way of illustration, the implementation of mixture modeling using the maximum likelihood approach to the cluster analysis of grid indentation data on shale G2IC-03 is first presented. Figure 3-10 displays the results of grid indentations on shale G2IC-03 tested in the x_3-direction and subjected to maximum indentation loads of $P = 0.3$ mN (a,b) and $P = 4.8$ mN (c,d). For both load cases, four groups were identified through cluster analysis, each of which is regarded as a mechanical active phase. Figures 3-10a and 3-10c display graphically the identified phases in the $M - H$ plane for the two load cases, respectively. Figures 3-10b and 3-10d show the corresponding estimated mix proportions and allocation rates for the different phases. Conveniently, the results presented in Figure 3-10 provide the appropriate frame of reference to examine some important trends derived from the EM-ML mixture analysis of all tested shale materials.

For all load cases ($P = 0.3, 1.2, 4.8, 10, 19.2$ mN) and indentation directions (x_1,x_3 directions), two main types of indentation modulus and hardness responses were identified. The first type corresponds consistently to a phase with large M, H values. This response is expected due to the presence of a dominant quartz inclusion phase from mineralogy composition data for all tested shale specimens, including shale G2IC-03. In Figure 3-10 for instance, phase 4 exhibits mean indentation modulus and hardness values of approximately $M \approx 60$ GPa, $H \approx 8$ GPa, for both load cases. The observations for all shale materials across the different experiments match in first order the expected properties of quartz ($M = 80 - 100$ GPa, $H = 12 - 14$ GPa, [43, 112, 122]). The discrepancies between the measured and expected values for the quartz phase are attributed to their different nature. Quartz grains in shale are often of de-

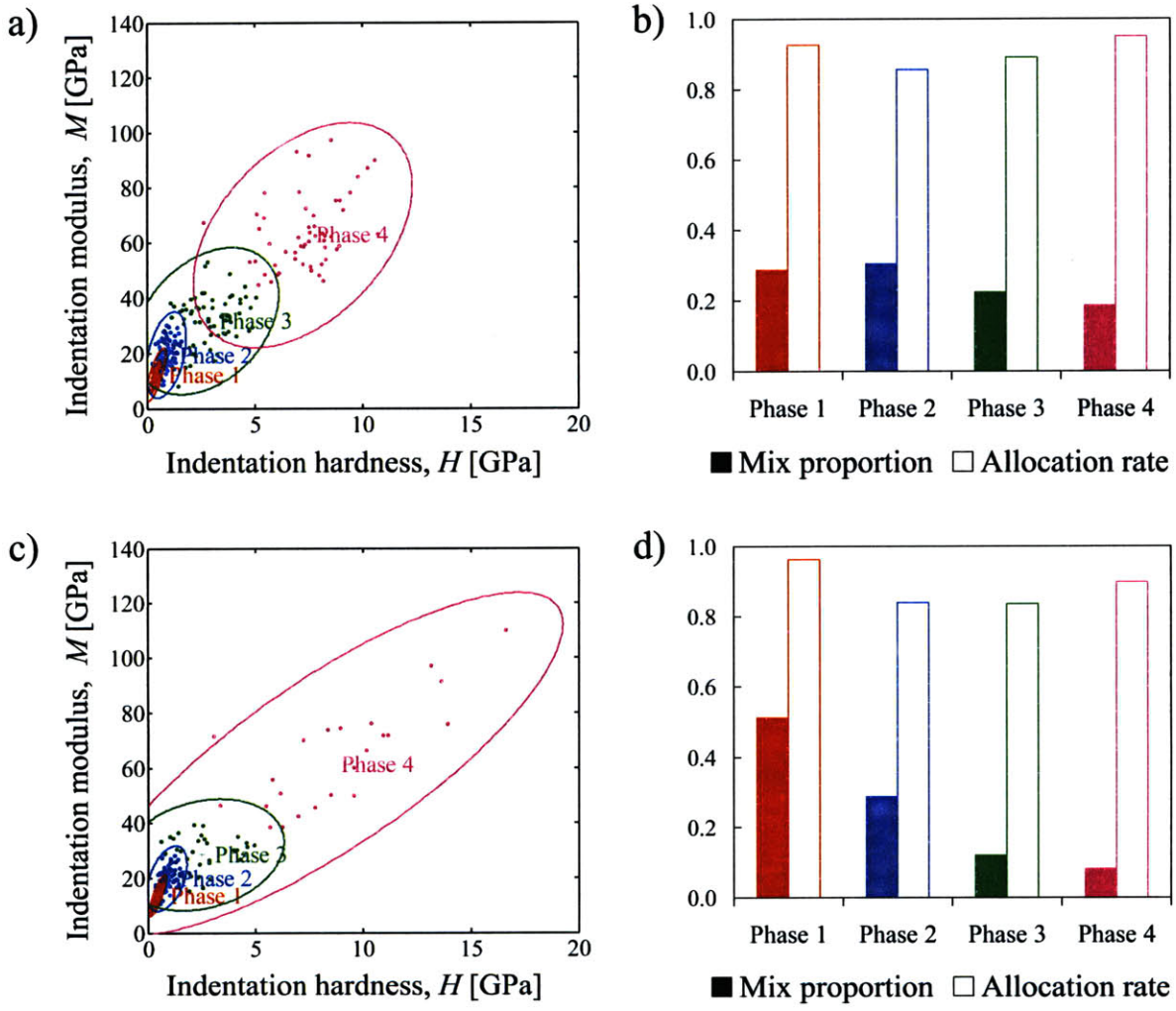

Figure 3-10: Mixture modeling of the grid indentation data for shale G2IC-03 in the x_3-direction. (a-b) correspond to tests with a maximum indentation load of $P = 0.3$ mN, and (c-d) to $P = 4.8$ mN. Plots a) and c) display the identified groupings, which in indentation testing correspond to active mechanical phases. Plots b) and d) show the values of the mix proportions and the allocation rates related to the identified mechanical phases.

trital nature, in addition to occurrences as either single grains or polycrystalline grains. If in polycrystal form, the expected mechanical properties would be of lesser values compared to behavior of single grains due to the presence of weak interphases at grain boundaries. A more refined assessment of this inclusion phase is due in future investigations. The second type of mechanical response corresponds to the remaining phases found through the cluster analysis, in addition to the quartz phase. These phases display significantly smaller values of indentation modulus and hardness compared to those of quartz[14].

In order to determine the sought porous clay, we recur to the derived mix proportion information from mixture modeling and the analysis of indentation load and depth data. Using as illustration the trends observed for shale G-03, it was observed that mix proportions showed similar magnitudes when sorted by their M, H values[15] for tests at $P = 0.3$ mN (see Fig. 3-10b). However for deeper indentations (consequently higher loads), the first phase typically displayed a larger mix proportion, while the subsequent phases displayed smaller ones (see Fig. 3-10d). For all forthcoming developments, phase 1 corresponds to the phase with the lowest indentation properties. This finding regarding mix proportions must be supplemented by the conditions of separability of length scales in continuum modeling. Bobko and Ulm [32] established that the adequate length scale for indentations on the porous clay in shale is approximately $0.5 < h < 3$ μm, based on considerations of particle sizes, surface roughness effects, and the continuum mechanics analysis used for inferring elastic and strength properties from indentation measurements. For all the shale materials tested, a maximum indentation load of $P = 0.3$ mN yielded indentation depths on the order of $250-500$ nm, while a load of $P = 4.8$ mN yielded indentation depths of approximately $1-2$ μm, which respects the indentation load–depth scaling of $P \propto h^2$ for conical indentations (see Section 3.5.1). Shallow indentations, such as those performed at $P = 0.3$ mN, may not provide accurate mechanical information since interference with surface roughness effects is likely to occur. Instead, deeper indentations may properly assess the properties of the indented shale material. These experimental observations may explain the trends in mix proportions observed in Figs. 3-10b and 3-10d. The knowledge that the tested

[14] It is important to mention that the mixture likelihood fitting was implemented for each set of data (i.e. a grid of indentations for a particular maximum load and material direction) using up to seven components/phases. Throughout our investigation, the majority of fits were accomplished with four to six phases.

[15] We observed that the presence of (nano)porosity affected the elasticity and hardness properties in similar manners: increasing indentation moduli values corresponded to increasing hardness (and viceversa).

shale materials posses large clay volume fractions (from mineralogy testing), in conjunction with a proper indentation depth during experiments, implies that the phase with the largest mix proportion should correspond to the porous clay composite. This phase tends to be the one with the lowest M, H values for the majority of tested shales. In contrast, experiments with indentation depths violating scale-separability conditions do not provide coherent information between mechanical properties and mix proportions; hence, the mix proportion trends for shallow indentations exhibit random relative magnitudes. Having determined the porous clay and quartz phases, the intermediate phases are regarded as composite phases, which may correspond to indentations at grain boundaries or on collapsed pore spaces.

As a way to synthesize the previous findings, Figures 3-11 through 3-13 compile the measured indentation modulus and hardness as functions of the maximum indentation load and depth for all tested specimens in both material directions. For each experimental case, the indentation properties for the phase with the largest mix proportion were used to build the figures. Whenever applicable, the mechanical properties measured with maximum indentation loads of $P = 4.8$ mN and higher appear relatively stable. It is worth noticing that, for indentation loads of $P = 19.2$ mN, the maximum indentation depths were of approximately $2 - 3$ μm, which remain within the length scale of validity. The derived properties displayed for experiments with deeper indentations (with load $P \geq 4.8$ mN) correspond consistently to phase 1, the porous clay composite, with the exception of a few experiments. The identified porous clay and quartz phases for the cases of deeper indentations also registered the highest allocation rates among all identified phases. This suggests that the mixture likelihood approach was able to cluster the data of the porous clay and quartz values into phases with higher degrees of certainty.

Among the tested shale materials (nine G2IC specimens and five Woodford specimens), two of them displayed significantly different experimental trends based on the cluster analysis: the Light and G2IC-08 (low-clay) shales. For the Light shale and its corresponding tested indentation loads, the phase with the largest mix proportions corresponded to clusters of indentations with M, H values much higher than those of the typical porous clay responses, reaching property levels of those of quartz ($M \approx 80$ GPa, $H \approx 10$ GPa). This observed behavior is related to the presence of a large quartz phase (the Light shale has the largest inclusion volume fraction,

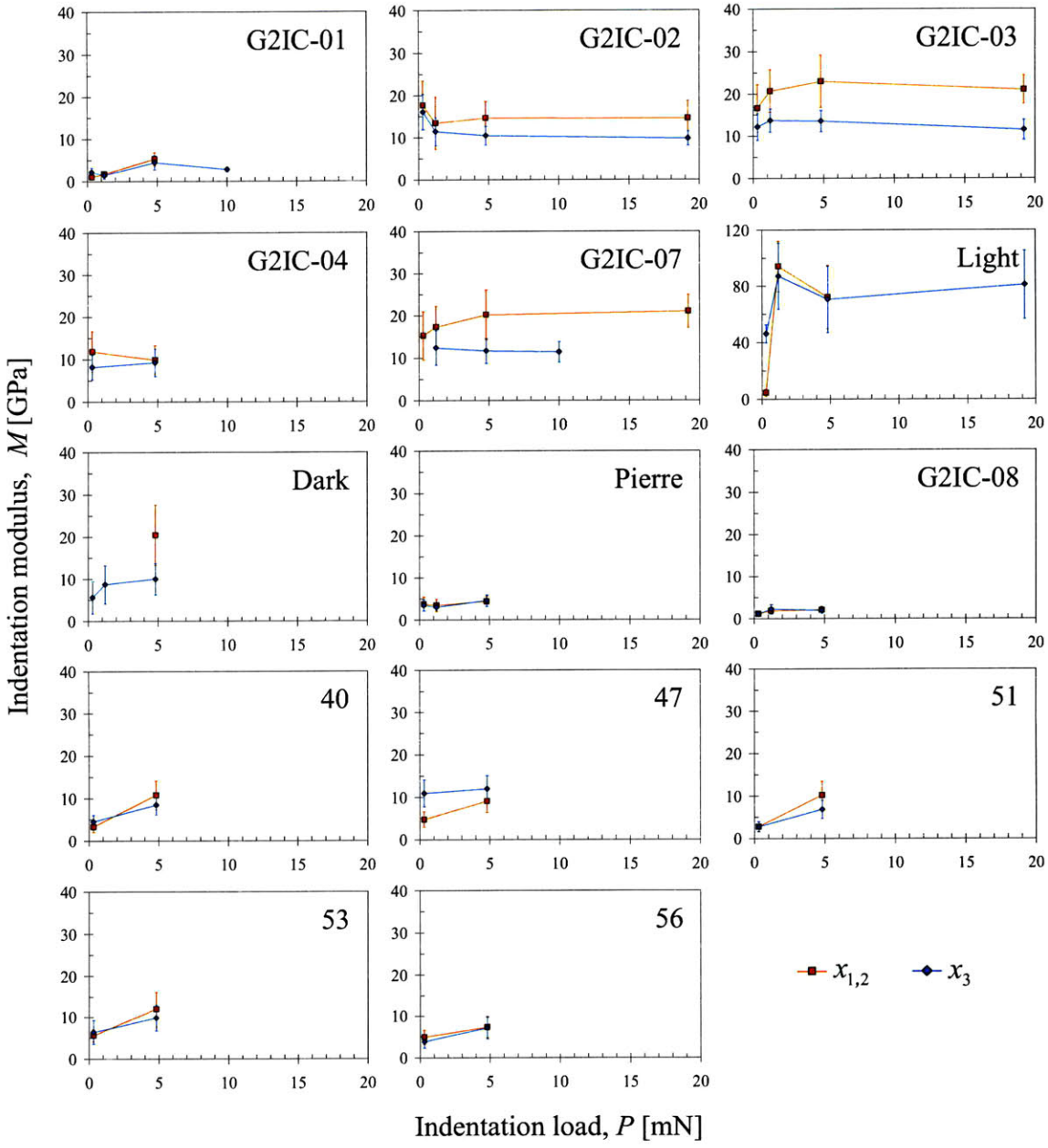

Figure 3-11: Measured indentation modulus M as a function of the maximum indentation load P in the x_1- and x_3-directions. The G2IC-series, Light, Dark, and Pierre specimes correspond to kerogen-free shale. Woodford specimes correspond to kerogen-rich shale.

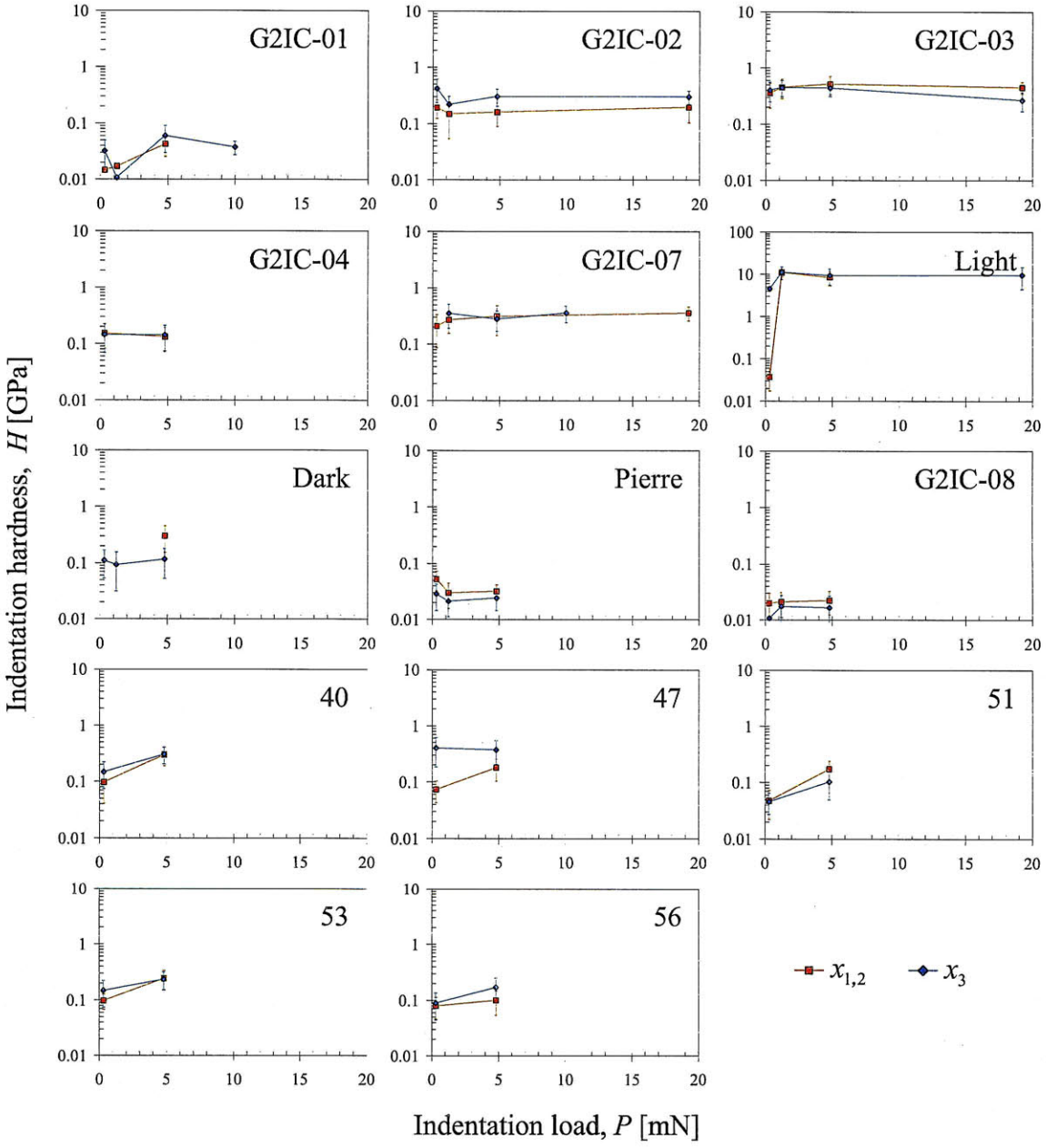

Figure 3-12: Measured indentation hardness H as a function of the maximum indentation load P in the x_1- and x_3-directions. The G2IC-series, Light, Dark, and Pierre specimes correspond to kerogen-free shale. Woodford specimes correspond to kerogen-rich shale.

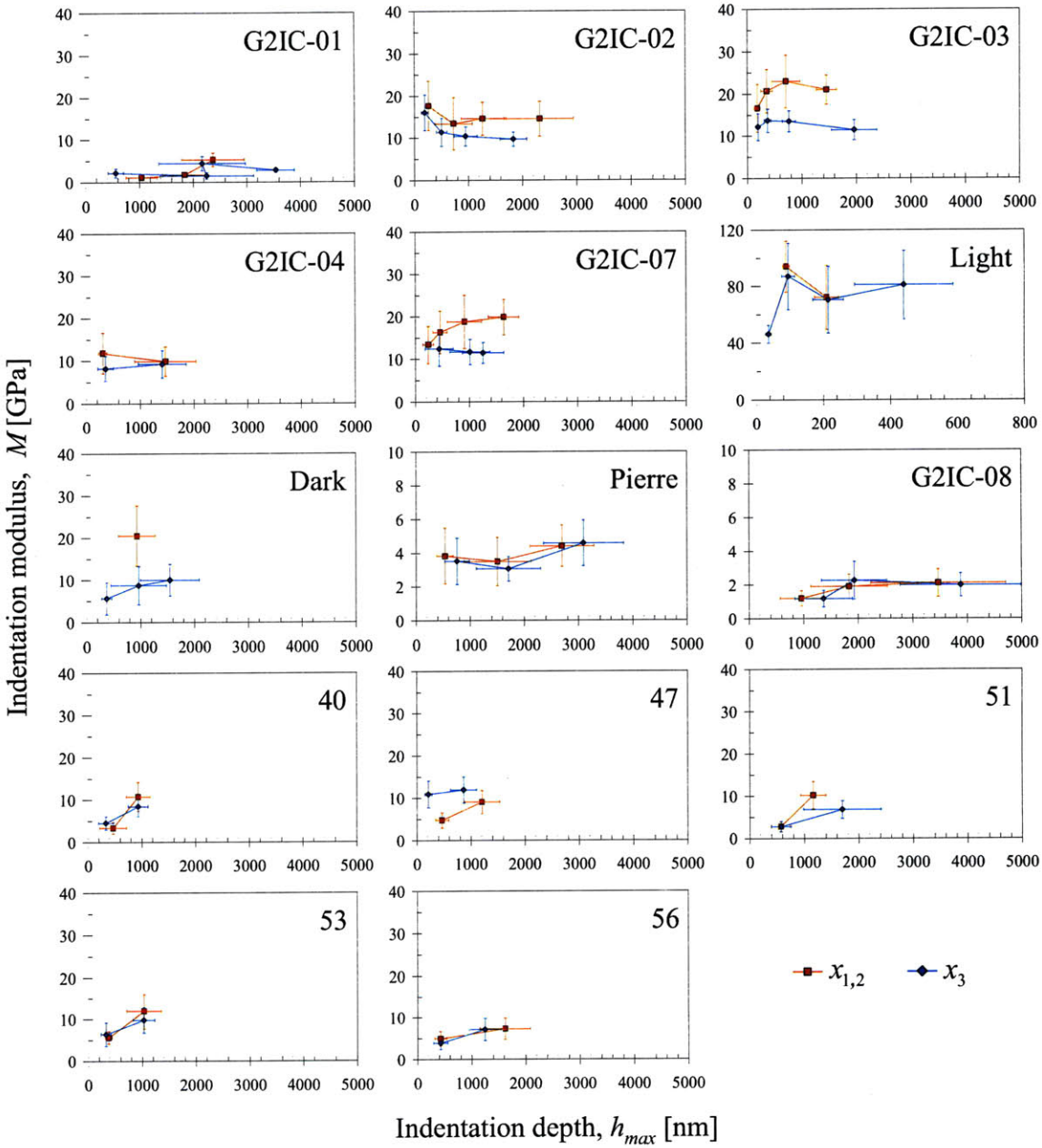

Figure 3-13: Measured indentation modulus M as a function of the maximum indentation depth $h_{\max}$ in the x_1- and x_3-directions. The G2IC-series, Light, Dark, and Pierre specimes correspond to kerogen-free shale. Woodford specimes correspond to kerogen-rich shale.

see Table 3.2). Thus, the nanoindentation campaign on this shale was not able to accurately probe the response of the porous clay. The G2IC-08, or Low-clay, shale instead displayed adequate trends in terms of the order of magnitude of mechanical properties for the porous clay composite for the different experimental cases. However, the identified mix proportions in most cases displayed similar magnitudes. Another peculiar experimental observation is the indentation depths ranging from 1 to 4 μm, which correspond to the bounding load cases $P = 0.3$ and $P = 19.2$ mN. Such indentation depths are somewhat larger than the trends of the remaining shale specimens. These observations from indentation analysis question the value of the indentation data for the Low-clay shale, in addition to the experimental difficulties encountered by [32] during sample preparation and indentation testing. The Light and Low-clay shales were dismissed for the forthcoming analyses as they may bring inaccurate information regarding the mechanical properties of the porous clay in shale.

After reanalyzing the data set of indentation properties for the porous clay composite obtained by grid nanoindentation, it is worth comparing the outputs of the EM-ML method for cluster analysis and the deconvolution technique. Figure 3-14 displays the comparison of the inferred indentation modulus and hardness values of the porous clay composite according to the statistical deconvolution approach used by Bobko and Ulm [32] and the mixture likelihood approach. In general, an excellent agreement exists between both approaches, with no fixed trends of under- or overestimation of the indentation properties by either technique. Evidently, the deconvolution procedure used in [32] and the present approach differ in some key aspects. While both methods are based on modeling components using normal distributions, the deconvolution procedure treats the indentation modulus and hardness data as sets of measurements with no links to specific indentation events. Nevertheless, Figure 3-14 corroborates the conjecture that the deconvolution technique is appropriate for porous composites in which the effects of porosity affect the elasticity and hardness properties in similar ways, as it is in fact the case of the porous clay composite. In addition to the multi-variate analysis capabilities, the EM-ML approach has the advantages of identifying the optimal number of phases and the degree of accuracy (in terms of allocation rates) of the clustering of data corresponding to each identified phase. The resulting data set of indentation properties for the G2IC and Woodford shales is detailed in Table 3.16.

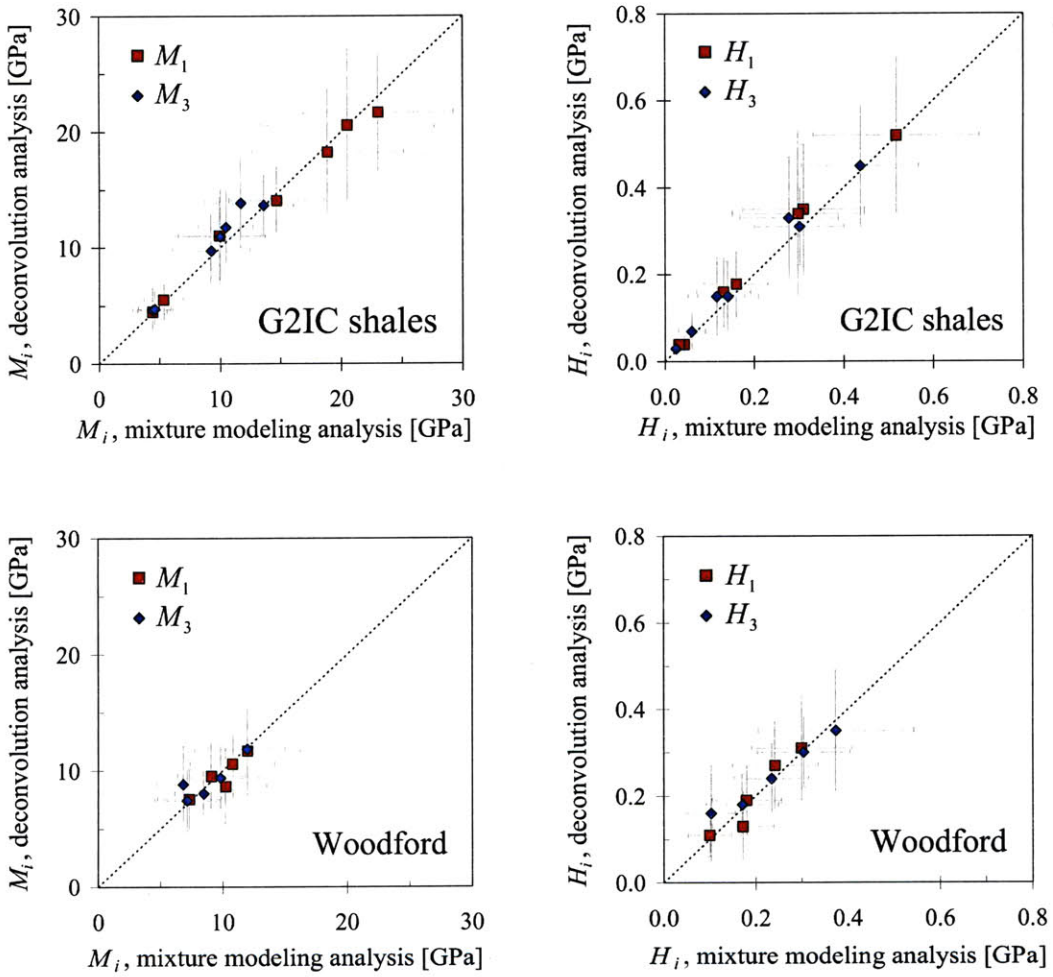

Figure 3-14: Comparison between indentation modulus values for the porous clay composite predicted by two different data analyses: statistical deconvolution and mixture likelihood approach.

Specimen	M_3 [GPa]		M_1 [GPa]		H_3 [GPa]		H_1 [GPa]	
	μ	σ	μ	σ	μ	σ	μ	σ
GeoGenome shales								
G2IC-01	4.44	1.66	5.32	1.59	0.06	0.03	0.04	0.02
G2IC-02	10.45	2.26	14.67	3.96	0.30	0.10	0.16	0.07
G2IC-03	13.56	2.50	23.03	6.19	0.44	0.13	0.52	0.18
G2IC-04	9.25	3.20	9.94	3.43	0.14	0.07	0.13	0.06
G2IC-07	11.68	2.95	18.85	6.28	0.28	0.11	0.31	0.14
Dark	10.01	3.73	20.49	7.16	0.12	0.06	0.30	0.15
Pierre	4.58	1.36	4.41	1.23	0.02	0.01	0.03	0.01
Woodford shales								
40	8.47	2.35	10.79	3.39	0.30	0.10	0.30	0.11
47	11.95	3.10	9.09	2.69	0.37	0.17	0.18	0.08
51	6.82	2.12	10.24	3.24	0.10	0.05	0.17	0.07
53	9.82	3.06	11.98	4.24	0.23	0.08	0.24	0.09
56	7.14	2.63	7.33	2.57	0.17	0.08	0.10	0.05

Table 3.16: Indentation moduli M_i and indentation hardness H_i properties of the porous clay fabric of shale materials tested by Bobko and Ulm [32] at maximum indentation loads of 4.8 mN. The grid indentation data was reanalyzed using the EM-ML approach. The indentation properties in the directions normal-to-bedding (x_3) and parallel-to-bedding (x_1,x_2) directions are presented in terms of mean (μ) and standard deviation (σ) values.

Scaling of Indentation Properties and Clay Packing Density

After reanalyzing the grid indentation data for G2IC and Woodford shale samples using the mixture likelihood approach, the relation between the measured indentation properties of the porous clay and the clay packing density is evaluated. Figure 3-15 displays the scaling between the indentation properties (modulus $M_{i=1,3}$ and hardness $H_{i=1,3}$) and the clay packing density η for the GeoGenome (kerogen-free) shale specimens. The displayed indentation modulus and hardness values correspond to the measurements at a maximum load of $P = 4.8$ mN, which provides stable estimates of elasticity properties that are also compliant with length scale separability conditions. Figure 3-15a also shows linear regressions for the experimental indentation modulus data in the normal-to-bending (x_3) and parallel-to-bedding (x_1) directions to highlight some important trends for elastic behavior. It is observed that increasing indentation modulus values correspond to increasing clay packing densities, and that the effective solid phase is anisotropic, with $M_1(\eta = 1) = 27.9$ GPa, $M_3(\eta = 1) = 15.3$ GPa. In addition, an apparent percolation threshold exists at packing densities between $\eta_0^{M_1} = 0.54$ and $\eta_0^{M_3} = 0.42$. The

occurrence of a percolation threshold hints toward a granular behavior of the porous clay composite in shale. For Woodford shales, differences in indentation moduli are somewhat reduced, as observed in Figure 3-16a. This reduced elastic anisotropy captured by nanoindentation is attributed to the presence of the kerogen phase with a pronounced amorphous morphology, instead of sheet-like kerogen structures that would result in enhanced structural anisotropy [74, 102].

Regarding the indentation hardness results for GeoGenome and Woodford shales, the trend of increasing hardness with increasing packing density is also observed in Figures 3-15b and 3-16b. However, the hardness – packing density scaling is more non-linear compared to the indentation modulus results. The hardness response also exhibits an apparent percolation threshold at packing densities similar to those observed for the indentation modulus data. A clear difference between the elastic and hardness behaviors shown in Figures 3-15 and 3-16 is the less apparent anisotropy for the hardness measurements. Shales G2IC-01, -02, and -04 show higher hardness values for the normal-to-bedding direction compared to those measured in the orthogonal direction (Figures 3-15b). In addition, the inspection of Figures 3-15b and 3-16b reveals that, despite the scatter in the data, the vertical error bars (the standard deviation of phase properties) in the hardness data are consistently overlapping. These arguments lead to considering an isotropic strength response for the porous clay phase in shale.

The granular, anisotropic elasticity signature of shale's porous clay solidifies the findings of Ulm and Abousleiman [265] and Bobko and Ulm [32], who used the deconvolution technique to interpret the same grid indentation data presented in this study. The remarkable scaling between nanoscale elasticity (expressed in indentation modulus values) and the clay packing density becomes the experimental baseline for modeling the anisotropy at level I of our multi-scale microporoelasticity model for shale. For strength modeling, a more advanced analysis is necessary for inferring the cohesive-frictional strength properties of shale from nanoindentation hardness measurements. The next section presents the results of Bobko [31] regarding a back-analysis of shale indentation hardness data to estimate the average strength properties of the solid clay phase.

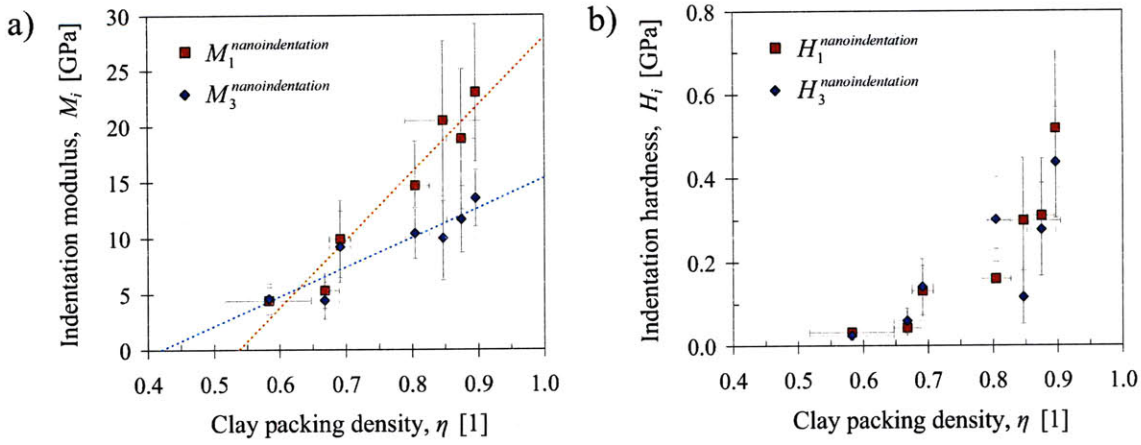

Figure 3-15: a) Porous clay stiffness M_i and b) hardness H_i versus clay packing density scaling η for the GeoGenome shale specimens. The vertical bars correspond to the standard deviation of the indentified phases from mixture modeling. The horizontal bars represent the variability of clay packing density estimates. By way of illustration, linear regressions have been included for the indentation modulus – clay packing density scaling to highlight the experimental trends (with r^2 values of $0.94, 0.84$ for M_1, M_3).

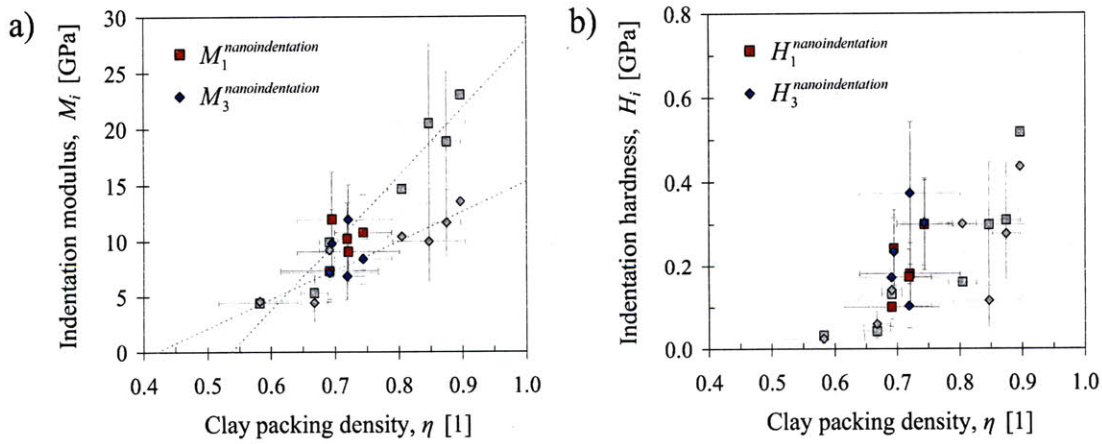

Figure 3-16: a) Porous clay stiffness M_i and b) hardness H_i versus clay packing density scaling η for the Woodford shale specimens. The vertical bars correspond to the standard deviation of the indentified phases from mixture modeling. The horizontal bars represent the variability of clay packing density estimates. The data for G2IC shales is presented in the background.

Inverse Analysis of Clay Strength Properties from Nanoindentation Hardness

The nanoindentation hardness - packing density scalings reviewed in Figures 3-15b and 3-16b describe an isotropic relation between the average hardness measured in orthogonal directions for the porous clay phase of several shale samples and their corresponding scaling with packing density. However, the multi-scale strength modeling of shale to be pursued in Part IV of this thesis requires the evaluation of the cohesive-frictional properties of the solid clay phase in shale. The assessment of clay strength properties from hardness measurements was conducted by Bobko [31], through an inverse analysis aiming at the translation of grid indentation data for the porous clay composite into information about the local packing densities associated with each indentation test and the solid strength properties of a particular sample. In addition to the grid indentation data, theoretical modeling based on linear micromechanics, yield design, and non-linear homogenization is employed to furnish scaling relations of the form (see e.g. (3.29)):

$$M^i_{(\beta)} = m^s_{(\beta)} \times \Pi_M \left(\eta^i\right) \tag{3.52a}$$

$$H^i = h^s \left(c^s, \alpha\right) \times \Pi_H \left(\alpha, \eta^i\right) \tag{3.52b}$$

between indentation moduli $M_{(\beta=1,3)}$ and hardness H probed for the porous clay composite[16], the packing density η, and solid clay properties at level 0 of the elementary building block (anisotropic moduli $m^s_{(\beta=1,3)}$, cohesion c^s, and friction coefficient α) [98, 202, 270]. The underlying concept of the indentation modulus-hardness-packing density ($M - H - \eta$) analysis approach is to link each indentation experiment, with measured modulus and hardness values $M^i_{(\beta)}, H^i$, to the properties of the solid phase $m^s_1, m^s_3, c^s, \alpha$ and the local packing density η^i. In an inverse application, the unknowns of the problem are the solid phase properties, and the N local packing densities η^i, for a total of $N+4$ unknowns. The results from each indentation test, $M^i_{(\beta)}$ and H^i, are known, for a total of $2N$ known quantities. The application of the inverse analysis relies on a large number of indentation tests, which is the case for grid indentation data, for the system of equations in (3.52) to be over-determined. However, the actual imple-

[16] For the implementation of the inverse analysis for shale data, the measured indentation hardness H was assumed isotropic, as noted in e.g. Figures 3-15b and 3-16b.

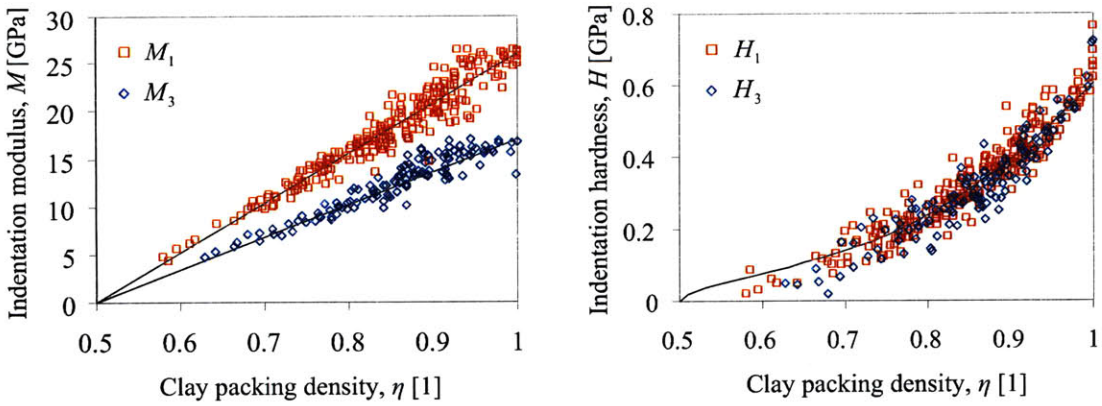

Figure 3-17: Sample of scaling results from the indentation modulus - hardness - packing density ($M - H - \eta$) scaling approach. The results correspond to shale G2IC-07. From [31]

mentation of the inverse analysis requires an error minimization approach between predicted and measured indentation data and a statistical analysis for retrieving the solid clay properties [31, 270].

Bobko [31] conducted the $M - H - \eta$ analysis for G2IC and Woodford shales, as well as for resedimented Boston Blue Clay specimens. Figure 3-17 displays the scaling results for shale G2IC-07, and shows the indentation modulus and hardness values versus the local packing density associated with each individual indentation test. The model lines correspond to the expressions in (3.52) with optimized solid parameters identified through the inverse analysis procedures.

Figure 3-18 shows the $M - H - \eta$ analysis results for the solid contact hardness h^s as a function of the clay packing density determined for each shale sample. This level 0 property is recovered for the limit case of packing density $\eta = 1$ for expression (3.29). From the results in Figure 3-18, the contact hardness and the clay packing density appear uncorrelated. Moreover, the porous clay phase in shale displays a relatively constant solid hardness despite variations in clay mineralogy [31]:

$$h^s = 0.69 \pm 0.09 \text{ GPa} \tag{3.53}$$

The solid contact hardness h^s is treated as a material invariant property of the solid clay phase in shale. In contrast to the solid contact hardness, the Drucker-Prager strength parameters, the

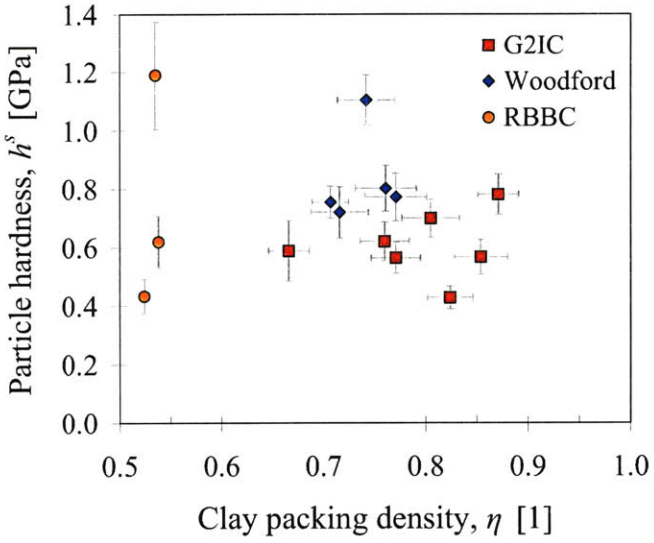

Figure 3-18: Particle hardness as a function of clay packing density from indentation analysis. Data obtained for G2IC shales, Woodford shales, and resedimented Boston Blue Clay samples. Error bars represent two standard deviations. From [31].

friction coefficient α and the solid cohesion c^s, vary considerably for the tested shale specimens and exhibit strong relationships with the clay packing density. The friction coefficient α, a measure of the pressure sensitivity of the solid clay, decreases with increasing values of packing density as shown in Figure 3-19a. In contrast, Figure 3-19b displays the results for the cohesion c^s, which follows the trend of increasing values with increasing packing densities. The inferred behavior for the cohesion derives from the form of the scaling relation for the solid contact hardness h^s in (3.30). These remarkable trends between the cohesive-frictional properties of the solid clay and the clay packing density are further discussed in Part IV of this thesis, as they will serve as crucial inputs to the multi-scale strength modeling of shale.

3.7 Macroscopic Characterization of Shale - Level II

The mechanical behaviors of shale in terms of deformation and strength have been derived mostly from extensive experimental testing at macroscopic length scales. In view of the different field applications related to shale such as reservoir modeling, oil recovery, and wellbore stability,

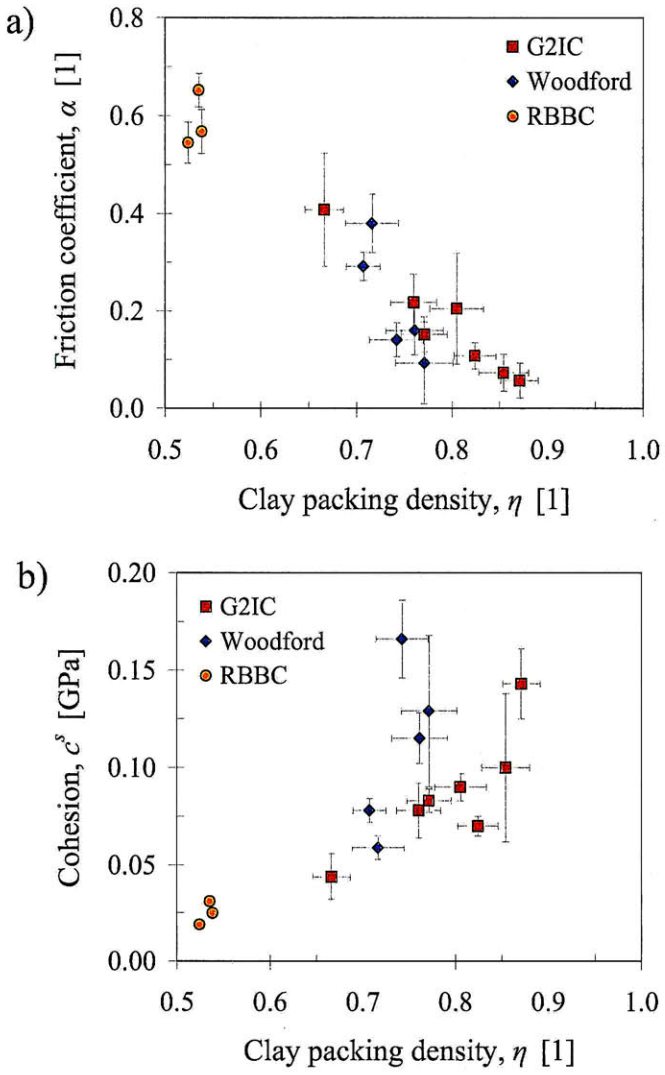

Figure 3-19: Scaling of clay strength properties with packing density. The experimental data corresponds to G2IC and Woodford shales and resedimented Boston Blue Clay samples. Error bars represent two standard deviations. From [31].

a variety of logging tools and data interpretation methods have been developed to assess the mechanical properties of rock formations in situ. The assessment of the complex anisotropic elasticity attributes of shale, for instance, has been the focus of seismic exploration techniques [283]. In addition to elasticity attributes, strength characterization has also been derived from logging data based on empirical correlations between different rock properties. Nevertheless, the field data developed to assess large rock formation volumes are typically supplemented with laboratory measurements of core specimens, which provide a more accurate assessment of physical properties. In this section, a brief introduction to the mechanical testing of shale at engineering scales is presented. The section is divided into elasticity and strength assessment of shale, based primarily on laboratory experiments that are recognized as benchmark methods for characterizing rock materials. The final objective is to compile sets of experimental data for shale elasticity and strength that will be used for the development of micromechanics models for shale.

3.7.1 Field and Laboratory Characterization of Rock Mechanics

The advances in the study of the physical properties of rocks have been driven by the progress in the past 50 years of seismic exploration techniques. In exploration seismology, seismic waves provide access to the sub-surface information of the rock formation and fluid properties in the form of wave travel times and reflection amplitude and phase variations. For applications in reservoir evaluation and enhanced oil recovery, seismic data used for evaluating the mechanical response of the formation derives from a variety of well logging tools. Sonic logging, for instance, provides a continuous record of seismic velocities that are used for determining rock elasticity properties using inversion techniques such as AVO (amplitude versus offset) [127]. However, log data is typically supplemented by core testing in an effort to improve the accuracy and reliability of interpretations. Core testing provides a direct means of characterizing the elasticity and strength properties of rocks, at the cost of sampling a rock formation only at discrete depths. Nevertheless, core data is instrumental in advancing the understanding of petrophysical properties of rocks and their relations to acoustic and strength attributes [176].

The elasticity of shale core specimens has been traditionally derived from static and dynamic laboratory measurements through e.g. triaxial testing and pulse transmission techniques, re-

spectively. Although both static and dynamic data are suitable for determining elastic moduli of a rock specimen in the laboratory, numerous studies have shown differences between the values determined by each technique. For dry rocks, the estimated dynamic modulus is of similar or larger magnitude compared to the static values [90, 242]. Potential sources that explain the discrepancies between static and dynamic measurements for natural rocks are the presence of cracks, the stress state of the rock during measurements, and strain amplitude [143, 281]. Experiments in shale specimens have revealed that the ratio of dynamic to static moduli is approximately constant at large stress levels (pressures up to 200 MPa) [60]. Disregarding pressure sensitivity effects, two main causes for the differences in static and dynamic measurements have been identified: strain amplitude and frequency [142]. Static measurements derived from stress-strain experiments are characterized by low frequencies and large strain amplitudes (10^{-4} or larger). In contrast, dynamic measurements obtained from both exploration seismology and laboratory acoustic experiments are related to high frequencies and small strain amplitudes (10^{-7} or smaller). Strain-amplitude mechanisms, which appear to be more a dominant effect in shale, are attributed to frictional losses at grain boundaries that are especially significant in static measurements [294]. Mechanisms dependent on frequency are generally linked to inertial and viscous effects associated with the wave propagation in saturated rocks [26]. The strength characterization of shale has been conducted primarily using the triaxial test method, although the low-permeability and sample preservation issues inherent to shale have motivated experimentalists to design special testing programs for achieving their experimental objectives [130, 245].

In the remaining parts of this section, the macroscopic characterization of shale's elasticity and strength properties will be presented based on the results of acoustic velocity measurements and triaxial testing. Dynamic measurements accomplished using pulse transmission techniques are the primary sources of elasticity data considered in this investigation. In addition to being a non-intrusive methodology, ultrasonic pulse velocity (UPV) measurements provide access to small strain-amplitude elasticity, similar to nanoindentation measurements that are used to probe shale at smaller length scales. Acoustic measurements and triaxial test results provide the adequate experimental context for understanding the mechanical response of shale at length scales representative of macroscopic properties.

3.7.2 Ultrasonic Pulse Velocity Measurements

For all shale specimens considered in this investigation, the classical ultrasonic pulse velocity (UPV) technique (see e.g. [27, 176]) has been employed to measure wave velocities and interpret the corresponding acoustic properties. The pulse-transmission technique consists in measuring the travel time of a solitary elastic pulse through a rock sample for a known wavepath length[17]. A typical experimental setup for UPV measurements of rock specimens is displayed in Figure 3-20. Compressional (P-) and shear (S-) waves are generated by piezoceramic elements, with central frequencies in the MHz range. The piezoceramics are placed at several locations on the shale specimen in order to capture its anisotropic properties. In particular, shale is generally agreed to exhibit transverse isotropic elastic properties [145, 228]. Within a Cartesian reference frame of orthonormal basis $[\underline{e}_1, \underline{e}_2, \underline{e}_3]$ of elastic properties of shale, where the plane $[\underline{e}_1, \underline{e}_2]$ corresponds to the bedding plane and $\underline{e}_3$ to the direction normal-to-bedding (symmetry axis), the transverse isotropic stiffness tensor in matrix form is:

$$[C_{ij}] = \begin{bmatrix} C_{11} & C_{12} & C_{13} & 0 & 0 & 0 \\ C_{12} & C_{11} & C_{13} & 0 & 0 & 0 \\ C_{13} & C_{13} & C_{33} & 0 & 0 & 0 \\ 0 & 0 & 0 & 2C_{66} = (C_{11} - C_{12}) & 0 & 0 \\ 0 & 0 & 0 & 0 & 2C_{44} & 0 \\ 0 & 0 & 0 & 0 & 0 & 2C_{44} \end{bmatrix} \tag{3.54}$$

where the Voigt notation is employed: $C_{11} = C_{1111}$, $C_{12} = C_{1122}$, $C_{13} = C_{1133}$, $C_{44} = C_{2323} = C_{1313}$, $C_{66} = C_{2121} = \frac{1}{2}(C_{11} - C_{12})$. Given its transverse isotropic character, common experimental setups for shale specimens include the measurement of a compressional wave velocity at 45° from the axis of symmetry, as shown in Figure 3-20. Single electrical pulses are emitted by a function generator. After passing through a dynamic amplifier, the amplitude-amplified pulse is converted into a mechanical vibration by the piezoceramics. This mechanical vibration then propagates through the rock specimen. A reverse process occurs at the receiving piezoceramics (the mechanical vibration is converted into an electrical pulse), after which both the emitted

[17] This section follows the thorough presentation of Sarout and Guéguen [226] regarding the implementation of the ultrasonic pulse velocity method.

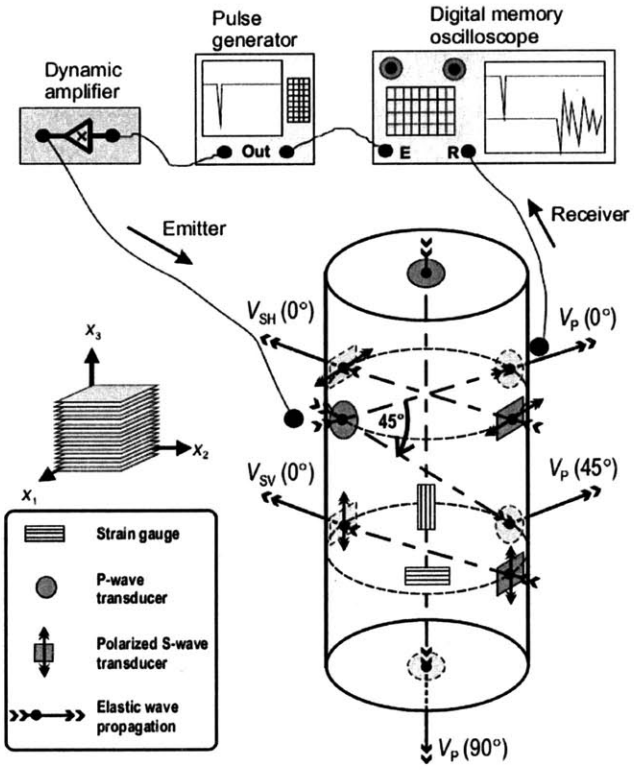

Figure 3-20: Diagram of the transducer arrangements for a shale sample used in UPV testing. The setup is coupled to a triaxial test apparatus. The rock bedding plane is perpendicular to the axis of the cylindrical sample. Adapted from [226], and reprinted with the kind permission of the authors.

and received waveforms are analyzed to determine the time delay between them. The setup for acoustic measurements is typically coupled with triaxial testing, which allows subjecting the specimen to various stress states aiming to simulate in situ conditions.

The next task involved in UPV measurements is the data analysis of the travel times. Improved procedures have been developed for UPV data interpretation to avoid dependencies on human errors, especially as the data analysis relies heavily on the accurate estimation of wave arrival times from waveform records (e.g. [129, 300]). Another important aspect of the data analysis is the treatment of oblique raypaths. In shale testing, the experimental setup is commonly designed such that raypaths coincide with the material axes of symmetry. For such scenario, pure wave modes are generated, which result in similar magnitudes for phase and group velocities [129]. However, the difference between phase and group velocities arises for

measurements at off-axis angles, such as the 45° measurement typically carried out for shale. The off-axis measurement is necessary to determine one of the five elastic constants, C_{13}, of the investigated shale specimen. Numerical schemes have been developed to quantify the relations of phase and group velocities measured in UPV experiments [77, 129]. The analysis of UPV measurements is commonly supplemented by detailed error evaluations of the estimated elastic moduli. These analyses are based on the uncertainties of parameters involved in the UPV experimental setup such as the specimen size, the specimen density, and the travel time (see e.g. [129, 146, 300]).

3.7.3 Acoustic Waves in Transverse Anisotropic Media

Classical results of acoustic waves in solids are presented in this section in order to determine stiffness from measured velocities in UPV experiments. The acoustic wave equations are commonly derived by adapting the acoustic field equations and constitutive relations. For a material with no acoustic energy losses (lossless material) in a source-free region, the acoustic field equations are [11]:

$$\nabla \cdot \boldsymbol{\sigma} = \rho \frac{\partial \underline{v}}{\partial t} \tag{3.55a}$$

$$\nabla_s \underline{v} = (\mathbb{C})^{-1} : \frac{\partial \boldsymbol{\sigma}}{\partial t} \tag{3.55b}$$

where $\boldsymbol{\sigma}$ is the stress field, ρ the mass density of the material, $\underline{v}$ the particle velocity field, $\mathbb{C}$ the fourth-order stiffness tensor of the material, and $\partial/\partial t$ the time derivative. The symbol ∇ represents the differential operator $\nabla = \frac{\partial}{\partial x_1}\underline{e}_1 + \frac{\partial}{\partial x_2}\underline{e}_2 + \frac{\partial}{\partial x_3}\underline{e}_3$, and ∇_s corresponds to the symmetric gradient of a vector field:

$$\nabla_s \underline{v} = \frac{1}{2}\left(\nabla \underline{v} + \nabla^t \underline{v}\right) \tag{3.56}$$

After manipulations of (3.55a) and (3.55b), the stress field is eliminated and the wave equation in terms of the velocity field is:

$$\nabla \cdot \mathbb{C} : \nabla_s \underline{v} = \rho \frac{\partial^2 \underline{v}}{\partial t^2} \tag{3.57}$$

The propagation of a uniform plane wave along the direction $\underline{n}$ has fields proportional to $e^{i(\omega t - k\underline{n}\cdot\underline{r})}$, which can be used in (3.57) to construct the wave equation as:

$$k^2 \left(\underline{n} \cdot \mathbb{C} \cdot \underline{n}\right) \cdot \underline{v} = k^2 \mathbf{\Gamma} \cdot \underline{v} = \rho\omega^2 \underline{v} \tag{3.58}$$

where k is the wave number and ω the wave frequency. Expression (3.58) is called the Christoffel equation, and the tensor $\mathbf{\Gamma}$ represents, in matrix notation, the Christoffel matrix. By inspection, the elements of the Christoffel tensor are functions of the elasticity constants C_{ijkl} of the solid and the direction of the plane wave propagation.

In wave acoustics, it is more convenient to consider the slowness surface, that is the inverse of the phase velocity $k/\omega = 1/V$ as a function of propagation direction $\underline{n}$, rather than the explicit form in (3.58), which scales with the wave frequency ω. Using the previous consideration, the Christoffel equation is typically rewritten as follows to determine the acoustic wave velocities of propagation:

$$\det\left(\mathbf{A} - V^2\mathbf{1}\right) = 0 \tag{3.59}$$

where $\mathbf{1}$ is second order unit tensor (or Kronecker Delta δ_{ij}), and $\mathbf{A}$ the undrained acoustic tensor,

$$\mathbf{A} = \frac{1}{\rho}\underline{n} \cdot \mathbb{C} \cdot \underline{n};\ A_{jk} = \frac{1}{\rho} n_i C_{ijkl} n_l \tag{3.60}$$

For shale, which is considered a transversely isotropic material at the macroscale, it is common practice to consider $\underline{n} = (\sin\theta, 0, \cos\theta)$, where $\theta = 0$ corresponds to the material's symmetry axis. A transversely isotropic of hexagonally symmetric medium contains one axis of rotational symmetry, which throughout this work is denoted as x_3. This direction in shale rocks is equivalent to the normal-to-bedding direction. The material properties in all directions perpendicular to x_3 are similar, and thus, the plane of symmetry is defined along the x_1, x_2 directions. The stiffness tensor of the solid medium is characterized by five, non-zero, independent elastic constants (see (3.54)). Using the following (3×6) matrix representation of the normal vector $\underline{n} = (n_1, n_2, n_3)$:

$$[n] = \begin{bmatrix} n_1 & 0 & 0 & \frac{1}{2}n_2\sqrt{2} & 0 & \frac{1}{2}n_3\sqrt{2} \\ 0 & n_2 & 0 & \frac{1}{2}n_1\sqrt{2} & \frac{1}{2}n_3\sqrt{2} & 0 \\ 0 & 0 & n_3 & 0 & \frac{1}{2}n_2\sqrt{2} & \frac{1}{2}n_1\sqrt{2} \end{bmatrix} \tag{3.61}$$

the acoustic tensor (3.60) can be calculated by matrix multiplication $\frac{1}{\rho}[n][C_{ij}][n]^t$,

$$[A_{jk}] = \frac{1}{\rho}\begin{bmatrix} C_{44}+\sin^2\theta\,(C_{11}-C_{44}) & 0 & (C_{13}+C_{44})\sin\theta\cos\theta \\ 0 & C_{44}+\sin^2\theta\,(C_{66}-C_{44}) & 0 \\ (C_{13}+C_{44})\sin\theta\cos\theta & 0 & C_{33}+\sin^2\theta\,(C_{44}-C_{33}) \end{bmatrix} \tag{3.62}$$

The wave velocities propagating in the plane of symmetry, that is the x_1,x_2 plane, are independent of the propagation direction in that plane. In the symmetry plane, the following wave modes are found:

$$V_{S1} = \sqrt{\frac{C_{66}}{\rho}};\ \text{pure shear mode polarized normal to the } x_3\text{-axis} \tag{3.63a}$$

$$V_{S3} = \sqrt{\frac{C_{44}}{\rho}};\ \text{pure shear mode polarized parallel to the } x_3\text{-axis} \tag{3.63b}$$

$$V_{P1} = \sqrt{\frac{C_{11}}{\rho}};\ \text{pure longitudinal mode} \tag{3.63c}$$

Wave propagation in the direction parallel to the symmetry axis results in the following modes:

$$V_{S3} = \sqrt{\frac{C_{44}}{\rho}};\ \text{pure shear mode polarized parallel to the } x_3\text{-axis} \tag{3.64a}$$

$$V_{P3} = \sqrt{\frac{C_{33}}{\rho}};\ \text{pure longitudinal mode} \tag{3.64b}$$

The wave propagation (and wave slowness surface) can be proven to be rotationally symmetric, since the Christoffel equation can be shown to be symmetric with respect to an arbitrary rotation about the axis of symmetry [11]. In this case, the following modes are determined:

$$V_{S\theta} = \sqrt{\frac{C_{44}\cos^2\theta + C_{66}\sin^2\theta}{\rho}};\ \text{pure shear mode} \tag{3.65a}$$

$$V_{qS\theta} = (2\rho)^{-\frac{1}{2}}\left(C_{11}\sin^2\theta + C_{33}\cos^2\theta + C_{44} - \varsigma\right)^{\frac{1}{2}};\ \text{quasi-shear wave} \tag{3.65b}$$

$$V_{qP\theta} = (2\rho)^{-\frac{1}{2}}\left(C_{11}\sin^2\theta + C_{33}\cos^2\theta + C_{44} + \varsigma\right)^{\frac{1}{2}};\ \text{quasi-longitudinal wave} \tag{3.65c}$$

where:

$$\varsigma = \sqrt{\left[(C_{11} - C_{44})\sin^2\theta + (C_{44} - C_{33})\cos^2\theta\right]^2 + (C_{13} + C_{44})^2 \sin^2(2\theta)} \tag{3.66}$$

For convenience, the five elastic constants related to the transverse isotropic elasticity of shale are expressed in terms of the acoustic wave velocities typically measured in UPV tests:

$$C_{11}^{UPV} = \rho V_{P1}^2 \tag{3.67a}$$

$$C_{33}^{UPV} = \rho V_{P3}^2 \tag{3.67b}$$

$$C_{66}^{UPV} = \frac{1}{2}\left(C_{11}^{UPV} - C_{12}^{UPV}\right) = \rho V_{S1}^2 \tag{3.67c}$$

$$C_{44}^{UPV} = \rho V_{S3}^2 \tag{3.67d}$$

$$C_{13}^{UPV} = -C_{44} + \alpha\sqrt{\left(C_{11} + C_{44} - 2\rho V_{45}^2\right)\left(C_{33} + C_{44} - 2\rho V_{45}^2\right)} \tag{3.67e}$$

where:

V_{P1} = pure longitudinal mode in the bedding direction

V_{P3} = pure longitudinal mode in the normal-to-bedding direction

V_{S1} = pure shear mode polarized normal to the axis of symmetry

V_{S3} = pure shear mode polarized parallel to the axis of symmetry

V_{qP45} = quasi-longitudinal $\alpha = (+1)$ or quasi-shear wave $\alpha = (-1)$ measured at 45° from the axis of symmetry

In the context of acoustic and anisotropic properties, a well-established measure of the degree of anisotropy is offered by Thomsen [256], who defined the following set of anisotropic parameters:

$$\varepsilon = \frac{C_{11} - C_{33}}{2C_{33}} \tag{3.68a}$$

$$\gamma = \frac{C_{66} - C_{44}}{2C_{44}} \tag{3.68b}$$

$$\delta^* = \frac{1}{2C_{33}^2}\left[2\left(C_{13} + C_{44}\right)^2 - \left(C_{33} - C_{44}\right)\left(C_{11} + C_{33} - 2C_{44}\right)\right] \tag{3.68c}$$

3.7.4 UPV Elasticity Data for Shale

In this section, we introduce ultrasonic pulse velocity (UPV) data measured from a variety of shale samples. This acoustic data will serve as the reference for the characterization of shale's elasticity at the macroscopic scale. With characteristic frequencies in the range of kHz – MHz, the UPV technique is able to quantify the elasticity content of shale at millimeter length scales, which corresponds to the length scale of level II of our multi-scale structure model presented in Section 2.3.

The elasticity data for shale specimens investigated as part of the work of the G2IC Industry Consortium and for those specimens documented in the open literature of shale are presented as functions of stress state. For simplicity, the values of elastic constants C_{ij} with the largest and smallest magnitudes and their corresponding applied stresses (confining, axial, and pore pressures; whenever applicable) are included in our compilation. By way of illustration, the measured UPV elasticity of shale G2IC-03 as a function of differential pressure (overburden minus pore pressure) is displayed in Figure 3-21. Additionally, the derived Thomsen parameters for the same shale are presented in the same figure. The marked elastic anisotropy of shale is clearly observed in Figure 3-21 and quantified by the large Thomsen parameter values.

Tables 3.17, 3.18, and 3.19 provide the acoustic data for the shale samples that will be used for model development. The elasticity data is presented in terms of the elastic constants C_{ij}. In addition, the stress states corresponding to the UPV measurements are presented, which are related to the levels of confining, axial, pore, or differential pressures used during acoustic testing (whenever applicable). Finally, Table 3.20 provides a summary of some relevant details of the experimental procedures followed in the different literature sources. For the data developed by the G2IC Industry Consortium, limited information has been provided due to proprietary issues. Nevertheless, the measurements are known to be of very high quality and reliability.

3.7.5 Macroscopic Strength Data for Shale

Compared to acoustic properties, the strength assessment of shale represents a more challenging task. Various technical problems arise in shale strength testing because of its extremely low permeability. Furthermore, well-preserved core samples are difficult to obtain [68]. The

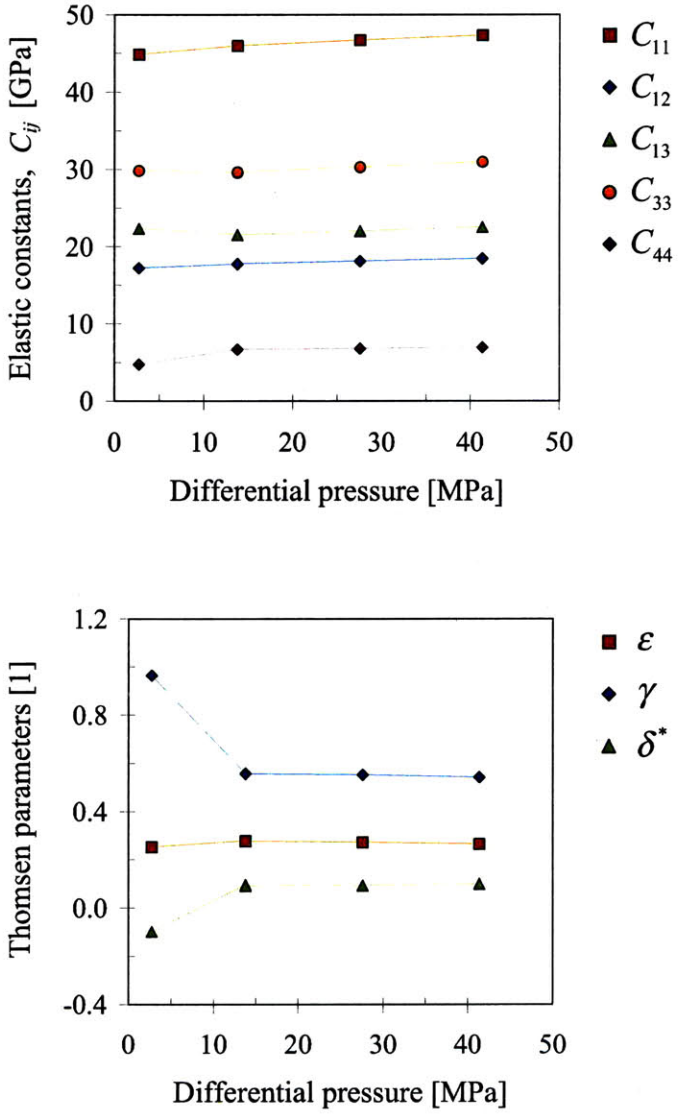

Figure 3-21: Elasticity constants C_{ij} of shale G2IC-03 as functions of differential pressure (top). Thomsen parameters derived from measured elastic constants as functions of differential pressure (bottom). The UPV data was generated by the G2IC.

Specimen	Pressure [MPa]			Elastic constants [GPa]				
	Overburden	Pore	Differential	C_{11}	C_{12}	C_{13}	C_{33}	C_{44}
G-01	19	16	3	18.6	8.5	7.3	11.8	3.6
	33	16	17	20.3	9.0	8.3	13.3	3.8
G-02	23	3	20	34.5	12.7	14.0	19.8	4.0
	47	20	27	35.4	13.3	14.8	20.6	4.1
G-03	3	1	3	44.9	17.2	21.5	29.6	6.6
	69	28	41	47.3	18.4	22.5	31.0	6.9
G-04	47	33	14	23.8	10.6	10.4	17.7	3.9
	53	33	21	25.0	11.7	13.8	19.2	4.5
G-05[a]	-	-	3	14.1	7.9	5.4	10.7	3.1
	-	-	20	16.2	9.1	6.8	12.3	3.4
G-06		N.A.		38.9	13.8	9.7	20.4	4.5
G-07		N.A.		45.8	17.7	14.1	29.7	8.9
G-08		N.A.		13.8	6.9	7.1	12.8	2.9
40	0	-	-	23.1	6.9	8.8	15.7	5.2
47	0	-	-	25.6	6.1	7.7	16.0	6.6
51	0	-	-	23.8	6.2	7.8	14.9	5.3
53	0	-	-	28.0	7.5	8.3	17.3	5.6
56	0	-	-	21.2	6.3	7.9	13.8	4.9
North sea[b]	2.5	-	-	32.5	-	-	23.4	-

Table 3.17: Macroscopic elasticity data for shale specimens gathered by the G2IC. The elasticity data were obtained from ultrasonic-pulse velocity measurements. The differential pressure represents the difference between the overdurben and pore pressures applied during testing. For some specimens, two sets of elastic properties are reported, which are related to the minimum and maximum elastic moduli and their corresponding stress states. N.A. (*non available*) refers to information not disclosed.

(a) The pressure during testing was reported as net pressure.

(b) The pressure during testing was reported as confining pressure. In addition, the elasticity for the North Sea shale specimen was calculated using the original UPV data and an estimate of the bulk density obtained from mineralogy and porosity.

Specimen	Pressure [MPa]			Elastic constants [GPa]				
	Confining	Differential	Pore	C_{11}	C_{12}	C_{13}	C_{33}	C_{44}
CRE	0.1	-	-	34.3	13.1	10.7	22.7	5.4
KIM	5	-	-	48.4	14.4	16.4	27.3	7.8
	80	-	-	56.2	18.4	20.5	36.4	10.3
JUR	5	-	-	33.4	14.2	14.8	22.5	5.0
	80	-	-	46.1	17.5	18.5	32.9	8.8
3492	1.5	0	1	28.8	7.4	3.8	19.9	9.3
	13	7	1	34.0	10.6	6.9	26.5	10.4
3506	1.5	0	1	28.0	10.6	3.5	21.8	6.9
	13	7	1	31.5	10.9	4.4	26.1	8.5
3525	1.5	0	1	23.7	6.5	4.5	19.6	8.1
	13	7	1	27.8	7.0	5.8	25.3	9.8
3536	1.5	0	1	31.8	8.2	4.7	19.3	5.6
	13	7	1	33.8	9.8	8.0	21.9	6.0
3564	1.5	0	1	26.9	8.3	3.4	19.0	8.6
	13	7	1	31.1	9.9	3.8	23.7	9.6
MUD	5	-	-	20.0	6.8	7.6	13.0	3.0
	60	-	-	27.0	9.5	16.2	18.0	4.5

Table 3.18: Macroscopic elasticity data for shale specimens gathered from literature sources. The list of specimens and their sources were introduced in Table 3.1. The differential pressure represents the difference between the axial and confining pressures applied during triaxial testing. Except for the CRE specimen, two sets of elastic properties are reported for each shale specimen, which are related to the minimum and maximum elastic moduli and their corresponding confining pressures at testing.

Specimen	Pressure [MPa]		Elastic constants [GPa]				
	Confining	Differential	C_{11}	C_{12}	C_{13}	C_{33}	C_{44}
108/111[a]	30	10	31.8	13.0	17.8	24.7	7.1
	45	40	35.5	13.5	16.5	29.5	8.9
9898[b]	15	170	-	-	-	31.9	16.6
9763[b]	15	230	-	-	-	57.7	24.2
	50	425	-	-	-	67.7	34.6
10151[b]	15	250	-	-	-	44.7	28.4
	50	240	-	-	-	30.0	19.3
6275[b]	50	202	-	-	-	35.8	14.6
7053[b]	15	135	-	-	-	54.7	18.0
	50	230	-	-	-	54.4	19.0
6853[b]	50	310	-	-	-	68.3	28.7
8675[b]	50	223	-	-	-	26.6	12.6
CO[c]	0	0	32.2	10.6	2.9	16.3	7.4
	15	0	32.9	10.9	3.6	17.4	7.6
[e]	-	-	34.5	11.5	10.8	23.6	8
CO[d]	0	0	35.3	14.3	10.9	22	7.1
	15	0	38.6	16	12.3	26.3	7.8
[e]	-	-	44.6	19	15	31.9	9.14

Table 3.19: Macroscopic elasticity data for shale specimens gathered from literature sources (continued). The list of specimens and their sources were introduced in Table 3.1. The differential pressure represents the difference between the axial and confining pressures applied during triaxial testing. For most specimens, two sets of elastic properties are reported for each shale specimen, which are related to the minimum and maximum elastic moduli and their corresponding stress states at testing.

(a) For specimen 108/111, the differential pressure refers to the difference between the confining and pore pressures applied during testing.

(b) For specimens 9898 through 8675 from Jizba [142], only isotropic properties are reported for these specimens. For the conversion from documented UPV data to elasticity constants, the density of the material was calculated using a linear combination of the densities of the clay and inclusion phases.

(c) The properties for specimen CO correspond to dry specimens tested at zero pore pressures.

(d) The properties for specimen CO correspond to wet specimens tested under undrained conditions.

(e) The sets of measured elasticity properties correspond to the highest moduli reached during isotropic stress loading, except for the elastic constants C_{13}, C_{33} in the dry case (b), which correspond to highest moduli reached during deviatoric stress loading.

Reference	Experimental procedures related to UPV measurements
[146]	Frequency of transducers: 1 MHz
	Confining pressure = 100 kPa
	Errors in elastic constants vary from +/- 4% for C_{11},C_{33} to +/- 50% for C_{13}
[129]	Frequency: 500 kHz for P-waves, 250 kHz for S-waves
	Confining pressures = 5 – 80 MPa
	Redundancy of measurements offers error estimates for all elastic constants
[138]	Frequency of transducers: 500-600 kHz
	Simulate in situ conditions by combination of:
	confining pressure = 1.5-13 MPa, axial load = 1.5-20 MPa
	constant pore-fluid pressure = 1 MPa
	Accurate estimate of C_{11},C_{12},C_{33},C_{44}.
	Less accurate for C_{13} due to use of only one off-axis receiver
[81]	Frequency: 0.75 MHz
	Pressure variations:
	Normally pressured state: confining = 45 MPa, pore = 5 MPa
	Highly overpressured state: confining = 30 MPa, pore = 20 MPa
	Differential pressure = difference between confining and pore pressures
	Same level of accuracy for all stiffness constants
[77]	Frequency: 0.6-1.0 MHz for P-waves, 0.2-0.4 MHz for S-waves
	Pore pressure = 5 MPa, Confining pressure = 10-65 MPa
	Errors in elastic constants < 1%, with exception of C_{13} ~2%
[142]	Central frequency for P- and S- waves: 1 MHz
	Confining pressures: 15, 50 MPa
	No assessment of the accuracy of acoustic measurements is presented
[226]	Central frequency for P- and S- waves: 1 MHz
	Hydrostatic and deviatoric stress paths were used during testing
	In situ conditions correspond to 15 MPa confining pressure
	Relative errors for elastic constants range between 9 and 19%

Table 3.20: Summary of experimental procedures used during UPV testing of the shale specimens documented in the open literature.

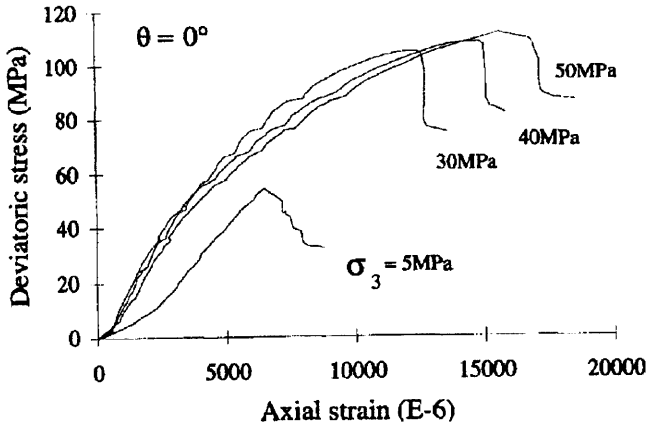

Figure 3-22: Deviatoric stress and axial strain during triaxial testing with various confining pressures (noted as σ_3). Data for Tournemire shale measured in the normal-to-bedding direction. From [195].

macroscopic knowledge base for shale strength properties has been developed based on the extensive use of triaxial testing, which allows the monitoring of pore pressures, hydrostatic, and deviatoric stresses that are applied independently on cylindrical rock samples [206].

The strength behavior of shale is certainly complex. Figure 3-22 displays the a typical deformation response of shale testing under a conventional triaxial setup, in which a radial and axial stresses are applied to the specimen. For low confining pressures, shale tends to exhibit a brittle behavior, whereas work-hardening is observed for higher states of confinement. These two different modes of deformation have been observed consistently for many shale materials [142, 298]. In addition, strength anisotropy has been reported [182, 195], although, the anisotropic behavior could be relatively small compared to other rock types (e.g. slates) [135].

In view of the exploratory character of the multi-scale strength investigation of shale, the focus of the strength assessment of shale is the unconfined compressive strength, a commonly reported parameter for the characterization of rocks [62]. In addition, unconfined compression is the conventional stress state used in most experimental programs. The review of the literature for shale strength yielded only a few sets of data which provide simultaneously strength properties and mineralogy and porosity information required for calculating the volumetric parameters (namely the clay packing density and the inclusion volume fraction) identified by the multi-scale model of shale. Unfortunately, macroscopic strength data was not developed yet by

Sample	Unconfined compressive strength (UCS) [MPa]
North Sea	21
RBBC-2	0.6
RBBC-4	1.1
RBBC-6	1.7
RBBC-8	2.3
RBBC-10	2.7
9898	110
10151	64
6275	98
7053	78
6853	149
8675	78
B	8.2
D	13
E	8
H	27
I	23
J	13
K	78
TOU	42
SH1	25

Table 3.21: Unconfined compressive strength data for shale samples from the literature, resedimented Boston Blue Clay samples, and the North Sea shale sample.

the G2IC, resulting in a more limited data set for strength modeling development compared to microporoelasticity.

The experimental data gathered from the open literature for shale strength is listed in Table 3.21. The strength data for the resedimented Boston Blue Clay is also employed for strength model development.

3.8 Chapter Summary

The presentation in this chapter of the database of material and mechanical properties for several shale samples sets the stage for the development of the multi-scale micromechanics modeling of shale. For the poroelasticity modeling, the mechanical characterization of shale at the grain-scale offers an unparalleled opportunity for devising effective mechanical descriptions

of the clay fabric's complex microstructure and composition. In addition, the multi-scale nature of the database herein developed complements the novel understanding of shale's nanomechanics with clay mineral properties at fundamental scales and conventional macroscopic acoustic data. Although different in nature, nanoindentation testing measurements and acoustic properties using ultrasonic pulse velocity techniques give access to the small-strain poroelastic behavior of shale. For shale strength, the interpretation of nanoindentation hardness measurements will aid our exploratory work of modeling and predicting macroscopic strength parameters by offering important insight into the nanomechanics interplay between cohesive and frictional characteristics of the clay phase in shale. The shale data collected in this chapter will be used in terms of collections or data sets that will assist model calibration and validation efforts.

Part III

Microporoelasticity of Shale

Chapter 4

Microporoelasticity of Shale

One of the most challenging tasks of rock physics is to link microstructure and composition of earth materials to acoustic velocity data that become accessible through increasingly sophisticated well logging tools in field applications and accurate laboratory measurements [115]. Classical approaches rely heavily on fitted empirical relations between velocity measurements and porosity, clay content, and other statistically significant parameters. Such empirical approaches have been implemented with some success for sandstones [88, 112] and limestones [99]. Some more refined methods have taken this approach a step further by linking porosity and clay content to seismic velocity through the application of effective medium theory [49, 221, 299]. However, modeling attempts have had a limited success when it comes to shale mainly due to the fact that shales –in contrast to sandstones, limestones, and synthetic clay-silt mixtures– are both highly heterogeneous and anisotropic from the micro- to the macroscale of engineering applications.

In Part III of this thesis, a microporoelastic model for shale is developed using a multi-scale structure approach. The aim of the model is to offer a universal description of the anisotropic poroelasticity of shale based on a specific set of material parameters defining the microstructure and composition. To this aim, Chapter 4 presents a comprehensive microporomechanics framework to model shale at the different length scales defined by the multi-scale structure thought model introduced in Chapter 2. In particular, the micromechanics framework allows for a complete description of the effects of material composition and microstructure on the poroelastic response of shale. Different sources of anisotropy related to the microstructure of

shale at microscopic scales such as particle geometries and orientations, as well as intrinsic elastic properties of the clay phase are incorporated in the model development.

The micromechanics modeling of shale continues in Chapter 5 with the calibration and validation of the model using a hypothesis testing approach. The different contributions to the macroscopic anisotropy of shale are translated into hypotheses of an elementary building block of solid clay, which is at the center of the developed upscaling scheme for poroelastic properties. The originality of the approach relies on the combination of the multi-scale micromechanics modeling and the use of extensive experimental data of shale elasticity. Various data sets inform and validate, independently, the modeled anisotropic elastic behavior of shale at different length scales. Of particular importance to the model development is the instrumented nanoindentation data generated by the GeoGenome Industry Consortium, and the inferred granular behavior of shale at sub-micrometer length scales. An effective description of the complex microstructure of shale's clay fabric will result from the model calibration and validation exercises, which will enable predictions of the macroscopic anisotropic behavior of shale based on parameters related to material composition and intrinsic material invariant properties of the clay phase.

Chapter 6 explores the applicability of the model established through the findings of the previous chapters. Chapter 6 will review the predictive capabilities of the adopted engineering model for shale at the different length scales in the context of the effectiveness of the elementary building block concept used for the modeling of the clay phase, the importance of particle geometries and orientation functions for the anisotropic description, and the relations of pressure and frequency dependencies to the measured poroelasticity and micromechanics model predictions. The proposed engineering model for shale will also be evaluated in terms of the predictions of poroelastic parameters, which are of importance for geomechanics and reservoir engineering applications. Finally, Chapter 7 presents an extension of the model for treating kerogen-rich shales and the results of two pilot studies aiming at the application of the model for characterizing shale formations.

4.1 Linear Microporoelasticity

Rocks, as many other natural composites, are heterogeneous materials with heterogeneities that manifest themselves from the nanoscale to the macroscale of engineering applications[1]. At sub-millimeter length scales, the rock specimen is composed of a complex fabric of grains and particles of diverse mineralogy, in addition to the occurrence of porosity. However, standard experimental techniques probe material samples on the order of centimeters in size. Consequently, the measured properties of the rock specimen represent the average properties of a heterogeneous composite material. If focusing on smaller scales, a similar observation can be made regarding single crystal grains, which are the result of specific atomic configurations and crystalline structures. The description of the transition from atomic scales (described by quantum and statistical mechanics) to the continuum scale (described by continuum physics) is the subject of condensed matter physics. In this work, the study of shale as a heterogeneous material begins at fundamental scales where the elementary constituents (clay minerals, nanoporosity) can be described using continuum mechanics theory. The natural objective is then to investigate the dependence of macroscopic properties of the heterogeneous composite based on the mechanical properties of its constituents and their spatial arrangement or microstructure.

To assist in the objective of modeling heterogeneous material systems, a variety of theoretical and computational frameworks have been developed such as finite element theory, discrete element theory, and periodic homogenization, among others. An attractive alternative to these methodologies are analytical and semi-analytical approaches using continuum micromechanics and random homogenization theory. In particular, the micromechanics approach for hierarchically structured materials systems has been successfully implemented in recent applications to natural composites such as concrete [21, 269], bone [93, 117], and shale [128, 267]. In micromechanics theory, not all the details of the complex microstructures and material phases are considered. Instead, only essential information regarding morphological features such as particle shapes and their orientations, mechanical properties, and volume fractions is considered in the homogenization problem.

Within the micromechanics approach, a variety of analytical methods are available for ap-

[1] This section is inspired in the presentation of Ponte Castañeda [217].

proaching the computation of homogenized properties of a heterogeneous material. Rigorous bounding methods have been extensively developed for estimating the effective behavior of heterogeneous materials. However in poromechanics, bounds may tend to be far apart and may not be of practical use for field applications [23]. Such situation requires the use of exact estimates provided by effective medium (mean-field) theories, which provide homogenization solutions for particular types of material microstructures.

In the remainder of this section, linear microporoelasticity is introduced as the methodology to be used for modeling the multi-scale, anisotropic poroelasticity of shale. This theoretical foundation will enable the development of a suit of micromechanics tools for linking the material composition and microstructure to the poroelastic material response of a multi-scale material system.

4.1.1 Elements of Continuum Mechanics and Homogenization Theory

The Representative Elementary Volume and Scale Separability

A critical element in the implementation of the continuum micromechanics approach is the concept of the representative elementary volume (*rev*), which is defined as an infinitesimal part of a three-dimensional structure or material system. The relevance of using the tools of integral and differential calculus offered by the continuum description are guaranteed when the characteristic length of the *rev* l is much smaller than the characteristic length scale of the structural system L. Furthermore, the size of the *rev* should be large enough to be representative of the material system, capturing the geometrical and physical properties relevant of the mechanical behavior under consideration. Hence, the *rev* should be much larger than that of local heterogeneities or deformation mechanisms, with characteristic length scale d. In addition, the scale of heterogeneities has to be compatible with the use of continuum mechanics concepts (e.g. strain and stress tensors). This implies a fourth length scale d_0, which serves as a lower bound below which continuum mechanics is no longer applicable. The previous descriptions are summarized in the *scale separability condition*, which serves as the necessary condition for the concept of the *rev* to be valid [301]:

$$d_0 \ll d \ll l \ll L \tag{4.1}$$

Homogenization Methodology

In constitutive modeling, the geometric deformation of a material system due to the application of forces prescribed from the outside is characterized by a macroscopic constitutive law. This macroscopic law aims at establishing a relation between the (macroscopic) forces applied to the system and the (macroscopic) strains, which determine the transformation of the elementary volume of the material system. The design of such macroscopic law can be typically derived from a purely phenomenological approach at the macroscale, which is based on the observation of the mechanical response of the material system to applied forces or displacements. However, homogenization theory provides an alternative approach to deriving the mechanical response of the material by solving a boundary value problem at the scale of the *rev*. Provided the appropriate scale of observation, the macroscopic behavior of the material considers the influence of the heterogeneous nature of the microstructure present in the *rev*. The objective of classical homogenization approaches is to replace the heterogeneous composite material by an equivalent homogeneous one that behaves mechanically in the same way at the global (macroscopic) scale.

The main components of the homogenization approach are summarized as follows [301]:

Description of the *rev* The first step in the homogenization approach is to describe the fundamental geometrical and mechanical features of the *rev*. Given the heterogeneous nature of the macroscopic material, statistical information is required in order to describe the relevant features[2]. The description of the *rev* begins with establishing the considered active mechanical phases and their mechanical attributes. In addition, statistical descriptions of their spatial distributions, or *morphology*, are necessary: volume fractions, texture functions, lattice orientations for crystalline particles, orientation distribution functions of fibers and voids and their aspect ratios, etc. From a practical perspective, a complete statistical description of the spatial distribution may be difficult to obtain, which opens the way for utilizing approximations or estimates based on the most salient morphological features according to the particular microstructure.

[2] In this investigation, we only consider materials with random microstructures. Materials with periodic microstructures can be treated with a different suit of homogenization theories.

Concentration or Localization The concentration or localization problem refers to the modeling of the interaction of mechanical phases present in the *rev* and their corresponding local stress and strain fields $\boldsymbol{\sigma}(\underline{z}), \boldsymbol{\varepsilon}(\underline{z})$ from the prescribed macroscopic stress and strain quantities $\boldsymbol{\Sigma}, \mathbf{E}$. The concentration problem at the *rev* level is an ill-posed problem since detailed constraints at the boundary of a *rev* are not known. In turn, a simpler problem is defined by considering *homogeneous boundary conditions* on the *rev*, also known as Hashin boundary conditions.

The *uniform stress boundary condition* represents the case of a *rev* subjected to a constant macroscopic stress state:

$$\boldsymbol{\sigma}'(\underline{z}) \cdot \underline{n}(\underline{z}) = \boldsymbol{\Sigma} \cdot \underline{n}(\underline{z}) \qquad (\forall \underline{z} \in \partial\Omega) \tag{4.2}$$

where $\underline{n}$ is unit outward normal at the boundary of the *rev* $\partial\Omega$. One can prove that $\boldsymbol{\Sigma}$ is equivalent to the volume average of the stress $\overline{\boldsymbol{\sigma}'}$ in the *rev* for any equilibrated, divergence-free[3] stress field $\boldsymbol{\sigma}'(\underline{z})$ which obeys (4.2):

$$\overline{\boldsymbol{\sigma}'} = \frac{1}{|\Omega|} \int_{\Omega} \boldsymbol{\sigma}'(\underline{z})\, dV_z = \boldsymbol{\Sigma} \tag{4.3}$$

In turn, the *uniform strain boundary condition* represents the case of a *rev* subjected to a regular displacement condition at its boundary:

$$\underline{\boldsymbol{\xi}}'(\underline{z}) = \mathbf{E} \cdot \underline{z} \qquad (\forall \underline{z} \in \partial\Omega) \tag{4.4}$$

Provided that the length scales of the heterogeneities are much smaller than that of the *rev* as prescribed in the scale separability condition (4.1), the macroscopic strain $\mathbf{E}$ is equivalent to the volume average of the strain $\overline{\boldsymbol{\varepsilon}'}$ for any strain field $\boldsymbol{\varepsilon}'(\underline{z})$ derived from its corresponding displacement field, and which obeys (4.4):

$$\overline{\boldsymbol{\varepsilon}'} = \frac{1}{|\Omega|} \int_{\Omega} \boldsymbol{\varepsilon}'(\underline{z})\, dV_z = \mathbf{E} \tag{4.5}$$

[3]The assumption of neglecting body forces in the formulation of the local problem is valid provided that $|\boldsymbol{\Sigma}| \gg |\rho \underline{f}| \times l$, where $\rho \underline{f}$ is a volume force, and l the characteristic length scale of the *rev*. This assumption is in fact relevant to the homogenization problem [83].

A remarkable consequence of applying the uniform boundary conditions (4.2) or (4.4) is the particular result called the Hill lemma, which consists in a similar average formulation for the case of the strain energy $\boldsymbol{\sigma}' : \boldsymbol{\varepsilon}'$:

$$\overline{\boldsymbol{\sigma}' : \boldsymbol{\varepsilon}'} = \overline{\boldsymbol{\sigma}'} : \overline{\boldsymbol{\varepsilon}'} = \boldsymbol{\Sigma} : \mathbf{E} \tag{4.6}$$

The Hill lemma states that the microscopic strain energy is equal to its macroscopic counterpart. With this result at hand, estimates for the stress and strain fields can be reached as functions of the macroscopically applied boundary conditions:

$$\boldsymbol{\sigma}'(\underline{z}) = \mathcal{B}(\boldsymbol{\Sigma}) \tag{4.7a}$$

$$\boldsymbol{\varepsilon}'(\underline{z}) = \mathcal{A}(\mathbf{E}) \tag{4.7b}$$

where $\mathcal{B}$ and $\mathcal{A}$ are the stress and strain concentration operators, respectively.

Homogenization The final step in the process of upscaling of mechanical properties is the *homogenization* itself. The objective of homogenization is to determine the appropriate expression for the macroscopic strain $\mathbf{E}$ associated with the microscopic strain field $\boldsymbol{\varepsilon}(\underline{z})$ when the *rev* is subjected to a (macroscopic) loading $\boldsymbol{\Sigma}$. Equivalently, the relation between the macroscopic stress $\boldsymbol{\Sigma}$ and the microscopic stress field $\boldsymbol{\sigma}(\underline{z})$ is sought when the *rev* is subjected to a (macroscopic) strain $\mathbf{E}$. Thus, combining the local constitutive relations $\boldsymbol{\sigma}(\boldsymbol{\varepsilon}), \boldsymbol{\varepsilon}(\boldsymbol{\sigma})$, the average relations (4.3) or (4.5), and the concentration operations in (4.7) yields the following upscaling relations according to the boundary condition (4.2) or (4.4):

$$\mathbf{E}'(\boldsymbol{\Sigma}) = \overline{\boldsymbol{\varepsilon}'(\boldsymbol{\sigma}')} = \overline{\boldsymbol{\varepsilon}'[\mathcal{B}(\boldsymbol{\Sigma})]} \tag{4.8a}$$

$$\boldsymbol{\Sigma}'(\mathbf{E}) = \overline{\boldsymbol{\sigma}'(\boldsymbol{\varepsilon}')} = \overline{\boldsymbol{\sigma}'[\mathcal{A}(\mathbf{E})]} \tag{4.8b}$$

For the particular case of linear elasticity, the microscopic and macroscopic stresses and strains are related by linear and homogeneous functions with respect to the loading parameters $\boldsymbol{\Sigma}$ and $\mathbf{E}$. Consequently, the concentration operators in (4.7) reduce to fourth-order tensor

fields:

$$\boldsymbol{\sigma}'(\underline{z}) = \mathbb{B}(\underline{z}) : \boldsymbol{\Sigma} \tag{4.9a}$$

$$\boldsymbol{\varepsilon}'(\underline{z}) = \mathbb{A}(\underline{z}) : \mathbf{E} \tag{4.9b}$$

These two results tend to be equivalent when the ratio d/l (that is, the ratio of the size of the local heterogeneities in the *rev* compared to the size of the *rev*) tends to zero (Hill-Mandel theorem, [125, 170]), which is enforced in view of the scale separability condition stated in (4.1). We extend the result (4.9b) for the case of describing the local stress field. In that case:

$$\boldsymbol{\sigma}'(\underline{z}) = \mathbb{C}(\underline{z}) : \mathbb{A}(\underline{z}) : \mathbf{E} \tag{4.10}$$

where $\mathbb{C}(\underline{z})$ is the material law describing the stiffness content of the material system at location $\underline{z}$. The use of the average rule (4.3) provides the following relation:

$$\boldsymbol{\Sigma}' = \overline{\boldsymbol{\sigma}'(\underline{z})} = \overline{\mathbb{C}(\underline{z}) : \mathbb{A}(\underline{z})} : \mathbf{E} \tag{4.11}$$

in which we readily identify the homogenized stiffness tensor $\mathbb{C}_{\text{hom}}$ that estimates the overall or effective stiffness response of the material system represented as a homogeneous medium:

$$\mathbb{C}_{\text{hom}} = \overline{\mathbb{C}(\underline{z}) : \mathbb{A}(\underline{z})} \tag{4.12}$$

In a similar manner, the result for the effective compliance of the heterogeneous medium is found:

$$\mathbb{S}_{\text{hom}} = \overline{\mathbb{S}(\underline{z}) : \mathbb{B}(\underline{z})} \tag{4.13}$$

The determination of the stress or strain concentration tensor is critical to the homogenization problem in linear poroelasticity. From a micromechanics perspective, the concentration tensors carry the relevant micromechanical information about the morphology and interaction of mechanical phases. With the appropriate estimates of these micromechanics quantities, estimates of elastic and poroelastic parameters can be accomplished. The determination of the concentration tensors is presented in the next section.

4.2 Localization and Microstructures

From expressions (4.12) and (4.13), the determination of the effective stiffness and compliance of the heterogeneous material, either as rigorous *bounds* or *estimates*, depend on the definitions of the concentrations tensors. Bounding approaches can be rigorously derived based on the available statistical description of the heterogeneous medium. The application of variational principles in elasticity theory yields the following bounds for the homogenized elasticity tensors (see e.g. [301]):

$$\boldsymbol{\Sigma} \;:\; \left(\overline{{}^{t}\mathbb{B} : \mathbb{S} : \mathbb{B}} - \mathbb{S}_{\text{hom}}\right) : \boldsymbol{\Sigma} \geq 0 \quad (\forall \boldsymbol{\Sigma}) \tag{4.14a}$$

$$\mathbf{E} \;:\; \left(\overline{{}^{t}\mathbb{A} : \mathbb{C} : \mathbb{A}} - \mathbb{C}_{\text{hom}}\right) : \mathbf{E} \geq 0 \quad (\forall \mathbf{E}) \tag{4.14b}$$

where ${}^{t}\mathbb{B}$ is the transpose of the components of $\mathbb{B}$, ${}^{t}B_{ijkl} = B_{klij}$. In the simplest case when the elasticity and the volume fractions of the constituents are known, the use of uniform fields in (4.9), that is, $\mathbb{B} = \mathbb{I}$ and $\mathbb{A} = \mathbb{I}$, gives the well-known Reuss and Voigt bounds, respectively:

$$\boldsymbol{\Sigma} \;:\; \left(\overline{\mathbb{S}} - \mathbb{S}_{\text{hom}}\right) : \boldsymbol{\Sigma} \geq 0 \quad (\forall \boldsymbol{\Sigma}) \tag{4.15a}$$

$$\mathbf{E} \;:\; \left(\overline{\mathbb{C}} - \mathbb{C}_{\text{hom}}\right) : \mathbf{E} \geq 0 \quad (\forall \mathbf{E}) \tag{4.15b}$$

Note that $\mathbb{I}$ is the fourth-order identity tensor ($I_{ijkl} = \frac{1}{2}\left(\delta_{ik}\delta_{jl} + \delta_{il}\delta_{jk}\right)$; δ_{ij} is the Kronecker delta). If the microstructure of the material system is statistically isotropic, a tighter set of bounds can be derived, known as the Hashin and Shtrikman bounds [114]. The incorporation of more refined statistical descriptions such as two-point correlations (a description of the positions of particles in a composite) provides rigorous ways for improving the construction of bounding schemes for e.g. linear elastic random composites , and non-linear composites [215, 248, 253].

In contrast to rigorous bounding methods, approximations for the effective stiffness that treat specific types of microstructures have also been proposed. These so-called *effective medium theory* estimates become suitable approaches as often the solutions of bounding methods may tend to be far apart [23]. In what follows, we recall a fundamental result of micromechanics, Eshelby's inclusion problem, which enables the development of a set of upscaling methods for

linear elastic composites[4]. In particular, the Eshelby's solution provides the foundation for estimating concentration tensors that are suitable for particulate and granular microstructures, which are of direct interest for poromechanics applications to geomaterials.

4.2.1 Eshelby's Inclusion Problem

In linear micromechanics, Eshelby's problem addresses the strain field in an ellipsoidal inclusion, embedded in an infinite homogeneous medium, with different elasticity, and subjected to uniform displacement boundary conditions at infinity. The ellipsoidal shape can account for a large variety of inhomogeneities found in composite materials, such as flat cracks or elongated needle shapes as extreme cases. The Eshelby's elastic inclusion problem adapted for the case of an inhomogeneity is depicted in Figure 4-1. The mechanics problem is presented as (see e.g. [83]):

$$\begin{aligned} &\operatorname{div}\boldsymbol{\sigma} = 0 && (\Omega) \\ &\boldsymbol{\sigma}(\underline{z}) = \mathbb{C}^{mat} : \boldsymbol{\varepsilon}(\underline{z}) + \boldsymbol{\sigma}^I(\underline{z}) && (\Omega) \\ &\underline{\xi}(\underline{z}) = \mathbf{E} \cdot \underline{z} && (\underline{z} \to \infty) \end{aligned} \tag{4.16}$$

where $\boldsymbol{\sigma}^I(\underline{z})$ is a fictitious stress field in the inclusion that characterizes the deviation from the homogeneous state induced by the inclusion:

$$\boldsymbol{\sigma}^I(\underline{z}) = \begin{cases} 0 & \left(\Omega^{mat}\right) \\ \delta\mathbb{C} : \boldsymbol{\varepsilon}(\underline{z}) & \left(\Omega^I\right) \end{cases} \tag{4.17}$$

where $\delta\mathbb{C} = \mathbb{C}^I - \mathbb{C}^{mat}$ is the contrast in elasticity content between the inclusion and homogeneous matrix. The remarkable result of Eshelby's inclusion problem (in which the original stress field $\boldsymbol{\sigma}^I(\underline{z})$ in (4.16) is assumed constant $\boldsymbol{\sigma}^I(\underline{z}) = \boldsymbol{\sigma}^I$ in Ω_I) is that the strain field is constant within an ellipsoidal inclusion:

$$\boldsymbol{\varepsilon}^I = -\mathbb{S}^{esh} : \left(\mathbb{C}^{mat}\right)^{-1} : \boldsymbol{\sigma}^I + \mathbf{E} \quad (\Omega_I) \tag{4.18}$$

[4] A comprehensive review of homogenization techniques for linear elastic composites is presented in [186].

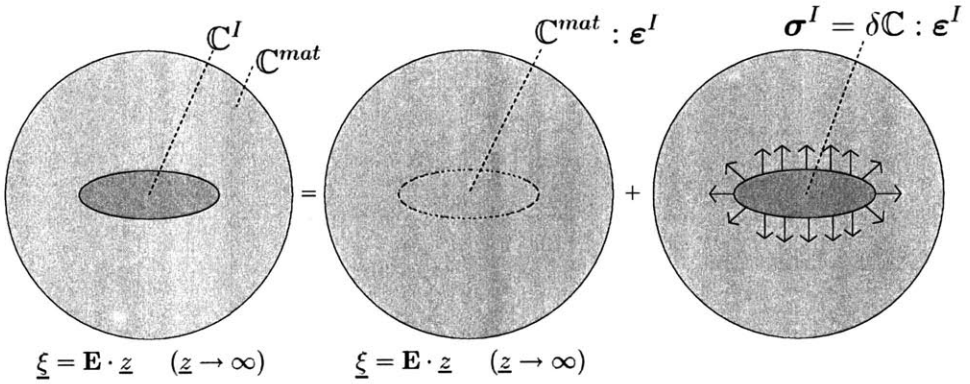

Figure 4-1: Eshelby's problem. Ellipsoidal inclusion of stiffness $\mathbb{C}^I$ embedded in an infinite matrix of stiffness $\mathbb{C}^{mat}$. Adapted from [264].

where $\mathbb{S}^{esh}$ is the Eshelby tensor. Furthermore, the Eshelby tensor is related to the fourth-order Hill concentration tensor (or P-tensor) $\mathbb{P}$ by:

$$\mathbb{S}^{esh} = \mathbb{P} : \mathbb{C}^{mat} \tag{4.19}$$

In synthesis, the P-tensor carries the information regarding the morphology and the orientation of the inclusion phase. A detailed description of the Hill tensor will be provided in a forthcoming section.

The fictitious stress $\boldsymbol{\sigma}^I$ is also constant in the inclusion, and it is linearly related to the macroscopic strain by:

$$\boldsymbol{\sigma}^I = \left[\mathbb{I} + \delta\mathbb{C} : \mathbb{S}^{esh} : \left(\mathbb{C}^{mat}\right)^{-1}\right] : \delta\mathbb{C} : \mathbf{E} \quad \left(\Omega^I\right) \tag{4.20}$$

Similarly, the relation between the microscopic strain in the inclusion and the macroscopic strain is, after manipulation:

$$\boldsymbol{\varepsilon}^I = \left[\mathbb{I} + \mathbb{S}^{esh} : \left(\left(\mathbb{C}^{mat}\right)^{-1} : \mathbb{C}^I - \mathbb{I}\right)\right]^{-1} : \mathbf{E} \quad \left(\Omega^I\right) \tag{4.21}$$

Expression (4.21) can be regarded as a strain concentration relation of the macroscopic strain prescribed at infinity into the inclusion phase, which in terms of the Hill concentration tensor

reads:

$$\boldsymbol{\varepsilon}^I = \overline{\mathbb{A}}^I : \mathbf{E} \tag{4.22a}$$

$$\overline{\mathbb{A}}^I = \left[\mathbb{I} + \mathbb{P} : \left(\mathbb{C}^I - \mathbb{C}^{mat}\right)\right]^{-1} \tag{4.22b}$$

4.2.2 Dilute Scheme

The first implementation of Eshelby's solution is for a set of aligned ellipsoids of similar shape and elasticity content that are distributed randomly in an elastic matrix phase. Furthermore, the concentration of inclusions is small, or *dilute*, which implies that the different inclusions are well separated from each other. Consequently, it is expected that the inclusions will not interact with each other. Within these constraints, the solution of Eshelby's inclusion problem is applicable, which expresses the average strain concentration tensor on the inclusion phase as $\overline{\mathbb{A}}^I$ in (4.22b):

$$\overline{\mathbb{A}}^I_{dilute} = \left[\mathbb{I} + \mathbb{P} : \left(\mathbb{C}^I - \mathbb{C}^{mat}\right)\right]^{-1} \tag{4.23}$$

For instance, the dilute approximation of the concentration tensor for an empty porous material, whose solid matrix and pore space have stiffness tensors $\mathbb{C}^s$ and $\mathbb{C}^p = 0$, respectively, yields:

$$\overline{\mathbb{A}}^p = (\mathbb{I} - \mathbb{P} : \mathbb{C}^s)^{-1} \tag{4.24}$$

Note that the concentration tensor satisfies the condition:

$$\overline{\mathbb{A}\,(\underline{z})} = \mathbb{I} \tag{4.25}$$

from the use of (4.9b) in (4.5). Using (4.24) and (4.25), the dilute estimate of the effective stiffness of the porous solid is:

$$\mathbb{C}_{\text{hom}} = \mathbb{C}^s : \left[\mathbb{I} - \phi_0 \left(\mathbb{I} - \mathbb{P} : \mathbb{C}^s\right)^{-1}\right] \tag{4.26}$$

where ϕ_0 represents the volume fraction corresponding to the pore space $\Omega^p = \phi_0 \Omega$.

The determination of the effective response of a composite material beyond the dilute concentration regime is a challenging task, for which advanced statistical means would be necessary

to describe the interaction between particles and their specific spatial arrangement within the material fabric. However, two types of effective medium theory schemes applicable to matrix-inclusion composites and granular materials account for inclusion interactions through the use of Eshelby's solution in microelasticity.

4.2.3 Mori-Tanaka Scheme

Within the framework of Eshelby's inhomogeneity problem, the interactions between inclusions for non-dilute inclusion concentrations can be captured by considering that the average strain in the homogeneous material surrounding the inclusion is:

$$\overline{\boldsymbol{\varepsilon}}^m = \mathbf{E}_0 \qquad (\Omega^m) \tag{4.27}$$

In this case, the strain in the inclusion phase is determined using (4.22):

$$\boldsymbol{\varepsilon}^I = \left[\mathbb{I} + \mathbb{P}^0 : \left(\mathbb{C}^I - \mathbb{C}^0\right)\right]^{-1} : \mathbf{E}_0 \qquad \left(\Omega^I\right) \tag{4.28}$$

where $\mathbb{C}^0$ is the reference stiffness of the surrounding matrix. It is left to relate the macroscopic strains $\mathbf{E}$ and $\mathbf{E}_0$, which is accomplished by using the strain average rule $\overline{\boldsymbol{\varepsilon}} = \mathbf{E}$:

$$\begin{aligned}
\mathbf{E} &= f^I \boldsymbol{\varepsilon}^I + \left(1 - f^I\right) \overline{\boldsymbol{\varepsilon}}^m && \text{(4.29a)} \\
&= \left(f^I \left[\mathbb{I} + \mathbb{P}^0 : \left(\mathbb{C}^I - \mathbb{C}^0\right)\right]^{-1} + \left(1 - f^I\right) \mathbb{I}\right) : \mathbf{E}_0 && \text{(4.29b)} \\
&= \overline{\left[\mathbb{I} + \mathbb{P}^0 : \left(\mathbb{C} - \mathbb{C}^0\right)\right]^{-1}} : \mathbf{E}_0 && \text{(4.29c)}
\end{aligned}$$

where $f^I = \Omega_I / \Omega$, and $\mathbb{C}$ represents the material phases $\left(\mathbb{C}^I, \mathbb{C}^0\right)$ involved in the averaging operation over the volumes $\left(\Omega^I, \Omega^{mat}\right)$ respectively. The use of (4.28) and (4.29) entail the following estimate of the average strain concentration tensor in the inclusion:

$$\overline{\mathbb{A}}^I = \left[\mathbb{I} + \mathbb{P}^0 : \left(\mathbb{C}^I - \mathbb{C}^0\right)\right]^{-1} : \overline{\left[\mathbb{I} + \mathbb{P}^0 : \left(\mathbb{C} - \mathbb{C}^0\right)\right]^{-1}}^{-1} \tag{4.30}$$

The choice of the reference medium in (4.30) determines a particular microstructure of the heterogeneous material. In the case of a composite with a characteristic matrix-inclusion

morphology, the reference medium corresponds to the solid matrix with stiffness $\mathbb{C}^0 = \mathbb{C}^s$. The resulting representation is commonly known in the literature as the *Mori-Tanaka* estimate [188]:

$$\overline{\mathbb{A}}^I_{mt} = \left[\mathbb{I} + \mathbb{P}^s : \left(\mathbb{C}^I - \mathbb{C}^s\right)\right]^{-1} : \overline{\left[\mathbb{I} + \mathbb{P}^s : \left(\mathbb{C} - \mathbb{C}^s\right)\right]^{-1}}^{-1} \tag{4.31}$$

For illustration, the application of the Mori-Tanaka scheme for a porous solid material using the strain concentration estimate (4.31) in (4.12), in addition to the average condition (4.25), yields the following estimate for the drained stiffness tensor:

$$\mathbb{C}_{\text{hom}} = \mathbb{C}^s : \left(\mathbb{I} - \phi_0 \left(\mathbb{I} - \mathbb{S}\right)^{-1} : \left[\left(1 - \phi_0\right)\mathbb{I} + \phi_0 \left(\mathbb{I} - \mathbb{S}\right)^{-1}\right]^{-1}\right) \tag{4.32}$$

where $\mathbb{S} = \mathbb{P}^s : \mathbb{C}^s$ is the Eshelby tensor. The drained response is a consequence of the pore space being emptied of any pore fluids.

The implementation of the Mori-Tanaka scheme provides useful stiffness estimates for matrix-inclusion type composite materials, especially for the cases of families of spherical or unidirectional, aligned ellipsoids [19], or a solid intermixed with a single family of randomly oriented ellipsoids [289]. However, Mori-Tanaka estimates for other configurations may lead to physically unrealistic predictions or violate rigorous bounds [217, 259].

4.2.4 Self-Consistent Scheme

In contrast to the matrix-inclusion morphology, other materials exhibit random microstructures in which none of the phases plays the apparent role of a matrix material. In this case, the *self-consistent* approximation is known to be a good estimate for polycrystalline materials and composites with granular microstructures. The self-consistent scheme was introduced by Hershey [121] and Kroner [154] in the context of elastic polycrystals, and by Budiansky [47] and Hill [124] for other types of aggregates and composites. The self-consistent approximation has been also developed by various authors in different contexts other than microelasticity (e.g. scattering theory [107]).

Within the framework of the self-consistent scheme, the interaction of particles are modeled by considering that all mechanical phases play the role of grains akin the composite response of a polycrystalline material. Given that no particular phase serves as a matrix, one can adapt

the results in (4.30) according to the choice that the reference medium $\mathbb{C}^0$ is the homogenized (self-consistent) material $\mathbb{C}^{sc}$:

$$\overline{\mathbb{A}}^I_{sc} = \left[\mathbb{I} + \mathbb{P}^{sc} : \left(\mathbb{C}^I - \mathbb{C}^{sc}\right)\right]^{-1} : \overline{\left[\mathbb{I} + \mathbb{P}^{sc} : \left(\mathbb{C} - \mathbb{C}^{sc}\right)\right]^{-1}}^{-1} \tag{4.33}$$

The self-consistent estimate $\mathbb{C}^{sc}$ is derived from (4.12):

$$\mathbb{C}^{sc} = \overline{\mathbb{C} : \left[\mathbb{I} + \mathbb{P}^{sc} : \left(\mathbb{C} - \mathbb{C}^{sc}\right)\right]^{-1}} : \overline{\left[\mathbb{I} + \mathbb{P}^{sc} : \left(\mathbb{C} - \mathbb{C}^{sc}\right)\right]^{-1}}^{-1} \tag{4.34}$$

It is worth noticing that the strain concentration tensor $\overline{\mathbb{A}}^I_{sc}$ is applicable to all the mechanical active phases, since each phase plays the role of an inclusion I.

By way of example, the self-consistent estimate of the drained stiffness behavior of a porous solid with granular microstructure is developed:

$$\begin{aligned} \mathbb{C}_{\text{hom}} \;=\; & \left(1-\phi_0\right)\mathbb{C}^s : \left[\mathbb{I} + \mathbb{P}^{sc} : \left(\mathbb{C}^s - \mathbb{C}^{sc}\right)\right]^{-1} : \\ & \left(\phi_0 \left[\mathbb{I} - \mathbb{P}^{sc} : \mathbb{C}^{sc}\right]^{-1} + \left(1-\phi_0\right)\left[\mathbb{I} + \mathbb{P}^{sc} : \left(\mathbb{C}^s - \mathbb{C}^{sc}\right)\right]^{-1}\right)^{-1} \end{aligned} \tag{4.35}$$

where the self-consistent reference medium stiffness is equivalent to the homogenized stiffness tensor $\mathbb{C}^{sc} = \mathbb{C}_{\text{hom}}$. The calculation of the P-tensor depends on the homogenized stiffness $\mathbb{P}^{sc} = \mathbb{P}^{sc}\left(\mathbb{C}_{\text{hom}}\right)$. By inspection, the solution of (4.35) could be implicit depending on the complexity of the P-tensor expression, in which case numerical techniques can assist in the calculations. For completeness, it is worth developing the expression (4.35) one step further for the case in which both inclusion types (solid particles and pores) exhibit the same geometry and orientation, which implies that the P-tensors for both phases are identical. Rewriting (4.34) as:

$$\overline{\left(\mathbb{C} - \mathbb{C}^{sc}\right) : \left[\mathbb{I} + \mathbb{P}^{sc} : \left(\mathbb{C} - \mathbb{C}^{sc}\right)\right]^{-1}} = 0 \tag{4.36}$$

it then follows from (4.36) when all P-tensors are identical that:

$$\overline{\left[\mathbb{I} + \mathbb{P}^{sc} : \left(\mathbb{C} - \mathbb{C}^{sc}\right)\right]^{-1}} = \mathbb{I} \tag{4.37}$$

This result provides a simplified form of (4.34):

$$\mathbb{C}^{sc} = \overline{\mathbb{C} : [\mathbb{I} + \mathbb{P}^{sc} : (\mathbb{C} - \mathbb{C}^{sc})]^{-1}} \tag{4.38}$$

which for the case of the porous solid in (4.35) yields:

$$\mathbb{C}_{\text{hom}} = (1 - \phi_0)\, \mathbb{C}^s : [\mathbb{I} + \mathbb{P}^{sc} : (\mathbb{C}^s - \mathbb{C}_{\text{hom}})]^{-1} \tag{4.39}$$

An important feature of the self-consistent scheme for porous materials, although not apparent from expressions (4.33) and (4.35), is the prediction of a percolation threshold at finite values of porosity. At the percolation threshold, the stiffness of the composite material vanishes. This characteristic modeling feature of the self-consistent scheme is most valuable for granular composites, and it will be used extensively in the development of a micromechanical model for shale. In forthcoming sections, a detailed analysis of the features of the self-consistent estimate for porous materials will be offered, in which we relate the predicted stiffness response of granular material to the percolation threshold and microstructural features such as particle shape and orientations.

4.2.5 Hill Concentration or P-Tensor

The last component of the micromechanics approach for modeling heterogeneous materials based on effective medium theory is the evaluation of the Hill concentration tensor, or P-tensor, $\mathbb{P}$ (4.19). Within the framework of Eshelby's inhomogeneity problem, the Hill tensor captures the morphology and orientation of the inclusion phases necessary for the estimation of the overall strain concentration tensors (e.g. see (4.22)).

The solution of the microstrain in the ellipsoidal inclusion (4.18) depends on the computation of the fourth-order Hill tensor $\mathbb{P}$:

$$P^0_{ijkl} = -\left[\frac{\partial^2}{\partial z_j \partial z_k}\left(\int_I G^0_{il}\left(\underline{z} - \underline{z}'\right) dV_{z'}\right)\right]_{(ij),(kl)} \tag{4.40}$$

in which the second-order Green function $\mathbf{G}^0\left(\underline{z} - \underline{z}'\right)$ expresses the displacement at point $\underline{z}$ in a linear elastic solid medium of stiffness $\mathbb{C}^0$ resulting from a unit force applied at a point $\underline{z}'$ in

the medium. Alternatively for the elasticity problem at hand, the Hill tensor may be expressed following Laws classical expressions [159], which in a slightly different form read [249]:

$$P_{ijkl} = \frac{1}{16\pi} \left(\mathcal{M}_{kijl} + \mathcal{M}_{kjil} + \mathcal{M}_{lijk} + \mathcal{M}_{ljik} \right) \tag{4.41}$$

where,

$$\mathcal{M}_{kijl} = \int_{S(\underline{\omega})} \frac{a_1 a_2 a_3}{\left(a_1^2 \omega_1^2 + a_2^2 \omega_2^2 + a_3^2 \omega_3^2 \right)^{3/2}} \Gamma_{kj}^{-1} \left(\underline{\omega} \right) \omega_i \omega_l dS_\omega \tag{4.42}$$

Parameters a_1, a_2, a_3 relate to the shape of the ellipsoid, $dS\left(\underline{\omega}\right)$ is the surface element of a unit ellipsoid of components $\omega_1, \omega_2, \omega_3$, and $\Gamma_{ik}\left(\underline{\omega}\right) = C^0_{ijkl}\omega_j\omega_l$ represents the Christoffel matrix denoting the stiffness of the matrix. Note that the fourth-order P-tensor is positive definite and obeys both major (diagonal) and minor symmetries, in contrast to the Eshelby tensor (4.19), which displays minor symmetry only.

The evaluation of expressions (4.41) and (4.42) depends on the particular stiffness properties of the reference medium $\mathbb{C}^0$ and the shape and orientation of the inclusion phase[5]. Many derivations of the Hill tensor are available in the literature for variations of the previously mentioned parameters (see e.g. [190, 238, 295]). In what follows, four different forms of the Hill tensor are presented, which are closely related to microstructures and stiffness properties of relevance to the micromechanics modeling of shale. These specific forms of the P-tensor are: spherical inclusions in an isotropic (homogenized) medium, spherical inclusions in a transverse isotropic medium, aligned spheroidal inclusions in an isotropic medium, and spheroidal inclusions with preferred orientation in a transverse isotropic medium. Clearly, the first three cases are retrieved under specific conditions from the last, more general case. Nevertheless, more succinct analytical and semi-analytical expressions are available for the first three cases.

Spherical Inclusions in an Isotropic Medium

The simplest case to be considered is that of the evaluation of the Hill concentration tensor for a spherical inclusion embedded in an isotropic (homogenized) medium. The resulting P-tensor

[5] For clarity, the superscript 0 in $\mathbb{C}^0$ will be dropped in the subsequent presentations of the P-tensor.

is readily available from standard micromechanics literature (see e.g. [83, 193]):

$$\mathbb{P} = \frac{\alpha}{3k}\mathbb{J} + \frac{\beta}{2g}\mathbb{K} \tag{4.43}$$

with,

$$\alpha = \frac{3k}{3k + 4g} \tag{4.44a}$$

$$\beta = \frac{6\,(k + 2g)}{5\,(3k + 4g)} \tag{4.44b}$$

where $J_{ijkl} = \frac{1}{3}\,(\delta_{ij}\delta_{kl})$ and $\mathbb{K} = \mathbb{I} - \mathbb{J}$.

Spherical Inclusions in a Transverse Isotropic Medium

Integral expressions of the Hill tensor for ellipsoidal inclusions in a transversely isotropic medium have been developed by Laws [159]. However, the evaluation of the Hill tensor can be specialized for (aligned) spherical inclusions within a transverse isotropic medium by taking advantage of the spherical symmetry [116]. The transversely isotropic stiffness of the reference medium is a function of five elastic constants. Within a Cartesian reference frame of orthonormal basis $[\underline{e}_1, \underline{e}_2, \underline{e}_3]$, where the plane $[\underline{e}_1, \underline{e}_2]$ corresponds to the plane of symmetry, the transverse isotropic stiffness tensor for the reference medium $\mathbb{C}$ in matrix form is[6]:

$$[C_{ij}] = \begin{bmatrix} C_{11} & C_{12} & C_{13} & 0 & 0 & 0 \\ C_{12} & C_{11} & C_{13} & 0 & 0 & 0 \\ C_{13} & C_{13} & C_{33} & 0 & 0 & 0 \\ 0 & 0 & 0 & 2C_{66} = C_{11} - C_{12} & 0 & 0 \\ 0 & 0 & 0 & 0 & 2C_{44} & 0 \\ 0 & 0 & 0 & 0 & 0 & 2C_{44} \end{bmatrix} \tag{4.45}$$

The calculation of the Christoffel matrix $\Gamma_{ik}\,(\underline{\omega}) = C_{ijkl}\omega_j\omega_l$ can be achieved through the use of matrix operations of the type $[w]\,[C]\,[w]^T$, in which the vector $\underline{\omega}$ is represented as a (3×6)

[6] Throughout this work, all matrix representations of second- and fourth-order tensors follow a normalized tensorial basis [119].

matrix:

$$[w] = \begin{bmatrix} w_1 & 0 & 0 & \frac{1}{2}w_2\sqrt{2} & 0 & \frac{1}{2}w_3\sqrt{2} \\ 0 & w_2 & 0 & \frac{1}{2}w_1\sqrt{2} & \frac{1}{2}w_3\sqrt{2} & 0 \\ 0 & 0 & w_3 & 0 & \frac{1}{2}w_2\sqrt{2} & \frac{1}{2}w_1\sqrt{2} \end{bmatrix} \tag{4.46}$$

$$[w]^T = \begin{bmatrix} w_1 & 0 & 0 \\ 0 & w_2 & 0 \\ 0 & 0 & w_3 \\ \frac{1}{2}w_2\sqrt{2} & \frac{1}{2}w_1\sqrt{2} & 0 \\ 0 & \frac{1}{2}w_3\sqrt{2} & \frac{1}{2}w_2\sqrt{2} \\ \frac{1}{2}w_3\sqrt{2} & 0 & \frac{1}{2}w_1\sqrt{2} \end{bmatrix} \tag{4.47}$$

Furthermore, the unit vector $\underline{\omega}$ is expressed in spherical coordinates $\theta \in [0, \pi]$; $\phi \in [0, 2\pi]$ by the following transformations:

$$\omega_1 = \sin\theta\cos\phi \tag{4.48a}$$

$$\omega_2 = \sin\theta\sin\phi \tag{4.48b}$$

$$\omega_3 = \cos\theta \tag{4.48c}$$

The non-zero terms in (4.41)-(4.42) are reduced to line integrals in $\xi = \cos\theta$, $d\xi = -\sin\theta d\theta$, whose evaluations are achieved numerically using standard software packages. The final expressions of the non-zero elements in Voigt notation of the P-Tensor, which will be heavily used in the multi-scale model of shale to be developed, are the following (see [116], except for a misprint corrected in the expressions below, [93]):

$$\begin{aligned} P_{11} = \frac{1}{16}\int_{-1}^{1} & \frac{\left(\xi^2-1\right)\left(-8\xi^4C_{33}C_{44} - 3\xi^4C_{12}C_{33} - 2\xi^4C_{13}^2 + 3\xi^4C_{12}C_{44}\ldots\right.}{D_1} \\ & \frac{\ldots - 5\xi^4C_{11}C_{44} + 5\xi^4C_{11}C_{33} - 4\xi^4C_{13}C_{44} + 6\xi^4C_{44}^2 - 6\xi^2C_{44}^2\ldots}{D_1} \\ & \frac{\ldots + 4\xi^2C_{13}C_{44} + 3\xi^2C_{12}C_{33} - 5\xi^2C_{11}C_{33} - 6\xi^2C_{12}C_{44} + 2\xi^2C_{13}^2\ldots}{D_1} \\ & \left.\frac{\ldots + 10\xi^2C_{11}C_{44} + 3C_{12}C_{44} - 5C_{11}C_{44}\right)}{D_1}d\xi \end{aligned} \tag{4.49}$$

$$P_{12} = -\frac{1}{16}\int_{-1}^{1} \frac{(\xi-1)^2(\xi+1)^2\left(C_{12}C_{44} - \xi^2 C_{12}C_{44} + \xi^2 C_{12}C_{33} + C_{11}C_{44}\ldots\right.}{D_1} \quad (4.50)$$
$$\frac{\left.\ldots - \xi^2 C_{11}C_{44} + \xi^2 C_{11}C_{33} - 2\xi^2 C_{13}^2 - 4\xi^2 C_{13}C_{44} - 2\xi^2 C_{44}^2\right)}{D_1} d\xi$$

$$P_{13} = -\frac{1}{4}(C_{13}+C_{44})\int_{-1}^{1} \frac{\xi^2\left(\xi^2-1\right)}{D_2} d\xi \quad (4.51)$$

$$P_{33} = \frac{1}{2}\int_{-1}^{1} \frac{\xi^2\left(-C_{11} + C_{11}\xi^2 - C_{44}\xi^2\right)}{D_2} d\xi \quad (4.52)$$

$$P_{44} = -\frac{1}{16}\int_{-1}^{1} \frac{\left(3\xi^2 C_{11}^2 - 2\xi^6 C_{13}^2 - C_{11}^2 - 4\xi^6 C_{11}C_{44} - 8\xi^6 C_{13}C_{44} - 4\xi^6 C_{33}C_{44}\ldots\right.}{D_1} \quad (4.53)$$
$$\frac{\ldots + 3\xi^6 C_{11}C_{33} - 3\xi^4 C_{11}^2 + C_{11}C_{22} + \xi^6 C_{11}^2 - \xi^6 C_{11}C_{12}\ldots}{D_1}$$
$$\frac{\ldots - \xi^6 C_{12}C_{33} + 4\xi^4 C_{12}C_{13} - 2\xi^2 C_{12}C_{13} + 2\xi^6 C_{11}C_{13}\ldots}{D_1}$$
$$\frac{\ldots + 2\xi^4 C_{13}^2 + \xi^4 C_{12}C_{33} + 8\xi^4 C_{11}C_{44} - 3\xi^4 C_{11}C_{33} - 4\xi^2 C_{11}C_{44}\ldots}{D_1}$$
$$\frac{\left.\ldots + 8\xi^4 C_{13}C_{44} - 4\xi^4 C_{11}C_{13} + 3\xi^4 C_{11}C_{12} - 3\xi^2 C_{11}C_{12} - 2\xi^6 C_{12}C_{13} + 2\xi^2 C_{11}C_{13}\right)}{D_1} d\xi$$

where:

$$D_1 = \left(\xi^2 C_{11} - C_{11} - 2\xi^2 C_{44} - \xi^2 C_{12} + C_{12}\right)(D_2) \quad (4.54)$$

$$D_2 = -\xi^4 C_{33}C_{44} + 2\xi^2 C_{13}C_{44} - \xi^2 C_{11}C_{33} - 2\xi^4 C_{13}C_{44} + \xi^4 C_{11}C_{33} \quad (4.55)$$
$$\ldots + 2\xi^2 C_{11}C_{44} + \xi^2 C_{13}^2 - \xi^4 C_{11}C_{44} - \xi^4 C_{13}^2 - C_{11}C_{44}$$

The previous expressions for the P-tensor readily reduce to (4.43) when the stiffness properties of the reference medium attain isotropic form.

Spheroidal Inclusions in an Isotropic Medium

The case of the Hill tensor for spheroidal inclusions in an isotropic medium is a classical result found in the literature. The spheroidal inclusions follow the characteristic equation to account for particle geometry:

$$\frac{(z_1)^2 + (z_2)^2}{a^2} + \frac{(z_3)^2}{c^2} = 1 \tag{4.56}$$

where $X = c/a$ stands for the particle aspect ratio, which is defined as the ratio of the length in the direction of the axis of symmetry over the diameter in the symmetry plane: $X < 1$ for oblates, $X > 1$ for prolates, and $X = 1$ for a sphere. The isotropic medium is characterized by the bulk and shear moduli k, g, respectively. Given the symmetry of the spheroidal inclusions, the P-tensor exhibits transversely isotropic symmetry, so that it follows a similar form of the tensor $\mathbb{C}$ in (4.45) [190, 218]:

$$[P_{ij}] = \begin{bmatrix} P_{11} & P_{12} & P_{13} & 0 & 0 & 0 \\ P_{12} & P_{11} & P_{13} & 0 & 0 & 0 \\ P_{13} & P_{13} & P_{33} & 0 & 0 & 0 \\ 0 & 0 & 0 & 2P_{66} = P_{11} - P_{12} & 0 & 0 \\ 0 & 0 & 0 & 0 & 2P_{44} & 0 \\ 0 & 0 & 0 & 0 & 0 & 2P_{44} \end{bmatrix} \tag{4.57}$$

where:

$$P_{11} = \frac{X\left(26gX^3\epsilon - 20g\xi X^2 - 35X\epsilon g + 15\xi k - 33X\epsilon k + 29\xi g + 6X^3\epsilon k + 12X^2\xi k\right)}{16\left(X^2-1\right)^{5/2}(3k+4g)\,g} \tag{4.58a}$$

$$P_{12} = \frac{X\left(-2gX^3\epsilon + 4g\xi X^2 - X\epsilon g - 3\xi k - 3X\epsilon k - \xi g - 6X^3\epsilon k + 12X^2\xi k\right)}{16\left(X^2-1\right)^{5/2}(3k+4g)\,g} \tag{4.58b}$$

$$P_{13} = -\frac{X\left(\xi g - 3X\epsilon g + 2g\xi X^2 - 9X\epsilon k + 6X^2\xi k + 3\xi k\right)}{4\left(X^2-1\right)^{5/2}(3k+4g)\,g} \tag{4.58c}$$

$$P_{33} = \frac{-5X\xi g - 9X^2\epsilon g + 8X^3\xi g - 9X^2\epsilon k + 6\epsilon g + 6X^3\xi k + 3X\xi k}{2\left(X^2-1\right)^{5/2}(3k+4g)\,g} \tag{4.58d}$$

$$P_{44} = \frac{3X^4\epsilon k - 9X^3\xi k + 9X^2\epsilon k + 4X^4\epsilon g - 6X^2\epsilon g - 9X\xi k - 6X\xi g + 6\epsilon k + 8\epsilon g}{8\left(X^2-1\right)^{5/2}(3k+4g)\,g} \tag{4.58e}$$

For the oblate case ($X < 1$), $\epsilon = \sqrt{1 - X^2}$ and $\xi = \arccos(X)$, whereas for the prolate case ($X > 1$), $\epsilon = \sqrt{X^2 - 1}$ and $\xi = \operatorname{arccosh}(X)$.

Spheroidal Inclusions with Preferred Orientation in a Transverse Isotropic Medium

We now consider the evaluation of the Hill tensor for the situation of spheroidal inclusions with preferential orientation embedded in a transversely isotropic reference medium. Giraud *et al.* [103] recently treated the evaluation of the Hill tensor for this general problem based on the integration of the exact Green's function provided by Pan and Chou [205] and the use of intermediate and global coordinate systems.

First, consider spheroidal particles that follow the characteristic equation to account for particle geometry:

$$\frac{(z_1^\chi)^2 + (z_2^\chi)^2}{a^2} + \frac{(z_3^\chi)^2}{c^2} = 1 \tag{4.59}$$

where χ refers to all quantities related to the inclusion χ. $X_\chi = c/a$ stands for the particle aspect ratio. It will be necessary to transition from the global coordinate system (z_1, z_2, z_3) to the local coordinate system $(z_1^\chi, z_2^\chi, z_3^\chi)$. To this end, the rotation operator $\mathbf{Q}^\chi$, defined as the product of two rotation matrices $\mathbf{Q}^\chi = \mathbf{Q}^{\theta\chi} \cdot \mathbf{Q}^{\varphi\chi}$, is introduced:

$$\left[Q_{ij}^{\theta\chi}\right] = \begin{bmatrix} 1 & 0 & 0 \\ 0 & \cos(\theta) & -\sin(\theta) \\ 0 & \sin(\theta) & \cos(\theta) \end{bmatrix} \; ; \; \left[Q_{ij}^{\varphi\chi}\right] = \begin{bmatrix} \cos(\varphi) & \sin(\varphi) & 0 \\ -\sin(\varphi) & \cos(\varphi) & 0 \\ 0 & 0 & 1 \end{bmatrix} \tag{4.60}$$

where the Euler angles φ ($0 \leq \varphi \leq 2\pi$) and θ ($0 \leq \theta \leq \pi$) are defined between the $z_1, z_1^{\varphi\chi}$ axes, and the $z_3, z_3^{\theta\chi}$ axes. The latter are the axes of symmetry in the global and local coordinate systems, respectively. The computation of the Hill tensor based on the Green's function solution of [205], which was originally developed for the coordinate system of a material with symmetry axis z_3, is adapted for computations in a coordinate system with one axis aligned to the axis of symmetry of the transversely isotropic material, that is $z_i^{\varphi\chi} = Q_{ij}^{\varphi\chi} z_j$. Likewise, the local coordinate system can be expressed in terms of an intermediate coordinate system $z_i^\chi = Q_{ij}^{\theta\chi} z_j^{\varphi\chi}$, and thus only the angle θ is considered for most computations.

After mathematical manipulations, Giraud et al. [103] provided expressions for the compo-

nents of the Hill tensor of general form (4.41)-(4.42) in intermediate coordinates and in terms of the arguments θ and $\underline{l}^{\varphi\chi}$:

$$P_{ijkl}^{\varphi\chi} = \int_{\Sigma} \left(p_l^{\varphi\chi} g_{kij}^{\varphi\chi} + p_l^{\varphi\chi} g_{kji}^{\varphi\chi} + p_k^{\varphi\chi} g_{lij}^{\varphi\chi} + p_k^{\varphi\chi} g_{lji}^{\varphi\chi} \right) d\omega \tag{4.61}$$

where the expressions for $p_i^{\varphi\chi} = p_i^{\varphi\chi}\left(\theta, \underline{l}^{\varphi\chi}, X^{\chi}\right)$ and $g_{ijk}^{\varphi\chi} = g_{ijk}^{\varphi\chi}\left(\underline{l}^{\varphi\chi}, C_{ij}\right)$ are provided hereafter for convenience[7]:

$$\begin{aligned}
p_1\left(\theta, \underline{l}, X\right) &= \frac{X^2 l_1}{X^2 {l_1}^2 + \left(l_3 \cos\left(\theta\right) + l_2 \sin\left(\theta\right)\right)^2 + X^2 \left(l_2 \cos\left(\theta\right) - l_3 \sin\left(\theta\right)\right)^2} \\
p_2\left(\theta, \underline{l}, X\right) &= \frac{1}{2} \frac{\left(1 + X^2\right) l_2 + \left(1 - X^2\right) \left(l_3 \sin\left(2\theta\right) - l_2 \cos\left(2\theta\right)\right)}{X^2 {l_1}^2 + \left(l_3 \cos\left(\theta\right) + l_2 \sin\left(\theta\right)\right)^2 + X^2 \left(l_2 \cos\left(\theta\right) - l_3 \sin\left(\theta\right)\right)^2} \\
p_3\left(\theta, \underline{l}, X\right) &= \frac{1}{2} \frac{\left(1 + X^2\right) l_3 + \left(1 - X^2\right) \left(l_3 \cos\left(2\theta\right) + l_2 \sin\left(2\theta\right)\right)}{X^2 {l_1}^2 + \left(l_3 \cos\left(\theta\right) + l_2 \sin\left(\theta\right)\right)^2 + X^2 \left(l_2 \cos\left(\theta\right) - l_3 \sin\left(\theta\right)\right)^2}
\end{aligned} \tag{4.62}$$

$$\begin{aligned}
g_{111}\left(\underline{l}, C_{ij}\right) = & -2\nu_1 A_1' l_1 \left(-8 \frac{{l_2}^2 {\nu_1}^2 {l_3}^2}{\rho^2} + \frac{{\nu_1}^2 {l_1}^2 {l_3}^2}{R_1^2} - 3{l_2}^2 + 2{\nu_1}^2 {l_3}^2 \right) \rho^{-4} R_1^{-1} \\
& -2\nu_2 A_2' l_1 \left(-8 \frac{{l_2}^2 {\nu_2}^2 {l_3}^2}{\rho^2} + \frac{{\nu_2}^2 {l_1}^2 {l_3}^2}{R_2^2} - 3{l_2}^2 + 2{\nu_2}^2 {l_3}^2 \right) \rho^{-4} R_2^{-1} \\
& -D l_1 \left(8 \frac{{\nu_3}^2 {l_2}^2 {l_3}^2}{\rho^2} + \frac{{\nu_3}^2 {l_2}^2 {l_3}^2}{R_3^2} - {l_1}^2 + 2{l_2}^2 - 2{\nu_3}^2 {l_3}^2 \right) \rho^{-4} R_3^{-1}
\end{aligned}$$

$$\begin{aligned}
g_{112}\left(\underline{l}, C_{ij}\right) = & -2\nu_1 A_1' l_2 \left(8 \frac{{\nu_1}^2 {l_1}^2 {l_3}^2}{\rho^2} + \frac{{\nu_1}^2 {l_1}^2 {l_3}^2}{R_1^2} + 2{l_1}^2 - {l_2}^2 - 2{\nu_1}^2 {l_3}^2 \right) \rho^{-4} R_1^{-1} \\
& -2\nu_2 A_2' l_2 \left(8 \frac{{\nu_2}^2 {l_1}^2 {l_3}^2}{\rho^2} + \frac{{\nu_2}^2 {l_1}^2 {l_3}^2}{R_2^2} + 2{l_1}^2 - {l_2}^2 - 2{\nu_2}^2 {l_3}^2 \right) \rho^{-4} R_2^{-1} \\
& -D l_2 \left(-8 \frac{{l_1}^2 {\nu_3}^2 {l_3}^2}{\rho^2} + \frac{{\nu_3}^2 {l_2}^2 {l_3}^2}{R_3^2} - 3{l_1}^2 + 2{\nu_3}^2 {l_3}^2 \right) \rho^{-4} R_3^{-1}
\end{aligned}$$

[7] For simplicity, the intermediate coordinate system symbols $\varphi\chi$ are omitted from the formulation.

$$
\begin{aligned}
g_{113}\left(\underline{l}, C_{ij}\right) &= 2{\nu_1}^3 A_1' l_3 \left(2{l_1}^2 - {l_2}^2 - \frac{{\nu_1}^2 {l_1}^2 {l_3}^2}{R_1^2}\right) \rho^{-4} R_1^{-1} \\
&\quad + 2{\nu_2}^3 A_2' l_3 \left(2{l_1}^2 - {l_2}^2 - \frac{{\nu_2}^2 {l_1}^2 {l_3}^2}{R_2^2}\right) \rho^{-4} R_2^{-1} \\
&\quad - D{\nu_3}^2 l_3 \left(\frac{{\nu_3}^2 {l_2}^2 {l_3}^2}{R_3^2} + {l_1}^2 - 2{l_2}^2\right) \rho^{-4} R_3^{-1}
\end{aligned}
$$

$$
\begin{aligned}
g_{121}\left(\underline{l}, C_{ij}\right) &= -2\nu_1 A_1' l_2 \left(8\frac{{\nu_1}^2 {l_1}^2 {l_3}^2}{\rho^2} + \frac{{\nu_1}^2 {l_1}^2 {l_3}^2}{R_1^2} + 2{l_1}^2 - {l_2}^2 - 2{\nu_1}^2 {l_3}^2\right) \rho^{-4} R_1^{-1} \\
&\quad - 2\nu_2 A_2' l_2 \left(8\frac{{\nu_2}^2 {l_1}^2 {l_3}^2}{\rho^2} + \frac{{\nu_2}^2 {l_1}^2 {l_3}^2}{R_2^2} + 2{l_1}^2 - {l_2}^2 - 2{\nu_2}^2 {l_3}^2\right) \rho^{-4} R_2^{-1} \\
&\quad + D l_2 \left(8\frac{{l_1}^2 {\nu_3}^2 {l_3}^2}{\rho^2} + \frac{{l_1}^2 {\nu_3}^2 {l_3}^2}{R_3^2} + 2{l_1}^2 - {l_2}^2 - 2{\nu_3}^2 {l_3}^2\right) \rho^{-4} R_3^{-1}
\end{aligned}
$$

$$
\begin{aligned}
g_{123}\left(\underline{l}, C_{ij}\right) &= 2\frac{{\nu_1}^3 A_1' l_1 l_2 l_3 \left(3\rho^2 + 2{\nu_1}^2 {l_3}^2\right)}{\rho^4 R_1^3} + 2\frac{{\nu_2}^3 A_2' l_1 l_2 l_3 \left(3\rho^2 + 2{\nu_2}^2 {l_3}^2\right)}{\rho^4 R_2^3} \\
&\quad - \frac{D{\nu_3}^2 l_1 l_2 l_3 \left(3\rho^2 + 2{\nu_3}^2 {l_3}^2\right)}{\rho^4 R_3^3}
\end{aligned}
$$

$$
g_{131}\left(\underline{l}, C_{ij}\right) = {\nu_1}^2 A_1 l_3 \left(1 - 2\frac{{l_1}^2}{\rho^2} - \frac{{l_1}^2}{R_1^2}\right) \rho^{-2} R_1^{-1} + {\nu_2}^2 A_2 l_3 \left(1 - 2\frac{{l_1}^2}{\rho^2} - \frac{{l_1}^2}{R_2^2}\right) \rho^{-2} R_2^{-1}
$$

$$
g_{312}\left(\underline{l}, C_{ij}\right) = 2k_1 {\nu_1}^3 A_1' l_1 l_2 l_3 \left(2\rho^{-2} + R_1^{-2}\right) \rho^{-2} R_1^{-1} + 2k_2 {\nu_2}^3 A_2' l_1 l_2 l_3 \left(2\rho^{-2} + R_2^{-2}\right) \rho^{-2} R_2^{-1}
$$

$$
g_{313}\left(\underline{l}, C_{ij}\right) = -2\frac{k_1 {\nu_1}^3 A_1' l_1}{R_1^3} - 2\frac{k_2 {\nu_2}^3 A_2' l_1}{R_2^3}
$$

$$
g_{331}\left(\underline{l}, C_{ij}\right) = \frac{k_1 {\nu_1}^2 A_1 l_1}{R_1^3} + \frac{k_2 {\nu_2}^2 A_2 l_1}{R_2^3}
$$

$$
g_{333}\left(\underline{l}, C_{ij}\right) = \frac{k_1 {\nu_1}^4 A_1 l_3}{R_1^3} + \frac{k_2 {\nu_2}^4 A_2 l_3}{R_2^3} \tag{4.63}
$$

where:

$$
\rho = \sqrt{l_1^2 + l_2^2}; \quad R_i^2 = \rho^2 + \nu_i^2 l_3^2 \quad ; \quad k_i = \frac{\frac{C_{11}}{\nu_i^2} - C_{44}}{C_{13} + C_{44}}
$$

$$
A_1 = \frac{1}{4} \frac{C_{13} + C_{44}}{\nu_1 \pi \left(\nu_2^2 - \nu_1^2\right) C_{33} C_{44}} \quad ; \quad A_2 = -\frac{\nu_1 A_1}{\nu_2}
$$

$$A_1' = \frac{1}{8}\frac{C_{44} - \nu_1^2 C_{33}}{\pi\left(\nu_2^2 - \nu_1^2\right)\nu_1^2 C_{33} C_{44}} \quad ; \quad A_2' = -\frac{1}{8}\frac{C_{44} - \nu_2^2 C_{33}}{\pi\left(\nu_2^2 - \nu_1^2\right)\nu_2^2 C_{33} C_{44}}$$

$$D = \frac{1}{4}\frac{1}{\pi C_{44}\nu_3} \quad ; \quad C_{13}^* = \sqrt{C_{11}C_{33}} \quad ; \quad C_{66} = \frac{1}{2}\left(C_{11} - C_{12}\right)$$

$$v_1 = \sqrt{\frac{\left(C_{13}^* - C_{13}\right)\left(C_{13}^* + C_{13} + 2C_{44}\right)}{4C_{33}C_{44}}} + \sqrt{\frac{\left(C_{13}^* + C_{13}\right)\left(C_{13}^* - C_{13} - 2C_{44}\right)}{4C_{33}C_{44}}}$$

$$v_2 = \sqrt{\frac{\left(C_{13}^* - C_{13}\right)\left(C_{13}^* + C_{13} + 2C_{44}\right)}{4C_{33}C_{44}}} - \sqrt{\frac{\left(C_{13}^* + C_{13}\right)\left(C_{13}^* - C_{13} - 2C_{44}\right)}{4C_{33}C_{44}}}$$

$$v_3 = \sqrt{\frac{C_{66}}{C_{44}}} \tag{4.64}$$

The remaining non-zero g_{ijk} terms are computed by the permutations of indices 1 and 2.

The unit vector $\underline{l}^{\varphi\chi}$ is expressed as a function of two angles for a spherical coordinate notation:

$$l_1^{\varphi\chi} = \cos\left(\zeta\right)\sin\left(\psi\right), \quad l_2^{\varphi\chi} = \sin\left(\zeta\right)\sin\left(\psi\right), \quad l_3^{\varphi\chi} = \cos\left(\psi\right) \tag{4.65}$$

and the integration over the unit sphere Ξ is:

$$\int_{\Xi} f\left(\theta, \underline{l}^{\varphi\chi}\right) d\omega = \int_{\zeta=0}^{\zeta=2\pi}\int_{\psi=0}^{\psi=\pi} f\left(\theta, \zeta, \psi\right)\sin\left(\psi\right) d\psi d\zeta \tag{4.66}$$

For a predetermined value of angle θ, (4.61) can be evaluated numerically using Gauss-Legendre quadrature in terms of the integration angles ψ, ζ. The Hill tensor $\mathbb{P}$ has monoclinic symmetry, and it is characterized by 13 independent constants in the intermediate $\underline{z}^{\varphi\chi}$ coordinates, which in matrix notation reads [103]:

$$\left[P_{ijkl}^{\varphi\chi}\right] = \begin{bmatrix} P_{1111}^{\varphi\chi} & P_{1122}^{\varphi\chi} & P_{1133}^{\varphi\chi} & 0 & 0 & \sqrt{2}P_{1123}^{\varphi\chi} \\ & P_{2222}^{\varphi\chi} & P_{2233}^{\varphi\chi} & 0 & 0 & \sqrt{2}P_{2223}^{\varphi\chi} \\ & & P_{3333}^{\varphi\chi} & 0 & 0 & \sqrt{2}P_{3323}^{\varphi\chi} \\ & & & 2P_{1212}^{\varphi\chi} & 2P_{1213}^{\varphi\chi} & 0 \\ & (sym) & & & 2P_{1313}^{\varphi\chi} & 0 \\ & & & & & 2P_{2323}^{\varphi\chi} \end{bmatrix} \tag{4.67}$$

From the examination of (4.61)-(4.64), the evaluation of the Hill tensor in the intermediate

coordinate system depends on the aspect ratio of the inclusion X^{χ}, the inclination angle θ of the inclusion, and the elastic properties of the reference medium:

$$P_{ijkl}^{\varphi\chi} = P_{ijkl}^{\varphi\chi}\left(X^{\chi}, \theta, C_{ijkl}\right) \tag{4.68}$$

It is important to note that for the case of a perfectly aligned inclusion (i.e. $\theta = 0$ rad), the computation of the Hill tensor presented in this section coincides with the analytical solutions of Withers [295].

4.2.6 Matrix-Inclusion versus Granular Microstructures

As a first application, some of the micromechanics developments presented in the previous sections are brought together to show classical results of homogenization theory for a porous solid with two contrasting microstructures: matrix-inclusion and granular. The matrix-inclusion (or particulate) microstructure represents a porous solid in which one phase clearly serves as the host or matrix material for inclusions (in this case, pores). The granular or polycrystal microstructure is instead relevant for composites in which all single grains or inclusions play a similar mechanical role, and therefore, no single constituent serves as a matrix-type material. For simplicity, the solid particles are assumed isotropic, with bulk modulus k^s and shear modulus g^s. Furthermore, the solid particles and pores are modeled as spherical inclusions.

The implementation of the two given microstructures suits the use of the Mori-Tanaka (MT) and the self-consistent (SC) schemes of micromechanics. For the given elastic and morphological features of the solid and pore space, the implementation of expressions (4.32) for the MT scheme and (4.39) for the SC scheme using the Hill tensor for spherical inclusions in an isotropic reference medium (4.43) yields the following homogenized stiffness properties for the porous solid as a function of packing density η (one minus the porosity ϕ_0):

$$\frac{k_{\text{hom}}^{MT}}{g^s} = \frac{4\eta r^s}{3\left(1-\eta\right)r^s + 4} \tag{4.69a}$$

$$\frac{g_{\text{hom}}^{MT}}{g^s} = \frac{\eta\left(9r^s + 8\right)}{3r^s\left(5-2\eta\right) + 4\left(5-3\eta\right)} \tag{4.69b}$$

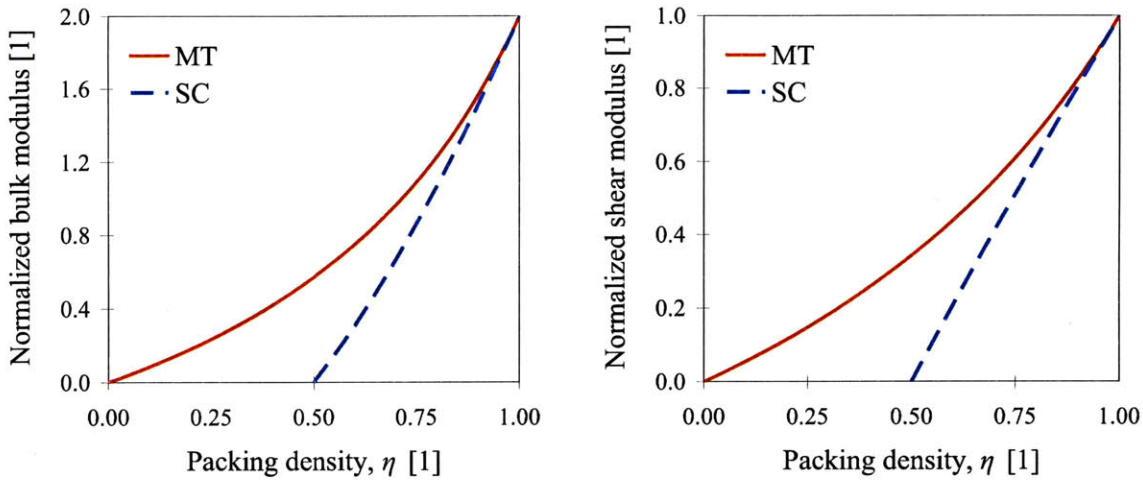

Figure 4-2: Homogenized stiffness properties for a porous solid with matrix/inclusion (particulate) and granular microstructures. These microstructures are modeled using the Mori-Tanaka (MT) and the self-consistent (SC) schemes, respectively, of micromechanics. The homogenized bulk and shear moduli are normalized by the solid shear moduli g^s, as in expressions (4.69a)-(4.70b). The displayed homogenization properties were calculated for $r^s = k^s/g^s = 2$.

$$\frac{k^{SC}_{\text{hom}}}{g^s} = \frac{4\eta r^s g^{SC}_{\text{hom}}/g^s}{4g^{SC}_{\text{hom}}/g^s + 3(1-\eta)r^s} \tag{4.70a}$$

$$\frac{g^{SC}_{\text{hom}}}{g^s} = \frac{1}{2} - \frac{5}{4}(1-\eta) - \frac{3}{16}(2+\eta)r^s + \frac{1}{16}\sqrt{144(1-r^s) - 480\eta + 400\eta^2 + 408\eta r^s - 120\eta^2 r^s + 9(2+\eta)^2 (r^s)^2} \tag{4.70b}$$

where $r^s = k^s/g^s$. These homogenization results for the porous solid based on the contrasting microstructures are displayed graphically in Figure 4-2. The Mori-Tanaka estimates of the stiffness response of the porous solid yield continuous elasticity predictions for all the range of packing density values (or porosity, alternatively). In contrast, the composite modeled through the self-consistent scheme predicts a percolation threshold at a solid packing density $\eta_0 = 0.5$, which is a well-known micromechanics result for the given configuration of the material system (i.e. isotropic solid and spherical inclusions). The existence of a percolation threshold is a trademark attribute of granular media, and the self-consistent scheme and its application in

micromechanics modeling capture the occurrence of solid percolation thresholds, below which the stiffness of the porous matrix vanishes. As we will explore in forthcoming sections, the accurate description of the percolation threshold plays a prominent role in the application of homogenization approaches to material systems in which the microstructures are intimately linked to specific particle geometries and orientations.

4.3 Microporomechanics Representation of Shale

The mechanical response of sedimentary rocks is affected by a variety of factors including its intrinsic rock properties, the properties of the saturating fluids, and the depositional environment. For shale in particular, its most prominent attribute, the seismic anisotropy (the change in wave velocity with propagation direction), is affected by numerous factors depending on the scale of observation. Large features affecting the anisotropy of shale are related to layering or aligned faults. Small-scale or microstructural features, which are most relevant to this micromechanics investigation, include the variations in spatial distributions of grains and minerals, particle/grain shape, the preferred orientation of particles, cracks, and pore spaces [168, 283]. However, an assessment of the particular contributions of each of these factors to the overall anisotropy is still lacking [271].

The success of predicting shale poromechanical and anisotropic behaviors relies on linking the different mechanical and microstructural attributes from the scale of clay mineralogy to the macroscopic scale. Multi-scale micromechanics approaches to modeling shale anisotropy, first pioneered by Hornby et al. [128] and Sayers [228], offered more robust alternatives to more traditional empirical approaches. In such schemes, microstructural features such as particle and pore geometries and their preferential alignments were regarded as the main contributors to the diversity of macroscopic anisotropic attributes of shales. These morphological descriptions of shale's fabric were derived from advanced visual and imaging techniques. Despite many attempts, progress in developing general micromechanics models that link material composition and microstructure to macroscopic measurements of shales has been limited due to the lack of experimental data defining the fundamental elastic properties of the so-called shale *elementary building block* [140], and links between those properties, microstructure, and macroscopic prop-

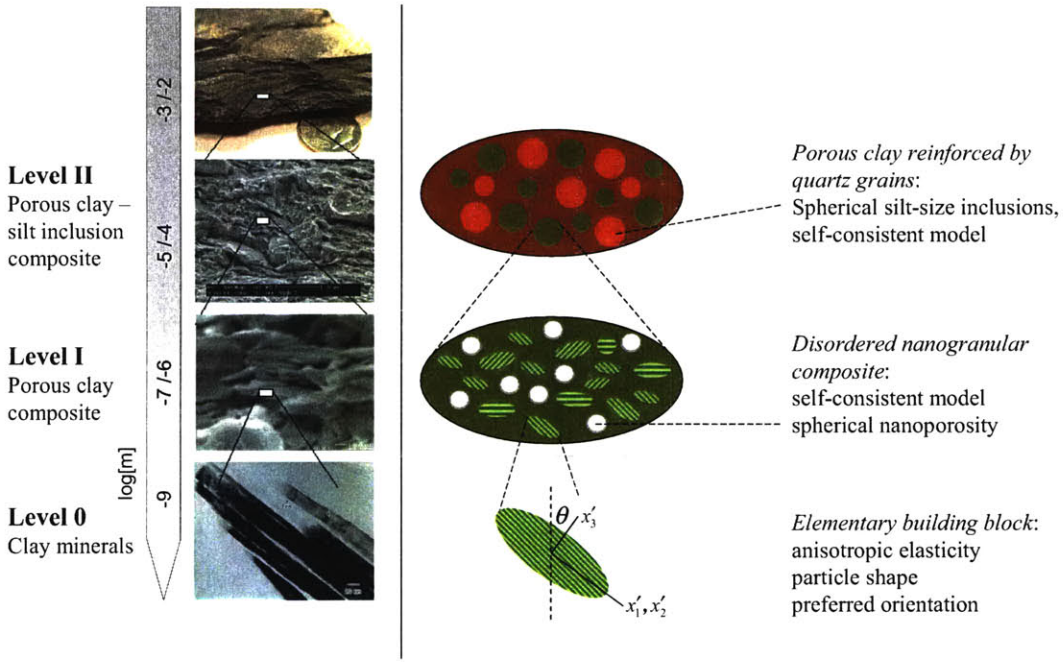

Figure 4-3: Multi-scale structure thought-model for shale and summary of the proposed micromechanics representation for poroelasticity modeling.

erties. Recent progress in nanomechanics and nanotechnology has made it possible to assess the in situ nano- and micromechanical properties of shales from instrumented indentation experiments. The experiments reported by Ulm and Abousleiman [265] and Bobko and Ulm [32] offered a first description of the nanomechanics of shale, which could provide a crucial contribution to the design of new mechanics models for shale. The rest of this section is devoted to the development of a general micromechanics representation of the most relevant mechanical and morphological features that could contribute to the poroelastic signature of shale materials at the different length scales. As a reference, we recall the multi-scale thought-model in Figure 4-3.

4.3.1 Level 0

The lowest level we consider is that of the elementary clay particles. From clay mineral chemistry (see Section 2.2.4), the clays are known to form groupings or packed ensembles of tens of nanometers in characteristic length during deposition and diagenetic compaction. In addition,

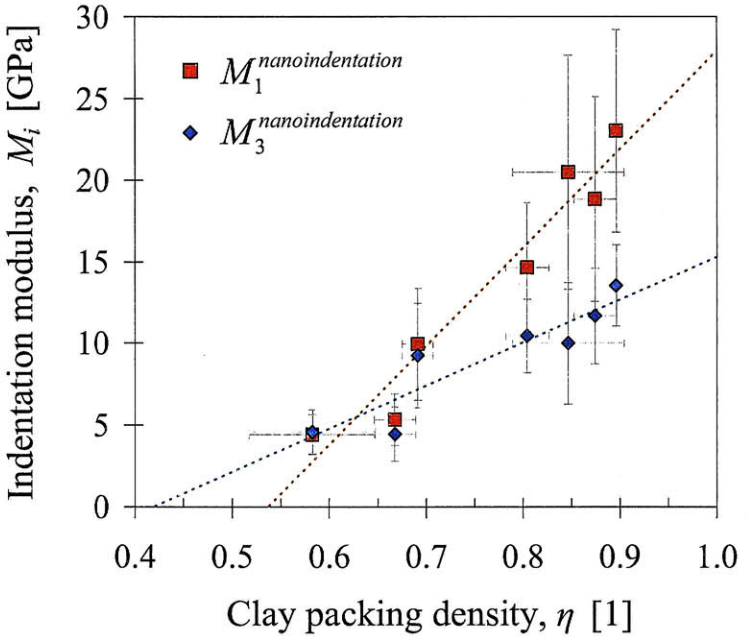

Figure 4-4: Porous clay stiffness M_i versus clay packing density scaling η for the G2IC shale specimens. The vertical bars correspond to the standard deviation of the indentified phases from mixture modeling. The horizontal bars represent the variability of clay packing density estimates. Recalled from Figure 3-15.

the strong chemical affinity between clay surfaces and water molecules or other cationic solutions creates interlayer structures between clay layers. Nuclear magnetic resonance and infrared spectroscopy studies suggest, for instance, that the influence of clay surface on water molecules may extend approximately to 1 nm [194]. These discrete clay layer – absorbed water structures define the clay phase in shale, which we represent as a continuous solid medium.

Assume that the effective solid clay exhibits linear elastic behavior. We now turn to the results of nanoindentation (see Section 3.6.6) to inform the appropriate characteristics of the level 0 elasticity modeling. The elasticity content of the porous clay composite (level I) exhibits a characteristic increasing anisotropy with increasing clay packing density (or decreasing nanoporosity) as shown in Figure 4-4.

This trend tends asymptotically to a solid clay phase (with packing density $\eta \rightarrow 1$) with intrinsic elastic anisotropy. For simplicity, the clay building block exhibits (at least) transverse

isotropic behavior, defined by the stiffness tensor $\mathbb{C}^s$ with five non-zero stiffness components. Within a Cartesian reference frame of orthonormal basis $[\underline{e}_1, \underline{e}_2, \underline{e}_3]$ of elastic properties of shale, where the plane $[\underline{e}_1, \underline{e}_2]$ corresponds to the bedding plane and $\underline{e}_3$ to the direction normal-to-bedding (symmetry axis), the transverse isotropic stiffness tensor for the solid clay in matrix form is:

$$\left[C^s_{ij}\right] = \begin{bmatrix} C^s_{11} & C^s_{12} & C^s_{13} & 0 & 0 & 0 \\ C^s_{12} & C^s_{11} & C^s_{13} & 0 & 0 & 0 \\ C^s_{13} & C^s_{13} & C^s_{33} & 0 & 0 & 0 \\ 0 & 0 & 0 & 2C^s_{66} = (C^s_{11} - C^s_{12}) & 0 & 0 \\ 0 & 0 & 0 & 0 & 2C^s_{44} & 0 \\ 0 & 0 & 0 & 0 & 0 & 2C^s_{44} \end{bmatrix} \tag{4.71}$$

The corresponding compliance tensor is $\mathbb{S}^s = (\mathbb{C}^s)^{-1}$. As a working assumption, $\mathbb{C}^s$ is unique to all shale materials, irrespective of the clay mineralogy; that is, $\mathbb{C}^s$ is a material invariant quantity characterizing the *in situ* behavior of clay in sedimentary rocks. Nanoindentation results already hint toward this material invariant character of the clay phase elasticity. This follows from the observed scaling relation between indentation moduli and packing density (Figure 4-4) for an array of shale minerals with varying mineralogy and porosity composition. We shall prove the relevance of this assumption through the calibration and validation of the model at different scales.

Finally, the elasticity content of in situ solid clay encompasses the interparticle contacts and the effects of the absorbed water in addition to the elasticity of clay layers. As noted in Section 3.5, the determination of the stiffness values for clay minerals remains a scientific challenge. Only limited data for certain clay minerals (e.g. muscovite) are available in the literature of clay minerals. Consequently, we establish the elasticity content of this *elementary building block* of in situ solid clay in shale as a degree-of-freedom to be resolved through this micromechanics investigation.

4.3.2 Level I

Level I of the multi-scale model of shale corresponds to the porous clay composite, the load bearing phase in shale. The solid clay and the nanoporosity form a poroelastic composite,

whose stiffness response depends on the contributions of the elasticity of the clay phase $\mathbb{C}^s$ and the (nano) porosity. The parameter that determines the mechanical contributions of the solid clay and the nanoporosity is the clay packing density η (refer to expression (3.5)), which neatly synthesizes the mineralogy and porosity information into one parameter at level I.

The additional ingredient to defining the poroelasticity of the porous clay is the characterization of the microstructure. For this, we turn to the mechanical behavior of shale assessed through nanoindentation, which offers a formidable window to the microstructural characteristics of the porous clay. In particular, the experimental finding of a clay packing percolation threshold as observed in Figure 4-4 hints toward a granular behavior of the porous clay at the nanoscale [32, 265] in view of the identified percolation threshold. Below the percolation threshold, the material exhibits no appreciable stiffness (at least in the GPa range probed by nanoindentation), as a continuous force path may cease to exist.

The nanogranular nature of the porous clay is captured in micromechanics by the self-consistent scheme. This homogenization scheme has the ability to replicate percolation thresholds. In addition, the self-consistent scheme is well suited for capturing the mechanical behavior of highly disordered composites, as it is the case of the porous clay in shale. Advanced observational techniques (e.g. SEM micrographs, refer to Section 2.3.2) have depicted the microfabric of shale as spatially highly-disordered media, which justify the use of the self-consistent scheme as a homogenization approach. However, it will be important to also consider microstructural features such as particle shapes and their preferred orientations, which are clearly visible in the SEM images. These geometrical parameters have been the foundation for most multi-scale modeling attempts for shale. Fortunately, the self-consistent scheme and its ability to model percolation thresholds is directly related to factors such as geometry and orientation distributions of particles. Finally, the nanoporosity at level I will be modeled as spherical inclusions in order to avoid introducing further sources of anisotropy.

4.3.3 Level II

At level II, the material is composed of the porous clay fabric intermixed with detrital grains, which are mainly quartz. The size of the quartz grains is typically above the micrometer size, thus satisfying the scale separability condition required for the application of micromechanics

theory. From SEM observations, quartz and other silt-size inclusions seem to be poorly sorted throughout the porous clay fabric. In addition, their occurrence as monocrystal and/or polycrystal solids is accompanied by a highly variable morphology. In a first approach, the silt inclusions are represented as spherical particles with linear elastic stiffness. Their disordered spatial location in the porous clay composite motivates the use of the self-consistent scheme to model the interaction between these two phases. The parameter that assists the quantification of the mechanical contributions of the porous clay and the silt inclusions is the inclusion volume fraction f^{inc}. Finally, the anisotropic elasticity content of the porous clay phase will result in overall anisotropic properties for the composite material at level II, which represents the macroscopic shale material at the sub-centimeter length scale of laboratory testing.

The micromechanics representation of shale is schematically summarized in Figure 4-3. The proposed representation will serve as the baseline for developing the poroelastic homogenization model for shale. Clearly, the suggested micromechanics representation of shale is reductionist in nature. The highly complex microstructure at different levels and the contributions of the different material phases in shale are characterized by a handful of micromechanics representations. Nevertheless, the objective of this investigation is to delineate a general multi-scale poroelastic model that reduces the macroscopically observed diversity of shale to a few material parameters of clear physical and/or chemical significance.

4.4 Multi-Scale Homogenization Model

We seek to develop a multi-scale model for upscaling the poroelastic properties of shale from the fine scales of clay particles to the macroscopic scale of engineering applications. The model development will follow the multi-scale structure thought-model presented here above. For each considered length scale, the relevant mechanical and microstructural features discussed in the previous section are translated into micromechanics quantities, which will then enable the determination of the poroelastic properties of shale at each scale based on the constitutive properties and microstructure of the scale below.

The primary tools for developing the multi-scale model for shale poroelasticity are those of continuum micromechanics theory. In particular, we will rely on the application of micro-

mechanics to porous material systems, or *microporomechanics*, developed by Dormieux and co-workers [54, 82, 83]. For all forthcoming micromechanics developments, the deformation of a *rev* at a particular scale is infinitesimal. Furthermore, small displacements in the *rev* are assumed to avoid introducing geometrical non-linearities due to prescribed mechanical loading.

4.4.1 Level I: Porous Clay Composite

The solid clay particles and nanoporosity form a porous clay composite, whose mechanical properties follow the classical relations of anisotropic poroelasticity, linking the strain average $\mathbf{E} = \overline{\boldsymbol{\varepsilon}(\underline{z})}$ and the pore pressure p to the overall stress average $\boldsymbol{\Sigma} = \overline{\boldsymbol{\sigma}(\underline{z})}$ and the change of nanoporosity $\varphi - \varphi_0$ [71]:

$$\boldsymbol{\Sigma} = \mathbb{C}^I_{\text{hom}} : \mathbf{E} - \boldsymbol{\alpha}^I p \tag{4.72a}$$

$$\varphi - \varphi_0 = \boldsymbol{\alpha}^I : \mathbf{E} + \frac{p}{N^I} \tag{4.72b}$$

where the superscript I indicates that the quantity is defined at level I, $\mathbb{C}^I_{\text{hom}}$ is the homogenized stiffness tensor, $\boldsymbol{\alpha}^I$ the second-order tensor of Biot pore pressure coefficients, and N^I the solid Biot modulus of the porous clay composite. Note that the variation $\varphi - \varphi_0$ of the (nano) porosity is defined in terms of a Lagrangian description, which proves useful for characterizing the pore volume changes. Linking the poroelastic properties $(\mathbb{C}^I_{\text{hom}}, \boldsymbol{\alpha}^I, N^I)$ and microscopic mechanical and morphological properties requires defining the appropriate mechanical problem on the *rev* of volume Ω, composed of the solid clay domain $\Omega^s = (1 - \varphi_0)\,\Omega$ and the pore space $\Omega^p = \varphi_0 \Omega$. Alternatively, the volume fraction used for the homogenization process at level I is the clay packing density $\eta = 1 - \varphi_0$, defined in (3.5). A convenient way to homogenize the behaviors of the linear elastic solid and the uniform microscopic stress field in the fluid is in the form of a continuous description of the stress field in the heterogeneous *rev* [83]:

$$\boldsymbol{\sigma}(\underline{z}) = \mathbb{C}(\underline{z}) : \boldsymbol{\varepsilon}(\underline{z}) + \boldsymbol{\sigma}^{\mathbf{T}}(\underline{z}) \qquad (\forall \underline{z} \in \Omega) \tag{4.73}$$

together with the distribution of elastic properties and eigenstresses:

$$\mathbb{C}(\underline{z}) = \begin{cases} 0 & (\Omega^p) \\ \mathbb{C}^s & (\Omega^s) \end{cases} \qquad \boldsymbol{\sigma}^{\mathbf{T}}(\underline{z}) = \begin{cases} -p\mathbf{1} & (\Omega^p) \\ 0 & (\Omega^s) \end{cases} \tag{4.74}$$

where $\mathbb{C}^s$ is the stiffness tensor of the solid clay phase.

The response of the *rev* characterized by the microscopic stress, strain, and displacements to the two loading parameters (the macroscopic strain $\mathbf{E}$ and the microscopic eigenstress $\boldsymbol{\sigma}^{\mathbf{T}}$) conform to the following relations:

$$\begin{aligned} &\operatorname{div}\boldsymbol{\sigma} = 0 && (\Omega) \\ &\boldsymbol{\sigma} = \mathbb{C}(\underline{z}) : \boldsymbol{\varepsilon} + \boldsymbol{\sigma}^{\mathbf{T}}(\underline{z}) && (\Omega) \\ &\underline{\xi} = \mathbf{E} \cdot \underline{z} && (\partial\Omega) \end{aligned} \tag{4.75}$$

Given the linearity of the problem with respect to the loading parameters $(\mathbf{E}, \boldsymbol{\sigma}^{\mathbf{T}})$, the problem is conveniently separated into two particular load cases.

1. The first load case corresponds to the application of the macroscopic strain $\mathbf{E}$ only, while the eigenstress is zero:

$$\begin{aligned} &\operatorname{div}\boldsymbol{\sigma}' = 0 && (\Omega) \\ &\boldsymbol{\sigma}' = \mathbb{C}(\underline{z}) : \boldsymbol{\varepsilon}' && (\Omega) \\ &\underline{\xi}' = \mathbf{E} \cdot \underline{z} && (\partial\Omega) \end{aligned} \tag{4.76}$$

   This boundary value problem is the well-known micromechanics problem of an empty porous medium subjected to uniform boundary conditions. Following the classical micromechanics result (see expression (4.9b)), the local strain field is related to the macroscopic strain through the fourth-order concentration tensor :

$$\boldsymbol{\varepsilon}'(\underline{z}) = \mathbb{A}(\underline{z}) : \mathbf{E} \tag{4.77}$$

   The corresponding macroscopic stress tensor is derived from the use of (4.77) in (4.73)

together with (4.74):

$$\boldsymbol{\Sigma}' = \overline{\boldsymbol{\sigma}'(\underline{z})} = \overline{\mathbb{C} : \mathbb{A}(\underline{z})} : \mathbf{E} \tag{4.78}$$

where the homogenized stiffness tensor of the porous medium emptied of a saturating fluid phase is identified:

$$\mathbb{C}^I_{\text{hom}} = \overline{\mathbb{C} : \mathbb{A}(\underline{z})} \tag{4.79}$$

Thus, the stiffness tensor $\mathbb{C}^I_{\text{hom}}$ corresponds to a drained condition. It is important to recognize that expression (4.79) is a particular case of the general result presented in (4.12).

2. The second load case corresponds to the application of the eigenstress field only, while the macroscopic strain is zero. The former condition implies zero microscopic displacements on the boundary of the *rev*:

$$\begin{aligned} &\operatorname{div} \boldsymbol{\sigma}'' = 0 && (\Omega) \\ &\boldsymbol{\sigma}'' = \mathbb{C}(\underline{z}) : \boldsymbol{\varepsilon}'' + \boldsymbol{\sigma}^{\mathbf{T}}(\underline{z}) && (\Omega) \\ &\underline{\xi}'' = 0 && (\partial\Omega) \end{aligned} \tag{4.80}$$

The corresponding macroscopic stress for this second load case $\boldsymbol{\Sigma}''$ is the average of the stress field $\boldsymbol{\sigma}''$ over the *rev* volume Ω. The application of Hill's lemma to the strain field $\boldsymbol{\varepsilon}'$ (4.77) and to the stress field $\boldsymbol{\sigma}''$ assists the derivation of the macroscopic stress as a function of the eigenstress:

$$\overline{\boldsymbol{\sigma}'' : \boldsymbol{\varepsilon}'} = \boldsymbol{\Sigma}'' : \mathbf{E} \tag{4.81}$$

Combining (4.80) and (4.81), we obtain:

$$\overline{\boldsymbol{\sigma}'' : \boldsymbol{\varepsilon}'} = \overline{\boldsymbol{\varepsilon}'' : \mathbb{C}(\underline{z}) : \boldsymbol{\varepsilon}'} + \overline{\boldsymbol{\sigma}^{\mathbf{T}}(\underline{z}) : \boldsymbol{\varepsilon}'} \tag{4.82}$$

A second application of Hill's lemma to the strain field $\boldsymbol{\varepsilon}''$ and $\boldsymbol{\sigma}'$, noting that $\overline{\boldsymbol{\varepsilon}''} = 0$ for this load case, yields $\overline{\boldsymbol{\varepsilon}'' : \mathbb{C}(\underline{z}) : \boldsymbol{\varepsilon}'} = 0$. As a result, the combination of expressions

(4.81), (4.82), and (4.77) yield:

$$\boldsymbol{\Sigma}'' = \overline{\boldsymbol{\sigma}^{\mathbf{T}}(\underline{z}) : \mathbb{A}(\underline{z})} \tag{4.83}$$

which corresponds to the classical Levin's theorem [164] (see also [54, 301]). Hence, the macroscopic stress $\boldsymbol{\Sigma}''$ represents the pressure variation under zero macroscopic strain conditions. Using the definition of the microscopic eigenstress (4.74), we obtain:

$$\boldsymbol{\Sigma}'' = \boldsymbol{\Sigma}^{\mathbf{T}} = -p\varphi_0 \mathbf{1} : \overline{\mathbb{A}}^p \tag{4.84}$$

The comparison of the microscopic eigenstress to its macroscopic counterpart allows recognition of the second-order tensor of Biot pore pressure coefficients $\boldsymbol{\alpha}^I$:

$$\boldsymbol{\alpha}^I = \varphi_0 \mathbf{1} : \overline{\mathbb{A}}^p = (1-\eta)\,\mathbf{1} : \overline{\mathbb{A}}^p \tag{4.85}$$

Finally, the macroscopic stress resulting from the combination of both load cases yields expression (4.72a).

The latter results are used to derive the micromechanics basis of the second state equation of poroelasticity at level I (4.72b). The variation of the Lagrangian porosity is a function of the strain field in the pore space:

$$\varphi - \varphi_0 = \varphi_0 \mathrm{tr}\overline{\boldsymbol{\varepsilon}}^p \tag{4.86}$$

Recall that the strain field solution $\boldsymbol{\varepsilon}$ of (4.75) is the sum of the sub-problem solutions $\boldsymbol{\varepsilon}'$ and $\boldsymbol{\varepsilon}''$. The first solution is readily derived from (4.77) and (4.85):

$$\varphi_0 \mathbf{1} : \overline{\boldsymbol{\varepsilon}'}^p = \varphi_0 \mathbf{1} : \overline{\mathbb{A}}^p : \mathbf{E} = \boldsymbol{\alpha}^I : \mathbf{E} \tag{4.87}$$

The solution to the second case satisfies the condition $\overline{\boldsymbol{\varepsilon}''} = 0$, which implies:

$$\varphi_0 \overline{\boldsymbol{\varepsilon}''}^p = -(1-\varphi_0)\,\overline{\boldsymbol{\varepsilon}''}^s \tag{4.88}$$

where $\overline{\boldsymbol{\varepsilon}''}^s$ is the mean strain field in the solid phase. The objective is to derive the strain field

in the pore space for the second load case as a function of the pore pressure p. Using the state equation in the solid domain, we obtain:

$$(1-\varphi_0)\,\overline{\boldsymbol{\varepsilon}''}^{s} = (1-\varphi_0)\,\mathbb{S}^{s} : \overline{\boldsymbol{\sigma}''}^{s} \tag{4.89}$$

In return, $\overline{\boldsymbol{\sigma}''}^{s}$ is derived from the average rule $\boldsymbol{\Sigma}'' = \overline{\boldsymbol{\sigma}''} = -p\boldsymbol{\alpha}^{I}$ and the definition $\overline{\boldsymbol{\sigma}''}^{p} = -p\mathbf{1}$:

$$(1-\varphi_0)\,\overline{\boldsymbol{\sigma}''}^{s} = p\left(\varphi_0\mathbf{1} - \boldsymbol{\alpha}^{I}\right) \tag{4.90}$$

This result is used in (4.88) and (4.89) to deliver the expression for the strain field $\overline{\boldsymbol{\varepsilon}''}^{p}$:

$$\varphi_0\mathbf{1} : \overline{\boldsymbol{\varepsilon}''}^{p} = p\mathbf{1} : \mathbb{S}^{s} : \left(\boldsymbol{\alpha}^{I} - \varphi_0\mathbf{1}\right) \tag{4.91}$$

Finally, the total change in porosity (4.72b) is obtained by the superposition of the results (4.87) and (4.91), where the solid Biot modulus is defined as:

$$\frac{1}{N^{I}} = \mathbf{1} : \mathbb{S}^{s} : \left(\boldsymbol{\alpha}^{I} - \varphi_0\mathbf{1}\right) = \mathbf{1} : \mathbb{S}^{s} : \left(\boldsymbol{\alpha}^{I} - (1-\eta)\,\mathbf{1}\right) \tag{4.92}$$

Expressions (4.79), (4.85), and (4.92) define the homogenized poroelastic properties of the porous clay composite at level I. These expressions depend on the clay packing density η (a volumetric parameter) and the fourth-order strain concentration tensor $\overline{\mathbb{A}\,(\underline{z})}$ (the micromechanics representation of the morphology and mechanical interaction between phases). The key feature in the application of the self-consistent scheme to modeling the poroelastic response of the porous clay in shale is the prediction of a percolation threshold. The evaluation of the strain concentration tensor within the framework of the self-consistent scheme is presented in detail hereafter. In particular, we show the explicit development of the drained stiffness tensor $\mathbb{C}^{I}_{\text{hom}}$ in view of the self-consistent scheme for different microstructural configurations.

Evaluation of the Drained Stiffness Tensor at Level I

Given the importance of the strain concentration tensor in the self-consistent formulation of the level I modeling of shale, a detailed presentation of the explicit forms of the homogenized drained stiffness tensor (4.79) is appropriate. Following the proposed micromechanics representation of

shale for level I, the porous clay composite, the general form of the granular structure of shale could display different material and microstructural configurations. The solid clay phase may exhibit different elasticity contents (isotropic or anisotropic elasticity), as well as different morphologies represented by particle shapes and orientation distributions.

The most general micromechanics description for the porous clay composite using the self-consistent scheme can be derived for the case of preferentially aligned inclusions (solid particles and pores) in a transversely isotropic medium. The two different families of inclusions (solid particles and pores) and their morphologies lead to the use of different forms of the Hill concentration tensor for the efficient implementation of the self-consistent scheme. The Hill concentration tensor for the pore space depends on its spherical morphology and the transversely isotropic elastic properties of the reference medium, that is, the homogenized medium itself. Consequently, the P-tensor for spherical inclusions in a transverse isotropic medium is used for this evaluation. The clay solid particles with preferential alignment are recognized by the Hill tensor for spheroidal inclusions with preferred orientation in a transversely isotropic reference medium. Anisotropic properties for the solid particles $\mathbb{C}^s$ are considered for the evaluation of the homogenized stiffness of the porous composite. As a result, we consider transverse isotropic properties for the solid particles that are aligned with their symmetry axes. The symmetric plane $(\underline{e}_1^s, \underline{e}_2^s)$ in the oblate spheroids with local coordinate system (z_1^s, z_2^s, z_3^s) coincide with the plane of symmetric elasticity properties, as in (4.71). The rotated configuration of the local stiffness properties of the solid particles resulting from their preferential alignment is expressed using the rotation operator $\mathbf{Q}^{\chi=s}$ (4.60):

$$C_{ijkl}^s(\varphi,\theta) = Q_{ip}^s Q_{jq}^s Q_{kr}^s Q_{ls}^s C_{pqrs}^s(0,0) \tag{4.93}$$

The effect of the particle orientation as described by an orientation distribution function (ODF) enters the micromechanics formulation through the evaluation of the strain concentration tensor $\overline{\mathbb{A}}$. The information about the particle alignment and shape in terms of inclination angles θ, φ and aspect ratio $X^{\chi=s}$ (for the solid inclusions) is carried in the homogenization scheme through the Hill tensor $\mathbb{P}_{X^s}^{sc}\left(\varphi, \theta, X^s, \mathbb{C}_{\text{hom}}^I\right)$. For the application of the self-consistent scheme to the porous clay composite with preferentially aligned solid particles, the homogenized properties

(4.35) at level I read in expanded form:

$$\begin{aligned}\mathbb{C}^I_{\text{hom}} &= \left\langle \eta\mathbb{C}^s(\varphi,\theta) : \left[\mathbb{I}+\mathbb{P}^{sc}_{X^s}\left(\varphi,\theta,X^s,\mathbb{C}^I_{\text{hom}}\right) : \left(\mathbb{C}^s(\varphi,\theta)-\mathbb{C}^I_{\text{hom}}\right)\right]^{-1}\right\rangle : \\ &\left\{(1-\eta)\left(\left[\mathbb{I}-\mathbb{P}^{sc}_{X^p}\left(X^p,\mathbb{C}^I_{\text{hom}}\right) : \mathbb{C}^I_{\text{hom}}\right]^{-1}\right)\right. \\ &\left.+\eta\left\langle\left[\mathbb{I}+\mathbb{P}^{sc}_{X^s}\left(\varphi,\theta,X^s,\mathbb{C}^I_{\text{hom}}\right) : \left(\mathbb{C}^s(\varphi,\theta)-\mathbb{C}^I_{\text{hom}}\right)\right]^{-1}\right\rangle\right\}^{-1}\end{aligned} \tag{4.94}$$

where the operator $\langle\rangle$ on any quantity $\mathbb{Y}$ represents:

$$\langle\mathbb{Y}\rangle = \frac{1}{4\pi}\int_{\varphi=0}^{\varphi=2\pi}\int_{\theta=0}^{\theta=\pi} W(\theta)\,\mathbb{Y}\sin(\theta)\,d\theta d\varphi \tag{4.95}$$

The term $W(\theta)$ in (4.95) represents an orientation distribution function, which defines the type of preferential alignment of the solid inclusions in the homogenized medium. The Hill tensor characterizing the solid clay particles $\mathbb{P}^{sc}_{X^s}\left(\varphi,\theta,X^s,\mathbb{C}^I_{\text{hom}}\right)$ is evaluated using (4.61) and its associated expressions. The Hill tensor characterizing the pore inclusions $\mathbb{P}^{sc}_{X^p}\left(X^p=1,\mathbb{C}^I_{\text{hom}}\right)$ is evaluated using expressions (4.49)-(4.55).

Given that all the tensors involved in $\langle\mathbb{Y}\rangle$-type operations in (4.94) are only a function of the inclination angle θ in the intermediate coordinate system, the evaluation of (4.94) can be further simplified. A first integration can be performed analytically in the intermediate coordinate system as any quantity $\mathbb{Y}^\varphi$ is independent of angle φ [103]:

$$\left\langle Y^\varphi_{ijkl}(\theta)\right\rangle = \frac{1}{2\pi}\int_{\varphi=0}^{\varphi=2\pi} Q^{\varphi\chi}_{pi}(\varphi)\,Q^{\varphi\chi}_{qj}(\varphi)\,Q^{\varphi\chi}_{rk}(\varphi)\,Q^{\varphi\chi}_{sl}(\varphi)\,Y^{\varphi\chi}_{pqrs}(\theta)\,d\varphi \tag{4.96}$$

The quantity $\left\langle Y^\varphi_{ijkl}(\theta)\right\rangle$ is then integrated numerically as a function of one variable, the inclination angle θ:

$$\langle Y_{ijkl}\rangle = \frac{1}{2}\int_{\theta=0}^{\theta=\pi} W(\theta)\left\langle Y^\varphi_{ijkl}(\theta)\right\rangle\sin(\theta)\,d\theta \tag{4.97}$$

Another relevant configuration of the porous clay composite modeled through the self-consistent scheme is introduced for the case of spherical inclusions (both solid particles and pores) in a transversely isotropic medium, which results from the intrinsic transversely isotropic elasticity of the solid clay. Although being spherical, the particles are perfectly aligned so that the material symmetry of the clay particles is aligned with the overall (resulting) transverse

isotropic material. This particular configuration of the porous clay yields a more compact formulation compared to the result in (4.94). The similar morphologies of clay particles and pores allow the use of the same form for the P-tensors describing their mechanical interactions. Consequently, the evaluation of the drained stiffness properties of the porous clay follows the simplified form for the self-consistent estimate given in (4.39):

$$\mathbb{C}^I_{\text{hom}} = \eta\mathbb{C}^s : \left[\mathbb{I} + \mathbb{P}^{sc} : \left(\mathbb{C}^s - \mathbb{C}^I_{\text{hom}}\right)\right]^{-1} \tag{4.98}$$

where $\mathbb{P}^{sc} = \mathbb{P}^{sc}\left(\mathbb{C}^I_{\text{hom}}\right)$ is the Hill tensor for spherical inclusions embedded in a transverse isotropic medium (see Section 4.2.5).

4.4.2 Level II: Porous Clay – Silt Inclusion Composite

At the macroscopic scale, shale is composed of porous clay and (mainly) quartz inclusions of approximately spherical shape and that are randomly distributed throughout the medium. Using the tools of microporomechanics, we aim to develop the homogenization scheme for a two-phase material composed of a porous solid phase governed by the poroelastic state equations (4.72) and elastic inclusions. The porous clay and silt inclusions occupy the volumes $\Omega^{pc} = \left(1 - f^{inc}\right)\Omega$ and $\Omega^{inc} = f^{inc}\Omega$ at the macroscopic scale. The non-clay inclusion volume fraction f^{inc} was introduced in (3.4a). A convenient way to homogenize the level II behavior is in form of a continuous description of the stress field in the heterogeneous *rev* [83][8]:

$$\boldsymbol{\sigma}\left(\underline{z}\right) = \mathbb{C}\left(\underline{z}\right) : \boldsymbol{\varepsilon}\left(\underline{z}\right) + \boldsymbol{\sigma}^{\mathbf{T}}\left(\underline{z}\right) \qquad \left(\forall \underline{z} \in \Omega\right) \tag{4.99}$$

together with the distribution of elastic properties and eigenstresses:

$$\mathbb{C}\left(\underline{z}\right) = \begin{cases} \mathbb{C}^I_{\text{hom}} & \left(\Omega^{pc}\right) \\ \mathbb{C}^{inc} & \left(\Omega^{inc}\right) \end{cases} \qquad \boldsymbol{\sigma}^{\mathbf{T}}\left(\underline{z}\right) = \begin{cases} -\boldsymbol{\alpha}^I p & \left(\Omega^{pc}\right) \\ 0 & \left(\Omega^{inc}\right) \end{cases} \tag{4.100}$$

where $\mathbb{C}^I_{\text{hom}}$ and $\boldsymbol{\alpha}^I$ are respectively the level I stiffness tensor (4.79) and the second-order tensor of Biot pore pressure coefficients (4.85), which characterize the poroelastic behavior of the

[8] A similar derivation has been previously presented in [267], in which the authors treated the homogenization problem for a two-phase material composed of a porous solid and elastic inclusions.

porous clay phase, while $\mathbb{C}^{inc} = 3k^{inc}\mathbb{J} + 2g^{inc}\mathbb{K}$ is the stiffness tensor of the (assumed isotropic) quartz inclusion phase. The macroscopic counterpart of those micromechanical stress–strain and eigenstress relations is recognized from classical micromechanics results:

$$\boldsymbol{\Sigma} = \overline{\boldsymbol{\sigma}\left(\underline{z}\right)} = \mathbb{C}^{II}_{\text{hom}} : \mathbf{E} + \boldsymbol{\Sigma}^{\mathbf{T}} \tag{4.101}$$

We proceed in a similar fashion as developed for the homogenization problem at level I, in which we decompose the problem into two particular load cases:

1. The first load case corresponds to the application of the macroscopic strain $\mathbf{E}$ only, while the eigenstress is zero. This is equivalent to a drained condition, for which the macroscopic strain tensor is related to the local strain field through the strain concentration tensor:

$$\boldsymbol{\varepsilon}'\left(\underline{z}\right) = \mathbb{A}\left(\underline{z}\right) : \mathbf{E} \tag{4.102}$$

The combination of the concentration expression (4.102) and the strain averaging (4.5) for the two-phase composite under consideration yields the following condition for the concentration tensor:

$$\overline{\mathbb{A}\left(\underline{z}\right)} = f^{inc}\overline{\mathbb{A}}^{inc} + \left(1 - f^{inc}\right)\overline{\mathbb{A}}^{pc} = \mathbb{I} \tag{4.103}$$

The macroscopic stress is derived from the use of (4.102) in (4.99) together with (4.100) and the application of volume averaging:

$$\boldsymbol{\Sigma}' = \overline{\boldsymbol{\sigma}'\left(\underline{z}\right)} = \mathbb{C}^{II}_{\text{hom}} : \mathbf{E} \tag{4.104}$$

where $\mathbb{C}^{II}_{\text{hom}}$ is the drained macroscopic stiffness of shale:

$$\mathbb{C}^{II}_{\text{hom}} = \overline{\mathbb{C} : \mathbb{A}\left(\underline{z}\right)} = \mathbb{C}^{I}_{\text{hom}} + f^{inc}\left(\mathbb{C}^{inc} - \mathbb{C}^{I}_{\text{hom}}\right) : \overline{\mathbb{A}}^{inc} \tag{4.105}$$

2. The second load case corresponds to the application of the eigenstress field only, while the macroscopic strain is zero. Based on Levin's theorem, the macroscopic eigenstress

$\boldsymbol{\Sigma}^{\mathbf{T}}$ and the microscopic eigenstress $\boldsymbol{\sigma}^{\mathbf{T}}(\underline{z})$ are related by:

$$\boldsymbol{\Sigma}'' = \boldsymbol{\Sigma}^{\mathbf{T}} = \overline{\boldsymbol{\sigma}^{\mathbf{T}}(\underline{z}) : \mathbb{A}(\underline{z})} = -\boldsymbol{\alpha}^{II} p \tag{4.106}$$

where $\boldsymbol{\alpha}^{II}$ is the second-order Biot coefficient tensor of the macroscopic composite:

$$\boldsymbol{\alpha}^{II} = \boldsymbol{\alpha}^{I} : \left(\mathbb{I} - f^{inc}\overline{\mathbb{A}}^{inc}\right) \tag{4.107}$$

Finally, one can derive the second macroscopic poro-elastic state equation for level II using the latter results. The change of porosity for the first subproblem is readily derived as:

$$(\phi - \phi_0)' = \boldsymbol{\alpha}^{II} : \mathbf{E} \tag{4.108}$$

For the second load case, we use the result for the porosity variation at the nanoscale and the volume fraction relation $\varphi_0 = \phi_0 / \left(1 - f^{inc}\right)$:

$$\begin{aligned} (\phi - \phi_0)'' &= \left(1 - f^{inc}\right)(\varphi - \varphi_0)'' && (4.109a) \\ &= \left(1 - f^{inc}\right)\left(\boldsymbol{\alpha}^{I} : \overline{\boldsymbol{\varepsilon}''}^{pc} + \frac{p}{N^I}\right) && (4.109b) \end{aligned}$$

The objective is then to substitute for the average strain in the porous clay $\overline{\boldsymbol{\varepsilon}''}^{pc}$ a suitable expression in function of the eigenstress. For this, we make use of the zero strain condition $\overline{\boldsymbol{\varepsilon}''} = 0$ used in the second load case to express the macroscopic stress:

$$\begin{aligned} \boldsymbol{\Sigma}'' &= f^{inc}\overline{\boldsymbol{\sigma}''}^{inc} + \left(1 - f^{inc}\right)\overline{\boldsymbol{\sigma}''}^{pc} && (4.110a) \\ &= \left(1 - f^{inc}\right)\left(\mathbb{C}^{I}_{\text{hom}} - \mathbb{C}^{inc}\right) : \overline{\boldsymbol{\varepsilon}''}^{pc} - \left(1 - f^{inc}\right)\boldsymbol{\alpha}^{I} p && (4.110b) \end{aligned}$$

The last result is combined with the expression for the macroscopic eigenstress (4.106):

$$\left(1 - f^{inc}\right)\overline{\boldsymbol{\varepsilon}''}^{pc} = \left(\mathbb{C}^{I}_{\text{hom}} - \mathbb{C}^{inc}\right)^{-1} : \left[-\boldsymbol{\alpha}^{II} + \left(1 - f^{inc}\right)\boldsymbol{\alpha}^{I}\right] p \tag{4.111}$$

Finally, combine (4.111) with (4.109). Together with the solution of the first load case (4.108),

we so obtain the second poroelastic state equation for level II:

$$\phi - \phi_0 = \boldsymbol{\alpha}^{II} \colon \mathbf{E} + \frac{p}{N^{II}} \tag{4.112}$$

where N^{II} is the macroscopic solid Biot modulus:

$$\frac{1}{N^{II}} = \frac{1 - f^{inc}}{N^{I}} + f^{inc} \boldsymbol{\alpha}^{I} : \left(\mathbb{C}^{inc} - \mathbb{C}^{I}_{\text{hom}}\right)^{-1} : \boldsymbol{\alpha}^{I} : \left(\mathbb{I} - \overline{\mathbb{A}}^{inc}\right) \tag{4.113}$$

Expressions (4.105), (4.107), and (4.113) define the homogenized poroelastic properties of the porous clay – silt inclusion composite at level II. These expressions depend on the inclusion volume fraction f^{inc} (a volumetric parameter) and the fourth-order strain concentration tensor $\overline{\mathbb{A}}^{inc}$ (the micromechanics representation of the morphology and mechanical interaction between the porous clay and the silt inclusions). For this homogenization step, the self-consistent estimate is also used to approximate the average strain concentration tensor in the inclusion $\overline{\mathbb{A}}^{inc}$, which is readily obtained by considering the heterogeneous stiffness distribution (4.100) in (4.33) while letting $\mathbb{C}^{SC} = \mathbb{C}^{II}_{\text{hom}}$. The evaluation of the concentration tensor $\overline{\mathbb{A}}^{inc}$ also involves the use of the P-tensor for spherical particles in a transverse isotropic medium, whose elements are detailed in expressions (4.49)-(4.55).

4.4.3 From Drained to Undrained Poroelastic Properties

We next rewrite the poroelastic state equations at levels I and II in a form that allows the comparison with acoustic measurements of shale specimens. Indeed, the application of acoustic measurement techniques to saturated shale corresponds to the case of undrained conditions due to the high frequencies employed in testing, which ensures that saturating fluids do not leave the pore domain [70][9]. Undrained estimates are achieved by first considering the mass content $m^I = \varphi \, \rho^{fl}(p)$ or $m^{II} = \phi \, \rho^{fl}(p)$ together with a linear state equation for the fluid density in function of the fluid pressure [70, 71]:

$$\rho^{fl} = \rho^{fl,0} \left(1 + \frac{p}{k^{fl}}\right) \tag{4.114}$$

[9] A thorough assessment of the prediction of acoustic properties of shale using poroelasticity theory will be presented in Chapter 6.

where $\rho^{fl,0}$ is the reference fluid density and k^{fl} the fluid bulk modulus. The substitution of (4.114) in the drained form of the poroelastic state equations yields the classical form of Biot's poroelasticity state equations:

$$\boldsymbol{\Sigma} = \mathbb{C}_{\text{hom}}^{J,un} : \left(\mathbf{E} - \mathbf{B}^J \frac{(m - m_0)^J}{\rho^{fl,0}} \right) \tag{4.115a}$$

$$\frac{(m - m_0)^J}{\rho^{fl,0}} = \boldsymbol{\alpha}^J : \mathbf{E} + \frac{p}{M^J} \tag{4.115b}$$

where $\mathbb{C}_{\text{hom}}^{J,un}$ is the undrained stiffness tensor (at level $J = I,II$), $\mathbf{B}^J$ the second-order tensor of Skempton coefficients, and M^J the overall Biot modulus, given by:

$$\mathbb{C}_{\text{hom}}^{J,un} = \mathbb{C}_{\text{hom}}^{J} + \left(M^J \boldsymbol{\alpha} \otimes \boldsymbol{\alpha} \right)^J \tag{4.116}$$

$$\mathbf{B}^J = M^J \mathbb{S}_{\text{hom}}^{J,un} : \boldsymbol{\alpha}^J \tag{4.117}$$

$$\frac{1}{M^J} = \frac{1}{N^J} + \frac{\phi_0^J}{k^{fl}} \tag{4.118}$$

with $\phi_0^I = \varphi_0 = 1 - \eta$ at level $J = I$, and $\phi_0^{II} = \varphi_0 \left(1 - f^{inc}\right)$ at level $J = II$.

4.4.4 Intrinsic Materials Invariant Phase Properties

One characteristic of our modeling approach is to assign material properties to elementary phases present in shale that could be, in first order, invariant across different material specimens. The first set of material invariant properties is composed of the five independent constants of the elementary building block of clay $\mathbb{C}^s$, as introduced in expression (4.71). The determination of the properties of in situ clay is a primary focus of this work, and will be pursued in subsequent chapters.

In turn, for the non-clay inclusions, the mechanical properties for natural quartz have been documented in the literature, showing that a single quartz crystal possesses trigonal symmetry (thus having, in addition to the five elasticity constants of transverse isotropic materials, a non-zero $C_{14} = C_{1123}$ term) [122]. On the other hand, since it is unlikely to encounter a single quartz crystal in shale microfabric, and since those crystals are expected to be randomly oriented, a first approach considers quartz inclusions with quasi-isotropic elastic properties defined by the

bulk modulus k^{inc} and shear modulus g^{inc}, which can be found in handbooks [175]:

$$k^{inc} = 37.9 \text{ GPa}; \; g^{inc} = 44.3 \text{ GPa} \tag{4.119}$$

The properties of quartz grains made out of polycrystals may differ from the values (4.119) due to the existence of weak crystal interfaces. Such occurrence may have some effect on sedimentary rocks such as sandstones, in which quartz and other sand-minerals alike constitute the load-bearing phase. Nevertheless, these effects might be of second order for the case of shales, which show moderate contents of quartz minerals.

Finally, the bulk modulus of the fluid phase saturating the pore space depends on the type of fluid (as well as on the fluid saturation). For all remaining developments, we shall consider shale as fully-saturated. In addition, the mechanical properties of the pore fluid are approximated by those of water[10]:

$$k^{fl} = 2.3 \text{ GPa} \tag{4.120}$$

4.5 Discussion of the Microporomechanics Representation of Shale

A general framework for the micromechanics modeling for shale has been established in the preceding sections. The foundations of the model rest in a multi-scale structure model and in the experimental observations of the mechanical response of shale at various length scales. In this discussion, we compare the present modeling approach with previous micromechanics models for shale and their approaches to modeling its microstructure and mechanics behaviors. This section will also focus on extended discussions of the important modeling aspects, assumptions, and clarifications related to our representation and micromechanics treatment of shale.

4.5.1 Comparisons with Existing Models

Research efforts in multi-scale modeling of shale anisotropic elasticity owe much to the pioneering work of Hornby et al. [128] and Sayers [228]. Hornby et al. introduced the concept

[10] For a few shale specimens considered in this study, the pore fluid is characterized as a brine solution with moderate salt concentrations. Hence, the compressibility of the pore fluid can be approximated by that of water.

of a 'perfect' shale at the smallest scale of relevance to mechanics. This elementary unit, or building block, represents the response of a bi-connected clay-fluid composite modeled through a combination of self-consistent and differential effective medium (DEM) theories [239]. The main feature of this modeling scheme for porous composites is the connectivity of phases over the entire range of relative concentrations, which ensures a finite stiffness for the composite material for all porosity values. Given the lack of elasticity data for clay minerals, isotropic elastic properties were assigned to the clay phase based on the combination of experimental data from clay-sand mixtures [171] and mechanics modeling. The anisotropic effective properties of the clay-fluid building block originated from considering inclusions as perfectly aligned, oblate spheroids. In addition to the geometric source of anisotropy linked to the particle shape of the clay-fluid unit, the model also recurred to the use of preferred particle orientations. Sayers pioneered the use of particle orientation distribution functions (ODF) to characterize shale's elastic-anisotropy measured by acoustic tests. The input for establishing the distributions of particle orientations is data extracted from advanced imaging techniques such as SEM micrographs. The final step in Hornby's model was to include the mechanical contribution of roughly spherical quartz inclusions at larger length scales compared to the clay fabric.

The multi-scale, micromechanics approach of Hornby et al. inspired several other models for shale. Jakobsen et al. [140] extended the model for an application to clay-rich, hydrate-bearing sediments. Draege et al. [85] combined Hornby et al.'s model to mechanical/chemical compaction models to predict effective elastic properties of cemented shales after diagenetic and temperature changes. Ulm et al. [267] also considered a similar multi-scale micromechanics approach, with the incorporation of mechanical behaviors of shale materials identified through nano- and microindentation testing. This model shares some essential features of previous attempts such as assigning the sources of anisotropy to shape and orientations of particles. In addition, Ulm et al. [267] consider the effects of layering on the response of the clay fabric at length scales comparable to those relevant to the silt inclusions. The model of Ulm et al. [267] has served as a reference framework for more recent modeling attempts such as Giraud et al. [103, 104] and the work herein presented.

It will be illustrative to summarize the key features of previous modeling attempts for characterizing shale in the perspective of the influential factors affecting the macroscopic response

of sedimentary rocks, as detailed in Table 4.1. Besides compositional aspects such as lithology, clay content, and bulk density, the most important attributes affecting the seismic responses of rocks are morphological features such as pore shape, fractures, and texture (understood as the shape of solid particles, sorting of particles, and grain-to-grain contacts). The traditional modeling of sedimentary rocks has assigned the most prominent role to geometrical aspects for defining macroscopic seismic attributes. The modeling of shale has indeed heavily relied on the effects of particle shape and orientations of particles to explain the macroscopically observed anisotropic elasticity. However, the elasticity of the clay phase and the mechanical response of the porous clay composite at nanoscales are the latest pieces of information to be added to the multi-scale approach for modeling shale. The nanomechanics of shale as measured by indentation testing hints towards the importance of an intrinsic anisotropy proper to the clay phase. Lastly, the models following the approach of Hornby et al. of using effective medium theory for modeling the micromechanical response of shale support the bi-connectivity of phases as an integral part of the approach. This connectivity of mechanical phases is regarded as a main characteristic of sedimentary rocks [128]. Clearly, the use of Biot's poroelasticity as the framework for our modeling approach is in line with the view of a connected pore space [239]. However, it is the microporomechanics approach of Dormieux et al. [54, 82, 83] and the experimental nanomechanics data of Ulm and co-workers [32, 265] that enrich the poroelastic description of shale through offering a physics-based link between the grain-scale properties and macroscopic behaviors of shale.

4.5.2 About the Microporomechanics Model of Shale

The general framework of the micromechanics model for shale poroelasticity has been developed throughout this chapter. In particular, Sections 4.3 and 4.4 outline the representation of shale for the application of a micromechanics modeling approach and the corresponding formulation for determining estimates of shale poroelasticity at different length scales. This section is devoted to supplementing those detailed presentations with additional notes regarding the applicability of the model and clarifications of modeling assumptions[11].

[11] This presentation has been enriched by the comments and suggestions made by the reviewers and editors of the journal publications [202, 203], for which the authors are very grateful.

Rock properties	*Fluid properties*	*Environment*
Compaction	Viscosity	Frequency
Consolidation history	Density	Stress history
Age	Wettability	Depositional environment
Cementation	Fluid composition	Temperature
Texture	Phase	Reservoir process
Bulk density	Fluid type	Production history
Clay content	Gas-oil, gas-water ratio	Layer geometry
Fractures	Saturation	Net reservoir pressure
Porosity		
Lithology		
Pore shape		

Table 4.1: Factors influencing the seismic properties of sedimentary rocks. Factors are listed with increasing importance from top to bottom. From Wang et al. [283].

Mechanical Representation of Porous Clay Composite at Level I

The micromechanics modeling for shale poroelasticity follows a *reductionist* approach, as we aim to simplify the complex mechanics of shale to a convenient set of parameters and descriptions. A crucial component of the model corresponds to the poromechanics description of the clay fabric in shale composed of the clay phase and the nanoscale porosity. The present approach assumes that there is a single porosity type that is entirely included in the clay fabric. We base this assumption on experimental observations from fluid-intrusion porosimetry results of shales, which show that the pore size distribution in highly compacted shales exhibits a single characteristic length scale (refer to Section 2.2.6, Figure 2-3). Typically, the pore throat radius is on the order of tens of nanometers, which is characteristic of the inter-clay grain size. Consequently, the poroelastic state equations (4.72) are valid for a single fluid phase saturating the pore space, which interacts purely mechanically with the assumed linear elastic solid clay. Thus, the case of partial saturation and chemical interactions at solid/fluid interfaces [71, 84] is not developed in this poroelastic study. The assumption of a single, fluid-filled porosity does not exclude the existence of an intra-particle porosity, whose size should be smaller than the interparticle porosity (i.e. in the sub-nanometer range, which is not accessible by conventional porosity testing). At the sub-nanometer length scale, the water molecules or liquids present in this sub-nanoporosity cannot be considered as a pore space filled by bulk water, as surface effects dominate this behavior. This bounded or structural water is instead part of the in situ

stiffness we consider at level 0.

Another modeling feature related to the pore space in shale is the treatment of the morphology of pores as spherical inclusion. The visual information provided by advanced imagining such as SEM micrographs depicts the various morphologies of solid particles. In contrast, the characterization of the pore space morphology is a more challenging topic. Computational approaches based on finite-element simulations have been developed to predict the mechanical behavior of rock, whose primary input are microstructural descriptions of the pore space obtained from tomographic images (see e.g. [76]). However, these expensive geometrical descriptions of the microstructure, and in particular of the pore space, are only restricted to small rock masses of millimeter length scales. Within the micromechanics approach, our modeling choice is justified by the need to reduce the different potential sources of anisotropy affecting the overall poroelastic response of shale to only a few relevant parameters.

Level II

One of the main challenges involved in the modeling of shale elasticity has been the identification and representation of the relevant sources of anisotropy. Earlier works on shale micromechanics (e.g. [128, 139]) assigned geometrical features of the clay fabric (particle shapes and orientations) as the sole sources of the anisotropy observed in laboratory testing of these materials. In addition, significant research in the area of elasticity of porous rocks has been developed based on the treatment of fractures and cracks as dominant factors controlling the anisotropic behavior [109, 131, 132, 257]. In our modeling effort, structural sources of anisotropy are not considered. Instead, we focus our model developments on advancing the understanding of the anisotropy of the clay fabric with the outlook of developing a baseline model for shale anisotropic poroelasticity for unperturbed (unfractured), in situ conditions. From a modeling perspective, the determination of the amount of cracks, usually quantified in terms of crack-like or soft porosity, represents a challenging task. Estimates of crack porosity, which is typically an extremely small fraction of the total porosity, are usually obtained from the difference between the measured total porosity and the extrapolation of high-pressure porosity versus pressure trends established from deformation experiments (see e.g. [173]). Being consistent with the treatment of unfractured media, the input parameters to our model, namely the clay packing density and

the silt inclusion volume fraction, are calculated based on the so-called equant or hard porosity [109]. This type of porosity is deemed to be pressure-insensitive, and it is equivalent to the total porosity ϕ_0 measured in experiments in the absence of crack porosity. Model predictions of acoustic properties at level II do not consider stiffening effects due to squirt-flow phenomena as a result of our treatment of shale as unfractured porous media. These topics will be further analyzed through the model validation work to be presented in forthcoming chapters. By focusing on the intrinsic anisotropic response of shale, the present modeling work may delineate the contributions of the different sources of anisotropy to the observed overall anisotropy of shale.

In so far related to the micromechanics representation of the contributions of the silt-size inclusions to the overall mechanical response of shale, our treatment of inclusions as quartz-like, isotropic elastic solids is shared by most other micromechanics models. Their relatively smaller volume fraction compared to the clay phase does not impose severe restrictions on their micromechanics representation. The assumed spherical shape corresponds, in context of the self-consistent scheme, to a morphology useful for describing random contact between particle surfaces. Furthermore, it precludes the silt inclusion phase from contributing to the overall anisotropic elasticity of shale, highlighting instead the commonly accepted primary role of the clay fabric on anisotropy. Finally, the underlying micromechanics formulation for the mechanical interaction between the silt inclusion and the porous clay composite assumes perfectly bonded phases. Any contributions from weak interfaces and partial transfer of forces resulting in reduced stiffness properties are not considered in the present poroelastic formulation.

4.6 Chapter Summary

In this chapter, a general micromechanics modeling framework has been established for the poroelastic assessment of shale. Based on linear micromechanics theory, the poroelastic responses of shale at the different length scales prescribed by our multi-scale structure thought-model can be properly estimated based on the microstructure and material properties at an scale below. The homogenization model has all the ingredients to characterize the multi-scale, anisotropic poroelasticity of shale, as it incorporates:

- Material composition information through volumetric parameters: the clay packing den-

sity, and the inclusion volume fraction.

- Mechanical properties of the relevant material phases: the clay fabric, the silt inclusions, and the saturating fluid. In particular, the mechanical behavior of the solid clay in shale is an unknown in the modeling problem, and it will be resolved through calibration and validation exercises.

- Microstructural features such as particle shapes and preferred orientation of particles.

All these modeling elements take root in the results and observations gathered from experimental testing on shale by means of advanced imaging techniques, nanoindentation testing, and conventional macroscopic acoustic experiments. In the following chapter, the micromechanics model will be tested against a series of hypotheses of the contributions of intrinsic material properties and microstructural features to the overall anisotropic, multi-scale behavior of shale elasticity. Through a series of calibration and validation exercises, the expected outcome of the hypothesis testing is a quantitative assessment of the different sources of anisotropy in shale, and to effectively predict the poroelastic behavior of shale at different length scales.

Chapter 5

Model Calibration and Validation

The microporomechanics framework developed in Chapter 4 provides a comprehensive mechanics description of various compositional and microstructural elements contributing to the multi-scale, anisotropic poroelasticity of shale. Structural sources of anisotropy, which have been traditionally regarded as the main sources of elastic anisotropy, are considered in the micromechanics formulation in the form of geometrical descriptions of particle shape and orientations. The nanogranular response of shale inferred from instrumented nanoindentation is also incorporated into the micromechanics developments through the contribution of the intrinsic anisotropy of the clay phase and the modeling of the percolation threshold.

The goal of this chapter is to establish a micromechanics model for the prediction of shale anisotropic poroelasticity based on a physics-based, effective descriptions of the microstructure and intrinsic material properties of shale. Particularly, we seek to determine the effective mechanical behavior of the clay fabric in shale, which governs its complex anisotropic behavior. The presentation of this chapter begins with the study of the relation between the percolation threshold, as observed for the porous clay at nanoscales, and the microstructure of granular media. The findings of that study will shed light on the effective ways to model microstructural features such as particle shape and orientation which would enable replicating the observed percolation threshold and the experimentally measured elastic response of the porous clay in shale. Armed with this understanding of granular micromechanics, the micromechanics model is then calibrated based on different hypotheses of the effective intrinsic properties and microstructure configurations of the porous clay, which are directly linked to the elasticity and morphology

of the elementary building block of shale at level 0 of the multi-scale structure model. These hypotheses represent sensible combinations of the different sources of anisotropic elasticity that ultimately define the macroscopic anisotropic behavior of shale. The different model hypotheses are then validated (or disproved) at the different length scales of the multi-scale approach using independent data sets of elasticity. The focus of calibration and validation exercises involved in model development is on shale with minimum organic content (kerogen-free shale)[1]. The expected outcome of the calibration and validation exercises is the systematic identification, from the pool of modeled elasticity attributes, of those that dominate the macroscopic diversity of shale's anisotropic poroelastic behavior.

5.1 Effects of Particle Shape and Orientation on the Mechanics of Granular Media

The results from nanoindentation experiments on shale materials presented have revealed a granular behavior of the clay fabric at nanometer scales through the identification of an apparent percolation threshold (refer to Figure 3-15). This distinct mechanical attribute unfolds a wealth of information regarding the link between the microstructure of the clay fabric and its effective mechanical response, within the framework of micromechanics modeling. More explicitly, morphological features such as particle shapes and their orientations dictate the specific packing of a granular ensemble and the potential occurrence of a percolation threshold packing, below which the material loses its ability to develop an elastic or strength response. Consequently, it is worth as a first application of the microporoelastic model to investigate the effects of particle shape and orientation on the percolation threshold of a porous solid representing the clay fabric in shale. For this application, some of the micromechanics developments introduced in Chapter 4 are implemented.

[1] The micromechanics model will be extended for the treatment of kerogen-rich shale. The corresponding model development and formulations will be presented in Chapter 7.

5.1.1 Percolation Threshold for Randomly Aligned Particles

The first case to be considered is the relation between percolation threshold and particle shape for material systems with randomly aligned particles. This random packing of particles has been a focus of attention in the granular physics community, and several researchers have investigated the effect of particle shape on packings of ellipsoids. Onoda and Liniger [201] determined that the random-loose packing fraction of uniform spheres ($X^s = c/a = 1$) at the limit of zero gravitational force is 0.555 ± 0.005, which corresponds to a sphere packing at its rigidity-percolation threshold. Buchalter and Bradley [46] performed Monte Carlo simulations of the pouring of oblate and prolate ellipsoids, and showed that increased asphericity yields lower percolation thresholds. Similar results have been obtained by Coelho et al. [67] and Sherwood [240] using sequential deposition algorithms for rigid particles of different shapes. These results become intuitive by recognizing that larger disk-like or needle-like particles may come easier into contact and create networks that percolate at smaller packing densities. Qualitatively, these results from granular physics for disordered media hint toward the correspondence of higher percolation thresholds to nearly spherical shapes, as observed in Figure 5-1.

The self-consistent scheme of continuum micromechanics (refer to Section 4.2.4) recognizes the percolation threshold associated with disordered granular materials. The original formulation of the scheme considered a perfectly random distribution of contact surfaces between particles [154]. This averaged random contact may be represented, mechanically, by a sphere. Irrespective of the elasticity of the particle, the percolation threshold of the polycrystal model for spherical particles is $\eta_0 = 0.5$, in close agreement with the random-loose packing fraction of spheres. While a sphere itself is a 'perfectly disordered' particle shape in the context of the self-consistent model [301], it will be of interest to review the results on the effects of non-spherical particles on the percolation threshold. For this, we summarize in this presentation the works of Fritsch et al. [91] and Sanahuja et al. [225].

Consider a porous medium composed of empty pores and aspherical solid particles, which are represented as spheroids of revolution of aspect ratio X^s (see expression (4.59)). Oblate spheroids correspond to $X^s < 1$ and prolate spheroids to $X^s > 1$. For simplicity, the pore space is represented as spherical inclusions. Given the different morphology and the orientation of the solid phase, the definition of the strain concentration of the solid particles (see expression

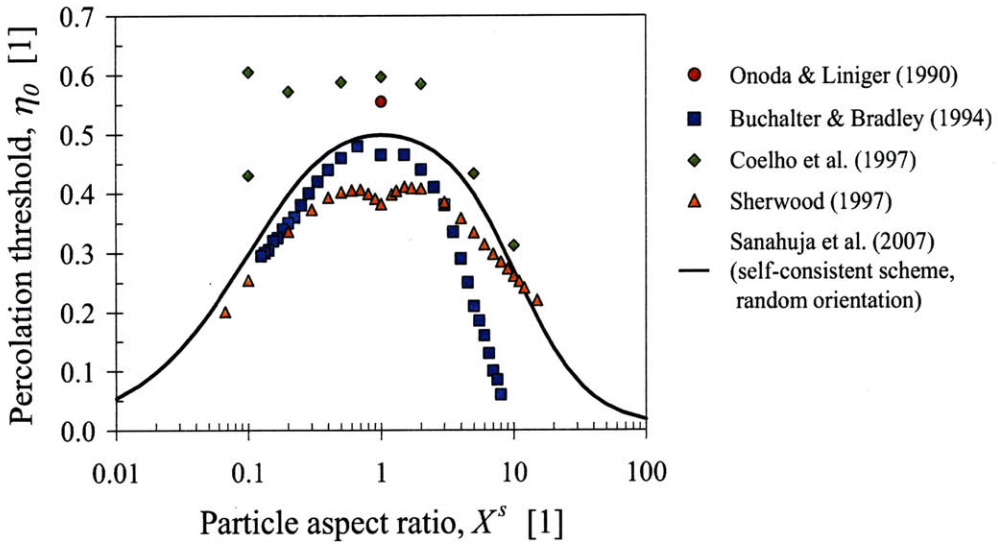

Figure 5-1: Percolation threshold η_0 for a porous solid modeled through the self-consistent scheme as function of solid particle aspect ratio X^s (< 1 oblates, > 1 prolates). Data points corresponds to selected results from granular physics simulations [46, 67, 201, 240]. The solid line corresponds to the implementations of the results of Fritsch et al. [91] and Sanahuja et al. [225] for a self-consistent model of a porous material with random particle orientations.

(4.28)) is modified accordingly to accommodate for the present situation. The uniform strain in the solid sphere depends on the orientation of the inclusion:

$$\boldsymbol{\varepsilon}^s(\varphi,\theta) = [\mathbb{I} + \mathbb{P}^{sc}(\varphi,\theta,X^s) : (\mathbb{C}^s - \mathbb{C}^{sc}_{\text{hom}})]^{-1} : \mathbf{E}_0 \qquad (\Omega^s) \tag{5.1}$$

where $\mathbb{P}^{sc}(\varphi,\theta,X^s)$ is the Hill tensor for a spheroid defined by the Euler angles φ,θ. The Hill tensor also depends on the elastic properties of the (yet to be determined) self-consistent medium $\mathbb{C}^{sc}_{\text{hom}}$ and the aspect ratio of the spheroidal particles X^s. The random arrangement of particles is modeled by a uniform distribution of orientations, which yields the following average strain estimate for the solid phase:

$$\overline{\boldsymbol{\varepsilon}}^s = \mathbb{L}^s : \mathbf{E}_0 \tag{5.2a}$$

$$= \left(\frac{1}{4\pi}\int_{\varphi=0}^{\varphi=2\pi}\int_{\theta=0}^{\theta=\pi} [\mathbb{I} + \mathbb{P}^{sc}(\varphi,\theta,X^s) : (\mathbb{C}^s - \mathbb{C}^{sc}_{\text{hom}})]^{-1}\sin(\theta)\,d\theta d\varphi\right) : \mathbf{E}_0 \tag{5.2b}$$

In contrast, the average strain in the pore space is given by:

$$\boldsymbol{\varepsilon}^p = \mathbb{L}^p : \mathbf{E}_0 \tag{5.3a}$$

$$= [\mathbb{I} - \mathbb{P}^{sc}(X_p = 1) : \mathbb{C}^{sc}_{\text{hom}}]^{-1} : \mathbf{E}_0 \tag{5.3b}$$

where the Hill tensor corresponds to the case of a spherical inclusion in an isotropic medium, as in (4.43). With these results, the effective stiffness of the porous solid given by the self-consistent scheme (4.33) is given by:

$$\mathbb{C}^{sc}_{\text{hom}} = \eta\mathbb{C}^s : \mathbb{L}^s : [(1-\eta)\,\mathbb{L}^p + \eta\mathbb{L}^s]^{-1} \tag{5.4}$$

where $\eta = 1 - \phi_0$ is the solid packing density (one minus the porosity). For the implementation of these results in Ref. [225], the symmetry of isotropic tensors (both stiffness and Hill tensors) is exploited. The computation of the Hill tensor for arbitrary orientations $\mathbb{P}^{sc}(\varphi,\theta,X^s)$ is accomplished using the expressions for the Hill tensor for aligned spheroidal inclusions in an isotropic medium (4.57)-(4.58), in combination with the rotation transformations in (4.60). The use of the Hill tensor expressions (4.57)-(4.58) for an isotropic reference medium are justified by

the a priori knowledge that an uniformly distributed set of particles will yield isotropic elastic properties for the homogenized medium.

The evaluation of (5.4) provides the relation between the effective elasticity of the porous solid to the packing of the material, characterized by the solid packing density η and the particle aspect ratio X^s. Moreover, the percolation threshold predicted by the self-consistent scheme for randomly oriented spheroids is found by identifying the critical packing density at which the homogenized elasticity of the material vanishes, i.e. $C^{sc}_{ijkl,\text{hom}} \rightarrow 0$. Figure 5-1 displays the predicted percolation thresholds as functions of the particle aspect ratio. The findings of Fritsch et al. [91] and Sanahuja et al. [225] are qualitatively in good agreement with the granular physics results. That is, more pronounced oblate or prolate shapes tend to lower percolation thresholds as less quantities of solid are needed to offer a continuous force path for developing rigidity in the porous material. In the limit case, the percolation threshold attribute disappears ($\eta_0 \rightarrow 0$) for extreme shapes: $X^s \rightarrow 0$ in the oblate case, and $X^s \rightarrow \infty$ in the prolate case. It is also observed in Figure 5-1 that the percolation threshold – aspect ratio relation is asymmetrical, supporting the intuitive understanding that an ensemble of needle-like particles (prolates) percolates with less volume fraction of solid compared to one of flattened disks (oblates). It is worth noting that the discussed results are independent of the elastic characteristics of the solid phase.

The results from granular physics and micromechanics modeling presented in Figure 5-1 confirm that the self-consistent scheme of linear micromechanics recognizes the percolation threshold associated with granular materials.

5.1.2 Percolation Threshold for Preferentially Aligned Particles

The next step in this survey of the effects of particle morphology and orientation on the percolation threshold of granular media is to address the case of aspherical particles with preferential alignment[2]. The implementation of the self-consistent scheme for this particular morphology requires a different methodology compared to the one presented in the previous section. For the case of partial alignment of particles, the resulting homogenized (self-consistent type) stiffness properties will exhibit anisotropic symmetry. In fact, the resulting transverse isotropic

[2] The work presented here has been published in [204].

symmetry is intimately related to the modeling of the inclusions as spheroidal particles.

The implementation of the self-consistent scheme for the case of preferentially aligned particles begins by defining a fictitious porous solid composed of aspherical solid particles and empty, spherical pores, akin to the model presented in Section 5.1.1. This porous solid emulates the porous clay composite in shale. Thus, we recall the derived expression for the homogenized stiffness response of the porous clay solid (4.94) for this examination of the percolation threshold behavior for preferentially aligned particles:

$$\begin{aligned}\mathbb{C}^{sc}_{\text{hom}} &= \left\langle \eta \mathbb{C}^{s}\left(\varphi,\theta\right) : \left[\mathbb{I} + \mathbb{P}^{sc}_{X^s}\left(\varphi,\theta,X^s,\mathbb{C}^{sc}_{\text{hom}}\right) : \left(\mathbb{C}^{s}\left(\varphi,\theta\right) - \mathbb{C}^{sc}_{\text{hom}}\right)\right]^{-1} \right\rangle : \\ &\quad \left\{ (1-\eta)\left(\left[\mathbb{I} - \mathbb{P}^{sc}_{X^p}\left(X^p,\mathbb{C}^{sc}_{\text{hom}}\right) : \mathbb{C}^{sc}_{\text{hom}}\right]^{-1} \right) \right. \\ &\quad \left. + \eta \left\langle \left[\mathbb{I} + \mathbb{P}^{sc}_{X^s}\left(\varphi,\theta,X^s,\mathbb{C}^{sc}_{\text{hom}}\right) : \left(\mathbb{C}^{s}\left(\varphi,\theta\right) - \mathbb{C}^{sc}_{\text{hom}}\right)\right]^{-1} \right\rangle \right\}^{-1}\end{aligned} \tag{5.5}$$

where the operator $\langle\rangle$ on any quantity $\mathbb{Y}$:

$$\left\langle \mathbb{Y} \right\rangle = \frac{1}{4\pi} \int_{\varphi=0}^{\varphi=2\pi} \int_{\theta=0}^{\theta=\pi} W\left(\theta\right) \mathbb{Y} \sin\left(\theta\right) d\theta d\varphi \tag{5.6}$$

involves the evaluation of a particular function describing the orientation distribution of particles. Following the work of Sayers [230], the term $W\left(\theta\right)$ in (5.6) represents an orientation distribution function, which defines the type of preferential alignment of the solid inclusions in the homogenized medium. The ODF considered here is of the form:

$$W\left(\theta,k\right) = \frac{k\cosh\left[k\cos\left(\theta\right)\right]}{\sinh\left(k\right)} \tag{5.7}$$

The parameter k quantifies the degree of alignment with respect to the axis of symmetry: $k = 0$ corresponds to the case of a random orientation of particles, and $k \to \infty$ represents a perfect alignment of particles with the axis of symmetry, as depicted in Figure 5-2.

We run simulations with the model described above to determine the percolation threshold from a vanishing elasticity ($C^{sc}_{ij,\text{hom}} \to 0$) for different degrees of alignment, monitored through the alignment factor k in (5.7), ranging from a random orientation ($k = 0$) to a perfect alignment of particles ($k \to \infty$). The simulation results are presented in Figure 5-3, in which a selected set

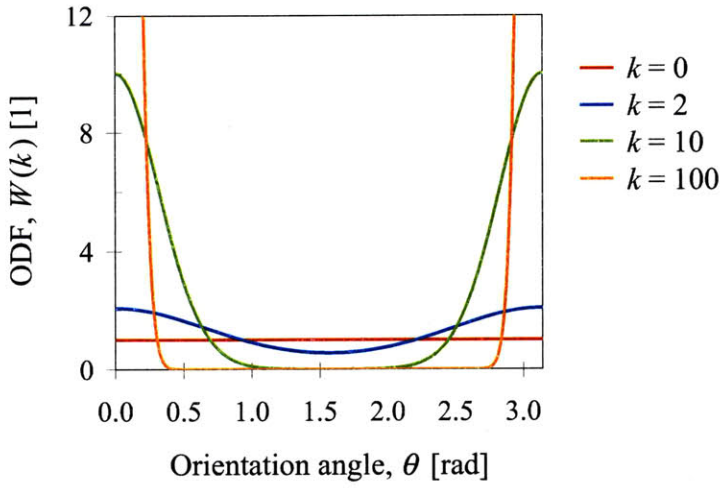

Figure 5-2: Orientation distribution function (ODF) used to characterize the preferential alignment of particles. The single parameter k defines the level of alignment, with limit cases $k = 0$ for a uniform distrubution of particle orientations (random alignment), and $k \to \infty$ (large k-value) for a perfectly aligned set of particles.

of data was generated within the validity of the application of the prescribed model[3]. For the purpose of validation, note that the case of random distributions of spheroidal particles ($k = 0$) is quantitatively in good agreement with granular physics results, as it perfectly matches the self-consistent solutions developed by Fritsch et al. [91] and Sanahuja et al. [225] for randomly oriented particles. In contrast, as one increases the degree of alignment ($k = 10, 100$), the effect of particle shape on the percolation threshold begins to vanish, and it approaches in the limit case of perfect alignment ($k \to \infty$) a percolation threshold of $\eta_0 = 0.5$, irrespective of particle shape. The numerical implementation of the latter case was accomplished for a large alignment parameter value ($k = 700$). This particular morphology of perfectly aligned, spheroidal particles in a transversely isotropic medium corresponds to the elastic field solution of Withers [295] in the context of Eshelby's inhomogeneity problem. As in the case of the solutions of Fritsch et al. [91] and Sanahuja et al. [225] for randomly oriented particles, the percolation thresholds

[3] In some special cases during the numerical iteration process required for solving the implicit equation (5.5), the resulting self-consistent estimates $C^{sc}_{ij,\text{hom}}$ violated the relation $\sqrt{C_{11}C_{33}} - C_{13} - 2C_{44} > 0$ in the expressions (4.64). This situation yields complex-number values in the evaluation of the P-tensor [205]. Recently, Tavara et al. [254] developed advanced numerical schemes for handling the cases of solving Eshelby's problem for transversely isotropic materials that follow the relation $\sqrt{C_{11}C_{33}} - C_{13} - 2C_{44} < 0$.

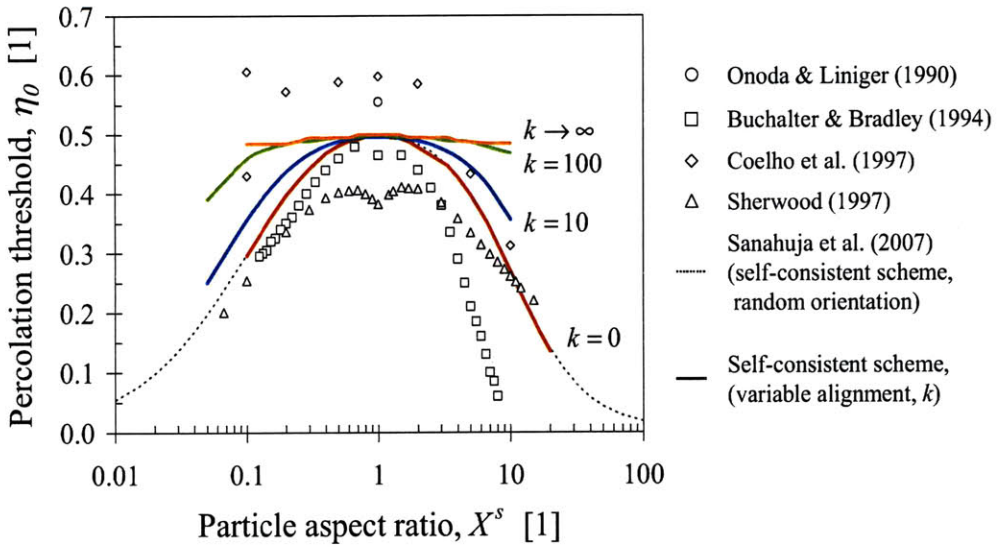

Figure 5-3: Percolation threshold η_0 for a porous solid modeled through the self-consistent scheme as function of solid particle aspect ratio X^s (< 1 oblates, > 1 prolates). The solid lines correspond to the implementation of the micromechanics model based on the self-consistent scheme for different cases of particle alignments. A random orientation corresponds to $k = 0$, while the case of perfect alignment corresponds to $k \to \infty$.

found for preferentially aligned particles are also independent of the elasticity content of the solid constituent.

5.1.3 Relation between Mechanical Percolation and Microstructure

The findings related to the mechanical percolation of granular ensembles modeled through the self-consistent scheme in micromechanics and its relation to particle geometry open new venues for modeling the complex microstructures of clay-bearing rocks. The numerous interpretations of micrographs taken for the clay fabric in shale through advanced imaging techniques have suggested arrangements of particles with geometries represented as spheroids with varying degrees of orientation (e.g. [128, 139, 267]). This knowledge about the microstructure of shale laid the foundation for developing the first micromechanics models, in which the primary sources of anisotropy were intimately related to the geometrical descriptions of particles. Based on the micromechanics approach presented in this section, the percolation threshold, identified

through the nanoindentation experiments of Ulm and co-workers [32, 265], is explicitly linked to specific microstructures. From the analysis of the results presented in Figure 5-3, a suitable micromechanics model could consider spheroidal particles with a practical range of aspect ratios of $0 < X^s \leq 1$ with high degrees of alignment. Such effective morphology could reproduce adequately the percolation behavior of the porous clay of approximately $\eta_0 = 0.5$ measured in nanoindentation experiments. The quest for an effective micromechanics model for shale poroelasticity has begun here with the assessment of effective microstructures linked to the identified percolation threshold at nanoscales. The task at hand is to supplement these findings with forthcoming model developments to effectively link the microstructure and material intrinsic properties of constituents for the prediction of the mechanical response of shale at different length scales.

5.2 Model Calibration

In the previous section, the implementation of the microporomechanics model based on the self-consistent scheme established a link between the microstructure of the granular, porous clay in shale and the percolation threshold determined from instrumented nanoindentation experiments. This new nanomechanics understanding complements the information furnished by advanced observational techniques regarding geometrical details of shale's microstructure.

Both structural sources of anisotropy and intrinsic properties of the clay phase in shale are incorporated into a hypothesis testing approach, which intends to establish an effective mechanical description for the microstructure and mechanical properties of material constituents useful for predictions of the macroscopic anisotropic poroelasticity of shale. This task is equivalent, within our micromechanics approach, to defining the elasticity and morphological characteristics of the elementary building block of shale, or level 0 of our multi-scale structure model. The elasticity content of the elementary building block represents the intrinsic elasticity of the clay phase, whose effective contribution to the overall anisotropy of shale has eluded many decoding attempts [227, 284]. In contrast, the morphological attributes are intimately related to the microstructural description of the porous clay phase at level I.

The different hypotheses of the elementary building block will be used for calibrating the mi-

cromechanics model developed in Chapter 4 for the specific attributes (elastic content, particle shape, particle orientation) considered by each hypothesis. The results of the model calibration exercises will be used in a forward implementation of the model, whose results will then be compared to experimental elasticity data at different scales to validate (or disprove) the different hypotheses.

5.2.1 Reverse Analysis Approach

The micromechanics developments established in Chapter 4 provide a robust framework for modeling the different contributions from material composition, microstructure, and intrinsic mechanical properties to the overall anisotropic poroelastic response of shale. In particular, the effects of particle shape, particle orientation distributions, and anisotropic elastic properties of the clay phase are considered explicitly in the application of the self-consistent scheme for the postulated granular porous clay. In a forward application, the model requires the following parameter as inputs to predict level I properties:

- The elasticity tensor of the (solid) clay phase $\mathbb{C}^s$ (4.71).
- The clay solid particle and pore aspect ratios X^s and X^p (4.59).
- The alignment factor k (5.7).
- The solid clay concentration or packing density η (3.5).

For predicting properties at level II, the model requires, in addition to some level I results:

- The inclusion elasticity constants $\mathbb{C}^{inc}$ (4.100).
- The inclusion aspect ratio X^{inc} (4.59)
- The fluid bulk modulus k^{fl} (4.114).
- The volume fraction f^{inc} (3.4a).

Following the suggestions presented in Section 4.4, the properties of quartz ($k^{inc} = 37.9$ GPa, $g^{inc} = 44.3$ GPa, see (4.119)) are assigned to the inclusion phase in view of the large presence

of this mineral in all investigated shale samples. For undrained elasticity predictions, the pore space is considered to be fully saturated with water ($k^{fl} = 2.3$ GPa, see (4.120)). In addition, the pore and inclusion geometries are assumed as spherical ($X^p = X^{inc} = 1$), which focuses our analysis on the well-documented importance of the morphology of the clay particles and restricts further sources of structural anisotropy. Finally, the clay packing density and the inclusion volume fraction (η, f^{inc}), which can be obtained from mineralogy and porosity measurements for shale materials, become the input parameters that synthesize the compositional characteristics of a shale specimen.

From the previous account of model parameters, only the full anisotropic tensor of elasticity constants of the solid phase $\mathbb{C}^s$ has not been assessed through experimental means. Thus, a reverse analysis approach is proposed, which seeks to determine or calibrate the elasticity constants C^s_{ij} of the level 0 - solid clay phase for different clay particle aspect ratios $\widehat{X^s}$ and degrees of particle alignment $\widehat{k}$. This reverse analysis approach is schematically shown in Figure 5-4. For its implementation, a calibration data set (CDS) is used, which provides a well-defined set of macroscopic measurements for various shale materials, that is the macroscopic elasticity $\mathbb{C}^{UPV}$ and calculated volumetric parameters η and f^{inc}.

The reverse analysis of C^s_{ij} properties is accomplished by minimizing the spectral norm of the relative error between experimentally measured values C^{UPV}_{ij} and undrained estimates $C^{II,un}_{ij,\text{hom}}$ defined by (4.116) and generated for a given set of $\left(\widehat{k}, \widehat{X^s}\right)$ properties:

$$\min_{\left(\widehat{k},\widehat{X^s},\mathbb{C}^s\right)} \left(\sum_{(CDS)} \left|\left| \left(\mathbb{C}^{II,un}_{\text{hom}} - \mathbb{C}^{UPV}\right) : \left(\mathbb{C}^{UPV}\right)^{-1} \right|\right|_2 \right) \tag{5.8}$$

subjected to:

$$\left.\begin{array}{c} C^s_{11} + C^s_{12} + C^s_{33} + \zeta > 0 \\ C^s_{11} + C^s_{12} + C^s_{33} - \zeta > 0 \\ C^s_{11} - C^s_{12} > 0 \\ C^s_{44} > 0 \\ \zeta = \sqrt{\left(C^s_{11}\right)^2 + \left(C^s_{12}\right)^2 + 8\left(C^s_{13}\right)^2 + \left(C^s_{33}\right)^2 + 2C^s_{11}C^s_{12} - 2C^s_{11}C^s_{33} - 2C^s_{12}C^s_{33}} \end{array}\right\} \tag{5.9}$$

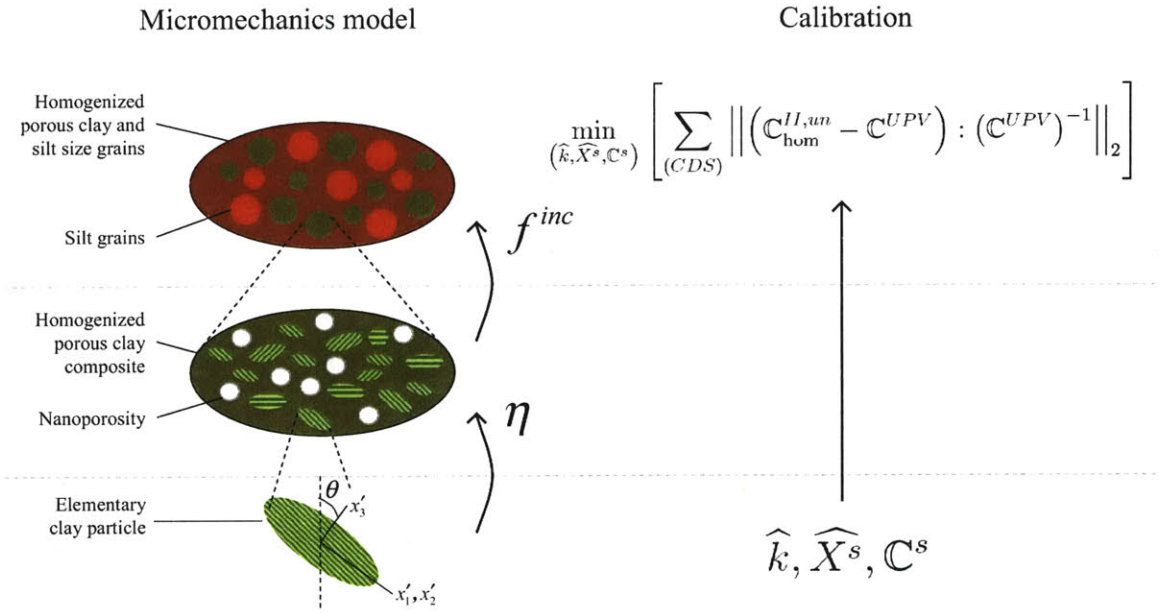

Figure 5-4: Schematic of the approach followed for the implementation of the reverse analysis. For a specific set of particle shape X^s and orientation distribution of particles defined by the parameter k, the elastic properties of the elementary building block at level 0 are optimized with regards to the resulting predictions at level II and the comparisons with experimental data. The calibration data set (CDS) facilitates the macroscopic elasticity data C_{ij}^{UPV} for eight shales measured in ultrasonic pulse velocity (UPV) experiments, as well as the porosity and composition data necessary to derive the clay packing density and inclusion volume fraction values.

The constraints in the minimization problem (5.8) ensure the positive definite character of the stiffness matrix $\mathbb{C}^s$ [247]. The numerical implementation is accomplished through the use of a sequential quadratic programming optimization routine available in Matlab [255]. It should be noted that the minimization problem is well-posed. The calibration data set will offer 8 (shale specimens) $\times$ 5 (elastic constants measured for each specimen) = 40 experimental values, which are used to determine 5 model parameters.

5.2.2 Calibration Data Set

A first data set is used for calibration of the microporoelastic model. The calibration data set (CDS) is composed of eight shales, for which the macroscopic elasticity constants and material composition properties are available. The choice of those materials for calibration purposes was based on the following considerations:

- The shale materials represent a large range of representative shale material compositions, varying in mineral compositions, porosity, and macroscopic elasticity properties. The macroscopic transversely isotropic elasticity was determined from ultrasonic pulse velocity (UPV) measurements translated into elastic constants using the classical velocity-stiffness relations for transversely isotropic materials (see expressions in Section 3.7.3).

- The mineral composition is available from XRD measurements, and porosity measurements are available from both MIP and drying porosity tests, and show consistent estimates.

- For each shale in the calibration set, the difference in clay packing density obtained by using respectively MIP and bulk density measurements in addition to the mineralogy is smaller than 5% on average.

Those considerations led to the CDS data set of eight shales listed in Table 5.1. The estimates for volumetric parameters (clay packing density and inclusion volume fraction) and measured UPV elasticity for the CDS shale samples are presented in Chapter 3.

Data set	Samples
CDS	G2IC-01, G2IC-02, G2IC-03, G2IC-04, G2IC-05, G2IC-06, G2IC-07, G2IC-08

Table 5.1: List of shale samples considered in the calibration data set, CDS. The experimental data for these samples were gathered by the G2IC.

5.2.3 Hypothesis Testing for Elementary Building Block of Shale

Performing the reverse analysis approach for model calibration requires first establishing different sets or combinations of elasticity content and morphologies for the elementary building block of clay. The intrinsic elasticity of this elementary unit at level 0 is associated to the effective stiffness properties C_{ij}^s of the solid clay phase in shale. In turn, the morphological features of the building block, its particle shape and orientation (characterized by parameters X^s,k), supplement the description of the microstructure of the porous clay at level I of the multiscale structure of shale. The experimental observations presented in Chapter 3 contribute to generating meaningful hypotheses of the form of the elementary building block of clay and its effects on the effective mechanical representation of the porous clay fabric. From visual analysis, different methods of observation (e.g. SEM, TEM) of the structure of the shale provide important insight into the microstructural arrangements of the clay fabric. To supplement these observations, indentation testing and micromechanics modeling of the mechanical properties of the porous clay composite furnish new means for understanding the links between mechanical behavior and particle geometries and alignments.

Four hypotheses about the structure and properties of the elementary building block will be tested:

- **Hypothesis 1.** The elementary building block is a preferentially aligned, oblate particle with anisotropic elasticity. Secondary electron micrographs (Figure 2-6a) provide evidence in favor of this hypothesis as individual clay platelets are apparent. Hornby et al. [128] championed this hypothesis, although the solid clay phase was assumed isotropic due to the lack of supporting experimental evidence. Furthermore, researchers have calibrated orientation distribution functions (ODFs) using data from digital analysis of SEM images [128, 230] and X-ray diffraction techniques [145, 166]. The macroscopic anisotropy of shale is introduced by considering some shape and preferred orientation of the solid particles.

The oblate particles posses an aspect ratio of $\widehat{X^s} = 1/20$, which has been considered as representative of some clay particles [128, 139]. The preferential alignment of the oblate particles is described by the parameter value $0 < \widehat{k} < \infty$, corresponding to a certain degree of alignment. The micromechanics analysis of nanoindentation experiments (Section 5.1) associates high degrees of particle alignment to the observed percolation threshold at clay packing densities of about $0.42 < \eta_0 < 0.54$ (see Figure 3-15). The lower bound of the percolation threshold behavior is considered for the implementation of hypothesis 1, for which an alignment parameter $\widehat{k} = 100$ replicates the percolation threshold of $\eta_0 = 0.42$ for $\widehat{X^s} = 1/20$ oblate particles. The proposed anisotropic elasticity for the solid clay phase displays transversely isotropic symmetry. In summary, hypothesis 1 combines all modeled effects: geometric factors (oblate particles with preferential alignment) and intrinsic particle anisotropy.

- **Hypothesis 2.** This hypothesis explores the effects of a purely geometric source of anisotropy through modeling the elementary unit of clay solid as perfectly aligned ($\widehat{k} \rightarrow \infty$), oblate particles with intrinsic isotropic elasticity. The perfect alignment implies that the axis of symmetry of all clay particles is oriented in the normal-to-bedding, or x_3-direction. Hypothesis 2 combines the geometric observations from image analysis regarding particle shape, while the perfect alignment reproduces the percolation threshold of $\eta_0 = 0.50$ from micromechanics modeling.

- **Hypothesis 3.** The elementary building block is a perfectly aligned, oblate particle with transversely isotropic elasticity. This intrinsic anisotropy is assumed to be intimately related to the structure of the solid particle, so that the axes of symmetry for shape and for elasticity properties coincide. Macroscopic anisotropy is a result of the combined effects of particle shape, preferred orientation, and intrinsic anisotropy. The material symmetry and the particle itself are oriented in the x_3-direction, which corresponds to the normal-to-bedding direction. The implementation of this hypothesis will consider three variations of the particle shape: $\widehat{X^s} = 1/100, 1/20, 1/2$.

- **Hypothesis 4.** The elementary building block is a spherical particle with transversely isotropic elasticity. While SEM images suggest platelet-like particle shapes, TEM images

Hypothesis	$\widehat{X^s}$	$\widehat{k}$	Elasticity
1	1/20	100	Transverse isotropic
2	1/20	700	Isotropic
3 – 1	1/100	700	Transverse isotropic
3 – 2	1/20	700	Transverse isotropic
3 – 3	1/2	700	Transverse isotropic
4	1	700	Transverse isotropic

Table 5.2: Hypothesis of the form of the elementary building block of clay used for reverse analysis its elasticity properties. $k = 100$ represents the case of partially aligned particles. $k = 700$ represents the case of (almost) perfect alignment.

from the literature and AFM images suggest lumped particle arrangements with little apparent preferred orientation (Figure 2-6b and c). In contrast to hypothesis 3, modeling based on hypothesis 4 discards any effects of particle shape by assigning a spherical morphology to the solid particles ($\widehat{X^s} = 1$). Modeling with spherical particle shapes also reflects the idea of a random orientation of particle-to-particle contact surfaces over which forces are transmitted in a spatially disordered material. The spherical particle cannot give rise to macroscopic anisotropy, so transversely isotropic elasticity (oriented in the x_3-direction) intrinsic to the solid particle is required.

The four hypotheses regarding the geometric and intrinsic elasticity contributions to the anisotropy of the porous clay in shale, which synthesize an array of combinations of particle aspect ratios, orientations of particles, and elasticity forms for the clay phase, are summarized in Table 5.2.

5.2.4 Implementation of the Micromechanics Model using the Reverse Analysis Approach

The implementation of the four hypotheses about the form and properties of the elementary building block of shale in the micromechanics multi-scale model begins by recalling the input values for the clay particle aspect ratio $\widehat{X^s}$ and the degree of alignment $\widehat{k}$. Four specific aspect ratios were chosen for model implementation, covering a practical range for oblate spheroids and the particular case of the sphere: $\widehat{X^s} = 1/100, 1/20, 1/2, 1$. Two forms of particle alignment are also considered: preferential orientation ($\widehat{k} = 100$) and perfect alignment ($\widehat{k} \to \infty$). The

partial alignment with $\widehat{k} = 100$ corresponds to a degree of orientation in which the majority of particles are within $\pm\pi/6$ rad from the axis of symmetry. The case of perfect alignment is implemented using a large value for the alignment parameter, $k = 700$. Finally, two forms for the elasticity content of the solid clay phase are considered: isotropy (two independent elastic constants) and transverse isotropy (five independent elastic constants).

For each hypothesis, the elastic constants C^s_{ij} are computed using the reverse analysis scheme from macroscopic elasticity data, as displayed schematically in Figure 5-4. The forward implementation of the micromechanics model to develop estimates of undrained elasticity $C^{II,un}_{ij,\text{hom}}$ at level II, and which are compared to UPV measurements C^{UPV}_{ij}, requires first the estimation of the (drained) properties of porous clay composite at level I, that is $C^{I}_{ij,\text{hom}}$. The stiffness tensor for the porous clay under drained conditions (refer to Section 4.4.1) is evaluated using the self-consistent homogenization scheme (4.33). For hypotheses 1 through 3, the explicit form of $\mathbb{C}^I_{\text{hom}}$ has been detailed in (4.94) (see also (5.5)). Additionally, the form of the orientation distribution function (ODF) is similar to (5.7). Expression (4.94) contains all the modeling dependencies: particle shape, orientation of particles, and anisotropic elasticities. For computational efficiency, the evaluation of hypothesis 4 is achieved using the more succinct formulation provided in (4.98), for the case in which the P-tensors for the solid and pore phases are identical (that is, perfect alignment and spherical morphologies).

5.2.5 Results of Model Calibration

The results of calibration of the micromechanics model using the reverse analysis approach and the different hypotheses of the elementary building block of clay are presented in Table 5.3. In addition to the elastic constants C^s_{ij}, the equivalent indentation moduli M^s_1, M^s_3 and isotropized elasticity values $M^s_{ISO}, k^s_{ISO}, g^s_{ISO}$ (indentation modulus, bulk modulus, and shear modulus, respectively) for the elementary unit of solid clay are presented. The equivalent indentation moduli were calculated using expressions in (3.28). The isotropized values were calculated using the Voigt-Reuss-Hill (VRH) average (3.10), an empirical estimate based on the arithmetic mean of the Voigt and Reuss averages, both of which provide rigorous bounds for the elastic properties of an isotropic aggregate of crystals [123]. Both the equivalent indentation moduli and isotropized moduli will be useful quantities for comparisons with experimental

Hypothesis	C^s_{11}	C^s_{12}	C^s_{13}	C^s_{33}	C^s_{44}	M^s_3	M^s_1	M^s_{ISO}	k^s_{ISO}	g^s_{ISO}
1	39.1	20.9	19.6	27.9	4.2	16.2	23.2	20.1	24.7	6.2
2	31.5	20.8	20.8	31.5	5.4	17.8	17.8	17.8	24.4	5.3
3 – 1	38.9	20.7	19.9	27.8	4.6	16.5	23.3	20.5	24.7	6.3
3 – 2	39.2	20.8	19.5	27.6	4.4	16.5	23.5	20.5	24.5	6.3
3 – 3	42.6	21.6	18.2	25.6	3.9	15.4	25.1	20.8	24.1	6.5
4	44.9	21.7	18.1	24.2	3.7	14.8	26.4	21.2	24.0	6.7

Table 5.3: Results of the reverse analysis of stiffness properties for the different hypotheses of the elementary building block of solid clay in shale (level 0). All elastic constants are in GPa.

values pursued in the model validation work.

In addition to the calibration results for each hypothesis, Table 5.4 presents the mean and the standard deviation of the relative errors, $\hat{e}$ and e_s [118]:

$$\hat{e} = \frac{1}{n}\sum e_i = \frac{1}{n}\sum \frac{x_i - y_i}{y_i} \tag{5.10}$$

$$e_s = \sqrt{\frac{1}{n-1}\sum (e_i - \hat{e})^2} \tag{5.11}$$

where the summation is performed over n number of shale specimens of the data set under consideration, x_i and y_i correspond to model predictions and experimental measurements, respectively. These statistical estimates quantify the errors involved in the results of the minimization algorithm (5.8) for the different elastic constants. Another metric that is used to quantify comparisons between predicted and experimental values is the correlation coefficient, r^2:

$$r = \frac{\sum_i^n (x_i - \widehat{x})\,(y_i - \widehat{y})}{\sqrt{\sum_i^n (x_i - \widehat{x})^2 \sum_i^n (y_i - \widehat{y})^2}} \tag{5.12}$$

where $\widehat{x} = \frac{1}{n}\sum_i^n x_i$ is the mean value. The correlation coefficients for each set of calibrations are also included in Table 5.4. Figure 5-5 shows graphically the results of the calibration procedure for, e.g. hypothesis 3 (with particle aspect ratio $\widehat{X^s} = 1/20$) by comparing the model stiffness properties $\mathbb{C}^{II,un}_{\text{hom}}$ of the eight shales with the experimental UPV stiffness. In general, the good agreement between the undrained model elasticity predictions and UPV elasticity measurements

Hypothesis	Relative error [%] C^s_{11}	C^s_{12}	C^s_{13}	C^s_{33}	C^s_{44}	r^2
1	-3 ± 20	-3 ± 7	-7 ± 21	-6 ± 19	-3 ± 39	0.93
2	-18 ± 22	-5 ± 7	-6 ± 21	-3 ± 21	-3 ± 46	0.86
$3-1$	-2 ± 20	-3 ± 8	-9 ± 21	-8 ± 22	-9 ± 47	0.93
$3-2$	-3 ± 19	-3 ± 7	-8 ± 20	-7 ± 20	-6 ± 43	0.93
$3-3$	-4 ± 16	-3 ± 7	-7 ± 21	-2 ± 16	-1 ± 35	0.95
4	-4 ± 14	-4 ± 7	-7 ± 21	-2 ± 17	0 ± 35	0.95

Table 5.4: Relative error statistics of the reverse analysis of stiffness properties for the different hypotheses of the elementary building block of solid clay in shale (level 0). The relative error values are presented in terms of the mean +/- the standard deviation of the relative error.

testifies to the good performance of the reverse analysis implementation.

In order to check the sensitivity of the calibration of a hypothesis with respect to the number of shales considered for calibration, a parametric study is conducted in which various combinations of shale samples from the CDS data set were selected for the calibration procedure. By way of illustration, Figure 5-6 shows the rapid convergence of the clay stiffness values with increasing number of shale samples for the calibration of hypothesis 4. The error bar in this figure represents the standard deviation from the specific combination of shales specimens. The parametric study shows that adequate convergence for all solid clay phase stiffness values is provided for five or more shale specimens used in the calibration procedure.

An interesting outcome of the calibration exercises is the similar order-of-magnitude of the elastic content for the effective solid clay at level 0. Although individual elastic constants C^s_{ij} may vary by as much as 13 GPa, the equivalent-isotropic values compare closely across all calibrated cases, with equivalent indentation moduli of $M^s_{ISO} \approx 20$ GPa, bulk moduli of $k^s_{ISO} \approx 24$ GPa, and shear moduli of $g^s_{ISO} \approx 6$ GPa. It appears that the elasticity content of the elementary building block of shale, at least from an isotropic representation, displays a characteristic magnitude. In addition, the review of the relative errors tabulated in Table 5.4 shows that the worst set of calibrations or fitting of C^s_{ij} constants corresponds to hypothesis 2 (clay building block with isotropic elasticity). The remaining calibrated hypotheses show comparable levels of relative errors between predicted and experimental elasticity at level II. In the next section, the different hypotheses of the elementary building block will be tested using the predictions of the micromechanics model in conjunction with independent data from

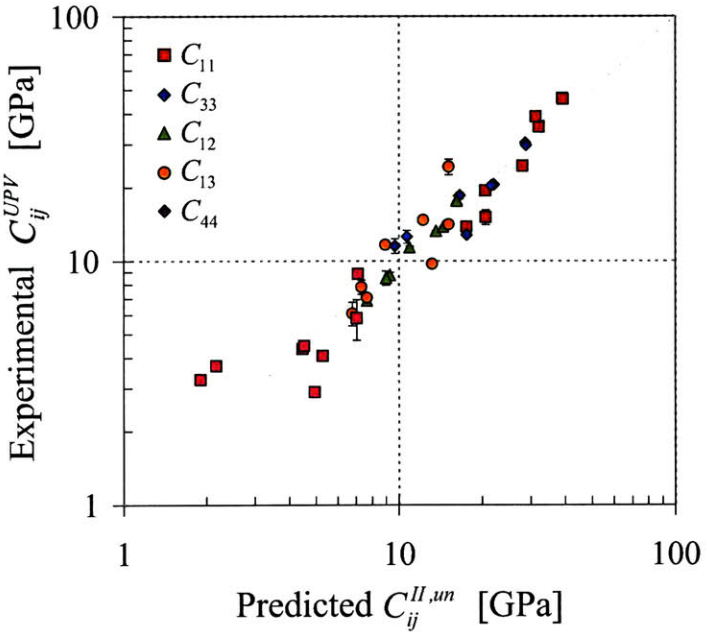

Figure 5-5: Comparison of model predictions based on hypothesis 3 (with particle aspect ratio $\widehat{X^s} = 1/20$) and experimental UPV elasticity measurements from the CDS data set for level II. Vertical error bars represent the variability of UPV stiffness as function of confining pressure.

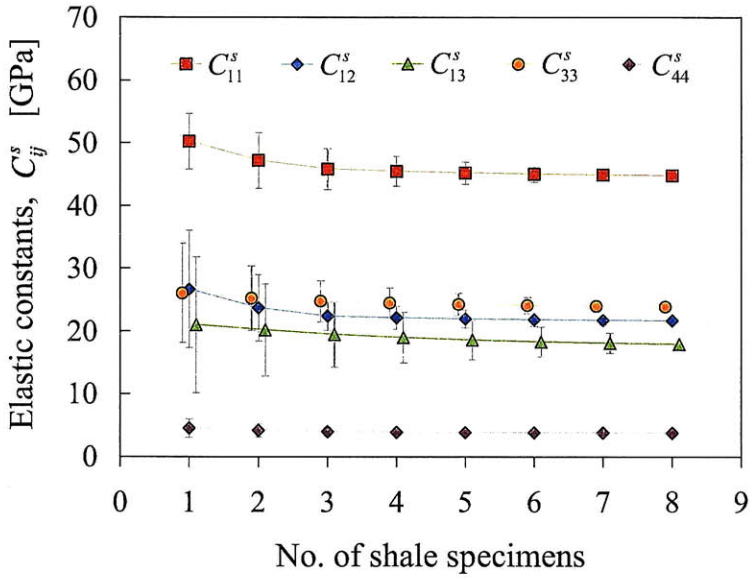

Figure 5-6: Convergence of calibration results for the elastic constants C^s_{ij} of the elementary building block of solid clay with increasing number of shale specimens considered from the CDS data set.

nanoindentation and acoustic experiments.

5.3 Model Validation

The different hypotheses of the elementary building block of clay are tested in this section against experimental data of shale elasticity at different scales; namely, macroscopic elasticity data (complete sets of transversely isotropic elastic constants), and instrumented nanoindentation data, which condense the elasticity content of the clay fabric into two elasticity constants, M_1 and M_3, as defined by expressions (3.28a)-(3.28b). Note that each data set alone is not able to provide a unique solution for the validation of the model. In fact, the indentation moduli M_1 and M_3, obtained from probing the clay fabric respectively into the bedding plane and normal-to-bedding plane, are functions of the five elasticity constants of the clay fabric stiffness $\mathbb{C}^I_{\text{hom}}$. Moreover, for each shale sample, the five macroscopic elasticity constants cannot be matched to the clay stiffness constants $\mathbb{C}^s$ without an intimate knowledge of the mineralogy and the porosity through the clay packing density and the silt inclusion volume fraction. The

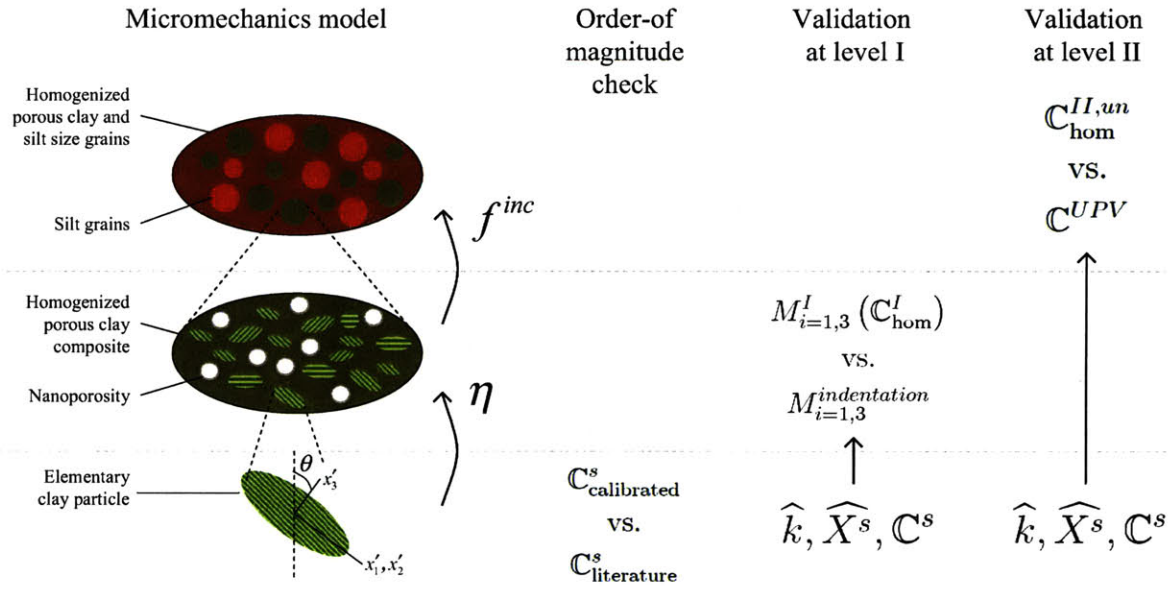

Figure 5-7: Schematic of the model validation process. At level 0, the stiffness properties of the calibrated modulus tensor $\mathbb{C}^s$ through the different hypotheses are compared with clay data from the literature. At level I, the model predictions for porous clay composite based on the different hypotheses of the clay elementary building block (with particle orientation k, shape X^s, and stiffness $\mathbb{C}^s$) are compared with nanoindentation data. At level II, macroscopic predictions for the porous clay - silt composite are compared with acoustic data for shale specimens not used for calibration.

approach for the validation of the micromechanics model is shown schematically in Figure 5-7. In addition to the model comparisons with anisotropic elasticity data at levels I and II, a first order-of-magnitude check is presented for the elastic properties of the elementary unit of clay at level 0. The elasticity content $\mathbb{C}^s$ of the different clay building block hypotheses is compared to data available in the open literature of clay minerals. The model validation exercises assists in achieving one of the key objective of this thesis, which is the definition of an effective micromechanics representation of the porous clay fabric that allows capturing the diverse anisotropic poroelastic behavior of shale at macroscopic scales.

5.3.1 Validation Data Sets

The model validations at levels I and II of the multi-scale structure model for shale are accomplished using independent sets of elasticity data. The nanoindentation experiments of Bobko

Data set	Samples
VDS-1	G2IC-01, G2IC-02, G2IC-03, G2IC-04, G2IC-07, Dark, Pierre
VDS-2	CRE, KIM, JUR, 3492, 3506, 3525, 3536, 3564, 108/111, MUD, CO, North Sea

Table 5.5: List of shale samples considered in the validation data sets, VDS-1 and VDS-2. The experimental data for these samples were gathered by the G2IC, as well as obtained from open literature sources.

and Ulm [32], which were reanalyzed in this thesis, form the first validation data set (VDS-1). The model validation at the macroscopic scale is accomplished using shale data collected from the open literature. The selected references offer complete descriptions of macroscopic elasticity and material composition. Table 5.5 displays the shale samples that constitute each of the validation data sets. The estimates for clay packing density and inclusion volume fraction and elasticity data for the VDS-1 and VDS-2 shale samples (nanoindentation moduli and UPV elastic constants, respectively) are detailed in Chapter 3.

5.3.2 Level 0 - Order of Magnitude Check

The concept of the clay elementary building block synthesizes the elasticity behavior of the solid component of the porous clay fabric in shale in the form of an effective mechanical phase. This first scale, or level 0 in our multi-scale micromechanics approach, can then be compared to the fundamental scale of clay minerals and their elastic properties.

The different hypotheses of the clay building block were calibrated using the reverse analysis approach, yielding different sets of stiffness properties as detailed in Table 5.3. The calibrated clay stiffness values C_{ij}^s exhibit significant anisotropy (except for the stiffness properties associated to hypothesis 2 which is modeled as an isotropic solid). Table 5.6 provides the calculated Thomsen parameters (expressions (3.68a)-(3.68c)) for various clay minerals and the anisotropic properties of the different calibrated hypothesis of C_{ij}^s. The Thomsen parameter values for quartz are also included for comparison. From the values listed in Table 5.6, only quartz qualifies as having elastic anisotropy in the weak-to-moderate range, i.e. $\varepsilon, \gamma, \delta^* < 0.2$ [256], whereas the elastic behavior of clay minerals and our calibrated clay values display considerable anisotropy.

A first order comparison of the different sets of C_{ij}^s elastic constants can be made with quasi-isotropic experimental values of clay elasticity introduced in Section 3.5. For the purpose of

Material	Reference	Thomsen parameters [1]		
		ε	γ	δ
Quartz	[122]	-0.09	-0.15	0.26
Muscovite	[7]	1.12	2.28	-1.24
Kaolinite	[148]	1.13	1.75	-0.70
Chlorite	[148]	0.44	2.24	-0.07
Hypothesis 1		0.20	0.57	-0.16
Hypothesis $3-1$		0.20	0.50	-0.09
Hypothesis $3-2$		0.21	0.54	-0.13
Hypothesis $3-3$		0.33	0.86	-0.26
Hypothesis 4		0.43	1.04	-0.26

Table 5.6: Thomsen parameters calculated for quartz, different clay single minerals, and for the calibrated clay stiffness properties associated with the different hypotheses of the elementary building block of shale. The data for muscovite, kaolinite, and chlorite was chosen due to their assumed transversely isotropic elastic properties, for which the computation of Thomsen parameters are applicable.

comparison, we resort to the equivalent bulk and shear moduli obtained through the application of the Voigt-Reuss-Hill averaging scheme. The comparison between the stiffness properties based on the different hypotheses of the clay elementary unit and those reported in the open literature is given in Table 5.7. The table is organized into two categories of elastic properties: elasticity of single clay minerals and elasticity of compacted or consolidated clay. The data obtained for single clay minerals through direct testing and numerical modeling ($k^s > 50$ GPa, $g^s > 20$ GPa) are clearly of a different magnitude compared to the properties inferred from actual rock testing and laboratory-made clay mixtures. The difference in behavior is directly attributed to the effects of confined absorbed water or other solutions in the interlayer and interparticle spaces and the mechanics of interparticle contacts. These effects undoubtedly reduce the otherwise stiff response of single clay layers. The range of averaged stiffness values for the different hypotheses of the clay elementary unit ($k^s \sim 24$ GPa, $g^s \sim 6$ GPa) are in agreement with clay data inferred from actual testing of clay-bearing rocks [20, 128, 147, 175]. The discrepancy with the bulk modulus of Vanorio et al. [273] may be attributed to the particular test methodologies used in that study, in which the clay powders were compacted into aggregates or diluted into water suspensions for experimentation. The good agreement of the VRH average of $\mathbb{C}^s$ with extrapolated data from rock testing is a first indication that our calibrated clay stiffness values are suitable representation of the in situ elastic behavior of clay

Material	Technique	Reference	k^s [GPa]	g^s [GPa]
Single mineral				
Muscovite	Ultrasonic	Aleksandrov & Ryzhova [7]	52.2	31.6
Muscovite	Brillouin scattering	Vaughan & Guggenheim[276]	59.1	34.4
Kaolinite	Velocity-density scaling	Katahara [148]	55.4	31.8
Chlorite	Velocity-density scaling	Katahara [148]	99.7	24.4
Muscovite	Molecular dynamics	Seo et al. [237]	80.5	49.3
Compacted clay				
	Data extrapolation	Hornby et al. [128]	22.9	10.6
	Data extrapolation	Berge and Berryman [20]	21.4	6.7
	Data extrapolation	Mavko et al. [175]	25	9
	Data extrapolation	Jorstad et al. [147]	26.6	7.5
	Acoustic measurements	Vanorio et al. [273]	12	6
	VRH average of $\mathbb{C}^s$		$24.0 - 24.7$	$5.3 - 6.7$

Table 5.7: Comparison of clay properties for single clay minerals and compacted clay in shale. Data for single clay mineral elasticity was presented in Table 3.13. Data for compacted clay in shale was presented in Table 3.12. The Voigt-Reuss-Hill (VRH) average of the elementary building block of clay with elasticity $\mathbb{C}^s$ corresponds to the range of values found throught the hypothesis calibration process.

in shale and clay-bearing rocks. It is worth noticing that this adequate agreement between these so-called compacted clays using quasi-isotropic, VRH averages does not imply the accuracy of the five transversely isotropic components of the stiffness tensor $\mathbb{C}^s$. The relevance of the full anisotropic properties of the elementary building block of shale will be tested at levels I and II of the multi-scale model.

5.3.3 Level I - Comparison with Nanoindentation Experiments

After performing an order-of-magnitude check for the elasticity properties of the elementary building block of shale at level 0, the next stage of comparisons between experimental results and theoretical predictions of shale elasticity corresponds to nanometer length scales, or level I in our multi-scale structure approach. The elasticity measured by grid nanoindentation provides a novel mechanics context for investigating the elastic content and the different combinations of geometric and intrinsic elasticity factors affecting the anisotropy of the porous clay phase in shale. According to the methodology displayed in Figure 5-7, the various hypotheses of the clay elementary unit based on combinations of particle orientations (controlled by the alignment parameter $\widehat{k}$), particle shapes (with aspect ratios $\widehat{X^s}$), and different intrinsic elasticities (calibrated

C^s_{ij} values listed in Table 5.3) are implemented in a forward application of the micromechanics model to obtain estimates of drained elasticity at level I. Nanoindentation on geomaterials such as shale is deemed as a drained-type test, because the associated nanometer length scales in mechanical experiments allow for almost instantaneous dissipations of pore pressures.

The nanoindentation used for model validation at level I corresponds to the validation data set 1 (VDS-1). This data set provides the complete mechanical characterization of seven shale samples in terms of their indentation properties. In addition, the VDS-1 provides the mineralogy, porosity, and density information necessary to determine the clay packing density, which is the key upscaling parameter for the homogenization modeling at level I. The stiffness properties of the porous clay for drained conditions, $\mathbb{C}^I_{\text{hom}}$ (4.79), are calculated using the microporomechanics formulation outlined in Section 4.4.1[4]. Figures 5-8 and 5-9 display the elasticity predictions for the porous clay modeled via the different hypotheses for the elementary unit of solid clay. The stiffness predictions $\mathbb{C}^I_{\text{hom}} = \mathbb{C}^I_{\text{hom}}\left(\mathbb{C}^s, \eta, \widehat{k}, \widehat{X^s}\right)$ are constructed as continuous functions of clay packing density η, and recasted into equivalent indentation moduli $M^I_{i,=1,3}$ using (3.28a) and (3.28b). Horizontal error bars represent the variability of clay packing density depending on the combination of tests used for its estimation: left-most η values were calculated using mineralogy and bulk density data, and right-most η values were calculated using mineralogy and porosity data; solid data points represent the mean value of these two estimates. The solid data points in the figures and their corresponding vertical error bars represent the mean and standard deviation of the experimental indentation modulus data compiled in the VDS-1. A degree of anisotropy expressed as the difference of indentation moduli $\Delta M = M_1 - M_3$ is also displayed in Figures 5-8 and 5-9.

The model indentation curves for hypothesis 1 (partially-aligned, transversely-isotropic, oblate particles) seem to follow the trends of nanoindentation data as shown in Figure 5-8a, especially for shale materials with large packing densities. An important feature of the model results for hypothesis 1 is the percolation threshold at $\eta_0 = 0.4$. Such a predicted attribute is related to the micromechanics response of the ensemble of oblate particles with particle aspect ratio $\widehat{X^s} = 1/20$ and partial alignment described by the parameter $k = 100$. The

[4]The described implementation of the micromechanics model for predicting level I properties follows a similar approach to that described in Section 5.2.4

modeled percolation threshold at $\eta_0 = 0.4$ matches the lower range of percolation behaviors ($\eta_0^{M_3} = 0.42$) identified by the linear scaling between the measured indentation moduli and the clay packing density shown in Figure 3-15. Hence, a combination of geometric factors and intrinsic anisotropy such as that of hypothesis 1 appears adequate for capturing the overall nanoelastic response of the porous clay in shale. The results for the degree of anisotropy displayed in Figure 5-8b predict large ΔM values for packing densities in the range of $\eta < 0.7$; although, small anisotropies are measured for shale samples in that packing density range.

The modeling of the porous clay via hypothesis 2 (perfectly-aligned, oblate particles with isotropic elasticity) yields poor predictions of nanoscale anisotropy as shown in Figures 5-8c and 5-8d. The geometric factors of an oblate particle shape and a perfect particle alignment generate significant elastic anisotropies for packing densities near the percolation threshold, $0.50 < \eta < 0.65$. The increasingly reduced anisotropy predicted by the model for increasing values of clay packing density contradicts the observed nanoindentation trends (Figure 5-8d). Asymptotically, the anisotropic behavior of the solid clay phase inferred from nanoindentation for packing densities $\eta \rightarrow 1$ cannot be replicated by isotropic clay properties, irrespective of particle shapes and orientation distribution. Consequently, geometric factors alone could not be the sole source of the nanoscale anisotropic behavior in shale.

The results for modeling a porous clay in shale through perfectly-aligned, oblate particles with varying aspect ratios and transversely isotropic elasticity are presented in Figure 5-9. The predicted scalings between indentation moduli and clay packing density for the different variants of hypothesis 3 adequately follow the trends of nanoindentation data. However, inspection of Figure 5-9b reveals some mismatches in trends for the degree of anisotropy ΔM between experimental data and model predictions for oblate aspect ratios $\widehat{X^s} = 1/100, 1/20$. Interestingly, the modeling approach based on hypothesis 4, which resorts to intrinsic anisotropic elasticity and to aligned, spherical particles ($\widehat{X^s} = 1$) as the sources of anisotropy of the porous clay, provides an optimal prediction of nanoelastic behavior, as shown in Figures 5-9c and 5-9d. Quantitative comparisons of the model's predictive capabilities based on the four hypotheses of the solid clay phase are given in Table 5.8, which emphasizes the observation that hypothesis 4 provides the most accurate modeling of the anisotropic elastic behavior of the porous clay.

The adequate comparisons between nanoindentation data and model predictions based on

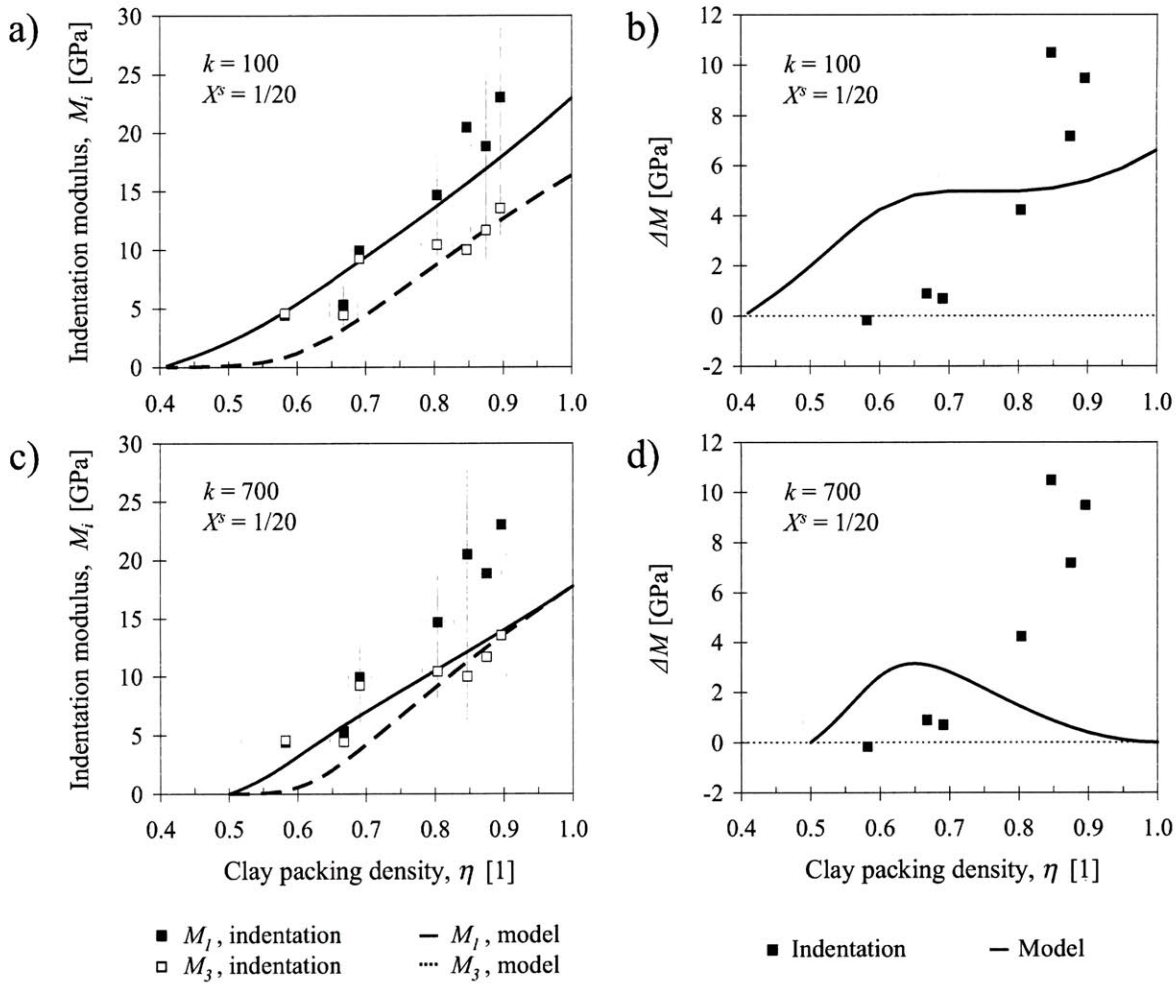

Figure 5-8: The nanoscale elasticity content of the porous clay in shale as a function of clay packing density. The elasticity is expressed in terms of indentation moduli $M_{i=1,3}$. The degree of anisotropy is expressed as the difference in indentation moduli $\Delta M = M_1 - M_3$. Modeling curves are presented for (a-b) hypothesis 1, and (c-d) hypothesis 2. The nanoindentation data corresponds to shales included in the validation data set VDS-1.

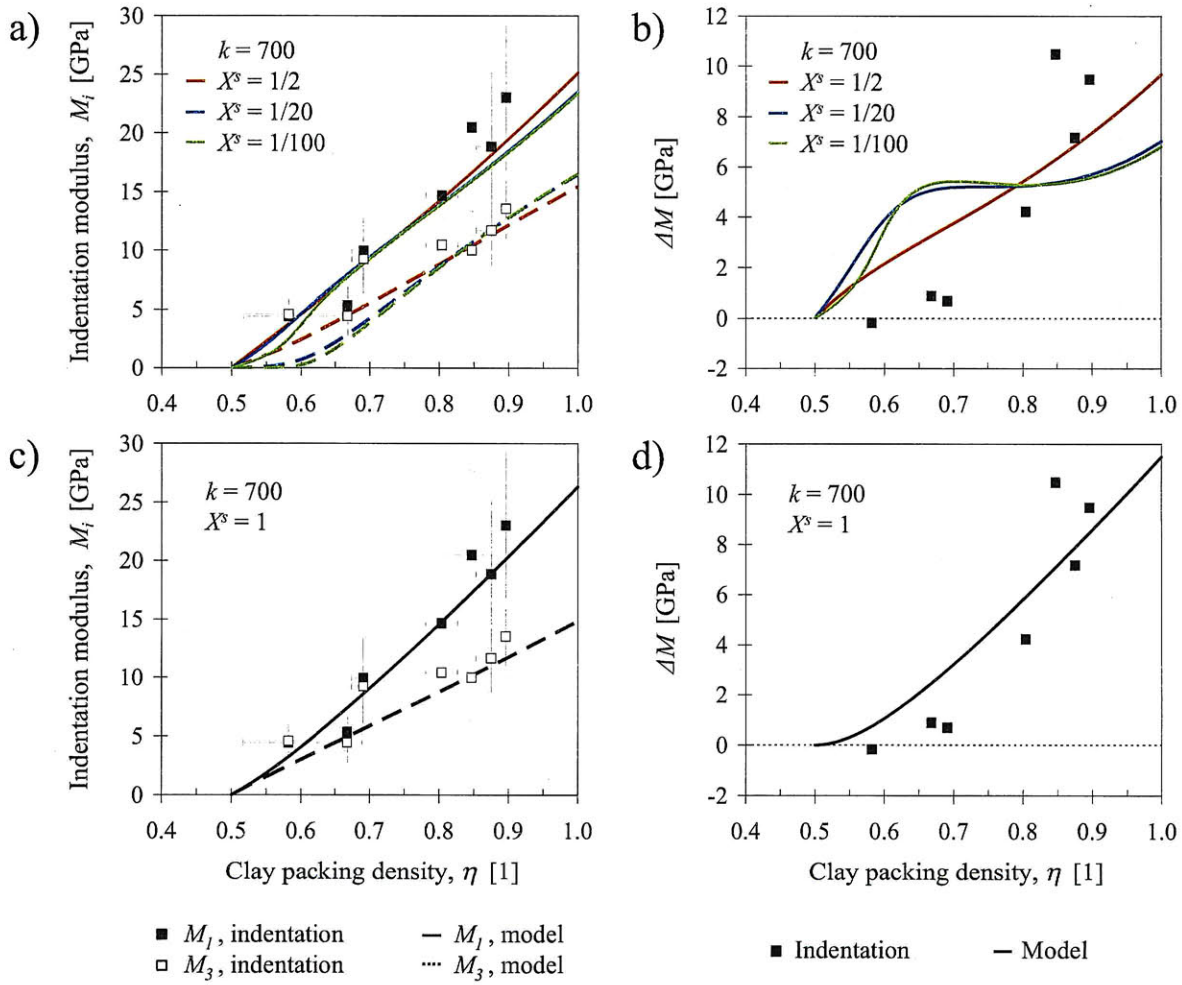

Figure 5-9: The nanoscale elasticity content of the porous clay in shale as a function of clay packing density. The elasticity is expressed in terms of indentation moduli $M_{i=1,3}$. The degree of anisotropy is expressed as the difference in indentation moduli $\Delta M = M_1 - M_3$. Modeling curves are presented for (a-b) hypothesis 3, and (c-d) hypothesis 4. The nanoindentation data corresponds to shales included in the validation data set VDS-1.

Hypothesis	Relative error [%] M_1	M_3
1	-2 ± 26	-26 ± 32
2	-29 ± 18	-26 ± 39
$3-1$	-10 ± 27	-32 ± 39
$3-2$	-5 ± 25	-29 ± 36
$3-3$	-3 ± 22	-18 ± 24
4	-4 ± 21	-15 ± 21

Table 5.8: Relative error statistics of the model validation at level I for the different hypotheses of the elementary building block of solid clay in shale (level 0). The relative error values are presented in terms of the mean +/- the standard deviation of the relative error.

aligned, spherical clay building blocks with intrinsic elastic anisotropy (captured in hypothesis 4) confirm the nanogranular nature of the porous clay phase in shale and highlight the prominent role of the intrinsic anisotropy of the in situ clay compared to structural sources such as particle shape and orientation. The comparisons between model predictions for level I and data from the VDS-1, which was not used for calibration, also validate independently the elastic content of the proposed elementary building block of shale at level 0, which was calibrated using the reverse analysis approach through macroscopic acoustic shale data. The final step in the validation process is to compare the model predictions based on the four hypotheses of the solid clay phase or elementary building block of shale with macroscopic experimental data.

5.3.4 Level II - Comparison with UPV Experiments

The final stage of testing and validating the different approaches to modeling the elastic anisotropy of shale based on the postulated four hypotheses of the clay elementary building block corresponds to comparisons between model predictions for level II of the multi-scale model and acoustic properties for several shales. The different hypotheses representing the effects of structural and intrinsic elastic anisotropies inherent to the clay building block translate, through model implementation, into different sources of the anisotropy observed in shale at macroscopic length scales. The acoustic measurements represent the customary laboratory testing used for the characterization of shale samples at the macroscopic scale. The data used for model validation at level II is gathered in the validation data set 2 (VDS-2). This validation data set provides a comprehensive characterization of acoustic properties for numerous shales

documented in the open literature, in addition to some data gathered by the G2IC. The VDS-2 also provides the mineralogy, porosity, and density information necessary to determine the clay packing density and inclusion volume fraction, which are the two volumetric parameters involved in the homogenization model for determining the properties of levels I and II.

Following the methodology displayed in Figure 5-7, the different hypotheses of the elementary building block of shale are implemented in a forward application of the micromechanics model to deliver estimates of undrained elasticity at level II. The first step in the two-scale homogenization model is to estimate the drained elastic properties for the porous clay composite at level I based on the proposed four hypotheses for the clay building block. These are implemented in the micromechanics model through the evaluation of $\mathbb{C}^I_{\text{hom}} = \mathbb{C}^I_{\text{hom}}(\eta, \mathbb{C}^s, X^s, k)$ using expressions (4.94) for hypotheses 1 through 3 and (4.98) for hypothesis 4. The second homogenization step is accomplished by first calculating the drained stiffness tensor of the porous clay - silt composite at level II, $\mathbb{C}^{II}_{\text{hom}}$, expressed in (4.105). The input parameters for this homogenization step are the drained stiffness properties for the porous clay at level I $\mathbb{C}^I_{\text{hom}}$ and the inclusion volume fraction f^{inc}. The assumed material invariant properties for the quartz inclusion and the fluid phase saturating the pore space were discussed in Section 4.4.4. Finally, undrained elastic properties are derived for the porous clay - silt composite using the expressions detailed in Section 4.4.3[5].

Figure 5-10 displays the comparisons between the macroscopic elasticity modeled via the four hypotheses listed in Table 5.2 and the measured ultrasonic pulse velocity (UPV) elasticity in terms of elasticity constants C^{UPV}_{ij} for shales in the VDS-2 data set. The horizontal error bars in Figure 5-10 correspond to the range of predicted elasticity values depending on the particular set of input parameters used for model implementation. Clay packing density and inclusion volume fraction estimates obtained from mineralogy and porosity information yielded higher-value elasticity constants, whereas estimates obtained from mineralogy and density information (used to derive an alternative porosity value) yielded lower-value predictions. The vertical error bars represent the range of UPV elasticity as a function of different levels of pressure (confining or triaxial) used during testing. The average values between elasticities at minimum

[5]The implementation of the model is accomplished using a similar approach to the reverse analysis approach presented in Section 5.2.1.

Hypothesis	Relative error [%] C_{11}^{UPV}	C_{12}^{UPV}	C_{13}^{UPV}	C_{33}^{UPV}	C_{44}^{UPV}	r^2
1	11 ± 20	15 ± 34	48 ± 90	13 ± 30	15 ± 49	0.84
2	-5 ± 20	14 ± 34	52 ± 93	15 ± 29	12 ± 45	0.78
$3-1$	11 ± 19	14 ± 34	46 ± 89	10 ± 30	10 ± 47	0.84
$3-2$	11 ± 19	14 ± 34	46 ± 89	12 ± 30	12 ± 47	0.84
$3-3$	11 ± 19	15 ± 34	47 ± 89	15 ± 29	16 ± 47	0.85
4	11 ± 19	14 ± 34	47 ± 89	16 ± 29	16 ± 47	0.85

Table 5.9: Relative error statistics of the validation of stiffness properties for the different hypotheses of the elementary building block of solid clay in shale (level 0). The relative error values are presented in terms of the mean +/- the standard deviation of the relative error.

and maximum pressure or stress states are used for comparison with model predictions, and are represented by the solid data points[6]. Table 5.9 shows the corresponding means and standard deviations of the relative errors in the predictions of elasticity properties.

The general trend inferred from Figure 5-10 and Table 5.9 reveals a uniform performance of the different variations of the micromechanics model in predicting the anisotropic elasticity of the shale materials in the VDS-2 data set. The mean relative errors between predicted and measured UPV elastic constants are on the order of 16 percent or less, with the exception of C_{13} with an associated mean relative error of approximately 50 percent. This is not surprising given that the experimental determination of the elastic constant C_{13} is generally recognized to suffer from higher uncertainties compared to the rest of the elastic constants as a result of standard practices in the inversion of elasticity data from UPV laboratory measurement [129]. Indeed, less accurate estimates for C_{13} compared to those of the remaining four elastic constants are reported for three of the studies included in the VDS-2 data (see Table 3.20).

[6]As reported often for shales, acoustic measurements could be sensitive to discontinuities such as cracks and elongated pores. Given our treatment of shale as uncracked porous media (refer to Section 4.5.2), it may be relevant to draw comparisons between model predictions and acoustic data at high pressures in view of the hypothesis of closere of cracks. For completeness, properties at low and high stress states are reported because we cannot guarantee the validity of assuming the complete closure of cracks at high pressures for all experimental data gathered for model validation. In addition, the choice of comparisons with the average of velocities at different pressure conditions is justified given the variability in experimental setups used for the deformation experiments gathered in the VDS-2 data set. Finally, the inspection of Figure 5-10 reveals that the effects of the pressure dependency of UPV elasticity are of similar magnitude compared to the range of model predictions caused by the variability in input parameters (namely the clay packing density and the inclusion volume fraction). A more detailed discussion of the pressure dependency and applicability of our model will be presented in a forthcoming section. Lastly, similar arguments justify the comparisons between model predictions and acoustic data for shale involved in the model calibration reported in Section 5.2.

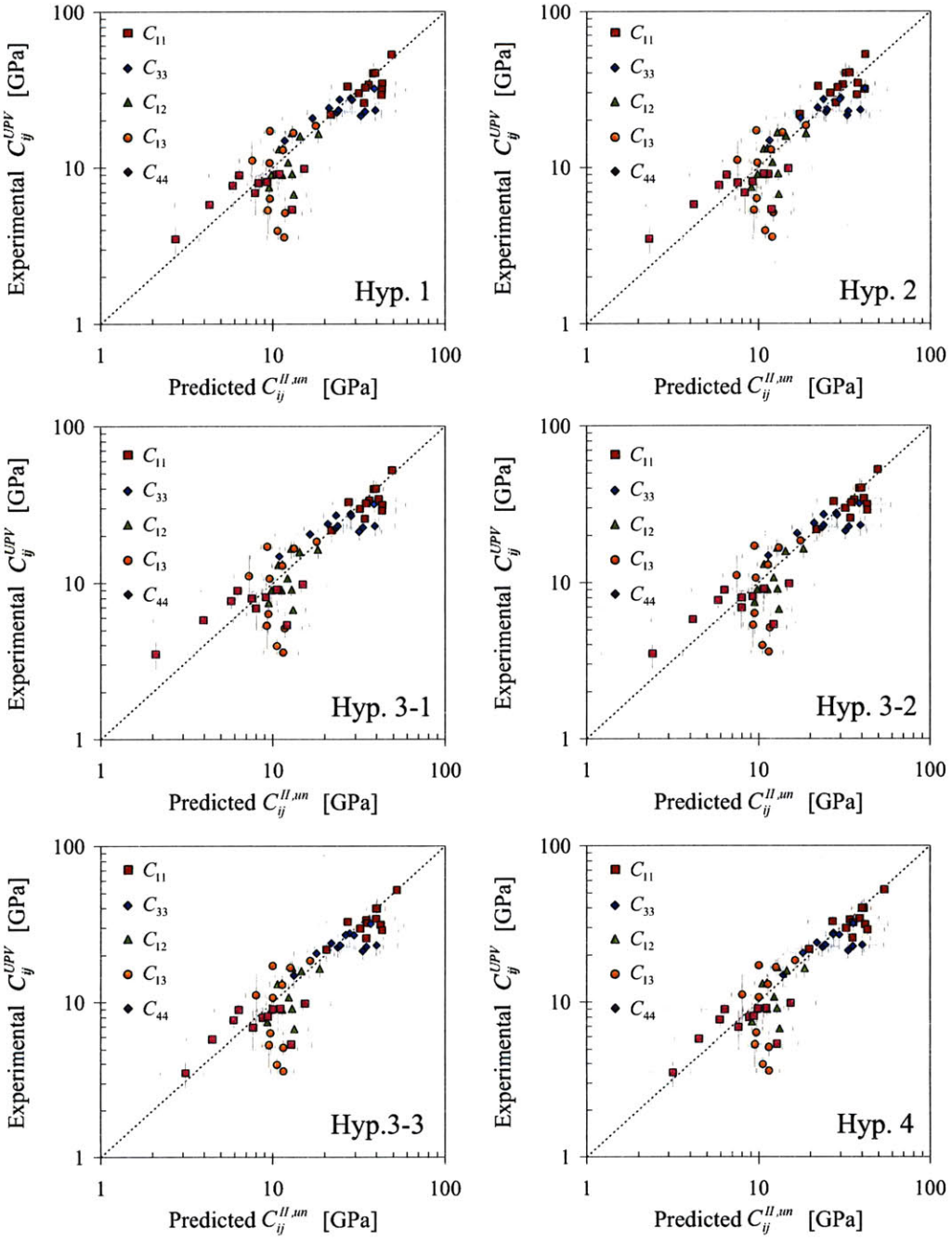

Figure 5-10: Comparison of predicted (undrained) stiffness values $C_{ij}^{II,un}$ and experimental UPV elasticity in terms of elastic constants C_{ij}^{UPV} from the VDS-2 data set for level II. Vertical error bars represent the variability of UPV stiffness as function of pressure state. Horizontal error bars represent the variability of model predictions depending on input volume fraction values.

Furthermore, the calibration of the C_{13}^s for the different hypotheses herein tested proved to be less accurate compared to the remaining elastic constants. From Table 5.4, the mean and standard deviation of the relative errors for C_{13}^s calibrations were among the highest of the set. The experimental uncertainties inherent to the assessment of C_{13} and its challenging model calibration may partially explain the scatter in relative errors for this parameter.

Given the overall favorable statistics for the comparisons between experimental and modeled UPV elasticity, it appears that the different combinations of geometric and intrinsic elasticity factors used for modeling the porous clay composite in shale translate into adequate modeling frameworks for capturing the macroscopic anisotropy of shale materials. The case of modeling the shale anisotropy based on purely geometric factors (hypothesis 2) exhibits the lowest accuracy in predictions compared to the rest of the cases considered in this set of comparisons. This observation highlights the importance of considering the intrinsic anisotropy of the clay phase in modeling the overall anisotropy of shale. Predictions based on the cases resorting to combinations of anisotropic sources (hypotheses 1 and 3) satisfactorily capture the measured macroscopic anisotropic behavior. Interestingly, optimal predictions are found for the case of purely intrinsic anisotropy (hypothesis 4), in which the only parameters specified for the elasticity upscaling using the proposed multi-scale micromechanics framework are the clay packing density and the inclusion volume fraction, in addition to the material invariant properties of the solid clay C_{ij}^s that were calibrated based on the given hypothesis. The perfect alignment and spherical morphology ($k \rightarrow \infty$, $X^s = 1$) reduce the number of model parameters to be measured or determined independently for an application of the model.

For completeness, a closer inspection of the validation results at level II is presented for the remarkable predictions of the micromechanics model based on hypothesis 4, which resorts to a compact set of model parameters: the (calibrated) stiffness of the solid clay phase $\mathbb{C}_s$ at level 0, and the clay packing density and inclusion volume fraction obtained from material composition and mineralogy data. In Figures 5-11 and 5-12, model predictions for specific shale specimens in the VDS-2 are compared directly to the UPV velocities measured through acoustic techniques. The elastic constants $C_{ij,\text{hom}}^{II,un}$ are converted into acoustic velocities using expressions (3.67a)-(3.67e). The displayed acoustic velocities are reported based on the customary compressional (P-) and shear (S-) wave velocities in the normal-to-bedding (x_3) and parallel-to-bedding

(x_1, x_2) directions. In addition, the (quasi) P-wave velocity at inclination angle $\theta = 45°$ is reported. Similar to Figure 5-10, the horizontal error bars in Figures 5-11 and 5-12 represent the range of predicted elasticity values given the two different input sets of estimates of clay packing density and inclusion volume fraction. The vertical error bars correspond to the range of reported UPV elasticity values resulting from varying pressure conditions. In addition to the comparisons in Figures 5-11 and 5-12, a summary of the relative errors between the measured and the predicted UPV elasticity is displayed graphically in Figure 5-13.

Excellent agreement between measured and predicted macroscopic acoustic properties is observed for the data obtained from the open literature: Hornby [129], Domnesteanu et al. [81], Dewhurst and Siggins [77], and Sarout and Guéguen [226], as well as the data for North Sea shale gathered by a G2IC member. For the shale data of these references, the relative errors are on the order of 10%, which indicates a very satisfactory comparison. The least satisfactory comparisons found are with the literature data from Jones and Wang [146] and Jakobsen and Johansen [138], displayed in Figures 5-11a and 5-11c. The discrepancy with the measurements by Jones and Wang could be attributed to the small confining pressures used during testing. In fact, the hydrostatic pressure applied during testing is in the sub-MPa range, which may not resemble the stress state of the rock formation. In fact, the application of the model would predict elastic properties related to some stress state relevant to the in situ behavior. A more detailed assessment of the pressure dependency of acoustic properties of shale with relation to the developed micromechanics model is due in a forthcoming chapter. The discrepancy with the measurements by Jakobsen and Johansen could be attributed to the relatively large volume fractions of unidentified minerals. For the implementation of the model, the so-called 'other' minerals (see Table 3.3) were assumed to belong to the clay type. Although the model captures the overall anisotropic behavior for this data set, only complete mineralogy information could help determining the sources for discrepancy between model predictions and measurements.

The present finding related to the effectiveness of treating the complex microstructure of the porous clay as a granular composite with an isotropic morphology and intrinsic anisotropic elasticity (hypothesis 4) agrees with the results of model validation at level I. The comparison of model predictions against nanoindentation data yielded an optimal match for the implementation of hypothesis 4. It appears that the nano- and macroelasticity of shale is dominated by

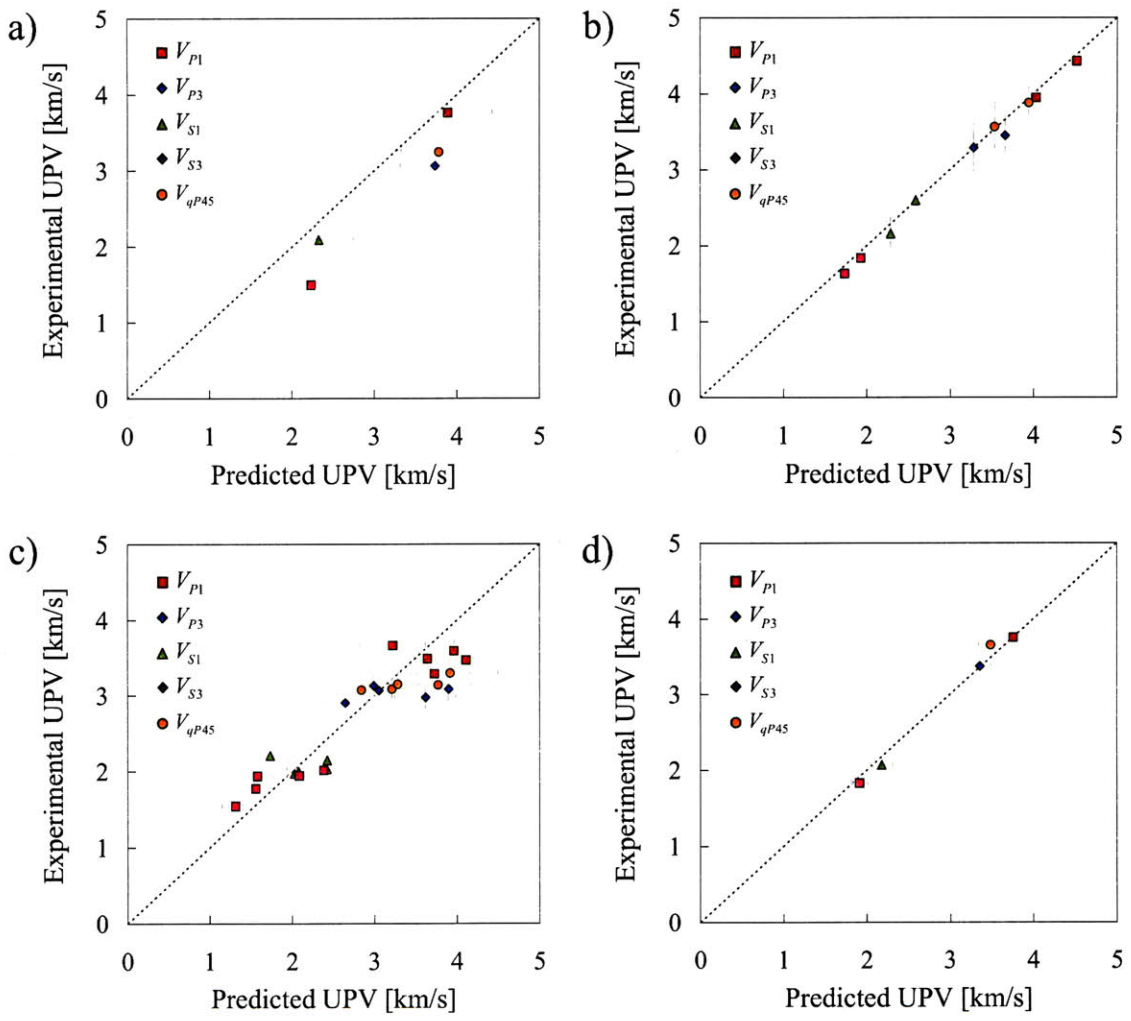

Figure 5-11: Comparison of predicted (undrained) stiffness and experimental UPV elasticity from a) Jones and Wang [146], b) Hornby [129], c) Jakobsen and Johansen [138], and d) Domnesteanu et al. [81]. Vertical error bars represent the variability of UPV stiffness as function of pressure state. Horizontal error bars represent the variability of model predictions depending on input volume fraction values.

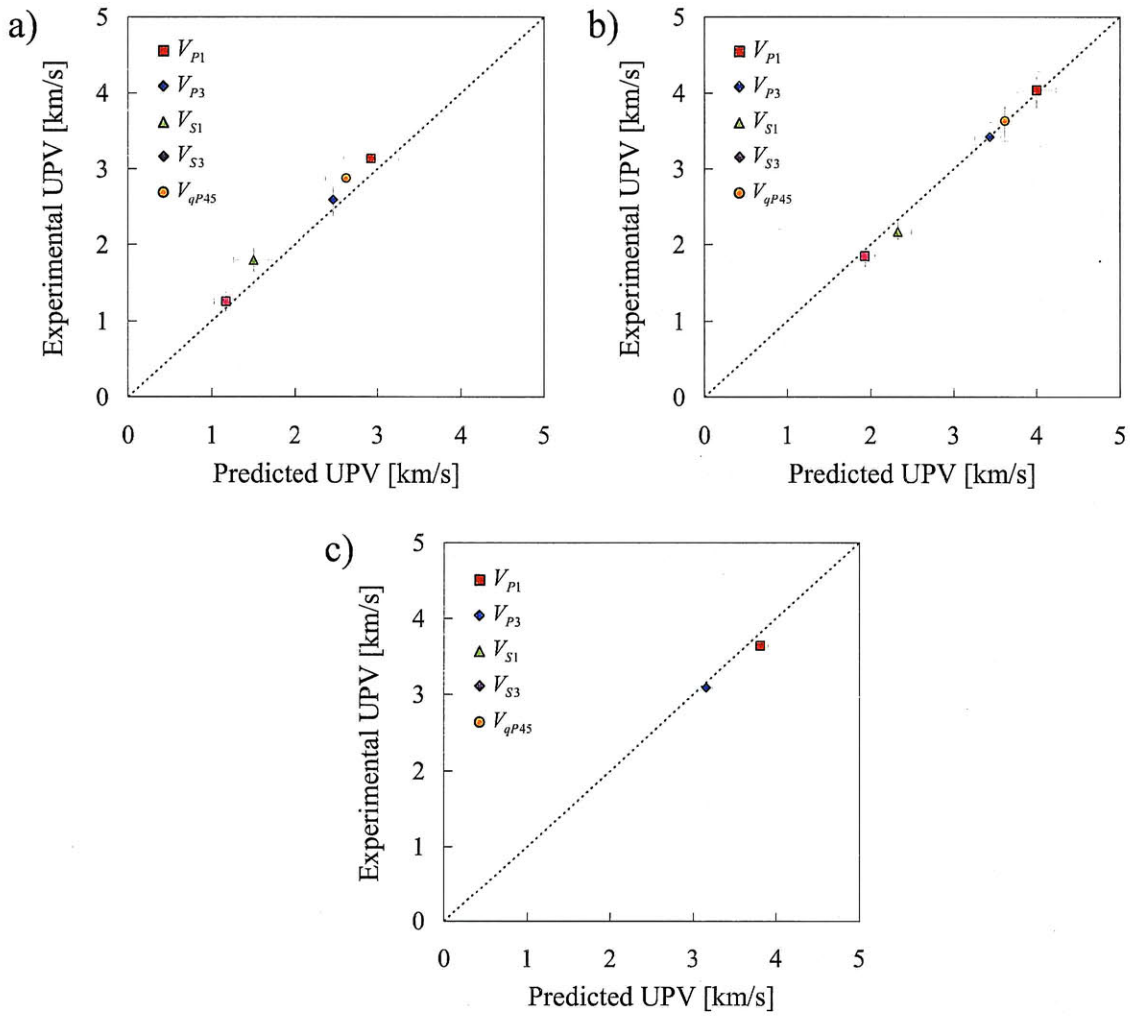

Figure 5-12: Comparison of predicted (undrained) stiffness and experimental UPV elasticity from a) Dewhurst and Siggins [77], and b) Sarout and Gueguen [226]. Comparisons in c) correspond to the North Sea (NS) sample, courtesy of StatoilHydro. Vertical error bars represent the variability of UPV stiffness as function of pressure state. Horizontal error bars represent the variability of model predictions depending on input volume fraction values.

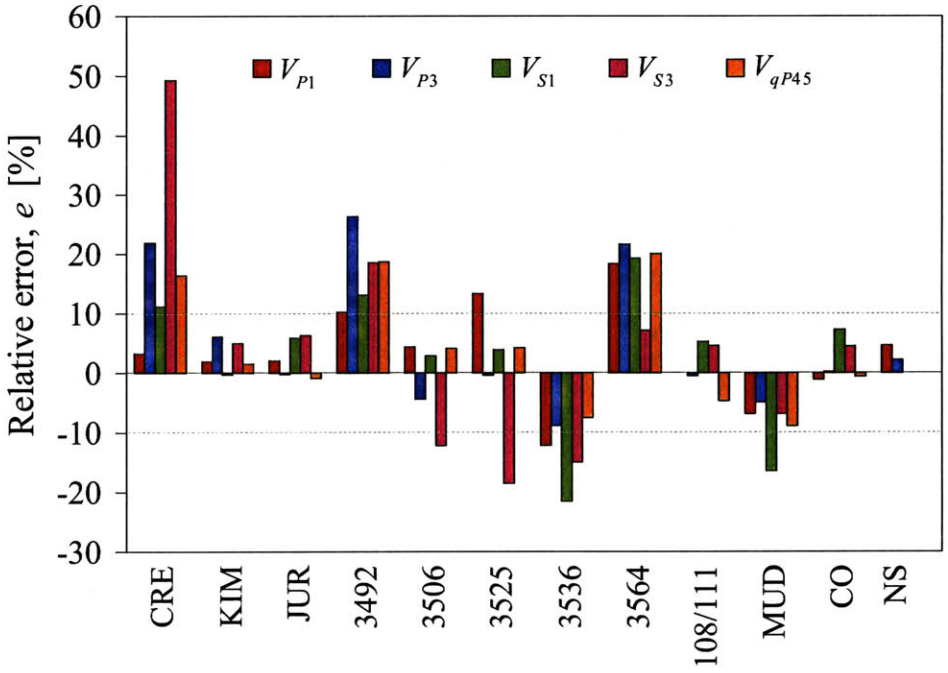

Figure 5-13: Relative errors (in percent) related to the prediction of acoustic velocities for the shale specimens in the VDS-2 data set.

the response of the intrinsically anisotropic clay phase, whereas structural sources of anisotropy such as particle geometries and orientations play a second-order role in defining the overall anisotropic behavior.

5.4 Chapter Summary

Conventional predictive models for the anisotropic elasticity of shale rely on the faithful translation of microstructural features such as the geometry and orientation of particles into modeling parameters. However, do these features represent the best descriptions of the origins of anisotropy in shale? In this chapter, a comprehensive micromechanics model for shale anisotropic poroelasticity was implemented. The model incorporates the elements of two schools of thought regarding the anisotropic mechanics of shale: the conventional approach, relying mostly on geometrical/structural sources of anisotropy, and the novel mechanics understanding inferred from nanoscale testing that underscores the prominent role of the intrinsic anisotropy of the clay fabric in shale. Using a hypothesis testing approach, the different sources of anisotropy in shale were quantified through a series of model calibration and validation exercises. The learned granular, anisotropic response of the clay fabric at nanoscales precludes any modeling attempt based on geometrical anisotropic sources alone. In contrast, combinations of structural sources such as particle shapes and orientation distributions and intrinsic anisotropic properties of the solid clay phase yield adequate descriptions of shale at different length scales.

Remarkably, the modeling of the porous clay scale based on intrinsic material anisotropy only yields an effective scheme for reproducing its poroelastic response and enabling the prediction of macroscale anisotropy. This intrinsic elasticity is represented through an elementary building block of solid clay, which appears to be in first order unique, or *invariant*, for shale materials. Also, the complex microstructure of the porous clay is translated into a micromechanics description rooted in the self-consistent scheme, in which the granular nature of shale is linked to the micromechanics response of highly aligned clay elementary building blocks with isotropic morphology. With the effective micromechanics description of the porous clay phase at hand, the material science paradigm for shale is fulfilled by relating the material composition to the mechanical response of shale at different scales. More specifically, the multi-scale

homogenization model for shale materials effectively predicts their anisotropic elasticity based on two shale-specific, volumetric parameters related to materials composition: the clay packing density and the inclusion volume fraction. The extensive data used for model development and the success of the validation process corroborates *a posteriori* the adequacy of the proposed multi-scale structure model for shale presented in Chapter 2.

In Chapter 6, the developments and findings of the micromechanics investigation presented thus far are translated and consolidated into an engineering model for shale multi-scale poroelasticity. The implications of the proposed effective definition of an elementary building block for shale and its success in enabling the prediction of shale anisotropic elasticity will be discussed in detail. In addition, the domain of applicability of the model as a predictive engineering tool will be further explored, especially in view of potential implementations of the model for laboratory and field applications.

Chapter 6

Microporoelastic Engineering Model

The challenge of developing predictive engineering models for complex heterogeneous materials such as shale rests in successfully establishing the relations between material microstructure, composition, and performance, while maintaining an acceptable balance for the number and nature of modeling parameters describing such interactions. In Chapter 5, a microporomechanics modeling framework aiming at the prediction of the multi-scale anisotropic elasticity of shale was evaluated based on a series of configurations of anisotropic factors arising from structural sources (particle shapes and particle orientation distributions) and intrinsic material properties (clay anisotropy). The main outcome of the evaluation was establishing the prominent role of the intrinsic anisotropic elasticity of the clay phase in shale. It was also found that the modeling of the complex microstructure of shale can be effectively undertaken without recurring to structural anisotropic attributes such as prescribed particle geometries or orientations. The porous clay composite is instead characterized using the self-consistent scheme of micromechanics, in which the concept of an elementary building block for the solid clay phase with isotropic morphology and intrinsic elastic anisotropy becomes the driving factor behind reproducing the granular nature of shale as measured by nanoindentation, as well as the diverse anisotropic poroelasticity of shale observed at macroscopic scales of engineering testing.

In this chapter, we synthesize the results from the calibration and validation exercises of Chapter 5 into a working engineering model for shale poroelasticity. The chapter begins with a presentation of the key features of the adopted micromechanics homogenization model, including the effective form of the elementary building block of shale and the upscaling model

parameters, which rely on material composition and porosity information. The presentation of the chapter continues with a detailed discussion of the physical basis of the elementary building block, which enables capturing the multi-scale mechanics of shale through the adopted homogenization scheme. Particular considerations are given to the intrinsic and invariant elastic properties of the elementary unit and its effective morphology, which define the properties of levels 0 and I in our multi-scale structure model. This chapter then explores the predictive capabilities and the applicability of the micromechanics model as an engineering tool for prediction of shale macroscopic properties. The predictive capabilities of the model in terms of anisotropic elasticity and poroelastic parameters are reviewed. The topics of stress dependency of macroscopic elastic properties and the effects of frequency on measured acoustic responses of shale are discussed in view of potential laboratory and field applications.

6.1 A Micromechanics Engineering Model for Shale Anisotropic Poroelasticity

The main finding from the calibration and validation exercises in Chapter 5 was the identification of a relevant and effective micromechanics approach for modeling the multi-scale anisotropic elasticity of shale materials from diverse origins and compositions. The key features of 'the' engineering model for shale elasticity are schematically summarized in Figure 6-1.

The multi-scale anisotropic elasticity of shale appears to be governed (in first order) by the intrinsic elasticity of the porous clay phase, which is represented by the properties of level 0 of the multi-scale structure model. The corresponding elementary building block of solid clay, with intrinsic, invariant elastic properties, is sufficient for modeling the nanomechanical response of shale at level I, without resorting to structural factors such as particle shapes and orientations. The nanogranular response of shale as sensed by nanoindentation and the complex microstructure of its clay fabric are typed into the model through the use of the self-consistent scheme of micromechanics of granular media, in which the elementary unit of clay is characterized by a spherical morphology. The scaling parameter for obtaining the poroelastic response of the porous clay composite at level I is the clay packing density η, which neatly synthesizes mineralogy and porosity information specific to a shale material. A second

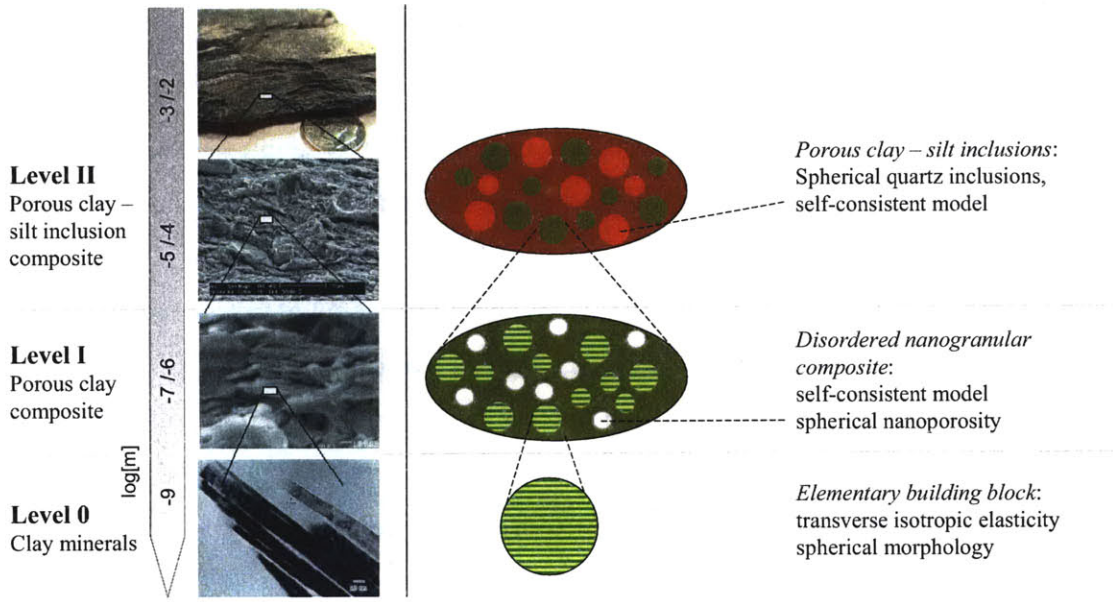

Figure 6-1: Engineering model for shale poroelasticity.

application of the self-consistent scheme facilitates determining the mechanical properties of the homogenized porous clay composite intermixed with silt inclusions at the macroscopic scale of shale. The homogenized poroelastic properties of the porous clay - silt inclusion composite depend on the second shale-specific parameter, the inclusion volume fraction f^{inc}. With the appropriate information regarding the compressibility of the fluid phase saturating the pore space, the micromechanics model yields predictions of the undrained poroelastic characteristics of shale materials. The features previously discussed of the adopted engineering model for shale anisotropic poroelasticity correspond to the implementation of hypothesis 4 (refer to Chapter 5).

Given the shale-invariant properties of the fundamental building block of shale, which had been appropriately calibrated and validated against independent data sets, it is recognized that the multi-scale poroelastic response of shale predominantly depends on the two shale-specific quantities: clay packing density and non-clay inclusion volume fraction. The clay packing density is recognized to be at the very origin of shale poroelastic sensitivity, while the presence of inclusion at larger scales weighs this sensitivity in proportion to the macroscopic porous clay volume fraction. The fact that those two parameters delimitate shale macroscopic

diversity makes the proposed two-parameter microporoelastic model an appealing alternative for geophysics and reservoir engineering applications. The remaining sections of this chapter are devoted to exploring the relevance of the proposed micromechanics model for shale, as well as its domain of application and its predictive capabilities.

6.2 Elementary Building Block of Shale - Level 0 Properties

Does a unique set of clay deposition stiffness values suffice to describe shale anisotropic elasticity? One of the scientific challenges presented in this thesis is the question whether is possible to identify a fundamental scale in shale rocks where the mechanical behaviors are governed by material invariant properties. Chapter 5 presented ample experimental evidence from instrumented nanoindentation and theoretical developments from microporomechanics to devise a multi-scale homogenization model capable of predicting the anisotropic elasticity of shale at different scales of observation. One of the key elements to achieve a predictive capability was the consideration of an elementary unit of clay. This so-called *elementary building block* at level 0 of our proposed multi-scale structure model with material properties that are unique or invariant (in first order) for shale materials across lithologies and formations answers the scientific question of identifying a fundamental mechanical unit for modeling. The rest of this section takes a closer look at the intrinsic and invariant nature of the elasticity content ascribed to the elementary building block of shale, which enables the successful modeling of the diverse macroscopic anisotropy of shale[1].

To guide the present discussion, Figure 6-2 recalls the results of nanoindentation on shale materials and the predictions of indentation moduli using the micromechanics engineering model for shale. The figure displays many of the important ingredients to examine the elastic properties of the elementary unit of solid clay.

The increasing anisotropic scaling of the porous clay stiffness with the clay packing density tends to a particular set of elastic properties, which in the asymptotic case $\eta \rightarrow 1$ corresponds to the stiffness tensor of elastic constants $\mathbb{C}^s$. It is worth recalling that the stiffness tensor was calibrated using a reverse analysis approach of macroscopic elastic properties of various

[1] The presentation of this section benefits from the fruitful discussions with C. Bobko, which translated into a recent journal comment [34].

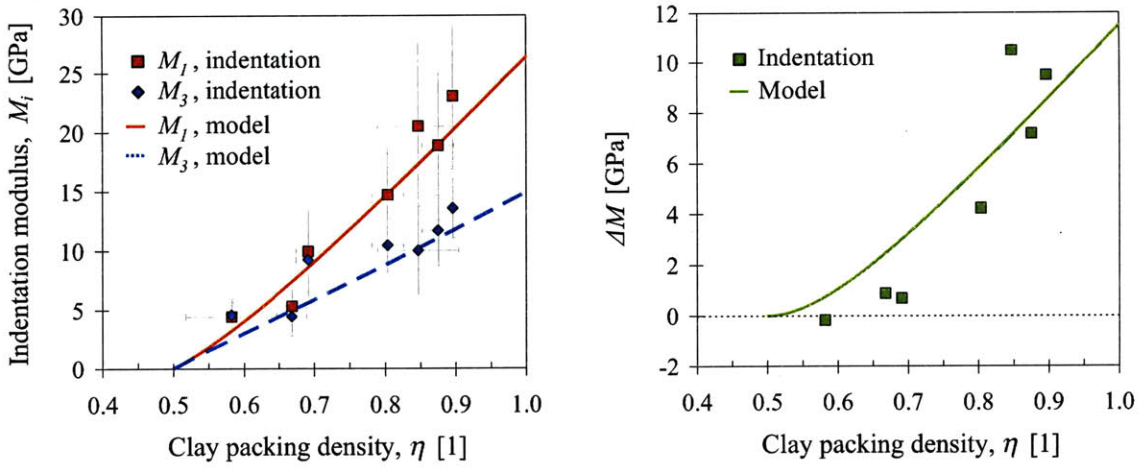

Figure 6-2: Stiffness of the porous clay composite as a function of clay packing density. The stiffness properties are expressed in terms of indentation moduli $M_{i=1,3}$. The degree of anisotropy is expressed as the difference in indentation moduli $\Delta M = M_1 - M_3$. The nanoindentation data corresponds to shales included in the validation data set VDS-1. The modeling curves correspond to the micromechanics engineering model adopted in Section 6.1.

shale samples. Consequently, this good agreement between the micromechanics model and the results from nanoindentation verifies the definition of a mechanical phase of solid clay, initially assumed for model development. The elastic properties $\mathbb{C}^s$, in terms of elastic constants and corresponding indentation moduli (in GPa):

$$[C^s_{ij}] = \begin{bmatrix} C^s_{11} = 44.9 & C^s_{12} = 21.7 & C^s_{13} = 18.1 & 0 & 0 & 0 \\ C^s_{12} = 21.7 & C^s_{11} = 44.9 & C^s_{13} = 18.1 & 0 & 0 & 0 \\ C^s_{13} = 18.1 & C^s_{13} = 18.1 & C^s_{33} = 24.2 & 0 & 0 & 0 \\ 0 & 0 & 0 & 2C^s_{66} = 23.2 & 0 & 0 \\ 0 & 0 & 0 & 0 & 2C^s_{44} = 7.4 & 0 \\ 0 & 0 & 0 & 0 & 0 & 2C^s_{44} = 7.4 \end{bmatrix} \tag{6.1}$$

$$M^s_1 = 26.4, \quad M^s_3 = 14.8 \tag{6.2}$$

or in the isotropized form (in GPa):

$$k^s_{ISO} = 24.0, \quad g^s_{ISO} = 6.7 \tag{6.3}$$

offer an estimate of the response of the clay fabric in shale in the absence of nanoporosity (one minus the packing density). In fact, the specific type of response of this calibrated $\mathbb{C}^s$ is in excellent agreement with data extrapolated from rock testing results, as noted in the discussion of Table 5.7. This so-called compacted or consolidated clay behavior represents the effective, in situ response of the solid clay phase in clay-bearing rocks, which is of a smaller order-of-magnitude compared to the measured elastic properties of single clay crystals. These contrasting behaviors could be reconciled in the light of some recent results from nanoindentation testing.

Zhang et al. [302] recently deployed nanoindentation techniques to measure elastic properties of two different clay minerals: muscovite and rectorite. The main differences between these two clay minerals are the bonding strengths in their layers and their interlayer spacings. Muscovite exhibits strong bonding in its 2:1 layer structure and small interlayer spacing, compared to rectorite and its weaker interlayer bonding and large interlayer spacings making it prone to water penetration. The highly crystalline, millimeter-sized samples were assumed to represent the properties of single minerals due to their crystal structure and the repeatable unit arrangement of clay layers and interlayer galleries. Compared to the acoustic and optical experimental techniques, which can assess the full elasticity tensor of the measured crystals, the nanoindentation approach of Zhang et al. provides quasi-isotropic elasticity values for the muscovite and rectorite specimens. The indentation results for these minerals yield the following indentation modulus properties[2]:

$$M^{muscovite} = 59 \text{ GPa} \tag{6.4a}$$

$$M^{rectorite} = 16 \text{ GPa} \tag{6.4b}$$

However, an in-depth analysis of Bobko et al. [34] argues that only the indentation measurement on muscovite may represent a meaningful estimate of the well-crystallized particle elasticity. The associated indentation depths in these experiments, in the micrometer range, probe the tested clay materials at characteristic length scales much larger than the individual unit structures (i.e. clay sheets plus interlayer material, on the nanometer range). However, in the case of

[2]The indentation properties correspond to the 'uncorrected' results of Zhang et al. [302], where pop-ins were smallest for both measured crystals. The indentation loads used for testing were on the order of 10 mN to 100 mN.

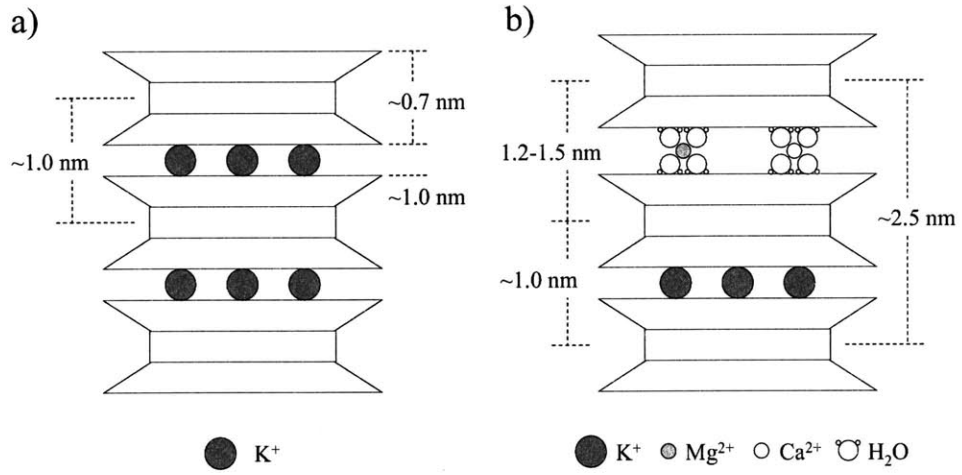

Figure 6-3: Schematic of the crystal structures of a) muscovite and b) rectorite. Adapted from [302].

muscovite, the relatively small interlayer gallery with little absorption of water or hydrated cations, as schematically shown in Figure 6-3, diminishes the mechanical contribution of a compliant interlayer to the otherwise stiff clay layers. In contrast, the indentation measurements on rectorite are seen as encompassing the responses of the clay layers and interlayer gallery, whose weak bonding and high absorption capacity for interlayer materials (e.g. water) may contribute significantly to the difference in elastic behavior as measured by nanoindentation.

These preliminary results from direct testing at the scale of clay minerals help to complete the understanding of the type of mechanics that is being modeled through the elementary building block concept. Rather than considering the stiff elastic properties of the clay layers or crystallized forms at the particle level such as muscovite crystals, the elementary unit of clay represents the combined response of agglomerated clay particles, an arrangement which encompasses the mechanical contributions of the clay platelets, the interlayer materials (absorbed water, hydrated cations, etc.), and the interparticle contacts. This elementary unit of 'solid' clay becomes the first continuum mechanics phase embodying the highly compacted, in situ elastic response of the clay phase in shale. Within this framework, the physical chemistry behavior at the sub-nanometer scales is not considered explicitly, such as double layer effects due to the presence of interlayer absorbed water or swelling pressures. Furthermore, the effects

of confined water residing in the interparticle spaces may prove difficult, at this moment, to be modeled or incorporated into a multi-scale continuum mechanics approach [17]. In loosely packed clays, those phenomena may play an important role, and even strongly influence the elasticity, as shown recently by Dormieux and co-workers [84].

An important attribute of the elasticity of the elementary building block of solid clay is its apparent insensitivity to clay mineralogy, at least in first order. This observation is inferred from the extensive validation of the micromechanics model with nanoindentation and acoustic data for shale materials of diverse compositions and origins. Although different clay minerals may exhibit contrasting properties (see Table 3.12), their direct contributions to the in situ mechanical response of shale at sub-micrometer length scales seem to be modulated by the compliant nature of interlayer and interparticle contact forces. Hence, the invariant character of the elastic properties of the elementary unit of clay may be intimately linked to the role of the interlayers in clay particles and the interparticle contacts. Clearly, this description is restricted to the elastic behavior only. The clay mineralogy is key to the description of other physical phenomena such as swelling and permeability.

Regarding the anisotropic nature of the elementary building block, those origins are intimately related to the depositional history of clay platelets and the ensuing stress history of buried shale. These processes lead to the alignment of clay minerals within local conglomerates. Furthermore, the atomic structure of clay, as it is clearly seen for muscovite, exhibit strong elastic anisotropic characteristics. Both the aligned structure and the anisotropy of the clay minerals lead to intrinsic (at least) transverse isotropy of the elementary building block. Previous modeling attempts that consider groupings of clay minerals tend to assume, for convenience, that these effective particles are elastically isotropic [128]. For shale materials, however, where the depositional history implies a certain overall alignment of individual clay particles, the anisotropy of the clay particle grouping must be considered.

6.3 Effective Form and Shape of Building Block - Structural Form at Level I

Apart from the intrinsic anisotropy of the elementary building block of shale, another crucial result from the calibration and validation exercises of Chapter 5 is its effective spherical morphology within our application of micromechanics and the self-consistent homogenization scheme. This raises the valid question of: *does clay particle shape really matter for shale modeling*? In this section, we present a series of arguments that consolidate the proposed effective mechanical representation of the porous clay microstructure through adopting a spherical morphology for the elementary clay unit.

The measured indentation moduli of porous clay at nanometer length scales through nanoindentation, as shown in Figure 6-2, furnish crucial information regarding the nanomechanical response of shale, which was not available to previous modeling attempts. To illustrate this point, Figure 6-4 displays the degree of anisotropy, in terms of Thomsen parameters, computed from the classical model results of Hornby et al. [128] for the elastic constants of the fully-aligned clay-fluid composite (see Figure 8, [128]). Their approach was based on an anisotropic formulation based on the self-consistent and the differential effective medium schemes to model the response of a bi-connected clay-fluid pseudo particle that controls the anisotropic response of shale. In addition, particle orientation distributions derived from SEM imaging analysis were incorporated into modeling to determine the effective elasticity of shale without the contribution of silt minerals.

The Thomsen parameter values displayed in Figure 6-2 are functions of packing density, which in this case is equal to one minus the fluid-filled porosity. The anisotropic response of the clay-fluid composite, which is analogous to level I of our multi-scale structure model, illustrates the ability of a continuum mechanics approach to model the sources of anisotropy in shale based solely on geometric parameters. However, a close comparison with indentation data, as illustrated in Figure 6-2 clearly establishes that geometric factors alone (i.e. shapes and orientation distributions of particles) cannot describe fully the nanoscale anisotropic elasticity of shale. A similar conjecture was derived from the hypothesis testing of case 2 (see Chapter 5), whose design followed a similar configuration for the porous clay composite: isotropic, oblate

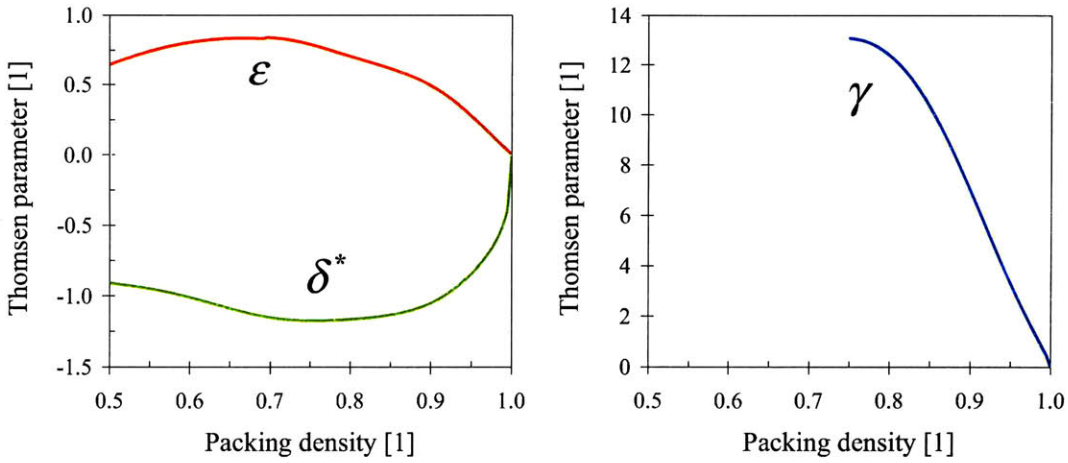

Figure 6-4: Thomsen parameters calculated from the elastic constants of the clay-fluid composite in shale modeled by Hornby et al. [128]. The numerical values for the elastic constants C_{ij} were obtained through digitizing the model results presented in Figure 8 [128]. The clay-fluid composite corresponds to an inclusion with aspect ratio of 1/20.

clay particles and nanoporosity. One must emphasize this particular shortcoming of previous modeling attempts, which certainly might have lacked the necessary evidence from small-scale mechanical testing such as e.g. nanoindentation. The work of Hornby et al. [128], for instance, has been referenced as a theoretical confirmation of experimental trends of decreasing anisotropy with decreasing porosity (see e.g. [129]). However, such assertion is a natural consequence of the asymptotic elastic behavior at zero porosity and irrespective of particle shape: the solid phase is isotropic. Having established that geometric arguments such as particle shape and orientation cannot alone predict the anisotropic response of shale at the scale of the clay fabric, the next two arguments drawn from micromechanics developments and advanced nanoindentation analysis address the importance (or not) of clay particle shape in the engineering modeling of shale.

The role of particle shape in the elastic anisotropy of the porous clay in shale is examined in Figure 6-5. The figure shows the normalized indentation stiffness $M_{i=1,3}/M^s_{i=1,3}$ as a function of packing density η. The modeling curves correspond to the implementation of the engineering model for estimating the homogenized properties at level I. For simplicity, the normalized model lines correspond to the results for indentation modulus in the direction x_1 and for oblate

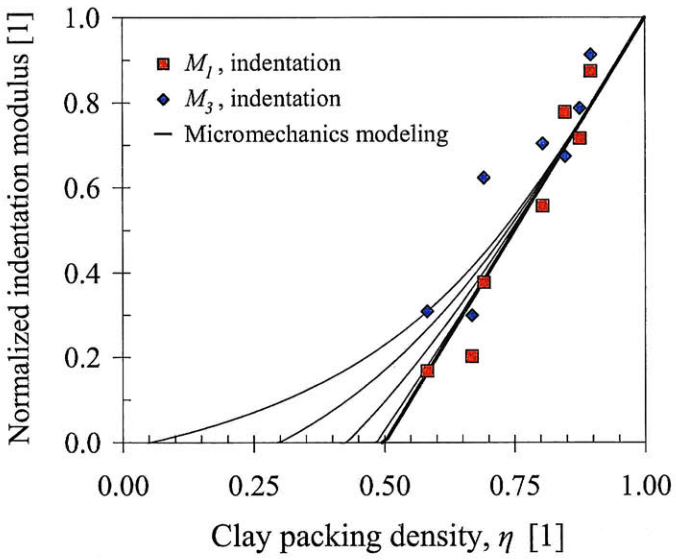

Figure 6-5: Normalized indentation modulus versus average packing density data for shale materials in the VDS-1. The indentation data was normalized by the solid indentation modulus $M^s_{i=1,3}$ displayed in (6.2). The modeling lines correspond to the self-consistent modeling of porous solid with isotropic particles with different oblate aspect ratios (from left to right): $X^s = 1/100, 1/10, 1/4, 1/2, 1$.

particles with random alignment[3]. A very similar set of normalized model lines could be found for the indentation modulus in the direction x_3. The experimental data corresponds to the VDS-1, which is also normalized by the solid clay values provided in (6.2). Most of the shale data belongs to a range of packing densities higher than $\eta > 0.6$, in which the effects of particle shape are not significant. It appears that for shale materials, with intrinsically high packing values, the micromechanics approach cannot resolve the order of the particle shape when predicting the mechanical response of shale's clay fabric. For other materials such as gypsum, which exhibit a broader range of packing densities (one minus porosity, at the appropriate length scale), particle shape may represent a first-order parameter for predictive modeling [225].

Another important piece of evidence, related to the relevance of considering particle shapes for understanding the nanoelasticity of the porous clay in shale, is drawn from advanced nanoin-

[3] Micromechanics results for partially aligned ensembles are not of added value to the discussion, as they would only modify the percolation threshold behavior for a particular particle shape.

dentation analysis [31, 270]. Ulm and co-workers investigated the scaling of elasticity and strength data generated from nanoindentation experiments for three nanocomposites (cement paste, bone, and shale) in order to identify intrinsic and structural sources of anisotropy. The indentation modulus-hardness-packing density ($M - H - \eta$) analysis employs each experiment from grid indentation on a material sample in combination with micromechanics modeling in order to infer distributions of packing densities and mechanical properties of the solid clay phase (refer to Section 3.6.6). The packing density distributions can be considered as mechanical assessments of the microstructure of the material. For each material system, orthogonal indentation measurements were conducted, and Figure 6-6 displays the indentation analysis results for apatite, the binding phase in bone, and the porous clay composite in shale, both of which materials are considered as macroscopically anisotropic. Figures 6-6a and c show the packing density scaling relations of indentation modulus M obtained from nanoindentation in orthogonal directions (x_1, x_3). Isotropic elastic properties are observed for apatite, whereas the porous clay in shale shows a marked anisotropic response. Figures 6-6b and d show the packing density distributions for the two materials inferred from indentation analysis in the two orthogonal directions. Apatite exhibits dissimilar packing density distributions for the two orthogonal directions. The porous clay composite of shale shows instead similar packing distributions. The finding that packing density distributions for the clay fabric are almost identical in orthogonal directions, as observed in Figure 6-6d hints towards an intrinsic anisotropy of the clay solid and an isotropic packing of particles, and thus an isotropic morphology sensed by nanoindentation, which contrasts the structural anisotropy observed for bone specimens, which exhibited different packing distributions in orthogonal directions.

The previous arguments highlight the apparent second-order effect of the particle shape in the nanomechanics of the clay fabric as sensed by instrumented indentation, compared to the first-order importance of the intrinsic elasticity of the clay phase. Mechanically, the role of particle shape is better understood by the overall behavior of clay conglomerates with high local alignment. The consideration of the elementary unit of clay as a spherical shape in a micromechanical morphology representation, which is able to replicate the percolation threshold behavior of $\eta_0 = 0.5$ inferred from nanoindentation, effectively reveals that particle-to-particle forces are transmitted over randomly oriented particle-to-particle contact surfaces. This gran-

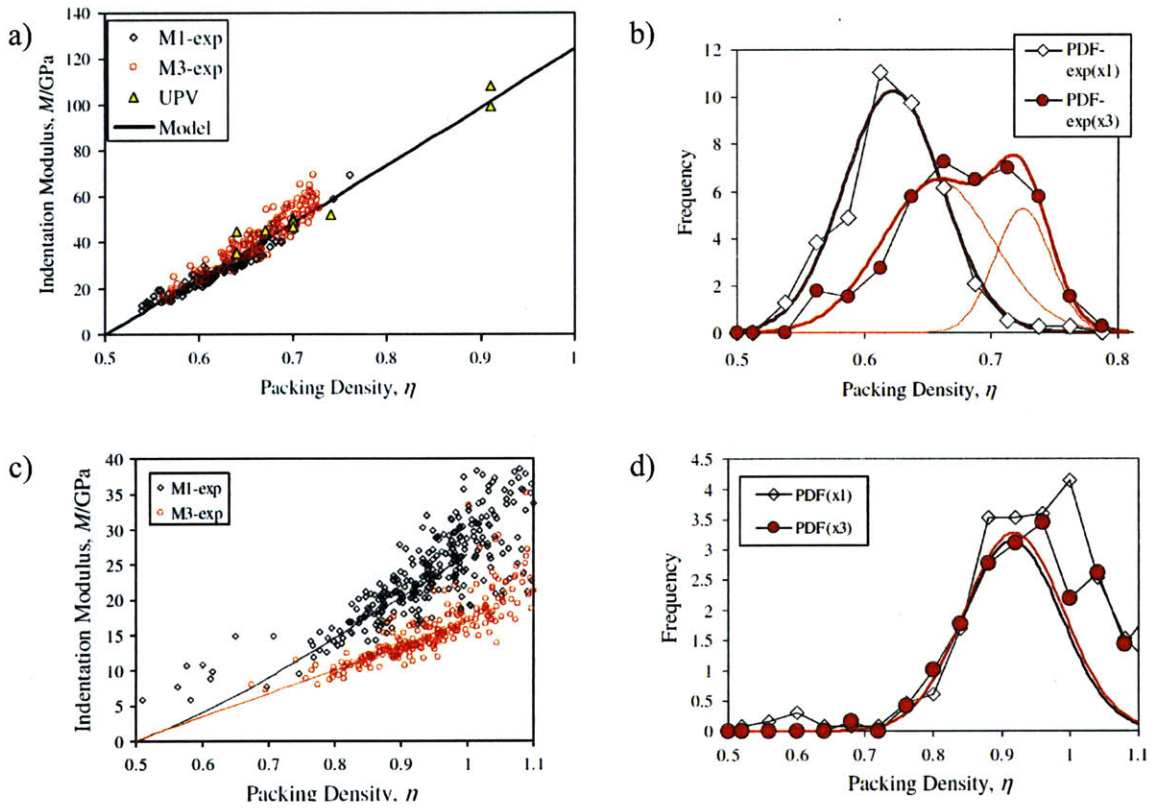

Figure 6-6: Indentation analysis for apatite mineral particle in anorganic bone (a-b) and the porous clay phase in shale (c-d). Packing density scaling relations of indentation modulus M in orthogonal directions (x_1, x_3) are displayed in (a,c). Probability density functions (PDF) of packing density are displayed in (b,d). Adapted from [270].

ular behavior is directly linked to the implementation of the self-consistent scheme in our modeling framework. Figure 6-7 displays and summarizes the conceptual framework for effectively modeling the microstructure and anisotropic elasticity of the porous clay in shale.

6.4 Domain of Model Application at Macroscopic Scales - Predictions at Level 2

The thorough comparisons between experimental measurements and model predictions at multiple length scales validate the use of the micromechanical model of shale as a tool for linking material composition (synthesized into volumetric parameters) to acoustic properties. In what follows, we explore the predictive capabilities of the engineering model through a detailed graphical representation of its domain of application. The resulting isoparametric plots delineate the acoustic signature of shale as function of the two model input parameters: the clay packing density and the inclusion volume fraction. The elastic anisotropy of shale, quantified in terms of Thomsen parameters, is also investigated using model results. The review of the macroscopic model predictions provides a context for later discussing important aspects of the use of the micromechanics model as a tool for engineering applications. The effects of frequency and pressure conditions on the predictions of acoustic properties, as well as the links between confining pressure, intrinsic anisotropy, and stress-induced anisotropy are presented. This series of discussions will help establish the domain of application and effectiveness of the model as an engineering tool for predicting the baseline anisotropic poroelasticity of shale rocks.

6.4.1 Isoparametric Plots for Acoustic Velocity Predictions

In this section, the engineering model for shale poroelasticity is examined through the display of predictions of acoustic velocities in the form of dimensionless isoparametric plots to visualize the wave velocity behaviors at the macroscopic scale in terms of the model input parameters. Figures 6-8 and 6-9 display the predicted compressional (V_P) and shear (V_S) velocities for the normal-to-bedding (x_3) and parallel-to-bedding (x_1, x_2) directions, respectively. For each plot, a form of the specific wave propagation velocity normalized by the corresponding velocity through the solid clay phase and a ratio of mass densities is displayed as a function of the

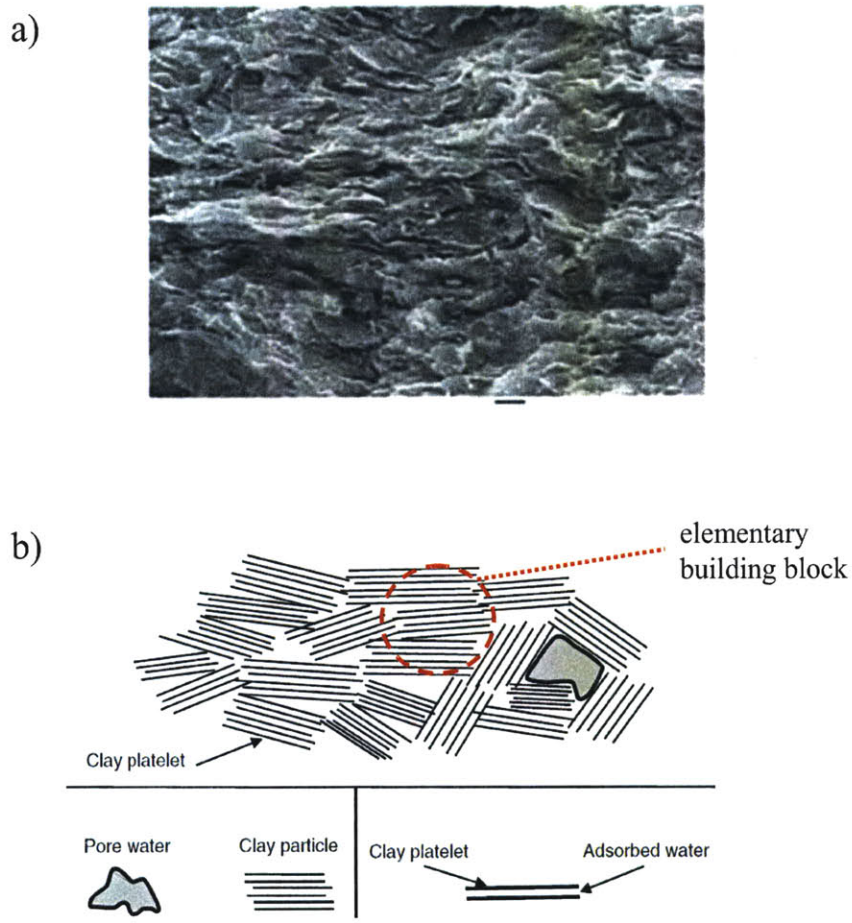

Figure 6-7: a) SEM image of shale G2IC-03, displaying the complex clay fabric in shale. Adapted from [267] b) Multi-scale illustration of the micro-, meso-, and macroscale of shale. Adapted from [227]. The groupings of clay particles, or clay domains, could be represented through the concept of an elementary building block of solid clay. The intrinsic elasticity is the result of the local degree of alignment. The spherical morphology recognizes, in a micro-mechanics framework, the randomness of the orientation of contact surfaces between particles and particle domains.

clay packing density for fixed values of inclusion volume fraction. The isoparametric curves are presented for inclusion volume fraction values ranging from $f^{inc} = 0$ (the case of no silt inclusions present in the shale material, i.e. the porous clay composite) to $f^{inc} = 1.0$ (the case of a pure silt solid). The saturating fluid used for the construction of the isoparametric plots was water, with a bulk modulus $k^{fl} = 2.3$ GPa. By way of example, the isoparametric curve corresponding to $f^{inc} = 0$ is described hereafter to highlight the effects of the nanogranular nature of shale on the acoustic properties. Below the percolation threshold of $\eta_0 = 0.5$, which relates to the absence of a continuous force path in the granular clay ensemble, the mechanical behavior is dictated by the response of the fluid saturating the pore domain. This is clearly observed by the hydraulic stiffening present in the compressional wave behavior, but it does not affect the shear wave propagation. For clay packing densities above the percolation threshold, a monotonically increasing, non-linear scaling is observed for both compressional and shear waves. The addition of (stiffer) silt inclusions increases the magnitude of acoustic velocities, tending to the maximum value of wave propagation in pure quartz (the case of $f^{inc} = 1.0$).

For all isoparametric plots displayed in Figures 6-8 and 6-9, the UPV experimental data for kerogen-free shales compiled in the CDS, VDS-1, and VDS-2 data sets have been superimposed to the model prediction curves to visualize the predictive coverage of the model. It is worth noticing that isoparametric plots such as those presented in Figures 6-8 and 6-9 could be generated for any direction of wave propagation, provided the identification of the angle of inclination from the bedding plane (i.e. information about angle θ, see Section 3.7.3). Having validated the predictive accuracy of the microporomechanics model, the isoparametric plots of acoustic velocities become useful tools for the seismic characterization of shale materials using strictly material composition information; and vice versa: velocities could be used to infer the rock composition (only in terms of clay type and non-clay (silt) type minerals).

6.4.2 Shale Anisotropic Behavior

Using the model results developed for constructing the isoparametric plots of acoustic velocities, the anisotropic seismic behavior of shale materials is now explored. The quantitative measures of anisotropy are the well-known Thomsen parameters (see expressions 3.68a, b, c). Figure 6-10 displays the model predictions for the P-wave anisotropy (ε), the S-wave anisotropy (γ), and the

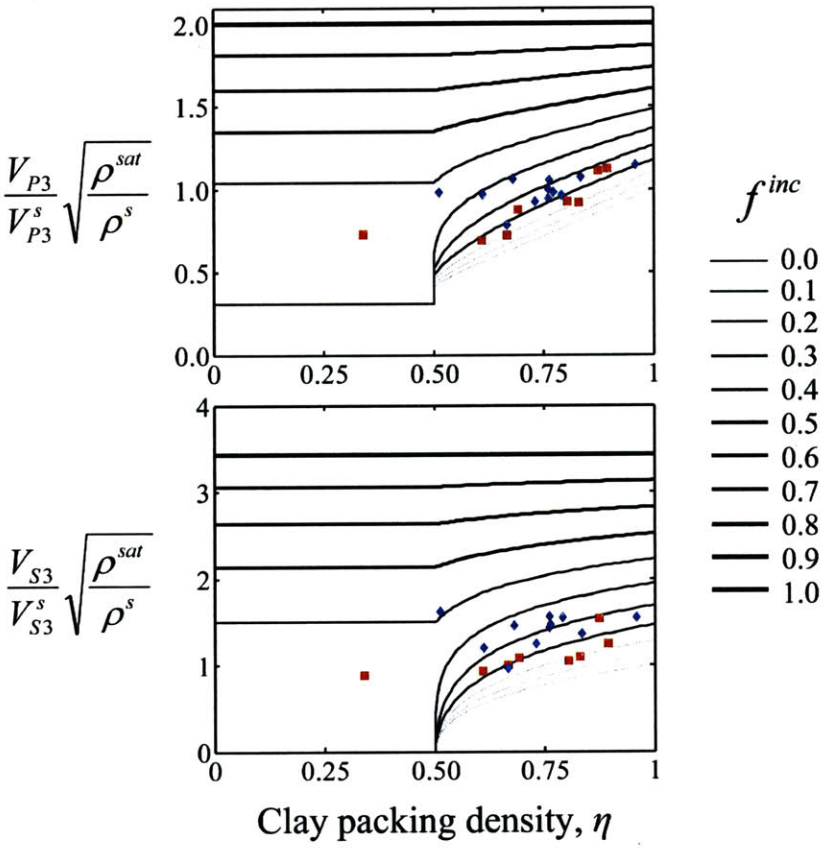

Figure 6-8: Isoparametric curves for compressional (V_P) and shear (V_S) acoustic wave velocity predictions in the normal-to-bedding direction. Squares correspond to the data from the CDS data set. Diamonds correspond to the VDS-1 and VDS-2 data sets. Experimental data has been plotted based on the calculated mean clay packing densities and measured wave velocity values.

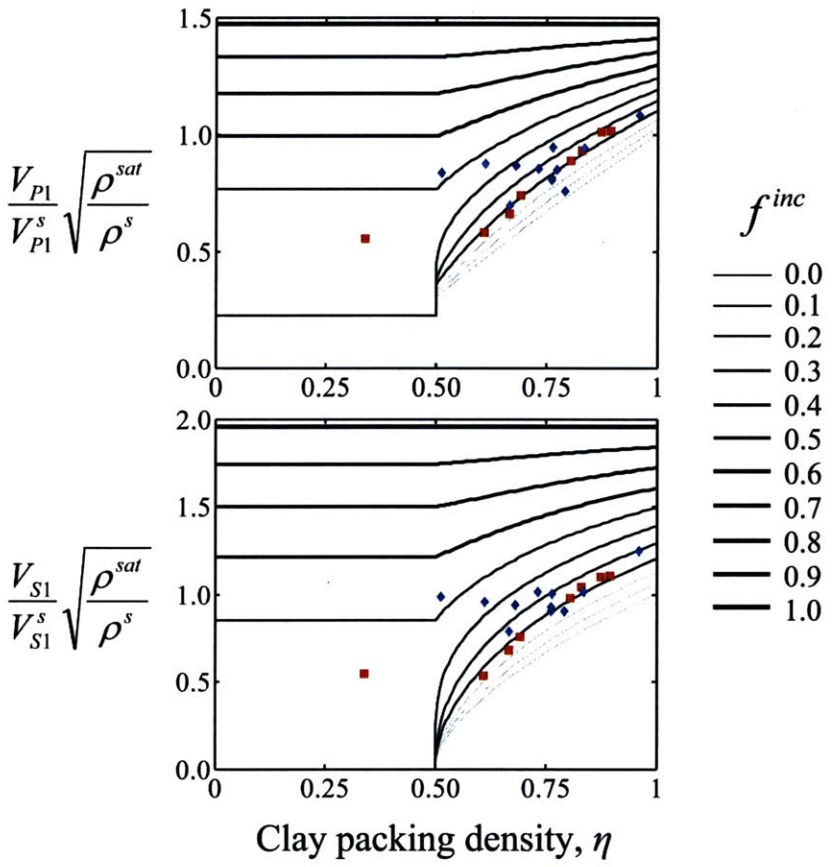

Figure 6-9: Isoparametric curves for compressional (V_P) and shear (V_S) acoustic wave velocity predictions in the parallel-to-bedding direction. Squares correspond to the data from the CDS data set. Diamonds correspond to the VDS-1 and VDS-2 data sets. Experimental data has been plotted based on the calculated mean clay packing densities and measured wave velocity values.

δ^* parameters as functions of clay packing density η. Each Thomsen parameter–clay packing density curve is plotted for a fixed value of inclusion volume fraction f^{inc}. The largest shale seismic anisotropies for all Thomsen parameters are clearly those for the case of the porous clay composite alone ($f^{inc} = 0$). In particular, the maximum anisotropy corresponds to that of the compacted clay, which is found for the asymptotic case of clay packing density equal to unity. As the clay packing density decreases (porosity increases), the seismic anisotropy is reduced. No anisotropy (i.e. $\varepsilon = \gamma = \delta^* = 0$) is observed below the percolation threshold $\eta_0 = 0.5$, irrespective of the silt inclusion volume. This behavior results from the uniform hydraulic stiffening provided by the fluid saturating the pore space and the (assumed) isotropic stiffness of the silt inclusions. Finally, the increase in silt inclusion volume fraction decreases the seismic anisotropy for all Thomsen parameters for clay packing densities above the percolation threshold.

The elastic anisotropy trend of decreasing anisotropy with increasing porosity is consistent with experimental observations of elastic anisotropy across shale specimens of different origin, porosity, and mineralogy composition [146, 277, 284]. It is worth noticing that those trends for shale were inferred based on total porosity information. In contrast, some authors have reported an opposite trend for anisotropy-porosity inferred from deformation experiments on shale . Higher confining pressures applied in the experiments have been related to reduced elastic anisotropies caused by a type of porosity that is pressure-sensitive. The so-called crack or soft porosity tends to close with increasing pressures. Although the trend of decreasing anisotropy with increasing confining pressures was clearly observed in [227], with anisotropy reductions at high pressures of half of the initial values, other authors have reported lesser amounts of reduction in anisotropy or even mixed trends in the relations of anisotropy and confining pressure [77, 138, 145]. The quantification of differences between structural anisotropy (due to the presence of crack porosity, which is typically only a very small fraction of the total porosity), and intrinsic anisotropy (under the assumption of complete closure of cracks at high pressures) in shale will require further investigation.

In addition to the model predictions, the experimental data on Thomsen parameters for the shale specimens from the CDS, VDS-1, and VDS-2, are displayed in Figure 6-10. In general, the microporomechanics model captures the main trends of elastic anisotropy for shale mate-

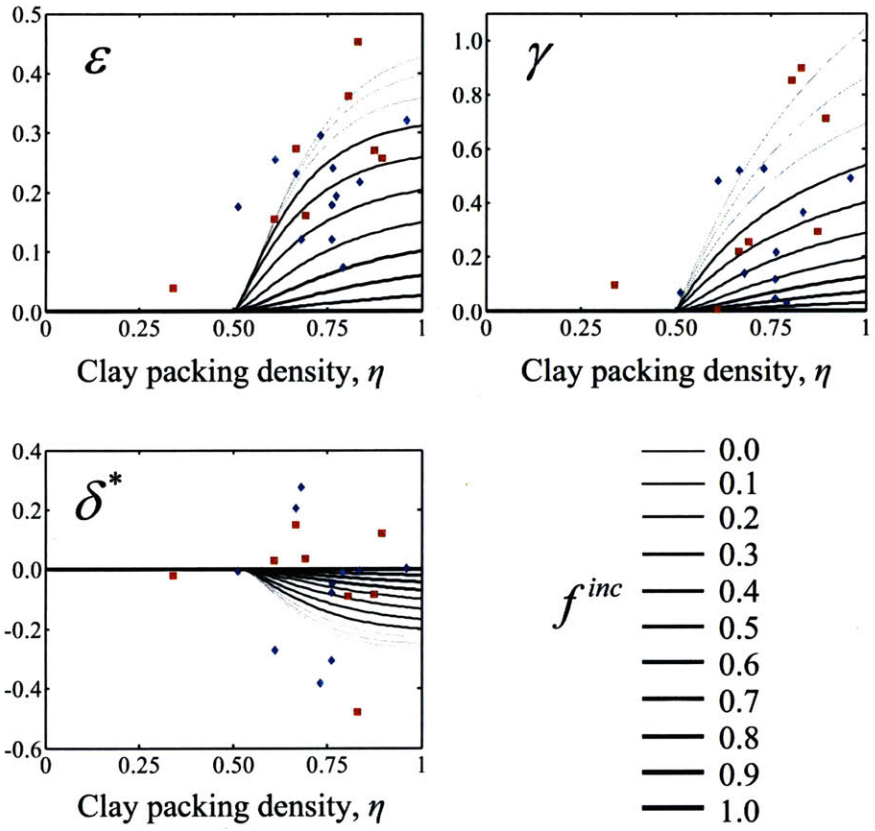

Figure 6-10: Model predictions of Thomsen parameters as functions of clay packing density for various fixed values of inclusion volume fraction. Squares correspond to the data from the CDS data set. Diamonds correspond to the VDS-1 and VDS-2 data sets. Each Thomsen parameter value corresponds to the average of two estimates, which are related to the minimum and maximum confining pressure conditions used for testing (if applicable). The variability of Thomsen parameters due to the effect of different confining pressures is relatively small for most shale specimens included in this study.

rials. For P-wave and S-wave anisotropies, the model covers the majority of the experimental values of Thomsen parameters. For the δ^*-parameter, the variability of experimentally measured values is significant, and the model can only predict a fraction of the observed range of δ^* anisotropies. The micromechanical model, as observed in Figure 6-10, predicts negative δ^* values for all clay packing density and inclusion volume fraction values. These results originate as a consequence of the particular stiffness properties of the compacted clay $\mathbb{C}^s$, especially the value for C_{13}^s. Experimental data has shown that shale materials indeed show positive and negative δ^* values, which also applies to the weak-anisotropy estimate of δ^* [256]. These experimental results have received significant attention from the geophysics community [229]; although, a conclusive understanding of the origins of δ^* anisotropy and correlations to shale's mineralogy or microstructure are still topics of ongoing debate. Moreover, the inherent difficulties and uncertainties in the determination of the elastic constant C_{13}, resulting from standard practices in the inversion of elasticity data from laboratory measurements [129], strongly affect the accuracy of measured C_{13} values and the derived Thomsen parameter δ^* values. Nevertheless, the contribution of the micromechanics model to the still open debate is that the intrinsic anisotropic elasticity of the in situ clay is not at the origin of positive δ^* values. Thus, positive δ^* values and the experimental data of ε and γ situated outside the modeling curves may originate from other sources of anisotropy that may well be structural such as the presence of microcracks [227, 257, 277], the existence of specific compliance conditions at contacts between clay particles, and the misalignment of clay particles [230].

6.4.3 Pressure Dependency of Shale Acoustic Properties

In addition to the previously discussed effect of stress-induced anisotropy, the magnitude of the acoustic properties of rocks is also affected by the imposed stress state or pressure condition. Figure 3-21 already showed the dependency of the measured elastic constants for shale G2IC-03 on the confining pressure state, whose general trend of increasing elasticity (inferred from the measured acoustic velocities) with increasing pressure is generally observed in the seismic assessment of reservoir rocks such as shale and sandstone. This well-known mechanics effect has been the focus of theoretical modeling for non-linear elasticity, in which higher-order constants must be defined and calibrated in order to capture the elasticity - confining pressure dependency

[296, 297]. The engineering model for shale, being rooted in linear microporomechanics theory, does not consider explicitly the link between acoustic property predictions and a prevailing stress state in the material. In a first approach, the development of the model through the calibration and validation exercises presented in Chapter 5 has been conducted considering for each shale sample its entire range of acoustic properties as function of pressure condition. That is, the comparisons between model predictions have involved the minimum and maximum values of acoustic/elastic properties, as displayed in Figure 5-10. The presented vertical error bars for experimental UPV data are directly related to the confining pressures used during testing: typically smaller acoustic property values correspond to lower confining pressure conditions, whereas higher acoustic property values correspond to higher pressures[4]. The convention of comparing model predictions and average acoustic properties from minimum and maximum pressure conditions was adopted in view of the variability in experimental setups used for the deformation experiments and related data considered in this study, as well as the diversity in shale samples with different origins and burial depths. From the results presented in figures such as Figure 5-10, it was observed that the magnitude of the pressure dependency of UPV properties was of similar or second-order compared to the range of modeled acoustic predictions, whose variability is caused by the estimation of the input parameters, namely the clay packing density and the inclusion volume fraction. Nevertheless, a refined discussion about the effect of pressure on model predictions is presented hereafter.

Since the engineering model is based on linear micromechanics, the link between pressure dependency of acoustic properties and model predictions is the definition of the stiffness properties of the solid clay phase, represented by the elementary building block at level 0 with stiffness tensor $\mathbb{C}^s$. The calibration of the C^s_{ij} elasticity constants, as presented in Chapter 5, involved the use of the calibration data set (CDS), which compiles the shale data on a series of samples provided by the G2IC. In addition to being a consistent set of data (e.g. the difference in clay packing density and inclusion volume fraction estimates are smaller than 5% on average), the shale samples were assumed to be representative of a diverse spectrum of shale properties. Furthermore, the stress states used for UPV testing of these materials should be representative

[4]In some cases, certain elastic constants such as C_{13} might exhibit a different behavior, in which higher magnitudes of stress result in lower acoustic properties. This opposite type of trend is rare, and only found in a few instances throughout the entire database of acoustic shale properties.

of their in situ conditions[5]. As a result, the calibration of the engineering model ensures, at least implicitly, that the clay phase properties are representative of shale for in situ conditions. This assertion is corroborated using the data presented in the studies of Hornby [129], Jakobsen and Johansen [138], and Sarout and Guéguen [226]. In these studies, the assessment of in situ stress conditions has been explicitly documented.

Jakobsen and Johansen [138] simulated in situ stress conditions in their UPV experiments using horizontal and vertical stress components of $\sigma_{11} = 13$ MPa, and $\sigma_{33} = 20$ MPa, respectively. Sarout and Guéguen [226] estimated an in situ hydrostatic stress using depth information of 15 MPa[6]. Using a similar approach, the in situ hydrostatic stress for the Kimmeridge shale sample tested by Hornby [129] correlates well with the maximum confining pressure of 80 MPa used during UPV testing. Based on these specific stress states, Table 6.1 shows the calculations for the relative errors between measured acoustic properties at specific pressure conditions (minimum, mean, maximum, and in situ) and model predictions. The acoustic properties associated with the mean pressure condition correspond to the arithmetic mean of those measured at the minimum and maximum pressures, and it has been used throughout this report for model comparisons. The relative errors were calculated using the five conventionally reported acoustic velocities (V_{P1}, V_{S1}, V_{P3}, V_{S3}, V_{qP45}) for each individual shale sample. With the exception of samples 3506 and 3536, the comparisons between model predictions and acoustic properties measured at in situ stress conditions yield the most optimal values. For the data of Hornby [129] and Jakobsen and Johansen [138], the in situ stress corresponds to the maximum stress condition used during testing. For Sarout and Guéguen [226], the comparison with mean acoustic properties relates well to that with in situ stress conditions.

The results presented in Table 6.1 support the value of the engineering model as a predictive tool for acoustic properties for shale under in situ conditions. This characteristic of the model could explain, for example, the overestimation of acoustic properties of the Cretaceous shale measured by Jones and Wang [146] and displayed in Figure 5-11. The set of acoustic properties for this shale sample was measured at very low confining pressure (0.1 MPa), which does not

[5] As it was already mentioned in this report, data originated from the G2IC consortium is sensitive to proprietary restrictions.

[6] The authors recognize that the assumption of hydrostatic overburden stress neglects any deviatoric stress contributions due to tectonic stress build-up.

Reference	Sample	Mean relative error [%]			
		Min	Mean	Max	In situ
[129]	KIM	9	3	-2	-2
[138]	3492	23	17	13	13
	3506	3	-1	-5	-5
	3525	6	1	-4	-4
	3536	-11	-13	-15	-15
	3564	22	17	13	13
[226]	CO	10	3	-3	2

Table 6.1: Comparisons between measured and predicted UPV elasticity for specific shale samples. The terms min, mean, max, and in situ correspond to the type of UPV data used for the comparison as they are to different pressure conditions. The mean relative errors for each pressure condition (min, mean, max, in situ) were calculated using the individual relative errors of velocity components V_{P1}, V_{S1}, V_{P3}, V_{S3}, V_{qP45} corresponding to each shale sample.

replicate the stress conditions of a rock sample retrieved from a 1.5 km depth.

Clearly, the intended application of the model for assessment of in situ elasticity will require further refinements, as in situ conditions could be sometimes difficult to characterize in field applications and to replicate field conditions for laboratory setups [77, 129]. Furthermore, the relations of pressure sensitivity due to crack or microfracture closure are not part of our modeling framework for shale as unfractured media. In its present form, the proposed engineering model captures the elastic anisotropy of shale resulting from geologic compaction and burial, in which case the stress states of the rock define the resulting mineralogy and porosity configuration.

6.4.4 Effect of Frequency on Acoustic Predictions

Velocity dispersion, a daunting aspect of geophysics, is a generally accepted cause for the variation of measured acoustic velocities with frequency in fluid-saturated rocks . This phenomenon is known to affect the three frequency bands of interest in exploration geophysics: seismic (10-100 Hz), sonic (1-10 kHz), and ultrasonic (0.1-1 MHz) [292]. An assessment of the effects of frequency on the accuracy of acoustic properties of shale is presented in this section. Having gained a thorough understanding of the poroelastic drained and undrained responses of shale through micromechanics (Section 6.1), the assessment of frequency effects on seismic and ultrasonic velocities is necessary, especially in view of the potential implementation of our engineering model predictions of undrained elasticity for laboratory and field applications.

Velocity dispersion in fluid-saturated rocks is attributed to several mechanisms, each of which can dominate depending on the conditions of frequency, strain amplitude, and saturation [293]. Frictional mechanisms, related to the sliding between grains, are associated with the dependency of velocities on strain amplitudes, and are of significance in the near field of seismic sources (e.g. earthquakes, explosions), where large strain amplitudes are present. Acoustic scattering occurs in heterogeneous materials, in which the acoustic wavelengths are of similar characteristic length scale as the material heterogeneities. The acoustic scattering reduces the velocity of the primary pulse, which results in a velocity reduction with increasing frequency. However, the effect in fluid-saturated rocks has not been clearly observed due to competing fluid-flow effects. These fluid flow mechanics appear to dominate the dispersion phenomena in rock at various scales: Biot-type dispersion at the macroscopic flow scale, and local-flow dispersion at the grain scale.

The macroscopic flow, or Biot mechanism [26], corresponds to the response of the solid frame 'dragging' the pore fluid during wave propagation. At low frequencies, the viscous skin depth is much larger than the characteristic pore size, and the solid-fluid composite behaves as a 'locked' system [291]. The poroelasticity theory of Biot for low frequencies corresponds to the expressions presented earlier by Gassmann [97], which allow the rigorous computation of undrained properties of a fluid-saturated composite from the properties of the dry frame and the fluid (see Section 4.4.3). In contrast, the viscous skin depth is small for high frequencies, causing the fluid to lag behind the response of the solid frame due to inertial effects. The result of the Biot mechanism is the increase of acoustic velocity with increasing frequency. Another dispersion effect due to fluid flow is the so-called local-flow. In this case, the heterogeneous nature of the pore space in rock causes the material system to respond unevenly during wave propagation. Pore pressure gradients are formed due to the low induced pressures in the so-called stiff pores (or equant porosity) compared to the high induced pressures in compliant pores (or crack-like porosity) upon wave compression. The generation of pore pressure gradients causes the rock to display a stiffer response at high frequencies, compared to the instance of low frequencies in which pore pressures are assumed equilibrated (see e.g. [87, 173, 174, 197]). The contribution of local-flow to the overall dispersion is significant at low pressure states, and it drastically decreases to almost Biot-type dispersion levels at high frequencies [291].

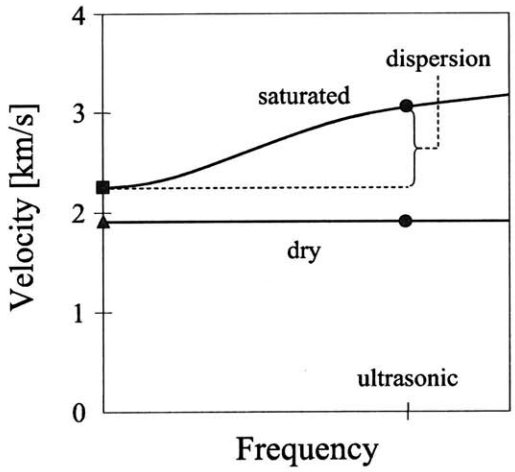

Figure 6-11: Schematic of the compressional wave velocity V_P as a function of frequency for a typical sandstone. Velocity in dry rock is generally assumed to be unaffected by dispersion. Dot-like data points correspond to ultrasonic laboratory measurements. The triangle-like data point corresponds to the extrapolated low frequency dry velocity. The square-like data point represents the velocity in saturated rock calculated dry rock velocity and zero-frequency theory. The total dispersion in saturated rock refers to the fractional increase of the high-frequency velocity compared the low-frequency velocity. Adapted from Winkler [292].

Figure 6-11 shows a schematic of the velocity dispersion phenomena as a function of frequency. The figure illustrates the total velocity dispersion attributed to flow dispersion mechanisms that is expected from extensive measurements on sandstones. From testing of many reservoir rocks, especially sandstone and granite, velocity measurements carried out at ultrasonic frequencies tend to be higher than velocities measured at seismic frequencies (see e.g. [152, 191, 292]) as expected due to the velocity dispersion across frequency bands. Furthermore, the frequency effects incorporated in Biot's theory do not account for the overall dispersion in rocks [285], and hence the theory of local-flow adequately complements the explanations of the observed acoustic behaviors. Interestingly, most of the knowledge of the velocity dispersion effect has been derived from measurements and analyses of sandstone rocks. In geophysics practice, the low-frequency Biot theory or equivalently Gassmann results are applicable only for seismic data for high-porosity, high-permeability rocks saturated with low viscosity fluids. For low-porosity, and low-permeability rocks, measured data at seismic frequencies are assumed to be similar to laboratory data [282].

Reference	Liu [165]	Sarout et al. [227]
Porosity, ϕ_0 [1]	0.04	0.10
Fluid viscosity, ν [Pa·s]	1×10^{-3}	1×10^{-3}
Fluid density, ρ^{fl} [kg/m^3]	1×10^{3}	1×10^{3}
Rock permeability, κ [m^2]	1×10^{-20}	$1 \times 10^{-21} - 100 \times 10^{-21}$
Biot-type frequency, f_{BIOT} [GHz]	6×10^{2}	$2 \times 10^{2} - 2 \times 10^{4}$

Table 6.2: Estimates of the Biot-type frequency for data gathered from the open literature of shale.

Given the different nature of shale as a sedimentary rock with low permeability and low porosity, an assessment of the effects of frequency on acoustic properties is due at this point. For this, we consider the differentiation between the practical limit between (relative) low and high frequencies. Focusing first on the Biot-type dispersion mechanism, the characteristic frequency separating low and high frequencies is [26]:

$$f_{\text{BIOT}} = \frac{\phi_0 \nu}{2\pi \rho^{fl} \kappa} \tag{6.5}$$

where ϕ_0 is the porosity, ν the fluid viscosity, ρ^{fl} the density of the pore fluid, and κ the rock permeability. Two estimates of (6.5) are calculated using data obtained from the open literature of shale. The first study corresponds to Liu [165], who compiled shale data for several shale materials from different formations. The second study of Sarout et al. [227] of the dynamic properties of Callovo-Oxfordian shale is similar to the one considered in this thesis (specimen CO [226], see Table 3.1). The data presented in these studies and the calculated characteristic Biot dispersion frequency are displayed in Table 6.2.

The calculated frequency is significantly larger than the frequency used for UPV experiments, typically carried out in the MHz range. The high value is directly related to the high permeability of shale, compared to other sedimentary rocks (see Figure 2-4).

A similar computation for the local-flow mechanism proves to be challenging. The characteristic frequency for local-flow requires estimating the squirt-flow length R [87]:

$$f_{\text{local-flow}} = \frac{\kappa F}{2\pi \nu \phi_0 R^2} \tag{6.6}$$

where:

$$F = \left(\frac{1}{k^{fl}} + \frac{1}{\phi_0 Q}\right)^{-1} \tag{6.7a}$$

$$Q = \frac{k_s}{1 - \phi_0 - k/k_s} \tag{6.7b}$$

are functions of the fluid bulk modulus k^{fl}, the solid (mineral) bulk modulus k^s, and the drained rock modulus k. Fortunately, Liu [165] offered a first order estimate of the characteristic dimension of the local flow length, $R = 100$ μm. Together with some rock and fluid properties ($k^{fl} = 2.3$ GPa, $k^s = 33$ GPa, $k = 28$ GPa), Liu reported an estimate for the local-flow frequency of $f_{\text{local-flow}} = 5$ Hz. For a squirt-type of dispersion mechanism, which is an equivalent assessment of the dispersion at the grain-scale, the assessment of the pore (crack) aspect ratio is necessary to establish the characteristic frequency [175, 197]:

$$f_{\text{squirt}} = \frac{k^s X^3}{\nu} \tag{6.8}$$

where X the pore aspect ratio. For a characteristic microcrack in shale $X = 1 \times 10^{-3}$, the squirt-flow frequency given by Liu [165] is $f_{\text{squirt}} = 33$ kHz. To summarize the calculations for characteristic dispersion frequencies, Figure 6-12 displays a schematic of the estimates for Biot and local-flow dispersion regimes with a focus on the different frequency bands of interest for geophysics applications.

Although the proposed estimates are only rough approximations given the complexity of shale rocks, the results in Figure 6-12 offer some insight into the applications of the engineering model for shale for laboratory and field applications. Figure 6-12 suggests that sonic log data and ultrasonic measurements in laboratory conditions might yield similar acoustic estimates without the necessity of frequency-dispersion corrections. However, the preliminary assessment presented in Figure 6-12 also suggests that local-flow dispersion may affect acoustic properties of shale across all frequency bands of interest, including that of UPV testing. As a result, the implementation of undrained poroelasticity theory to predict ultrasonic acoustic velocities, which is perfectly fit for shale because of the high-frequency dispersion threshold at the GHz range, may still be linked to velocity dispersion due to local flow.

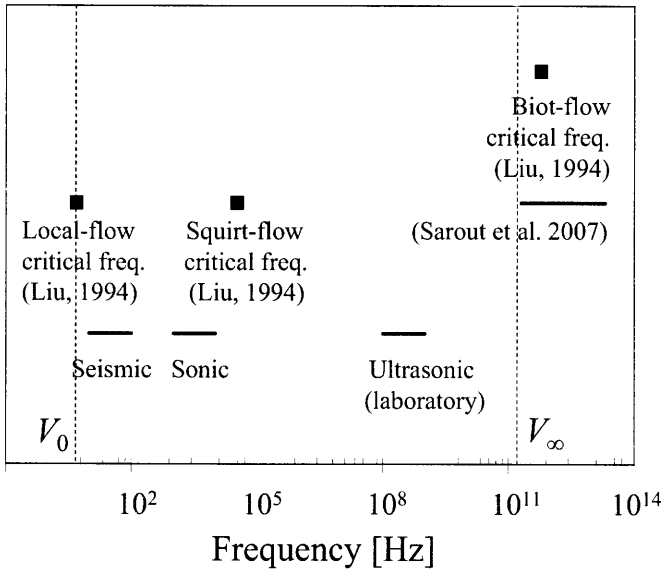

Figure 6-12: Schematic of the frequency range for the three frequency bands of interest in geophysics applications. The results for velocity thresholds corresponding to the low (V_0) and high (V_∞) frequencies estimated for shale are also displayed. The estimates correspond to data from [165, 227].

Certainly, the engineering micromechanics model for shale herein proposed considers shale as an uncracked medium. Consequently, the analysis of the anisotropic response of shale is entirely based on the properties of shale's microstructure and intrinsic elastic properties, and any effects of crack-like porosity or fractures are not included. This precludes the use of any additional theoretical tools that could incorporate corrections for local-flow dispersion. In fact, local-flow models are recognized to be of poorly predictive capabilities because they are extremely dependent on microstructural features that are difficult to quantify [283, 293]. Nevertheless, it is certainly important to quantify the expected dispersion effects of velocity prediction based on our (zero frequency) undrained poroelasticity.

The task of quantifying the true magnitude of dispersion that might affect our model predictions is a challenging task. Fortunately, its magnitude in relation to acoustic measurements of shale could be of second-order importance given the typically significant magnitude of in situ states of stress, which are also emulated in laboratory testing. Although dispersion analysis is still lacking for shale materials, data for other reservoir rocks shows that dispersion between zero and ultrasonic frequencies is on the order of 10% at low confining stresses, and tends to only a few percent at higher stresses [292]. Another component of the dispersion phenomenon is the type of fluid saturating the specific rock. Oil saturated rocks exhibit significantly more dispersion compared to brine-saturated, which is the case of most shales considered in this study [291]. The effects of high confining pressures and low-viscosity saturating fluids relate well to the shale data sets used for model development, for which most specimens are saturated by low-viscosity fluids, and tested at effective stresses typically larger than 10 MPa. In order to verify these arguments, Figure 6-13 displays the velocity predictions for the data of Sarout and Guéguen [226] for dry and wet shale specimens. Among all shale literature references, this particular one presents one of the most complete and rigorous experimental programs on shale characterization.

The figure includes the cross-comparisons of measured and predicted drained and undrained acoustic properties for similar shale specimens. The drained case is of significance as acoustic properties of dry rocks are generally known to exhibit no dispersion [175, 292].

The model predicts very accurately the anisotropic acoustic properties for undrained conditions, as it was already noted in Section 5.3.4. The average relative error for the different

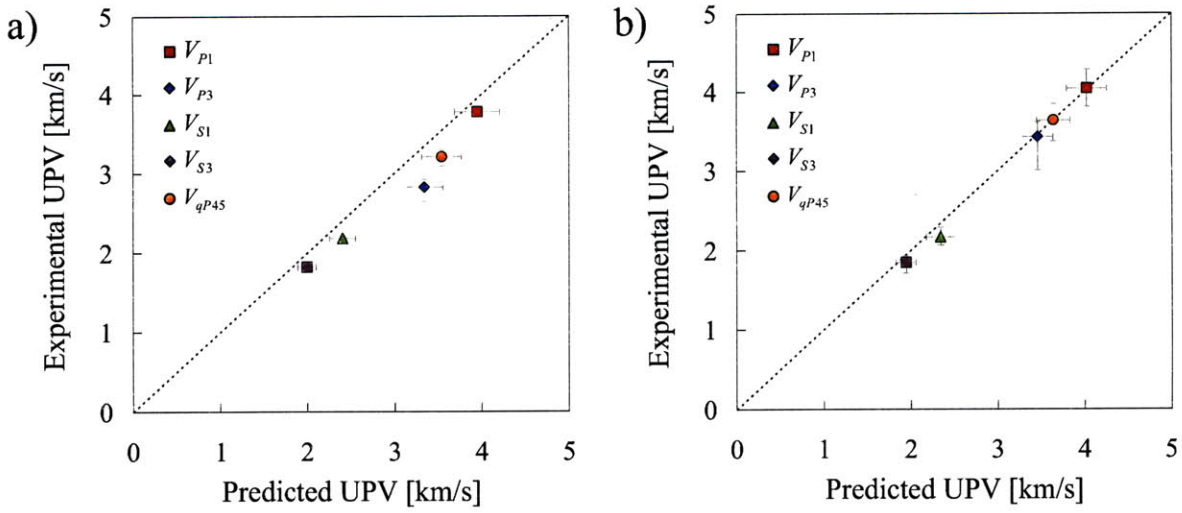

Figure 6-13: Comparisons between predicted and measured a) drained and b) undrained acoustic properties obtained from UPV testing [226].

compressional and shear wave velocities was found to be approximately 3%. The comparisons between measured and model predictions for drained (dry) conditions yield an average overprediction of 10%. Without more data available for directing a more rigorous verification, the results from Figure 6-13 could shed some light on the effects of dispersion on the predictions of acoustic properties. Provided that the model calibration efforts of section 5.2 were based on comparisons between undrained poroelastic predictions and UPV measurements, the consistent overprediction observed in Figure 6-13 is in line with the expected behavior as in Figure 6-11 if local-flow dispersion were to be present. The relative errors involved in this comparison are encouraging for the application of the engineering micromechanics model to predict sonic and ultrasonic wave velocities. However, caution must be necessary for potential implementations for field applications, in which issues related to poor consolidation, presence of gas phases, and most importantly, partial saturation conditions, could significantly alter the magnitude of the dispersion phenomena affecting the measured acoustic properties.

6.5 Prediction of Poroelastic Constants

The nanogranular behavior of shale has some important consequences on the poromechanical properties of shale materials at different scales. Poroelastic parameters defining the intrinsic behavior of the rock formation are critical input parameters to reservoir engineering and drilling applications [5, 6]. To illustrate their importance, it is good practice to combine the undrained form of Biot's state equation (4.115b) with the mass balance equation ($\partial m/\partial t = -\nabla \cdot \underline{w}$) and a Darcy fluid conduction law ($\underline{w}/\rho_0^{fl} = -\mathbf{k}/\eta^{fl} \cdot \nabla p$), which yields for the single fluid saturated case (see, for instance, [4]):

$$\frac{\partial p}{\partial t} = \mathcal{M}^J \left(-\boldsymbol{\alpha}^J : \frac{\partial \mathbf{E}}{\partial t} + \frac{\mathbf{k}^J}{\eta^{fl}} : \mathbf{H}(p) \right) \tag{6.9}$$

or equivalently, using (4.115a):

$$\frac{\partial p}{\partial t} = -\mathbf{B}^J : \frac{\partial \boldsymbol{\Sigma}}{\partial t} + \mathcal{M}^J \left(1 - \boldsymbol{\alpha}^J : \mathbf{B}^J\right) \frac{\mathbf{k}^J}{\eta^{fl}} : \mathbf{H}(p) \tag{6.10}$$

where $\mathbf{k}^J$ is the intrinsic permeability of the porous material (of dimension $\left[\mathbf{k}^J\right] = L^2$), η^{fl} is the dynamic viscosity of the fluid (of dimension $\left[\eta^{fl}\right] = L^{-1}MT^{-1}$), and $\mathbf{H}(p) = \nabla(\nabla p)$ is the Hessian function of the pressure p. These two classical relations of flow through (saturated) deformable porous media show the importance of the Biot pore pressure coefficients α_{ij}^J, and the Skempton coefficients B_{ij}^J. Due to the application of strain or stresses, the fluid pressure locally increases, which sets the fluid in motion until the fluid pressure is re-equilibrated. The focus of the next three sections is to shed light on the effect of the nanogranular nature of shales at two different scales on these two poroelastic properties and their combination in the term $\left(1 - \boldsymbol{\alpha}^J : \mathbf{B}^J\right)$, all of which affect the fluid flow through the highly anisotropic microstructure of shales.

6.5.1 Biot Pore Pressure Coefficients

The Biot pore pressure coefficient α is a key parameter in reservoir engineering and wellbore drilling applications, as it weighs the influence of pore pressures within the context of (elastic) effective stress analysis of rocks. Specifically, the Biot coefficient quantifies the compressibility

of the skeleton of the porous material with respect to its solid phase, and provides a sense of the overall compressibility of the rock structure [8]. In the isotropic case, the expression for this pore pressure coefficient was first obtained by Gassmann in 1951 [97] for the case of a micro-homogeneous porous media, and by Brown and Korringa in 1975 [45] and Rice and Cleary in 1976 [222] for general porous media with multiple minerals as constituents (see also [22, 236]):

$$\phi_0 \leq \alpha = 1 - \frac{K}{k^s} \leq 1 \tag{6.11}$$

where K is the drained bulk modulus of the porous material, and k^s is the bulk modulus of the solid phase. The generalization of the isotropic micromechanics relation (6.11) to general anisotropic two-phase solid-pore space composite materials is due to Dormieux et al. [54, 82, 83]; and it is used in our approach at level I of the porous clay composite, i.e. relation (4.85), which can be rewritten with the help of (4.79) in the form:

$$\varphi_0 \mathbf{1} \leq \boldsymbol{\alpha}^I = \mathbf{1} : \left(\mathbb{I} - \mathbb{S}^s : \mathbb{C}^I_{\text{hom}}\right) \leq \mathbf{1} \tag{6.12}$$

where $\varphi_0 = 1 - \eta$ is the nanoporosity of the porous clay phase. The lower bound of the pore pressure coefficient in (6.11) and (6.12) corresponds to the Voigt bound, whereas the upper bound corresponds to the case of a (generalized) incompressible solid phase, which forms the backbone of Terzaghi's soil mechanics theory. In the particular case of a transversely isotropic solid phase and a transversely isotropic porous clay phase with similar axis of symmetry (in this case x_3), the tensor of Biot coefficients reduces to a diagonal form $\boldsymbol{\alpha}^I = \text{diag}\left(\alpha^I_{11}, \alpha^I_{11}, \alpha^I_{33}\right)$, where $\alpha^I_{11} = \alpha^I_{22}$ is the pore pressure coefficient characterizing the in-bedding plane poromechanical coupling behavior, and α^I_{33} characterizes the normal-to-bedding behavior:

$$\alpha^I_{11} = 1 - \left(S^s_{11} + S^s_{12}\right)\left(C^I_{11} + C^I_{12}\right) - S^s_{13}\left(C^I_{11} + C^I_{12} + 2C^I_{13}\right) - S^s_{33}C^I_{13} \tag{6.13a}$$

$$\alpha^I_{33} = 1 - 2S^s_{11}C^I_{13} - 2S^s_{12}C^I_{13} - 2S^s_{13}\left(C^I_{13} + C^I_{33}\right) - S^s_{33}C^I_{33} \tag{6.13b}$$

where $S^s_{ij} = \left(C^s_{ij}\right)^{-1}$ are the components of the clay deposition compliance tensor, and $C^I_{ij} = C^I_{ij}(\eta)$ are the components of the porous clay stiffness tensor (4.79). In contrast to the isotropic expression (6.11), which is recovered from (6.13) in the form $\alpha^I_{11} = \alpha^I_{33} = \frac{1}{3}\text{tr}\,\boldsymbol{\alpha}^I = 1 -$

$(S^s_{11}+2S^s_{12})\,(C^I_{11}+2C^I_{12})$ for a micro- and macro- isotropic material, an experimental approach to the determination of the pore pressure coefficients of the transversely isotropic material would require the experimental determination of four components of C^I_{ij}. As an alternative, the micromechanics model provides a means to estimate $C^I_{ij}=C^I_{ij}(\eta)$ for any shale material from the sole knowledge of the clay packing density η, and to determine the Biot pore pressure coefficients as continuous functions $\alpha^I_{11}(\eta)$ and $\alpha^I_{33}(\eta)$ of this clay packing density. The result, which is displayed in Figure 6-14 as $\alpha_{ij}\left(\eta, f^{inc}=0\right)$, faithfully translates the polycrystal or granular structure of the porous clay phase into Biot pore pressure coefficients, with $\alpha^I_{11}=\alpha^I_{33}=1$ below the solid percolation threshold, $\eta<\eta_0=0.5$, for which $C^I_{ij}=0$; and $\alpha^I_{11}=\alpha^I_{33}=0$ for the asymptotic pure solid state, $\eta=1$. In between those asymptotic values, $\alpha^I_{11}(\eta)$ and $\alpha^I_{33}(\eta)$ follow unique scaling relations, with α^I_{11} being marginally greater in magnitude than α^I_{33} for the range of clay packing densities $0.5<\eta<1$. This quasi-isotropy of the Biot pore pressure coefficients can be explained by recognizing that although shale macroscopic anisotropy originates from the transversely isotropic nature of the elementary building block, the transverse isotropy (almost) cancels out in the tensor contraction $\mathbb{S}^s:\mathbb{C}^I_{\text{hom}}$ in (6.12). As a result, $\alpha^I_{11}(\eta)$ and $\alpha^I_{33}(\eta)$ take almost the same values in Figure 6-14. In fact, if $C^I_{ij}=C^I_{ij}(\eta)$ scaled perfectly linearly with the packing density, $\alpha^I_{11}(\eta)$ and $\alpha^I_{33}(\eta)$ would take exactly the same values. Indeed, using $\mathbb{C}^I_{\text{hom}}=(2\eta-1)\,\mathbb{C}^s$ for the range $0.5<\eta<1$ in (6.12) (which is a good first approximation), the corresponding tensor of Biot pore pressure coefficients is $\boldsymbol{\alpha}^I=2\varphi_0\mathbf{1}$.

Figure 6-14 also displays the macroscopic (level II) Biot pore pressure coefficients $\alpha^{II}_{11}\left(\eta, f^{inc}\right)$ and $\alpha^{II}_{33}\left(\eta, f^{inc}\right)$ determined from (4.107) in the form of isoparametric curves for various inclusion volume fraction values, as well as data points corresponding to shale-specific volume fractions defined in the CDS, VDS-1, and VDS-2 data sets. From the very definition (4.107) of $\boldsymbol{\alpha}^{II}$, it is readily understood that the macroscopic Biot coefficients are situated between the following bounds defined by the level I Biot coefficients:

$$\left(1-f^{inc}\right)\boldsymbol{\alpha}^I(\eta)\leq\boldsymbol{\alpha}^{II}\left(\eta,f^{inc}\right)\leq\boldsymbol{\alpha}^I(\eta) \tag{6.14}$$

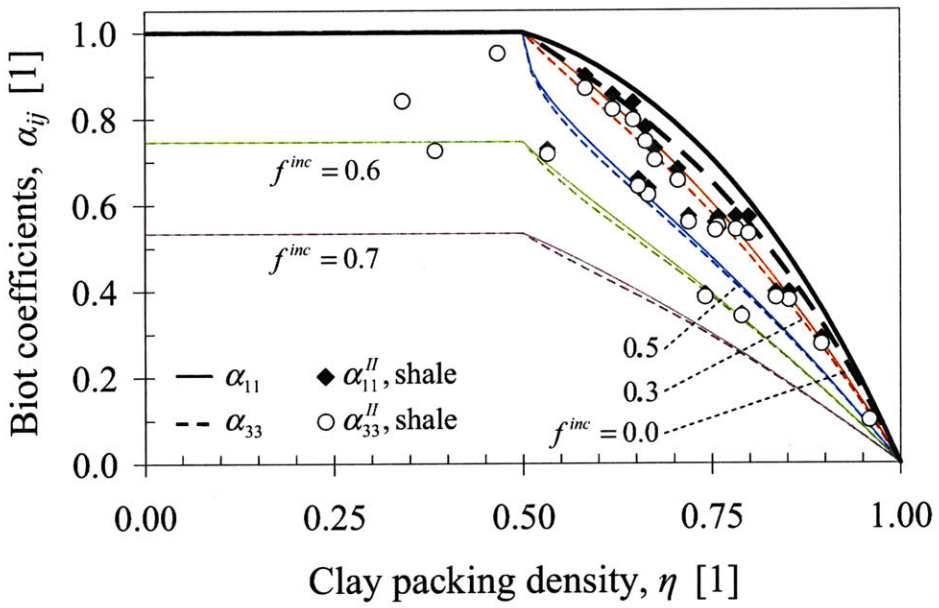

Figure 6-14: Model predictions of the Biot pore pressure coefficients α_{ij}, as continuous functions of clay packing density for level I ($f^{inc} = 0$) and level II ($f^{inc} > 0$). Data points correspond to the level II model predictions for shale-specific volume fractions defined in the CDS, VDS-1, and VDS-2 data sets. Clay packing density and inclusion volume fraction estimates for the shale data were obtained from mineralogy and bulk density information.

where f^{inc} is the (non-clay) inclusion volume fraction. Those bounds are confirmed in Figure 6-14: At the level of the porous clay–silt composite (level II), the pore pressure coefficients $\alpha_{11}^{II}, \alpha_{33}^{II}$ are all smaller in magnitude compared to those from level I due to the presence of the silt inclusions. Furthermore, the difference in magnitude between $\alpha_{11}^{II}\left(\eta, f^{inc}\right)$ and $\alpha_{33}^{II}\left(\eta, f^{inc}\right)$ is even smaller than the difference between $\alpha_{11}^{I}\left(\eta\right)$ and $\alpha_{33}^{I}\left(\eta\right)$, due to the isotropy of the added silt inclusions.

In summary, despite the pronounced anisotropy of shale macroscopic elasticity, there is some evidence that the macroscopic pore pressure sensitivity of shale is close to isotropic. That is, in a strain-driven drilling situation carried out under undrained conditions, the fluid pressure variation induced by strain (see expression (6.9)) is expected to be (almost) independent of the direction of strain application.

6.5.2 Skempton Coefficients

In contrast to the Biot pore pressure coefficient, which specifies the coupling between strain application and pore pressure variation, the Skempton coefficient (or Skempton's pore-pressure build-up parameter) specifies the link between stress application and pore pressure variation. Originally introduced by A.W. Skempton in 1954 [243], it is a common quantity employed in poroelasticity to quantify the pressure build-up under undrained conditions as a consequence of a macroscopic stress application (see, for instance, [24, 25, 70]). In the linear elastic isotropic undrained case, the Skempton coefficient quantifies the fraction of the macroscopic mean stress $\Sigma_m = \frac{1}{3}\mathrm{tr}\left(\boldsymbol{\Sigma}\right)$ carried by the fluid pressure, and is defined by [70]:

$$\mathrm{B_S} = -\frac{p}{\Sigma_m}|_{m=m_0} = \frac{M\alpha}{k^{un}} \tag{6.15}$$

where M is the overall Biot modulus, α the pore pressure coefficient, and $k^{un} = k + M\alpha^2$ the undrained bulk modulus of the porous material. In the general anisotropic case, the pore-pressure build up under undrained conditions is governed by the second-order tensor of Skempton coefficients (4.117) [118]:

$$\mathbf{B} = -p\boldsymbol{\Sigma}^{-1}|_{m=m_0} = M\mathbb{S}_{\mathrm{hom}}^{un} : \boldsymbol{\alpha} \tag{6.16}$$

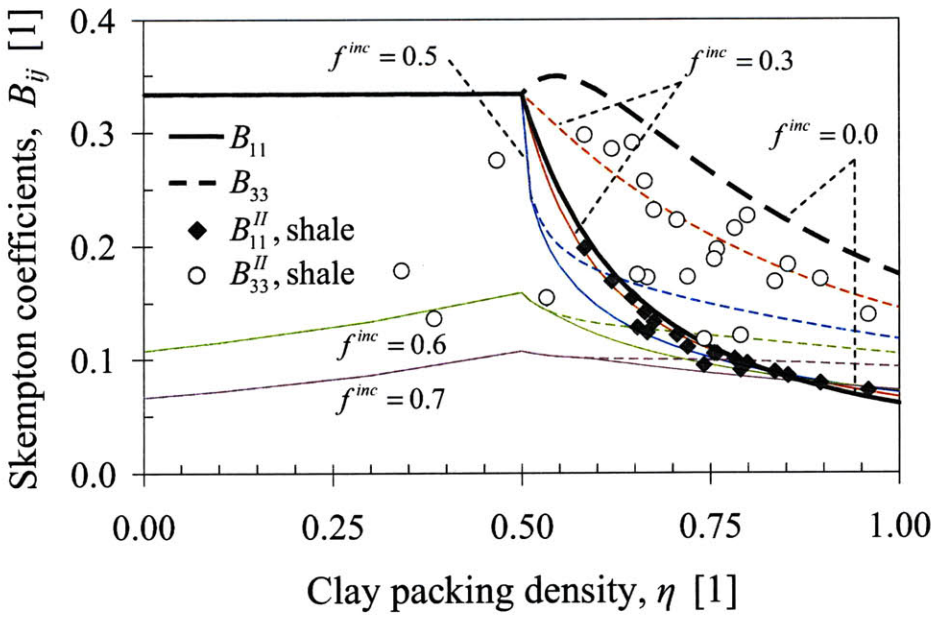

Figure 6-15: Model predictions of Skempton coefficients B_{ij} as continuous functions of clay packing density for level I ($f^{inc} = 0$) and level II ($f^{inc} > 0$). Data points correspond to the level II predictions for shale-specific volume fractions (from mineralogy and bulk density) defined in the CDS, VDS-1, and VDS-2 data sets.

where $\mathbb{S}_{\text{hom}}^{un} = (\mathbb{C}_{\text{hom}} + M\boldsymbol{\alpha} \otimes \boldsymbol{\alpha})^{-1}$ is the undrained elastic compliance tensor, and $\boldsymbol{\alpha}$ the second-order tensor of Biot pore pressure coefficients. In the transversely isotropic case, the previous expression reduces to a diagonal form $\mathbf{B} = \text{diag}\,(B_{11}, B_{11}, B_{33})$, with:

$$B_{11} = M\left[(S_{11}^{un} + S_{12}^{un})\,\alpha_{11} + S_{13}^{un}\alpha_{33}\right] = M\frac{\alpha_{11}C_{33}^{un} - \alpha_{33}C_{13}^{un}}{C_{33}^{un}\,(C_{11}^{un} + C_{12}^{un}) - 2\,(C_{13}^{un})^2} \tag{6.17a}$$

$$B_{33} = M\left[2S_{13}^{un}\alpha_{11} + S_{33}^{un}\alpha_{33}\right] = M\frac{\alpha_{33}\,(C_{11}^{un} + C_{12}^{un}) - 2\alpha_{11}C_{13}^{un}}{C_{33}^{un}\,(C_{11}^{un} + C_{12}^{un}) - 2\,(C_{13}^{un})^2} \tag{6.17b}$$

where S_{ij}^{un} are the components of $\mathbb{S}_{\text{hom}}^{un} = (\mathbb{C}_{\text{hom}}^{un})^{-1}$. Note that the isotropic case (6.15) is recovered from (6.16) and (6.17) by letting $\text{B}_\text{S} = \text{tr}\,(\mathbf{B}) = 3M\alpha\,(S_{11}^{un} + 2S_{12}^{un})$. The focus of this section is to quantitatively assess the Skempton coefficients at the two scales where shale manifests itself as a porous medium; namely at the scale of the porous clay composite (level I) and at the macroscopic scale of porous clay–silt inclusion composite (level II).

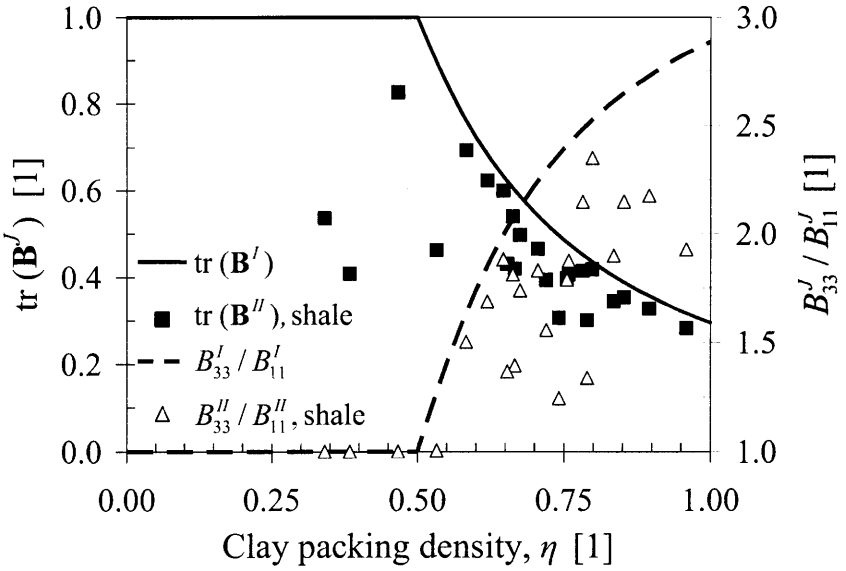

Figure 6-16: Behavior of Skempton coefficients expressed in terms of $\mathrm{tr}(\mathbf{B}^J)$ and the ratio B^J_{33}/B^J_{11}. Level I predictions are displayed as continuous functions of clay packing density. Level II predictions correspond to shale data.

At level I, the Skempton coefficients $B^I_{11}(\eta)$ and $B^I_{33}(\eta)$ are readily determined as continuous functions of the clay packing density η, from the sole knowledge of the solid stiffness tensor $\mathbb{C}^s$ and the fluid bulk modulus k^{fl}. The results are displayed in Figure 6-15 as $B^I_{ij}(\eta) = B_{ij}\left(\eta, f^{inc}=0\right)$: Below the percolation threshold $\eta < \eta_0 = 0.5$, where $C^I_{ij,\mathrm{hom}} = 0$ and $\boldsymbol{\alpha} = \mathbf{1}$, the Skempton coefficients take a unique value $\mathbf{B}^I = \frac{1}{3}\mathbf{1}$. As expected, in the absence of the solid phase contributing to the (drained) stiffness, any stress applied is entirely carried by the fluid phase, i.e. $\mathrm{B_S} = \mathrm{tr}\left(\mathbf{B}^I\right) = 1$. Above the percolation threshold, $B^I_{33}(\eta)$ is consistently greater than $B^I_{11}(\eta)$ for the range of clay packing densities $0.5 < \eta < 1$; a trend which is contrary to the tendency of Biot pore pressure coefficients observed in Figure 6-14. To examine this behavior, we remind ourselves that the pore pressure coefficients in Figure 6-14 are comparable in magnitude, so that one can let $\alpha^I_{11} \approx \alpha^I_{33}$ in (6.17) to obtain the following simplified form of the ratio of Skempton coefficients:

$$\frac{B^I_{33}}{B^I_{11}} \approx \frac{C^{I,un}_{11} + C^{I,un}_{12} - 2C^{I,un}_{13}}{C^{I,un}_{33} - C^{I,un}_{13}} \tag{6.18}$$

Furthermore, since $C_{12}^{I,un}$ and $C_{13}^{I,un}$ are of similar magnitude (see for instance Figure 5-10), $B_{33}^{I}(\eta) \geq B_{11}^{I}(\eta)$ appears in the first place as a consequence of the intrinsic anisotropy of shale materials: the ratio B_{33}^{I}/B_{11}^{I} increases with the packing density from the percolation threshold, where $B_{33}^{I}/B_{11}^{I} = 1$, to the asymptotic solid state, $\eta \to 1$, where $B_{33}^{I}/B_{11}^{I} \approx 3$ (Figure 6-16). In all cases, $\text{tr}\left(\mathbf{B}^{I}\right) \leq 1$ as shown in Figure 6-16.

A second factor that affects the Skempton coefficients is the fluid compressibility. To illustrate this dependency, Figure 6-17 shows a parametric study of the behavior of Skempton coefficients at level I (the porous clay composite) predicted by the microporomechanical model for different fluid compressibility values (expressed alternatively in terms of fluid bulk modulus units). In addition to the compressibility of water ($k^{fl} = 2.7$ GPa at $p = 40$ MPa and 30°C), a compressibility of oil ($k^{fl} = 1.8$ GPa at $p = 20$ MPa and 31°C [286]) and a large, arbitrary compressibility value were considered in Figure 6-17a. While the values of both Skempton coefficients, B_{33}^{I} and B_{11}^{I}, tend to become larger with increasing fluid bulk modulus (i.e. more incompressible fluids), as it is expected due to the higher hydraulic stiffening of the composite material, the ratio B_{33}^{I}/B_{11}^{I} displayed in Figure 6-17b is unaffected by the fluid's compressibility, which confirms the point that the anisotropy of the pore pressure build up in the porous clay of shales is directly related to the solid's intrinsic anisotropy. Finally, the values of the Skempton coefficients for all three cases comply with the condition $\text{tr}\left(\mathbf{B}^{I}\right) \leq 1$ for all clay packing densities.

Lastly, Figures 6-15 and 6-16 also display the macroscopic (level II) Skempton coefficients $B_{11}^{II}\left(\eta, f^{inc}\right)$ and $B_{33}^{II}\left(\eta, f^{inc}\right)$, predicted by the poromechanical model in the form of isoparametric curves for various inclusion volume fraction values, as well as data points corresponding to shale-specific volume fractions defined in the CDS, VDS-1, and VDS-2 data sets. As expected, the addition of isotropic silt inclusions to the porous clay phase reduces the Skempton coefficients, so that:

$$\mathbf{B}^{II}\left(\eta, f^{inc}\right) \leq \mathbf{B}^{I}(\eta) \tag{6.19}$$

The differences between B_{11}^{I} and B_{11}^{II} appear to be minimal for shale materials with clay packing densities above the percolation threshold $\eta > \eta_0 = 0.5$. Another effect of the silt inclusions is observed in Figure 6-16 for the ratio B_{33}^{II}/B_{11}^{II}, which is smaller than B_{33}^{I}/B_{11}^{I} for all clay packing densities above the percolation threshold. This behavior is attributed to the

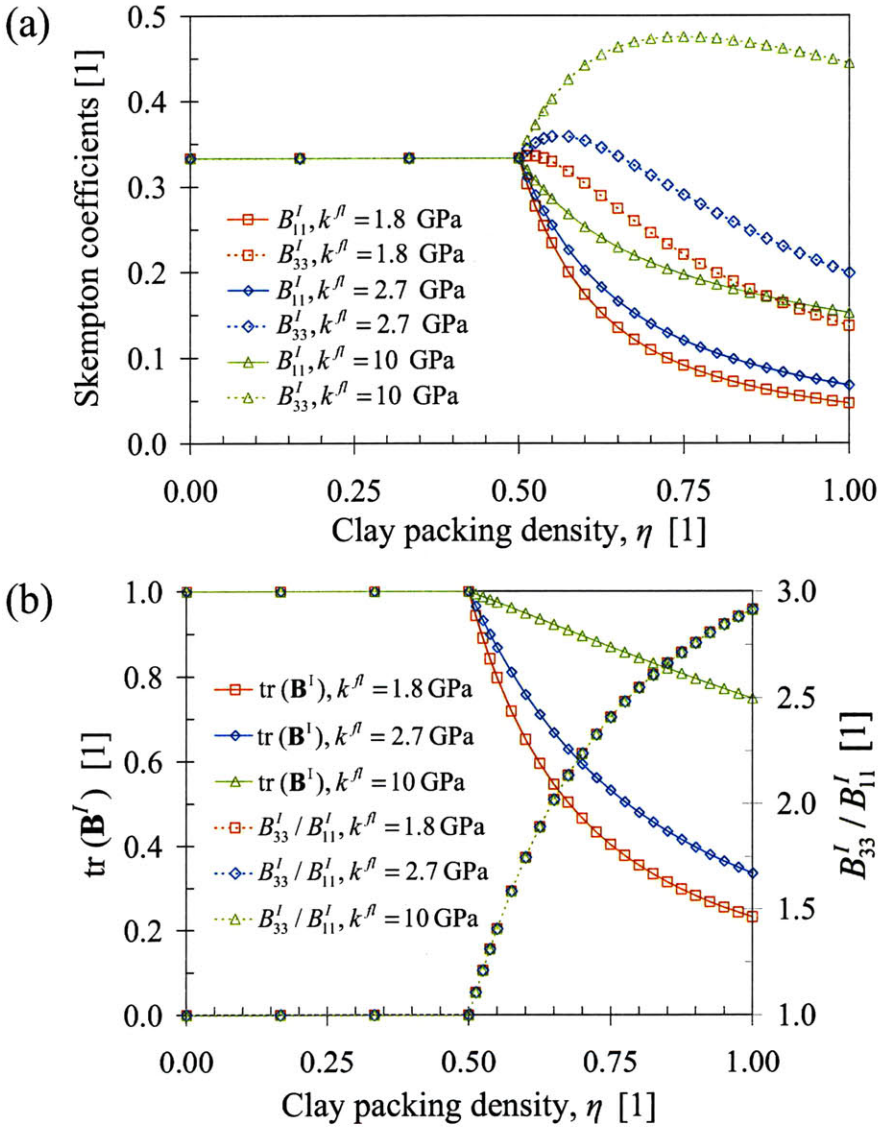

Figure 6-17: a) Effect of fluid compressibility k^{fl} (expressed in bulk modulus units) on predictions of Skempton coefficients at level I, B^I_{ij}. $k^{fl} = 1.8$ GPa represents the bulk modulus of Carnation oil at $p = 21$ MPa and 31°C. $k^{fl} = 2.7$ GPa represents the bulk modulus of water at $p = 40$ MPa and 30°C. $k^{fl} = 10$ GPa represents a large, arbitrary modulus used for illustration. b) Behavior of Skempton coefficients expressed in terms of $\mathrm{tr}(B^I)$ and the ration B^I_{33}/B^I_{11}.

level II homogenization of the transverse isotropic porous clay composite at level I and the added isotropic silt inclusions. Nevertheless, the Skempton coefficient B_{33}^{II} is generally greater than B_{11}^{II} by at least 40% for the shale materials presented in Figure 6-15 with clay packing densities above the percolation threshold. As a consequence, any change of stress normal to the bedding plane affects the pore pressure more than a change of the in-plane stresses. This behavior contrasts the strain-driven undrained situation, which is (almost) independent of the direction of strain application.

6.5.3 Gassmann-Berryman Poroelastic Coupling Parameter

Thus far, $\boldsymbol{\alpha}^J$ and $\mathbf{B}^J$ show different scaling with the packing density of the porous clay phase, and the non-clay volume fraction. A convenient way to combine those two poroelastic constants is in form of the Gassmann–Berryman poroelastic coupling parameter, $1-\boldsymbol{\alpha}^J\colon \mathbf{B}^J$, which scales the fluid transport term in (6.10). In the isotropic case, this scalar factor expresses the ratio of drained–to–undrained bulk modulus (see [22, 51, 97]):

$$1-\alpha \mathrm{B_S} = \frac{k}{k^{un}} \tag{6.20}$$

where k^{un} is the undrained bulk modulus, k the drained bulk modulus, α the isotropic pore pressure coefficient (6.11), and $\mathrm{B_S}$ the Skempton coefficient (6.15). The Gassmann–Berryman coupling parameter (6.20), which is used in reservoir engineering along with other derived results from Gassmann's work [97] as tools for fluid identification, estimates the strength of the coupling between mechanical and hydraulic effects within the framework of poroelasticity analysis [304]. Indeed, for $\alpha \mathrm{B_S} \ll 1$, there is little difference between drained and undrained conditions, for which reason the hydraulic stiffening of the porous medium under undrained conditions becomes negligible. From available water-saturated rock data, Zimmerman [304] showed that the poroelastic coupling parameter ranges from $(1-\alpha \mathrm{B_S}) = 0.43$ to $(1-\alpha \mathrm{B_S}) = 0.90$; thus testifying to the considerable hydromechanical coupling in rocks. The focus of this section is to quantitatively assess this coupling parameter for shale, both at the scale of the porous clay composite and at the macroscopic scale (levels I and II of our multi-scale structure model) by using the developed microporomechanics model.

To start with, the generalization of (6.20) to the anisotropic case yields:

$$1 - \boldsymbol{\alpha}^J \colon \mathbf{B}^J = \mathbb{S}^{J,un}_{\text{hom}} :: \mathbb{C}^J_{\text{hom}} - 5 \tag{6.21}$$

where the operation :: represents a fourth-order tensor contraction operation. Since both $\mathbb{S}^{J,un}_{\text{hom}}$ and $\mathbb{C}^J_{\text{hom}}$ $(J = I, II)$ are accessible by the microporomechanics model, the coupling coefficient $1 - \boldsymbol{\alpha}^J \colon \mathbf{B}^J$ is obtained as a mere application of our model, based on the knowledge of the solid stiffness tensor $\mathbb{C}^s$ and the fluid bulk modulus k^{fl} as the shale invariant input parameters, and the clay packing density η and the inclusion volume fraction f^{inc} as shale-specific data.

The resulting curve for level I (denoted by $f^{inc} = 0$) is displayed in Figure 6-18. Below the percolation threshold $\eta < \eta_0 = 0.5$, where $\boldsymbol{\alpha}^I = \mathbf{1}$ and $\text{tr}\left(\mathbf{B}^I\right) = 1$, the coupling scalar is zero due to the zero drained elastic stiffness of the porous clay phase below the percolation threshold. Above the percolation threshold, the value of the coupling factor monotonically increases towards $\lim_{\eta \to 1} \left(1 - \boldsymbol{\alpha}^I \colon \mathbf{B}^I\right) = 1$ which is reached for the asymptotic solid state, $\eta \to 1$, for which obviously all hydromechanical coupling cancels out.

The effect of the addition of silt-inclusions (of volume fraction f^{inc}) on the coupling coefficient $1 - \boldsymbol{\alpha}^{II} \colon \mathbf{B}^{II}$ at the macroscopic scale (level II) is also shown in Figure 6-18. Because $\boldsymbol{\alpha}^I(\eta) \geq \boldsymbol{\alpha}^{II}\left(\eta, f^{inc}\right)$ and $\mathbf{B}^I(\eta) \geq \mathbf{B}^I\left(\eta, f^{inc}\right)$ (see expressions (6.14) and (6.19)), it is readily understood that:

$$1 - \boldsymbol{\alpha}^{II} \colon \mathbf{B}^{II} \geq 1 - \boldsymbol{\alpha}^I \colon \mathbf{B}^I \tag{6.22}$$

In particular, below the percolation thresholds of both the clay phase and the inclusion phase, $\eta < 0.5$ and $f^{inc} < 0.5$, where neither clay nor silt contribute to the drained stiffness, we observe that $1 - \boldsymbol{\alpha}^{II} \colon \mathbf{B}^{II} = 0$, which is a consequence of the self-consistent model applied on both level I and level II. In turn, when the clay packing density is below the percolation threshold, $\eta < 0.5$, and $f^{inc} > 0.5$, so that the load bearing phase is the non-clay inclusion phase (representing *de facto* a 'clean' sandstone), the coupling coefficient quickly increases, as shown by the isoparametric curves at level II in Figure 6-18 (curves labeled $f^{inc} = 0.6$ and $f^{inc} = 0.7$). On the other hand, when the load bearing phase is the clay phase ($\eta > 0.5$), the hydromechanical coupling $1 - \boldsymbol{\alpha}^{II} \colon \mathbf{B}^{II}$ is recognized to be dominantly driven by the level I properties. This is the case of most shale materials of the CDS, VDS-1, and VDS-2 data sets considered in this study, displayed as data points in Figure 6-18. The computed values for

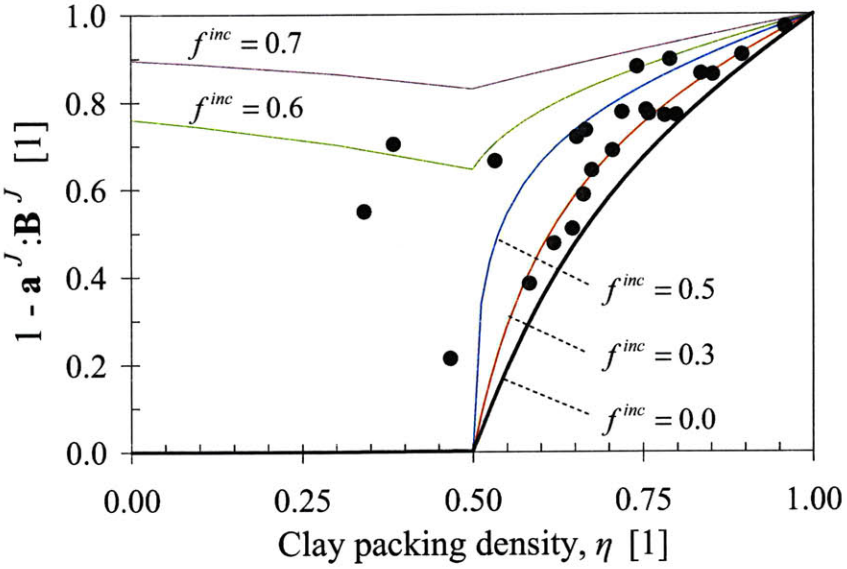

Figure 6-18: Model predictions of the Gassmann-Berryman poroelastic coupling parameter $1 - \boldsymbol{\alpha}^J : \mathbf{B}^J$, as continuous functions of clay packing density for level I ($f^{inc} = 0$) and level II ($f^{inc} > 0$). Data points correspond to the level II model predictions for shale-specific volume fractions (obtained from mineralogy–density and mineralogy–porosity) defined in the CDS, VDS-1, and VDS-2 data sets.

the Gassmann–Berryman parameter for most shale materials range between 0.39 to 0.97, an observation which is in very close agreement with the values reported for water-saturated rock data by Zimmerman [304]. This finding justifies a posteriori the use of the microporomechanics theory for shale; that is, the poroelastic coupling in shale is of critical importance for the accurate prediction of shale's transversely isotropic poroelastic behavior.

6.5.4 Sensitivity to Model Input Parameters

The present discussion cannot be closed without a sensitivity study of the model with respect to the two shale-specific model input parameters, the clay packing density, η, and the (non-clay) inclusion volume fraction, f^{inc}. Both η and f^{inc} exhibit some variability depending on the particular experimental means for assessing the porosity of shale (see Figure 3-1).

Figure 6-19 displays the comparison between two sets of model predictions of the Biot pore pressure coefficients α_{ij}, and the Skempton coefficients B_{ij}, at the macroscopic scale (level II) for all shales in the CDS, VDS-1, and VDS-2 data sets. The first set of model predictions (displayed in Figure 6-19 on the y-axis) was calculated using input parameters derived from bulk density information (namely $\eta_{\min}, f^{inc}_{\min}$). The second set of model predictions (displayed in Figure 6-19 on the x-axis) was calculated using input parameters derived from porosity information (namely $\eta_{\max}, f^{inc}_{\max}$; refer to Tables 3.9 and 3.10). The general trend found in the cross-plots of Figure 6-19 is that the use of the bulk density for porosity determination (using relation (3.1)) yields greater values for the Biot and Skempton coefficients than the use of direct porosity measurements. This trend translates into poroelastic constants the well-known observation that direct porosity measurement techniques (like MIP) underestimate the actual porosity (and thus overestimate the clay packing density and the inclusion volume fraction) compared to indirect measurements using e.g. bulk density values [79]. Since the poroelastic coefficients $\alpha^{II}_{ij}, B^{II}_{ij}$ scale inversely proportional with the input parameters η, f^{inc} (see Figures 6-14,6-15), it is therefore not surprising that lower $\left(\alpha^{II}_{ij}, B^{II}_{ij}\right)$ values are obtained with $(\eta_{\max}, f^{inc}_{\max})$ compared to the $\left(\alpha^{II}_{ij}, B^{II}_{ij}\right)$ values obtained with $(\eta_{\min}, f^{inc}_{\min})$. As Figure 6-19 shows, this trend is more pronounced for the Biot pore pressure coefficients than for the Skempton coefficients.

The results of a quantitative analysis of the sensitivity of the poroelastic coefficients $\left(\alpha^{II}_{ij}, B^{II}_{ij}\right)$, are presented in Table 6.3. The table shows how the variability of the model input parameters

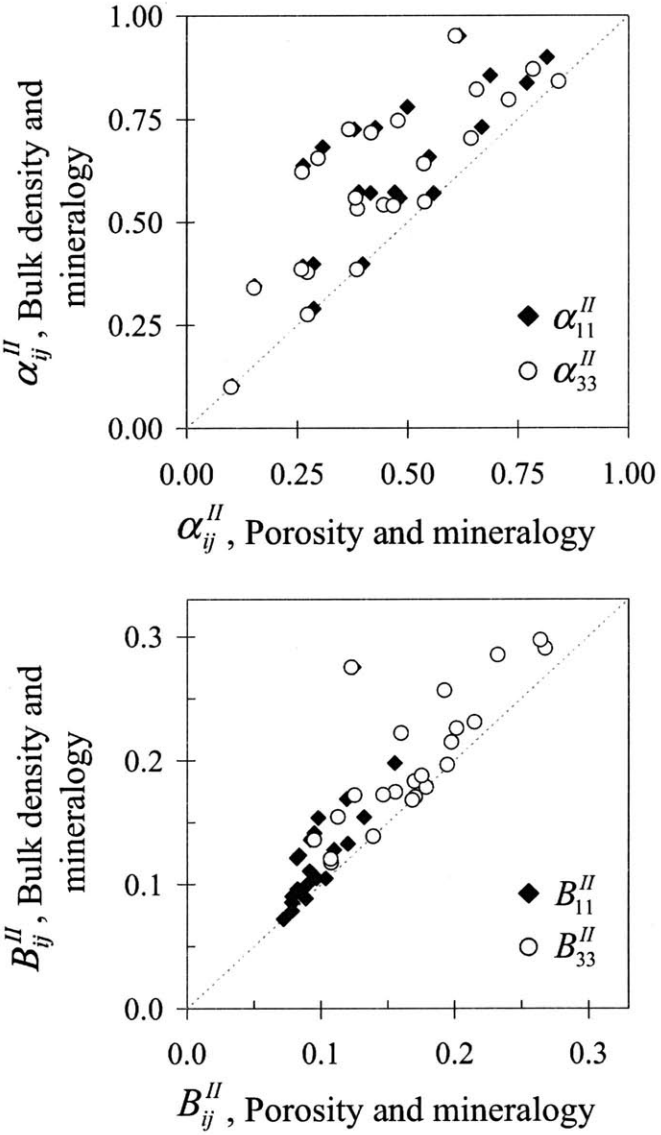

Figure 6-19: Comparisons of model predictions of Biot pore pressure coefficients α_{ij} (top) and Skempton coefficients B_{ij} (bottom) obtained from porosity and bulk density information in addition to mineralogy. Data points correspond to model predictions at the macroscopic scale (level II) for all the shale materials reported in the CDS, VDS-1, and VDS-2 data sets.

	Input parameters				Model prediction							
	η		f^{inc}		α_{11}^{II}		α_{33}^{II}		B_{11}^{II}		B_{33}^{II}	
	$\hat{e}$	e_s	$\hat{e}$	e_s	$\hat{e}$	e_s	$\hat{e}$	e_s	$\hat{e}$	e_s	$\hat{e}$	e_s
CDS	5	3	4	2	−14	10	−15	10	−11	7	−8	4
VDS(1)	22	18	12	7	−37	19	−37	19	−28	15	−24	15

Table 6.3: Sensitivity of model predictions of Biot pore pressure coefficients and Skempton coefficients due to the variability of input parameters η and f^{inc}.
The mean and the standard deviation of the relative errors (variability), $\hat{e}$ and e_s, for the input parameters were calculated between their minimum and maximum estimates obtained from mineralogy-bulk density and mineralogy-porosity information, respectively. The mean and the standard deviation of the relative errors for the model predictions were calculated between model results obtained from minimum η,f^{inc} values and those obtained from maximum η,f^{inc} values. The reference values for relative error calculations are the input parameters obtained from mineralogy and bulk density information. Relative errors are presented in percent units.
(1) The VDS data set encompases the information from the VDS-1 and VDS-2 data sets. Repeated shale specimens in the CDS and VDS-1 data sets are only considered in the CDS data set for relative error computations.

$\left(\eta, f^{inc}\right)$ translates into the variability of model output parameters $\left(\alpha_{ij}^{II}, B_{ij}^{II}\right)$. The variability of both input and output parameters is expressed in the form of relative errors between different estimates: one using bulk density information, the other, porosity information. It is found that the variability in $\left(\eta, f^{inc}\right)$ entails a variability of the same order of the Skempton coefficients B_{ij}^{II}, while it is twice (for CDS) and three times (for VDS) higher for the Biot pore pressure coefficients α_{ij}^{II}. This underlines the importance of an accurate determination of the porosity of shale as a prerequisite for a successful prediction of poroelastic properties.

6.6 Chapter Summary

This chapter has presented an extended discussion of the microporoelastic engineering model for shale and its critical elements. A fundamental building block of shale elasticity behavior has been identified. This elementary unit of solid clay is (at least) transversely isotropic, and characterized by a set of unique in situ stiffness properties. These stiffness properties appear to be little affected by the specific shale mineralogy, and are well below reported stiffness values for pure clay minerals. The orientation of the building blocks is governed by the shale deposition direction; and it is thus a consequence of the burial diagenesis of this depository rock. This intrinsic anisotropy of the elementary building block is at the core of shale macroscopic anisotropy. At the level of the porous clay fabric, the oriented clay particles in shale behave

at the microscale like a nanogranular material, transmitting forces over randomly oriented contact surfaces that activate the intrinsic elastic anisotropy of the elementary building block. The nanogranular nature of shale and the randomness of the contact surface orientation are typed into our approach through the application of a self-consistent micromechanical model of spherical fundamental building blocks of transversely isotropic properties, which mimics well the experimentally found clay packing density threshold $\eta_0 = 0.5$. The 'effective' porous clay properties, therefore, are governed by both the shale-invariant properties and the shale-specific clay packing density. This packing density neatly summarizes the porosity and clay mineralogy information about the material into one simply understood parameter. In contrast to previous approaches, there is no need in our model to consider additional orientation functions of the clay particles to enhance the intrinsic anisotropy. The second parameter relating to mineralogy that affects shale macroscopic behavior is the (non-clay) silt inclusion volume fraction. While the addition of silt inclusions obviously stiffens the effective porous clay properties, the essence of shale macroscopic behavior originates from the transversely isotropic nature of the clay fabric.

This multi-scale micromechanical picture of shale elasticity translates into a unique poroelastic signature of shale materials, which is critical for the accurate prediction of shale acoustic behavior: Due to the intrinsic anisotropy of the elementary building block and the scaling of this anisotropy with the clay packing density, the Biot pore pressure coefficients a are almost isotropic. By contrast, the Skempton coefficients, which quantify the pore pressure build-up under undrained conditions in consequence of a macroscopic stress application, are highly anisotropic, with an anisotropy that scales with the packing density. Finally, the Gassmann-Berryman parameter, which neatly summarizes both Biot coefficients and Skempton coefficients into one single parameter that characterizes the hydromechanical coupling, provides clear evidence that such coupling in shale is of considerable magnitude that cannot be neglected in poroelasticity analysis of shale. Moreover, given the shale-invariant properties of the fundamental building block of shales, it is recognized that the poroelastic response of shale predominantly depends on the two shale-specific properties: clay packing density η, and non-clay inclusion volume fraction f^{inc}. More specifically, the clay packing density is recognized to be at the very origin of shale poroelastic sensitivity, while the presence of inclusion at larger scales weighs this sensitivity in proportion of the macroscopic porous clay volume fraction. The fact that

those two parameters, η and f^{inc}, delimitate shale macroscopic diversity, makes the proposed two-parameter microporoelastic model even more appealing for geophysics and exploitation engineering applications, although issues related to pressure and frequency dependencies of acoustic properties would still require further investigation.

Chapter 7

Microporoelastic Model Extension and Field Applications

The micromechanics model developed in Chapters 4 through 6 was validated as a predictive engineering tool for the multi-scale anisotropic poroelasticity of shale. Its original development focused on kerogen-free shales, i.e. shale rocks with minimum organic content. In this chapter, the realm of the microporoelastic framework is extended to the modeling of kerogen-rich shale, in which the presence of kerogen results in a more compliant elastic response. The chapter continues with the presentation of two pilot studies related to the application of the model for the poroelastic characterization of shale formations. The microporoelastic model, which has been implemented in a software package, uses as inputs the mineralogy and porosity information from state-of-the-art logging tools employed in petroleum industry operations. These sample field applications of the model highlight its potential as an engineering tool and bring forward several aspects of its implementation that will require further investigation.

7.1 Microporoelasticity of Kerogen-Rich Shale

7.1.1 Model Extension to Kerogen-Rich Shale

The importance of hydrocarbon source rocks as major oil and gas plays has increased in the past decades [2]. The presence of kerogen, a precursor of oil and gas, significantly alters the

mechanical response of source rocks in terms of their acoustic response and anisotropy [277, 278]. The microporoelastic engineering model for shale is extended to accommodate the prediction of acoustic velocities for kerogen-rich shales by modifying the homogenization treatments at levels 0 and I of the multi-scale structure thought-model[1].

Advanced observational methods have shown kerogens in hydrocarbon-bearing shales as aggregates of various sizes, ranging from sub-micrometers to tens of micrometers. TEM observations revealed that kerogen manifests itself as lamellar structures with nanometer thicknesses forming sheets [102] or as amorphous organic matter with granular and homogeneous morphologies [74]. At micrometer scales, SEM images of the microstructure of kerogen-rich shales characterized it as a dispersion of kerogen in the form of microlayers among clay phases, as well as layers containing clay particles [278] (Figure 7-1). Given the similar length scales, the introduction of the kerogen phase and its effects on the mechanical response of shale are modeled through the homogenization of elastic properties of the kerogen and solid clay phases at level 0, with resulting properties:

$$\mathbb{C}^s_{\text{hom}} = \mathbb{C}^k + \left(1 - f^k\right)\left(\mathbb{C}^s - \mathbb{C}^k\right) : \overline{\mathbb{A}}^s \tag{7.1}$$

where $\mathbb{C}^k$ is the stiffness tensor of the kerogen phase and f^k the relative volume fraction of kerogen. The homogenized clay/kerogen stiffness $\mathbb{C}^s_{\text{hom}}$ enters the multi-scale formulation at level I by substituting $\mathbb{C}^s_{\text{hom}}$ instead of the compacted clay stiffness $\mathbb{C}^s$ in (4.98). With this proposed upscaling methodology, kerogen is treated akin to a clay mineral phase, and thus the relative volume fraction of kerogen is calculated as (see Section 3.4):

$$f^k = \frac{V^k}{\sum_{i=1}^{i=CM} V^i} \tag{7.2}$$

where V^k is the volume of kerogen and $\sum_{i=1}^{i=CM} V^i$ the total volume of clay mineral (CM) phases and kerogen. The computation of the clay packing density in (3.5) also is modified accordingly. The stiffness of the solid kerogen phase is given by data available in the literature: bulk modulus $k^k = 6.8$ GPa, and shear modulus $g^k = 3.6$ GPa [278], which in tensor notation reads as:

[1] The work presented here has been published in [203].

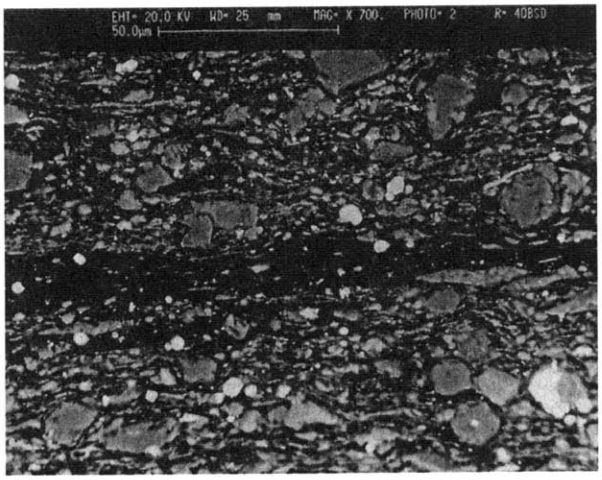

Figure 7-1: SEM micrograph of black shale. Kerogen (shown in black) is distributed in the microstructure in the form of microlayers among the clay matrix, as well as layers containing numbers of clay particles. Image from [278].

$$\mathbb{C}^k = 3k^k\mathbb{J} + 2g^k\mathbb{K} \tag{7.3}$$

The choice of modeling kerogen as a solid phase is in accordance with laboratory experimental conditions during ultrasonic pulse velocity measurements on various Woodford shale specimens used for model validation. In situ mechanical characterization of kerogen-rich shales might require incorporating temperature effects, because organic materials are viewed as amorphous composites prone to liquefaction with increasing temperature [278]. The mechanical interaction between the clay and kerogen phases is modeled using the self-consistent scheme (refer to Section 4.2.4). In addition, we model the kerogen phase with a spherical morphology. Although simplifying the complex morphology of the kerogen phase, these modeling choices recognize the disordered nature of the kerogen-rich clay fabric in shale and do not introduce structural sources of anisotropy resulting from particle shapes. The relevance of these assumptions shall be assessed through comparisons with experimental data at levels I and II. This first approach to modeling the effect of kerogen, namely, the homogenization of clay/kerogen at level 0 and the introduction of porosity at level I, includes the necessary elements for the prediction of nano- and macroscopic elasticity of kerogen-rich shale. The low stiffness properties of kero-

gen are expected to reduce the acoustic properties at micro- and macroscales. In addition, the model is equipped to yield predictions for kerogen-rich shales with non-negligible porosities, in contrast to previous modeling attempts [278]. Finally, the present model extension does not quantify the effects of kerogen maturation on elastic anisotropy.

7.1.2 Comparisons with Nanoindentation and UPV Experiments

The microporoelastic model extension for kerogen-rich shales is validated at levels I and II of the multi-scale structure model through comparisons with nanoindentation and UPV measurements gathered for five Woodford shale specimens. The clay packing density, inclusion volume fraction, and relative kerogen volume fraction values for the Woodford shale samples are detailed in Chapter 3, and represent the input parameters to generate model predictions at the different length scales.

For validation at level I, the model is implemented in a forward application to develop drained stiffness estimates $C^I_{ij,\text{hom}}$ (4.98) using as inputs the clay stiffness properties (7.1) and the clay packing density calculated for each shale specimen. The stiffness values are then compressed into equivalent indentation moduli M_1, M_3 using the expressions (3.28a)-(3.28b), which represent the elasticity content sensed by an indentation test in the direction normal to the axis of material symmetry (x_1, x_2 axes) and in the direction of material symmetry (x_3-axis), respectively. The resulting continuous functions are displayed in Figure 7-2. Two sets of predicted moduli are displayed for different relative volume fractions of kerogen $f^k = 0, 0.4$. The indentation modulus curves for $f^k = 0$ correspond to kerogen-free conditions, whereas the curves for kerogen-rich shale were generated for an average value of $f^k = 0.4$ which is characteristic of the Woodford samples considered in this study. The solid data points and vertical error bars correspond to the mean and standard deviation of the experimental indentation moduli measured for the porous clay phases of the Woodford shale specimens. The horizontal error bar denotes the variability of the clay packing density depending on the information used for computation (either mineralogy/porosity or mineralogy/bulk density). In addition to the Woodford shale data, indentation data for G2IC shales is displayed in Figure 7-2. The predicted indentation response for Woodford shale samples tends to slightly underpredict the measured nanoindentation moduli. Compared to G2IC shales, the differences in elastic

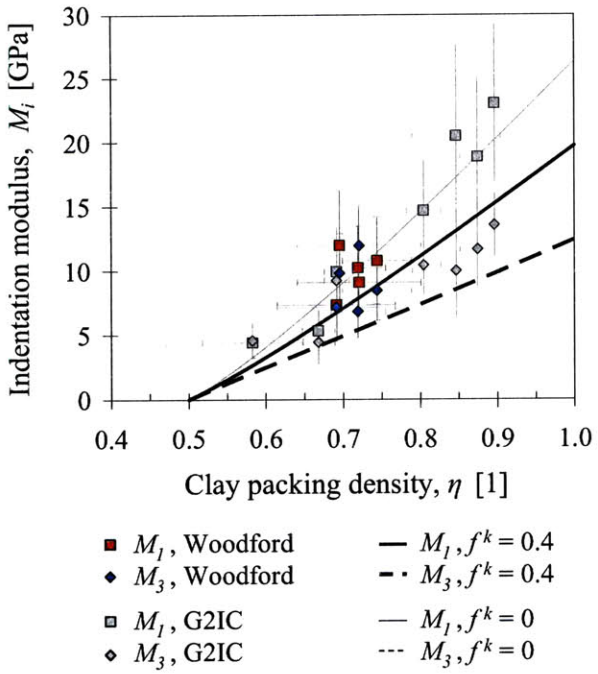

Figure 7-2: Comparison between model predictions (lines) and nanoindentation results (data points) for level I - the porous clay phase in shale. The predicted indentation modulus curves are displayed for two values of the relative kerogen volume fraction $f^k = 0, 0.4$. The curves for $f^k = 0$ correspond to kerogen-free conditions. The curves for $f^k = 0.4$ are representative of the Woodford shale samples. Vertical error bars in the experimental data represent the standard deviations of indentation results. Horizontal error bars represent the variability of clay packing density estimates. The Woodford shale indentation data was provided in Table 3.16.

moduli are also somewhat reduced for Woodford shales. This reduced anisotropic response captured by nanoindentation is attributed to the presence of a kerogen phase with pronounced amorphous morphology, instead of sheet-like kerogen structures that would result in an increased structural anisotropy.

The performance of the model extension for kerogen-rich shale as a predictive tool for macroscopic elasticity is tested by comparing acoustic predictions at level II to UPV measurements. The model is implemented in a forward application to develop undrained stiffness estimates in the form of acoustic velocities for the composite of porous clay and silt inclusions (see Section 4.4). Predicted acoustic velocities are reported in the customary compressional- and shear-wave velocities in the normal-to-bedding and parallel-to-bedding directions. In addition, the (quasi)

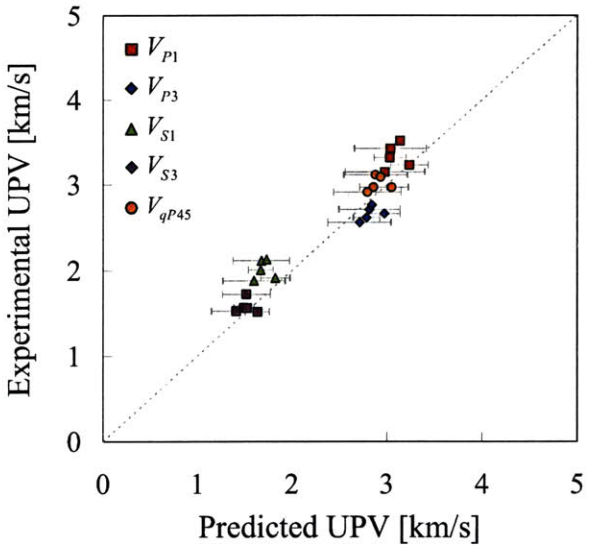

Figure 7-3: Comparison of predicted acoustic velocities and experimental UPV measurements for Woodford shale data. Horizontal error bars represent the variability of model predictions depending on input volume fraction values.

P-wave velocity at 45° is reported. The input data for the implementation of the model are the clay packing density η and inclusion volume fraction f^{inc}, which are calculated for each shale specimen from reported mineralogy and porosity measurements, and alternatively from mineralogy and density measurements. Figure 7-3 displays the comparisons between experimental and predicted acoustic velocities for the Woodford shale data. The horizontal error bars represent the range of predicted elasticity values given the two different sets of clay packing density and inclusion volume fraction estimates. Based on the results presented in Figure 7-3, predicted acoustic velocities compare adequately to UPV measurements for the kerogen-rich Woodford shales.

7.1.3 Effects of Kerogen

The presence of kerogen has long been recognized as a significant factor modifying the physical and mechanical properties of shale. In particular, kerogen-rich shales exhibit low porosities and bulk densities, and high acoustic anisotropies [278]. After validation of the model predictions for kerogen-rich shales using the Woodford shale data, the focus of this section is to assess

quantitatively the effects of kerogen on the anisotropic acoustic behavior of shale.

Figure 7-4 displays isoparametric curves of acoustic velocities in the normal- and parallel-to-bedding directions as functions of clay packing density for two characteristic values of inclusion volume fraction: $f^{inc} = 0$ (the porous clay composite) and $f^{inc} = 0.4$ (a representative value for shale materials). In addition, isoparametric curves for relative kerogen volume fractions, $f^k = 0, 0.1, 0.3, 0.5$ are presented in the figure. Although there are minor differences in the plotted scales between the compressional- and shear-wave velocity graphs, the softening behavior of kerogen is observed to have a larger effect on the parallel-to-bedding acoustic properties compared with normal-to-bedding. In addition, the stiffness softening appears to have similar magnitudes for both cases of inclusion volume fractions.

Figure 7-4 also shows the parametric curves of Thomsen parameters (3.68a)-(3.68c) for the two cases of inclusion volume fraction, $f^{inc} = 0, 0.4$, and different kerogen volume fractions. The overall trend emerging from the analysis of these plots is the decrease in anisotropy values for all Thomsen parameters. The observed predictions are a direct consequence of the assumed isotropic elasticity and morphology of the kerogen phase at level 0 of the multi-scale model. The acoustic properties of isolated kerogen have been characterized, at best, by quasi-isotropic values, as used in our model (see (7.3)). This available isotropic description of kerogen translates into a decreasing degree of elastic anisotropy at levels I and II. In addition, the modeling choice of treating the kerogen phase as polycrystal grains with spherical morphology does not enhance the anisotropy of model predictions. The model predictions for kerogen-rich shales, represented by the Woodford shale specimens, display very good agreement with UPV elasticity data as observed in Figure 7-3. Consequently, there is an adequate agreement between the experimental data shown in Figure 7-4 a-d and the isoparametric curves, i.e. most experimental data are situated close to the curves with $f^{inc} = 0.40$ and $f^k = 0.3$–0.5. For Thomsen parameters, it seems that the model predictions compare well for only the S-wave anisotropy (γ parameter). The poorest comparisons are observed for the δ^* parameter, and may hint to the existence of structural sources of anisotropy in these kerogen-rich materials.

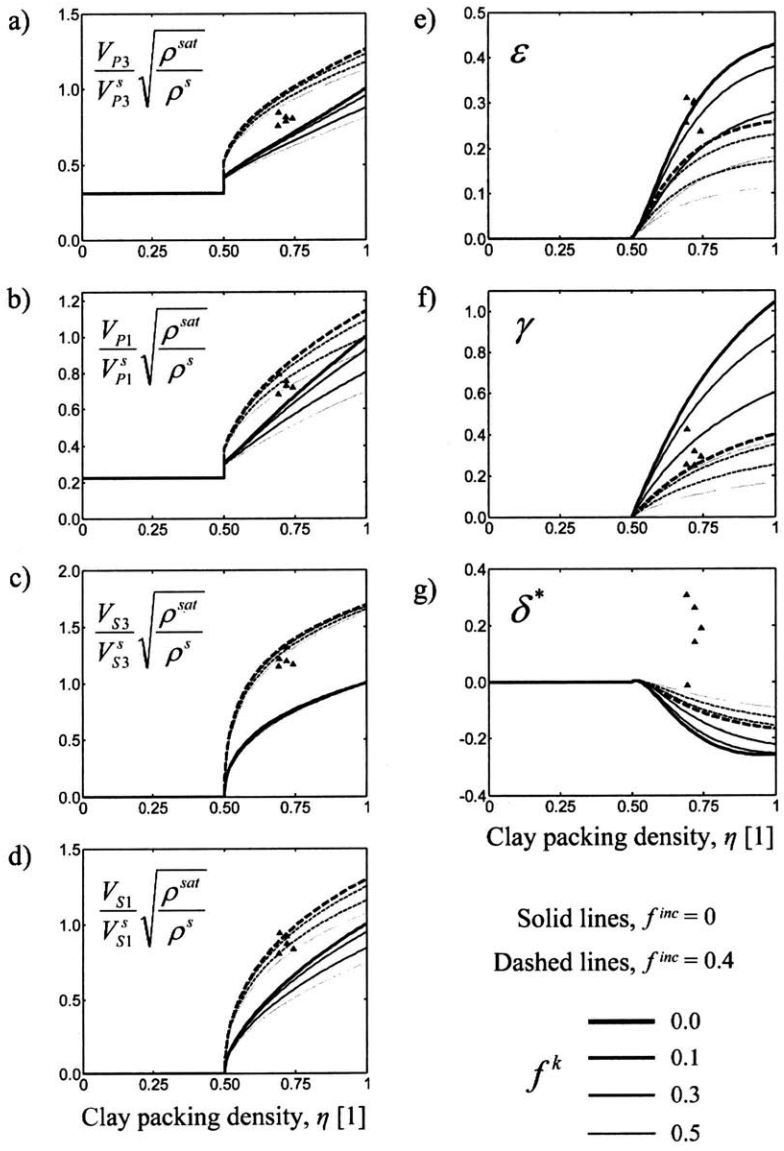

Figure 7-4: Effects of kerogen on (a-d) the acoustic properties in the form of isoparametric curves, and (e-g) the elastic anisotropy in terms of Thomsen parameters of shale materials. Triangles correspond to experimental data on Woodford shale, which have been plotted based on the calculated mean clay packing density and measured acoustic wave velocities.

7.2 Field Applications

7.2.1 Industrial Motivation

The increasing importance of many shale formations as prolific sources of natural gas in the U.S. has challenged the oil and gas industries to develop improved solutions for their exploitation. The profitable production from gas shale, due to its intrinsically low permeabilities, rests on the success of horizontal well drilling and hydraulic fracturing operations [172], which in turn depend on the adequate characterization of the anisotropic poromechanics of the formation [89]. Current technologies used for the estimation of mechanical properties of sub-surface formations such as advanced sonic logs are primarily designed to assess elastic properties parallel to the borehole axis. In contrast, laboratory testing of core samples can reliably estimate the full anisotropic characteristics of shale at the costs of time-consuming and expensive core retrieval operations. A pressing need exists for the real-time assessment of the anisotropic poroelasticity of shale formations.

The microporoelastic engineering model detailed in this thesis is proposed as a potential solution for the field characterization of shale. Based on input parameters related to mineralogy and porosity, the model has been adapted to predict the anisotropy and poroelastic parameters of shale formations in real-time applications through the use of recently developed geochemical logs [208]. The rest of this section showcases the first field applications of the microporoelastic model for shale. The MIT-OU GeoGenome Industry Consortium has conducted two pilot studies in which a shallow well (70 m) in a Woodford shale formation (Arkoma basin, Oklahoma) and a deep well (2.5 km) in a Barnett shale formation (Fort Worth basin, Texas) have been cored and logged. The objectives of these field tests, complemented by core data analyses, were to compare sonic log and ultrasonic pulse velocity data with model predictions and to evaluate the applicability of the model as a tool for petroleum engineering applications[2].

[2] The work presented here has been published in [2, 3, 261]. The field studies and the implementation of the model in a software package for the real-time characterization of shale formations have been conducted by M. Tran and S. Hoang from the University of Oklahoma.

7.2.2 Implementation of the Microporoelastic Model in Pilot Studies

The microporoelastic model for shale has been implemented into a software package called Quantitative GeoGenome Mineralogy Simulator[3], QGGMS©. The software analyzes mineralogy and porosity data obtained from logging tools, and provides estimates of the anisotropic, poroelastic properties of the investigated shale formation. Recall that mineralogy and porosity constitute the information necessary for calculating the two input parameters for the microporoelastic engineering model: the clay packing density and the inclusion volume fraction. For the investigations of the Woodford and Barnett formations, a suite of logs including Element Capture Spectroscopy (ECS), log porosity, and Sonic Scanner was run for each well. The ECS sonde (developed by Schlumberger [233]) targets the mineralogy evaluation of a formation by measuring and processing gamma ray spectra. Tran et al. [3] determined good correlations between the mineralogy estimates obtained from ECS logs and laboratory measurements performed on selected core sample using X-ray diffraction (XRD) analysis. Figure 7-5 displays graphically the mineralogy composition of the Woodford and Barnett shales as obtained from ECS logging. In contrast to comparable measurements between ECS and laboratory-derived mineralogies, the assessments of porosity in field and laboratory setups may yield different results. Data obtained for the Woodford shale formation showed relative differences of approximately 24% between log-porosity and porosity measured by mercury intrusion porosimetry (MIP) in laboratory conditions [261]. Before its use for modeling, the log-porosity was calibrated using MIP values, as shown in Figure 7-6. The use of porosity estimates based on the MIP method is considered more relevant for the application of the microporoelastic model, which treats the porosity in the composite medium as interconnected. The mineralogy compositions provided by ECS logs and the calibrated log-porosities served as the inputs for generating predictions of poroelastic properties for the Woodford and Barnett formations.

The results of the implementation of the model for the characterization of the Woodford formation along with the poroelastic properties measured in sonic logging and UPV experiments are shown in Figure 7-7. The acoustic properties measured by the Sonic Scanner log (developed by Schlumberger [232]) were only available for the normal-to-bedding direction, which coincides

[3]The software package is property of the PoroMechanics Institute, University of Oklahoma.

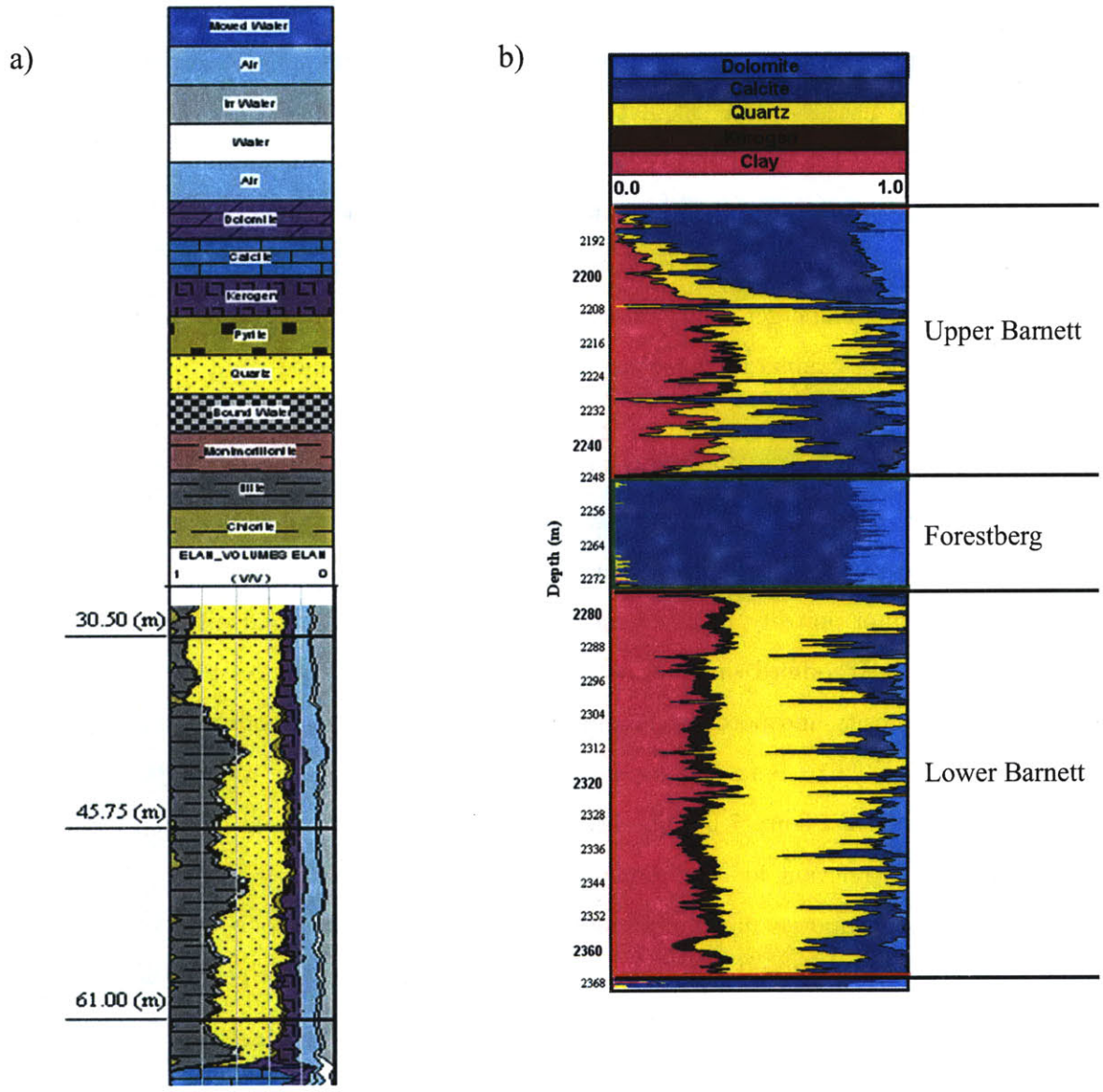

Figure 7-5: Summary of mineralogy results obtained from Element Capture Spectroscopy (ECS) logs for a) the Woodford formation, and b) the Barnett formation. Adapted from [3].

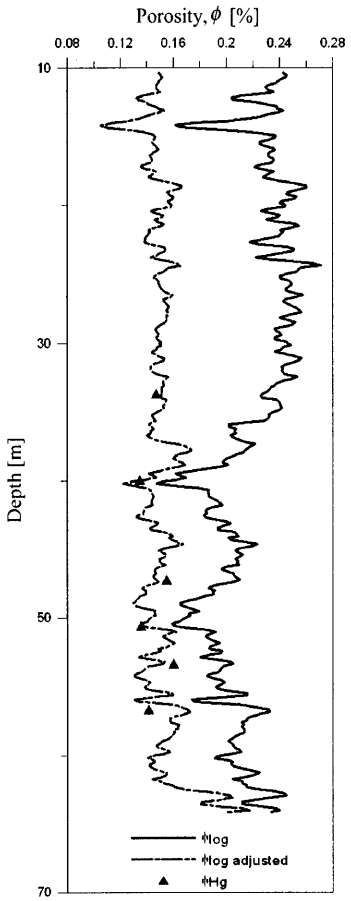

Figure 7-6: Porosity estimates for the Woodford formation: log porosity $\phi_{\log}$, calibrated log porosity, $\phi_{\log,calibrated}$, and MIP porosity ϕ_{Hg}. Adapted from [3].

with the borehole axis. The elastic properties are given in terms of engineering moduli, which are related to the elastic constants C_{ij} by:

$$E_3 = \frac{C_{11}C_{33} + C_{12}C_{33} - 2C_{13}^2}{C_{11} + C_{12}} \tag{7.4a}$$

$$G_3 = C_{44} \tag{7.4b}$$

$$\nu_{13} = \frac{C_{13}}{C_{11} + C_{12}} \tag{7.4c}$$

In addition to the elastic constants, the sonic log also provides an estimate for the Biot pore pressure coefficient α_3 in the direction normal-to-bedding (see Section 6.5). The UPV data displayed in Figure 7-7 corresponds to core samples analyzed in laboratory conditions. In general, the simulated elastic properties using the microporoelastic model compared adequately to the UPV data at selected intervals. This finding was already presented in Section 7.1, as the UPV data generated for some of the core samples was employed for the validation of the microporoelastic model extension to kerogen-rich shale. The model predictions and UPV data corresponding to the Young's modulus E_3 and shear modulus G_3 shown in Figure 7-7 tend to be larger than the responses measured through sonic logging. Improved comparisons are found for the Poisson's ratio ν_{13} and the Biot pore pressure coefficient α_3.

The results for the characterization of the Barnett formation are presented in Figure 7-8. Unfortunately, core samples were not available for laboratory characterization. For this shale formation, a similar suite of logs as that obtained for the Woodford formation was run. The sonic data and the model predictions are displayed for two geological intervals that are separated by the Forestberg calcite lense [3]. A good agreement between sonic data and simulated Young's and shear moduli is observed in Figure 7-8. The mean relative errors for the engineering moduli corresponding to the Upper Barnett section are approximately 15%, whereas those estimated for the Lower Barnett section are less than 7% [3].

These two pilot studies represent the first implementations of the model for the field characterization of shale formations. The better quantitative comparisons reached for Barnett shale are attributed to the calibration of the microporoelastic model using shale data obtained at moderate confining pressures. As discussed in Section 6.4.3, the pressure sensitivity of acoustic properties is not explicitly considered by the microporoelastic model. There are also several

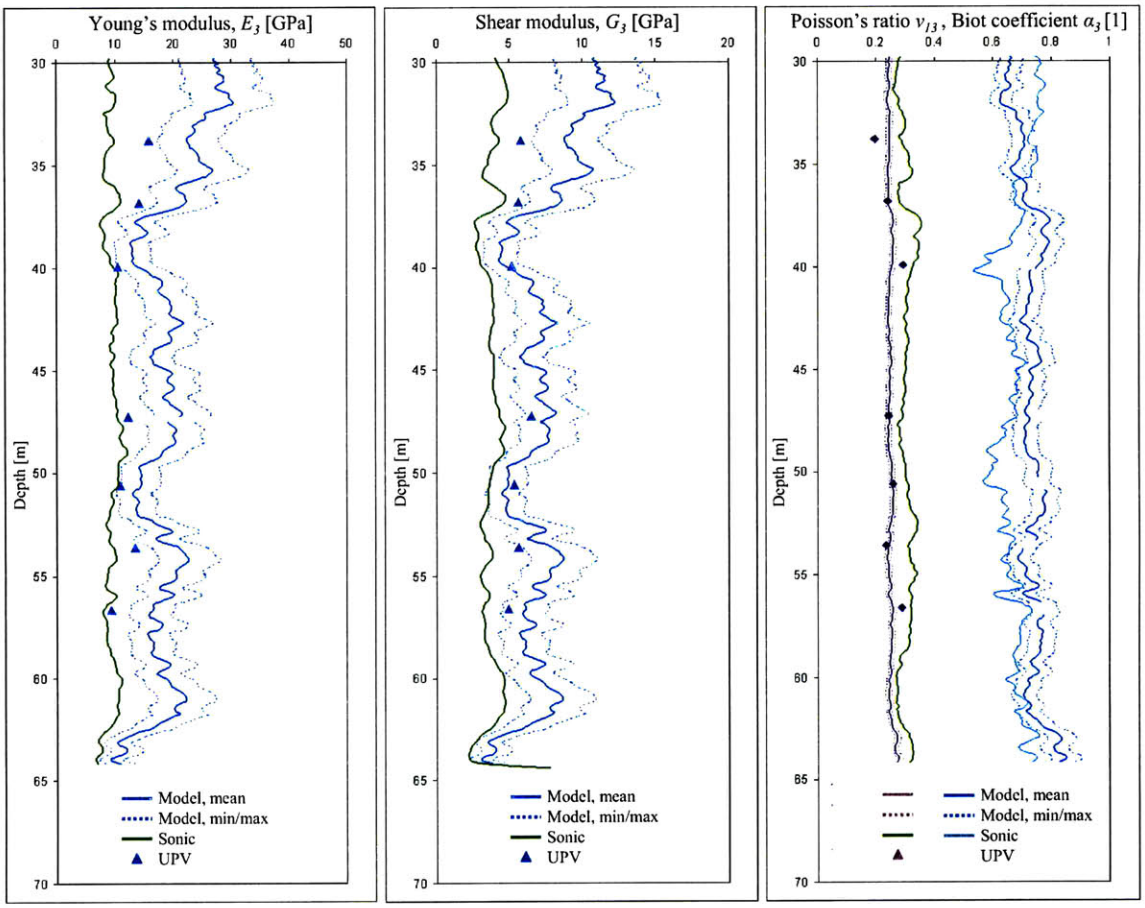

Figure 7-7: Comparison of engineering elastic constants in the normal-to-bedding direction estimated by Sonic Scanner, UPV measurements, and model predictions for the Woodford formation. The Biot pore pressure coefficient is also reported. Adapted from [3, 261].

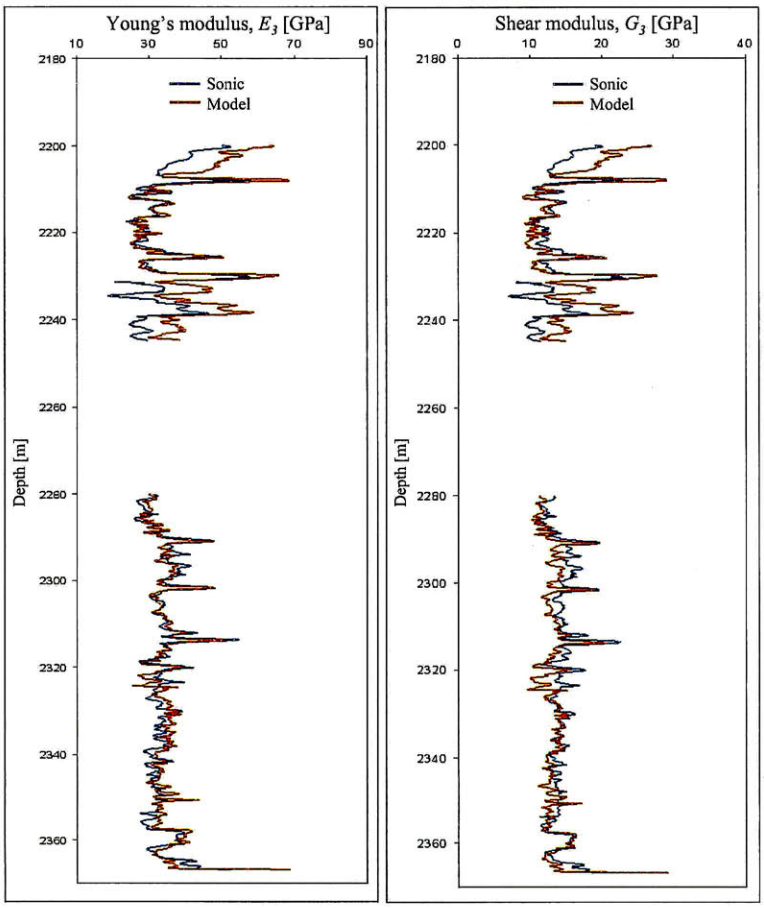

Figure 7-8: Comparison of engineering elastic constants in the normal-to-bedding direction estimated by Sonic Scanner and model predictions for the Barnett formation. Adapted from [3].

aspects that require further investigation in order to ensure the use of the microporoelastic model as an engineering tool for field applications. The assessments of porosity in field and laboratory setups tend to differ depending on the techniques. Consequently, correlation studies between different methods should be developed as porosity is a key parameter for estimating the clay packing density and the inclusion volume fraction. For the characterization of deep formations, temperature variations could have considerable effects on the predictions of poroelastic properties. The model extension discussed in Section 7.1 considers kerogen as a quasi-solid in view of laboratory conditions associated to UPV experiments. A different scenario could be encountered in deep shale formations, in which the kerogen phase at elevated temperatures could behave as a more compliant mechanical phase. The presence of different pore fluids and unsaturated conditions are common occurrences in shale formations, and are not supported by the model. The mechanical properties of water and fully saturated conditions are assumed as representative for these field implementations of the model. The dependency of acoustic properties on frequency also requires further experimental studies, although the preliminary calculations presented in Section 6.4.4 suggest that dispersion effects for the sonic and ultrasonic frequency ranges may be of similar magnitudes. Nevertheless, the quantification of dispersion effects in acoustic measurements is crucial for appropriate field characterization. Finally, the application of the microporoelastic model to large formations neglects any large scale discontinuities such as fractures or dislocations. The original development of the model is restricted to intact shale rock. Such configuration is associated with laboratory testing (e.g. UPV experiments) of bench-size rock specimens. However, the results from the two field applications described in this chapter encourage the potential use of the microporoelastic engineering model as a baseline characterization of the intrinsic anisotropy of shale formations.

7.3 Chapter Summary

In this chapter, the engineering model for anisotropic poroelasticity was adapted for the prediction of properties of kerogen-rich shale materials. The decrease in stiffness induced by the addition of the kerogen phase at the porous clay composite level allows the micromechanical model to predict effectively the macroscopic elastic behaviors of hydrocarbon bearing rocks.

The model has been implemented in two pilot studies of actual shale formations in an effort to investigate its applicability for formation characterization. Using only on mineralogy and porosity information, the model appears to capture the trends of acoustic properties for the Woodford and Barnett formations as estimated by sonic logging tools. These pilot field applications represent the first steps toward extending the model originally developed for laboratory bench-scale samples to in situ formation characterization. Further studies will be needed for the satisfactory evaluation of the effects of formation pressures, frequency dependence of acoustic properties, fractures, and high temperatures on the in situ poroelasticity predictions for shale rocks.

Part IV

Strength Predictability of Shale

Chapter 8

Strength Homogenization of Shale

The modeling and prediction of the strength properties of geomaterials such as rocks, soils, and, concrete continue to be challenging research fields for the mechanics community. The current knowledge of the cohesive-frictional behaviors of geomaterials has been derived mainly from macroscopic testing, and the modeling pursued from a purely phenomenological perspective. Typically, the macroscopic strength is characterized by a criterion defining the onset of plastic deformation (the elastic limit or yield strength, [56]). The simplest forms of strength criteria for geomaterials are linear relations such as the well-known Mohr-Coulomb [69] and Drucker-Prager [86] criteria, which capture a pressure-dependent strength development. Other yield criteria follow non-linear envelopes such as elliptical forms proposed for clay plasticity models (e.g. the Cam-clay model [234]), and hyperbolic forms proposed for strength of rocks (e.g. Hoek-Brown model [126]). All these criteria depend on strength parameters that must be calibrated for the specific material under investigation. As an alternative to purely phenomenological approaches, developments in micromechanics have enabled the prediction of macroscopic strength criteria for composite materials based on the strength behaviors of material constituents.

Part IV of this thesis is devoted to an exploratory work aiming at the implementation of the micromechanics approach to the modeling of the cohesive-frictional properties of shale. Similarly to the microporoelastic model developed in Part III, the objective of the strength upscaling model is to determine the macroscopic behavior of shale based on compositional and microstructural information. Chapter 8 is dedicated to the presentation of the micromechanics framework for the upscaling of strength properties of shale, which follows the multi-scale

structure thought-model used in the microporoelasticity investigation. A non-linear homogenization approach based on the linear comparison composite (LCC) theory [98] is employed in the development of the strength model. Given the novelty of the adopted theoretical framework, the multi-scale strength model is analyzed in detail to define its domain of application for predictive purposes. The assessment of the model includes detailed comparisons with existing micromechanics models and studies of the effects of material composition and microstructure on predicted strength domains. In an original development, the model is extended to treat a cohesive-frictional solid with dual-porosity, a material configuration of relevance to many geomaterials.

The implementation of the strength upscaling model for the characterization of strength properties of shale is pursued in Chapter 9. The strength model is calibrated and validated using independent data sets of strength properties. Hardness measurements obtained through instrumented nanoindentation experiments define the behavior of shale at grain-scales, and elucidate important trends of the cohesive-frictional response of the clay fabric. These learned behaviors are linked, through the application strength homogenization model, to the macroscopic strength response of shale materials as measured by conventional methods. Based on the results of the calibration and validation exercises, the ability and limitations of the model in delivering strength predictions of shale are finally discussed.

8.1 Elements of Strength Homogenization

The application of micromechanics theory has been largely devoted to the determination of elastic properties of material systems. Part III of this thesis attests to the extensive use of linear microporomechanics as a modeling framework for dealing with complex geomaterials like shale, which exhibits multi-scale properties, highly heterogeneous microstructures, and structural and intrinsic sources of anisotropy. In contrast, the development and application of micromechanics techniques to non-linear composites is a more recent and emerging research field [301].

A particular branch of non-linear micromechanics addresses the problem of upscaling strength properties. The objective of strength homogenization is to derive the macroscopic strength domain for a heterogeneous material from the specific microscopic strength responses of the

material constituents. The first contributions to strength upscaling schemes focused on composite materials with constituents governed by purely cohesive strength behaviors (see e.g. [141, 162, 248]). Strength upscaling schemes have been extended to the modeling of composite materials with cohesive-frictional strength attributes, which pertain directly to the behavior of rocks. The characterizations of strength domains for cohesive-frictional materials intermixed with porosity [83] or reinforced with rigid grains or inclusions [16, 163] have been recently derived. Important applications and extensions of the micromechanics approach have been also pursued. Cariou et al. [50] employed the strength homogenization approach for the assessment of cohesive-frictional properties of porous materials from nanoindentation hardness measurements. Maghous et al. [167] developed an extension of the micromechanics approach for strength properties within the framework of non-associated plasticity. Gathier and Ulm [98] have further advanced the modeling of cohesive-frictional materials through the implementation of the linear comparison composite (LCC) theory of Ponte Castañeda [214, 215, 216], which offers an improved treatment of the non-linear behavior inherent to the strength homogenization problem.

The multi-scale strength upscaling model for shale presented in this chapter follows the theoretical developments of Gathier and Ulm [98]. Meticulous analyses of the domain of application and predictive capabilities of the multi-scale theoretical framework are also developed. The presentation of the strength homogenization model for shale begins with the introduction of yield design theory, which forms the foundation for the strength modeling approach. The variational formulation rooted in the linear comparison composite theory is then presented as a means for addressing the non-linear strength homogenization problem. This theoretical background sets the stage for the introduction of the multi-scale strength model for shale, which is then compared to existing strength homogenization solutions for benchmark microstructural configurations. Finally, the predictive capabilities of the model are detailed, with emphases on the different strength regimes (elliptical and hyperbolic domains) and on the effects of rigid inclusions, interface conditions, and underlying microstructures on homogenized strengths. In an original development, the multi-scale model is extended to address the strength behavior of a two-scale porosity composite.

8.1.1 Yield Design Theory

The problem of strength homogenization is framed within the mechanics theory of plastic limit analysis or yield design. The objective of yield design is to determine the load-bearing capacity of a plastic material system. In the limit of plastic collapse, the material has exhausted its capacity to store any additional external work δW_{ext} into recoverable free energy $\dot{W}$. The formal expression of this process is given by the Clausius-Duhem inequality, which at the material system level and for isothermal evolutions is expressed as [266]:

$$\dot{D} = \delta W_{ext} - \dot{W} \geq 0 \tag{8.1}$$

where $\dot{D}$ refers to the rate of energy dissipation. At plastic collapse, the recoverable free energy reduces to $\dot{W} \equiv 0$, and consequently, the additional external work rate δW_{ext} is entirely dissipated into heat form through plastic yielding:

$$\dot{D} = \delta W_{ext} \geq 0 \tag{8.2}$$

Yield design focuses on the critical work increment leading to plastic collapse for a given geometry and set of prescribed loads without referring to specific energy states of the material system prior to failure, thus obviating the need to perform a complete elasto-plastic analysis.

The implementation of the yield design approach is intimately related to the following concepts [55, 224, 266]:

1. Plastic collapse occurs once the material or structure has exhausted its capacity to develop, in response to prescribed loads, stress fields that are statically compatible with the external loading and plastically admissible with the strength behavior of the material system. This stress-strength approach refers to the capacity of the material system to sustain additional loading through developing stresses that satisfy equilibrium considerations and that comply to the local strength of the material.

2. At plastic collapse, the external work supplied to the material system is dissipated through plastic yielding in the material bulk and/or along plastic slippage planes. The failure mechanisms, which cannot be controlled from outside of the system, follow the kinematics

of plastic flow developing in the material or structure. This kinematics approach evaluates how the plastic collapse occurs by determining the capacity of the material system for plastic dissipation along failure mechanisms.

The combination of these two concepts define the plastic collapse load in yield design, and consequently, the sought strength of the material system[1].

8.1.2 The Stress-Strength and Dual Approaches

The stress-strength approach focuses on the evaluation of stress fields that are statically compatible with prescribed forces and simultaneously compatible with the strength capacities of the material constituents. Consider the application of the stress-strength approach to the *rev* of a heterogeneous material system. The microscopic stress field $\boldsymbol{\sigma}'(\underline{z})$ is statically admissible (s.a.) with a given macroscopic stress state $\boldsymbol{\Sigma}$ provided it satisfies:

$$\begin{aligned} \operatorname{div} \boldsymbol{\sigma}' &= 0 && (\Omega) \\ \underline{t}(\underline{z}) &= \boldsymbol{\Sigma} \cdot \underline{n}(\underline{z}) && (\partial\Omega) \end{aligned} \tag{8.3}$$

where $\underline{t}$ is a uniform traction condition. Additionally, the material strength must sustain everywhere in the *rev* the stress fields induced by the macroscopic stress:

$$\boldsymbol{\sigma}'(\underline{z}) \in G(\underline{z}) \quad (\forall \underline{z} \in \Omega) \tag{8.4}$$

where $G(\underline{z})$ denotes the local, ultimate domain of plastically admissible stress states[2]. The strength domain $G(\underline{z})$ is assumed to be strictly convex, and it is described by means of a convex strength criterion $\mathcal{F}(\boldsymbol{\sigma}')$:

$$G = \left\{\boldsymbol{\sigma}', \mathcal{F}\left(\boldsymbol{\sigma}'\right) \leq 0\right\} \tag{8.5}$$

[1] The introduction of the yield design theoretical framework for strength homogenization follows the presentations of [83, 98, 167, 266].

[2] The term *ultimate* precludes any hardening effects since the material system has exhausted its capacity to store additional external work into recoverable free energy, including hardening energy [266].

A combination of conditions (8.3)-(8.4) defines the set of admissible stress states:

$$\overline{G} = \left\{ \boldsymbol{\Sigma}', \exists \boldsymbol{\sigma}' \text{ s.a. with } \boldsymbol{\Sigma}',\ \boldsymbol{\sigma}'(\underline{z}) \in G(\underline{z}) \quad (\forall \underline{z} \in \Omega) \right\} \tag{8.6}$$

Alternatively, the strength of a material can be expressed by a dual definition within the context of yield design theory. This dual definition is based on the premise that, at plastic collapse, the material system has exhausted its capacity to store external work into recoverable energy, and hence it is plastically dissipated into heat. The external work rate supplied to the *rev* is obtained by the application of the Hill Lemma (4.6) for the uniform traction condition in (8.3):

$$\delta W_{ext} = \frac{1}{|\Omega|} \int_{\partial\Omega} \underline{t}(\underline{z}) \cdot \underline{v}'(\underline{z})\, dS = \overline{\boldsymbol{\sigma}(\underline{z}) : \mathbf{d}(\underline{z})} = \boldsymbol{\Sigma} : \mathbf{D} \tag{8.7}$$

where $\mathbf{d}(\underline{v}'(\underline{z}))$ is the microscopic strain rate field related to the macroscopic strain $\mathbf{D}$:

$$\mathbf{d}\left(\underline{v}'(\underline{z})\right) = \frac{1}{2}\left(\mathbf{grad}\,\underline{v}' + {}^{t}\mathbf{grad}\,\underline{v}'\right) \tag{8.8a}$$

$$\mathbf{D} = \overline{\mathbf{d}(\underline{z})} \tag{8.8b}$$

The velocity field $\underline{v}'$ is kinematically admissible in the sense of yield design theory. Given that plastic collapse cannot be prescribed by constraining the velocity to non-zero values, the velocity field $\underline{v}'$ is only left to satisfy a zero-velocity boundary condition. The prescription of uniform stress boundary conditions (8.3) imposes no restrictions on the velocity field $\underline{v}'$. Nevertheless, the only restriction of the dissipated work rate at plastic collapse is that it must remain finite, as the material cannot sustain infinite stresses locally. These considerations lead to the definition of a support function $\pi(\mathbf{d})$, which denotes the maximum possible plastic dissipation capacity of the material:

$$\pi(\mathbf{d}) = \sup_{\boldsymbol{\sigma}'(\underline{z}) \in G(\underline{z})} \left\{ \boldsymbol{\sigma}' : \mathbf{d} \right\} \tag{8.9}$$

The support function has the characteristic of being a homogeneous function of degree 1:

$$\pi(t\mathbf{d}) = t\pi(\mathbf{d}) \qquad \left(\forall t \in \mathbb{R}^{+}\right) \tag{8.10}$$

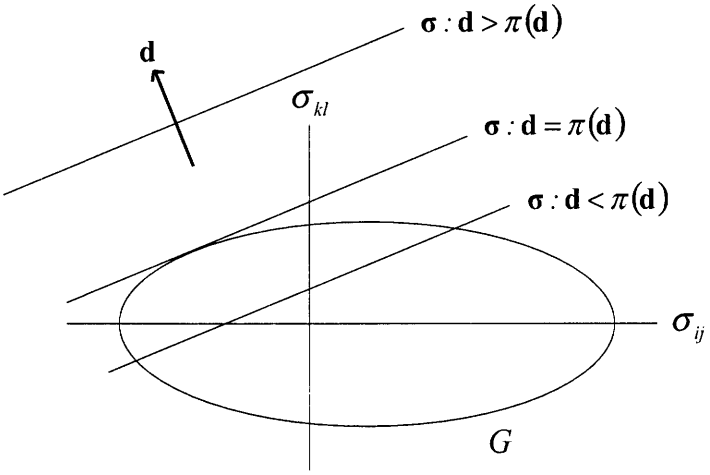

Figure 8-1: Geometrical interpretation of the support function (from [83]).

Furthermore, differentiating (8.10) with respect to $t > 0$ yields:

$$\frac{\partial \pi}{\partial \mathbf{d}}(\mathbf{d}) : (\mathbf{d}) = \pi(\mathbf{d}) \tag{8.11}$$

It follows that if a stress $\boldsymbol{\sigma}$ is on the boundary of the local strength domain G and maximizes the local work rate, that is $\pi(\mathbf{d}) = \boldsymbol{\sigma} : \mathbf{d}$, then the stress and strain rates are uniquely related by:

$$\boldsymbol{\sigma} = \frac{\partial \pi}{\partial \mathbf{d}}(\mathbf{d}) \tag{8.12}$$

Expression (8.9) represents the dual definition of the local strength domain of the material system based on its maximum plastic dissipation capacity. A geometrical interpretation of the support function is provided in Figure 8-1.

The dual definition of the local material strength is implemented in the strength homogenization problem of the heterogeneous *rev*. By noting that the stress field $\boldsymbol{\sigma}'(\underline{z})$ in definition (8.9) is strength compatible with the local response $G(\underline{z})$, it follows:

$$\boldsymbol{\sigma}' : \mathbf{d}\left(\underline{v}'(\underline{z})\right) \leq \pi\left(\underline{z}, \mathbf{d}\left(\underline{v}'\right)\right) \qquad (\forall \underline{z} \in \Omega) \tag{8.13}$$

The substitution of this expression into the volume average operation (8.7) gives:

$$\delta W_{ext} = \boldsymbol{\Sigma} : \mathbf{D} \leq \overline{\pi\left(\underline{z}, \mathbf{d}\left(\underline{v}'\right)\right)} \tag{8.14}$$

which provides an alternative characterization of the macroscopic stress that can be potentially supported by the material system in terms of a dissipation capacity.

8.1.3 Limit Analysis

The elements of yield design are a statically and plastically admissible stress state and a kinematically compatible velocity field subjected to the normality rule of plastic flow. Limit analysis focuses on determining bounds to the plastic collapse problem by relaxing either condition. The underlying idea of a stress-strength approach is the compatibility between conditions (8.3) and (8.4), without evoking the compatibility of the stress field and the kinematics of plastic flow associated with the actual stress field solution. Assume that the macroscopic stress $\boldsymbol{\Sigma}$, the corresponding microscopic stress field $\boldsymbol{\sigma}\left(\underline{z}\right)$, and a velocity field $\underline{v}\left(\underline{z}\right)$ satisfy:

$$\boldsymbol{\Sigma} : \mathbf{D} = \overline{\boldsymbol{\sigma}\left(\underline{z}\right) : \mathbf{d}\left(\underline{v}\left(\underline{z}\right)\right)} = \overline{\pi\left(\underline{z}, \mathbf{d}\left(\underline{v}\right)\right)} \tag{8.15}$$

It can be shown from convex analysis that [224, 266]:

$$\boldsymbol{\sigma}\left(\underline{z}\right) : \mathbf{d}\left(\underline{z}\right) = \sup_{\boldsymbol{\sigma}\left(\underline{z}\right) \in G\left(\underline{z}\right)} \left\{\boldsymbol{\sigma} : \mathbf{d}\right\} = \pi\left(\mathbf{d}\left(\underline{z}\right)\right) \qquad \left(\forall \underline{z} \in \Omega\right) \tag{8.16}$$

and that:

$$\boldsymbol{\Sigma}' : \mathbf{D} \leq \boldsymbol{\Sigma} : \mathbf{D} \qquad \left(\forall \boldsymbol{\Sigma}' \in \overline{G}\right) \tag{8.17}$$

Inequality (8.17) shows that any macroscopic stress $\boldsymbol{\Sigma}'$ that is compatible with definition (8.6) underestimates the maximum dissipation capacity of the material system at plastic collapse, given by:

$$\Pi_{\text{hom}}\left(\mathbf{D}\right) = \sup_{\boldsymbol{\Sigma} \in \overline{G}} \left\{\boldsymbol{\Sigma} : \mathbf{D}\right\} \tag{8.18}$$

with $\overline{G} = G_{\text{hom}}$ from the duality between the strength and dissipation capacity definition of yield design. Expression (8.18) represents the macroscopic counterpart of local material dissipation

(8.9), and hence, the solution to the yield design problem:

$$\boldsymbol{\Sigma} : \mathbf{D} = \Pi_{\text{hom}}(\mathbf{D}) \ , \ \boldsymbol{\Sigma} = \frac{\partial \Pi_{\text{hom}}}{\partial \mathbf{D}}(\mathbf{D}) \tag{8.19}$$

In contrast to the stress-strength approach, a kinematics approach offers an upper bound to the estimation of the maximum plastic dissipation of the material. At plastic collapse, the material undergoes free plastic flow. The corresponding strain rate is purely plastic, and its orientation is specified by the normality rule:

$$\mathbf{d} \overset{def}{=} \mathbf{d}^{pl} = \overset{\circ}{\lambda} \frac{\partial \mathcal{F}}{\partial \boldsymbol{\sigma}}(\boldsymbol{\sigma}) \tag{8.20}$$

where $\overset{\circ}{\lambda}$ is the plastic multiplier, which expresses the intensity of the plastic flow. The application of the associated plastic flow rule entails that the material is assumed to dissipate the externally applied work at the highest (yet finite) possible rate. From the convexity of the strength domain $\mathcal{F}(\boldsymbol{\sigma})$, it follows for a given strain rate $\mathbf{d}'$ and its associated stress field $\boldsymbol{\sigma}'$:

$$\boldsymbol{\sigma} : \mathbf{d}' \leq \sup_{\boldsymbol{\sigma}'(\underline{z}) \in G(\underline{z})} \left\{ \boldsymbol{\sigma}' : \mathbf{d}' \right\} = \pi \left(\mathbf{d}' = \overset{\circ}{\lambda} \frac{\partial \mathcal{F}}{\partial \boldsymbol{\sigma}'}(\boldsymbol{\sigma}') \right) \tag{8.21}$$

Let us define a set of velocity fields:

$$\mathcal{U}(\mathbf{D}) = \left\{ \underline{v}', \mathbf{D} = \overline{\mathbf{d}(\underline{v}'(\underline{z}))} \quad (\forall \underline{z} \in \Omega) \right\} \tag{8.22}$$

and establish that the macroscopic stress $\boldsymbol{\Sigma}$ is the solution to the yield design problem with associated velocity field $\underline{v}$. Considering a velocity field $\underline{v}' \in \mathcal{U}(\mathbf{D})$, the application of (8.14) yields:

$$\delta W_{ext} = \overline{\boldsymbol{\sigma}(\underline{z}) : \mathbf{d}(\underline{v}'(\underline{z}))} = \boldsymbol{\Sigma} : \mathbf{D} \leq \overline{\pi(\underline{z}, \mathbf{d}(\underline{v}'))} \quad \left(\forall \underline{v}' \in \mathcal{U}(\mathbf{D}) \right) \tag{8.23}$$

whereas for the actual velocity field solution (8.15), we obtain:

$$\delta W_{ext} = \overline{\boldsymbol{\sigma}(\underline{z}) : \mathbf{d}(\underline{v}(\underline{z}))} = \boldsymbol{\Sigma} : \mathbf{D} = \overline{\pi(\underline{z}, \mathbf{d}(\underline{v}))} = \Pi_{\text{hom}}(\mathbf{D}) \tag{8.24}$$

The combination of (8.23) and (8.24) yields:

$$\Pi_{\text{hom}}(\mathbf{D}) = \overline{\pi(\mathbf{d}(\underline{v}), \underline{z})} \leq \overline{\pi(\underline{z}, \mathbf{d}(\underline{v}'))} \quad (\forall \underline{v}' \in \mathcal{U}(\mathbf{D})) \tag{8.25}$$

This result shows that any kinematically admissible velocity field $\underline{v}'$ delivers an upper bound to the actual dissipation capacity of the material system:

$$\Pi_{\text{hom}}(\mathbf{D}) = \inf_{\underline{v}' \in \mathcal{U}(\mathbf{D})} \left\{ \overline{\pi(\underline{z}, \mathbf{d}(\underline{v}'))} \right\} \tag{8.26}$$

It is worth noting that the derivations herein presented were based on the application of the uniform stress boundary condition (8.3) and the intrinsic average (8.8b). More generally, the velocity field $\underline{v}'$ can be restricted by the application of a homogeneous strain rate boundary condition complying to:

$$\mathcal{U}(\mathbf{D}) = \left\{ \underline{v}', \underline{v}'(\underline{z}) = \mathbf{D} \cdot \underline{z} \quad (\forall \underline{z} \in \partial\Omega) \right\} \tag{8.27}$$

which directly satisfies the condition (8.8b). In addition, this kinematic boundary condition does not alter the expression of the external work rate (8.7), which is assumed to be entirely dissipated into heat form at plastic collapse. However, instead of serving as a true boundary condition to the otherwise unrestricted plastic collapse, the homogeneous strain rate condition in (8.27) serves as a constraint to the optimization problem (8.26) [98].

8.2 Non-Linear Homogenization

8.2.1 Variational Formulation

The homogenization problem of the heterogeneous *rev* composed of $i = 1, N$ material phases consists in solving the following set of equations[3]:

$$\operatorname{div} \boldsymbol{\sigma} = 0 \qquad (\Omega) \tag{8.28a}$$

$$\boldsymbol{\sigma}(\underline{z}) = \frac{\partial \pi^i}{\partial \mathbf{d}}(\mathbf{d}(\underline{z})) \qquad (\Omega^i) \tag{8.28b}$$

$$\mathbf{d} = \frac{1}{2}\left(\mathbf{grad}\,\underline{v} + {}^t\mathbf{grad}\,\underline{v}\right) \qquad (\Omega) \tag{8.28c}$$

$$\underline{v}(\underline{z}) = \mathbf{D} \cdot \underline{z} \qquad (\Omega) \tag{8.28d}$$

From convex analysis, the boundary value problem (8.28) can be alternatively formulated as a variational problem of the form [217]:

$$\Pi_{\text{hom}}(\mathbf{D}) = \inf_{\underline{v}' \in \mathcal{U}(\mathbf{D})} \frac{1}{|\Omega|} \int_{\Omega} \pi\left(\underline{z}, \mathbf{d}\left(\underline{v}'\right)\right) dV = \inf_{\underline{v}' \in \mathcal{U}(\mathbf{D})} \left\{ \overline{\pi\left(\underline{z}, \mathbf{d}\left(\underline{v}'\right)\right)} \right\} \tag{8.29}$$

where $\mathcal{U}(\mathbf{D})$ is the set of kinematically admissible strain rates defined in (8.27). Expression (8.29) is in fact associated with the kinematic approach to limit analysis (see (8.26)). At first glance, the problem in (8.28) may appear similar to the linear elasticity problem (see e.g. (4.75)) by replacing the strain rate $\mathbf{d}$ by the strain $\boldsymbol{\varepsilon}$, and the dissipation function $\pi(\mathbf{d})$ by a strain energy function, e.g. $\omega(\boldsymbol{\varepsilon}, \underline{z}) = \frac{1}{2}\boldsymbol{\varepsilon} : \mathbb{C}(\underline{z}) : \boldsymbol{\varepsilon}$. However, the dissipation function $\pi(\mathbf{d}) = \sup\{\boldsymbol{\sigma} : \boldsymbol{\varepsilon}\}$ is a homogeneous function of degree 1, whereas the strain energy function $\omega(\boldsymbol{\varepsilon})$ of linear elasticity obeys a quadratic form. Consequently, the non-linearity introduced in (8.28b) precludes the use of conventional linear homogenization techniques. Methodologies such as the effective strain rate approach (see e.g. [16, 248]) have been proposed to address the non-linearity of the boundary value problem (8.28). In this work, the solution to the strength homogenization problem resorts to the linear comparison composite (LCC) theory introduced by Ponte Castañeda [214, 215, 216], which aims at approximating the non-linear behavior by a linear elastic one with suitable model parameters.

[3] The condition $\boldsymbol{\sigma} = 0$ must be added to the set if the heterogeneity is porosity, with reference volume Ω^p.

8.2.2 Linear Comparison Composite Approach

Variational Problem Based on the LCC

The linear comparison composite (LCC) approach estimates the effective behavior of a non-linear composite in terms of an effective modulus tensor for a suitably chosen linear elastic comparison composite with a similar underlying microstructure as the non-linear composite. For the strength homogenization problem, the LCC method frames the determination of the dissipation function of the material system $\Pi_{\text{hom}}(\mathbf{D})$ as the solution to an elastic problem with an infinite number of phases [213].

The formulation of our variational problem using the LCC approach begins by considering a strain rate energy density function (or potential function) associated with a linear heterogeneous comparison composite material with non-uniform, positive-definite modulus tensor $\mathbb{C}_0(\underline{z})$[4]:

$$\omega_0(\underline{z}, \mathbf{d}) = \frac{1}{2}\mathbf{d} : \mathbb{C}_0(\underline{z}) : \mathbf{d} \tag{8.30}$$

The weaker-than-quadratic character of the dissipation function $\pi(\underline{z}, \mathbf{d})$ (i.e. $\pi(\underline{z}, \lambda\mathbf{d}) = \lambda\pi(\underline{z}, \mathbf{d})$ compared to $\omega_0(\underline{z}, \lambda\mathbf{d}) = \lambda^2\omega_0(\underline{z}, \mathbf{d})$) implies that $\pi(\underline{z}, \mathbf{d}) - \omega_0(\underline{z}, \mathbf{d}) \to -\infty$ for infinitely large strains. This suggests the following definition [217]:

$$\nu(\underline{z}, \mathbb{C}_0) = \sup_{\mathbf{d}} \{\pi(\underline{z}, \mathbf{d}) - \omega_0(\underline{z}, \mathbf{d})\} \tag{8.31}$$

Noting that $\nu(\underline{z}, \mathbf{d})$ is a convex function of $\mathbb{C}_0(\underline{z})$, it follows that:

$$\pi(\underline{z}, \mathbf{d}) \leq \omega_0(\underline{z}, \mathbf{d}) + \nu(\underline{z}, \mathbb{C}_0) \tag{8.32}$$

It is then concluded by taking the minimum over $\mathbb{C}_0(\underline{z})$:

$$\pi(\underline{z}, \mathbf{d}) \leq \inf_{\mathbb{C}_0 > 0} \{\omega_0(\underline{z}, \mathbf{d}) + \nu(\underline{z}, \mathbb{C}_0)\} \tag{8.33}$$

where the notation $\mathbb{C}_0 > 0$ denotes the positive-definite character of the modulus tensor. The

[4]The term modulus, within the context of the LCC theory, refers to the set of parameters that characterize the linear elastic comparison composite.

result (8.33) is used in (8.29) to reformulate the variational problem:

$$\Pi_{\text{hom}}(\mathbf{D}) = \inf_{\underline{v}' \in \mathcal{U}(\mathbf{D})} \left\{ \overline{\inf_{\mathbb{C}_0 > 0} \{\omega_0(\underline{z}, \mathbf{d}(\underline{v}')) + \nu(\underline{z}, \mathbb{C}_0)\}} \right\} \tag{8.34}$$

or equivalently, after interchanging the order of infima [214]:

$$\Pi_{\text{hom}}(\mathbf{D}) = \inf_{\mathbb{C}_0 > 0} \left\{ \overline{\mathcal{W}_0(\mathbf{D}) + \mathcal{V}(\mathbb{C}_0)} \right\} \tag{8.35}$$

where:

$$\mathcal{W}_0(\mathbf{D}) = \inf_{\underline{v}' \in \mathcal{U}(\mathbf{D})} \left\{ \overline{\omega_0(\underline{z}, \mathbf{d}(\underline{v}'))} \right\} \tag{8.36a}$$

$$\mathcal{V}(\mathbb{C}_0) = \overline{\nu(\underline{z}, \mathbb{C}_0)} \tag{8.36b}$$

The expression for the macroscopic dissipation function $\Pi_{\text{hom}}(\mathbf{D})$ in (8.35) is now expressed in terms of a variational principle for a linear comparison heterogeneous material, whose properties are given by the strain rate energy of a suitably chosen linear comparison composite $\mathcal{W}_0(\mathbf{D})$ and the function $\mathcal{V}(\mathbb{C}_0)$ measuring the non-linearity of the original material.

LCC Approximation for a N-Phase Composite

It is worth noting that the modulus tensor for the LCC material $\mathbb{C}_0(\underline{z})$ in (8.35) is a varying quantity over the heterogeneous *rev*, which makes the solution of the variational problem as cumbersome as the original one. Fortunately, the formulation in (8.35) can be extended for discrete forms of $\mathbb{C}_0(\underline{z})$ that allow for a simplified implementation of the method [215, 216].

First, consider a comparison composite in which the behavior of each material phase is given by:

$$\boldsymbol{\sigma} = \mathbb{C}^i : \mathbf{d} + \boldsymbol{\tau}^i \tag{8.37}$$

where $\mathbb{C}^i$ is the positive-definite modulus tensor and $\boldsymbol{\tau}^i$ an eigenstress, which becomes instrumental for subsequent model developments. The corresponding piecewise-constant strain rate

energy of the composite materials is:

$$\omega_0(\underline{z}, \mathbf{d}) = \sum_i \chi(\underline{z})\ \omega^i(\mathbf{d}) \tag{8.38}$$

where:

$$\chi(\underline{z}) = \begin{cases} = 1 \text{ if } \underline{z} \in \Omega^i \\ = 0 \text{ if } \underline{z} \notin \Omega^i \end{cases} \tag{8.39a}$$

$$\omega^i(\mathbf{d}) = \frac{1}{2}\mathbf{d} : \mathbb{C}^i : \mathbf{d} + \boldsymbol{\tau}^i : \mathbf{d} \tag{8.39b}$$

The pursued reformulation of (8.35) in a discrete form will yield an upper bound for the true dissipation capacity. Then, recalling the classical inequality [216]:

$$\inf_x \{f(x) + g(x)\} \geq \inf_x \{f(x)\} + \inf_x \{g(x)\} \tag{8.40}$$

and applying it to $\omega_0 = \pi + (\omega_0 - \pi)$, it follows that:

$$\inf_{\underline{v}' \in \mathcal{U}(\mathbf{D})} \left\{\overline{\omega_0(\underline{z}, \mathbf{d}(\underline{v}'))}\right\} \geq \inf_{\underline{v}' \in \mathcal{U}(\mathbf{D})} \left\{\overline{\pi(\underline{z}, \mathbf{d}(\underline{v}'))}\right\} + \inf_{\underline{v}' \in \mathcal{U}(\mathbf{D})} \left\{\overline{\omega_0(\underline{z}, \mathbf{d}(\underline{v}')) - \pi(\underline{z}, \mathbf{d}(\underline{v}'))}\right\} \tag{8.41}$$

where we recognize the term $\Pi_{\text{hom}}(\mathbf{D})$, which then yields:

$$\Pi_{\text{hom}}(\mathbf{D}) \leq \inf_{\underline{v}' \in \mathcal{U}(\mathbf{D})} \left\{\overline{\omega_0(\underline{z}, \mathbf{d}(\underline{v}'))}\right\} - \inf_{\underline{v}' \in \mathcal{U}(\mathbf{D})} \left\{\overline{\omega_0(\underline{z}, \mathbf{d}(\underline{v}')) - \pi(\underline{z}, \mathbf{d}(\underline{v}'))}\right\} \tag{8.42}$$

The first term of the right hand side of (8.42) is the macroscopic strain rate energy of the LCC:

$$\mathcal{W}_0(\mathbf{D}) = \inf_{\underline{v}' \in \mathcal{U}(\mathbf{D})} \left\{\overline{\omega_0(\underline{z}, \mathbf{d}(\underline{v}'))}\right\} \tag{8.43}$$

The second term in (8.42) can be overestimated by:

$$-\inf_{\underline{v}' \in \mathcal{U}(\mathbf{D})} \left\{\overline{\omega_0(\underline{z}, \mathbf{d}(\underline{v}')) - \pi(\underline{z}, \mathbf{d}(\underline{v}'))}\right\} \geq \sum_i f^i \mathcal{V}^i \tag{8.44}$$

where $\mathcal{V}^i$ is constant in each phase of volume fraction f^i:

$$\mathcal{V}^i = \sup_{\mathbf{d}} \left\{ \pi^i (\mathbf{d}) - \omega^i (\mathbf{d}) \right\} \tag{8.45}$$

Finally, the following upper bound is obtained for the macroscopic dissipation capacity of the comparison composite material:

$$\Pi_{\text{hom}} (\mathbf{D}) \leq \mathcal{W}_0 (\mathbf{D}) + \sum_i f^i \mathcal{V}^i \tag{8.46}$$

The goal is to find the modulus parameters of the comparison composite that lead to the lowest possible upper bound for (8.46), therefore yielding the best possible estimate of Π_{hom}. However, as discussed in [216], preserving an upper bound status may prove to be a difficult task. Instead, it is of interest to consider a generalized version of (8.46) by replacing the extremal points by stationary points. The resulting estimates are then stationary estimates and not bounds, in the sense of (8.35). The stationary estimate of $\Pi_{\text{hom}} (\mathbf{D})$ is:

$$\widetilde{\Pi}_{\text{hom}} (\mathbf{D}) = \underset{\mathbb{C}^i, \boldsymbol{\tau}^i}{\text{stat}} \left\{ \mathcal{W}_0 (\mathbf{D}) + \sum_i f^i \mathcal{V}^i \right\} \tag{8.47}$$

with:

$$\mathcal{V}^i = \underset{\mathbf{d}}{\text{stat}} \left\{ \pi^i (\mathbf{d}) - \omega^i (\mathbf{d}) \right\} \tag{8.48}$$

There are usually different points of stationarity, hence each particular case must be analyzed separately [216].

Steps for Determining Homogenized Strength Properties based on the LCC Approach

The LCC methodology is used to determine the macroscopic strength criterion for a composite material through the following steps [98]:

- Compute the expression for the macroscopic strain rate energy $\mathcal{W}_0 (\mathbf{D})$ of the LCC composite. Relevant results from linear micromechanics are used to furnish the macroscopic strain rate energy.

- Compute the function $\mathcal{V}^i$ for each phase. This function measures the non-linearity of the original material and contains the information about the local strength capacities through the material dissipation functions $\pi^i(\mathbf{d})$.

- Generate the system of stationarity equations (8.47)-(8.48) and solve the system in terms of the modulus properties $\mathbb{C}^i$ and the eigenstress $\boldsymbol{\tau}^i$.

- Use the estimated dissipation capacity $\widetilde{\Pi}^{\text{hom}}(\mathbf{D})$ to derive the macroscopic strength domain through the yield design definition (8.19).

8.3 Multi-Scale Homogenization Model

8.3.1 Micromechanics Representation of Shale

Following the microporoelasticity model development presented in Part III, we adopt the multi-scale structure thought-model for shale (Section 2.3) as the reference for building the strength homogenization model. The micromechanics description of shale for modeling its strength properties also benefits from the results gathered from microporoelasticity, especially in terms of the treatment of the microstructure through effective particle morphologies and homogenization schemes for granular media.

At level 0, the scale of the elementary clay particles is represented by an elementary building block of solid clay. The strength modeling of shale begins by assuming that this elementary unit follows isotropic strength properties, as suggested by nanoindentation hardness measurements (see Figure 3-15). Similarly to the elementary building block for elasticity, the properties of the elementary unit for strength modeling are assumed to be material invariant quantities. The characteristic cohesive-frictional properties of the solid clay used for model development will be further explored in Chapter 9, in which model calibration and validation exercises will link the grain-scale strength of shale to macroscopic measurements.

The porous clay composite or level I is characterized by the strength properties of the solid clay phase and the weakening contribution from the nanoporosity. The granular microstructure of the porous clay is modeled through the self-consistent scheme, in which the effective morphologies of the elementary units of clay and nanoporosity are represented as spherical in-

clusions. The parameter that quantifies the mechanical contributions of the two phases at level I is the clay packing density.

Finally, the macroscopic scale of shale formed by the porous clay composite intermixed with silt inclusions is modeled as a two-phase composite consisting of the cohesive-frictional porous clay and rigid inclusions. The premise of rigid inclusions implies their unbounded strength, and it constitutes a first approach to the homogenization problem herein development. To enhance the description of the strength behavior at the macroscale, the interface behavior between porous clay and inclusion phases considers two limit conditions: perfectly adherent and slip (non-frictional) interfaces. In an original development, a second configuration for the level II homogenization step is investigated, in which the rigid inclusions are replaced by pores. The corresponding material system is a two-scale porosity medium, with a nanoporosity assigned to level I and a macroporosity assigned to level II. The proposed variation of the multi-scale model represents a model extension of interest to the modeling of geomaterials such as sandstones, in which the pore space manifests itself at different length scales. The micromechanics representation of shale for strength upscaling and modeling is schematically summarized in Figure 8-2.

8.3.2 Level 0 - Cohesive-Frictional Solid Clay

The lowest level we consider is that of the solid clay phase with cohesive-frictional strength properties. It is generally recognized that the clay phase in shale and soils, in general, display a pressure-sensitive response in which the shear (or deviatoric) strength increases with increasing confinement [187]. This pressure-sensitive behavior of the solid is captured by the Drucker-Prager criterion, which depends on two invariants of the stress state sustained by the material: the mean stress $\sigma_m = \frac{1}{3} I_1 = \frac{1}{3} \mathrm{tr}\,(\boldsymbol{\sigma})$, and the deviatoric stress $\mathbf{s} = \boldsymbol{\sigma} - \sigma_m \mathbf{1}$. The Drucker-Prager failure criterion is expressed as:

$$\mathcal{F}^s\,(\boldsymbol{\sigma}) = \sqrt{J_2} + \alpha \sigma_m - c^s \leq 0 \tag{8.49}$$

where $J_2 = \frac{1}{2}\mathbf{s} : \mathbf{s}$, and α, c^s are the Drucker-Prager friction coefficient and cohesion that characterize the intrinsic strength properties of the solid phase. It is important to notice that

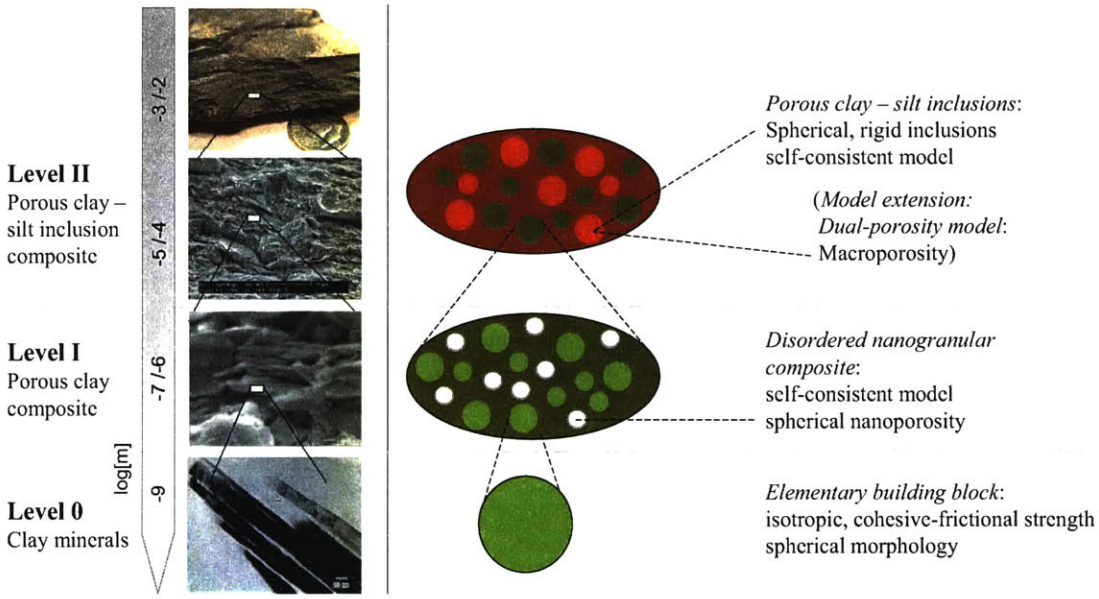

Figure 8-2: Summary of the proposed micromechanics representation of shale for strength homogenization modeling.

the Drucker-Prager friction coefficient is limited to $\alpha < \sqrt{3}/2$, which corresponds to a Mohr-Coulomb friction angle of 90° [75]. Recent results of micromechanics modeling have shown that the continuum Drucker-Prager criterion can represent the strength behavior of a polycrystalline solid with Coulomb-type failure prescribed at crystal interfaces [92]. These results encourage the choice of the Drucker-Prager model to describe the strength properties of the elementary building block of solid clay, which from the microporoelasticity investigation is understood as a conglomerate of clay units composed of platelets and compliant interlayers.

The dual definition of the Drucker-Prager strength domain prescribed for the clay solid phase (8.49) is given by the support function $\pi^s(\mathbf{d})$ [224]:

$$\boldsymbol{\sigma} \in G^s(\underline{z}) \Leftrightarrow \pi^s(\mathbf{d}) = \sup\{\boldsymbol{\sigma} : \mathbf{d}\} = \begin{cases} \dfrac{c^s}{\alpha} d_v & \text{if } d_v \geq 2\alpha d_d \\ \infty & \text{else} \end{cases} \tag{8.50}$$

where $d_v = \operatorname{tr}(\mathbf{d})$ and $d_d = \sqrt{\frac{1}{2}\boldsymbol{\delta} : \boldsymbol{\delta}} = \sqrt{J_2'}$ are the strain rate invariants of the strain rate tensor $\mathbf{d} = \boldsymbol{\delta} + \frac{1}{3} d_v \mathbf{1}$. It is convenient for upcoming developments to formulate expressions

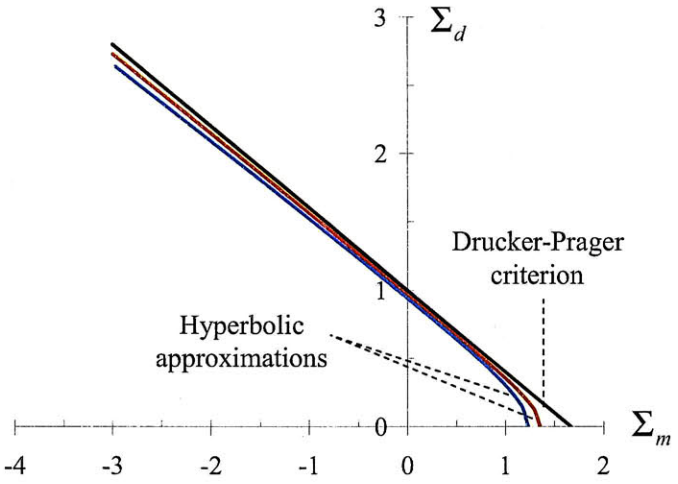

Figure 8-3: Approximation of a Drucker-Prager strength domain by a set of hyperbolic domains.

(8.49) and (8.50) as strictly convex functions for the application of the LCC variational approach to strength homogenization. Consequently, the following regularized strength criterion that asymptotically tends to the Drucker-Prager criterion and also circumvents the point of singularity ($J_2 = 0, \sigma_m = c^s/\alpha$) is considered:

$$\mathcal{F}(\boldsymbol{\sigma}) = 1 - \left(\frac{\sigma_m - S_0}{A}\right)^2 + \left(\frac{\sigma_d}{B}\right)^2 \leq 0 \tag{8.51}$$

where $\sigma_d = \sqrt{J_2}$. The set of hyperbolas in (8.51) are defined by the scalar quantities A, B, and S_0. The Drucker-Prager criterion (8.49) is retrieved as a special limit case for the following conditions:

$$\begin{cases} B = \alpha A \\ S_0 = \dfrac{c^s}{\alpha} \\ A \to 0 \end{cases} \tag{8.52}$$

The regularization of the Drucker-Prager strength criterion is shown schematically in Figure 8-3.

Similarly, the regularized dual definition of the strength domain in terms of the support

function $\pi(\mathbf{d})$ is obtained from the following set of conditions [266]:

$$\mathbf{d} = \overset{\circ}{\lambda} \frac{\partial \mathcal{F}}{\partial \boldsymbol{\sigma}} (\boldsymbol{\sigma}) \tag{8.53a}$$

$$\mathcal{F}(\boldsymbol{\sigma}) = 0 \tag{8.53b}$$

$$\boldsymbol{\sigma} : \mathbf{d} = \pi(\mathbf{d}) \tag{8.53c}$$

The $6+1+1=8$ equations enable the determination of the unknowns: $\pi(\mathbf{d})$, $\overset{\circ}{\lambda}$, and $6 \times \sigma_{ij}$ at the boundary of the strength domain $\partial\mathcal{F}(\boldsymbol{\sigma})$. For the regularized hyperbolic criterion (8.51), we make use of:

$$\frac{\partial \mathcal{F}}{\partial \boldsymbol{\sigma}} (\boldsymbol{\sigma}) = \frac{1}{3} \frac{\partial \mathcal{F}}{\partial \sigma_m} (\sigma_m, \sigma_d) + \frac{1}{2\sigma_d} \frac{\partial \mathcal{F}}{\partial \sigma_d} (\sigma_m, \sigma_d) \, \mathbf{s} \tag{8.54}$$

Thus, expression (8.53a) gives:

$$\begin{cases} \sigma_m - S_0 = -\frac{A^2 d_v}{\overset{\circ}{\lambda}} \\ \sigma_d = \frac{B^2 d_d}{\overset{\circ}{\lambda}} \end{cases} \tag{8.55}$$

while the value of $\overset{\circ}{\lambda}$ is given by (8.53b):

$$\left(\overset{\circ}{\lambda}\right)^2 = \left(\frac{A d_v}{2}\right)^2 - (B d_d)^2 \tag{8.56}$$

It then follows:

$$\pi(\mathbf{d}) = \pi(d_v, d_d) = S_0 d_v - \sqrt{(A d_v)^2 - (2 B d_d)^2} \tag{8.57}$$

The Drucker-Prager support function (8.50) is exactly retrieved when (8.57) is subjected to the set of conditions (8.52).

8.3.3 Level I: Porous Clay Composite

The homogenization step at level I establishes the strength behavior of the porous clay composed of the pore space and the solid clay phase that follows the Drucker-Prager model. The application of the LCC methodology to deliver the homogenized strength domain for the porous clay composite follows the approach formulated in Section 8.2.2. For reasons of convexity, the regularized dual form of the Drucker-Prager criterion (8.57) is preferred for the forthcoming developments.

Strain Rate Energy Function $\mathcal{W}_0^I(\mathbf{D})$ of the Porous Clay Composite

The first step for solving the strength homogenization problem of the porous clay composite is determining the strain rate energy function $\mathcal{W}_0^I(\mathbf{D})$ of the linear elastic comparison composite at level I. A convenient way to homogenize this behavior is to apply a continuous description of the microscopic stress field:

$$\boldsymbol{\sigma}(\underline{z}) = \mathbb{C}(\underline{z}) : \mathbf{d}(\underline{z}) + \boldsymbol{\tau}(\underline{z}) \qquad (\forall \underline{z} \in \Omega) \tag{8.58}$$

where the microscopic modulus tensor $\mathbb{C}(\underline{z})$ and the eigenstress $\boldsymbol{\tau}(\underline{z})$ have the following spatial distributions within the *rev*:

$$\mathbb{C}(\underline{z}) = \begin{cases} \mathbb{C}^s = 3k^s\mathbb{J} + 2g^s\mathbb{K} & (\Omega^s) \\ 0 & (\Omega^p) \end{cases} \qquad \boldsymbol{\tau}(\underline{z}) = \begin{cases} \tau\mathbf{1} & (\Omega^s) \\ 0 & (\Omega^p) \end{cases} \tag{8.59}$$

and $\Omega^s = (1-\varphi)\,\Omega$, $\Omega^p = \varphi\Omega$ are the domains occupied by the clay phase and the nanoporosity, respectively. The volume fraction used for the homogenization at level I is the clay packing density[5] $\eta = 1 - \varphi$. Using Levin's theorem [83], the corresponding macroscopic stress equation of state reads:

$$\boldsymbol{\Sigma} = \mathbb{C}^I_{\text{hom}} : \mathbf{D} + \mathbf{T}^I \tag{8.60}$$

where $\mathbb{C}^I_{\text{hom}}$ and $\mathbf{T}^I$ are the macroscopic modulus tensor and eigenstress given by:

$$\mathbb{C}^I_{\text{hom}} = \overline{\mathbb{C}(\underline{z}) : \mathbb{A}(\underline{z})} = \eta\mathbb{C}^s : \overline{\mathbb{A}}^s = 3k^I_{\text{hom}}\mathbb{J} + 2g^I_{\text{hom}}\mathbb{K} \tag{8.61a}$$

$$\mathbf{T}^I = \overline{\boldsymbol{\tau}(\underline{z}) : \mathbb{A}(\underline{z})} = \eta\tau\mathbf{1} : \overline{\mathbb{A}}^s = \tau\mathbf{1} : (\mathbb{C}^s)^{-1} : \mathbb{C}^I_{\text{hom}} = \tau\frac{k^I_{\text{hom}}}{k^s}\mathbf{1} \tag{8.61b}$$

$$k^I_{\text{hom}} = \eta k^s\mathbb{J} : \overline{\mathbb{A}}^s = g^s\mathcal{K}^I\left(\frac{k^s}{g^s}, \eta\right) \tag{8.62a}$$

$$g^I_{\text{hom}} = \eta g^s\mathbb{K} : \overline{\mathbb{A}}^s = g^s\mathcal{M}^I\left(\frac{k^s}{g^s}, \eta\right) \tag{8.62b}$$

[5] In contrast to the microporoelastic case, the formal development of the strength criterion considers the pore volume fraction φ to correspond to the current configuration of the microstructure, which is in fact the relevant configuration for the analysis of failure [83].

with $\mathbb{A}(\underline{z})$ the forth-order strain (rate) localization tensor, and $\overline{\mathbb{A}}^s$ the volume average of $\mathbb{A}(\underline{z})$ over the solid phase. The second parts of the expressions in (8.62) are readily obtained from dimensional analysis, where the dimensionless functions $\mathcal{K}^I$ and $\mathcal{M}^I$ are the inclusion morphology factors for level I. These dimensionless functions depend on the bulk-to-shear modulus ratio, the clay packing density, and the morphological features of the microstructure. They will be presented in a forthcoming section.

The general strain energy function in terms of strain rates for a two-phase composite $\mathcal{W}_0(\mathbf{D})$ is given from classical thermoelasticity [158, 164]:

$$\begin{aligned}\mathcal{W}_0(\mathbf{D}) &= \frac{1}{2}\mathbf{D}:\mathbb{C}_{\text{hom}}:\mathbf{D}+\left[\left(\boldsymbol{\tau}^1-\boldsymbol{\tau}^2\right):\left(\mathbb{C}^1-\mathbb{C}^2\right)^{-1}:\left(\mathbb{C}_{\text{hom}}-\mathbb{C}^2\right)+\boldsymbol{\tau}^2\right]:\mathbf{D} \\ &\quad +\frac{1}{2}\left(\boldsymbol{\tau}^1-\boldsymbol{\tau}^2\right):\left[\left(\mathbb{C}^1-\mathbb{C}^2\right)^{-1}:\left(\mathbb{C}_{\text{hom}}-\mathbb{C}^2\right)-f^1\mathbb{I}\right]:\left(\mathbb{C}^1-\mathbb{C}^2\right)^{-1}:\left(\boldsymbol{\tau}^1-\boldsymbol{\tau}^2\right)\end{aligned} \tag{8.63}$$

For our purposes, the strain rate energy function adapted to the porous clay configuration and in isotropic form simplifies to:

$$\begin{aligned}\mathcal{W}_0^I(D_v,D_d) &= \frac{1}{2}k_{\text{hom}}^I D_v^2+2g_{\text{hom}}^I D_d^2+\frac{k_{\text{hom}}^I}{k^s}\tau D_v+\frac{1}{2k^s}\left(\frac{k_{\text{hom}}^I}{k^s}-\eta\right)\tau^2 \\ &= \frac{1}{2}g^s\mathcal{K}^I D_v^2+2g^s\mathcal{M}^I D_d^2+\frac{g^s}{k^s}\tau\mathcal{K}^I D_v+\frac{1}{2k^s}\left(\frac{g^s}{k^s}\mathcal{K}^I-\eta\right)\tau^2\end{aligned} \tag{8.64}$$

where $D_v=\text{tr}(\mathbf{D})$ and $D_d=\sqrt{\frac{1}{2}\boldsymbol{\Delta}:\boldsymbol{\Delta}}$, with $\boldsymbol{\Delta}=\mathbf{D}-\frac{1}{3}D_v\mathbf{1}$.

$\mathcal{V}$ Function or Measure of Non-Linearity

The second step in the strength homogenization of level I consists in determining the $\mathcal{V}^s$ function (8.48), which provides a measure of the non-linear behavior of the solid phase (the value of $\mathcal{V}^p$ for the nanoporosity domain is zero). For its implementation, the expression of the π^s function (8.57) is required, along with an expression for the strain rate energy of the solid:

$$\omega^s(\mathbf{d})=\frac{1}{2}k^s d_v^2+2g^s d_d^2+\tau d_v \tag{8.65}$$

The application of the stationarity condition to the $\mathcal{V}^s$ function yields:

$$\frac{\partial \mathcal{V}^s}{\partial d_v} = \frac{\partial \left(\pi^s - \omega^s\right)}{\partial d_v} = S_0 - \frac{A^2 d_v}{\sqrt{\left(Ad_v\right)^2 - \left(2Bd_d\right)^2}} - k^s d_v - \tau = 0 \tag{8.66a}$$

$$\frac{\partial \mathcal{V}^s}{\partial d_d} = \frac{\partial \left(\pi^s - \omega^s\right)}{\partial d_d} = \frac{4B^2 d_d}{\sqrt{\left(Ad_v\right)^2 - \left(2Bd_d\right)^2}} - 4g^s d_d = 0 \tag{8.66b}$$

The introduction of the eigenstress provides a means for ensuring that the microscopic moduli k^s, g^s are positive by manipulating (8.66):

$$\tau = S_0 - \frac{2A^2 d_v}{\sqrt{\left(Ad_v\right)^2 - \left(2Bd_d\right)^2}} \tag{8.67a}$$

$$k^s = \frac{A^2}{\sqrt{\left(Ad_v\right)^2 - \left(2Bd_d\right)^2}} > 0 \tag{8.67b}$$

$$g^s = \frac{B^2}{\sqrt{\left(Ad_v\right)^2 - \left(2Bd_d\right)^2}} > 0 \tag{8.67c}$$

Consequently, only two parameters are independent for the behavior of the comparison composite, namely g^s and τ, since:

$$\frac{k^s}{g^s} = \frac{A^2}{B^2} = cst. \tag{8.68}$$

For the Drucker-Prager case (8.52), the previous expression reduces to:

$$\frac{k^s}{g^s} = \frac{A^2}{B^2} = \frac{1}{\alpha^2} \tag{8.69}$$

These results yield the sought expression of the non-linearity function $\mathcal{V}^s$ for a hyperbolic criterion as a function of the independent parameters g^s and τ:

$$\mathcal{V}^s = \frac{1}{4g^s}\left[\frac{B\left(S_0 - \tau\right)}{A}\right]^2 - \frac{B^2}{2g^s} \tag{8.70}$$

which for the Drucker-Prager case (8.52) simplifies to:

$$\mathcal{V}^s = \frac{1}{4g^s}\left(c^s - \alpha\tau\right)^2 \tag{8.71}$$

Stationarity of the Dissipation Function $\widetilde{\Pi}^I_{\text{hom}}$

The third step consists in evaluating the stationarity of the homogenized dissipation function for the porous clay composite $\widetilde{\Pi}^I_{\text{hom}}$ (8.47). The result in (8.68) reduces the degrees of freedom from three (k^s, g^s, τ) to two (g^s, τ), such that the evaluation of (8.47) takes the form:

$$\widetilde{\Pi}^I_{\text{hom}} = \underset{g^s,\tau}{\text{stat}} \left\{ \mathcal{W}^I_0 \left(D_v, D_d \right) + \eta \mathcal{V}^s \right\} \tag{8.72}$$

This condition is expressed explicitly as:

$$\frac{\partial \widetilde{\Pi}^I_{\text{hom}}}{\partial g^s} = \frac{\partial k^s}{\partial g^s} \frac{\partial \mathcal{W}^I_0}{\partial k^s} + \frac{\partial \mathcal{W}^I_0}{\partial g^s} + \eta \frac{\partial \mathcal{V}^s}{\partial g^s} = 0 \tag{8.73a}$$

$$\frac{\partial \widetilde{\Pi}^I_{\text{hom}}}{\partial \tau} = \frac{\partial \mathcal{W}^I_0}{\partial \tau} + \eta \frac{\partial \mathcal{V}^s}{\partial \tau} = 0 \tag{8.73b}$$

Using (8.64) and (8.70) in (8.73b), while making use of (8.68) yields:

$$\tau = \frac{A^2 \left(2 g^s \mathcal{K}^I D_v - \eta S_0 \right)}{\eta A^2 - 2 \mathcal{K}^I B^2} \tag{8.74}$$

Substituting (8.74) into the solution of (8.73a) gives:

$$(g^s)^2 = \frac{\eta B^2 \left[\eta A^2 \left(S_0^2 - A^2 \right) + \mathcal{K}^I B^2 \left(2A^2 - S_0^2 \right) \right]}{A^2 \left[\eta \mathcal{K}^I A^2 D_v^2 + 4 \left(\eta \mathcal{M}^I A^2 - 2 \mathcal{K}^I \mathcal{M}^I B^2 \right) D_d^2 \right]} \tag{8.75}$$

Finally, using the expressions of (g^s, τ) corresponding to the stationarity of $\widetilde{\Pi}^I_{\text{hom}}$ in (8.72) provides the following estimate for $\widetilde{\Pi}^I_{\text{hom}}$:

$$\widetilde{\Pi}^I_{\text{hom}} \left(\mathbf{D} \right) = \widetilde{\Pi}^I_{\text{hom}} \left(D_v, D_d \right) = \Sigma^I_{\text{hom},0} D_v - \text{sign} \left(2 \mathcal{K}^I B^2 - \eta A^2 \right) \sqrt{\left(A^I_{\text{hom}} D_v \right)^2 + \left(2 B^I_{\text{hom}} D_d \right)^2} \tag{8.76}$$

where:

$$\left(A^I_{\text{hom}}\right)^2 = \frac{\eta^2 B^2 \mathcal{K}^I \left[\eta A^2 \left(S_0^2 - A^2\right) + B^2 \mathcal{K}^I \left(2A^2 - S_0^2\right)\right]}{\left(\eta A^2 - 2B^2 \mathcal{K}^I\right)^2} \tag{8.77a}$$

$$\left(B^I_{\text{hom}}\right)^2 = \frac{\eta B^2 \mathcal{M}^I \left[\eta A^2 \left(S_0^2 - A^2\right) + B^2 \mathcal{K}^I \left(2A^2 - S_0^2\right)\right]}{A^2 \left(\eta A^2 - 2B^2 \mathcal{K}^I\right)} \tag{8.77b}$$

$$\Sigma^I_{\text{hom},0} = \frac{\eta B^2 \mathcal{K}^I}{2B^2 \mathcal{K}^I - \eta A^2} S_0 \tag{8.77c}$$

The comparison of expressions (8.76) and (8.57) reveals that $\widetilde{\Pi}^I_{\text{hom}}$ is the support function of a hyperbolic criterion provided that $2\mathcal{K}^I B^2 - \eta A^2 > 0$. In return, the support function for the case $2\mathcal{K}^I B^2 - \eta A^2 < 0$ corresponds to an elliptical strength criterion.

The expressions in (8.77) for the Drucker-Prager case reduce to the following homogenization factors:

$$\left(\frac{A^I_{\text{hom}}}{c^s}\right)^2 = \frac{\eta^2 \mathcal{K}^I \left(\eta - \alpha^2 \mathcal{K}^I\right)}{\left(\eta - 2\alpha^2 \mathcal{K}^I\right)^2} \tag{8.78a}$$

$$\left(\frac{B^I_{\text{hom}}}{c^s}\right)^2 = \frac{\eta \mathcal{M}^I \left(\eta - \alpha^2 \mathcal{K}^I\right)}{\eta - 2\alpha^2 \mathcal{K}^I} \tag{8.78b}$$

$$\frac{\Sigma^I_{\text{hom},0}}{c^s} = \frac{\eta \alpha \mathcal{K}^I}{2\alpha^2 \mathcal{K}^I - \eta} \tag{8.78c}$$

The class of criterion is determined by the sign of $\varrho = 2\alpha^2 \mathcal{K}^I - \eta$: $\varrho > 0$ for a hyperbola, $\varrho < 0$ for an ellipse.

Strength Criterion for Porous Clay Composite

With the homogenized support function for the porous clay composite $\widetilde{\Pi}^I_{\text{hom}}$ at hand, the strength criterion is derived using the yield design definition (8.19):

$$\Sigma_m = \frac{1}{3}\text{tr}\left(\boldsymbol{\Sigma}\right) = \frac{\partial \widetilde{\Pi}^I_{\text{hom}}}{\partial D_v} \tag{8.79a}$$

$$\Sigma_d = \frac{1}{2}\frac{\partial \widetilde{\Pi}^I_{\text{hom}}}{\partial D_d} \tag{8.79b}$$

where $\Sigma_d = \sqrt{\frac{1}{2}\mathbf{S} : \mathbf{S}}$, and $\mathbf{S} = \boldsymbol{\Sigma} - \Sigma_m \mathbf{1}$. The application to (8.76) yields the sought homoge-

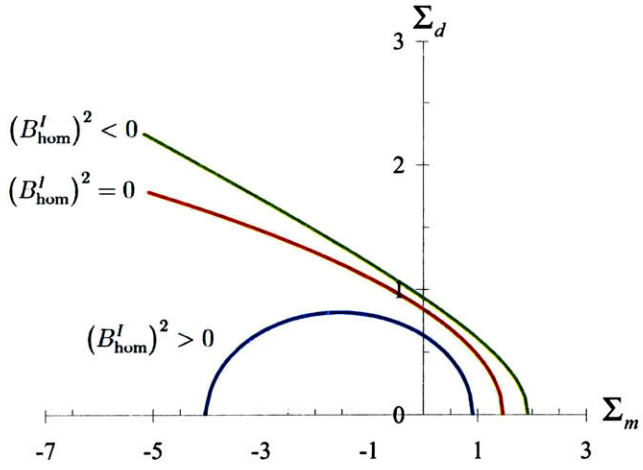

Figure 8-4: Schematic of the different strength criteria: elliptical $\left(B^I_{\text{hom}}\right)^2 > 0$, limit parabola $\left(B^I_{\text{hom}}\right)^2 = 0$, and hyperbolic $\left(B^I_{\text{hom}}\right)^2 < 0$.

nized strength criterion for level I:

$$\mathcal{F}^I(\boldsymbol{\Sigma}) = \left(\frac{\Sigma_m - \Sigma^I_{\text{hom},0}}{A^I_{\text{hom}}}\right)^2 + \left(\frac{\Sigma_d}{B^I_{\text{hom}}}\right)^2 - 1 \leq 0 \tag{8.80}$$

By inspection of (8.80), the homogenized criterion can be either a hyperbola or an ellipse depending on the sign of the term $\left(B^I_{\text{hom}}\right)^2$, as displayed schematically in Figure 8-4. From (8.78b), the sign of the term $\left(B^I_{\text{hom}}\right)^2$ for the Drucker-Prager case depends on:

$$\eta - 2\alpha^2 \mathcal{K}^I\left(\frac{k^s}{g^s} = \frac{1}{\alpha^2}, \eta\right) \begin{cases} < 0 & \text{Hyperbolic criterion} \\ = 0 & \text{Limit parabola} \\ > 0 & \text{Elliptical criterion} \end{cases} \tag{8.81}$$

Inclusion Morphology Factors for Level I

The only terms missing for the evaluation of (8.80) are the inclusion morphology factors for the porous clay composite:

$$\frac{k^I_{\text{hom}}}{g^s} = \mathcal{K}^I\left(\frac{k^s}{g^s},\eta\right) \tag{8.82a}$$

$$\frac{g^I_{\text{hom}}}{g^s} = \mathcal{M}^I\left(\frac{k^s}{g^s},\eta\right) \tag{8.82b}$$

Their definitions in expressions (8.61) and (8.62) enable the use of linear micromechanics for their determination. The morphology of the porous clay composite follows a similar configuration as the one adopted for the microporoelastic engineering model for shale, in which the elementary building block of clay and the nanoporosity are represented as spherical inclusions. In addition, the isotropic strength behavior assumed in the linear comparison composite approach for level I enables the use of the Hill concentration tensor for spherical inclusions in an isotropic medium (refer to Section 4.2.5). The upscaling strength model for shale, akin to the microporoelastic model, requires the implementation of the self-consistent model to describe the granular microstructure and mechanics of the porous clay composite. For completeness, the estimates for $\mathcal{K}^I, \mathcal{M}^I$ based on the Mori-Tanaka homogenization scheme are presented.

The evaluation of the morphology factors for the porous clay composite using linear micromechanics theory (see e.g. expressions (4.32) and (4.39) for the Mori-Tanaka and self-consistent estimates, respectively) yields:

$$\mathcal{K}^I_{MT} = \frac{4\eta}{3(1-\eta)+4\alpha^2} \tag{8.83a}$$

$$\mathcal{M}^I_{MT} = \frac{\eta\left(9+8\alpha^2\right)}{15-6\eta+(20-12\eta)\,\alpha^2} \tag{8.83b}$$

$$\mathcal{K}^I_{SC} = \frac{4\eta\,\mathcal{M}^I_{SC}}{4\alpha^2\,\mathcal{M}^I_{SC}+3(1-\eta)} \tag{8.84a}$$

$$\mathcal{M}^I_{SC} = \frac{1}{2}-\frac{5}{4}(1-\eta)-\frac{3}{16\alpha^2}(2+\eta)+ \frac{1}{16\alpha^2}\sqrt{144\left(\alpha^4-\alpha^2\right)-480\alpha^4\eta+400\alpha^4\eta^2+408\alpha^2\eta-120\alpha^2\eta^2+9(2+\eta)^2} \tag{8.84b}$$

in which the solid clay bulk-to-shear modulus ratio is replaced by (8.69). Similar to stiffness homogenization, the application of the Mori-Tanaka scheme exhibits a percolation threshold at $\eta_0 = 0$, hence offering a continuous development of strength for the entire range of packing densities. In contrast, the application of the self-consistent scheme to spherical morphologies is characterized by the percolation threshold at $\eta_0 = 0.5$.

The application of either description of microstructure defines a critical packing density η^{cr}, which separates the elliptical and hyperbolic strength domains:

$$\eta - \eta^{cr}(\alpha) \begin{cases} > 0 & \text{Hyperbolic criterion} \\ = 0 & \text{Limit parabola} \\ < 0 & \text{Elliptical criterion} \end{cases} \tag{8.85}$$

For the Mori-Tanaka type of morphology, substitution of (8.83a) in (8.81) delivers:

$$0 < \eta^{cr}_{MT} = 1 - \frac{4}{3}\alpha^2 \leq 1 \tag{8.86}$$

where the lower bound corresponds to the limit case $\alpha = \sqrt{3}/2$. For the self-consistent scheme, substitution of (8.84a) in (8.81) delivers:

$$\frac{2}{3} < \eta^{cr}_{SC} = 1 - \frac{\sqrt{1216\alpha^4 + 432\alpha^2 + 81} - \left(16\alpha^2 + 9\right)}{2\left(3 + 20\alpha^2\right)} \leq 1 \tag{8.87}$$

The critical packing densities for both homogenization schemes are displayed in Figure 8-5. The figure shows that the effect of microstructure is more significant for higher friction values of the solid phase.

8.3.4 Level II: Porous Clay - Silt Inclusion Composite

The macroscopic scale of shale corresponds to the porous clay composite intermixed with silt-size inclusions such as quartz. For the homogenization step at level II, the aim is to derive the strength behavior for the two-phase material composed of the porous clay phase governed by the strength criterion (8.80) and rigid silt inclusions. The model development follows a similar procedure to that used for level I.

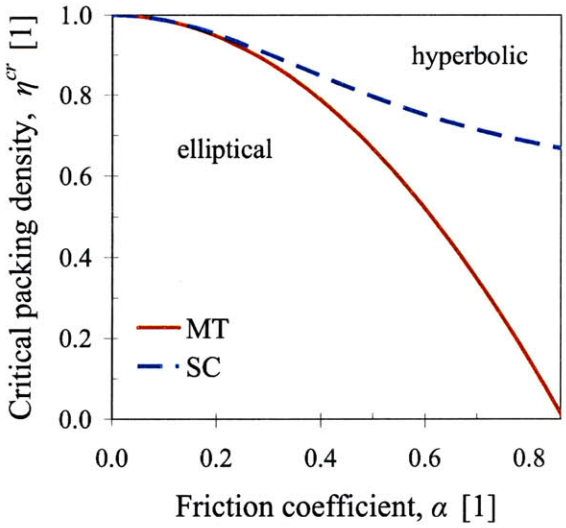

Figure 8-5: Critical packing density η^{cr} as a function of the friction coefficient α. The microstructure of the porous clay is modeled by the Mori-Tanaka (MT) and self-consistent (SC) schemes.

Strain Rate Energy Function $\mathcal{W}_0^{II}(\mathbf{D})$ of the Porous Clay - Silt Inclusion Composite

Consider the composite formed by the porous clay phase and rigid inclusions and occupying the volumes $\Omega^{pc} = \left(1 - f^{inc}\right)\Omega$ and $\Omega^{inc} = f^{inc}\Omega$, respectively, at the macroscopic scale or level II. For convenience, a continuous description of the stress field in the heterogeneous *rev* is assumed:

$$\boldsymbol{\sigma}(\underline{z}) = \mathbb{C}(\underline{z}) : \mathbf{d}(\underline{z}) + \boldsymbol{\tau}(\underline{z}) \qquad (\forall \underline{z} \in \Omega) \tag{8.88}$$

together with the following spatial description of the modulus tensor and the eigenstress:

$$\mathbb{C}(\underline{z}) = \begin{cases} \mathbb{C}^{pc} = 3k^{pc}\mathbb{J} + 2g^{pc}\mathbb{K} & (\Omega^{pc}) \\ \infty & (\Omega^{inc}) \end{cases} \qquad \boldsymbol{\tau}(\underline{z}) = \begin{cases} \tau^{pc}\mathbf{1} & (\Omega^{pc}) \\ 0 & (\Omega^{inc}) \end{cases} \tag{8.89}$$

where $\mathbb{C}^{pc}$ and τ^{pc} are the modulus tensor and eigenstress of the porous clay at level I given by the LCC approach. The corresponding macroscopic stress state equation for a solid reinforced with inclusions is:

$$\boldsymbol{\Sigma} = \mathbb{C}_{\text{hom}}^{II} : \mathbf{D} + \mathbf{T}^{II} \tag{8.90}$$

with:

$$\mathbb{C}_{\text{hom}}^{II} = \overline{\mathbb{C}(\underline{z}) : \mathbb{A}(\underline{z})} = 3k_{\text{hom}}^{II}\mathbb{J} + 2g_{\text{hom}}^{II}\mathbb{K} \tag{8.91a}$$

$$\mathbf{T}^{II} = \overline{\boldsymbol{\tau}(\underline{z}) : \mathbb{A}(\underline{z})} = \tau^{pc}\mathbf{1} \tag{8.91b}$$

Similar to (8.62), the homogenized moduli are presented in a dimensionless form:

$$k_{\text{hom}}^{II} = g^{pc}\mathcal{K}^{II}\left(\frac{k^{pc}}{g^{pc}}, f^{inc}\right) \tag{8.92a}$$

$$g_{\text{hom}}^{II} = g^{pc}\mathcal{M}^{II}\left(\frac{k^{pc}}{g^{pc}}, f^{inc}\right) \tag{8.92b}$$

where the inclusion morphology factors $\mathcal{K}^{II}$,$\mathcal{M}^{II}$ will be detailed later on. With this information, the general expression of the strain rate energy (8.63) is adapted to the case of the porous clay reinforced with rigid inclusions:

$$\mathcal{W}_0^{II}(D_v, D_d) = \frac{1}{2}g^{pc}\mathcal{K}^{II}D_v^2 + 2g^{pc}\mathcal{M}^{II}D_d^2 + \tau^{pc}D_v \tag{8.93}$$

$\mathcal{V}$ Function or Measure of Non-Linearity

The next step consists in determining the $\mathcal{V}^{pc}$ function for the (homogenized) porous solid phase (the value of $\mathcal{V}^{inc}$ for the rigid inclusion phase is zero). The support function of the porous clay composite $\pi^{pc}(\mathbf{d})$ is adapted from (8.76):

$$\pi^{pc}(\mathbf{d}) = \widetilde{\Pi}_{\text{hom}}^{I}(\mathbf{D} \to \mathbf{d}) = \Sigma_{\text{hom},0}^{I}d_v - \text{sign}(\varrho)\sqrt{\left(A_{\text{hom}}^{I}d_v\right)^2 + \left(2B_{\text{hom}}^{I}d_d\right)^2} \tag{8.94}$$

where $\varrho = 2\alpha^2\mathcal{K}^I - \eta$ distinguishes the hyperbolic ($\varrho > 0$) and elliptical ($\varrho < 0$) strength domains, and the morphology factors $\Sigma_{\text{hom},0}^{I}, A_{\text{hom}}^{I}, B_{\text{hom}}^{I}$ are specified in (8.78). The strain rate energy function for the porous solid phase is akin to (8.65):

$$\omega^{pc}(\mathbf{d}) = \frac{1}{2}k^{pc}d_v^2 + 2g^{pc}d_d^2 + \tau^{pc}d_v \tag{8.95}$$

Given the familiar forms of $\pi^{pc}(\mathbf{d})$ and $\omega^{pc}(\mathbf{d})$ when compared to their counterparts at level I, previous developments can be used for deriving the $\mathcal{V}^{pc}$ function provided that the form of

the support function $\widetilde{\Pi}^I_{\text{hom}}$ is associated with a hyperbolic strength criterion. Recall that the derivation of (8.70) began with a hyperbolic criterion that included a minus sign and $B^2 > 0$ (see (8.57)). Therefore, one can adapt the result (8.70) to the form of (8.76) for the case when the strength criterion of the porous clay at level I is a hyperbola by replacing $\left(B^I_{\text{hom}}\right)^2$ by $-\left(B^I_{\text{hom}}\right)^2$:

$$\mathcal{V}^{pc}\left(\varrho > 0\right) = \frac{\left(B^I_{\text{hom}}\right)^2}{2g^{pc}} - \frac{1}{4g^{pc}}\left[\frac{B^I_{\text{hom}}\left(\Sigma^I_{\text{hom},0} - \tau^{pc}\right)}{A^I_{\text{hom}}}\right]^2 \tag{8.96}$$

together with:

$$\beta = \frac{k^{pc}}{g^{pc}} = -\operatorname{sign}\left(\varrho\right)\left(\frac{A^I_{\text{hom}}}{B^I_{\text{hom}}}\right)^2 = cst. \tag{8.97}$$

where $-\operatorname{sign}\left(\varrho\right)$ accounts for the fact that $\left(B^I_{\text{hom}}\right)^2 < 0$ in the hyperbolic case.

In contrast, the general procedure for calculating the stationarity condition of the $\mathcal{V}^{pc}$ function is followed for the case when the support function $\widetilde{\Pi}^I_{\text{hom}}$ is associated with an elliptical strength criterion ($\varrho < 0$):

$$\frac{\partial \mathcal{V}^{pc}}{\partial d_v} = \Sigma^I_{\text{hom},0} + \frac{\left(A^I_{\text{hom}}\right)^2 d_v}{\sqrt{\left(A^I_{\text{hom}} d_v\right)^2 + \left(2B^I_{\text{hom}} d_d\right)^2}} - k^{pc} d_v - \tau^{pc} = 0 \tag{8.98}$$

$$\frac{\partial \mathcal{V}^{pc}}{\partial d_d} = \frac{4\left(B^I_{\text{hom}}\right)^2 d_d}{\sqrt{\left(A^I_{\text{hom}} d_v\right)^2 + \left(2B^I_{\text{hom}} d_d\right)^2}} - 4g^{pc} d_d = 0 \tag{8.99}$$

The consideration of the eigenstress ensures the positivity of the moduli k^{pc}, g^{pc}:

$$\tau^{pc} = \Sigma^I_{\text{hom},0} \tag{8.100a}$$

$$k^{pc} = \frac{\left(A^I_{\text{hom}}\right)^2}{\sqrt{\left(A^I_{\text{hom}} d_v\right)^2 + \left(2B^I_{\text{hom}} d_d\right)^2}} > 0 \tag{8.100b}$$

$$g^{pc} = \frac{-\operatorname{sign}\left(\varrho\right)\left(B^I_{\text{hom}}\right)^2}{\sqrt{\left(A^I_{\text{hom}} d_v\right)^2 + \left(2B^I_{\text{hom}} d_d\right)^2}} > 0 \tag{8.100c}$$

and consequently:

$$\beta = \frac{k^{pc}}{g^{pc}} = -\operatorname{sign}\left(\varrho\right)\left(\frac{A^I_{\text{hom}}}{B^I_{\text{hom}}}\right)^2 = cst. \tag{8.101}$$

The expression for the $\mathcal{V}^{pc}$ function for the elliptical case is therefore:

$$\mathcal{V}^{pc}\left(\varrho<0\right)=\frac{\left(B_{\mathrm{hom}}^{I}\right)^{2}}{2g^{pc}} \tag{8.102}$$

Stationarity of the Dissipation Function $\widetilde{\Pi}_{\mathrm{hom}}^{II}$ and Hyperbolic Strength Criterion

The macroscopic strength related to the case of a hyperbolic strength criterion governing the behavior of the porous clay composite at level I is first considered. The two degrees of freedom for the application of the stationarity condition are g^{pc}, τ^{pc}:

$$\widetilde{\Pi}_{\mathrm{hom}}^{II}=\underset{g^{pc},\tau^{pc}}{\mathrm{stat}}\left\{\mathcal{W}_{0}^{II}\left(D_{v},D_{d}\right)+\left(1-f^{inc}\right)\mathcal{V}^{pc}\right\} \tag{8.103}$$

Using (8.93) and (8.96), the stationarity condition with respect to τ^{pc} yields:

$$\tau^{pc}=\Sigma_{\mathrm{hom},0}^{I}+\frac{2g^{pc}D_{v}}{1-f^{inc}}\left(\frac{A_{\mathrm{hom}}^{I}}{B_{\mathrm{hom}}^{I}}\right)^{2} \tag{8.104}$$

In addition, the stationarity condition with respect to g^{pc} delivers the following expression:

$$\frac{\partial\widetilde{\Pi}_{\mathrm{hom}}^{II}}{\partial g^{pc}}=\frac{1}{2}\mathcal{K}^{II}D_{v}^{2}+2\mathcal{M}^{II}D_{d}^{2}+\frac{1-f^{inc}}{2\left(g^{pc}\right)^{2}}\left(\frac{1}{2}\left[\frac{B_{\mathrm{hom}}^{I}\left(\Sigma_{\mathrm{hom},0}^{I}-\tau^{pc}\right)}{A_{\mathrm{hom}}^{I}}\right]^{2}-\left(B_{\mathrm{hom}}^{I}\right)^{2}\right)=0 \tag{8.105}$$

The strength domain for level II can be found by replacing the macroscopic strain rates D_v, D_d in the stationarity conditions (8.104) and (8.105) by their corresponding expressions provided through the state equations of the linear elastic comparison composite (8.90):

$$D_{v} = \frac{\Sigma_{m}-\tau^{pc}}{k_{\mathrm{hom}}^{II}} \tag{8.106a}$$

$$D_{d} = \frac{\Sigma_{d}}{2g_{\mathrm{hom}}^{II}} \tag{8.106b}$$

yielding:

$$\mathcal{F}^{II}\left(\boldsymbol{\Sigma}\right)=\left(\frac{\Sigma_{m}-\Sigma_{\mathrm{hom},0}^{II}}{A_{\mathrm{hom}}^{II}}\right)^{2}+\left(\frac{\Sigma_{d}}{B_{\mathrm{hom}}^{II}}\right)^{2}-1\leq0\qquad\left(\varrho>0\right) \tag{8.107}$$

where:

$$\left(A^{II}_{\text{hom}}\right)^2 = 2\left(A^{I}_{\text{hom}}\right)^2 + \left(1-f^{inc}\right)\mathcal{K}^{II}\left(B^{I}_{\text{hom}}\right)^2 \tag{8.108a}$$

$$\left(B^{II}_{\text{hom}}\right)^2 = \left(1-f^{inc}\right)\mathcal{M}^{II}\left(B^{I}_{\text{hom}}\right)^2 \tag{8.108b}$$

$$\Sigma^{II}_{\text{hom},0} = \Sigma^{I}_{\text{hom},0} \tag{8.108c}$$

The strength criterion in (8.107) corresponds to the porous clay – silt inclusion composite whose porous clay phase is governed by a hyperbolic strength domain (i.e. $\left(B^{I}_{\text{hom}}\right)^2 < 0$). Furthermore, it is evident that the macroscopic composite is also described by a hyperbolic criterion at level II since $\left(B^{II}_{\text{hom}}\right)^2 < 0$.

Stationarity of the Dissipation Function $\widetilde{\Pi}^{II}_{\text{hom}}$ and Elliptical Strength Criterion

The macroscopic strength related to the case of an elliptical strength criterion governing the behavior of the porous solid at level I is now considered. Given that expression (8.100a) fixes the value of the eigenstress τ^{pc}, the stationarity condition for $\widetilde{\Pi}^{II}_{\text{hom}}$ depends solely on g^{pc}, yielding the following relation:

$$\frac{\partial \widetilde{\Pi}^{II}_{\text{hom}}}{\partial g^{pc}} = \frac{1}{2}\mathcal{K}^{II}D_v^2 + 2\mathcal{M}^{II}D_d^2 - \frac{\left(1-f^{inc}\right)\left(B^{I}_{\text{hom}}\right)^2}{2\left(g^{pc}\right)^2} = 0 \tag{8.109}$$

In a similar development as for the evaluation of the hyperbolic strength criterion, the solution to the stationarity condition for $\widetilde{\Pi}^{II}_{\text{hom}}$ and the substitution of the strain rates D_v, D_d by their corresponding expressions provided through the state equations of the linear elastic comparison composite (8.90) deliver the macroscopic strength criterion for the case of the porous clay governed by an elliptical strength criterion:

$$\mathcal{F}^{II}\left(\boldsymbol{\Sigma}\right) = \left(\frac{\Sigma_m - \Sigma^{II}_{\text{hom},0}}{A^{II}_{\text{hom}}}\right)^2 + \left(\frac{\Sigma_d}{B^{II}_{\text{hom}}}\right)^2 - 1 \leq 0 \qquad (\varrho < 0) \tag{8.110}$$

where:

$$\left(A^{II}_{\text{hom}}\right)^2 = \left(1 - f^{inc}\right) \mathcal{K}^{II} \left(B^{I}_{\text{hom}}\right)^2 \tag{8.111a}$$

$$\left(B^{II}_{\text{hom}}\right)^2 = \left(1 - f^{inc}\right) \mathcal{M}^{II} \left(B^{I}_{\text{hom}}\right)^2 \tag{8.111b}$$

$$\Sigma^{II}_{\text{hom},0} = \Sigma^{I}_{\text{hom},0} \tag{8.111c}$$

It is found that the macroscopic composite with a porous clay phase governed by an elliptical strength domain (i.e. $\left(B^{I}_{\text{hom}}\right)^2 > 0$) is described by an elliptical criterion at level II since $\left(B^{II}_{\text{hom}}\right)^2 > 0$.

Inclusion Morphology Factors for Level II

The evaluations of the homogenized strength criteria (8.107) and (8.110) at level II require the definition of the inclusion morphology factors $\mathcal{K}^{II}, \mathcal{M}^{II}$. Following a similar configuration as proposed for the microporoelastic engineering model, the microstructure of the porous clay - silt inclusion composite is represented as spherical inclusions with isotropic properties. The mechanical interaction between the two material phases is described by the self-consistent scheme for granular materials. For completeness, the case of a matrix-inclusion type of microstructure modeled by the Mori-Tanaka scheme is also presented.

The determination of the inclusion morphology factors resorts to the results from linear micromechanics for a two-phase linear comparison composite with modulus properties as defined by (8.89), i.e. the porous clay is characterized by the moduli k^{pc}, g^{pc} while the consideration of rigid inclusions imply $(k^{inc}, g^{inc} \to \infty)$. In particular, the ratio of bulk-to-shear moduli k^{pc}/g^{pc} is expressed in view of (8.97) (or (8.101)) and the homogenization results for level I (8.78) as:

$$\beta = \frac{k^{pc}}{g^{pc}} = -\operatorname{sign}(\varrho) \left(\frac{A^{I}_{\text{hom}}}{B^{I}_{\text{hom}}}\right)^2 = \frac{\eta \mathcal{K}^{I}}{\mathcal{M}^{I} \left|\eta - 2\alpha^2 \mathcal{K}^{I}\right|} > 0 \tag{8.112}$$

The linear micromechanics solutions for a two-phase material description in the context of the Mori-Tanaka and self-consistent schemes (refer to Section 4.2) provide the following $\mathcal{K}^{II}, \mathcal{M}^{II}$

morphology factors for the case of perfect adherence between interfaces:

$$\mathcal{K}^{II}_{MT,A} = \frac{4f^{inc}+3\beta}{3\left(1-f^{inc}\right)} \tag{8.113a}$$

$$\mathcal{M}^{II}_{MT,A} = \frac{\left(9f^{inc}+6\right)\beta+8f^{inc}+12}{6\left(1-f^{inc}\right)\left(2+\beta\right)} \tag{8.113b}$$

$$\mathcal{K}^{II}_{SC,A} = \frac{\left[18-42f^{inc}+15\left(f^{inc}\right)^2\right]\beta+4f^{inc}\left(3-f^{inc}\right)+f^{inc}\kappa_A}{18\left(1-f^{inc}\right)\left(1-2f^{inc}\right)} \tag{8.114a}$$

$$\mathcal{M}^{II}_{SC,A} = \frac{\left(15f^{inc}-6\right)\beta+\left(12-4f^{inc}\right)+\kappa_A}{24\left(1-2f^{inc}\right)} \tag{8.114b}$$

with:

$$\kappa_A = \sqrt{9\left(5f^{inc}-2\right)^2\beta^2-24\left(f^{inc}+2\right)\left(5f^{inc}-3\right)\beta+16\left(f^{inc}-3\right)^2} \tag{8.115}$$

The inclusion volume fraction associated to the self-consistent estimates and perfect bonding between interfaces is bounded by $f^{inc} < 1/2$. In contrast, the slip or non-frictional interface condition is characterized by a purely normal stress vector acting on the interface. Hence, the classical solution of Eshelby's problem has been adapted for rigid inclusions with non-frictional interface conditions [16, 61]. The corresponding expressions of the inclusion morphology factors for the Mori-Tanaka and self-consistent estimates are [14]:

$$\mathcal{K}^{II}_{MT,S} = \frac{3\beta+4f^{inc}}{3\left(1-f^{inc}\right)} \tag{8.116a}$$

$$\mathcal{M}^{II}_{MT,S} = \frac{\left(9f^{inc}+15\right)\beta+8f^{inc}+24}{3\left(5-2f^{inc}\right)\beta+12\left(2-f^{inc}\right)} \tag{8.116b}$$

$$\mathcal{K}^{II}_{SC,S} = \frac{3\left[12-23f^{inc}+8\left(f^{inc}\right)^2\right]\beta+8f^{inc}\left(3-2f^{inc}\right)+f^{inc}\kappa_S}{18\left(1-f^{inc}\right)\left(2-3f^{inc}\right)} \tag{8.117a}$$

$$\mathcal{M}^{II}_{SC,S} = \frac{24-16f^{inc}-\left(15-24f^{inc}\right)\beta+\kappa_S}{24\left(2-3f^{inc}\right)} \tag{8.117b}$$

with:

$$\kappa_S = \sqrt{9\left(8f^{inc}-5\right)^2\beta^2 + \left[720 - 1392f^{inc} + 528\left(f^{inc}\right)^2\right]\beta + 64\left(2f^{inc}-3\right)^2} \tag{8.118}$$

The volume fraction of rigid inclusions associated to the self-consistent estimates and slip interface conditions is bounded by $f^{inc} < 2/3$. It is worth noting that the relevance of the solutions for slip interface conditions may be physically questionable for tensile stress conditions. For the purpose of this study, the validity of expressions (8.116)-(8.117) is restricted to scenarios of macroscopic compression loading.

8.3.5 Level II (Model Extension): Porous Clay - Macroporosity Composite

The level II of the multi-scale structure model for shale is modified to accommodate for an extension to the strength upscaling of a two-scale porosity medium. The rigid inclusion phase considered in the model development for shale is substituted by a second pore space, which is denoted as macroporosity. Consequently, the macroscale volumetric partition of the dual-porosity material system follows a similar form as the one considered for shale (see (3.3)):

$$\text{Level II: } \phi_0^I + \phi_0^{II} + f^c = 1 \tag{8.119}$$

where ϕ_0^I, ϕ_0^{II} represent the nano- and macroporosity, respectively. In addition, the clay packing density η is modified accordingly:

$$\eta = \frac{f^c}{1-\phi_0^{II}} = 1 - \frac{\phi_0^I}{1-\phi_0^{II}} \tag{8.120}$$

Strain Rate Energy Function $\mathcal{W}_0^{II}(\mathbf{D})$ of the Dual-Porosity Composite

Consider the composite formed by a porous solid phase (with nanoporosity) and a macroporosity with volumetric domains $\Omega^{pc} = \left(1-\phi_0^{II}\right)\Omega$ and $\Omega^{mp} = \phi_0^{II}\Omega$, respectively. A continuous description of the stress field in the heterogeneous *rev* is assumed:

$$\boldsymbol{\sigma}(\underline{z}) = \mathbb{C}(\underline{z}) : \mathbf{d}(\underline{z}) + \boldsymbol{\tau}(\underline{z}) \qquad (\forall \underline{z} \in \Omega) \tag{8.121}$$

together with the following spatial description of the modulus tensor and the eigenstress:

$$\mathbb{C}(\underline{z}) = \begin{cases} \mathbb{C}^{pc} = 3k^{pc}\mathbb{J} + 2g^{pc}\mathbb{K} & (\Omega^{pc}) \\ 0 & (\Omega^{mp}) \end{cases} ; \boldsymbol{\tau}(\underline{z}) = \begin{cases} \tau^{pc}\mathbf{1} & (\Omega^{pc}) \\ 0 & (\Omega^{mp}) \end{cases} \tag{8.122}$$

where $\mathbb{C}^{pc}$ and τ^{pc} are the modulus tensor and eigenstress of the porous solid at level I. The macroscopic stress state equation governing the behavior at level II is:

$$\boldsymbol{\Sigma} = \mathbb{C}^{II}_{\text{hom}} : \mathbf{D} + \mathbf{T}^{II} \tag{8.123}$$

with:

$$\mathbb{C}^{II}_{\text{hom}} = \overline{\mathbb{C}(\underline{z}) : \mathbb{A}(\underline{z})} = 3k^{II}_{\text{hom}}\mathbb{J} + 2g^{II}_{\text{hom}}\mathbb{K} \tag{8.124a}$$

$$\mathbf{T}^{II} = \overline{\boldsymbol{\tau}(\underline{z}) : \mathbb{A}(\underline{z})} = \tau^{pc}\frac{k^{II}_{\text{hom}}}{k^{pc}}\mathbf{1} \tag{8.124b}$$

where the homogenized moduli in dimensionless form are:

$$k^{II}_{\text{hom}} = g^{pc}\mathcal{K}^{II}\left(\frac{k^{pc}}{g^{pc}}, \phi^{II}_0\right) \tag{8.125a}$$

$$g^{II}_{\text{hom}} = g^{pc}\mathcal{M}^{II}\left(\frac{k^{pc}}{g^{pc}}, \phi^{II}_0\right) \tag{8.125b}$$

With this description of the macroscopic composite, the corresponding expression of the strain rate (8.63) for the porous solid intermixed with macroporosity is:

$$\begin{aligned} \mathcal{W}^{II}_0(D_v, D_d) = {} & \frac{1}{2}g^{pc}\mathcal{K}^{II}D_v^2 + 2g^{pc}\mathcal{M}^{II}D_d^2 + \frac{g^{pc}}{k^{pc}}\tau^{pc}\mathcal{K}^{II}D_v \\ & + \frac{1}{2k^{pc}}\left[\frac{g^{pc}}{k^{pc}}\mathcal{K}^{II} - \left(1 - \phi^{II}_0\right)\right](\tau^{pc})^2 \end{aligned} \tag{8.126}$$

$\mathcal{V}$ Function or Measure of Non-Linearity

This step consists in determining the $\mathcal{V}^{pc}$ function for the (homogenized) porous solid (the value of $\mathcal{V}^{mp}$ for the macroporosity is zero), whose calculation can take advantage of previous developments. The results derived for the case of a porous solid reinforced with rigid inclusions are relevant to the present formulation given the similar inputs: the support function for the

porous solid $\pi^{pc}(\mathbf{d}) = \widetilde{\Pi}^{I}_{\text{hom}}(\mathbf{D} \rightarrow \mathbf{d})$ (see (8.76)), and the strain rate energy function of the porous solid phase $\omega^{pc}(\mathbf{d})$ akin to (8.65). Consequently, for the case of the support function associated with a hyperbolic criterion governing the porous solid at level I, the following function is obtained (see (8.96)):

$$\mathcal{V}^{pc}(\varrho > 0) = \frac{\left(B^{I}_{\text{hom}}\right)^2}{2g^{pc}} - \frac{1}{4g^{pc}}\left[\frac{B^{I}_{\text{hom}}\left(\Sigma^{I}_{\text{hom},0} - \tau^{pc}\right)}{A^{I}_{\text{hom}}}\right]^2 \tag{8.127}$$

Similarly for the case of the support function associated with an elliptical criterion at level I, we obtain (see (8.102)):

$$\mathcal{V}^{pc}(\varrho < 0) = \frac{\left(B^{I}_{\text{hom}}\right)^2}{2g^{pc}} \tag{8.128}$$

For both expressions, the results (8.97) and (8.101) also apply:

$$\beta = \frac{k^{pc}}{g^{pc}} = -\operatorname{sign}(\varrho)\left(\frac{A^{I}_{\text{hom}}}{B^{I}_{\text{hom}}}\right)^2 = cst. \tag{8.129}$$

Stationarity of the Dissipation Function $\widetilde{\Pi}^{II}_{\text{hom}}$ - Hyperbolic/Elliptical Strength Criterion

First, consider the case of a hyperbolic strength criterion governing the behavior of the porous solid at level I. The macroscopic dissipation function is computed using (8.126) and (8.127). In addition, the two degrees of freedom related to the estimation of the macroscopic dissipation function are g^{pc}, τ^{pc}:

$$\widetilde{\Pi}^{II}_{\text{hom}} = \underset{g^{pc},\tau^{pc}}{\text{stat}}\left\{\mathcal{W}^{II}_{0}(D_v, D_d) + \left(1 - \phi^{II}_{0}\right)\mathcal{V}^{pc}\right\} \tag{8.130}$$

The stationarity conditions are expressed explicitly as:

$$\frac{\partial \widetilde{\Pi}^{II}_{\text{hom}}}{\partial g^{pc}} = \frac{\partial k^{pc}}{\partial g^{pc}}\frac{\partial \mathcal{W}^{II}_{0}}{\partial k^{pc}} + \frac{\partial \mathcal{W}^{II}_{0}}{\partial g^{pc}} + \left(1 - \phi^{II}_{0}\right)\frac{\partial \mathcal{V}^{pc}}{\partial g^{pc}} = 0 \tag{8.131a}$$

$$\frac{\partial \widetilde{\Pi}^{II}_{\text{hom}}}{\partial \tau^{pc}} = \frac{\partial \mathcal{W}^{II}_{0}}{\partial \tau^{pc}} + \left(1 - \phi^{II}_{0}\right)\frac{\partial \mathcal{V}^{pc}}{\partial \tau^{pc}} = 0 \tag{8.131b}$$

with a similar approach to that used in the strength homogenization for the porous clay - rigid inclusion composite, the results of the stationarity conditions (8.131) and the macroscopic state equations for the linear comparison composite (8.123) are used to deliver the homogenized strength domain at level II of the dual-porosity medium:

$$\mathcal{F}^{II}(\boldsymbol{\Sigma}) = \left(\frac{\Sigma_m - \Sigma^{II}_{\text{hom},0}}{A^{II}_{\text{hom}}}\right)^2 + \left(\frac{\Sigma_d}{B^{II}_{\text{hom}}}\right)^2 - 1 \leq 0 \qquad (\varrho > 0) \tag{8.132}$$

where:

$$\left(A^{II}_{\text{hom}}\right)^2 = \frac{\left(1-\phi_0^{II}\right)^2 B^2 \mathcal{K}^{II}\left[A^2\left(1-\phi_0^{II}\right)\left(A^2-S_0^2\right)+B^2\mathcal{K}^{II}\left(2A^2-S_0^2\right)\right]}{\left[\left(1-\phi_0^{II}\right)A^2+2B^2\mathcal{K}^{II}\right]^2} \tag{8.133a}$$

$$\left(B^{II}_{\text{hom}}\right)^2 = \frac{\left(1-\phi_0^{II}\right) B^2 \mathcal{M}^{II}\left[A^2\left(1-\phi_0^{II}\right)\left(A^2-S_0^2\right)+B^2\mathcal{K}^{II}\left(2A^2-S_0^2\right)\right]}{A^2\left[\left(1-\phi_0^{II}\right)A^2+2B^2\mathcal{K}^{II}\right]} \tag{8.133b}$$

$$\Sigma^{II}_{\text{hom},0} = \frac{\left(1-\phi_0^{II}\right) B^2 \mathcal{K}^{II}}{\left(1-\phi_0^{II}\right)A^2+2B^2\mathcal{K}^{II}} S_0 \tag{8.133c}$$

with $A = A^I_{\text{hom}}, B = B^I_{\text{hom}}, S_0 = \Sigma^I_{\text{hom},0}$. The strength criterion (8.132) is applicable to the case of the porous clay composite at level I governed by a hyperbolic strength domain (i.e. $\left(B^I_{\text{hom}}\right)^2 < 0$ or $\varrho > 0$). The particular shape of the macroscopic criterion (8.132) depends on the sign of $\varpi = A^2\left[\left(1-\phi_0^{II}\right)A^2+2B^2\mathcal{K}^{II}\right]$: $\varpi < 0$ for a hyperbola, $\varpi > 0$ for an ellipse.

Stationarity of the Dissipation Function $\widetilde{\Pi}^{II}_{\text{hom}}$ - Elliptical Strength Criterion

Expressions (8.126) and (8.128) are implemented in a similar development as followed in the previous section to determine the strength criterion for the dual-porosity material for the case of the porous solid governed by an elliptical strength domain. The derived macroscopic criterion is:

$$\mathcal{F}^{II}(\boldsymbol{\Sigma}) = \left(\frac{\Sigma_m - \Sigma^{II}_{\text{hom},0}}{A^{II}_{\text{hom}}}\right)^2 + \left(\frac{\Sigma_d}{B^{II}_{\text{hom}}}\right)^2 - 1 \leq 0 \qquad (\varrho < 0) \tag{8.134}$$

where:

$$\left(A^{II}_{\text{hom}}\right)^2 = \frac{B^2\mathcal{K}^{II}}{A^4}\left[A^2\left(1-\phi_0^{II}\right)\left(A^2-S_0^2\right)+B^2S_0^2\mathcal{K}^{II}\right] \tag{8.135a}$$

$$\left(B^{II}_{\text{hom}}\right)^2 = \frac{B^2\mathcal{M}^{II}}{A^4}\left[A^2\left(1-\phi_0^{II}\right)\left(A^2-S_0^2\right)+B^2S_0^2\mathcal{K}^{II}\right] \tag{8.135b}$$

$$\Sigma^{II}_{\text{hom},0} = \frac{B^2\mathcal{K}^{II}}{A^2}S_0 \tag{8.135c}$$

with $A = A^I_{\text{hom}}, B = B^I_{\text{hom}}, S_0 = \Sigma^I_{\text{hom},0}$. The macroscopic criterion (8.134) corresponds to the case of the porous solid governed by an elliptical criterion (i.e. $\left(B^I_{\text{hom}}\right)^2 > 0$ or $\varrho < 0$). By inspection, it is determined that the criterion (8.134) is also defined by an elliptical shape since $\left(B^{II}_{\text{hom}}\right)^2 > 0$.

Inclusion Morphology Factors for Level II - Dual-Porosity Material

The definition of the morphology factors $\mathcal{K}^{II}, \mathcal{M}^{II}$ used for the evaluation of the homogenized strength criteria (8.132) and (8.134) takes advantage of previous results. The dual-porosity solid at level II is composed of a (homogenized) porous solid at level I and a second type of porosity (macroporosity), both of which are modeled as spherical inclusions. This configuration resembles the modeling at level I of the porous clay composite. The main difference for the implementation of (8.83)-(8.84) is the definition of the effective properties of the linear comparison composite, namely the bulk-to-shear moduli ratio. For level I, the solid clay properties used for the computation of the morphology factors were related by (see (8.69)):

$$\frac{k^s}{g^s} = \frac{1}{\alpha^2} \tag{8.136}$$

Instead, the properties for the homogenized porous solid correspond to (see (8.129)):

$$\beta = \frac{k^{pc}}{g^{pc}} = -\operatorname{sign}(\varrho)\left(\frac{A^I_{\text{hom}}}{B^I_{\text{hom}}}\right)^2 \tag{8.137}$$

The Mori-Tanaka and self-consistent estimates for the inclusion morphology factors used for the level II homogenization of the dual-porosity solid are:

$$\mathcal{K}_{MT}^{II} = \frac{4\left(1-\phi_0^{II}\right)\beta}{4+3\phi_0^{II}\beta} \tag{8.138a}$$

$$\mathcal{M}_{MT}^{II} = \frac{\left(1-\phi_0^{II}\right)(8+9\beta)}{8+9\beta+6\phi_0^{II}(2+\beta)} \tag{8.138b}$$

$$\mathcal{K}_{SC}^{II} = 4\frac{\left(1-\phi_0^{II}\right)\beta\mathcal{M}_{SC}^{II}}{4\mathcal{M}_{SC}^{II}+3\phi_0^{II}\beta} \tag{8.139a}$$

$$\mathcal{M}_{SC}^{II} = \frac{1}{2}-\frac{3}{16}\beta\left(1-\phi_0^{II}\right)-\frac{3}{8}\beta-\frac{5}{4}\phi_0^{II}+ \frac{1}{16}\sqrt{64+144\beta+81\beta^2-\phi_0^{II}\left(54\beta^2+168\beta+320\right)+\left(\phi_0^{II}\right)^2\left(9\beta^2-120\beta+400\right)} \tag{8.139b}$$

The consideration of particular microstructures at the material levels I and II defines a critical macroporosity, which separates the elliptical and hyperbolic strength domains associated to the macroscopic material for the case of a hyperbolic criterion governing the porous clay at level I:

$$\phi_0^{II}-\left(\phi_0^{II}\right)^{cr}\begin{cases} <0 & \text{Hyperbolic criterion} \\ =0 & \text{Limit parabola} \\ >0 & \text{Elliptical criterion} \end{cases} \tag{8.140}$$

For the Mori-Tanaka and self-consistent schemes defining the microstructure of the macroscopic material at level II, the critical macroporosity factors are:

$$\left(\phi_0^{II}\right)_{MT,II}^{cr} = -\frac{4}{3}\left(\frac{B_{\text{hom}}^I}{A_{\text{hom}}^I}\right)^2 \tag{8.141}$$

$$\left(\phi_0^{II}\right)_{SC,II}^{cr} = \frac{16\left(B_{\text{hom}}^I\right)^2-9\left(A_{\text{hom}}^I\right)^2+\sqrt{81\left(A_{\text{hom}}^I\right)^4-432\left(A_{\text{hom}}^I\right)^2\left(B_{\text{hom}}^I\right)^2+1216\left(B_{\text{hom}}^I\right)^4}}{2\left[3\left(A_{\text{hom}}^I\right)^2-20\left(B_{\text{hom}}^I\right)^2\right]} \tag{8.142}$$

For a particular microstructure at level II, the critical macroporosity depends, through the homogenization factors A_{hom}^I, B_{hom}^I, on the packing density η, the friction coefficient α, and the microstructure at level I. Figure 8-6 displays graphically the predicted critical macroporosities

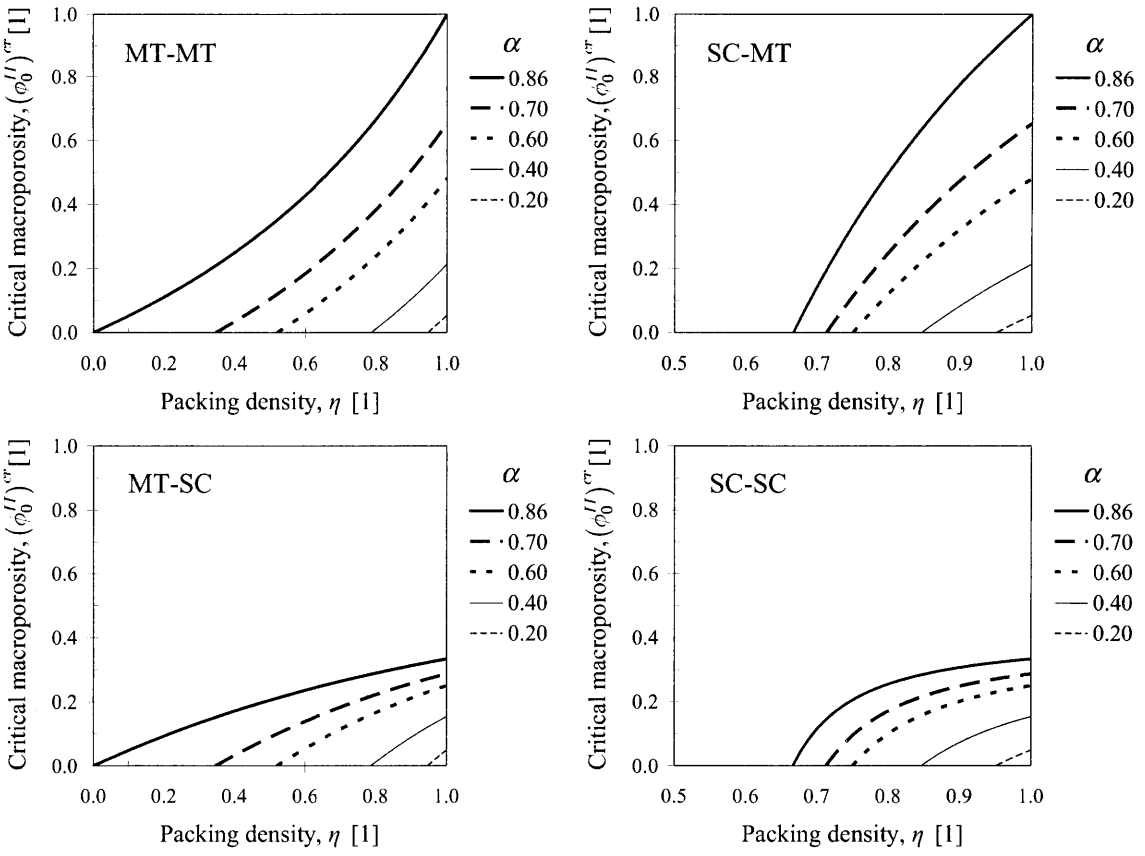

Figure 8-6: Critical macroporosity $\left(\phi_0^{II}\right)^{cr}$ as a function of the packing density η and the friction coefficient α. The microstructures at levels I and II of the dual-porosity material are modeled by the Mori-Tanaka (MT) and self-consistent (SC) schemes.

for different microstructural configurations.

8.4 Analysis of the Strength Upscaling Model for Shale

The novelty of the strength homogenization approach established by Gathier and Ulm [98] calls for a thorough analysis. Before its application to shale, it will be instructive to assess the predictive capabilities of the multi-scale strength upscaling model by first comparing it to existing strength homogenization solutions. The predictive capabilities of the strength model are then investigated at the length scales of the porous solid (level I) and of the porous solid reinforced

with rigid inclusions (level II). In particular, the model review focuses on the two types of strength domains predicted by the model (elliptical and hyperbolic domains), the effects of inclusion reinforcement, and the two types of interface conditions defining the interactions between phases. In these studies, the matrix-inclusion and granular morphologies are considered in order to highlight the strength behaviors predicted for different modeled microstructures. Finally, the theoretical predictions of the strength model for a dual-porosity material are presented.

8.4.1 Comparisons with Existing Models

Gurson's Hollow Sphere Model

The first case considered is the classical result of Gurson's hollow sphere model [110]. The model describes the yield criterion for a porous ductile material, in which the matrix is treated as rigid-perfectly plastic obeying a von Mises yield criterion. Based on the kinematic approach of limit analysis, Gurson's model is known to be an upper bound solution to the described homogenization problem [106, 160, 262]. The Gurson's yield criterion is expressed as:

$$\mathcal{F}\left(\Sigma_m, \Sigma_{eqv} = \sqrt{3}\Sigma_d\right) = 2\left(1-\eta\right)\left[\cosh\left(\frac{3\Sigma_m}{2Y^s}\right) - 1\right] + \left(\frac{\Sigma_{eqv}}{Y^s}\right)^2 - \eta^2 \leq 0 \tag{8.143}$$

where $Y^s = \sqrt{3}c^s$ is the uniaxial strength of the von Mises solid phase with solid concentration or packing density η. A suitable comparison with Gurson's model is the matrix-inclusion morphological representation of the microstructure for level I. The non-frictional behavior of the solid phase corresponds to the limit case $\alpha \to 0$, for which the strength domain of the porous solid in (8.80) results in an elliptical form. The corresponding homogenization factors (8.78) are:

$$\left(\frac{A^I_{\text{hom}}\left(\alpha=0\right)}{c^s}\right)^2 = \frac{4\eta^2}{3\left(1-\eta\right)} \tag{8.144a}$$

$$\left(\frac{B^I_{\text{hom}}\left(\alpha=0\right)}{c^s}\right)^2 = \frac{3\eta^2}{5-2\eta} \tag{8.144b}$$

$$\frac{\Sigma^I_{\text{hom},0}\left(\alpha=0\right)}{c^s} = 0 \tag{8.144c}$$

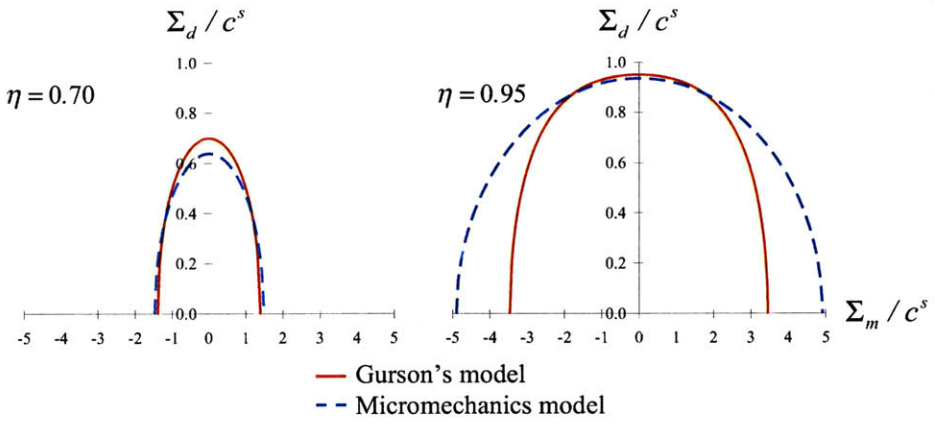

Figure 8-7: Comparisons between micromechanics results and Gurson's model for a von Mises porous solid.

The result in (8.144) for the strength homogenization of a von Mises porous matrix is a well-established micromechanics solution (see e.g. [213, 248, 252]). A graphical comparison between the model results and Gurson's predictions is presented in Figure 8-7. The elliptical strength domain (8.144) improves the upper bound solution of Gurson's model for the deviatoric loading. However, the elliptical criterion offers a poor prediction for purely hydrostatic stresses, especially for low porosity values (or alternatively, large packing densities). The inadequate predictions are attributed to the inability of high-order averages of the deviator strain rate (within the framework of the effective strain rate approach) to capture the heterogeneous strain fields around the cavity of the hollow sphere [15, 83].

Effective Strain Rate Approach for Cohesive-Frictional Composites

The effective strain rate method developed by Dormieux and co-workers [15, 16, 83, 163] approaches the homogenization problem (8.28) akin to a viscous flow problem, in which the behavior of the solid phase is described by a viscous state equation:

$$\boldsymbol{\sigma}(\underline{z}) = \frac{\partial \pi^s}{\partial \mathbf{d}}(\mathbf{d}(\underline{z})) = \mathbb{C}^s(\mathbf{d}(\underline{z})) : \mathbf{d}(\underline{z}) \qquad (\forall \underline{z} \in \Omega^s) \tag{8.145}$$

This material behavior differs from classical linear elasticity as the strain rate $\mathbf{d}(\underline{z})$ and the modulus tensor $\mathbb{C}^s(\mathbf{d}(\underline{z}))$ are heterogeneous within the material domain. Furthermore, the modulus tensor $\mathbb{C}^s(\mathbf{d}(\underline{z}))$ also depends on the load level. The nature of this problem has been addressed by the so-called secant methods of non-linear homogenization, which aim to represent the load dependency of $\mathbb{C}^s(\mathbf{d}(\underline{z}))$ through reference strain rate fields[6]. The reference strain rate $\mathbf{d}^r$ approximates the true heterogeneous tensor by a uniform tensor in the solid material domain:

$$\mathbb{C}(\underline{z}) = \mathbb{C}^s(\mathbf{d}(\underline{z})) \approx \mathbb{C}^s(\mathbf{d}^r) \qquad (\forall \underline{z} \in \Omega^s) \tag{8.146}$$

The practical implementation of (8.146) differs in the type of the reference strain rate [248]. The suitable choice of quadratic averages of strain rate fields has been proven to deliver adequate approximations for effective strain rates in the solution of strength homogenization problems. The effective strain rate approach has been successfully applied to the strength homogenization of two representative material systems: a porous solid, and a solid intermixed with rigid inclusions. In this section, the solutions based on the effective strain rate approach are compared to the LCC model results.

Porous Solid Configuration The strength homogenization of a cohesive-frictional porous solid has been addressed by Barthélémy and Dormieux [15] (see also [50, 83]). Based on the effective strain rate approach, the predicted strength domain for a porous medium with a Drucker-Prager solid phase follows an elliptical form. Using a similar form of the strength domain derived in (8.80), the homogenization factors for the elliptical criterion are [50]:

$$\left(\frac{A^I_{\text{hom}}}{c^s}\right)^2 = \frac{\eta^3 \widehat{\mathcal{K}}^I}{\left(\eta - \alpha^2 \widehat{\mathcal{K}}^I\right)^2} \tag{8.147a}$$

$$\left(\frac{B^I_{\text{hom}}}{c^s}\right)^2 = \frac{\eta^2 \widehat{\mathcal{M}}^I}{\eta - \alpha^2 \widehat{\mathcal{K}}^I} \tag{8.147b}$$

$$\frac{\Sigma^I_{\text{hom},0}}{c^s} = \frac{\alpha \eta \widehat{\mathcal{K}}^I}{\alpha^2 \widehat{\mathcal{K}}^I - \eta} \tag{8.147c}$$

[6] This strategy has been proposed for extensions of Darcy flow problems involving power-law fluids (see e.g. [83]).

where $\widehat{\mathcal{K}}^I = \mathcal{K}^I(\alpha = 0)$, $\widehat{\mathcal{M}}^I = \mathcal{M}^I(\alpha = 0)$ are the inclusion morphology factors (8.82) evaluated for an incompressible solid ($k^s \to \infty \Longleftrightarrow \alpha = 0$). The incompressible character of the fictitious viscous solid is an inherent trait of the effective strain rate homogenization approach. The LCC strength homogenization approach offers a less restrictive solution to the non-linear homogenization problem as the linear comparison composite moduli are defined by the relation $k^s/g^s = 1/\alpha^2$ (see (8.69)).

Figures 8-8 and 8-9 offer quantitative comparisons between the predictions generated by the LCC and effective strain rate models, as functions of the two variables involved in the homogenization problem: the packing density η and the friction coefficient α. The comparisons are developed for three specific stress states:

- *Unconfined compressive strength* (UCS): This stress state is associated with the failure of a material under uniaxial compression in unconfined conditions. The unconfined compressive load Σ^{UCS} is related to the mean and deviatoric stress invariants as follows:

$$\Sigma_m = -\frac{1}{3}\Sigma^{UCS} \; ; \; \Sigma_d = \frac{\sqrt{3}}{3}\Sigma^{UCS} \tag{8.148}$$

The predicted UCS strength is obtained by substituting the particular stress state (8.148) into the elliptical strength domain (e.g. (8.80)):

$$\Sigma^{UCS} = \frac{3}{3\left(A^{II}_{\text{hom}}\right)^2 + \left(B^{II}_{\text{hom}}\right)^2}\left(-\Sigma^{II}_{\text{hom},0}\left(B^{II}_{\text{hom}}\right)^2 + \sqrt{\left(A^{II}_{\text{hom}}\right)^2\left(B^{II}_{\text{hom}}\right)^4 + 3\left(A^{II}_{\text{hom}}\right)^4\left(B^{II}_{\text{hom}}\right)^2 - 3\left(A^{II}_{\text{hom}}\right)^2\left(B^{II}_{\text{hom}}\right)^2\left(\Sigma^{II}_{\text{hom},0}\right)^2}\right) \tag{8.149}$$

- *Pure deviatoric stress*: This stress state is represented in the invariant stress space as:

$$\Sigma_m = 0 \; ; \; \Sigma_d = \pm\Sigma^{dev} \tag{8.150}$$

The prediction of the deviatoric failure stress based on the elliptical strength criterion is:

$$\Sigma^{dev} = \frac{B^I_{\text{hom}}}{A^I_{\text{hom}}}\sqrt{\left[\left(A^I_{\text{hom}}\right)^2 - \left(\Sigma^I_{\text{hom},0}\right)^2\right]} \tag{8.151}$$

- *Hydrostatic tension*: This stress state is represented in the invariant stress space as:

$$\Sigma_m = \Sigma^{hyd} \; ; \; \Sigma_d = 0 \tag{8.152}$$

The prediction of hydrostatic tension based on the elliptical strength criterion is:

$$\Sigma^{hyd} = \Sigma^I_{\text{hom},0} + A^I_{\text{hom}} \tag{8.153}$$

These stress states offer practical reference points in the invariant stress space to quantitatively compare the predicted strengths by the two models. In addition, the matrix-inclusion and granular microstructures, modeled by the Mori-Tanaka and self-consistent schemes, respectively, are implemented for the comparisons. The contour plots in Figures 8-8 and 8-9 represent the absolute difference between normalized predictions of the LCC and the effective strain rate (ESR) models:

$$|\Delta| = \frac{1}{c^s} \left| \Sigma^J_{ESR} - \Sigma^J_{LCC} \right| \tag{8.154}$$

where $J = UCS, dev, hyd$. The inspection of the figures reveals that the differences between the strength predictions obtained by the two models are relatively small. The largest difference between predictions is observed for the unconfined compressive strength case, which can reach values of $|\Delta| = 0.10$ for the self-consistent morphology. It is worth noting that the comparisons in Figures 8-8 and 8-9 were established only for the elliptical strength regime, which is in accordance to the applicability of the effective strain rate model [50].

In summary, the LCC homogenization model improves upon the effective strain rate model, allowing the consideration of a larger range of frictional values. In return, the difference may only be substantial in specific cases related to strong deviator states and large values of the solid's friction coefficient.

Solid Reinforced with Rigid Inclusions Solutions for the case of a Drucker-Prager solid intermixed with rigid inclusions have been proposed by Lemarchand et al. [163] and Barthélémy and Dormieux [16]. The strength criterion for level II is adapted for the case of a solid phase

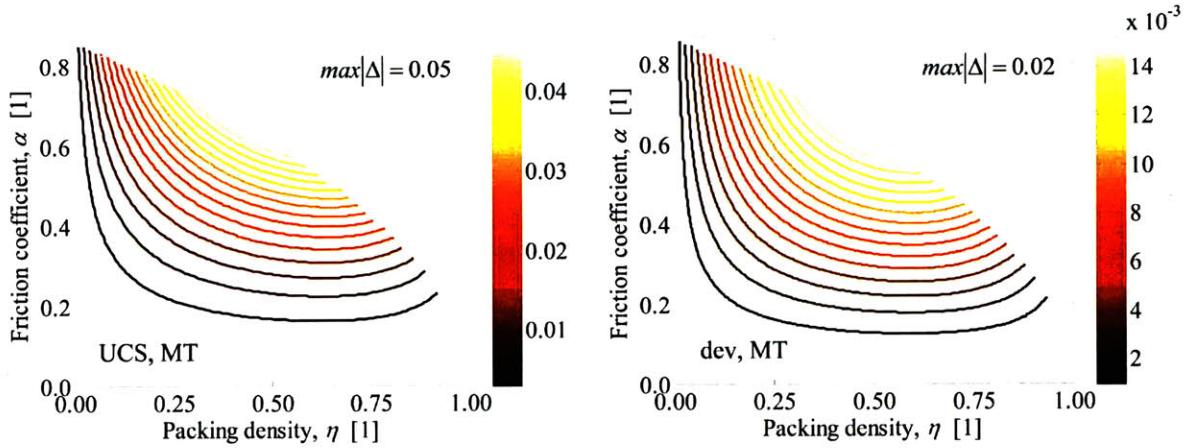

Figure 8-8: Comparisons between predictions of the LCC and effective strain rate models for specific strength types: unconfined compressive strength (UCS), and pure deviatoric stress (dev). The microstructure of the porous solid is modeled by the Mori-Tanaka scheme. The contour plots of the absolute difference between predictions $|\Delta|$ are generated as functions of the friction coefficient α and the packing density η. The case of hydrostatic tension is not shown given that both models offer equivalent predictions (the homogenization factors $\Sigma^I_{\text{hom},0}$, A^I_{hom} are identical in both modeling approaches).

in level I, which implies:

$$\begin{cases} \left(B^I_{\text{hom}}\right)^2 = -\alpha^2 \left(A^I_{\text{hom}}\right)^2 \\ \Sigma^I_{\text{hom},0} = \frac{c^s}{\alpha} \\ \left(A^I_{\text{hom}}\right)^2 \to 0 \end{cases} \tag{8.155}$$

The resulting macroscopic criterion (8.107) yields:

$$\mathcal{F}^{II}(\boldsymbol{\Sigma}) = \Sigma_d + \alpha_{\text{hom}} \left(\Sigma_m - \frac{c^s}{\alpha}\right) \leq 0 \tag{8.156}$$

which corresponds to a Drucker-Prager criterion with a homogenized (macroscopic) friction coefficient:

$$\alpha_{\text{hom}} = \alpha \sqrt{\frac{\left(1 - f^{inc}\right) \mathcal{M}^{II}}{2 - \alpha^2 \mathcal{K}^{II} \left(1 - f^{inc}\right)}} \tag{8.157}$$

The solution by Lemarchand et al. [163] for the homogenized friction coefficient based on a mixed-secant method is:

$$\alpha_{\text{hom}} = \alpha \sqrt{1 + \frac{3}{2} f^{inc}} \tag{8.158}$$

.

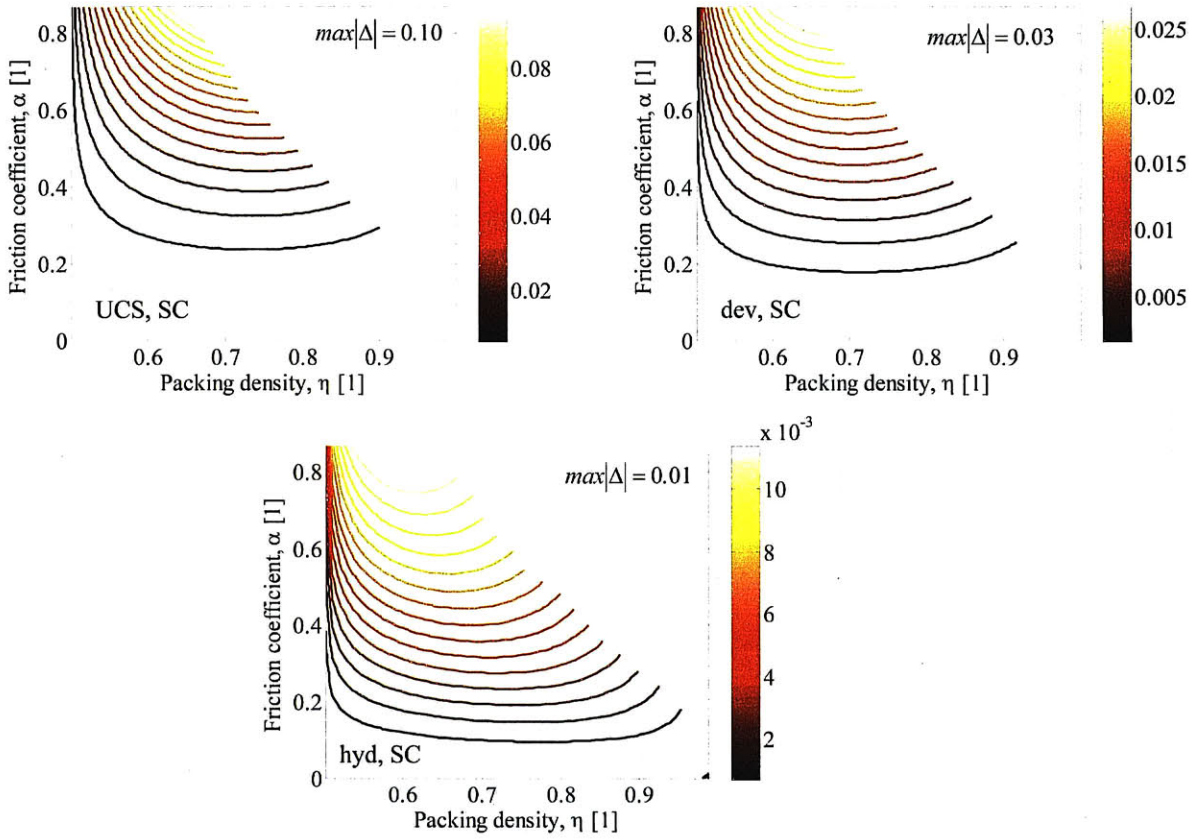

Figure 8-9: Comparisons between predictions of the LCC and effective strain rate models for specific strength types: unconfined compressive strength (UCS), pure deviatoric stress (dev), and hydrostatic tension (hyd). The microstructure of the porous solid is modeled by the self-consistent scheme. The contour plots of the absolute difference between predictions $|\Delta|$ are generated as functions of the friction coefficient α and the packing density η.

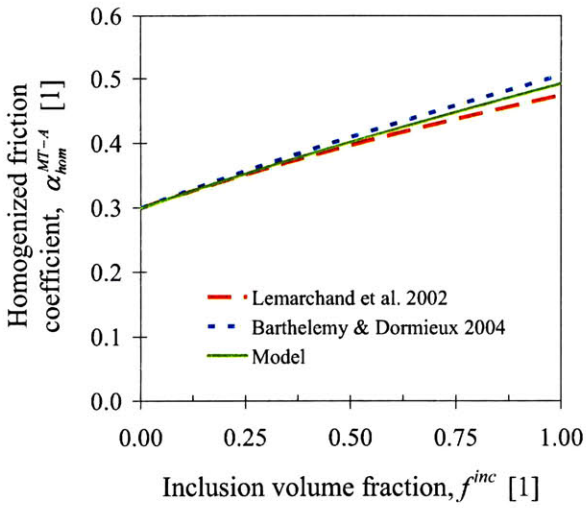

Figure 8-10: Predictions of the homogenized friction coefficient for a Drucker-Prager solid reinfored with rigid inclusions. The microstructure is modeled by the Mori-Tanaka scheme and considers perfectly adherent interface conditions.

whereas the solutions by Barthélémy and Dormieux [16] based on adherent and slip conditions read:

$$\alpha_{\text{hom}}^{MT,A} = \alpha\sqrt{\frac{1+\frac{3}{2}f^{inc}}{1-\frac{4}{3}\alpha^2 f^{inc}}} \tag{8.159a}$$

$$\alpha_{\text{hom}}^{MT,S} = \alpha\sqrt{\frac{(1-f^{inc})\left(1+\frac{3}{2}f^{inc}\right)}{\left(1-\frac{2}{5}f^{inc}\right)\left(1-\frac{4}{3}\alpha^2 f^{inc}\right)}} \tag{8.159b}$$

These micromechanics solutions were derived based on a matrix-inclusion morphology, which is properly modeled by the Mori-Tanaka scheme. Figures 8-10 and 8-11 display the homogenized friction coefficient predictions by the LCC and effective strain rate models, showing adequate comparisons between them. A strict comparison between the model of Lemarchand et al. and the two remaining models cannot be formulated. The mixed-secant method does not consider the local flow rule associated with the Drucker-Prager criterion of the solid phase [16].

8.4.2 Strength Predictions - Level I

The assessment of the strength model begins at level I of the multi-scale structure thought

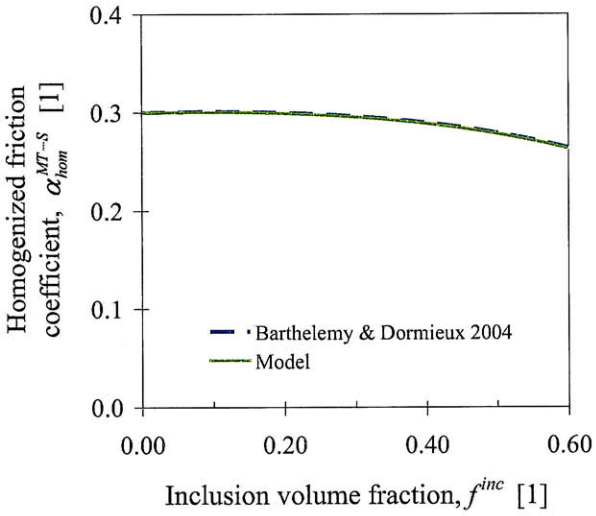

Figure 8-11: Predictions of the homogenized friction coefficient for a Drucker-Prager solid reinforced with rigid inclusions. The microstructure is modeled by the Mori-Tanaka scheme and considers non-frictional (slip) interface conditions.

model. As noted in Section 8.4.1, the model based on the effective strain rate approach predicts an elliptical strength domain for the case of a porous solid [50]. The form of the strength criterion (8.80) derived through the LCC approach yields a smooth transition between a closed ellipse ($\eta < \eta^{cr}$) and an open hyperbola ($\eta > \eta^{cr}$). Note that the critical packing density η^{cr} is strictly defined by the friction coefficient α and the modeled microstructure. The limit case of a parabolic domain, which serves as a transition between the elliptical and hyperbolic regimes, is not supported by the strength criterion (8.80). An example of the parabolic domain (i.e. $\eta = \eta^{cr}$) is developed here to illustrate the smooth transition between domains predicted for level I. For this application, the matrix-inclusion microstructure, by through the Mori-Tanaka scheme, is used for analytical derivations. The parabolic strength domain is obtained from the expression of the homogenized dissipation function (8.76) for the limit case $\eta \to \eta^{cr}$. The resulting function $\lim_{\eta \to \eta^{cr}} \widetilde{\Pi}^{I}_{\text{hom}}(\mathbf{D})$ is used in conjunction with the yield design definition (8.19) to deliver the strength domain for the parabolic limit case:

$$\mathcal{F}^{I}_{par}(\boldsymbol{\Sigma}) = \frac{\Sigma_m}{A^{I}_{par}} + \left(\frac{\Sigma_d}{B^{I}_{par}}\right)^2 - 1 \leq 0 \tag{8.160}$$

where:

$$A^I_{par} = \frac{3-4\alpha^2}{6\alpha} \tag{8.161a}$$

$$\left(B^I_{par}\right)^2 = \frac{128\alpha^6 - 48\alpha^4 - 144\alpha^2 + 81}{9\left(16\alpha^4 + 16\alpha^2 + 9\right)} \tag{8.161b}$$

Figure 8-12 illustrates an implementation of the parabolic domain (8.160). The figure also shows sample elliptical and hyperbolic domains obtained for packing density values close to the critical packing density defining the parabolic domain. To verify the smooth transition between elliptical and hyperbolic domains, the particular case of unconfined compressive strength (akin to (8.149)) is developed as a function of packing density. Figure 8-13 displays UCS predictions based on the general strength criterion for level I (8.80) and the particular estimate for the parabolic domain (8.160). The figure also displays the predictions for a granular material modeled by the self-consistent scheme[7]. The evolution of the predicted strength for the self-consistent scheme displays a percolation threshold at $\eta_0 = 0.5$, whereas the Mori-Tanaka predictions cover the entire range of packing densities. As shown in Figure 8-13, the smooth transition between the elliptical and hyperbolic regimes is verified by the application of the results associated with the parabolic domain. The micromechanics model based on the LCC formulation offers strength predictions for the entire range of packing densities, depending on the modeled microstructure.

8.4.3 Strength Predictions - Level II

This section examines the effects of rigid inclusions on the strength predictions of the multi-scale model for level II. The type of homogenization scheme, interface condition, and volume fraction of inclusions modify the strength behavior of the macroscopic composite.

Effect of Homogenization Scheme

The reinforcing effect of rigid inclusions on the strength properties of the porous solid is described graphically in Figure 8-14. The porous solid at level I is modeled by the self-consistent scheme. At level II, the macroscopic material (porous solid and rigid inclusions) is modeled by

[7]The UCS value corresponding to the transition between domains in view of the implementation of the self-consistent scheme was computed numerically.

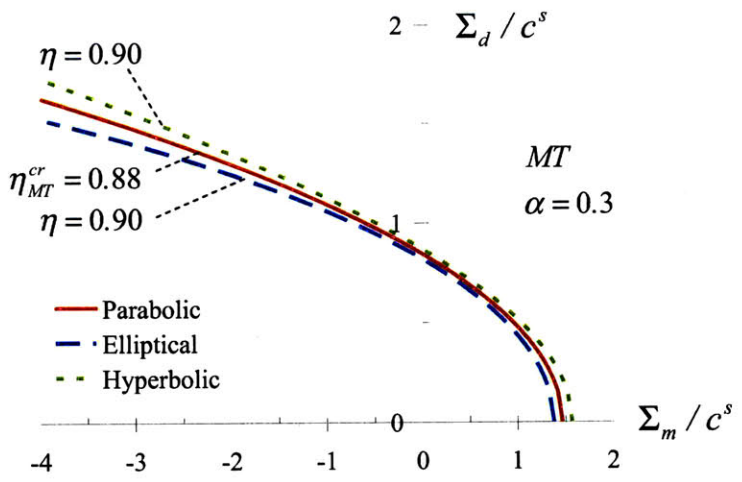

Figure 8-12: Illustration of the different types of strength domains predicted by the LCC strength model for level I. The porous solid is modeled by the Mori-Tanaka (MT) scheme. The friction coefficient for the solid phase is $\alpha = 0.3$, which results in a critical packing density $\eta^{cr}_{MT} = 0.88$.

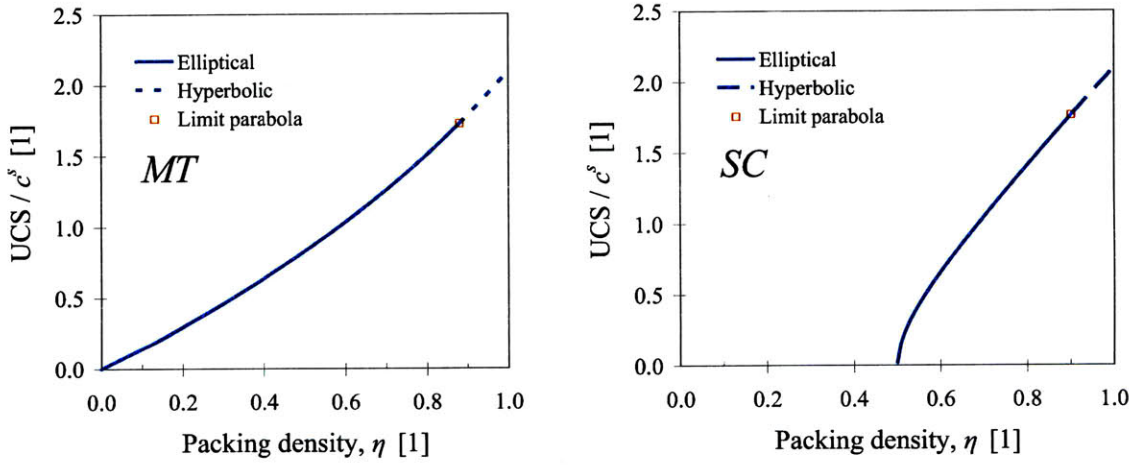

Figure 8-13: Predictions of the normalized unconfined compressive strength (UCS) as a function of packing density η for a porous solid modeled by the Mori-Tanaka (MT) and self-consistent (SC) schemes. The solid friction coefficient is $\alpha = 0.3$. The solid lines correspond to the predictions associated with the elliptical strength regime ($\eta < \eta^{cr}$), whereas the dashed lines to those associated with the hyperbolic strength regime ($\eta > \eta^{cr}$). The solid data point corresponds to the prediction from the limit parabolic criterion.

the Mori-Tanaka and self-consistent schemes describing matrix-inclusion and granular media, respectively. In addition, perfect bonding is assumed between material interfaces. Different amounts of inclusion volume fraction $f^{inc} = 0.2, 0.4$ are used for the strength predictions displayed in Figure 8-14. As observed in the figure, the granular microstructure tends to amplify more significantly the reinforcing effect of rigid inclusions compared to the matrix-inclusion microstructure. The disordered nature of the granular material, modeled through the self-consistent scheme, appears to strengthen the composite response of the macroscopic medium.

Effect of Interface Condition

A similar set of comparisons as presented in Figure 8-14 is developed for the case of slip (non-frictional) interface conditions between the two material phases at level II. Figure 8-15 shows the predicted strength domains for implementations of the Mori-Tanaka and self-consistent homogenization schemes modeling the microstructures at level II, and for different amounts of inclusion volume fraction $f^{inc} = 0.2, 0.4$. As expected, the predicted strength domains for level II based on slip interface conditions are smaller in magnitude compared to those obtained for perfectly bonded interfaces. The self-consistent predictions display an overall increase in the size of the strength domain. Instead, the increase of the inclusion volume fraction related to the Mori-Tanaka predictions translates into a decreased strength capacity for some deviatoric stress states and an increased strength for mostly hydrostatic stresses. As noted in Section 8.3.4, one should interpret the strength predictions for slip interface conditions for tensile stress states with caution given the modeling of the interface based on assumed transmission of loads only through normal stresses.

Transition between Elliptical and Hyperbolic Strength Domains

The analysis of the elliptical and hyperbolic strength regimes for the porous clay composite revealed a smooth transition between them as a function of the clay packing density. The objective of this section is to study such transition at level II, which incorporates the strength reinforcement due to the addition of rigid inclusions. Although not crucial to the modeling of shale, which is characterized by the implementation of the self-consistent scheme at levels I and II, the multi-scale model can accommodate different combinations of microstructures

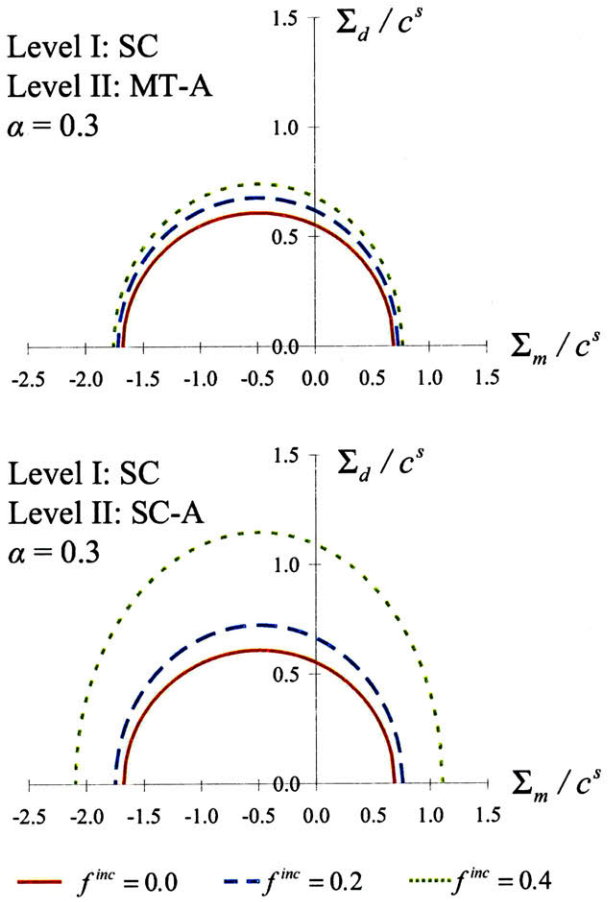

Figure 8-14: Effect of rigid inclusions with perfect adherence on the homogenized strength at level II. The porous clay at level I ($f^{inc} = 0$) is modeled by the self-consistent scheme, with a packing density $\eta = 0.7$ and friction coefficient $\alpha = 0.3$. The level II properties are predicted for a Mori-Tanaka (MT) and self-consistent (SC) estimates.

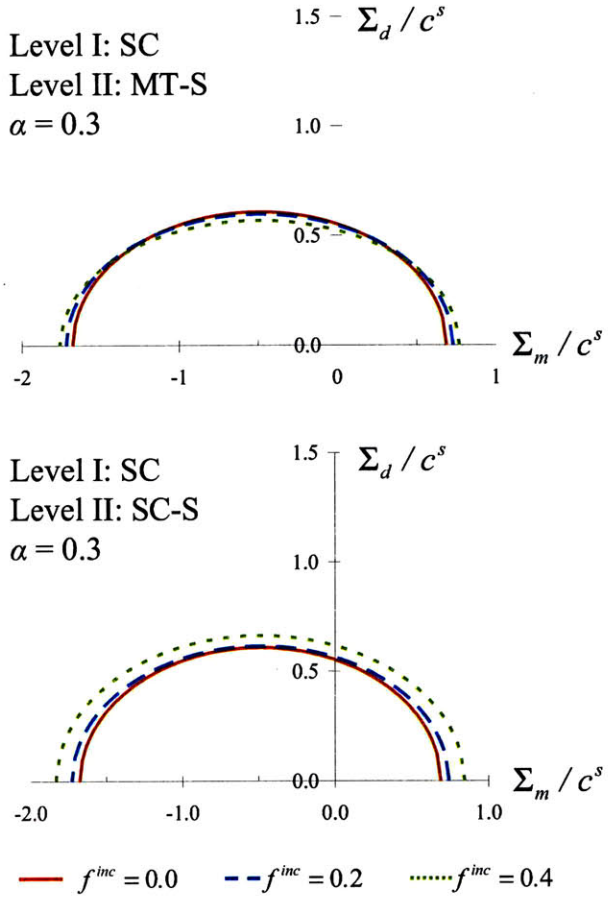

Figure 8-15: Effect of rigid inclusions with slip interface on the homogenized strength at level II. The porous clay at level I ($f^{inc} = 0$) is modeled by the self-consistent scheme, with a packing density $\eta = 0.7$ and friction coefficient $\alpha = 0.3$. The level II properties are predicted for Mori-Tanaka (MT) and self-consistent (SC) estimates.

at the different levels. The two types of microstructures, namely the matrix-inclusion and granular microstructures modeled by the Mori-Tanaka (MT) and self-consistent (SC) schemes, yield a total of four combinations of structural configurations for a two-scale homogenization: MT-MT, MT-SC, SC-MT, and SC-SC. These different microstructural configurations exhibit particular homogenized strength properties. For instance, Figure 8-16 displays the evolution of the predicted unconfined compressive strength for a material with MT-MT configuration and inclusion volume fraction $f^{inc} = 0.4$. As observed in the figure, the development of the predicted UCS strength follows the expected trend of increasing values with increasing packing densities for a fixed value of the inclusion volume fraction. It can be shown that such consistent trend is observed for the MT-MT and SC-MT configurations and perfectly adherent interface properties[8]. The trend of increasing strength with increasing packing density for a fixed value of the inclusion volume fraction is also attained for MT-SC and SC-SC configurations in the elliptical strength regime. However, the strength modeling of level II based on the self-consistent scheme presents particular cases in which inadequate transitions between the elliptical and hyperbolic domains are observed. To illustrate such behavior, a sample study is presented hereafter that sheds light on the effect of rigid inclusions on the transition of strength regimes at level II. For the purpose of illustration, only perfectly-adherent interface conditions are considered in the study.

Consider the strength domains for a macroscopic composite presented in Figure 8-17. The hyperbolic domains correspond to two different levels of inclusion volume fraction ($f^{inc} = 0.20, 0.34$). In addition to the hyperbolic domains obtained for a packing density $\eta = 0.90$, the limit cases of the parabolic domains ($\eta = \eta^{cr}(\alpha)$), which mark the transition between the elliptical and hyperbolic strength regimes, are also included in Figures 8-17a and 8-17b[9]. The microstructure at level I is defined by the Mori-Tanaka scheme. For the strength domains corresponding to $f^{inc} = 0.20$ in Figure 8-17a, the effect of increasing the packing density from $\eta = \eta^{cr}(\alpha = 0.3) = 0.88$ to $\eta = 0.90$ yields the expected behavior of an enlarged strength domain for the macroscopic material. For the case of a larger inclusion volume fraction value ($f^{inc} = 0.34$), the strength domain for a packing density of $\eta = 0.90$ delivers lower strengths

[8] The microstructural configurations MT-MT and SC-MT with slip interface are not considered, given that the macroscopic UCS predictions decrease in magnitude with increasing inclusion volume fraction values.

[9] The derivation of the parabolic limit case is achieved numerically using a standard software package.

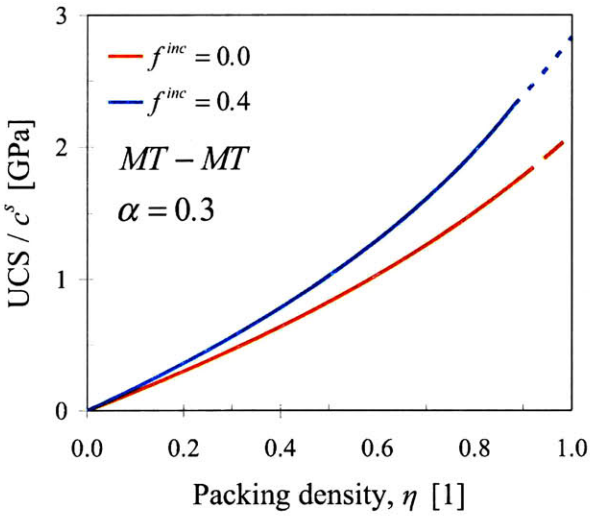

Figure 8-16: Predictions of the normalized unconfined compressive strength (UCS) for levels I ($f^{inc} = 0$) and II ($f^{inc} = 0.4$) as functions of the packing density η for a MT-MT microstructural configuration. The solid friction coefficient is $\alpha = 0.3$. The predicted UCS values for the elliptical regime are displayed in solid lines, whereas those corresponding to the hyperbolic regime are displayed in dashed lines.

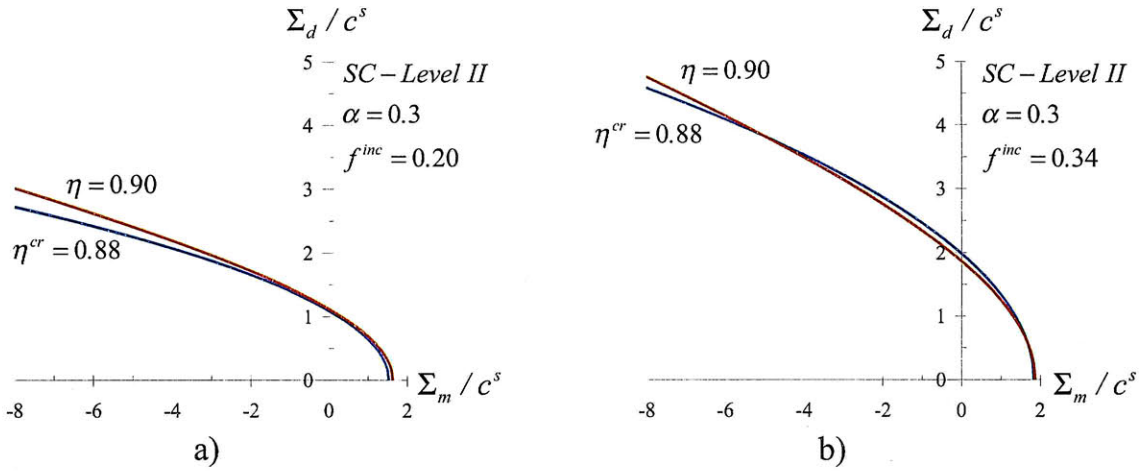

Figure 8-17: Predictions of strength domains for level II modeled by the self-consistent scheme. Two values of inclusion volume fraction are considered: a) $f^{inc} = 0.2$, and b) $f^{inc} = 0.34$. The properties of the porous solid at level I are: Mori-Tanaka microstructure, and friction coefficient $\alpha = 0.3$. For each case, two strength domains with different clay packing density values ($\eta = \eta^{cr} = 0.88$, and $\eta = 0.90$) are shown.

than predicted by the parabolic domain ($\eta = \eta^{cr} = 0.88$) for a particular range of stress states as observed in Figure 8-17b. Clearly, such behavior violates the expected strength development for the composite material.

To investigate this behavior, we return to the yield design framework in which the material strength is directly related to its plastic dissipation capacity. Figure 8-18 displays the corresponding normalized dissipation capacities $\widetilde{\Pi}^{II}_{\text{hom}}(\xi = D_d/D_v)$ of the material configurations analyzed in Figure 8-17b. The results from Figure 8-18 show that for the range of strain rates $(\xi' \leq \xi \leq \xi'')$ one verifies:

$$\widetilde{\Pi}^{II}_{\text{hom}}\left(\eta = 0.88, f^{inc} = 0.34\right) > \widetilde{\Pi}^{II}_{\text{hom}}\left(\eta = 0.90, f^{inc} = 0.34\right) \tag{8.162}$$

which clearly violates the expected dissipation behavior of a material. The increase in packing density (or decrease of porosity) should result in an increased capacity of the material for plastic dissipation. The range of strain rates $\left[\xi', \xi''\right]$ for which the decreased dissipation capacity is

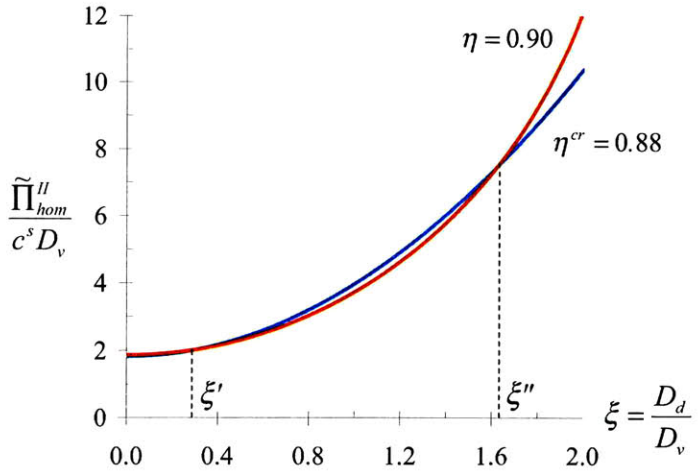

Figure 8-18: Normalized maximum dissipation capacity for the strength response at level II, $\widetilde{\Pi}^{II}_{\text{hom}}/\left(c^s D_v\right)$, as a function of the ratio of strain rates $\xi = D_d/D_v$. The dissipation functions correspond to the strength domains displayed in Figure 8-17b.

observed are transformed into stress states using the yield design definitions (8.19):

$$\Sigma_m = \frac{\partial \widetilde{\Pi}^{II}_{\text{hom}}}{\partial D_v}(\xi) \tag{8.163a}$$

$$\Sigma_d = \frac{1}{2}\frac{\partial \widetilde{\Pi}^{II}_{\text{hom}}}{\partial D_d}(\xi) \tag{8.163b}$$

The results are displayed in Figure 8-19, which define the stress range $[\Sigma', \Sigma'']$ over which the strength predictions are not valid. This stress range encompasses the previously identified domain in which the strength predictions for $\eta = 0.90$ are of lesser magnitude compared to those generated for $\eta = \eta^{cr} = 0.88$.

From the results of this sample study, it is recognized that specific amounts of rigid inclusions (quantified by f^{inc}) cannot be modeled by the LCC strength homogenization approach in view of a granular microstructure represented by the self-consistent scheme. A series of parametric studies were conducted in order to delineate the ranges of inclusion volume fraction for which the strength homogenization model deliver sensible strength predictions. Figures 8-20 and 8-21 display the critical inclusion volume fraction values for different strength measures (UCS, pure deviatoric stress, hydrostatic tension) as functions of the friction coefficient α. The friction

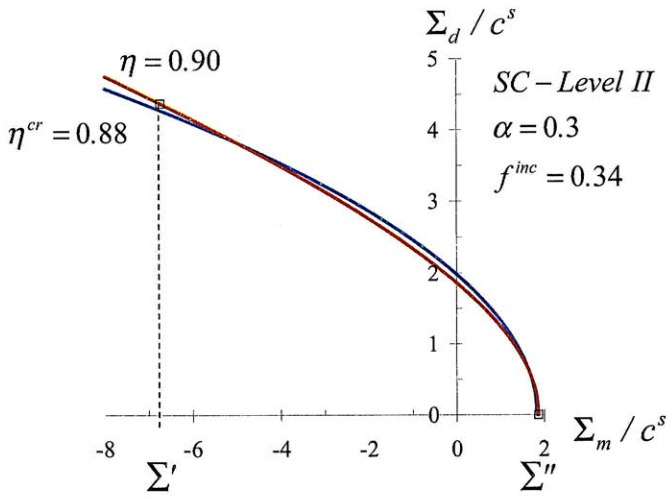

Figure 8-19: Domain of strength predictions $[\Sigma', \Sigma'']$ over which the evaluation of the macroscopic dissipation capacity is altered by the effect of rigid inclusions.

coefficient determines the characteristic packing density separating the elliptical and hyperbolic strength domains. The critical inclusion volume fraction establishes the characteristic amount of rigid inclusions below which strength predictions remain valid for the entire range of admissible packing densities ($0 < \eta < 1$ for the Mori-Tanaka scheme, and $0.5 < \eta < 1$ for the self-consistent scheme). Strength predictions are otherwise restricted to packing densities below the critical packing density $\eta < \eta^{cr}$ (see (8.85)). The range of packing densities $\eta < \eta^{cr}$ corresponds to strengths at level I defined by an elliptical domain.

8.4.4 Strength Behavior of a Dual-Porosity Material

The development of the dual-porosity model offers a theoretical context for investigating the effects of pore spaces at two different length scales in a cohesive-frictional solid on the macroscopic strength response. Recall that the macroscopic partitioning of the composite material accounts for a nanoporosity ϕ_0^I and a macroporosity ϕ_0^{II}, in addition to the solid (clay) volume fraction f^c, with $\phi_0^I + \phi_0^{II} + f^c = 1$. The solutions presented in Section 8.3.5 satisfy the two limit cases for distributions of the pore space:

- In the case of zero nanoporosity $\phi_0^I = 0$, the packing density at level I is $\eta = 1$, and

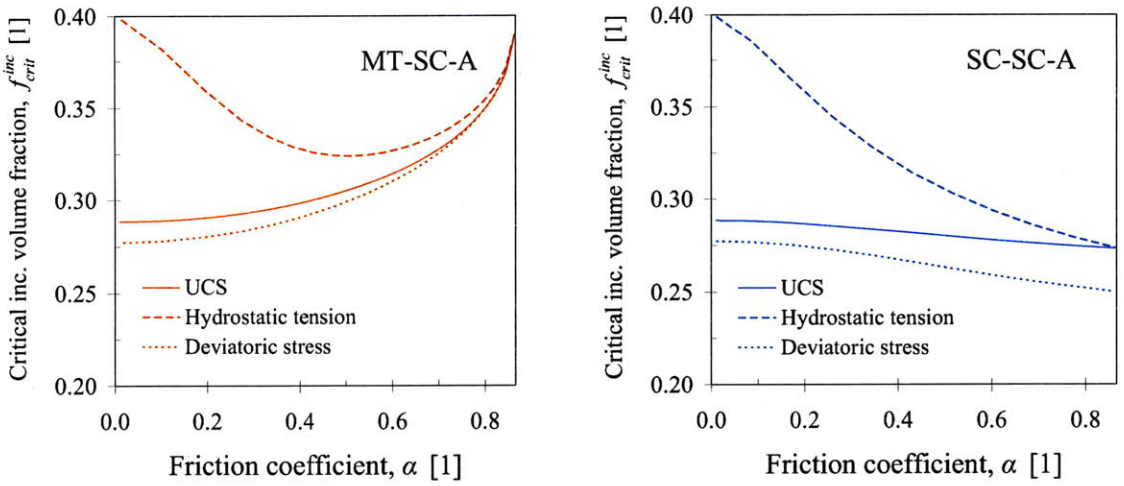

Figure 8-20: Critical inclusion volume fraction f_{crit}^{inc} as a function of the solid friction coefficient α, for MT-SC and SC-SC configurations at levels I and II, respectively, and perfectly adherent interfaces (A). Below the critical values f_{crit}^{inc}, the strength homogenization model for level II adequately predictics strength properties for the complete range of admissible packing densities.

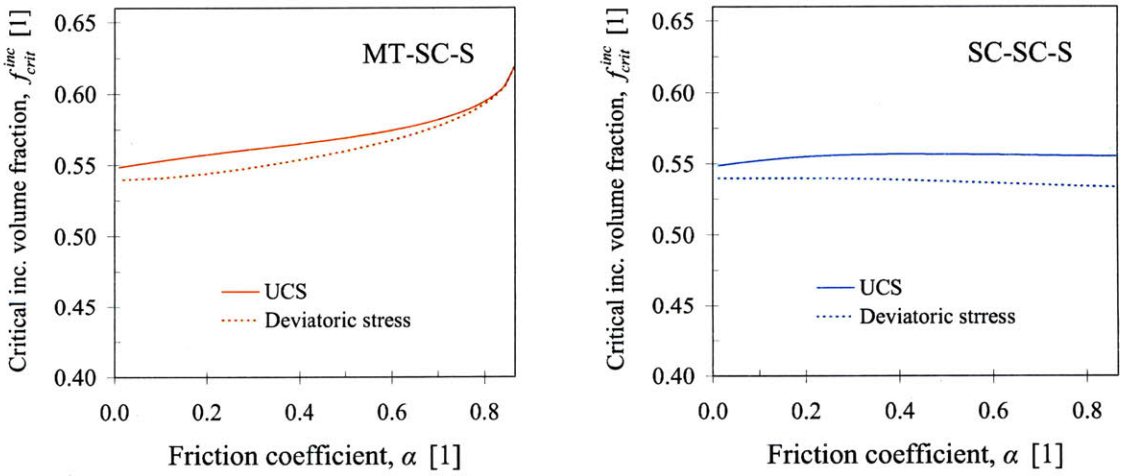

Figure 8-21: Critical inclusion volume fraction f_{crit}^{inc} as a function of the solid's friction coefficient α, for MT-SC and SC-SC configurations at levels I and II, respectively, and slip (non-frictional) interfaces (S). Below the critical values f_{crit}^{inc}, the strength homogenization model for level II adequately predictics strength properties for the complete range of admissible packing densities.

the homogenization step at level I retrieves the Drucker-Prager strength domain (8.49). The homogenization step at level II in the dual-porosity model is then equivalent to the solution for a level I homogenization step as detailed in Section 8.3.3.

- In the case of zero macroporosity $\phi_0^{II} = 0$, the result of the homogenization step at level II is equivalent to the solution of the level I homogenization.

However, in the case of finite values of nano- and macroporosities, the strength predictions for the composite material display particular trends, which depend on the type of microstructure of the material as modeled by the Mori-Tanaka and self-consistent schemes. To investigate the effects of a two-scale porosity, a fictitious material system is established with characteristic values of the friction coefficient α and total porosity $\phi_0 = \phi_0^I + \phi_0^{II}$. The distribution of porosity is monitored by the variable f^{mp}, the relative volume fraction of macroporosity, defined as:

$$f^{mp} = \frac{\phi_0^{II}}{\phi_0} = \frac{\phi_0^{II}}{\phi_0^I + \phi_0^{II}} \tag{8.164}$$

The values $f^{mp} = 0$ and $f^{mp} = 1$ correspond to the limit cases of pore space distributions between length scales that were previously described. The specific types of strength predictions used for model implementation are the unconfined compressive strength, pure deviatoric strength, and hydrostatic tension (see e.g. expressions (8.149),(8.151),(8.153)).

Figure 8-22 displays the different predicted strengths as functions of the relative volume fraction of macroporosity f^{mp}. The microstructure is modeled by the Mori-Tanaka scheme. The total porosity for the fictitious solid is $\phi_0 = 0.4$, and two friction coefficients are considered $\alpha = 0.2, 0.6$. The predicted strengths Σ^* in Figure 8-22 represent normalized values involving the result for the limit case $f^{mp} = 0$ (or equivalently $f^{mp} = 1$):

$$\Sigma^* = \frac{\Sigma^J\left(f^{mp}\right)}{\Sigma^J\left(f^{mp} = 0\right)} \tag{8.165}$$

where $J = UCS, dev, hyd$. The results in Figure 8-22 reveal that a distribution of the pore space between different length scales, modeled by $0 < f^{mp} < 1$, tends to weaken the strength response of the composite material with matrix-inclusion microstructure. However, this weakening effect appears to be relatively small (approximately $5 - 8\%$ for the considered total porosity $\phi_0 = 0.4$,

and tends to be smaller for lower porosity values).

A similar analysis is also presented in Figure 8-23 for the case of a granular microstructure modeled by the self-consistent scheme. The occurrence of a two-scale porosity in the granular medium shows a significant contrast compared to the model predictions for a matrix-inclusion microstructure. For all cases considered in Figure 8-23, the distribution of the pore space between the nano- and macroscale yields an enhancement of the strength response of the material. Figures 8-23a through 8-23c display strength predictions for a similar value of the solid friction coefficient $\alpha = 0.2$, whereas the total porosity varies by $\phi_0 = 0.2, 0.3, 0.4$. The increased strength effect is more significant for larger values of porosity, reaching levels of $20 - 30\%$ for $\phi_0 = 0.4$ compared to 5% for $\phi_0 = 0.2$. Clearly, these results are understood in the perspective of relative strength increases due to dual-porosity effects. The absolute strength of the material, as quantified by the definitions of UCS, pure deviatoric stress, and hydrostatic tension, is approximately 46% for a total porosity $\phi_0 = 0.4$ compared to the strength associated with a porosity of $\phi_0 = 0.2$.

Figures 8-23c and 8-23d offer information regarding the role of the friction coefficient on the dual-porosity strength behavior. The figures are generated for a similar total porosity $\phi_0 = 0.4$, while two friction coefficients are considered: $\alpha = 0.2, 0.6$. The increased friction capacity of the solid modifies the different strength definitions dissimilarly:. the UCS behavior is further enhanced, whereas the hydrostatic tension capacity is diminished. The deviatoric stress capacity is only slightly modified with increased friction. Finally, the maximum levels of strength enhancement recognized for the granular, two-scale porosity composite correspond to a relatively even distribution of pore space (with a relative macroporosity volume fraction of $f^{mp} \approx 0.57$). The results presented in Figures 8-22 and 8-23 provide a first micromechanics analysis of the strength of dual-porosity systems. This theoretical framework will have to be rigorously validated against experimental data in future studies.

8.5 Chapter Summary

A multi-scale micromechanics model for the upscaling of strength properties of shale has been presented in this chapter. Based on the linear comparison composite theory, the non-linear

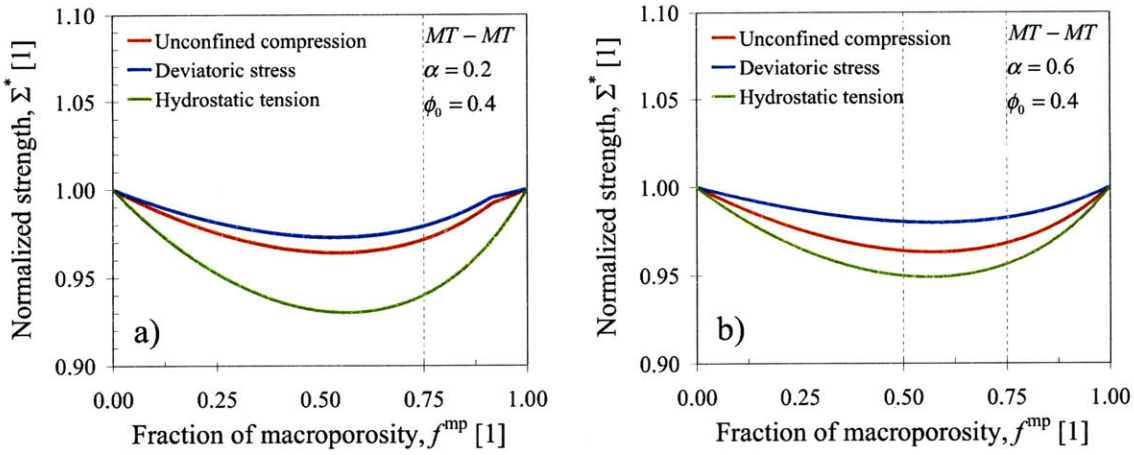

Figure 8-22: The effect of dual-porosity on the strength response of a cohesive-frictional solid with matrix-inclusino microstructure modeled by the Mori-Tanaka scheme.

homogenization approach of Gathier and Ulm [98] offers a general methodology which allows the consideration of a larger range of frictional behaviors in strength upscaling problems. This represents an improvement upon more restrictive strength homogenization models. The domain of application of the strength model was thoroughly analyzed. For the homogenization step related to the porous clay composite at level I, the model shows a smooth transition between elliptical and hyperbolic strength domains. For the homogenization step at level II, the addition of rigid inclusions representing silt minerals to the granular porous clay composite is limited to specific volume fractions. In addition to the development of the strength upscaling model for shale, a theoretical extension of the model was presented to address the effects of a dual-porosity on the strength of a cohesive-frictional solid. Parametric studies showed that the homogenized strength response of a granular composite is enhanced for the case in which the total porosity is allocated at two different length scales. In contrast, the presence of a two-scale porosity distribution on a composite with matrix-inclusion morphology has a small impact on its overall strength response.

In the following chapter, the strength upscaling framework is implemented for the modeling of shale, aiming at the link between grain-scale measurements from nanoindentation and macroscopic strength properties derived from conventional experiments.

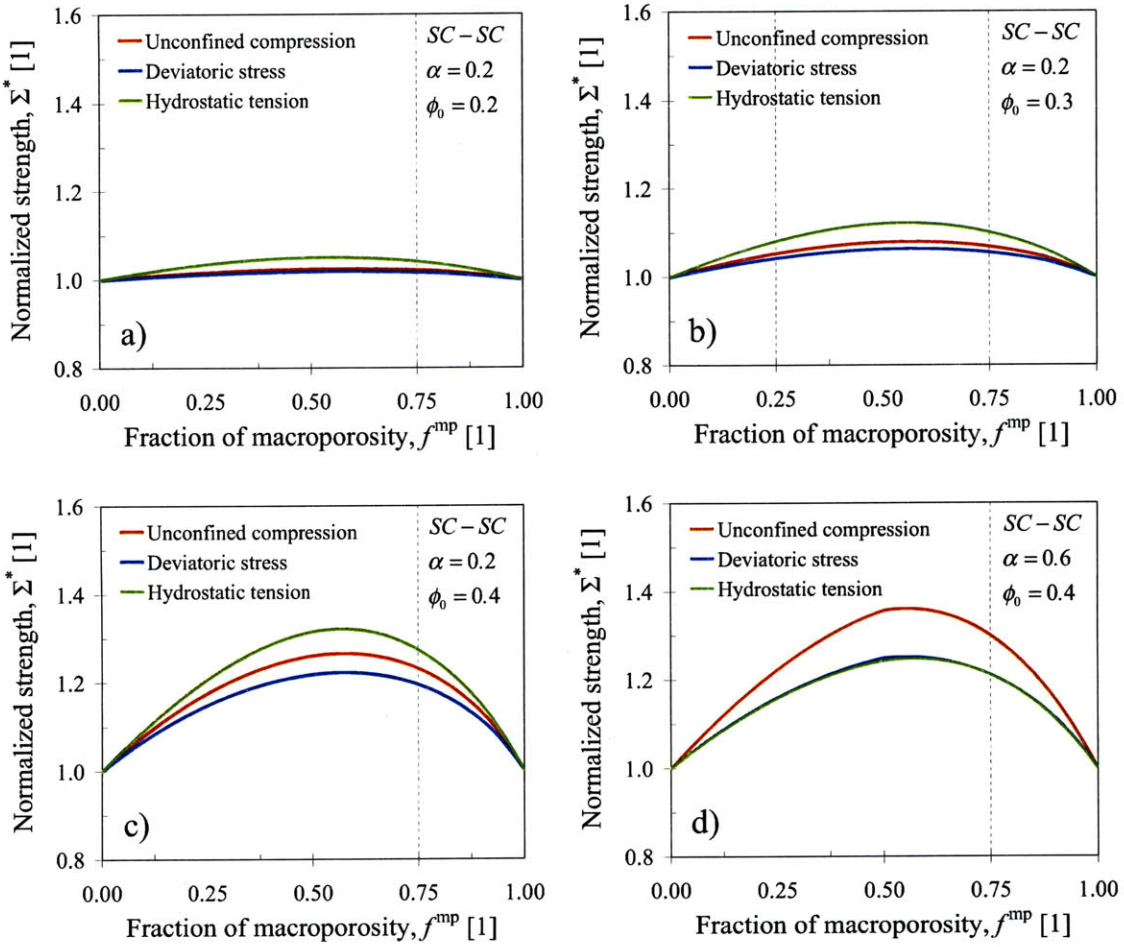

Figure 8-23: The effect of dual-porosity on the strength response of a cohesive-frictional solid with granular microstructure modeled by the self-consistent scheme.

Chapter 9

Strength Upscaling Model for Shale

The development of a micromechanics model for shale strength began in Chapter 8 with the presentation of a theoretical framework directed at the homogenization of strength properties at different length scales. The strength homogenization approach followed the multi-scale structure thought-model for shale introduced in Chapter 2, and incorporates some of the solutions developed through the microporoelasticity investigation in Part III of this thesis. The strength modeling framework recognizes the granular nature of the clay fabric assessed by nanoindentation, and employs an effective micromechanics description for the microstructure of shale. These features, in conjunction with the appropriate definitions for material invariant properties at the grain-scale of the clay fabric, were found to delineate the macroscopic diversity of shale's poroelastic behaviors.

The objective of this chapter is to implement the multi-scale strength homogenization model for the prediction of shale strength properties. Similar to microporoelasticity modeling, the prediction of strength properties of shale requires linking material composition, microstructure, and an adequate set of material invariant properties at the fundamental scale of the load-bearing clay phase. This chapter first focuses on the review of the cohesive-frictional behaviors of the clay phase as inferred from nanoindentation measurements and scaling analysis. The fundamental strength behaviors of the highly consolidated clay in shale are analyzed using a fractal packing model [32], which elucidates the relations between cohesion, friction, and packings of particles. The nanomechanics understanding of shale's strength behavior sets the stage for the implementation and validation of the strength upscaling model. The cohesive-

frictional properties of clay at level 0 of our multi-scale structure thought-model are used for constructing macroscopic predictions for shale samples gathered for an independent data set. From the results of validation procedures, we evaluate the predictive capabilities of the strength upscaling model. The chapter concludes with discussions of the nature of multi-scale strength behaviors of shale, and the domain of application and limitations of the proposed strength model.

9.1 Model Calibration

The implementation of the multi-scale homogenization model for the prediction of shale strength properties follows a different format compared to the microporoelasticity modeling presented in Chapter 5. A challenge for the latter investigation was the appropriate representation of the microstructure of shale at the scale of the clay fabric. Based on a thorough calibration and validation of the poroelastic model, the visually complex porous clay phase in shale was effectively characterized as a nanogranular composite, in which the intrinsic properties of the solid clay dominate the grain-scale mechanical response compared to the contributions from geometrical aspects of the microstructure and varying clay mineralogies. This micromechanics representation of the microstructure of shale was assumed to be relevant to the solution of the strength homogenization problem. The identified nanogranular nature of shale was typed into the strength upscaling model developed in Chapter 8 through the considerations of isotropic particle morphologies (spherical elementary units of clay and nanoporosity) and of the self-consistent homogenization scheme of micromechanics.

The standing challenge for the development of the strength predictive model for shale rests on the definition of the cohesive-frictional properties of the load-bearing clay phase. These properties enter the multi-scale formulation at level 0, that of the elementary building block. The lack of extensive data and the complex nature of the strength assessment of shale at macroscopic scales negate a back-analysis calibration approach for strength properties emulating the one pursued for the microporoelasticity model. Instead, the fundamental strength behavior of the elementary unit of clay is derived from grid nanoindentation hardness measurements. The rest of this section is devoted to the review of results from Chapter 3 regarding the cohesion

and friction behaviors of the solid clay inferred from nanoindentation scaling analysis. The section then introduces a fractal packing model [31] which provides an appropriate framework for understanding the relations derived from nanoindentation between friction and cohesion properties and the packing of clay mineral aggregates. The knowledge of the strength responses of shale at the scale of clay aggregates serves as the baseline for attempting the prediction of properties at macroscopic scales of engineering testing.

9.1.1 Review of the Cohesive-Frictional Properties of Clay in Shale

Scaling Relations of Cohesion and Friction Properties with Clay Packing Density

The indentation scaling analysis of Bobko [31] provided further insight on grid indentation results for shale materials. The so-called indentation modulus–hardness–packing density ($M-H-\eta$) analysis combines the measurements from individual indentation tests probing the porous clay in orthogonal directions and micromechanics scaling relations between intrinsic material properties (level 0) and measured indentation quantities (level I) to infer packing density distributions (see discussion in Section 3.6.6) and strength properties of the solid clay phase. The latter results are of particular importance to the strength modeling of shale as they provide a first means for characterizing the cohesive and frictional behaviors of the elementary material unit at level 0 of the multi-scale structure model.

Recall the form of the scaling relation derived from yield analysis and non-linear homogenization between the indentation hardness H, the solid's cohesion c^s and friction coefficient α (for a Drucker-Prager type solid), and the clay packing density η (see (3.29))

$$H = h^s\left(c^s, \alpha\right) \times \Pi_H\left(\alpha, \eta\right) \tag{9.1}$$

where $h^s\left(c^s, \alpha\right) = \lim_{\eta \to 1} H$ is the asymptotic contact hardness of the solid clay phase, and $\Pi_H\left(\alpha, \eta\right)$ is a dimensionless function provided in (3.31). A remarkable result from the $M-H-\eta$ scaling analysis is the apparent constant value of $h^s = 0.69$ GPa for the tested shale samples with varying mineralogy compositions. This finding presents the solid hardness as an intrinsic parameter characterizing the clay strength response in shale. In contrast to the invariant character of the solid hardness, an interplay between the solid's cohesion and friction with the

clay packing density was identified from the $M - H - \eta$ scaling analysis. Figure 9-1 displays the trends between the cohesion and friction behaviors of the elementary unit of solid clay and the clay packing density (see also discussion in Section 3.6.6). The significant dependency of the strength behavior of the clay phase on the packing density for individual shale specimens differs from the elastic behavior, which is characterized by a constant and invariant set of anisotropic properties at level 0. The solid clay friction coefficient decreases with increasing values of packing density, and tends towards a minimum value for packing densities close to $\eta = 1$ (Figure 9-1a). Alternatively, the cohesive behavior scales proportionally with the packing density, from a minimum value close to the percolation threshold at $\eta = 0.5$ to larger values with increasing packing densities (Figure 9-1b).

The relationship between the cohesion and friction properties and the clay packing density, which synthesizes porosity and mineralogy information, is an intriguing attribute ascribed to the elementary building block of shale in the context of its strength properties. The knowledge derived from the nanoelasticity of the elementary unit as the collective response of conglomerates of clay particles encompassing clay mineral layers and interlayer galleries offers the appropriate context for the understanding of strength behaviors at the fundamental scales of shale. Bobko [31] suggested that the interface and interparticle behaviors may indeed modulate the cohesive-frictional properties of the solid clay phase. The underlying physical mechanisms related to the cohesion-friction-packing density dependencies were explained by linking experimental evidence to concepts of coordination number, bond distances, friction models, and fractal packings. Particularly, the framework of space-filling bearings and fractal packing models provided a rational basis for establishing a scaling relation between the frictional response of the solid clay phase as a function of the clay packing density.

Cohesion, Coordination Number, and Bond Distance

Coordination number, which denotes the average number of contacts for a particle, was proposed as the geometrical parameter for explaining the relation of cohesion and packing density [31]. In essence, the coordination number for a particle assembly offers a quantification of its degree of packing. Figure 9-2 shows the mean coordination numbers determined experimentally for randomly packed mono-sized and two-sized spherical assemblies as functions of packing density,

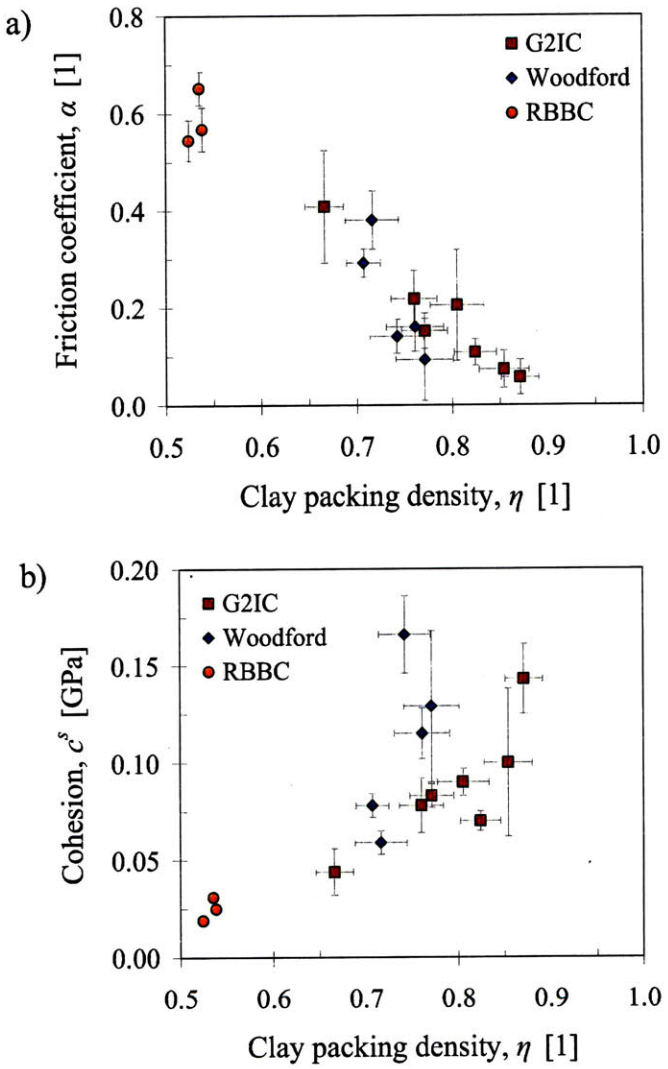

Figure 9-1: Scaling of clay strength properties with packing density (recalled from Section 3.6.6). The experimental data corresponds to G2IC and Woodford shales and resedimented Boston Blue Clay samples. Uncertainties represent two standard deviations. From [31].

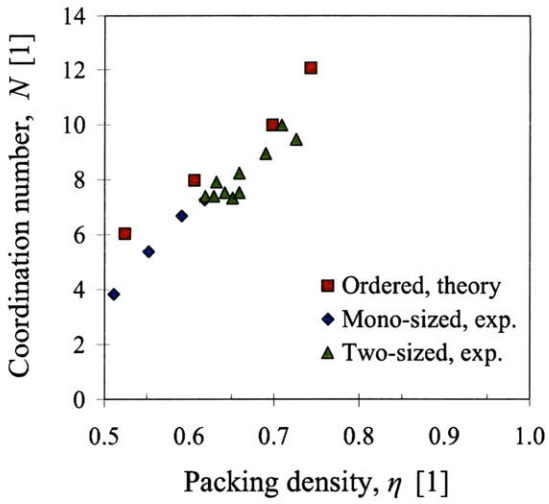

Figure 9-2: Mean coordination numbers determined for theoretical packings of particles and for experiments on random packings of mono-sized and two-sized glass beads. Data from [198], replotted in terms of packing density values.

as well as theoretical results for packings of spheres. The trend between coordination number and packing density is relatively linear, and compares qualitatively with the cohesion–packing density trend displayed in Figure 9-1. Bonding forces resulting from cementations between particles or combinations of ionic and electrostatic forces at the grain-scale may be linked to the concept of coordination number. These attractive forces lead to the development of cohesion in clay depending on bonding distances, which highlights a potential relation between cohesion and the spacing or packing between particles in the highly compacted clay fabric of shale.

Friction and Particle-Pore Interactions

The physical origins of friction in granular media remains a challenging research endeavor [155, 223]. Adding to the discourse, the experimental data and mechanics interpretations for the frictional behavior of shale were explored in context of interactions between particles and pore spaces at nanoscales [31]. Among the different theoretical models for understanding friction, a classical perspective is given by the Amontons-Coulomb law for the contact between two solids (see e.g. [96]), which denotes a linear relation between the friction force and the load

pushing the solids together, while remaining independent of the contact surface. This definition of friction is entirely based on a geometric argument relating the frictional behavior to the presence of asperities between contiguous surfaces. More sophisticated theories have explored the phenomenon of friction with relations to the effects of absorbed mobile molecules on material surfaces [192] and to the propagation of self-healing cracks [100]. A crucial notion in these theories is the requirement for space between particles in order to generate a frictional response.

A relationship between the frictional behavior of clay and interactions between particles and pore spaces was postulated in [31] based on the experimental indentation investigation of shale materials. Figure 9-3 shows the trend between the average pore throat radius obtained from mercury intrusion porosimetry and the clay packing density determined for G2IC and Woodford shales. The observed trend of decreasing packing density with increasing pore throat radius is used in Figure 9-4 to redisplay the relation between the friction coefficient behavior (see Figure 9-1a) and the pore throat radius. The friction coefficient scales with the characteristic size of the pore space, which hints towards a generation of frictional mechanisms upon the availability of interparticle space understood in the sense of porosity. Consequently, this observation seems to agree with the postulates from the theoretical models previously reviewed, in which looser arrangements of particles could potentially allow for the activation of asperities in the classical friction model and the necessary space for mobile molecules or microcracks to enhance the frictional behavior [100, 192]. The inferred frictional behavior for the solid clay in shale from advanced grid indentation analysis and the concept of particle-pore interactions motivate the use of a fractal packing model to formally explain the relationship between the clay friction and packing density.

9.1.2 Fractal Packing Model

Bobko [31] developed a model based on space-filling bearings and fractal packings as a means to derive a relationship between the frictional behavior of the elementary unit of solid clay and the packing density as inferred from nanoindentation scaling analysis. The development was motivated by the nature of the highly compacted arrangement of clay particles in shale, which could translate into packing densities beyond the maximum packing of $\eta = 0.74$ corresponding to a face-centered cubic packing [80]. From clay mineralogy, the varying characteristic sizes of

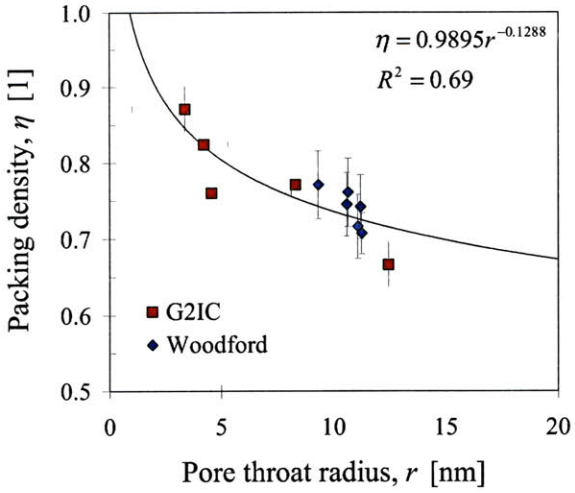

Figure 9-3: Relation between the average pore throat radius obtained from mercury intrusion porosimetry r, and the clay packing density obtained from indentation scaling analysis η. Data corresponds to G2IC and Woodford shales. Uncertainties for experimental data are represented by one standard deviation. The solid line is a power-law fit, underscoring the decrease in packing density with increase in pore throat radius. From [31].

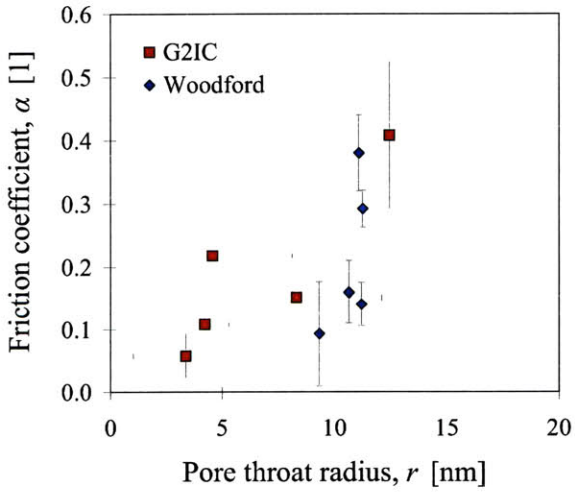

Figure 9-4: Friction coefficient determined from indentation scaling analysis as a function of the pore throat radius determined from mercury intrusion porosimetry for G2IC and Woodford shales. Uncertainties for experimental data are represented by one standard deviation. From [31].

clay crystals hint towards highly dispersed arrangements in shale. In this sense, a limit case of dense packings with disperse grain sizes is the space-filling bearing [120], an arrangement which almost perfectly fills a three-dimensional space[1]. A particular case relevant for quantitative analysis is the Apollonian packing of spheres, which represents a perfect space-filling packing starting with a tetrahedron arrangement of mutually touching spheres. Solid spheres then fit recursively the existing pores by maximizing the occupied volumes. Such recursive filling is associated with the concept of fractals.

In fractal packing, the number of spheres with radii larger than ϵ follows an asymptotic relation [36]:

$$N(\epsilon) \sim \epsilon^{-D} \tag{9.2}$$

in which D is the packing fractal dimension, which can also be determined from other quantities such as the sum of perimeters $s(\epsilon)$, the sum of surface areas $p(\epsilon)$, and the sum of volumes $v(\epsilon)$ of spheres:

$$s(\epsilon) \sim \epsilon^{1-D} \tag{9.3a}$$

$$p(\epsilon) \sim \epsilon^{2-D} \tag{9.3b}$$

$$v(\epsilon) \sim \epsilon^{3-D} \tag{9.3c}$$

For the Apollonian packing of spheres, the fractal dimension has been rigorously computed to be $D = 2.474$ [36]. The fractal packing model of Bobko [31] targeted the identification of the fractal dimension for the packing of clay particles as a potential link between clay packing and the space-filling bearing using two different types of available experimental data for shale samples. The first approach consisted in deriving a relation between clay porosity and the pore throat radius. Figure 9-5 redisplays the data presented in Figure 9-3 in terms of the clay nanoporosity $\varphi_0 = 1 - \eta$, which is used to compute a power function representative of a volume fractal of the form:

$$\varphi_0 = \left(\frac{\epsilon}{\epsilon_0}\right)^{3-D} \quad ; \quad \epsilon_0 = 168 \text{ nm} \tag{9.4}$$

where ϵ_0 is the characteristic size or correlation length. The corresponding fractal dimension

[1] The property defining a bearing is the allowed slipless rotation around an arbitrary axis.

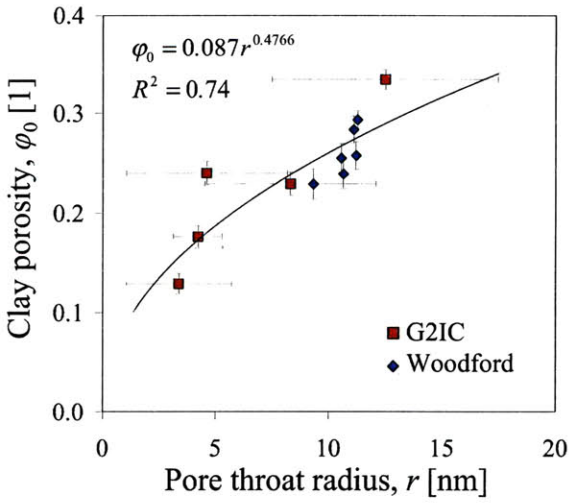

Figure 9-5: Clay porosity determined from nanoindentation scaling analysis φ_0 as a function of pore throat radius r for G2IC and Woodford shales. The solid line represents the power-law fit given by the displayed equation. Uncertainties for experimental data represent one standard deviation. From [31].

for the porosity–pore size relation is $D = 2.523$.

The second approach in determining a fractal dimension for the packing of clays in shale is to establish a scaling between friction and packing density. From the classical Amontons-Coulomb law for friction, the frictional force is proportional to the normal loading applied to the two surfaces while remaining independent of the contact surface. The Coulomb-type friction coefficient is given by:

$$\mu = \frac{|F_t|}{F_n} \tag{9.5}$$

where F_t, F_n are the tangential and normal forces, respectively. The analysis of the frictional behavior is pursued through dimensional analysis in an extended base dimension system in order to derive a link between the different length dimensions involved in the problem. Consider an extended $L_n L_t MT$ base dimension system [133], where L_n refers to the length dimension measured in the normal direction, and L_t to the length dimension in the contact plane of the two surfaces, such that the dimension function of any quantity Q can be expressed as:

$$[Q] = L_n^{\alpha} L_t^{\beta} M^{\gamma} T^{\delta} \tag{9.6}$$

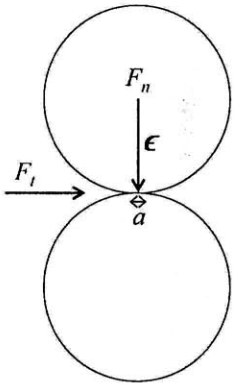

Figure 9-6: Schematic of the friction behavior between two spheres, which suggests the use of an extended base dimension system for the dimensional analysis of the contact problem. The normal length scale ϵ is much larger than the tangential length scale a.

The extended base dimension system is appropriate for describing the friction problem, where the magnitude of the length associated with the normal dimension is larger than that of the contact area. Figure 9-6 presents a schematic of the distorted system related to the friction problem. The dimension functions for the normal and tangential forces in the extended base dimension system are:

$$[F_t] = L_t M T^{-2} \tag{9.7a}$$

$$[F_n] = L_n M T^{-2} \tag{9.7b}$$

and consequently:

$$[\mu] = \frac{[F_t]}{[F_n]} = \frac{L_t}{L_n} \tag{9.8}$$

The length dimensions in (9.8) can be related to the asymptotic relations in (9.3) defined by fractal packing. In particular, consider the perimeter of a sphere measured along any circle $s = 2\pi\epsilon$ whose normal passes through the center of the sphere. In the extended base dimension system, the perimeter depends on the dimension L_n, without requiring a tangential measure:

$$[s] = L_n \tag{9.9}$$

The surface area of a sphere corresponds to the measurement of a tangential area with dimension L_t along tangent planes:

$$[p] = L_t^2 \tag{9.10}$$

These dimensional considerations are used in the dimension function for the friction coefficient (9.8), yielding:

$$[\mu] = \frac{L_t}{L_n} = \frac{[p]^{\frac{1}{2}}}{[s]} \tag{9.11}$$

The substitution of the fractal relations (9.3a) and (9.3b) in (9.11) provides an asymptotic scaling relation for the friction coefficient:

$$\mu \sim \frac{\sqrt{p(\epsilon)}}{s(\epsilon)} = \frac{\sqrt{\epsilon^{2-D}}}{\epsilon^{1-D}} = \epsilon^{\frac{D}{2}} \tag{9.12}$$

The development of the relation (9.12) was based on the packing of solid particles, whereas (9.4) considered the porosity and pore throat radii. Based on a generalized pore-solid fractal modeling approach, the combination of the fractal friction coefficient and fractal porosity scalings yields[2]:

$$\mu \sim \left(\varphi_0^{\frac{1}{3-D}}\right)^{\frac{D}{2}} = \varphi_0^{\varkappa} \quad ; \quad \varkappa = \frac{D}{6-2D} \tag{9.13}$$

which allows determining the fractal dimension from the relation between friction and porosity. The friction coefficient μ is computed from the experimental data for shale by converting the Drucker-Prager values α using the relation between the Mohr-Coulomb friction coefficient $\mu = \tan\phi$ and the internal cone of the Drucker-Prager criterion [235]:

$$\sin\phi = \sqrt{\frac{3\alpha^2}{3-\alpha^2}} \tag{9.14}$$

Figure 9-7 displays the relation between the friction coefficient μ and the clay porosity φ_0, and the data fitting using a power-function with coefficient $\varkappa = 2.0769$. Consequently, the use of (9.13) provides an estimate for the fractal dimension from the friction–porosity scaling of $D = 2.418$. This estimate of the fractal dimension compares well with the result derived

[2]The generalized pore-solid fractal model features symmetry of fractal scalings and equivalent fractal dimensions for pore and solid size relations. However, fractal symmetry may not exist between pore and solid sizes when a cutoff on fractal scaling exists [210].

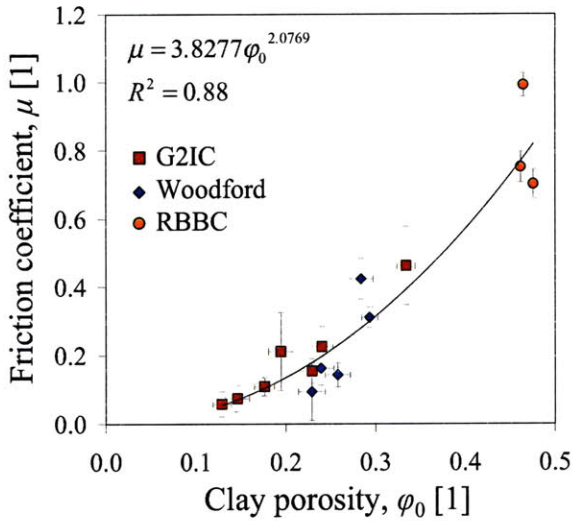

Figure 9-7: Scaling between the Mohr-Coulomb friction coefficient μ and the clay porosity φ_0 for G2IC shales, Woodford shales, and resedimented Boston Blue Clay samples. The Mohr-Coulomb type friction coefficient was derived from experimental data using expression (9.14). The solid line represents the power-law fit given by the displayed equation. Uncertainties for experimental data represent one standard deviation. From [31].

from the porosity–pore throat radius scaling. Bobko [31] suggested that the apparent friction coefficient at the scale of clay particles in the elementary building block exhibits fractality, with a fractal dimension similar to that of the Apollonian packing. This implies that the packing of the porous clay in shale may come close to a perfect packing as a result of sedimentary and diagenetic processes. Compared to the perfect packing with zero porosity and frictionless conditions, the presence of nanoporosity yields instead an imperfect space-filling mechanism that introduces a frictional behavior as noted from considerations of particle-pore interactions.

9.1.3 Fractal Scaling Relations for Friction, Cohesion, and Packing Density

The development of the fractal packing model by Bobko [31] offers a quantitative relation between the frictional behavior and packing density for the fundamental scale of shale materials. The scaling relation between the Mohr-Coulomb friction coefficient and porosity derived from the fractal packing model (9.13) can be expressed in an alternative form. Considering the internal cone equation for the Drucker-Prager criterion (9.14) and the clay porosity in terms of

the packing density $\eta = 1 - \varphi_0$, a relation between the friction coefficient α and packing density is obtained:

$$\sin^{-1}\left(\sqrt{\frac{3\alpha^2}{3-\alpha^2}}\right) = \tan^{-1}\left[3.8277\,(1-\eta)^{2.0769}\right] \tag{9.15}$$

The cohesion of the elementary building block can be calculated using the result for the friction coefficient from fractal scaling (9.15) and the function (3.30) derived from yield design and non-linear homogenization considerations:

$$c^s = \frac{h^s}{a\left[1 + b\alpha + (c\alpha)^3 + (d\alpha)^{10}\right]} \tag{9.16}$$

where h^s is the solid hardness, and

$$\begin{cases} a = 4.7644 \\ b = 2.5934 \\ c = 2.1860 \\ d = 1.6777 \end{cases}$$

An estimate for the solid hardness of $h^s = 0.69$ GPa was determined from nanoindentation analysis (refer to Section 3.6.6). Figure 9-8 shows the data inferred from indentation scaling analysis for the friction coefficient and cohesion as functions of packing density, as well as the results from fractal scaling. The conversion of the fractal scaling relation (9.13) into a Drucker-Prager type friction – packing density form fits the experimental data adequately, as seen in Figure 9-8a. A similar observation is made for the cohesion-packing density scaling shown in Figure 9-8b. The scaling relation (9.15) derived on the basis of the fractal packing model of Bobko [31] and the corresponding determination of the cohesion from expression (9.16) constitute the cohesive-frictional material properties describing the strength behavior of the elementary building block of solid clay at level 0 of the multi-scale structure model for shale.

9.2 Model Validation

The definition of material properties for level 0, the elementary unit of clay, represents a crucial component for the implementation of the strength model in a predictive mode. The nanogranular nature of shale and its microstructure have already been addressed through effective de-

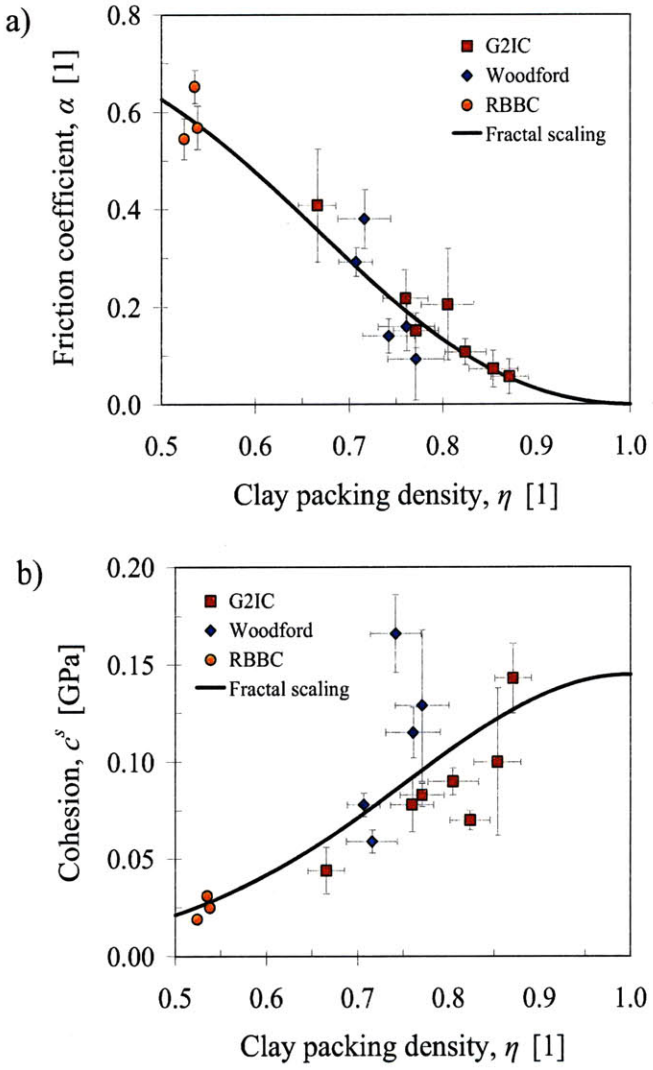

Figure 9-8: Scalings between the packing density η and a) the Drucker-Prager friction coefficient α, and b) the cohesion c^s. The experimental data corresponds to G2IC and Woodford shales and resedimented Boston Blue Clay samples. The fractal scaling relations derived for both strength properties are also displayed [31]. Uncertainties represent two standard deviations.

finitions deduced from microporoelasticity modeling. Hence, the validation of the strength upscaling model for shale depends on the confirmation of the cohesion-friction-packing density relations discussed in Section 9.1. The developed understanding of the cohesive-frictional behavior of shale at the scale of the elementary unit of solid clay is tested in this section through its implementation in the multi-scale strength homogenization model presented in Chapter 8. The objective of the model validation is to compare the model predictions for level II (the porous clay - silt inclusion composite) with macroscopic strength data for a set of shale samples gathered in this exploratory work of strength modeling. An independent validation of the model at level I (the porous clay composite) is not viable given that the experimental nanoindentation data generated by the G2IC [31] served as the baseline for developing the cohesion-friction-packing density scaling relations for level 0 properties.

9.2.1 Validation Data Set

The validation data set for strength modeling corresponds to shale data collected from the open literature, as well as data for one shale sample from the G2IC and several resedimented Boston Blue Clay samples. The selected literature references furnish complete descriptions of mineralogy composition, porosity, and unconfined compressive strength (UCS) values for several shale materials of diverse origins. Table 9.1 displays the list of shale samples included in the validation data set for strength modeling (VDS-S). The estimates of clay packing density and inclusion volume fraction and strength data for the VDS-S shale samples are detailed in Chapter 3. Figure 9-9 displays graphically the volumetric parameters estimated for the shale samples in the VDS-S data set. The broad range of packing densities and inclusion volume fractions ensure the adequacy of the VDS-S for model validation.

9.2.2 Level II - Comparison with UCS Experiments

The validation of the strength upscaling model is accomplished through its implementation in a forward approach to generate unconfined compressive strength (UCS) predictions for the shale samples considered in the VDS-S data set. The material properties for the elementary unit of solid clay at level 0 correspond to the scaling relations between cohesive-frictional properties and packing density summarized in expressions (9.15) and (9.16). The key elements in these

Data set	Reference	Samples
VDS-S	[142]	9898, 10151, 6275, 7053, 6853, 8675,
	[130]	B, D, E, H, J, K,
	[195]	TOU
	[68]	SH1
	G2IC	North Sea
	[1]	RBBC-2, RBBC-4, RBBC-6, RBBC-8, RBBC-10

Table 9.1: List of shale samples considered in the validation data set for strength modeling, VDS-S. The experimental data for these samples was gathered from open literature sources. The data for the resedimented Boston Blue Clay (RBBC) was generated at MIT. The North Sea sample was investigated by the G2IC.

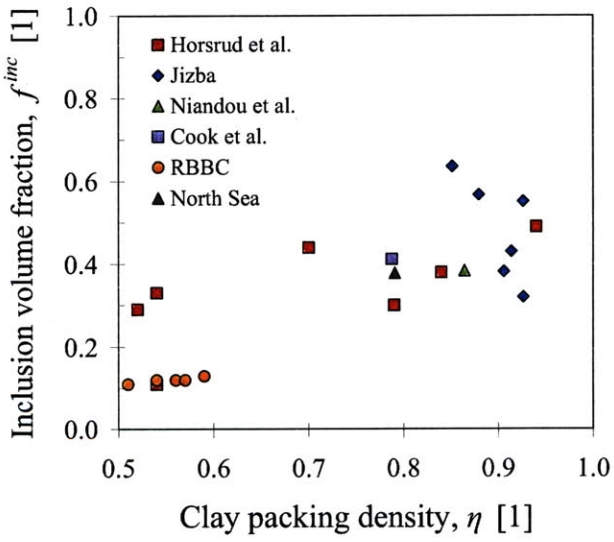

Figure 9-9: Clay packing density η and silt inclusion volume fraction f^{inc} estimated for the shale samples considered in the VDS-S validation data set. The displayed volume fractions are calculated based on mineralogy and porosity data.

relationships are the explicit dependency of the solid's cohesion and friction coefficient on the clay packing density and the order-of-magnitude of the intrinsic cohesion of the solid clay phase scaled by the solid hardness, $h^s = 0.69$ GPa. In addition to the properties of the elementary building block, the other model parameters involved in strength upscaling are the clay packing density and the inclusion volume fraction, determined from mineralogy and porosity information for each shale sample in the VDS-S. The volumetric parameters and material behaviors at level 0 represent the complete set of input parameters necessary for the prediction of strength domains at level II, whose expressions are detailed in Section 8.3.4. The parameters defining the strength domains $(\Sigma^{II}_{\text{hom},0}, A^{II}_{\text{hom}}, B^{II}_{\text{hom}})$ are then used to calculate the modeled UCS strengths (see e.g. expression (8.149)):

$$\Sigma^{UCS} = \frac{3}{3\left(A^{II}_{\text{hom}}\right)^2 + \left(B^{II}_{\text{hom}}\right)^2}\left(-\Sigma^{II}_{\text{hom},0}\left(B^{II}_{\text{hom}}\right)^2 + \sqrt{\left(A^{II}_{\text{hom}}\right)^2\left(B^{II}_{\text{hom}}\right)^4 + 3\left(A^{II}_{\text{hom}}\right)^4\left(B^{II}_{\text{hom}}\right)^2 - 3\left(A^{II}_{\text{hom}}\right)^2\left(B^{II}_{\text{hom}}\right)^2\left(\Sigma^{II}_{\text{hom},0}\right)^2}\right) \tag{9.17}$$

The predictions of UCS properties for level II are generated for two different interface conditions between the (rigid) silt inclusions and the homogenized porous clay phase; namely perfect bonding and slip (non-frictional) conditions. These modeling features enhance the mechanical description of the macroscopic composite by delineating two limit conditions for interface behaviors. The comparisons between predicted and measured UCS strengths for the VDS-S data are presented in Figure 9-10. The horizontal error bars for the Tournemire and North Sea shale samples are related to the alternative sets of volumetric properties (η, f^{inc} obtained from mineralogy-porosity and mineralogy-density information) used for model implementation. The remaining shale samples in the VDS-S are characterized by volumetric properties obtained exclusively from mineralogy and porosity data. Three shale samples (9898, 7053, 6853) cannot be modeled assuming perfectly bonded interfaces as their corresponding inclusion volume fractions exceed the limit value of $f^{inc} = 0.5$ associated with such interface condition (refer to Section 8.3.4). The case of slip-type interfaces restricts the range of inclusion volume fraction values to $f^{inc} < 2/3$, which allows the modeling of all shale specimens in the VDS-S data set.

The analysis of Figures 9-10a and 9-10b readily reveals an overprediction of UCS strengths associated with modeling results. Interestingly, the observed overprediction for both types

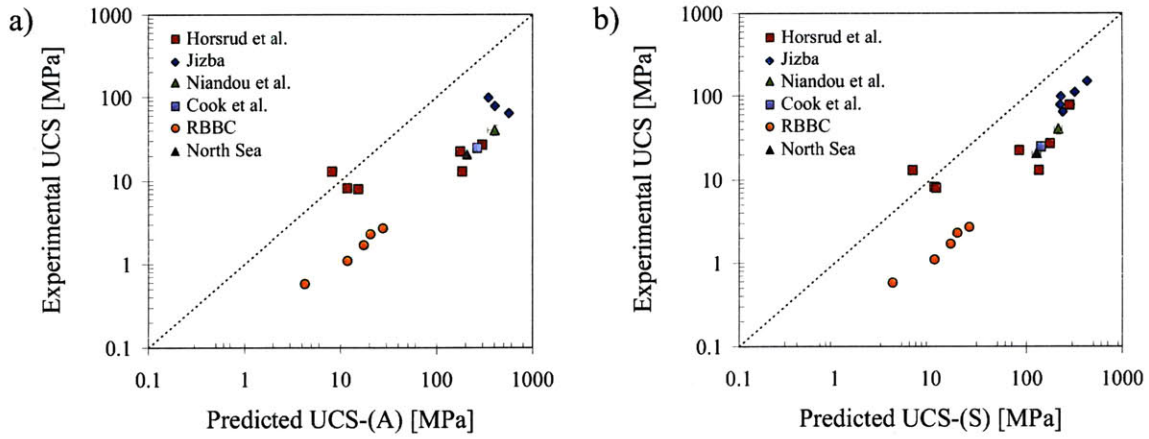

Figure 9-10: Comparisons of unconfined compressive strength (UCS) between experimentally measured values and model predictions. The modeling results correspond to macroscopic (level II) predictions for two types of interface conditions: a) perfectly adherent interfaces, and b) slip-type interfaces.

of modeled interface conditions displays a somewhat consistent trend, except for three shale samples (B,D,E) which exhibit relatively low strengths compared to others in the particular set [130]. The observed overprediction is verified for the strength predictions based on slip interface conditions with a correlation coefficient $r^2 = 0.88$. The correlation coefficient for the set of comparisons based on model predictions assuming perfect interface conditions is $r^2 = 0.45$. Nevertheless, the results in Figure 9-10 suggests that the strength upscaling model for shale based on the cohesion-friction-packing density relations (9.15)-(9.16) and scaled by the solid cohesion h^s from nanoindentation analysis cannot be applied for the prediction of macroscopic strength properties. Yet, the apparently consistent overprediction of properties furnished by the present form of the multi-scale strength homogenization model deserves further analysis.

9.3 Discussion of the Multi-Scale Strength Behavior of Shale

Although the comparisons between model predictions and macroscopic strength data presented in Figure 9-10 invalidate the use of the strength upscaling model for shale in its present form, the consistent overprediction of properties is analyzed in this section. The aim of this extended

investigation is to delineate the potential causes for such overpredictive tendency of the model, which otherwise seems to capture the macroscopic strength response for shale samples of distinct origin and compositional characteristics.

9.3.1 Adjusted Contact Hardness

The consistent overestimation in UCS strength properties hints towards a difference between experimental and predicted values that scales by a proportionality factor. From the review of model input parameters, the variable modulating the order-of-magnitude of predicted strength behaviors is solid hardness h^s, which enters the formulation through the solid's cohesion c^s in (9.16). The estimate for the solid hardness of $h^s = 0.69$ GPa was determined from the scaling analysis of grid indentation data obtained at nanometer length scales in shale [31]. Although established as a material invariant property, its order-of-magnitude represents a potential source for the mismatch between strength measurements and predictions.

In order to define an effective value for the solid hardness, we pursue a back-calculation analysis to determine an adjusted parameter $\widehat{h^s}$, which in turn could enable adequate macroscopic strength predictions. The back-calculation approach is similar to the reverse analysis of anisotropic elasticity properties for the elementary unit detailed in Section 5.2.1. The strength model is implemented in a forward application using the clay strength properties derived from fractal scaling analysis (9.15)-(9.16), while keeping the value $\widehat{h^s}$ as a degree-of-freedom. The parameter calibration is accomplished by minimizing the relative error between the experimental UCS strength values for the VDS-S data and the corresponding model predictions generated for a given $\widehat{h^s}$ value:

$$\min_{\widehat{h^s}} \left(\sum_{(VDS-S)} \left| \frac{\Sigma^{UCS}_{predicted} - \Sigma^{UCS}_{measured}}{\Sigma^{UCS}_{measured}} \right| \right) \tag{9.18}$$

The back-calculation of the adjusted solid hardness $\widehat{h^s}$ was conducted for both types of interface conditions (perfect bonding and slip interface) used in modeling of the strength response at level II. Figures 9-11a and 9-11b display the new sets of comparisons between predicted and measured UCS strength properties for the VDS-S shale samples based on the following adjusted

Interface condition	Mean relative error [%] [142]	[130]	[195]	[68]	North Sea	RBBC	r^2
Perfect adherence	−48	−23	−12	6	−12	−16	0.45
Slip interface	−48	−31	−7	0	8	55	0.88

Table 9.2: Mean relative error statistics for the comparisons between measured unconfined compressive strengths (UCS) and model predictions for the VDS-S shale data. For each interface condition, the correlation coefficient is calculated for the complete set of data.

solid hardness values for perfectly adherent (A) and slip (S) interface conditions, respectively:

$$\widehat{h_A^s} = 0.06 \text{ GPa} \tag{9.19a}$$

$$\widehat{h_S^s} = 0.12 \text{ GPa} \tag{9.19b}$$

These values represent 9% and 18% of the solid hardness h^s determined from nanoindentation. Table 9.2 reports the relative errors involved in the UCS strength predictions based on the adjusted values for the solid hardness.

The results presented in Figure 9-11 and Table 9.2 suggest that the strength upscaling model for shale can capture the strength behavior of shale samples over two orders of magnitude in UCS strengths provided the solid hardness h^s is adjusted properly. Encouraging results are obtained for the majority of shale samples considered in the VDS-S data set, especially for the data of Niandou et al. [195], Cook et al. [68], and the RBBC and North Shale specimens. In general, the strength model considering a slip-type interface condition delivers improved predictions, with an overall relative error $e_S = -5 \pm 56\%$, compared to the modeling based on perfectly bonded interfaces with $e_A = -23 \pm 48\%$. Although an acceptable predictive capability of the shale strength model has been verified based on the use of an adjusted cohesion $c^s\left(\widehat{h^s}\right)$ for the clay solid, an important question remains: are the nanoscale cohesive-frictional behaviors (9.15)-(9.16), established for the elementary building block of shale, the factors enabling the predictions of UCS strengths observed in Figure 9-11? The next section addresses this question.

9.3.2 Validation of Nanoscale Cohesive-Frictional Properties of Shale

The strength upscaling scheme for shale achieved a predictive status with the adjustment of the solid hardness h^s in the expression of the solid cohesion c^s (9.16). However, the apparent ability

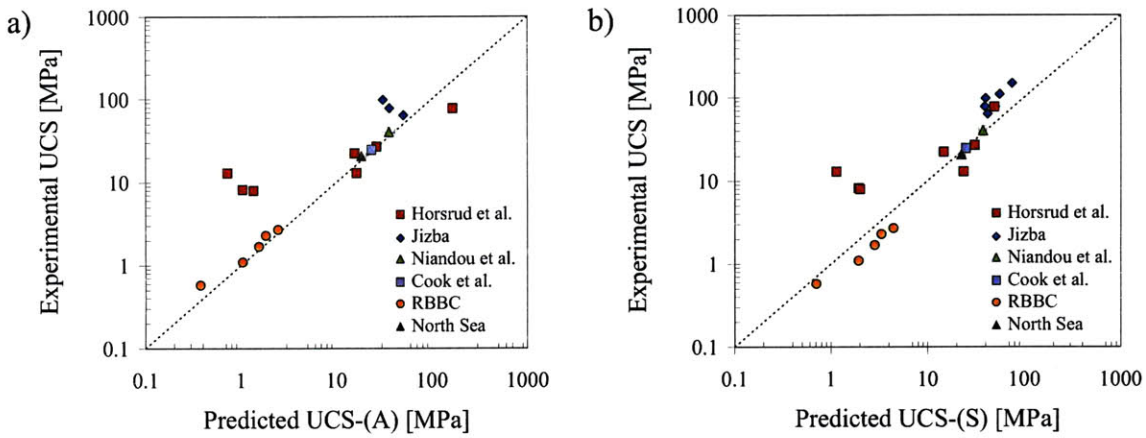

Figure 9-11: Comparisons of unconfined compressive strength (UCS) between experimentally measured values and model predictions. The modeling results correspond to macroscopic (level II) predictions for two types of interface conditions: a) perfectly adherent interfaces, and b) slip-type interfaces. The results in this figure differ from those in Figure 9-10 due to the use of adjusted properties for the solid contact hardness $\widehat{h^s}$ as given in (9.19a).

of the strength model to capture the macroscopic behavior of shale materials deserves further scrutiny. The focus of the analysis presented in this section is to determine the relevance of the cohesion-friction-packing density scaling relations to the multi-scale strength modeling of shale.

Recall from the microporoelasticity investigation that the development of the engineering predictive model was based on the successful specification of an elementary building block of solid clay with material invariant properties. For strength modeling, the equivalent approach relies on the characterization of the cohesive-frictional character of the load-bearing clay phase from nanoindentation data and scaling analysis. Section 9.3.1 explored the order-of-magnitude of the solid clay cohesion c^s as modulated by the solid hardness h^s. The remaining key aspect of the cohesive-frictional properties at level 0 of shale is their marked dependency on the clay packing density, as established in expressions (9.15) and (9.16). It will be instructive to probe these functional relationships using the strength upscaling model and the macroscopic strength data provided by the VDS-S data set as an alternative means for validating their relevance to the description of the multi-scale strength behavior of shale.

The proposed alternative analysis of the cohesive-frictional properties of the elementary

building block is accomplished using a similar approach to that presented in Section 9.3.1. In a forward application of the model, the material properties at level 0 are calibrated in order for the model to deliver optimal macroscopic predictions when compared to the experimental data gathered in the VDS-S data set. The cohesion of the solid clay c^s is derived from the indentation hardness relation for a Drucker-Prager material (see (3.30)), which was obtained from yield design and non-linear homogenization theory. The cohesion behavior remains equivalent with the form used thus far for model development (see (9.16)), and which is dependent on the solid hardness and the friction coefficient. Based on the analysis of the nanoscale solid hardness, the adjusted value $\widehat{h_S^s} = 0.12$ GPa is used in the expression of the cohesion (9.16) to avoid the overprediction of UCS properties as analyzed in Section 9.2 [3]. The degree-of-freedom to be monitored in this alternative approach to the properties of clay building block is the Drucker-Prager friction coefficient α, whose calibration is accomplished by minimizing the relative error between experimental and predicted UCS strengths for each shale sample in the VDS-S generated for a given $\widehat{\alpha}$ value:

$$\min_{\widehat{\alpha}} \left(\frac{\Sigma^{UCS}_{predicted} - \Sigma^{UCS}_{measured}}{\Sigma^{UCS}_{measured}} \right) \tag{9.20}$$

The estimation of $\widehat{\alpha}$ values is accomplished using the strength upscaling model assuming slip interfaces when modeling the interaction between silt inclusions and the porous clay composite. This type of interface condition appeared to yield slightly improved predictions compared to those associated with perfectly bonded interfaces. The objective of the calibration of the friction coefficient behavior is to verify its dependency on the clay packing density corresponding to each particular shale sample.

Figure 9-12 displays the friction coefficient behavior as a function of the clay packing density determined from nanoindentation scaling analysis for G2IC shales, Woodford shales, and RBBC samples, as well as the relationship derived from fractal packing analysis (9.15). Figure 9-12 also displays the results of the back-analysis of friction coefficients $\widehat{\alpha}$ from macroscopic data for shale samples in the VDS-S, except for six samples: B, D, E [130] and 9898, 7053, 6853 [142].

[3] The value for the solid hardness $\widehat{h_S^s} = 0.12$ GPa was allowed to vary within a range of $\pm 10\%$ for the numerical implementation of the back-analysis algorithm.

The first three samples correspond to specimens with low UCS strengths that the strength model cannot capture (see e.g. Figure 9-11). The latter three samples exhibit the largest inclusion volume fractions in the VDS-S. A potentially excessive reinforcement effect due to large amounts of rigid inclusions might obliterate the modeled contribution of the clay phase to the composite strength behavior, hence not allowing any sensible results from the back-analysis of clay friction properties. The trend of decreasing friction coefficient with increasing packing density is retrieved for the back-calculated values from macroscopic measurements associated with the remaining shale samples in the VDS-S. This finding may confirm the nanogranular behavior assessed through nanoindentation, micromechanics, and fractal packing considerations, and could establish the friction behavior of the elementary building block of solid clay of the form (9.15) as a scale-independent property for shale rocks. In addition to the clay packing density and inclusion volume fraction, which weigh the contributions of the porous clay and (rigid) inclusions to the macroscopic strength, the cohesion-friction-packing density relations for level 0 may represent important factors for capturing the multi-scale strength behavior of shale using the micromechanics framework herein proposed. However, the order-of-magnitude of the cohesion, scaled by the solid hardness, becomes a material property which cannot be implemented directly for strength upscaling.

9.3.3 Scale Effects for Hardness and Cohesion of the Elementary Building Block

The micromechanics modeling investigation of the multi-scale strength properties of shale suggests that the particular descriptions of the cohesion-friction-packing density relationships for the elementary unit of solid clay obtained from nanoindentation analysis could be instrumental for the prediction of macroscopic strength of shale. However, the successful implementation of the model depends on the appropriate estimation of the order-of-magnitude of the cohesive behavior ascribed to the clay phase. At the core of such determination is the value of the solid hardness h^s described by the functional relation (9.16), which for a first application of the model corresponded to the experimental evidence gathered from nanohardness experiments (refer to Section 9.2). The use of $h^s = 0.69$ GPa, determined from nanoindentation, in the upscaling model led to an overprediction of the unconfined compressive strengths of shale samples. A sub-

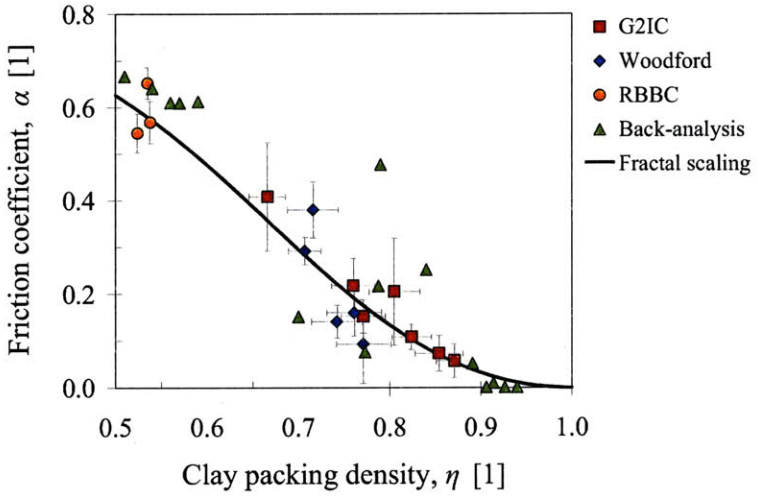

Figure 9-12: Scaling between the Drucker-Prager friction coefficient α and clay packing density η. The experimental data for G2IC shales, Woodford shales, and resedimented Boston Blue Clay samples was derived from nanoindentation scaling analysis. The fractal scaling relations correspond to the results of a fractal packing model by expression (9.15) [31]. The results of the back-analysis of friction properties for the elementary unit of solid clay from macroscopic data are also presented in the figure. These results follow the friction-packing density trends observed for experimental data and fractal scaling.

sequent implementation of the model using adjusted values of the solid hardness (and hence the solid cohesion) e.g. $\widehat{h_S^s} = 0.12$ GPa for slip interface conditions, yielded adequate comparisons with experimental data. The difference between the experimental and adjusted solid hardness values hints towards a potential size or scale effect. The existence of a scale effect affecting the hardness behavior of shale may explain the deviation of its macroscopic strength behavior from the one predicted by the strength upscaling model based on yield design and non-linear homogenization theory.

Size effects in indentation testing have been extensively documented for many materials including metals, ceramics, and polymers (see review in [59]). In metals, the size dependence is attributed to large numbers of dislocations governing the plastic deformation at micrometer length scales. These dislocations result in strain gradients modifying strongly the stress response of the material system [134]. The measured hardness values generally tend to decrease with increasing indentation load or depth [59]. Phenomenological models have been developed to characterize the indentation size effect. The depth dependency of hardness for crystalline materials, for instance, follows the form [196]:

$$\frac{H}{H_0} = \sqrt{1 + \frac{h^*}{h}} \tag{9.21}$$

where H is the hardness for a given indentation depth h, H_0 the limit constant hardness, and h^* a characteristic length scale related to the depth dependence of hardness. Figure 9-13 shows an application of the model (9.21) for the depth dependence of hardness in copper. Characterizations of the indentation scale effect have been implemented in strain gradient plasticity models, which attribute the strengthening effects to large strain gradients. Consequently, these effects are more significant when the material system is plastically deformed in small volumes [196]. In addition to indentation size effects related to specific materials, size effects are also attributed to measurement-related issues such as surface roughness, surface films, and indenter tip configurations [59].

In applications of instrumented indentation to cohesive-frictional materials such as cements and shale, scale effects associated with hardness have not been fully characterized. From the experimental perspective, the issues of surface roughness and intender geometries have been

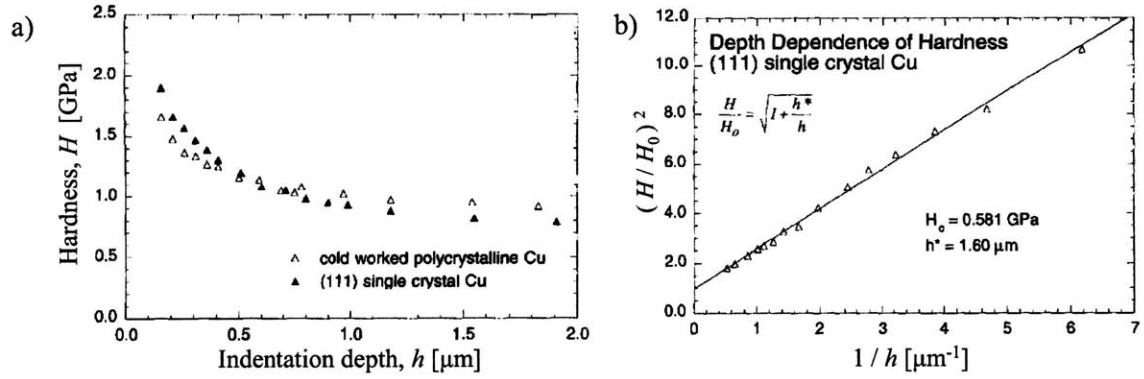

Figure 9-13: a) Dependence of indentation hardness on indentation depth for copper (from [177, 196]). b) Depth dependence for (111) single-crystal copper plotted according to equation (9.21). Adapted from [196].

carefully addressed given their effects on the quality and accuracy of indentation modulus and hardness data [64, 185]. Discarding any size effects related to surface roughness considerations in view of adequate surface preparation procedures, a first assessment of the potential influence of size effects on the indentation response of cohesive-frictional materials was presented by Vandamme [274]. The study aimed at deriving estimates of the composite response of a heterogeneous material in the form of homogenized indentation modulus and hardness values $M_{\text{hom}}, H_{\text{hom}}$ on the basis of grid indentation data M_i, H_i generated at smaller scales. The so-called self-consistent indentation technique for multi-phase materials employed linear micromechanics and yield design theories to determine the homogenized indentation properties for heterogeneous granular materials. For the indentation modulus, the modeled homogenized response of a virtual heterogeneous composite is given by [274]:

$$\sum_{i=1}^{N} \frac{1}{1+\frac{1}{2}\left(M_i/M_{\text{hom}}-1\right)} = \sum_{i=1}^{N} \frac{M_i/M_{\text{hom}}}{1+\frac{1}{2}\left(M_i/M_{\text{hom}}-1\right)} \tag{9.22}$$

The proposed estimate depends on the set of indentation moduli $\{M_i\}_{i=1,N}$ measured through a grid of indentations. Similar expressions, although mathematically more complex, were also derived for the homogenized indentation hardness estimate H_{hom}.

The application of the self-consistent indentation technique for multi-phase materials was

directed at the cement paste in concrete materials, which is composed of hydration phases, residual clinker phases, and capillary porosities. In particular, the grid nanoindentation experiments targeted the individual C-S-H (calcium silicate hydrates) phases, which represent the main products of hydration. Average indentation depths of approximately $h_{\max}^{nano} \approx 200$ nm were used in the grid nanoindentation experiments. The homogenized indentation modulus and hardness estimates $M_{\hom}, H_{\hom}$ from grid nanoindentation were compared with microindentation experiments, for which the average indentation depths were approximately $h_{\max}^{micro} \approx 20$ μm. The microindentations probed the cement paste at a scale in which its behavior tends to be homogeneous. The contrast in length scales probed by nano- and microindentations satisfy the scale separability condition necessary for the application of micromechanics methods (see Section 4.1.1).

Figure 9-14 shows a comparison between the measured microindentation modulus and hardness values for three cement pastes with different water-to-cement ratios ($w/c = 0.15, 0.30, 0.40$) and the corresponding homogenized estimates obtained from grid nanoindentation experiments and micromechanics analysis. The microindentation values correspond to the means and standard deviations for sets of 50 measurements, whereas the homogenized properties were computed for grids of hundreds of nanoindentations experiments. The average difference between measured and estimated microindentation modulus values is 6%. This adequate comparison for the indentation modulus properties (Figure 9-14a) shows the validity of the homogenization scheme proposed by Vandamme [274] for the elastic behavior. In contrast, the measured and estimated hardness properties showed large differences of approximately 50% on average. As observed in Figure 9-14b, the homogenized hardness estimates tend to significantly overpredict the composite response of the cement pastes as assessed by microindentation. The decrease in hardness properties with increasing indentation depth is a clear manifestation of size effects influencing the strength response of cement pastes at different scales. Although not directly assessed by experimental means such as microindentation, the indentation hardness response for shale appears to exhibit similar size effects. The larger value for the solid hardness h^s in shale compared to the adjusted value $\widehat{h_S^s}$ obtained from micromechanics modeling was indeed determined by grid indentations at nanometric length scales corresponding to the porous clay composite.

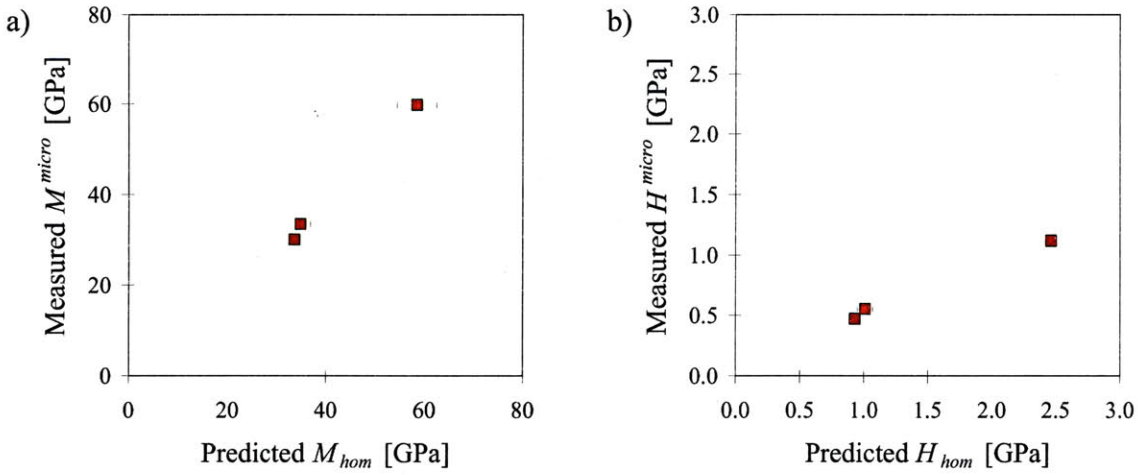

Figure 9-14: Comparisons for indentation modulus and hardness of cement pastes obtained from microindentation experiments M^{micro}, H^{micro} and estimates of homogenized properties $M_{\text{hom}}, H_{\text{hom}}$ derived from grid nanoindentation data and micromechanics analysis [274].

As noted for metallic materials, strong size effects are directly related to non-uniform plastic deformations at the micrometer and sub-micrometer length scales [134, 288]. The enhanced strengths associated with larger indentation hardness values for shale (as well as cement-based materials) at nanoscales testifies to the presence of characteristic length scales affecting the strength response in cohesive-frictional natural composites. In the proposed multi-scale structure thought-model for shale, the homogenization of elastic properties was viable between the scales of the elementary building block of solid clay, the nanoscale of the porous clay, and the macroscale of the porous clay – silt inclusion composite. For strength upscaling, a characteristic length scale at the sub-micrometer level may exist, for which the strength behavior is controlled by an alternative mechanism such as microfracturing that is not considered in the yield design approach. The appearance of size effects in shale opens a new research area, in which the understanding of the physical phenomena driving the strength properties of cohesive-frictional composites would require more exhaustive experimental testing and the extension of homogenization approaches considering scale-dependent variables such as fracture properties.

9.3.4 Model Limitations

The multi-scale prediction of strength properties for shale within the framework of yield design as proposed in this micromechanics investigation is a first attempt to address such a challenging endeavor. The modeling approach resorted to important simplifications in order to keep the strength homogenization problem for a cohesive-frictional, multi-phase composite tractable. The well-known anisotropic strength response of shale is not considered, which also becomes an imposed assumption in view of the isotropic data commonly reported in the literature of shale. The finding of size effects defines the need to identify intrinsic material scales and incorporate alternative mechanisms such as fracture and interface conditions in the strength upscaling schemes, at least when considering material behaviors at sub-micrometer length scales. The strength behavior assigned to the elementary building block of clay requires further scrutiny. While adding to the discourse about the potential origins of friction and cohesion in clay-bearing rocks from the experimental nanoindentation and micromechanics perspectives, the material model for clay used for strength upscaling must be further validated by experimental means or atomistic simulations. Finally, the experimental evidence of strength responses coming from hardness measurements at the porous clay level and from conventional compression tests at the macroscopic level should be properly categorized. The hardness measurements, obtained from nanoindentation, and unconfined compressive experiments involve different types of stress fields and plastic deformation patterns. The consideration of extensive data from indentation experiments at different scales and triaxial data will help solidify the development and improvement of strength homogenization solutions.

9.4 Chapter Summary

In this chapter, the multi-scale strength upscaling model developed in Chapter 8 was implemented for the prediction of macroscopic strength properties of shale. In addition to the clay packing density and the inclusion volume fraction derived from mineralogy and porosity information, the remaining key element to the strength upscaling problem is the cohesive-frictional behavior of the elementary building block of solid clay. These grain-scale properties, originally determined from indentation analysis and modeling of fractal packings, were confirmed to be

strongly dependent on the packing density of shale materials. A series of comparisons between macroscopic strength data for various shale samples and model predictions showed that the frictional behavior of the elementary unit of clay represents a scale-independent material property. In contrast, the cohesive response of the elementary building block is modified by scale effects. The hardness parameter associated to the clay cohesion appears to be magnified for measurements at nanometric length scales, which is consistent with observations made for other cohesive-frictional composites. While recalling the different simplifications and limitations of the proposed model, this multi-scale investigation of strength properties of a complex geomaterial such as shale represents a leap forward in the advancement of strength homogenization schemes.

Part V

Conclusions

Chapter 10

Summary of Results and Future Perspectives

The overall objective of this thesis was the development of a microporomechanics framework for translating the grain-scale mechanics sensed by nanoindentation experiments into macroscopic predictive schemes for the poroelastic and strength properties of shale. This chapter presents a summary of the knowledge generated through the development and validation of the micromechanics models. Based on the findings and contributions, some limitations and future research directions are proposed.

10.1 Summary of Main Findings

This study revealed the following scientific findings about the links between microstructure, material composition, and mechanical performance of shale:

- Based on a closed loop approach of calibration and validation of elastic and strength properties at multiple scales, it was possible to deconstruct shale to a scale of elementary material units with mechanical behaviors governed by invariant properties, and to upscale these behaviors from the nanoscale to the macroscale of engineering applications. The identified building block of shale represents the effective mechanical response of clay conglomerates encompassing clay platelets, interlayer galleries, and interparticle contacts. The stiffness of the elementary building block is invariant with respect to clay mineralogy.

- The nanogranular behavior of the porous clay fabric in shale as sensed by nanoindentation is confirmed by means of microporomechanics modeling and the inversion of poroelastic properties from comprehensive macroscopic data. This signature behavior of shale at nanoscales, characterized by a percolation threshold in the poroelastic and strength responses at packing densities close to $\eta = 0.5$, is mechanically representative of a highly aligned, granular ensemble of particles.

- The intrinsic anisotropy of the porous clay fabric is the dominant factor driving the multi-scale anisotropic elasticity of unfractured shale compared to the contributions of geometrical sources related to shapes and orientations of clay particles. This intrinsic anisotropy is intimately related to the local alignment of clay conglomerates resulting from depositional processes and to the anisotropic nature of individual clay minerals.

- Having established the material invariant properties of the elementary building block and the adequate micromechanics modeling of the microstructure of shale, it is demonstrated that its poroelastic diversity predominantly depends on two shale-specific properties: the clay packing density and the silt inclusion volume fraction. These volumetric parameters neatly synthesize the mineralogy and porosity information of individual shale samples.

- The nanogranular and anisotropic behaviors of shale translate into a unique poroelastic signature. Due to the intrinsic anisotropy of the solid clay and to the scaling of the porous clay elasticity with the packing density, the Biot pore pressure coefficients are almost isotropic. By contrast, the Skempton coefficients, which quantify the pore pressure build-up under undrained conditions in consequence of a macroscopic stress application, are highly anisotropic, with an anisotropy that scales with the packing density.

- The frictional behavior of the solid clay phase is found to be an invariant, scale-independent material property defining the multi-scale strength properties of shale. In contrast, scale effects modify the cohesive properties of the elementary building block determined from nanoindentation hardness measurements. The scale effect associated with nanohardness measurements for shale materials is consistent with similar phenomena observed for metals and cement-based composites.

10.2 Research Contributions

Progress in micromechanics modeling for the predictions of poroelasticity and strength properties of shale materials required the following developments:

- A suit of microporomechanics analytical and modeling tools was generated to properly characterize the multi-scale mechanics of shale. Novel developments in poroelasticity were related to the modeling of anisotropy based on geometric descriptions of the underlying microstructure of shale (particle shapes and orientation distributions of particles) and intrinsic elastic properties of material constituents.

- The yield design approach for the homogenization of strength properties based on the LCC theory is fully developed in this work. This homogenization method offers an improved framework for the modeling of strength properties for cohesive-frictional materials compared to existing formulations. The predictive capabilities of the model in terms of supported strength regimes and the effects of inclusion reinforcement and material interface conditions are systematically characterized. The extensive analysis of the LCC-based strength homogenization model ensures a well-defined domain for its application.

- The multi-scale microporomechanics approach developed in this thesis represents a comprehensive modeling framework that could be extended to other geomaterials such as sedimentary rocks, soils, and cement-based composites. In particular, the implementation of microporomechanics theory for the characterization of nanoscale mechanical behaviors advances the true objective of multi-scale modeling of linking grain-scale and engineering properties.

10.3 Industrial Benefits

The micromechanics approach for the prediction of poroelasticity and strength becomes a novel, physics-based alternative for industrial applications. Departing from purely empirical methods, the modeling framework pursued in this thesis demonstrates the significance of incorporating grain-scale behaviors probed by nanotechnologies into engineering predictive models. The micromechanics analysis of the poroelastic response of the clay fabric measured by nanoindentation

experiments enabled the appropriate modeling of the otherwise visually complex microstructure of shale. By resolving the contributions of microstructural features, a link is established between compositional information, readily available from advanced logging tools in petroleum and reservoir applications, and material performance. The resulting microporoelastic model for shale represents a baseline model for the prediction of anisotropic properties of unfractured samples. In addition, the model offers a suitable theoretical framework for incorporating other relevant aspect affecting mechanical behavior such as multi-scale porosities, morphological descriptions of microstructure, and fracture mechanisms.

10.4 Current Limitations and Future Perspectives

The developments of the microporomechanical models for shale poroelasticity and strength recognize some limitations. From these limitations and other considerations, potential directions for future research are identified.

At the center of the modeling efforts presented in this thesis, the successful definition of an elementary unit of solid clay common to all shale materials represents the foundation for the multi-scale prediction of poroelastic and strength properties. Although the continuum mechanics understanding of this fundamental scale of clay agglomerates has been validated in this work, the precise natures of mechanisms encompassed by the effective response of this elementary unit are yet to be established, such as the roles of interlayer galleries and interparticle interfaces in the deformation and strength responses. The postulated local alignment of clay particles yielding the overall anisotropic behavior of the solid clay phase is a first-order approximation, which may not be representative for shale materials in certain depositional environments. Regarding mineralogy, the significant presence of clay minerals such as smectite can modify the elastic response of shale materials, highlighting the need for a chemomechanical approach to better delineating the properties of the elementary unit of solid clay. The extension of nanoindentation techniques for probing individual clay crystals and the use of atomistic simulations have the potential to assess fundamental mechanisms at the level of the elementary building block that are not accessible to the continuum micromechanics approach.

The complex, multi-scale mechanical behaviors of shale called for a reductionist approach

to modeling, and many mechanisms of relevance to the poroelastic behavior were not directly addressed by the proposed micromechanics model. The well-known pressure dependency of elastic properties in shale cannot be captured by the linear micromechanics approach herein developed, and will require the use of non-linear poroelasticity methods. In addition, the predictions for acoustic properties were developed for fully saturated conditions. Depending on the frequency of acoustic measurements, the effect of partial saturation may be significant and should be incorporated in predictive models to deliver accurate estimates of velocity dispersion. Finally, the baseline predictions for anisotropic elasticity are associated with unfractured shale materials. The presence of microcracks and crack-like porosity, which are often difficult to characterize or quantify, introduces structural sources of anisotropy that could significantly alter the macroscopic response of shale. While experimental techniques such as X-ray tomography are advancing the microstructural assessment of shale, future developments related to micromechanics modeling may include fracture formulations in order to fully simulate and predict the behaviors of shale rock masses at scales relevant to engineering applications.

Although the micromechanical frameworks were shown to be relevant alternatives for predictive modeling, the treatment of shale strength is limited compared to the comprehensive microporoelastic approach. The known anisotropic nature of shale was not considered in the strength investigation, since the present formulation is bounded to isotropic behaviors. The consideration of rigid inclusions with unbounded strengths for the description of silt-size particles in shale represents a first approach. Furthermore, the strength homogenization approach based on yield design cannot capture size effects potentially associated to the strength response of the clay fabric at sub-micrometer length scales. The field of strength homogenization is still emerging, and this particular application to shale represents a first step towards developing micromechanics-based predictive models. Improvements for the strength modeling of shale will also require the generation of more comprehensive data sets, including multi-scale strength measurements and complete characterizations of mineralogy and porosity.

Bibliography

[1] Abdulhadi, N. O. (2009). "An experimental investigation into the stress-dependent mechanical behavior of cohesive soil with application to wellbore instability." PhD dissertation, Massachusetts Institute of Technology, Cambridge.

[2] Abousleiman, Y., Tran, M., Hoang, S., Bobko, C., Ortega, J. A., and Ulm, F. J. (2007). "Geomechanics field and lab characterization of Woodford shale: The next gas play." In: Society of Petroleum Engineers Annual Technical Conference and Exhibition, Anaheim, SPE 110120.

[3] Abousleiman, Y., Tran, M., Hoang, S., Ortega, J. A., and Ulm, F. J. (2009). "Geomechanics field characterization of two prolific US Mid-west gas plays with advanced wire-line logging tools." In: Society of Petroleum Engineers Annual Technical Conference and Exhibition, New Orleans, SPE 124428.

[4] Abousleiman, Y., Cheng, A. H. D., Cui, L., Detournay, E., and Roegiers, J. C. (1996). "Mandel's problem revisited." Geotechnique, 46(2), 187-195.

[5] Abousleiman, Y., and Cui, L. (1998). "Poroelastic solutions in transversely isotropic media for wellbore and cylinder." International Journal of Solids and Structures, 35(34-35), 4905-4929.

[6] Abousleiman, Y., and Ekbote, S. (2005). "Solutions for the Inclined Borehole in a Porothermoelastic Transversely Isotropic Medium." Journal of Applied Mechanics, 72(1), 102-114.

[7] Aleksandrov, K. S., and Ryzhova, T. V. (1961). "Elastic properties of rock-forming minerals. II. Layered silicates." Bull. USSR Acad. Sci., Geophys. Ser., 9, 1165–1168.

[8] Al-Tahini, A., Abousleiman, Y., and J., B. (2005). "Acoustic and quasistatic laboratory measurement and calibration of the pore pressure prediction coefficient in the poroelastic theory." In: Society of Petroleum Engineers Annual Technical Conference and Exhibition, Dallas, SPE 95825.

[9] American Society of Civil Engineers (1996). Rock Foundations, ASCE Press, New York.

[10] Antonangeli, D., Krisch, M., Fiquet, G., Badro, J., Farber, D. L., Bossak, A., and Merkel, S. (2005). "Aggregate and single-crystalline elasticity of hcp cobalt at high pressure." Physical Review B, 72(13), 134303.

[11] Auld, B. A. (1990). Acoustic fields and waves in solids, Robert E. Krieger Publishing Company, Malabar.

[12] Aylmore, L. A., and Quirk, J. P. (1960). "Domain or turbostratic structures of clay." Nature, 187, 1046-1048.

[13] Barenblatt, G. I. (1996). Scaling, self-similarity, and intermediate asymptotics, Cambridge University Press, Cambridge.

[14] Barthélémy, J.-F. (2005). "Approche micromécanique de la rupture et de la fissuration dans les géomatériaux," Thèse de l'Ecole Nationale des Ponts et Chaussés.

[15] Barthélémy, J.-F., and Dormieux, L. (2003). "Determination of the macroscopic strength criterion of a porous medium by nonlinear homogenization." Comptes Rendus Mécanique, 331(4), 271-276.

[16] Barthélémy, J.-F., and Dormieux, L. (2004). "A micromechanical approach to the strength criterion of Drucker-Prager materials reinforced by rigid inclusions." International Journal for Numerical and Analytical Methods in Geomechanics, 28(7-8), 565-582.

[17] Bellissent-Funel, M. C., Chen, S. H., and Zanotti, J. M. (1995). "Single-particle dynamics of water molecules in confined space." Physical Review E, 51(5), 4558-4569.

[18] Bennett, R. H., O'Brien, N. R., and Hulbert, M. H. (1991). "Determinants of clay and shale microfabric signatures: processes and mechanisms." In: Microstructure of fine grained sediments: from mud to shale, R. H. Bennet, N. R. O'Brien, and M. H. Hulbert, eds., Springer, New York, 5-32.

[19] Benveniste, Y. (1987). "A new approach to the application of Mori-Tanaka's theory in composite materials." Mechanics of Materials, 6(2), 147-157.

[20] Berge, P. A., and Berryman, J. G. (1995). "Realizability of negative pore compressibility in poroelastic composites." Journal of Applied Mechanics, 62, 1053-1062.

[21] Bernard, O., Ulm, F.-J., and Lemarchand, E. (2003). "A multiscale micromechanics-hydration model for the early-age elastic properties of cement-based materials." Cement and Concrete Research, 33(9), 1293-1309.

[22] Berryman, J. G. (2002). "Extension of poroelastic analysis to double-porosity materials: new technique in microgeomechanics." Journal of Engineering Mechanics, 128(8), 840-847.

[23] Berryman, J. G. (2005). "Up-scaling analysis with rigorous error estimates for poromechanics in random polycrystals of porous laminates." In: Poromechanics III - Biot Centennial (1905-2005), Y. Abousleiman, A. H.-D. Cheng, and U. Franz-Josef, eds., A.A.Balkema, Norman, 79-84.

[24] Berryman, J. G., and Milton, G. W. (1991). "Exact results for generalized Gassmann's equations in composite porous media with two constituents." Geophysics, 56(12), 1950-1960.

[25] Berryman, J. G., and Wang, H. F. (1995). "The elastic coefficients of double-porosity models for fluid transport in jointed rock." Journal of Geophysical Research, 100(B12), 24611-24627.

[26] Biot, M. A. (1956). "Theory of propagation of elastic waves in a fluid saturated porous solid: I. Low frequency range and II. higher frequency range." Journal of the Acoustical Society of America, 28, 168-191.

[27] Birch, F. (1960). "The velocity of compressional waves in rocks to 10 kilobars, Part 1." Journal of Geophysical Research, 65(4), 1083-1102.

[28] Blangy, J. D. (1992). "Integrated seismic lithologic interpretations: the petrophysical basis." PhD dissertation, Stanford University, Palo Alto.

[29] Boggs Jr., S. (2003). Petrology of sedimentary rocks, The Blackburn Press, Caldwell.

[30] Bobko, C. (2005). "Material invariant properties and reconstruction of microstructure of sandstones by nanoindentation and microporoelastic analysis," S.M. thesis, Massachusetts Institute of Technology, Cambridge.

[31] Bobko, C. (2008). "Assessing the mechanical microstructure of shale by nanoindentation: the link between mineral composition and mechanical properties." PhD dissertation, Massachusetts Institute of Technology, Cambridge.

[32] Bobko, C., and Ulm, F.-J. (2008). "The nano-mechanical morphology of shale." Mechanics of Materials, 40(4-5), 318-337.

[33] Bobko, C., and Ulm, F. J. (2008). "Assessing the mechanical microstructure of shale by nanoindentation: the link between mineral composition and mechanical properties." CEE Research Report R08-03, Massachusetts Institute of Technology, Cambridge.

[34] Bobko, C., Ortega, J. A., and Ulm, F. J. (2009). "Comment on 'Elastic modulus and hardness of muscovite and rectorite determined by nanoindentation'." Applied Clay Science, in print.

[35] Bolshakov, A., and Pharr, G. M. (1998). "Influences of pile-up on the measurement of mechanical properties by load and depth sensing indentation techniques." Journal of Materials Research, 13(4), 1049-1058.

[36] Borkovec, M., De Paris, W., and Peikert, R. (1994). "The fractal dimension of the Apollonian sphere packing." Fractals, 2(4), 521-526.

[37] Borodich, F. M. (1989). "Hertz contact problems for an anisotropic physically nonlinear elastic medium." Strength of Materials, 21(12), 1668-1676.

[38] Borodich, F. M. (1998). "Similarity methods in Hertz contact problems and their relations with the Meyer hardness test." Technical Report TR/MAT/FMB/98-98, Glasgow Caledonian University, Glasgow, 1-45.

[39] Borodich, F. M., and Galanov, B. A. (2002). "Self-similar problems of elastic contact for non-convex punches." Journal of the Mechanics and Physics of Solids, 50(11), 2441-2461.

[40] Borodich, F. M., Keer, L. M., and Korach, C. S. (2003). "Analytical study of fundamental nanoindentation test relations for indenters of non-ideal shapes." Nanotechnology, 14(7), 803-808.

[41] Brace, W. F. (1980). "Permeability of crystalline and argillaceous rocks." International Journal of Rock Mechanics and Mining Sciences & Geomechanics Abstracts, 17(5), 241-251.

[42] Brinell, J. A. (1901). "Mémoire sur les épreuves à bille en acier." In: Congres International des Methodes d'Essai des Materiaux de Construction, Paris, 83-94.

[43] Broz, M. E., Cook, R. F., and Whitney, D. L. (2006). "Microhardness, toughness, and modulus of Mohs scale minerals." American Mineralogist, 91(1), 135-142.

[44] Bryant, W. R., Bennett, R. H., Burkett, P. J., and Rack, F. R. (1991). "Microfabric and physical property characteristics of a consolidated clay section: ODP Site 697, Weddell Sea." In: Microstructure of fine-grained sediments: From mud to shale, R. H. Bennett, W. R. Bryant, and M. H. Hulbert, eds., Springer-Verlag, New York.

[45] Brown, R. J. S., and Korringa, J. (1975). "On the dependence of the elastic properties of a porous rock on the compressibility of the pore fluid." Geophysics, 40(4), 608-616.

[46] Buchalter, B. J., and Bradley, R. M. (1994). "Orientational order in amorphous packings of ellipsoids." Europhysics Letters, 26(3), 159-164.

[47] Budiansky, B. (1965). "On the elastic moduli of some heterogeneous materials." Journal of the Mechanics and Physics of Solids, 13(4), 223-227.

[48] Bulychev, S. I., Alekhin, V. P., Shorshorov, M. K., Ternovskii, A. P., and Shnyrev, G. D. (1975). "Determination of Young's modulus according to indentation diagram." Zavodskaya Laboratoria (Transl: Industrial Laboratory), 41, 1409–1412.

[49] Carcione, J. M., Gurevich, B., and Cavallini, F. (2000). "A generalized Biot-Gassmann model for the acoustic properties of shaley sandstones." Geophysical Prospecting, 48(3), 539-557.

[50] Cariou, S., Ulm, F.-J., and Dormieux, L. (2008). "Hardness-packing density scaling relations for cohesive-frictional porous materials." Journal of the Mechanics and Physics of Solids, 56(3), 924-952.

[51] Carroll, M. M. (1980). "Mechanical response of fluid-saturated porous materials." In: Proceedings of 15th International Congress of Theoretical and Applied Mechanics, F. P. J. Rimrott and B. Tabarrok, eds., Amsterdam, 251–262.

[52] Castagna, J. P., Batzle, M. L., and Eastwood, R. L. (1985). "Relationships between compressional-wave and shear-wave velocities in clastic silicate rocks." Geophysics, 50(4), 571-581.

[53] Castagna, J. P., Batzle, M. L., and Kan, T. K. (1993). "Rock physics - the link between rock properties and AVO response." Investigations in Geophysics, 8, 135-171.

[54] Chateau, X., and Dormieux, L. (2002). "Micromechanics of saturated and unsaturated porous media." International Journal for Numerical and Analytical Methods in Geomechanics, 26(8), 831-844.

[55] Chen, W.-F. (1975). Limit analysis and soil plasticity, Elsevier Scientific Pub. Co., Amsterdam.

[56] Chen, W. F., and Han, D. J. (1988). Plasticity for Structural Engineers, Springer-Verlag, New York.

[57] Chen, B., and Evans, J. R. G. (2006). "Elastic moduli of clay platelets." Scripta Materialia, 54(9), 1581-1585.

[58] Cheng, Y.-T., and Cheng, C.-M. (1998). "Scaling approach to conical indentation in elastic-plastic solids with work hardening." Journal of Applied Physics, 84(3), 1284-1291.

[59] Cheng, Y.-T., and Cheng, C.-M. (2004). "Scaling, dimensional analysis, and indentation measurements." Materials Science and Engineering: R: Reports, 44(4-5), 91-149.

[60] Cheng, C. H., and Johnston, D. H. (1981). "Dynamic and static moduli." Geophys. Res. Lett., 8(1), 39-41.

[61] Christensen, R. M., and Lo, K. H. (1979). "Solutions for effective shear properties in three phase sphere and cylinder models." Journal of the Mechanics and Physics of Solids, 27(4), 315-330.

[62] Colmenares, L. B., and Zoback, M. D. (2002). "A statistical evaluation of intact rock failure criteria constrained by polyaxial test data for five different rocks." International Journal of Rock Mechanics and Mining Sciences, 39(6), 695-729.

[63] Constantinides, G., Ulm, F.-J., and Van Vliet, K. (2003). "On the use of nanoindentation for cementitious materials." Materials and Structures, 36(257), 191-196.

[64] Constantinides, G. (2006). "Invariant mechanical properties of calcium-silicate-hydrates in cement-based materials: instrumented nanoindentation and microporomechanical modeling." PhD dissertation, Massachusetts Institute of Technology, Cambridge.

[65] Constantinides, G., Ravi Chandran, K. S., Ulm, F. J., and Van Vliet, K. J. (2006). "Grid indentation analysis of composite microstructure and mechanics: Principles and validation." Materials Science and Engineering: A, 430(1-2), 189-202.

[66] Constantinides, G., and Ulm, F.-J. (2007). "The nanogranular nature of C-S-H." Journal of the Mechanics and Physics of Solids, 55(1), 64-90.

[67] Coelho, D., Thovert, J. F., and Adler, P. M. (1997). "Geometrical and transport properties of random packings of spheres and aspherical particles." Physical Review E, 55(2), 1959-1978.

[68] Cook, J. M., Sheppard, M. C., and Houwen, O. H. (1991). "Effects of strain rate and confining pressure on the deformation and failure of shale." SPE Drilling Engineering, 6(2), 100-104.

[69] Coulomb, C. A. (1773). "Essai sur une application des règles de Maximis et Minimis à quelques problèmes de statique relatifs à l'architecture." Mémoire à l'Académie Royale des Sciences, Paris.

[70] Coussy, O. (1995). Mechanics of porous continua, Wiley, Chichester.

[71] Coussy, O. (2004). Poromechanics, Wiley, Chichester.

[72] Delafargue, A., and Ulm, F.-J. (2004). "Explicit approximations of the indentation modulus of elastically orthotropic solids for conical indenters." International Journal of Solids and Structures, 41(26), 7351-7360.

[73] Dempster, A. P., Laird, N. M., and Rubin, D. B. (1977). "Maximum lilkelihood from incomplete data via EM algorithm." J. R. Stat. Soc. Ser. B-Methodol., 39(1), 1-38.

[74] Deniau, I., Derenne, S., Beaucaire, C., Pitsch, H., and Largeau, C. (2001). "Morphological and chemical features of a kerogen from the underground Mol laboratory (Boom Clay Formation, Oligocene, Belgium): structure, source organisms and formation pathways." Organic Geochemistry, 32(11), 1343-1356.

[75] Desrues, J. (2002) "Limitations du choix de l'angle de frottement pour le critère de plasticité de Drucker-Prager." Revue Française de Génie Civil, 6, 853-862.

[76] Desrues, J., Viggiani, G., and Besuelle, P. (2006). Advances in X-ray tomography for geomaterials., Proceedings of the GeoX 2006, ISTE, Aussois, France.

[77] Dewhurst, D. N., and Siggins, A. F. (2006). "Impact of fabric, microcracks and stress field on shale anisotropy." Geophysical Journal International, 165(1), 135-148.

[78] Dewhurst, D. N., Yang, Y., and Aplin, A. C. (1999). "Permeability and fluid flow in natural mudstones." In: Muds and mudstones: physical and fluid-flow properties, A. C. Aplin, A. J. Fleet, and J. H. S. Macquaker, eds., Geological Society Special Publications, London, 23-43.

[79] Diamond, S. (2000). "Mercury porosimetry: An inappropriate method for the measurement of pore size distributions in cement-based materials." Cement and Concrete Research, 30(10), 1517-1525.

[80] Donev, A., Cisse, I., Sachs, D., Variano, E. A., Stillinger, F. H., Connelly, R., Torquato, S., and Chaikin, P. M. (2004). "Improving the density of jammed disordered packings using ellipsoids." Science, 303(5660), 990-993.

[81] Domnesteanu, P., McCann, C., and Sothcott, J. (2002). "Velocity anisotropy and attenuation of shale in under- and overpressured conditions." Geophysical Prospecting, 50(5), 487-503.

[82] Dormieux, L., Molinari, A., and Kondo, D. (2002). "Micromechanical approach to the behavior of poroelastic materials." Journal of the Mechanics and Physics of Solids, 50(10), 2203-2231.

[83] Dormieux, L., Kondo, D., and Ulm, F.-J. (2006). Microporomechanics, Wiley, Chichester.

[84] Dormieux, L., Lemarchand, E., and Sanahuja, J. (2006). "Macroscopic behavior of porous materials with lamellar microstructure." Comptes Rendus Mécanique, 334(5), 304-310.

[85] Draege, A., Jakobsen, M., and Johansen, T. A. (2006). "Rock physics modelling of shale diagenesis." Petroleum Geoscience, 12(1), 49-57.

[86] Drucker, D. C., and Prager, W. (1952). "Soil mechanics and plastic analysis or limit design." Quarterly of Applied Mathematics, 10, 157-165.

[87] Dvorkin, J., Mavko, G., and Nur, A. (1995). "Squirt flow in fully saturated rocks." Geophysics, 60(1), 97-107.

[88] Eberhart-Phillips, D., Han, D. H., and Zoback, M. D. (1989). "Empirical relationships among seismic velocity, effective pressure, porosity, and clay content in sandstone." Geophysics, 54(1), 82-89.

[89] Ekbote, S., and Abousleiman, Y. (2006). "Porochemoelasticsolution for an inclined borehole in a transversely isotropic formation." Journal of Engineering Mechanics, 132(7), 754-763.

[90] Fjaer, E. (2009). "Static and dynamic moduli of a weak sandstone." Geophysics, 74(2), WA103-WA112.

[91] Fritsch, A., Dormieux, L., and Hellmich, C. (2006). "Porous polycrystals built up by uniformly and axisymmetrically oriented needles: homogenization of elastic properties." Comptes Rendus Mécanique, 334(3), 151-157.

[92] Fritsch, A., Dormieux, L., Hellmich, C., and Sanahuja, J. (2007). "Micromechanics of crystal interfaces in polycrystalline solid phases of porous media: fundamentals and application to strength of hydroxyapatite biomaterials." J. Mater. Sci., 42(21), 8824-8837.

[93] Fritsch, A., and Hellmich, C. (2007). "Universal microstructural patterns in cortical and trabecular, extracellular and extravascular bone materials: Micromechanics-based prediction of anisotropic elasticity." Journal of Theoretical Biology, 244(4), 597-620.

[94] Galin, L. A. (1953). Contact problems in the theory of elasticity, Gostekhizdat, Moscow.

[95] Ganneau, F. P., Constantinides, G., and Ulm, F. J. (2006). "Dual-indentation technique for the assessment of strength properties of cohesive-frictional materials." International Journal of Solids and Structures, 43(6), 1727-1745.

[96] Gao, J., Luedtke, W. D., Gourdon, D., Ruths, M., Israelachvili, J. N., and Landman, U. (2004). "Frictional forces and Amontons' Law: from the molecular to the macroscopic scale." Journal of Physical Chemistry B, 108(11), 3410-3425.

[97] Gassmann, F. (1951). "On the elasticity of porous media." Vierteljahrsschrift der Naturforschenden Gesellschaft in Zürich (in German), 96, 1-23.

[98] Gathier, B., and Ulm, F. J. (2008). "Multiscale strength homogenization - application to shale nanoindentation." CEE Research Report R08-01, Massachusetts Institute of Technology, Cambridge.

[99] Gaviglio, P. (1989). "Longitudinal waves propagation in a limestone: The relationship between velocity and density." Rock Mechanics and Rock Engineering, 22(4), 299-306.

[100] Gerde, E., and Marder, M. (2001). "Friction and fracture." Nature, 413(6853), 285-288.

[101] Germaine, J. T. (1982). "Development of the direction shear cell for measuring cross-anisotropic clay properties." ScD dissertation, Massachusetts Institute of Technology, Cambridge.

[102] Gillaizeau, B., Derenne, S., Largeau, C., Berkaloff, C., and Rousseau, B. (1996). "Source organisms and formation pathway of the kerogen of the Göynük Oil Shale (Oligocene, Turkey) as revealed by electron microscopy, spectroscopy and pyrolysis." Organic Geochemistry, 24(6-7), 671-679.

[103] Giraud, A., Huynh, Q. V., Hoxha, D., and Kondo, D. (2007). "Effective poroelastic properties of transversely isotropic rock-like composites with arbitrarily oriented ellipsoidal inclusions." Mechanics of Materials, 39(11), 1006-1024.

[104] Giraud, A., Hoxha, D., Huynh, Q. V., Do, D. P., and Magnenet, V. (2008). "Effective porothermoelastic properties of transversely isotropic rock-like composites." International Journal of Engineering Science, 46(6), 527-550.

[105] Gmira, A., Zabat, M., Pellenq, R., and Van Damme, H. (2004). "Microscopic physical basis of the poromechanical behavior of cement-based materials." Materials and Structures, 37(1), 3-14.

[106] Gologanu, M., Leblond, J.-B., Perrin, G., and Devaux, J. (1997). "Recent extensions of Gurson's model for porous ductile metals." In: Continuum Micromechanics, P. Suquet, ed., Springer-Verlag, Berlin, 61-130.

[107] Gubernatis, J. E., and Krumhansl, J. A. (1975). "Macroscopic engineering properties of polycrystalline materials: Elastic properties." Journal of Applied Physics, 46(5), 1875-1883.

[108] Guggenheim, S., Adams, J. M., Bain, D. C., Bergaya, F., Brigatti, M. F., Drits, V. A., Formoso, M. L. L., Galan, E., Kogure, T., and Stanjek, H. (2006). "Summary of recommendations of nomenclature committees relevant to clay mineralogy: report of the Association Internationale pour l'Etude des Argiles (AIPEA) Nomenclature Committee for 2006." Clay Minerals, 41(4), 863-877.

[109] Gurevich, B. (2003). "Elastic properties of saturated porous rocks with aligned fractures." Journal of Applied Geophysics, 54(3-4), 203-218.

[110] Gurson, A. L. (1977). "Continuum theory of ductile rupture by void nucleation and growth: part I - yield criteria and flow rules for porous ductile media." Journal of Engineering Materials and Technology, 99, 2-15.

[111] Hall, P. L., Mildner, D. F. R., and Borst, R. L. (1983). "Pore size distribution of shaley rock by small angle neutron scattering." Applied Physics Letters, 43(3), 252-254.

[112] Han, D.-H., Nur, A., and Morgan, D. (1986). "Effects of porosity and clay content on wave velocities in sandstones." Geophysics, 51(11), 2093-2107.

[113] Hashin, Z., and Shtrikman, S. (1962). "On some variational principles in anisotropic and nonhomogeneous elasticity." Journal of the Mechanics and Physics of Solids, 10(4), 335-342.

[114] Hashin, Z., and Shtrikman, S. (1963). "A variational approach to the theory of the elastic behaviour of multiphase materials." Journal of the Mechanics and Physics of Solids, 11(2), 127-140.

[115] Hearst, J. R., Nelson, P. H., and Paillet, F. L. (2000). Well logging for physical properties: a handbook for geophysicists, geologists, and engineers, Wiley, Chichester.

[116] Hellmich, C., Barthélémy, J.-F., and Dormieux, L. (2004). "Mineral-collagen interactions in elasticity of bone ultrastructure - a continuum micromechanics approach." European Journal of Mechanics - A/Solids, 23(5), 783-810.

[117] Hellmich, C., Ulm, F.-J., and Dormieux, L. (2004). "Can the diverse elastic properties of trabecular and cortical bone be attributed to only a few tissue-independent phase properties and their interactions?" Biomechanics and Modeling in Mechanobiology, 2(4), 219-238.

[118] Hellmich, C., and Ulm, F.-J. (2005). "Drained and undrained poroelastic properties of healthy and pathological bone: a poro-micromechanical investigation." Transport in Porous Media, 58(3), 243-268.

[119] Helnwein, P. (2001). "Some remarks on the compressed matrix representation of symmetric second-order and fourth-order tensors." Computer Methods in Applied Mechanics and Engineering, 190(22-23), 2753-2770.

[120] Herrmann, H. J., Mahmoodi Baram, R., and Wackenhut, M. (2003). "Searching for the perfect packing." Physica A: Statistical Mechanics and its Applications, 330(1-2), 77-82.

[121] Hershey, A. V. (1954). "The elasticity of an isotropic aggregate of anisotropic cubic crystals." Journal of Applied Mechanics, 21, 226–240.

[122] Heyliger, P., Ledbetter, H., and Kim, S. (2003). "Elastic constants of natural quartz." Journal of the Acoustical Society of America, 114(2), 644-650.

[123] Hill, R. (1952). "The Elastic Behaviour of a Crystalline Aggregate." Proceedings of the Physical Society. Section A, 65, 349-354.

[124] Hill, R. (1965). "A self-consistent mechanics of composite materials." Journal of the Mechanics and Physics of Solids, 13(4), 213-222.

[125] Hill, R. (1967). "The essential structure of constitutive laws for metal composites and polycrystals." Journal of the Mechanics and Physics of Solids, 15(2), 79-95.

[126] Hoek, E., and Brown, E. T. (1997). "Practical estimates of rock mass strength." International Journal of Rock Mechanics and Mining Sciences, 34(8), 1165-1186.

[127] Holt, R. M., Fjaer, E., Torsaeter, O., and Bakke, S. (1996). "Petrophysical laboratory measurements for basin and reservoir evaluation." Marine and Petroleum Geology, 13(4), 383-391.

[128] Hornby, B. E., Schwartz, L. M., and Hudson, J. A. (1994). "Anisotropic effective-medium modeling of the elastic properties of shales." Geophysics, 59(10), 1570-1583.

[129] Hornby, B. E. (1998). "Experimental laboratory determination of the dynamic elastic properties of wet, drained shales." Journal of Geophysical Research-Solid Earth, 103(B12), 29945-29964.

[130] Horsrud, P., Sonstebo, E. F., and Boe, R. (1998). "Mechanical and petrophysical properties of North Sea shales." International Journal of Rock Mechanics and Mining Sciences and Geomechanics Abstracts, 35(12), 1009-1020.

[131] Hudson, J. A., Liu, E., and Crampin, S. (1996). "The mechanical properties of materials with interconnected cracks and pores." Geophysical Journal International, 124(1), 105-112.

[132] Hudson, J. A., Pointer, T., and Liu, E. (2001). "Effective-medium theories for fluid-saturated materials with aligned cracks." Geophysical Prospecting, 49(5), 509-522.

[133] Huntley, H. E. (1967). Dimensional Analysis, Dover, New York.

[134] Hutchinson, J. W. (2000). "Plasticity at the micron scale." International Journal of Solids and Structures, 37(1-2), 225-238.

[135] Ibanez, W. D., and Kronenberg, A. K. (1993). "Experimental deformation of shale: Mechanical properties and microstructural indicators of mechanisms." International Journal of Rock Mechanics and Mining Sciences & Geomechanics Abstracts, 30(7), 723-734.

[136] Igarashi, S., Bentur, A., and Mindess, S. (1996). "Characterization of the microstructure and strength of cement paste by microhardness testing." Advances in Cement Research, 8(30), 877-892

[137] Israelachvili, J. N. (1991). Intermolecular and surface forces, Academic Press, London.

[138] Jakobsen, M., and Johansen, T. A. (2000). "Anisotropic approximations for mudrocks: A seismic laboratory study." Geophysics, 65(6), 1711-1725.

[139] Jakobsen, M., Hudson, J. A., Minshull, T. A., and Singh, S. C. (2000). "Elastic properties of hydrate-bearing sediments using effective medium theory." Journal of Geophysical Research, 105(B1), 561-577.

[140] Jakobsen, M., Hudson, J. A., and Johansen, T. A. (2003). "T-matrix approach to shale acoustics." Geophysical Journal International, 154(2), 533-558.

[141] Jiang, M., Jasiuk, I., and Ostoja-Starzewski, M. (2002). "Apparent elastic and elasto-plastic behavior of periodic composites." International Journal of Solids and Structures, 39(1), 199-212.

[142] Jizba, D. (1991). "Mechanical and acoustical properties of sandstones and shales." PhD dissertation, Stanford University, Palo Alto.

[143] Jizba, D., and Nur, A. (1990). "Static and dynamic moduli of tight gas sandstones and their relation to formation properties." In: 31st Annual Logging Symposium, Society of Professional Well Log Analysts, Paper BB.

[144] Johnson, K. L. (1985). Contact mechanics, Cambridge University Press, Cambridge.

[145] Johnston, J. E., and Christensen, N. I. (1995). "Seismic anisotropy of shales." Journal of Geophysical Research 100(B4), 5991-6003.

[146] Jones, L. E. A., and Wang, H. F. (1981). "Ultrasonic velocities in Cretaceous shales from the Williston basin." Geophysics, 46(3), 288-297.

[147] Jorstad, A., Mukerji, T., and Mavko, G. (1999). "Model-based shear-wave velocity estimation versus empirical regressions." Geophysical Prospecting, 47(5), 785-797.

[148] Katahara, K. W. (1996). "Clay mineral elastic properties." SEG Technical Program Expanded Abstracts, 15(1), 1691-1694.

[149] Katsube, T. J., Mudford, B. S., and Best, M. E. (1991). "Petrophysical characteristics of shales from the Scotian shelf." Geophysics, 56(10), 1681-1689.

[150] Katti, D. R., Schmidt, S. R., Ghosh, P., and Katti, K. S. (2005). "Modeling the response of pyrophyllite interlayer to applied stress using steered molecular dynamics." Clays and Clay Minerals, 53(2), 171-178.

[151] Kholmyansky, M., Kogan, E., and Kovler, K. (1994). "On the hardness determination of fine grained concrete." Materials and Structures, 27(10), 584-587.

[152] King, M. S. (1966). "Wave velocities in rocks as a function of changes in overburden pressure and pore fluid saturants." Geophysics, 31(1), 50-73.

[153] Krakowiak, K., Ortega, J. A., and Ulm, F.-J. (2009). "Analysis of shale indentation data using a maximum likelihood approach to clustering". In preparation.

[154] Kröner, E. (1958). "Berechnung der elastischen Konstanten des Vielkristalls aus den Konstanten des Einkristalls." Zeitschrift für Physik A Hadrons and Nuclei, 151(4), 504-518.

[155] Kruyt, N. P. (2003). "Contact forces in anisotropic frictional granular materials." International Journal of Solids and Structures, 40, 3537-3556.

[156] Lambe, T. W., and Whitman, R. V. (1969). Soil Mechanics, John Wiley & Sons, New York.

[157] Larsson, P. L., Giannakopoulos, A. E., SÖderlund, E., Rowcliffe, D. J., and Vestergaard, R. (1996). "Analysis of Berkovich indentation." International Journal of Solids and Structures, 33(2), 221-248.

[158] Laws, N. (1973). "On the thermostatics of composite materials." Journal of the Mechanics and Physics of Solids, 21(1), 9-17.

[159] Laws, N. (1985). "A note on penny-shaped cracks in transversely isotropic materials." Mechanics of Materials, 4(2), 209-212.

[160] Leblond, J.-B. (2003). Mécanique de la rupture fragile et ductile. Etudes en mécanique des matériaux et des structures, Hermes Science, Paris.

[161] Lee, S. Y., Hyder, L. K., and Alley, P. D. (1991). "Microstructural and mineralogical characterization of selected shales in support of nuclear waste repository studies." In: Microstructure of Fine-Grained Sediments, from Mud to Shale, R. H. Bennet, W. R. Bryant, and M. H. Hulbert, eds., Springer-Verlag, New York, 545-560.

[162] Lee, B. J., and Mear, M. E. (1992). "Effective properties of power-law solids containing elliptical inhomogeneities. I. rigid inclusions, II. voids." Mechanics of Materials, 14(4), 313-335, 337-356.

[163] Lemarchand, E., Ulm, F.-J., and Dormieux, L. (2002). "Effect of inclusions on friction coefficient of highly filled composite materials." Journal of Engineering Mechanics, 128(8), 876-884.

[164] Levin, V. M. (1967). "Thermal expansion coefficients of heterogeneous materials." Mekhanika Tverdogo Tela, 2, 83-94.

[165] Liu, X. (1994). "Nonlinear elasticity, seismic anisotropy and petrophysical properties of reservoir rocks." PhD dissertation, Stanford University, Palo Alto.

[166] Lonardelli, I., Wenk, H.-R., and Ren, Y. (2007). "Preferred orientation and elastic anisotropy in shales." Geophysics, 72(2), D33-D40.

[167] Maghous, S., Dormieux, L., and Barthélémy, J. F. (2009). "Micromechanical approach to the strength properties of frictional geomaterials." European Journal of Mechanics - A/Solids, 28(1), 179-188.

[168] Mainprice, D., Popp, T., Guegen, Y., Huenges, E., Rutter, E. H., Wenk, H.-R., and Burlini, L. (2003). "Physical properties of rocks and other geomaterials, a special volume to honour Professor H. Kern." Tectonophysics, 370(1-4), 1-311.

[169] Manevitch, O. L., and Rutledge, G. C. (2003). "Elastic Properties of a Single Lamella of Montmorillonite by Molecular Dynamics Simulation." The Journal of Physical Chemistry B, 108(4), 1428-1435.

[170] Mandel, J. (1972). Plasticité classique et viscoplasticité, CISM Lecture Notes No. 97, Springer, Wein.

[171] Marion, D., Nur, A., Yin, H., and Han, D. (1992). "Compressional velocity and porosity in sand-clay mixtures." Geophysics, 57(4), 554-563.

[172] Mathews, H. L., Schein, G., and Malone, M. (2007). "Stimulation of gas shales: They're all the same - right?" In: SPE Hydraulic Fracturing Technology Conference, College Station, 106070-MS.

[173] Mavko, G., and Jizba, D. (1991). "Estimating grain-scale fluid effects on velocity dispersion in rocks." Geophysics, 56(12), 1940-1949.

[174] Mavko, G. M., and Nur, A. (1979). "Wave attenuation in partially saturated rocks." Geophysics, 44(2), 161-178.

[175] Mavko, G., Mukerji, T., and Dvorkin, J. (1998). The Rock Physics Handbook, Cambridge University Press, Cambridge.

[176] McCann, C., and Sothcott, J. (1992). "Laboratory measurements of the seismic properties of sedimentary rocks." Geological Society, London, Special Publications, 65(1), 285-297.

[177] McElhaney, K. W., Vlassak, J. J., and Nix, W. D. (1998). "Determination of indenter tip geometry and indentation contact area for depth-sensing indentation experiments." Journal of Materials Research, 13(5), 1300-1306.

[178] McLachlan, G. J., and Basford, K. E. (1988). Mixture models: Inference and Applications to Clustering, Marcel Dekker, New York.

[179] McLachlan, G. J., and Krishnan, T. (2008). The EM algorithm and extensions, 2nd Ed., Wiley, Hoboken.

[180] McLachlan, G. J., and Peel, D. (2001). Finite mixture models, Wiley, New York.

[181] McLachlan, G. J., Peel, D., Basford, K. E., and Adams, P. (1999). "Fitting of mixtures of normal and t-components." Journal of Statistical Software, 4(2).

[182] McLamore, R., and Gray, K. E. (1967). "The mechanical behaviour of anisotropic sedimentary rocks." ASME Journal of Engineering and Industry, 89, 62-76.

[183] McNeil, L. E., and Grimsditch, M. (1993). "Elastic moduli of muscovite mica." Journal of Physics: Condensed Matter, 5(11), 1681-1690.

[184] Middleton, G. V. (2003). "Encyclopedia of sediments & sedimentary rocks." In: Encyclopedia of sediments & sedimentary rocks, G. V. Middleton, ed., Kluwer Academic Publishers, Dordrecht.

[185] Miller, M., Bobko, C., Vandamme, M., and Ulm, F.-J. (2008). "Surface roughness criteria for cement paste nanoindentation." Cement and Concrete Research, 38(4), 467-476.

[186] Milton, G. W. (2002). The theory of composites, Cambridge University Press, Cambridge.

[187] Mitchell, J. K., and Soga, K. (2005). Fundamentals of soil behavior, John Wiley & Sons, Hoboken, N.J.

[188] Mori, T., and Tanaka, K. (1973). "Average stress in matrix and average elastic energy of materials with misfitting inclusions." Acta Metallurgica, 21(5), 571-574.

[189] Moon, C. F., and Hurst, C. W. (1984). "Fabric of muds and shales: an overview." Geological Society, London, Special Publications, 15(1), 579-593.

[190] Mura, T. (1987). Micromechanics of defects in solids, 2nd Ed., Martinus Nijhoff Publishers, Dordrecht.

[191] Murphy, W. F., III. (1984). "Acoustic measures of partial gas saturation in tight sandstones." Journal of Geophysical Research, 89(B13), 11549-11559.

[192] Müser, M. H., Wenning, L., and Robbins, M. O. (2001). "Simple Microscopic Theory of Amontons's Laws for Static Friction." Physical Review Letters, 86(7), 1295.

[193] Nemat-Nasser, S., and Hori., M. (1993). Micromechanics: overall properties of heterogeneous materials, North-Holland, Amsterdam.

[194] Newman, A. C. D. (1987). Chemistry of clays and clay minerals, Longman Scientific & Technical, Harlow.

[195] Niandou, H., Shao, J. F., Henry, J. P., and Fourmaintraux, D. (1997). "Laboratory investigation of the mechanical behaviour of Tournemire shale." International Journal of Rock Mechanics and Mining Sciences, 34(1), 3-16.

[196] Nix, W. D., and Gao, H. (1998). "Indentation size effects in crystalline materials: A law for strain gradient plasticity." Journal of the Mechanics and Physics of Solids, 46(3), 411-425.

[197] O'Connell, R. J., and Budiansky, B. (1977). "Viscoelastic properties of fluid-saturated cracked solids." Journal of Geophysical Research, 82, 5719-5736.

[198] Oda, M. (1977). "Co-ordination number and its relation to the shear strength of granular material." Soils and Foundations, 17(2), 29-42.

[199] Oliver, W. C., and Pharr, G. M. (1992). "An improved technique for determining hardness and elastic modulus using load and displacement sensing indentation experiments." Journal of Materials Research, 7(6), 1564-1583

[200] Oliver, W. C., and Pharr, G. M. (2004). "Measurement of hardness and elastic modulus by instrumented indentation: Advances in understanding and refinements to methodology." Journal of Materials Research, 19(1), 3-20.

[201] Onoda, G. Y., and Liniger, E. G. (1990). "Random loose packings of uniform spheres and the dilatancy onset." Physical Review Letters, 64(22), 2727-2730.

[202] Ortega, J. A., Ulm, F.-J., and Abousleiman, Y. (2007). "The effect of the nanogranular nature of shale on their poroelastic behavior." Acta Geotechnica, 2(3), 155-182.

[203] Ortega, J. A., Ulm, F.-J., and Abousleiman, Y. (2009). "The nanogranular acoustic signature of shale." Geophysics, 74(3), D65-D84.

[204] Ortega, J. A., Ulm, F. J., and Abousleiman, Y. (2009). "The effect of particle shape and grain-scale properties of shale: A micromechanics approach." International Journal for Numerical and Analytical Methods in Geomechanics, Online, DOI: 10.1002/nag.850.

[205] Pan, Y. C., and Chou, T. W. (1976). "Point force solution for an infinite transversely isotropic solid." Journal of Applied Mechanics-Transactions of the Asme, 43(4), 608-612.

[206] Parry, R. H. G. (2004). Mohr Circles, Stress Paths, and Geotechnics, Spon Press, London.

[207] Pearson, F. J. (1999). "What is the porosity of mudrock?" In: Muds and mudstones: physical and fluid-flow properties, A. C. Aplin, A. J. Fleet, and J. H. S. Macquaker, eds., Geological Society Special Publications, London, 9-21.

[208] Pemper, R., Sommer, A., Guo, P., Jacobi, D., Longo, J., Bliven, S., Rodriguez, E., Mendez, F., and Han, X. (2006). "A new pulsed neutron sonde for derivation of formation lithology and mineralogy." In: SPE Annual Technical Conference and Exhibition, San Antonio, 102770-MS.

[209] Peng, S., and Zhang, J. (2007). Engineering geology for underground rocks, Springer, Berlin; New York.

[210] Perrier, E., Bird, N., and Rieu, M. (1999). "Generalizing the fractal model of soil structure: the pore-solid fractal approach." Geoderma, 88(3-4), 137-164.

[211] Pharr, G. M., and Bolshakov, A. (2002). "Understanding nanoindentation unloading curves." Journal of Materials Research, 17(10), 2660-2671

[212] Picard, M. D. (1971). "Classification of fine-grained sedimentary rocks." Journal of Sedimentary Petrology, 41(1), 179-195.

[213] Ponte Castañeda, P. (1991). "The effective mechanical properties of nonlinear isotropic composites." Journal of the Mechanics and Physics of Solids, 39(1), 45-71.

[214] Ponte Castañeda, P. (1992). "New variational principles in plasticity and their application to composite materials." Journal of the Mechanics and Physics of Solids, 40(8), 1757-1788.

[215] Ponte Castañeda, P. (1996). "Exact second-order estimates for the effective mechanical properties of nonlinear composite materials." Journal of the Mechanics and Physics of Solids, 44(6), 827-862.

[216] Ponte Castañeda, P. (2002). "Second-order homogenization estimates for nonlinear composites incorporating field fluctuations: I–theory." Journal of the Mechanics and Physics of Solids, 50(4), 737-757.

[217] Ponte Castañeda, P. (2005). "Heterogeneous materials." Lecture notes. Department of Mechanics, Ecole Polytechnique.

[218] Ponte Castañeda, P., and Willis, J. R. (1995). "The effect of spatial distribution on the effective behavior of composite materials and cracked media." Journal of the Mechanics and Physics of Solids, 43(12), 1919-1951.

[219] Potter, P. E., Maynard, J. B., and Pryor, W. A. (1980). Sedimentology of shale :study guide and reference source, Springer-Verlag, New York

[220] Prasad, M., Kopycinska, M., Rabe, U., and Arnold, W. (2002). "Measurement of Young's modulus of clay minerals using atomic force acoustic microscopy." Geophysical Research Letters, 29(8), 13-01, 13-04.

[221] Pratson, L. F., Stroujkova, A., Herrick, D., Boadu, F., and Malin, P. (2003). "Predicting seismic velocity and other rock properties from clay content only." Geophysics, 68(6), 1847-1856.

[222] Rice, J. R., and Cleary, M. P. (1976). "Some basic stress-diffusion solutions for fluid saturated elastic porous media with compressible constituents." Reviews of Geophysics and Space Physics, 14, 227–241.

[223] Roux, J.-N. (2000). "Geometric origin of mechanical properties of granular materials." Physical Review E, 61(6), 6802.

[224] Salençon, J. (1990). "An introduction to the yield design theory and its application to soil mechanics." European Journal of Mechanics - A/Solids, 9(5), 477-500.

[225] Sanahuja, J., Dormieux, L., and Chanvillard, G. (2007). "Modelling elasticity of a hydrating cement paste." Cement and Concrete Research, 37(10), 1427-1439.

[226] Sarout, J., and Guéguen, Y. (2008). "Anisotropy of elastic wave velocities in deformed shales: Part 1 - Experimental results." Geophysics, 73(5), D75-D89.

[227] Sarout, J., Molez, L., Guéguen, Y., and Hoteit, N. (2007). "Shale dynamic properties and anisotropy under triaxial loading: Experimental and theoretical investigations." Physics and Chemistry of the Earth, Parts A/B/C, 32(8-14), 896-906.

[228] Sayers, C. M. (1994). "The elastic anisotropy of shales." Journal of Geophysical Research-Solid Earth, 99(B1), 767-774.

[229] Sayers, C. M. (2004). "Seismic anisotropy of shales: what determines the sign of Thomsen's delta parameter?" SEG Technical Program Expanded Abstracts, 103-106.

[230] Sayers, C. M. (2005). "Seismic anisotropy of shales." Geophysical Prospecting, 53(5), 667-676.

[231] Savage, W. Z., and Braddock, W. A. (1991). "A model for hydrostatic consolidation of Pierre shale." International Journal of Rock Mechanics and Mining Sciences & Geomechanics Abstracts, 28(5), 345-354.

[232] Schlumberger. (2005). "Sonic Scanner." www.slb.com/oilfield.

[233] Schlumberger. (2006). "ECS Elemental Capture Spectroscopy Sonde." www.slb.com/oilfield.

[234] Schofield, A., and Wroth, P. (1968). Critical state soil mechanics, McGraw-Hill, New York.

[235] Schweiger, H. F. (1994). "On the use of Drucker-Prager failure criteria for earth pressure problems." Computers and Geotechnics, 16(3), 223-246.

[236] Scott, T. E., and Abousleiman, Y. (2005). "Acoustic measurements of the anisotropy of dynamic elastic and poromechanics moduli under three stress/strain pathways." Journal of Engineering Mechanics, 131(9), 937-946.

[237] Seo, Y.-S., Ichikawa, Y., and Kawamura, K. (1999). "Stress-strain response of rock-forming minerals by molecular dynamics simulation." Materials Science Research International, 5(1), 13-20.

[238] Sevostianov, I., Yilmaz, N., Kushch, V., and Levin, V. (2005). "Effective elastic properties of matrix composites with transversely-isotropic phases." International Journal of Solids and Structures, 42(2), 455-476.

[239] Sheng, P. (1990). "Effective-medium theory of sedimentary rocks." Physical Review B, 41(7), 4507-4512.

[240] Sherwood, J. D. (1997). "Packing of spheroids in three-dimensional space by random sequential addition." Journal of Physics A: Mathematical and General, 30(24), L839-L843.

[241] Sheriff, R. E. (2002). "Encyclopedic Dictionary of Applied Geophysics." Society of Exploration Geophysics.

[242] Simmons, G., and Brace, W. F. (1965). "Comparison of static and dynamic measurements of compressibility of rocks." Journal of Geophysical Research, 70(22), 5649-5656.

[243] Skempton, A. W. (1954). "The pore-pressure coefficients A and B." Geotechnique, 4, 143–147.

[244] Sneddon, I. N. (1977). Application of integral transforms in the theory of elasticty, Springer Verlag, Wien.

[245] Steiger, R., and Leung , P. K. (1991). "Consolidated undrained triaxial test procedure for shales." In: Rock Mechanics as a Multidisciplinary Science, J. C. Roegiers, ed., Balkema, 637-646.

[246] Stephansson, O., Hudson, J. A., and Jing, L. (2004). Coupled thermo-hydro-mechanical-chemical processes in geo-systems: fundamentals, modelling, experiments and applications, Elsevier, Amsterdam.

[247] Strang, G. (1998). Introduction to linear algebra, 3rd Ed., Wellesley-Cambridge Press, Wellesley.

[248] Suquet, P. (1997). "Effective behavior of nonlinear composites." In: Continuum Micromechanics, P. Suquet, ed., Springer-Verlag, Berlin, 197-264.

[249] Suvorov, A. P., and Dvorak, G. J. (2002). "Rate form of the Eshelby and Hill tensors." International Journal of Solids and Structures, 39(21-22), 5659-5678.

[250] Swadener, J. G., and Pharr, G. M. (2001). "Indentation of elastically anisotropic half-spaces by cones and parabolae of revolution." Philosophical Magazine A, 81(2), 447 - 466.

[251] Tabor, D. (1948). "A Simple Theory of Static and Dynamic Hardness." Proceedings of the Royal Society of London. Series A. Mathematical and Physical Sciences, 192(1029), 247-274.

[252] Talbot, D. R. S., and Willis, J. R. (1992). "Some simple explicit bounds for the overall behaviour of nonlinear composites." International Journal of Solids and Structures, 29(14-15), 1981-1987.

[253] Talbot, D. R. S., and Willis, J. R. (1997). "Bounds of third order for the overall response of nonlinear composites." Journal of the Mechanics and Physics of Solids, 45(1), 87-111.

[254] Távara, L., Ortiz, J. E., Mantic, V., and París, F. (2008). "Unique real-variable expressions of displacement and traction fundamental solutions covering all transversely isotropic elastic materials for 3D BEM." International Journal for Numerical Methods in Engineering, 74(5), 776-798.

[255] The MathWorks, Inc (2006) Optimization toolbox for MATLAB, fmincon function. Online manual, http://www.mathworks.com.

[256] Thomsen, L. (1986). "Weak elastic anisotropy." Geophysics, 51(10), 1954-1966.

[257] Thomsen, L. (1995). "Elastic anisotropy due to aligned cracks in porous rock." Geophysical Prospecting, 43(6), 805-829.

[258] Titterington, D. M., Smith, A. F. M., and Makov, U. E. (1985). Statistical analysis of finite mixture distributions, Wiley, Chichester, New York.

[259] Torquato, S. (2002). Random heterogeneous materials: microstructure and macroscopic properties, Springer, New York.

[260] Tourtelot, H. A. (1960). "Origin and use of the word shale." American Journal of Science, 258, 335-343.

[261] Tran, M. H., Abousleiman, Y. N., Hoang, S. K., Ortega, J. A., and Ulm, F.-J. (2009). "The make-up of nanoindentation in engineering applications." In: Poromechanics IV, H. I. Ling, A. Smyth, and R. Betti, eds., DEStech Publications, New York, 758-764.

[262] Trillat, M., and Pastor, J. (2005). "Limit analysis and Gurson's model." European Journal of Mechanics - A/Solids, 24(5), 800-819.

[263] Tucker, M. E. (1991). Sedimentary petrology :an introduction to the origin of sedimentary rocks, Blackwell Scientific Publications, Oxford.

[264] Ulm, F.-J. (2006). Mechanics of durability of solids. Lecture notes. Massachusetts Institute of Technology.

[265] Ulm, F.-J., and Abousleiman, Y. (2006). "The nanogranular nature of shale." Acta Geotechnica, 1(2), 77-88.

[266] Ulm, F. J., and Coussy, O. (2003). Mechanics and durability of solids - Volume 1: Solid mechanics, Prentice Hall, Upper Saddle River.

[267] Ulm, F.-J., Delafargue, A., and Constantinides, G. (2005). "Experimental microporomechanics." In: Applied Micromechanics of Porous Materials, L. Dormieux and F.-J. Ulm, eds., Springer, Wien, 207-288.

[268] Ulm, F.-J., Constantinides, G., Delafargue, A., Ewy, R., Duranti, L., and McCarty, D. K. (2005). "Material invariant poromechanics properties of shales." In: Poromechanics III. Biot Centennial (1905-2005), Y. Abousleiman, A. H.-D. Cheng, and F.-J. Ulm, eds., A. A. Balkema Publishers, Norman, OK, 627-644.

[269] Ulm, F., Constantinides, G., and Heukamp, F. (2004). "Is concrete a poromechanics materials?—A multiscale investigation of poroelastic properties." Materials and Structures, 37(1), 43-58.

[270] Ulm, F. J., Vandamme, M., Bobko, C., Ortega, J. A., Tai, K., and Ortiz, C. (2007). "Statistical indentation techniques for hydrated nanocomposites: Concrete, bone, and shale." Journal of the American Ceramic Society, 90(9), 2677-2692.

[271] Valcke, S. L. A., Casey, M., Lloyd, G. E., Kendall, J. M., and Fisher, Q. J. (2006). "Lattice preferred orientation and seismic anisotropy in sedimentary rocks." Geophysical Journal International, 166(2), 652-666.

[272] van Olphen, H. (1977). An introduction to clay colloid chemistry, John Wiley & Sons, New York.

[273] Vanorio, T., Prasad, M., and Nur, A. (2003). "Elastic properties of dry clay mineral aggregates, suspensions and sandstones." Geophysical Journal International, 155(1), 319-326.

[274] Vandamme, M. (2008). "The nanogranular origin of concrete creep: A nanoindentation investigation of microstructure and fundamental properties of calcium-silicate-hydrates." PhD dissertation, Massachusetts Institute of Technology, Cambridge.

[275] Vandamme, M., and Ulm, F.-J. (2009). "Nanogranular origin of concrete creep." Proceedings of the National Academy of Sciences, 106(26), 10552-10557.

[276] Vaughan, M. T., and Guggenheim, S. (1986). "Elasticity of muscovite and its relationship to crystal structure." J. Geophys. Res., 91(B5), 4657–4664.

[277] Vernik, L., and Liu, X. (1997). "Velocity anisotropy in shales: A petrophysical study." Geophysics, 62(2), 521-532.

[278] Vernik, L., and Nur, A. (1992). "Ultrasonic velocity and anisotropy of hydrocarbon source rocks." Geophysics, 57(5), 727-735.

[279] Vlassak, J. J., Ciavarella, M., Barber, J. R., and Wang, X. (2003). "The indentation modulus of elastically anisotropic materials for indenters of arbitrary shape." Journal of the Mechanics and Physics of Solids, 51(9), 1701-1721.

[280] Walpole, L. J. (1966). "On bounds for the overall elastic moduli of inhomogeneous systems–I." Journal of the Mechanics and Physics of Solids, 14(3), 151-162.

[281] Walsh, J. B., and Brace, W. F. (1966). "Elasticity of rock: A review of some recent theoretical studies." Rock Mechanics and Engineering Geology, 4, 283-297.

[282] Wang, Z. (2000). "The Gassmann equation revisited: comparing laboratory data with Gassmann's predictions." In: Seismic and Acoustic Velocities in Reservoir Rocks, 3: Recent Developments, Z. Wang and N. Amos, eds., Society of Exploration Geophysicists, 8-23.

[283] Wang, Z. (2001). "Fundamentals of seismic rock physics." Geophysics, 66(2), 398-412.

[284] Wang, Z. (2002). "Seismic anisotropy in sedimentary rocks, part 1: A single-plug laboratory method – part 2: Laboratory data." Geophysics, 67(5), 1415-1422 (part 1), 1423-1440 (part 2).

[285] Wang, Z., and Nur, A. (1990). "Dispersion analysis of acoustic velocities in rocks." The Journal of the Acoustical Society of America, 87(6), 2384-2395.

[286] Wang, Z., Cates, M. E., and Langan, R. T. (1998). "Seismic monitoring of a CO2 flood in a carbonate reservoir: A rock physics study." Geophysics, 63(5), 1604-1617.

[287] Wang, Z., Wang, H., and Cates, M. E. (2001). "Effective elastic properties of solid clays." Geophysics, 66(2), 428-440.

[288] Wei, Y., and Hutchinson, J. W. (2003). "Hardness trends in micron scale indentation." Journal of the Mechanics and Physics of Solids, 51(11-12), 2037-2056.

[289] Weng, G. J. (1992). "Explicit evaluation of Willis' bounds with ellipsoidal inclusions." International Journal of Engineering Science, 30(1), 83-92.

[290] Willis, J. R. (1977). "Bounds and self-consistent estimates for the overall properties of anisotropic composites." Journal of the Mechanics and Physics of Solids, 25(3), 185-202.

[291] Winkler, K. W. (1985). "Dispersion analysis of velocity and attenuation in Berea sandstone." Journal of Geophysical Research, 90(B8), 6793-6800.

[292] Winkler, K. W. (1986). "Estimates of velocity dispersion between seismic and ultrasonic frequencies." Geophysics, 51(1), 183-189.

[293] Winkler, K. W., and Murphy III, W. F. (1995). "Acoustic velocity and attenuation in porous rocks." In: Rock physics and phase relations, T. J. Ahrens, ed., AGU Reference Shelf, Washington, 20-34.

[294] Winkler, K., Nur, A., and Gladwin, M. (1979). "Friction and seismic attenuation in rocks." Nature, 277(5697), 528-531.

[295] Withers, P. J. (1989). "The determination of the elastic field of an ellipsoidal inclusion in a transversely isotropic medium, and its relevance to composite materials." Philosophical Magazine A, 59(4), 759 - 781.

[296] Winkler, K. W., and Liu, X. (1996). "Measurements of third-order elastic constants in rocks." The Journal of the Acoustical Society of America, 100(3), 1392-1398.

[297] Winkler, K. W., and McGowan, L. (2004). "Nonlinear acoustoelastic constants of dry and saturated rocks." Journal of Geophysical Research, 109, B10204.

[298] Wong, R. C. K. (2001). "Strength of two structured soils in triaxial compression." International Journal for Numerical and Analytical Methods in Geomechanics, 25(2), 131-153.

[299] Xu, S. Y., and White, R. E. (1995). "A new velocity model for clay-sand mixtures." Geophysical Prospecting, 43(1), 91-118.

[300] Yin, H. (1992). "Acoustic velocity and attenuation of rocks: isotropy, intrinsic anisotropy, and stress induced anisotropy." PhD dissertation, Stanford University, Palo Alto.

[301] Zaoui, A. (2002). "Continuum Micromechanics: Survey." Journal of Engineering Mechanics, 128(8), 808-816.

[302] Zhang, G., Wei, Z., and Ferrell, R. E. (2009). "Elastic modulus and hardness of muscovite and rectorite determined by nanoindentation." Applied Clay Science, 43(2), 271-281.

[303] Zhang, G., Wei, Z., and Ferrell, R. E. (2009). "Reply to comment by Bobko et al. on Elastic modulus and hardness of muscovite and rectorite determined by nanoindentation." Applied Clay Science, in print.

[304] Zimmerman, R. W. (2000). "Coupling in poroelasticity and thermoelasticity." International Journal of Rock Mechanics and Mining Sciences, 37(1-2), 79-87.